Implementation of the Laser-Based Femtosecond Precision Synchronization System at FLASH

Dissertation

zur Erlangung des Doktorgrades
des Fachbereichs Physik
der Universität Hamburg

vorgelegt von

Dipl.-Phys. Sebastian Schulz
aus Brühl bei Köln

Hamburg
2011

Gutachter der Dissertation	PD Dr. Bernhard Schmidt Prof. Dr. Markus Drescher
Gutachter der Disputation	PD Dr. Bernhard Schmidt Dr. Jens Osterhoff
Datum der Disputation	11. Mai 2011
Vorsitzende des Prüfungsausschusses	Prof. Dr. Caren Hagner
Vorsitzender des Promotionsausschusses	Prof. Dr. Günter Huber
Dekan der Fakultät für Mathematik, Informatik und Naturwissenschaften	Prof. Dr. Heinrich Graener

Abstract

FLASH, the high-gain free-electron laser (FEL) in Hamburg, enables the generation of light pulses with wavelengths in the soft X-ray region and durations down to a few femtoseconds. To fully exploit this capability in time-resolved pump-probe experiments, and for the projected externally seeded operation, the critical components of the accelerator and several external laser systems have to be synchronized with a temporal accuracy at least in the same order of magnitude. This can not be realized purely with established RF-based systems and therefore, an optical, laser-based synchronization system is required.
In this thesis, the optical synchronization system of FLASH has been, based on previous successful proof-of-principle experiments, massively extended. One major topic is the comprehensive characterization of the timing reference of the system and a comparison of different types of such master laser oscillators, as well as studies on their short- and long-term stability. Similar investigations have been carried out for the upgraded and newly installed length-stabilized fiber links, which connect the remote locations at the accelerator to the optical timing reference. The successful demonstration of an all-optical synchronization of a Ti:sapphire oscillator with sub-10 femtosecond timing jitter and the connection of the photo injector laser system to the synchronization system mark further important key experiments of this thesis. The robustness of the actual implementations played a key role, as the synchronization system forms the basis for the future, operator-friendly arrival time feedback.

Kurzdarstellung

FLASH, der hochverstärkende Freie-Elektronen-Laser (FEL) in Hamburg, kann Pulse weicher Röntgenstrahlung mit Dauern von wenigen Femtosekunden erzeugen. Um das volle Potenzial dieser Lichtpulse in zeitaufgelösten Anrege-Abfrage-Experimenten ausnutzen zu können, und für den zukünftigen Betriebsmodus mit einem externen Saat-Laser ist eine Synchronisation der kritischen Komponenten des Beschleunigers und der externen Lasersysteme mindestens in der gleichen zeitlichen Größenordnung erforderlich. Diese Präzision ist mit elektrischen Hochfrequenzsystemen nicht zu erreichen und erfordert ein optisches, laser-basiertes Synchronisationssystem.
Im Rahmen dieser Arbeit wurde, aufbauend auf früheren erfolgreichen Machbarkeitsstudien, das optische Synchronisationssystem bei FLASH massiv erweitert. Dabei lag ein Schwerpunkt auf der umfangreichen Charakterisierung der Zeitreferenz des Systems und dem Vergleich zweier verschiedener Typen solcher Master-Laseroszillatoren, sowie Studien zu deren Kurz- und Langzeitstabilität. Diese wurde auch an den ebenfalls erweiterten längenstabilisierten Glasfaserstrecken, die zur Ankopplung der verschiedenen Stationen am Beschleuniger an die optische Zeitreferenz dienen, studiert. Die erfolgreich demonstrierte optische Synchronisation eines Titan:Saphir-Laseroszillators mit weniger als 10 Femtosekunden Zeitjitter und die Anbindung des Photoinjektor-Lasers an das Synchronisationssystem stellen weitere Schlüsselexperimente dieser Arbeit dar. Dabei wurde besonderer Wert auf die Robustheit der eigentlichen Implementationen gelegt, da das Synchronisationssystem das Fundament der geplanten aktiven Ankunftszeitstabilisierung im Beschleuniger bildet.

“ Die ganze Welt ist voll von Sachen, und es ist wirklich nötig, dass jemand sie findet. ”

Pippi Langstrumpf

Contents

List of Figures

List of Tables

Introduction

X-ray pulses with high intensity and ultra-short durations enable experiments on the femtosecond time scale with atomic spatial resolution in many fields of science – ranging from physics, chemistry and material science to biology and medicine. Such pulses can only be generated by linear accelerator (linac)-driven high-gain free-electron lasers (FELs), like the Free-Electron Laser in Hamburg (FLASH) at Deutsches Elektronen-Synchrotron (DESY), the Linac Coherent Light Source (LCLS) at Stanford Linear Accelerator Center (SLAC) in the United Stated, FERMI@Elettra in Italy or the upcoming European XFEL with unprecedented brilliance – see figure i.1.

Most commonly, experiments are carried out in a pump-probe geometry, where specimen are excited by a pump light pulse followed by probing the development of the excitation in the system with many consecutive pulses, each with a different temporal delay. Depending on the particular experiment, the X-ray pulse is used for probing the system while an optical laser pulse excited it initially, or vice versa. In any case, it is mandatory to synchronize the two light pulses as they are generated by independent sources and fluctuations in their relative timing, the timing jitter, will degrade the temporal resolution of the experiment. Ideally, the accuracy of the synchronization is in the order of the X-ray pulse duration or better, which can be less than 10 fs [AAA+07, EAA+10].

Presently, the basis for the generation of the FEL radiation at most accelerator facilities is self-amplified spontaneous emission (SASE). In this process, spontaneous radiation of an electron bunch is amplified in an undulator. The statistical pulse energy and timing fluctuations, caused by the start from noise, can not be compensated. However, additional sources of timing jitter of the electron bunch at the entrance of the undulator, and thus the FEL pulse, include the instability of the laser system which is used to produce the electron bunch in a photoinjector and the electron gun, the instabilities of the phase and amplitude in the accelerating fields and the jitter introduced by the bunch compression process.

Another possibility to initiate the FEL process in the undulator is to imprint the required density modulation with an external laser at the desired output wavelengths [LHG+08]. This technique is called direct seeding, and a corresponding experiment is presently being installed and commissioned at the FLASH facility. The advantage of this approach is to overcome the fluctuations of the SASE process, since here the seed pulse defines the temporal and spectral properties of the generated radiation. Furthermore, a nearly perfect synchronization is given between the seed and the FEL pulse for pump-probe experiments as both are originate from the same source. The drawback is the fact that laser systems at ultraviolet wavelengths are not readily available and hence, high-harmonics of a high-power laser have to be generated, for instance in a noble gas. Furthermore, the timing jitter between the electron bunch to be seeded and the seed laser pulse remains, as the bunch still under-

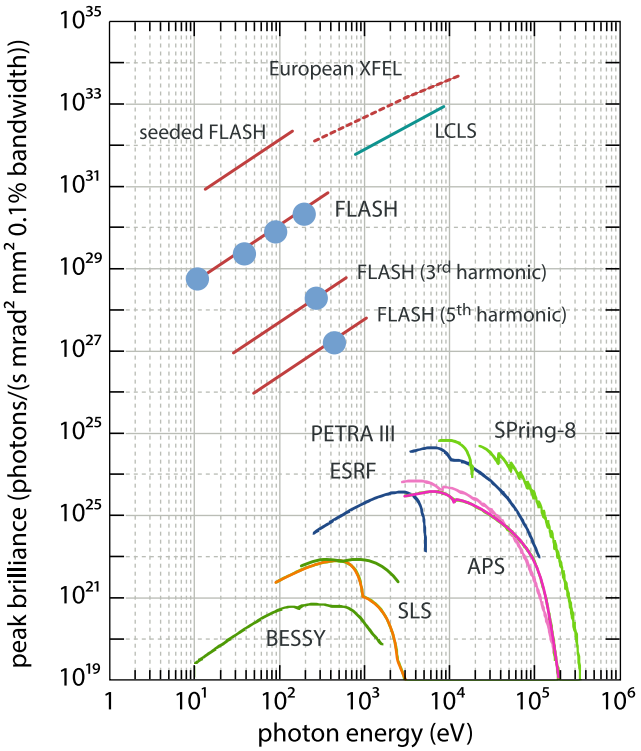

Figure i.1 | Peak brilliance of selected free-electron lasers and synchrotron radiation sources. The peak brilliance is defined as $b_{peak} = 4\,\Phi / \lambda^2 = 4\,N_{ph} / (\lambda^2\,\sigma_t\,\sigma_\omega)$ and describes the number of photons N_{ph} in a pulse with the duration σ_t at the radiation wavelength λ within the spectral width σ_ω of typically 0.1%. The advantage of the free-electron lasers FLASH, LCLS and the upcoming European XFEL compared to storage ring-based light sources like PETRA III, APS or SPring-8 is obvious (adapted from [Sch10b]).

lies the sources of jitter in the acceleration process. In order to achieve a timing jitter of the electron bunch which is comparable to its duration, or even less, the timing critical components of the accelerator, such as the acceleration modules, have to be synchronized in the same order of magnitude. This leads to demanding requirements for the acceleration radio frequency (RF), with an amplitude stability of better than 10^{-4} and a phase stability of 0.005 deg, corresponding to 10 fs at 1.3 GHz. The long-term stable transport of such signals across the accelerator facility using traditional coaxial distribution schemes is practically not possible.

Laser-Based Synchronization with Femtosecond Accuracy

Therefore, an optical, laser-based synchronization system as sketched in figure i.2 had been proposed [KIK+04, KCCK08]. The timing information is the precise repetition rate of a train of sub-picosecond pulses emitted by a passively mode-locked laser oscillator with ultra-low timing phase noise. This master laser oscillator (MLO) is synchronized to the master RF oscillator (MO) of the accelerator facility, due to the better long-term stability of RF oscillators. The timing information is then distributed to the remote locations via length- and consequently transit time-stabilized optical fiber links. All-optical measurement schemes allow for a stabilization on the sub-micrometer length- and thus femtosecond time-scale. For this, the center wavelength of the system had been chosen as the telecommunication standard of 1550 nm, since numerous different fiber-optical components are readily available at comparatively low cost. Furthermore, at this wavelength, dispersion compensating fiber is available, which is crucial for the fiber link stabilization scheme and to provide short pulse

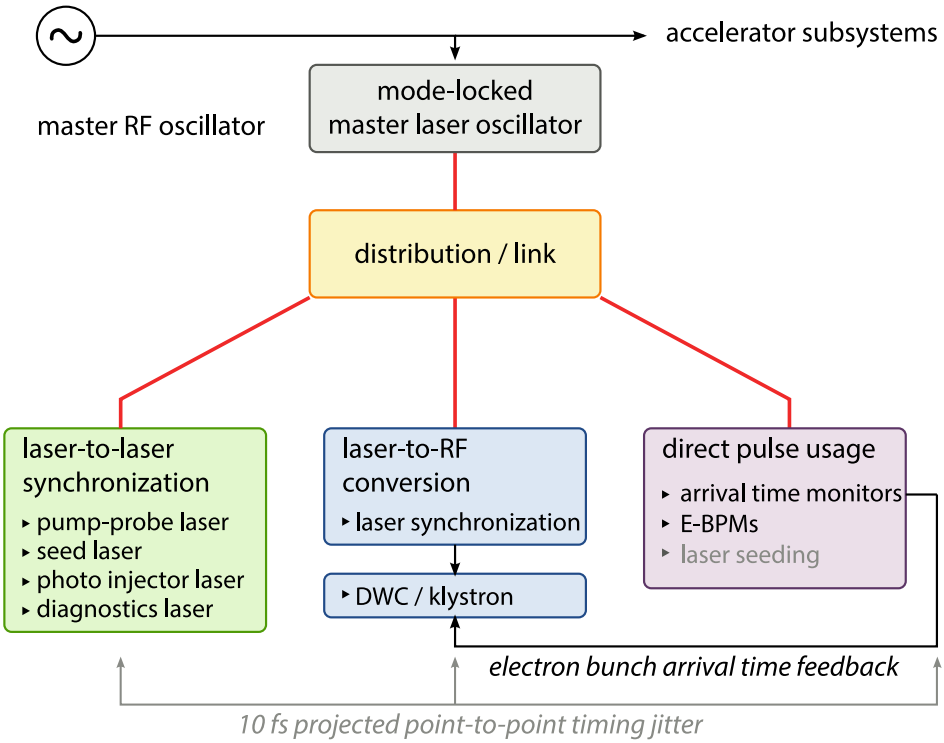

Figure i.2 | Sketch of the laser-based synchronization topology at FLASH. A femtosecond mode-locked laser provides the timing reference for the system as its repetition rate. The pulses are distributed across the facility on stabilized optical fibers. At the remote locations, they can be used to synchronize external laser systems based on all-optical timing detection, or radio-frequency (RF) signals can be extracted. Additionally, they can be utilized directly for precise diagnostic methods.

durations at the link ends at the same time. At the remote locations in the accelerator tunnel or in external laboratories, which can be hundreds of meters or even kilometers away from the master laser oscillator, the applications are basically threefold and related to the timing jitter and synchronization needs of the accelerator in different ways:

- The optical pulse train can be used directly for electron bunch arrival time measurements with femtosecond resolution. When this is done after the final compression of the electron bunch, the measured arrival times can be used to sort the data of a pump-probe experiment after recording. Furthermore, the arrival time information can be used as input for a feedback on the acceleration modules (denoted DWC/klystron in the figure). By this, the arrival time of the FEL pulses can be stabilized, helping improve the temporal resolution of pump-probe experiments.
- A unique feature of the pulsed optical synchronization is the capability to lock external, pulsed laser systems to the distributed reference laser pulse train by an optical cross-correlation scheme with sub-10 fs timing jitter. This is of particular importance for the pump-probe-, the seed- and the photoinjector laser, but also for bunch diagnostics, such as the electro-optic experiments.

- Highly phase-stable RF signals can be extracted at practically all harmonics of the fundamental repetition rate of the master laser oscillator with different techniques. These can be used to control the accelerating modules, thus, when used in combination with the other cases, the complete timing of the accelerator is referenced to the master laser.

At FLASH, the implementation of an optical synchronization system based on this scheme began already in 2004. In this thesis, finished years later, the system has been enormously extended on the basis of former, successful proof-of-principle experiments. During the upgrade, many critical components underwent a comprehensive survey, while new devices have been added. These include an important optical setup as part of the distribution, an optical cross-correlator for the synchronization of a Ti:sapphire laser, and similarly an optical cross-correlator for the photoinjector laser oscillator.

Content, Structuring and Organization of This Thesis

This thesis is divided into eight chapters, beginning with a description of the accelerator facility, starting on the next page. In chapters 2 (pages 21 ff.) and 3 (pages 47 ff.), basics of mode-locked lasers in general, fiber- and nonlinear optics are discussed. A more detailed description of the implementation and the upgrade of the optical synchronization system is given in chapter 4 (starting at page 61). Chapter 5 (pages 71 ff.) is devoted to the comparison of two different types of master laser oscillators (MLOs) – a self-built erbium-doped fiber laser (EDFL) and a commercial SESAM- (semiconductor saturable absorber mirror) based laser, where the suitability as master laser oscillator for the optical synchronization is the main focus. Additionally, the setup for stable delivery of the generated reference pulse train to up to 16 fiber links is evaluated, and presents results from its commissioning. The experiences and results of the fiber link stabilization units, which have been commissioned as engineered versions here, but were designed in a former thesis, are discussed in chapter 6 (pages 131 ff.). In chapters 7 and 8 (pages 151 ff. and 167 ff., respectively), the novel optical cross-correlators (OXCs) for the synchronization of a Ti:sapphire and the photoinjector laser are presented with their first, promising results. In combination with a bunch arrival time monitor upstream of the first magnetic chicane, the latter allows for the first time investigations of timing jitter in the injector section of the accelerator. Those measurements revealed several timing instabilities in the injector of the accelerator, and identified a pathway for their mitigation or elimination in the future.

It should be noted that the electron beam diagnostics and in particular the bunch arrival time monitors, which are enabled by the possibilities of the optical synchronization system are not part of this thesis, but rather the main topic of [Boc13]. There, also the different aspects of longitudinal feedback strategies, as well as a comprehensive investigation of the fiber link stabilization scheme is included. In a sense, that thesis continues where [Loe09] came to an end, while the thesis at hand continues more or less where [Win08] left off.

PACS codes: 41.60.Cr, 42.15.Eq, 42.55.Wd, 42.60.By, 42.60.Fc, 42.60.Mi, 42.79.Hp, 42.81.Uv

HEP keywords:[1] crystal, DESY FLASH, erbium, feedback, fibre, free electron laser, laser, measurement methods, optics, soliton, time resolution

[1] from http://www-library.desy.de/schlagw2.html, accessed May 2011

1 FLASH – Linear Accelerator and Free-Electron Laser

FLASH, the Free-Electron Laser in Hamburg, was the first FEL (free-electron laser) user facility in the vacuum-ultraviolet (VUV) and soft X-ray spectral region. It evolved from the TESLA test facility (TTF) linac, which was build to conduct several experiments related to the TESLA Linear Collider Project and to demonstrate the feasibility of a SASE FEL. The accelerator and user facilities underwent several upgrades to achieve shorter wavelengths with higher beam energies, for the installations of new experiments and subsystems and continuous improvements of the beam diagnostics.

In the following section, a more detailed view of the machine and important components after its latest upgrade in 2010 [HFF+10, SFF+10] is given, along with their physical principles. Many explanations are based on [SDR08, Wie98a, Wie98b] with the FLASH-specific details mainly from [Fel10, Ste07, Win08, Loe09, Hac10] and additional literature quoted therein.

1.1 Overview of the Accelerator Facility

The FLASH accelerator facility can be divided into four major parts: the injector and booster section, the superconducting linac including the bunch compressors, the undulator section and the experimental area. The total length of the accelerator up to the experimental endstations in a dedicated hall is approximately 315 m. Figure 1.1 schematically shows the first two sections.

The photocathode inside the RF gun is impinged by the laser pulses of a special photoinjector laser system. The RF gun was exchanged during the last FLASH shutdown, and also an improved photoinjector drive laser had been commissioned (see section 8.1, pages 168). Downstream of the gun, after a short diagnostic section, the electron bunches are boosted in the first acceleration module (ACC1) to energies up to 170 MeV, before the pass the so-called third-harmonic module. This acceleration module, installed during the 2010-upgrade, is operated at three times the nominal acceleration frequency using corresponding cavities. In combination with the preceding acceleration module, it allows for a linearization of the phase space and by this the generation of high-current electron bunches with several hundreds of femtoseconds duration, as explained later in section 1.4 on page 11 f. The following magnetic chicane[1] is used to compress the electron bunch based on the energy chirp of the electron bunches, when they are accelerated off-crest in the booster. The corresponding bunch compression monitor (BCM, see section 1.8.2, page 18 f.) has also been improved during the

[1] For historical reasons, the first bunch compressor is named "BC2" and the second "BC3". This nomenclature will be used in this thesis.

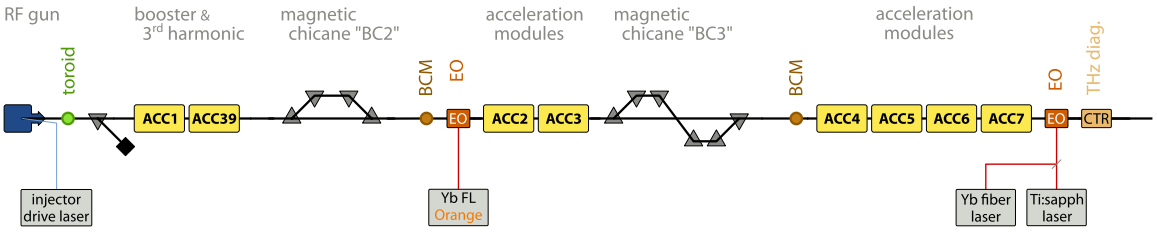

Figure 1.1 | Schematic view of the FLASH injector and linac section. The required laser systems for the photoinjector and special beam diagnostic methods are also shown.

2010-upgrade, and a complete electro-optic (EO, see section 1.8.1, pages 16 f.) beam diagnostic setup, based on an ytterbium fiber laser, has been installed in the tunnel for non-destructive, on-line longitudinal bunch profile measurements. Using six further acceleration modules, grouped as ACC23 and ACC4567, the electron beam can be accelerated up to 1.25 GeV. The last module, ACC7, was also installed as part of the accelerator upgrade, allowing for the generation of SASE FEL pulses at wavelengths down to 4.12 nm reaching into the water window [DES10]. Between the two groups of acceleration modules, another magnetic chicane, called BC3, is installed for further compression of the bunch at an intermediate energy in the order of 450 MeV.

The main linac section is followed by a diagnostic section with a coherent transition radiation (CTR) beamline to a laboratory outside the accelerator tunnel, for instance for spectroscopic or electro-optic investigations of the generated THz radiation. A laser beamline from the same laboratory allows for bunch length diagnostics in another electro-optic setup in the tunnel, both with an ytterbium and a Ti:sapphire laser system. The latter was used for the all-optical synchronization investigations discussed in chapter 7 on pages 151 ff.

After the energy collimator, the electron beam enters the undulator section, as shown in Fig. 1.2, beginning with the undulator section of the optical replica synthesizer (ORS) experiment. These are followed by the new undulator section of the sFLASH experiment, which was also installed during the latest shutdown [MAB+09]. The seed pulses, produced in a high-harmonic generation (HHG) source from a Ti:sapphire laser/amplifier system in an external laboratory, are injected into the accelerator beamline at the last dipole of the collimator. After the undulators, the generated FEL radiation is coupled out from the electron beamline with a small magnetic chicane and send to an experimental hutch. A fraction of the radiation of the seed laser amplifier system can also be guided into this hutch through an evacuated beamline, which will enable pump-probe experiments with an extremely tight synchronization, as the laser and the FEL radiation would originate from the same source.

The next section has also been redesigned in the accelerator upgrade and allows for electron bunch diagnostics, for example by means of the transverse deflecting structure (transverse deflecting structure (TDS), denoted “LOLA” in the figure, which moved from another position) or the timing electro-optic (TEO) setup [Azi09].

Afterwards, the electron beam enters the main undulators, consisting of six 4.5 m long undulator segments, where the VUV- and soft X-ray FEL radiation is generated based on the SASE principle. In addition to the main undulators, another undulator is installed, which can be used for the generation

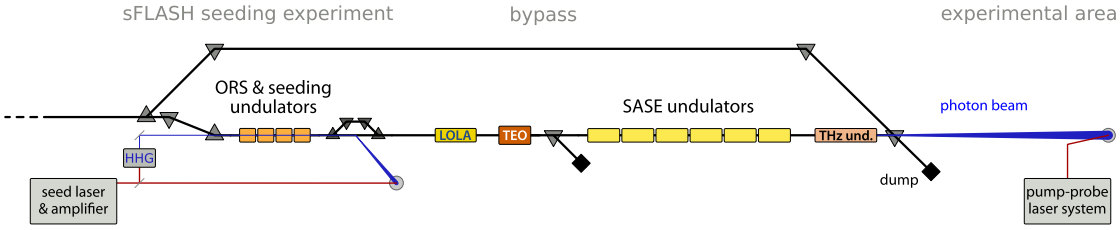

Figure 1.2 | Schematic view of the FLASH undulator section. The required laser systems for pump-probe user experiments and the sFLASH seeding project are also shown.

of infrared/THz pulses with wavelengths up to several hundred micrometers [GHR+07]. Finally, the electron beam is separated from the photon beam(s) with a dipole magnet and is dumped, whereas the VUV-, X-ray and possible infrared pulses arrive into the area for user experiments.

There, the FEL beam can be switched to five experimental stations at five beamlines, which have different focusing optics. Two beamlines are provided by a monochromator, which can not only be used for limiting the spectral bandwidth, but also to suppress the fundamental of the FEL radiation enabling experiments at higher harmonics. In one beamline, the infrared radiation of the THz undulator is available.

At all experimental stations, the radiation of the so-called "pump-probe Ti:sapphire laser" system installed in a hutch in the hall, is available [WRD+05, RASA+11]. A detailed description of the user facility can be found for example in [TAvB+09].

All laser systems mentioned above are presently phase-locked to the master RF oscillator of the accelerator. The projected connection and integration of those to the optical synchronization system is described in chapter 4 on pages 61 ff.

1.2 Free-Electron Lasing Process

To generate the FEL radiation, the accelerated and longitudinally compressed electron bunches are send through an undulator, which is a periodic structure of magnets with an alternating polarity of the magnetic field B_u, separated by the so-called undulator period λ_u, as illustrated in Fig. 1.3. Typically, the period is in the order of a few centimeter and much smaller than the length of the undulator, $\lambda_u \ll L_u$. At FLASH, the undulator has a period of 27.3 mm, a total length of 27 m and an on-axis peak magnetic field of 0.47 T, separated in six undulator structures of 4.5 m length with additional beam diagnostics in between the segments.

The underlying principle is the tangential emission of synchrotron radiation by a relativistic electron, when it propagates on a curved trajectory induced by a magnetic field. Unlike bending magnets in synchrotrons or storage rings, however, the on-axis magnetic field of a planar undulator is nearly harmonic, $B_y = B_u \sin(k_u z)$ with $k_u = 2\pi/\lambda_u$, which forces the electrons onto a sinusoidal trajectory (see 1.3). By this, the generated radiation consists of narrow spectral lines and is contained in a narrow cone along the undulator axis. It can be shown, that the wavelength λ_{ph} of the emitted radiation

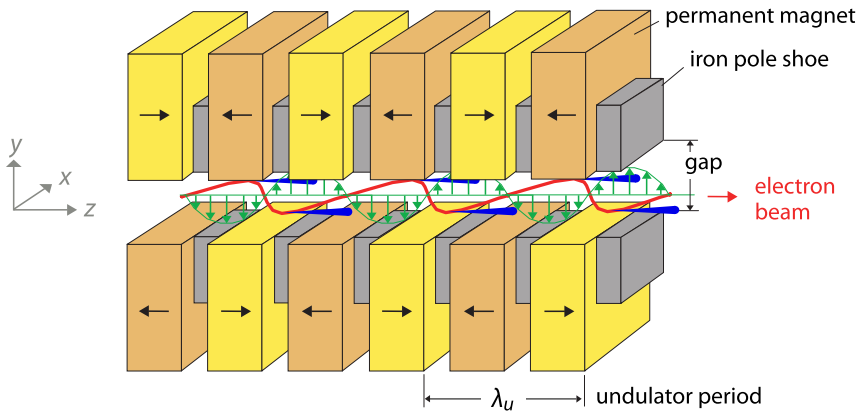

Figure 1.3 | Sketch of a planar undulator magnet. The alternating magnetic field forces the electron beam onto a sinusoidal trajectory (drawn strongly exaggerated). The undulator period λ_u is the distance between two equal poles (adapted from [SDR08]).

is given in very good approximation by

$$\lambda_{\mathrm{ph}} = \frac{\lambda_{\mathrm{u}}}{2\gamma_{\mathrm{rel}}^2}\left(1 + \frac{K_{\mathrm{u}}^2}{2}\right) \qquad \text{with} \qquad K_{\mathrm{u}} = \frac{eB_{\mathrm{u}}\lambda_{\mathrm{u}}}{2\pi m_e c_0}\,. \tag{1.1}$$

where K_{u} is called the undulator parameter. Due to the LORENTZ factor $\gamma_{\mathrm{rel}} = (1-\beta^2)^{-1/2}$ with $\beta = v/c_0$ in Eq. 1.1, the wavelength of the FEL radiation can be tuned by a variation of the electron beam energy $W = \gamma_{\mathrm{rel}} m_e c_0$.

An important consideration for the generation of coherent radiation in a high-gain FEL is the sustained energy transfer from the electron bunch to the light wave over the length of the undulator in a single pass. This is enabled by a process of self-organization within the electron bunch, which is known as microbunching and related to the gain length L_g. Electrons, which loose energy to the light wave travel a longer path in the sinusoidal magnetic field in the undulator, while electrons, which gain back energy from the light wave travel on a shorter path. This results in an electron density modulation with the light's wavelength. These slices, or microbunches, radiate in phase, and their light adds coherently to the light generated by the other microbunches. This leads to a quadratic enhancement of the emitted intensity. Since the number of electrons N_c emitting coherently is in the order of 10^4 to 10^6, the increase of the intensity is enormous. The microbunch formation is furthered with the increasing coherent light field and the increased energy transfer, resulting in an exponential growth of the power $P(z)$ along the undulator:

$$P(z) \propto \exp\left\{\frac{z}{L_g}\right\} \qquad \text{for} \qquad z \gtrsim 2\,L_g \quad \text{and} \quad L_g^{(1\mathrm{d})} \propto \left(\frac{\sigma_\perp^2}{I_0}\right)^{1/3}\,. \tag{1.2}$$

In the one-dimensional (1d) FEL theory, the gain length depends on the transverse beam size $\sigma_\perp$ and the peak current of the electron bunch I_0. Hence, to keep the gain length sufficiently short, peak

currents of several thousand ampere are required. In a three-dimensional model, it can be shown that also the transverse emittance and the energy spread must be sufficiently small. Additionally, the FEL gain is reduced due to betatron oscillations, which lead to different phase shifts of the electrons and the light wave.

The process of microbunch formation from shot noise is called self-amplified spontaneous emission (SASE), where the spontaneous radiation in the first section of a long undulator serves as seed radiation for the remaining section. By this, the resonance condition, Eq. 1.1, can be fulfilled at every wavelength, which is a major advantage for the generation of radiation in the X-ray region compared to other schemes. However, the radiation exhibits reduced longitudinal coherence and statistical fluctuations from shot to shot, even if the shot noise of the charge fluctuation is neglected.

For completeness, it should be noted that the additional infrared/THz undulator consists with nine periods of 40 cm length. In this undulator, infrared pulses at wavelengths between 50 µm and several hundred micrometer can be generated based on spontaneous radiation, where all electrons contribute. Since both the VUV and the infrared pulse are arise from the same electron bunch, they are inherently synchronized to each other, and can, after the propagation to the experimental area, be exploited in pump-probe experiments [FWG+09]. There are, however, mechanisms influenced by machine parameters which change the relative timing of the pulses, see [Loe09].

1.3 Direct-Seeding of the FEL Process with an External Laser

The motivation for the seeded FEL operation is to overcome the fluctuations of the generated radiation based on the SASE principle. In this scheme, the light wave of an external laser is superimposed to the electron bunch at the beginning of the undulator to initiate the microbunching process. By this, the temporal and spectral profiles of the FEL radiation are defined by those properties of the driving laser, which can be controlled with a high precision. Presently, the generation of the seed pulses at the desired wavelength in the XUV region, fulfilling the resonance condition of the undulator, is based on high-harmonic generation (HHG) in a noble gas. The drive laser is usually a high-power Ti:sapphire oscillator/amplifier system to produce the high-harmonics at sufficiently high pulse energies. By tapping off a fraction of the fundamental radiation, for pump-probe experiments nearly perfectly synchronized optical laser pulses and FEL pulses are available. However, the remaining challenge is the synchronization of the seed laser to the electron bunch to provide consistent overlap, as fluctuations of their relative timing results in changes of the FEL output power. This directly relates the seeded operation to the optical synchronization system, as it will not only be used to measure and stabilize the electron bunch arrival time to the optical reference, but also enable the tight synchronization of the seed laser to that reference (see chapters 4 and 7 on pages 61 ff. and 151 ff.).

The sFLASH seeding project has been installed and technically commissioned during the major accelerator upgrade. First results and a discussion of the required subsystems, such as the HHG source and the undulators, along with diagnostics and techniques for establishing spatial and temporal overlap with sub-picosecond resolution, are presented in [BAC+10, CAB+10, TAB+10, MAB+09, DHMR+09] and the references quoted therein.

1.4 Electron Bunch Compression

Electron bunches with a peak current in the order of several kiloampere required for the SASE FEL process can not be generated in the injector gun, since then enormous space-charge forces would destroy the bunch within a short distance. Therefore, electron bunches with a current of about 50 A are generated and longitudinally compressed by approximately two orders of magnitude. The compression takes place at highly relativistic energies, where the repulsive COULOMB forces are compensated for by attractive magnetic forces and the longitudinal degree of freedom is frozen.

For this, electrons are accelerated *off-crest* (see also next section), where the electrons in the head of the bunch gain less energy than the ones in the tail of the bunch. Due to the imprinted energy chirp, the trailing electrons travel a shorter path length in a magnetic chicane following the acceleration module, and by this they catch up to the electrons in the bunch head. The principle is illustrated in Fig. 1.4, where the quantity δp denotes the momentum deviation of an electron with respect to a reference particle of the momentum p. Most commonly, the final compression is realized in two

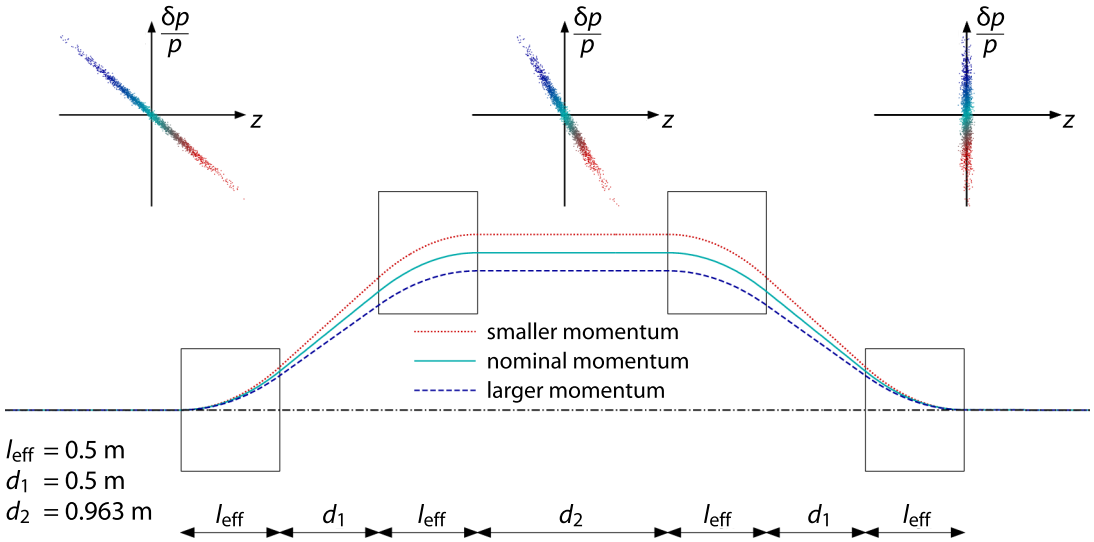

Figure 1.4 | Schematic view of the FLASH C-type magnetic chicane BC2. Particles with a smaller momentum travel a longer path through the magnetic chicane while consequently particles with higher momentum travel a shorter path, resulting in longitudinal bunch compression (adapted from [Loe09]).

stages to reduce the influence of collective effects, such as coherent synchrotron radiation. At FLASH, the first bunch compressor "BC2" has a C-type magnetic chicane, as shown in the figure, whereas the second bunch compressor "BC3" is based on a symmetric S-type chicane. The beam energy at the entrances of the chicanes are typically 150 MeV and 450 MeV, respectively.

Since the initial length of the bunch generated in the gun covers more than 2 deg, or more than 4.3 ps, of an 1.3 GHz oscillation, the sinusoidal curvature of the accelerating field induces a nonlinear energy chirp. This results in a nonlinear bunch compression and leads to a charge distribution with a short spike at the head of the bunch and a much longer tail. The peak current of the spike, whose

duration is in the order of 50 fs rms, is then large enough for the SASE FEL process, whereas the tail with a duration of several picoseconds contributes only negligible to the generated FEL radiation. The use of two bunch compressors also reduces the effect of this nonlinearity, since the bunch is already compressed at the entrance of the second chicane.

While being essential for the generation of the high peak current electron bunches, the compressors are at the same time one of the most critical components of the accelerator with regard to timing jitter. Since any variation of the energy chirp is converted into a variation of the arrival time after the chicane, the requirements for the amplitude and phase stability are very demanding (see section 4.1, pages 62 f.). The timing jitter $\delta t_{\text{bunch}}{}^2$ after the first magnetic chicane is, according to [SAL+05], given by

$$\delta t_{\text{bunch}}^2 \approx \left(\frac{R_{56}}{c_0}\frac{\sigma_A}{A}\right)^2 + \left(\frac{C-1}{C}\right)^2 \cdot \left(\frac{\sigma_\varphi}{\omega_{\text{RF}}}\right)^2 + \frac{1}{C^2}\,\delta t_{\text{in}}^2\,. \tag{1.3}$$

The dispersion R_{56} of the magnetic chicane is about −180 mm for BC2 and −70 mm for BC3 at FLASH. In the European XFEL, chicanes with 100 mm and 15 . . . 25 mm are planned [ABC+07]. The compression factor C is in the range of 20 and 100 depending on the particular setup of the accelerator, $\omega_{\text{RF}} = 2\pi f_{\text{RF}}$ is the angular frequency of the accelerating field, σ_A/A and σ_φ/φ are its relative amplitude and phase stability, and σ_{in} is the incoming bunch arrival time jitter caused by the injector (see section 1.6.2, pages 14 f.). Taking the second accelerating section, ACC23, and the second chicane into account, the timing jitter can be derived as [Hac10]

$$\delta t_{\text{bunch}}^2 \approx \left(\left(R_{56,1} + \frac{E_1}{E_2}R_{56,2}\right)\cdot\frac{\sigma_{A_1}}{c_0 A_1}\right)^2 + \left(R_{56,2}\,\frac{E_2-E_1}{E_2}\,\frac{\sigma_{A_2}}{c_0 A_1}\right)^2 + \left(\frac{C-1}{C}\cdot\frac{\sigma_{\varphi_1}}{\omega_{\text{RF}}}\right)^2 + \frac{1}{C^2}\,\delta t_{\text{in}}^2\,, \tag{1.4}$$

where the index j in $R_{j,56}$, A_j and E_j refers to the corresponding acceleration section, and $C = C_1 \cdot C_2$ is the total compression factor. Equation 1.4 has to be considered in the design of an arrival time feedback, as it was used during the proof-of-principle experiments for the optical synchronization system, as briefly described in section 4.5 on pages 69 f. Detailed discussions on the longitudinal feedback are given for example in [LAF+10, Hac10, GBF+10a, KBB+10, Boc13].

Linearization of the Phase Space

The advantage of the nonlinear, or "roll-over" compression scheme with a short spike is the capability to produce FEL pulses with durations down to a few 10 fs at the cost, that only about 10% – 20% of the bunch charge contributes to the lasing process. In order to gain better control of the compression process, a superconducting module with four nine-cell cavities operated at $f_{39} = 3.9$ GHz has been installed in the injector section during the FLASH upgrade as mentioned earlier.

It enables imprinting a more linearized energy chirp onto the electron bunch by linearizing the accelerating RF wave. In that way, a much larger fraction of the charge gets compressed into a single pulse with high peak current required for the generation of FEL radiation in the undulators. Due to the more uniformly distributed charge along the bunch, the total charge can be reduced, while

saturation is maintained. The lower charge helps to reduce negative impact from space-charge and coherent synchrotron radiation. Although a longer pulse duration might not desirable for all user experiments, it is essential for the sFLASH commissioning and operation, as a comparatively long bunch with durations in the order of ~ 250 fs to ~ 400 fs with a uniformly distributed charge counteracts the relative arrival time fluctuations of the electron bunch and the seed laser pulses.

The principle of the linear compression scheme can be found for example in [Emm01], whereas FLASH-specific details are discussed for instance in [VAB+10] and [EBH10].

1.5 Acceleration Modules

The electron bunches are accelerated by alternating electric fields in superconducting nine-cell RF cavities developed for the TESLA project. Their resonance frequency is f_{RF} = 1.3 GHz and the cavities are excited at their TEM_{010} mode where the electric field is parallel to their axis. Since the length of the cells is $c_0/(2f_{RF})$, a particle with the speed $v \approx c_0$ needs half a period of the accelerating frequency to pass the cell. When the particle enters a cell at the zero-crossing of the electric field, it is accelerated along the whole cell and leaves it at the next zero-crossing of the field. In multi-cell cavities excited at their π-mode, a standing wave pattern arises with an alternating electric field from cell to cell. By this, a particle leaving one cell, in which it was accelerated, experiences in the next cell again an accelerating field due to the phase advance of π between the cells. The phase setting φ_{ACC} of the driving RF for this maximum energy gain is referred to as *on-crest* acceleration, whereas in all other cases the electrons gain less (*off-crest* acceleration) or even loose energy (deceleration).

At FLASH, each of the seven acceleration modules, called ACC1 to ACC7, consist of eight nine-cell cavities and are, partly in groups, powered by several klystrons. The amplitude and phase of the fields in the modules are controlled by adjusting amplitude and phase of the corresponding klystron. The cavities are furthermore equipped with pick-up antennas to determine their fields, and the complex field amplitudes are added vectorially. This vector sum (VS) is used by the low-level radio frequency (LLRF) controller to regulate phase and amplitude of the modules.

1.6 Injector and Booster

The term "injector and booster" usually refers to the first section of the accelerator up to the first magnetic chicane, consisting of the RF electron gun, its driving laser, the first acceleration module and after the latest upgrade also the third-harmonic module. This first section is in particular critical, as the beam energy after the gun is around 5 MeV and thus space-charge effects are still strong. Several diagnostic elements, among them a toroid charge monitor, are installed after the gun. Apart from that, the first acceleration module is installed as close as possible.

1.6.1 Electron Source

The requirements for the electron beam driving high-gain FEL are demanding. At the entrance of the undulator, the electron bunch has to have a high peak current and at the same time a very low emittance. Such beams, suitable for the mandatory bunch compression, can be generated in special thermionic guns, or, as in the case of FLASH, using a photoinjector. The utilized caesium telluride (CsTe) photocathode requires photon energies in the order of 3.5 eV for the photoemission process, and therefore laser pulses in the ultraviolet (UV) region are required. These are generated by a special, actively mode-locked laser system, which is described in section 8.1 on pages 168 f. below. In Fig. 1.5 the electron gun is depicted schematically. The photocathode is located at the backplane of a 1.5-

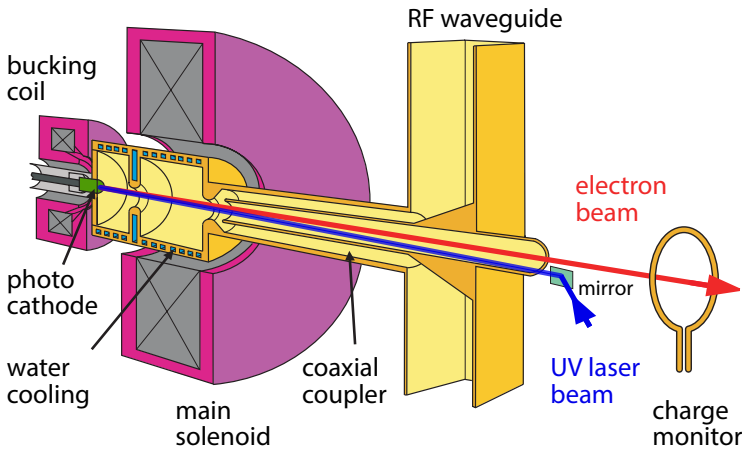

Figure 1.5 | Sketch of the FLASH radio-frequency electron gun. It is based on photoemission from a cesium telluride (Cs_2Te) cathode impinged by UV picosecond laser pulses in a 1.5-cell normal conducting RF cavity (courtesy of K. Flöttmann).

cell copper, i.e. normal-conducting (NC) cavity, also operating at 1.3 GHz. At the cathode surface an electrical field of ~ 40 MV/m, delivered by a 5 MW klystron, accelerates the generated electron bunches away from the cathode. The main solenoid counteracts the emittance growth due to the repulsive space charge effects by focusing the electron beam. The magnetic field on the cathode surface, where the electrons have a low energy, is cancelled by a second solenoid, called bucking coil. In order to avoid time-dependent RF-induced transverse kicks of the beam, a cylindrical coupler is used to feed the RF, which is equipped with forward- and reflected-power monitors, into the cavity. The emission phase φ_{gun} of the RF has to be well adjusted and very stable for this photoemission mechanism. Since the gun is not equipped with mechanical tuners, the resonance frequency is set and tuned by a carefully designed water cooling system with a sensor mounted in the iris of the gun. At a steady state, the temperature is stabilized to 0.06°C, which corresponds to 1.2 kHz, but with operation at the maximum RF pulse length of 800 µs the resonance frequency change can be as high as 8 kHz. These phase changes and also the stability of the powering RF play an important role for the arrival time at the first acceleration module, ACC1, and by that the complete dynamics of the electron bunch along the accelerator and ultimately its lasing performance. It is therefore crucial to

stabilize the phase of the of the electron gun in the planned longitudinal feedback system.

1.6.2 Arrival Time Upstream of the First Chicane

In addition to the phase of the RF gun, the relative timing between the RF field and the arrival time of the photo injector laser pulses critically influence the arrival time of the electron bunch. Furthermore, since the electrons are not yet relativistic, the dynamics at the beginning of the accelerator is dominated by space-charge forces and the longitudinal bunch profile is changed by different electron velocities. The influence of those changes of the RF gun phase and the injector laser timing had been studied in [Loe09] by means of numerical simulations with ASTRA. Here, the results for the arrival time at the entrance of the magnetic chicane are summarized, as they are important for the interpretation of the results discussed in chapter 8, page 167 ff. Accordingly, the timing change $\delta t_{\mathrm{bunch}}$ of the electron beam is given by

$$\delta t_{\mathrm{bunch}} = G_{\mathrm{laser}}\,\delta t_{\mathrm{laser}} + G_{\mathrm{gun}}\,\delta t_{\mathrm{gun}} + G_{\mathrm{ACC1}}\,\delta t_{\mathrm{ACC1}} \tag{1.5}$$

where the factors G_j weigh the influence of timing changes induced by the laser $\delta t_{\mathrm{laser}}$, the RF gun δt_{gun} and the first acceleration module δt_{ACC1}, respectively. The timing changes of the gun and the acceleration module are

$$\delta t_{\mathrm{gun}} = \frac{\delta\varphi_{\mathrm{gun}}}{\omega_{\mathrm{RF}}} \quad \text{and} \quad \delta t_{\mathrm{ACC1}} = \frac{\delta\varphi_{\mathrm{ACC1}}}{\omega_{\mathrm{RF}}} \quad \text{with} \quad \omega_{\mathrm{RF}} = 2\pi f_{\mathrm{RF}}\,. \tag{1.6}$$

Since a timing change of the components must cause a timing shift of the beam by equal amount, the factors G_j must sum up to unity

$$G_{\mathrm{laser}} + G_{\mathrm{gun}} + G_{\mathrm{ACC1}} = 1 \tag{1.7}$$

This is equivalent to the statement, that timing changes per degree phase change have to add up to 2.137 ps/deg at f_{RF}. The characteristics of the factors G_j are shown in Fig. 1.6 as function of the gun emission phase. It can be seen that the influence of the first acceleration module is almost negligible, as it amounts to G_{ACC1} =0.6% for on-crest acceleration. The influence increases for off-crest acceleration, but was found to stay less than 1.5% for typical phase setpoints. At the nominal operation phase setpoint[2] $\varphi_{\mathrm{nom}} = -38$ deg, the timing changes induced by the laser and the gun phase affect the electron bunch arrival differently. The factors amount to $G_{\mathrm{laser}} \approx 60\%$ and $G_{\mathrm{gun}} \approx 40\%$.

In this thesis it has been tested experimentally, whether the run of the curve of G_{gun} can be extrapolated up to the point, where gun phase changes do not affect the arrival time of the electron bunch anymore, as will be discussed in chapter 8 on pages 167 ff.

It should be noted that the simulations did not account for the third-harmonic module, and did not include the assumed phase setpoint of $\varphi_0 \equiv \varphi_{\mathrm{nom}} - 20$ deg where $G_{\mathrm{gun}} = 0$. New simulations will,

[2] The phase $\varphi_{\mathrm{gun}} = 0$ is defined, when the toroid charge monitor can not detect a charge anymore in a scan approaching this phase setting (see Fig. 8.15, page 183).

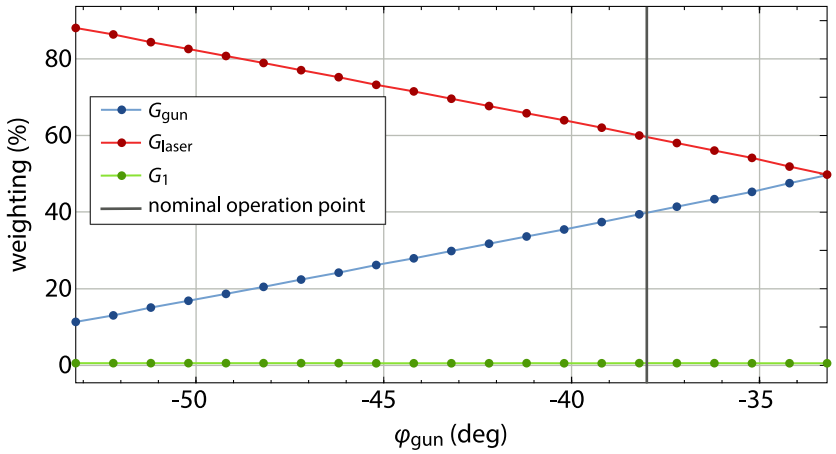

Figure 1.6 | Weighting factors for timing changes of the electron beam in the injector. Simulated contribution of the photoinjector laser, the RF gun and the first acceleration module on the arrival time at the entrance of the first magnetic chicane at FLASH (from [Loe09]).

in addition to that, also incorporate the longer pulse duration of the new photoinjector laser, and the now routinely set bunch charge of 0.5 nC compared to the values before the FLASH upgrade.

1.7 Bunch Pattern / Time Structure of the Accelerator

In superconducting cavities the accelerating field can be sustained over a long duration due to their low losses and high quality factors compared to normal conducting cavities. At FLASH, the maximum RF pulse duration is 800 µs, in which a maximum number of 800 bunches with an intra-train repetition rate of f_{bunch} = 1 MHz can be accelerated. There are, however, several discrete settings for

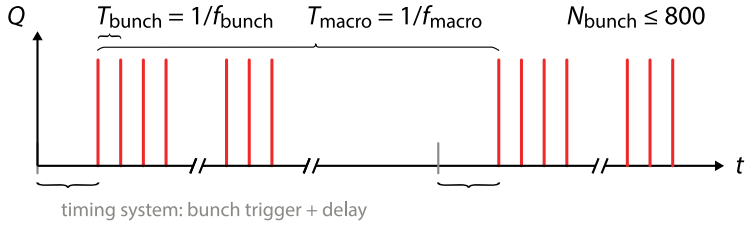

Figure 1.7 | Time structure and bunch pattern at FLASH. The macro-pulses are usually separated by the macro-pulse repetition time $T_{macro} = 1/f_{macro} = 0.1$ s, wherein up to $N_{bunch} = 800$ electron bunches with a repetition rate of 1 MHz are possible. For lower repetition rates within the train, the number of bunches reduces accordingly.

the intra-train repetition rate from 1 MHz down to 25 kHz with an accordingly reduced number of maximum bunches.[3] The sequence of electron bunches is also called macro-pulse. The repetition rate

[3] A special operation mode for high-current operation, as it would be required for the International Linear Collider (ILC), with f_{bunch} = 3 MHz and N_{max} = 2400 is also available, but routinely not used.

of the macro-pulses, sometimes referred to as bunch trigger, is typically $f_{\text{macro}} = 10\,\text{Hz}$, but can also be set to 5 Hz as it used to be before the latest FLASH upgrade, and to 1 Hz for special experiments. Figure 1.7 shows a sketch of this time structure, or "bunch pattern", respectively.

1.8 Beam Diagnostic Instrumentation and Methods

At FLASH, numerous beam diagnostic instrumentation and experiments are installed. These range from standard methods such as beam position monitors (BPMs) to longitudinal bunch profile reconstruction from coherent radiation (see for example [Beh10, Weso8]; the position of coherent transition radiation (CTR) setups are shown in Figs. 1.1 and 1.2 or using a transverse deflecting structure (TDS) [Roeo8, BGZo9], noted as "LOLA" in the figure).

With respect to the optical synchronization system and the planned longitudinal feedback, two diagnostic methods are briefly explained in the following two sections. The electron bunch arrival time monitors (BAMs) are discussed seperately in section 4.4 on pages 67 ff. as integral components of the optical synchronization system.

1.8.1 Electro-Optic Techniques

The longitudinal charge density distribution and the arrival time of an electron bunch can be measured non-destructively utilizing the Pockels effect in electro-optic (EO) crystals like gallium phosphide (GaP) or zinc telluride (ZnTe). When a relativistic electron bunch passes such a crystal within a few hundreds of micrometers, the bunch's transient Coulomb field, whose strength is proportional to the bunch charge distribution, induces a birefringence in the crystal. A resulting change of the state of polarization (SOP) of a co-propagating laser pulse can, for example, be detected with high sensitivity in a crossed-polarizer setup. By that, the temporal profile of the electric field and thus the longitudinal bunch structure can be reconstructed. The total phase retardation in an EO crystal of the length L is given by

$$\Gamma(t) = \frac{2L}{\lambda}\, n_0^3\, \mathrm{Re}\left\{ \int_0^\infty e^{-i\omega t}\, \tilde{E}(\omega)\, G_{\mathrm{EO}}(\omega)\, \mathrm{d}\omega \right\} \tag{1.8}$$

where n_0 is the refractive index of the crystal in absence of a field, $\tilde{E}(\omega)$ the Fourier transform of the electric field, while the electro-optic response function $G_{\mathrm{EO}}(\omega)$ takes the crystal's geometric and electro-optic properties properties for a laser pulse at a wavelength λ and of finite duration into account [Steo7, SAB+o9].

For the detection of the induced polarization change, several schemes were developed in the past. In all methods, the EO crystal, which is required to be inside the electron beam pipe, is placed between two crossed polarizers. In the simplest method, known as electro-optic sampling (EOS), the electric field is probed with relatively short laser pulses in a step-scan fashion by varying the optical delay between the electron bunch and the laser pulse shot by shot. A schematic setup for this technique is shown in Fig. 1.8a. While this scheme provides the best temporal resolution, it is

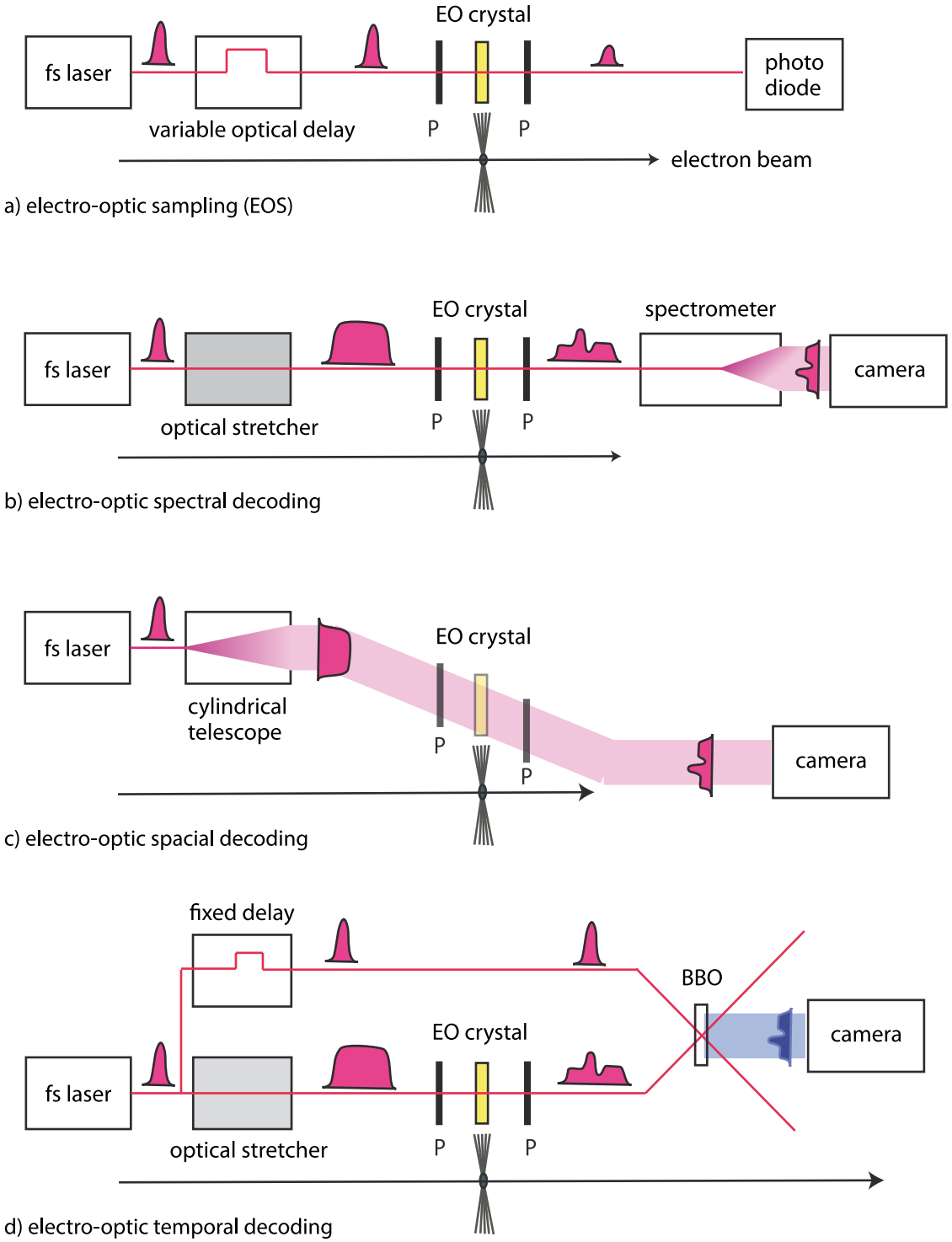

Figure 1.8 | Schematic arrangements of different electro-optic techniques. In all schemes, information on the electron bnch is decoded from a modulated laser pulse (illustration donated by B. Schmidt).

presently limited by the timing jitter between the laser pulse and the electron bunch, and shot-to-shot fluctuations of the bunch profile. So far, resolutions in the order of 50 fs have been demonstrated at another accelerator site [vTM+08]. However, the influence of the timing jitter can be reduced with the optical synchronization system. When the laser system used for probing the electro-optic effect is synchronized to the master laser oscillator and the electron bunch arrival time is measured relative to this optical reference, the recorded data can be sorted with respect to the arrival times of every shot. It is obvious that the EOS technique requires many shots for the pump-probe data acquisition and has therefore only limited use for electron bunch diagnostics.

For this, different single-shot methods can be applied: For the technically comparatively simple electro-optic spectral decoding (EOSD), shown in Fig. 1.8b, a short laser pulse is stretched to a few picoseconds using a dispersive material generating a wavelength chirp. After passing the electro-optic crystal, the time domain modulation is decoded in a wavelength modulation and can be detected with a combination of spectrometer and camera. However, this method has intrinsic limitations of the temporal resolution and is best used for picosecond bunch lengths. To partly overcome this limitation, an ytterbium-doped fiber laser (YDFL) is used in the EO monitor downstream the first magnetic chicane at FLASH (see Fig. 1.1, page 6 and [BSSW10, Bre11]), as the velocity mismatch between the Coulomb field and the laser pulses in the crystal is reduced at the wavelength emitted by the ytterbium laser compared to the use of a Ti:sapphire laser. At the EO diagnostic station after the accelerating section, both ytterbium and a Ti:sapphire lasers are available [WAB+09, Wis12]. The latter has been used for arrival time measurements comparing the EO method and the BAM which resulted in a relative timing jitter of 80 fs rms after all [AFK+08].

In another scheme, a short laser pulse travels through the electro-optic crystal at an angle with respect to the electron beam direction. In this non-collinear cross-correlation of the Coulomb field and the laser pulse, the different transverse positions in the laser pulse experience different electron bunch timings and the bunch profile is decoded in the spatial profile of the pulse, which is measured single-shot with a camera, see Fig. 1.8c. In [Azi09], a resolution of 75 fs of this electro-optic spatial decoding technique has been demonstrated.

The electro-optic temporal decoding (EOTD) method is also based on single-shot non-collinear cross-correlation, but therein, a BBO crystal is used for the correlation of the modulated laser pulse with a reference pulse from the same pulse train, as shown in Fig. 1.8d. This technique provides a better time resolution of about 60 fs [SAB+09] compared to the other schemes at the cost of a more complex setup in the accelerator tunnel.

1.8.2 Bunch Compression Monitor

The principle of operation of the bunch compression monitor (BCM) at FLASH are based on the coherent radiation effects of the electron bunch. For electron bunches, whose radiation process can be described as a superposition of the electric fields N electrons, it can be shown [LS97] that the total

intensity $I_N(\omega)$ can be written as

$$I_N(\omega) = I_1(\omega)\left(N + N(N-1)\cdot|F(\omega)|^2\right) \ , \qquad F(\omega) = \frac{1}{Q}\int \rho(\boldsymbol{r}) e^{-i\boldsymbol{k}\boldsymbol{r}}\,\mathrm{d}\boldsymbol{r} \tag{1.9}$$

where $F(\omega)$ the form factor of the charge distribution $\rho(\boldsymbol{r})$ and $I_1(\omega)$ the single electron spectrum. For highly relativistic bunches, the radiation is usually emitted into a narrow cone with an opening angle of $\Theta = 1/\gamma$. In this case, it is sufficient to consider only the longitudinal form factor

$$F_L(\lambda) = \frac{1}{Q}\int \rho(z)\, e^{-i\,2\pi z/\lambda}\,\mathrm{d}z\,. \tag{1.10}$$

For an electron bunch with a longitudinally Gaussian profile with the length σ_z, the total radiated intensity is proportional to σ_z^{-1} and also under realistic conditions, a strong correlation exists between the bunch length and the coherent intensity. Therefore, a single detector integrating over a broad spectral range, such as pyroelectric sensors can be used as monitors for the bunch compression and suppress fluctuations by means of a feedback. The upgraded BCMs (see also Fig. 1.1, page 6) are described in [BNSW10, Wes12] and will be integrated into the arrival time feedback described in section 4.5 on pages 69 f.

2 Laser Basics

In this chapter, some fundamental principles of laser pysics relevant for this thesis are introduced. Based on Maxwell's equations, the propagation of Gaussian laser beams through an optical system is derived, which is particularly important for the optimization of the free-space distribution unit discussed in chapter 5. The propagation of laser pulses in an optical fiber is described by the nonlinear Schrödinger equation, along with the effects of dispersion and nonlinearities occurring in this case. Furthermore, various techniques for pulsed operation of a laser by means of mode-locking are introduced, as these are relevant for the different laser systems in conjunction with the synchronization system. The last section gives a brief summary of the erbium-doped fiber amplifiers (EDFAs), which are required in several subsystems of the synchronization system.

2.1 Fundamental Theory

Laser radiation is an electromagnetic phenomenon and thus Maxwell's equations form the basis for the following mathematical framework for the description of the propagation in free-space and in optical fibers. They read:

$$\nabla \cdot \boldsymbol{D} = \rho_\mathrm{f} \tag{2.1a}$$

$$\nabla \cdot \boldsymbol{B} = 0 \tag{2.1b}$$

$$\nabla \times \boldsymbol{E} = -\frac{\partial \boldsymbol{B}}{\partial t} \tag{2.1c}$$

$$\nabla \times \boldsymbol{H} = \boldsymbol{j} + \frac{\partial \boldsymbol{D}}{\partial t}\,, \tag{2.1d}$$

where $\boldsymbol{E}$ and $\boldsymbol{H}$ are the electric and magnetic field vectors, while $\boldsymbol{D}$ and $\boldsymbol{B}$ are the corresponding electric and magnetic flux density. The response of a medium to an external or internal electric or magnetic field is described by the material equations

$$\boldsymbol{D}(\boldsymbol{E}) = \varepsilon_0 \boldsymbol{E} + \boldsymbol{P}(\boldsymbol{E}) \tag{2.2}$$

$$\boldsymbol{B}(\boldsymbol{H}) = \mu_0 \boldsymbol{H} + \mu_0 \boldsymbol{M}(\boldsymbol{H})\,, \tag{2.3}$$

with the induced electric polarization $\boldsymbol{P}$ and the induced magnetization $\boldsymbol{M}$. The vacuum permittivity ε_0 and the vacuum permeability μ_0 fulfill the relation $1/c_0^2 = \varepsilon_0 \mu_0$. The charge density of free carriers ρ_f and the current density vector $\boldsymbol{j}$ in Eq. 2.1a and 2.1d are sources for electric fields, and assumed to be zero in the context of the description of laser phenomena in the following. Furthermore, a

nonmagnetic and homogeneous material is assumed, for example in both the core and the cladding of an optical fiber. In this case, the wave equation for the electric field vector $\boldsymbol{E}$ can be derived as

$$\nabla^2 \boldsymbol{E} - \frac{1}{c^2}\frac{\partial^2 \boldsymbol{E}}{\partial t^2} = \mu_0 \frac{\partial^2 \boldsymbol{P}}{\partial t^2}\,. \tag{2.4}$$

A general solution can not be given, and further assumptions and boundary conditions are needed to describe a specific problem. This is particularly true for the pulse propagation in optical fibers as discussed in section 2.3.1 on page 25, where the nonlinear Schrödinger equation (NLSE) is derived from the wave equation.

2.2 Gaussian Optics and Free-Space Laser Pulse Propagation

In case of vacuum where $\boldsymbol{P} = 0$ the most simple solutions of the wave equation 2.4 are plane waves

$$\boldsymbol{E}(\boldsymbol{x}, t) = \boldsymbol{E}_0\, e^{i\boldsymbol{k}\boldsymbol{x} - i\omega t} \tag{2.5}$$

with the dispersion relation $k^2 = \omega^2/c_0^2$ and the wave number $k = 2\pi/\lambda$. In cases when only the magnitude of the electric field, but not the direction is of interest, the field vector can be written as $\boldsymbol{E} = E \cdot \boldsymbol{e}$ with the constant unit vector $\boldsymbol{e}$. Then, the scalar wave equation is given by

$$\nabla^2 E - \frac{1}{c^2}\frac{\partial^2 E}{\partial t^2} = 0\,. \tag{2.6}$$

For the description of real radiation fields, however, the spatial distribution has to be considered, because the radiation field is not infinite in space as plane waves are. This can be achieved with the paraxial approximation, which is also known as the slowly varying envelope approximation (SVEA). It states that a laser beam with a finite intensity distribution $E_0(x, y, z)$ travels nearly parallel to one direction of propagation, which is assumed to be z in the following. Using the ansatz

$$E(x, y, z) = E_0(x, y, z)\, e^{ikz - i\omega t} \tag{2.7}$$

the scalar wave equation 2.6 becomes

$$\frac{\partial^2 E_0}{\partial x^2} + \frac{\partial^2 E_0}{\partial y^2} + \frac{\partial}{\partial z}\left(\frac{\partial E_0}{\partial z} + 2ikE_0\right) = 0\,. \tag{2.8}$$

In the SVE approximation, $\partial E_0/\partial z \ll kE_0$ is assumed and leads to the paraxial wave equation

$$\frac{\partial^2 E_0}{\partial x^2} + \frac{\partial^2 E_0}{\partial y^2} + 2ik\frac{\partial E_0}{\partial z} = 0 \tag{2.9}$$

in Cartesian coordinates. Since laser resonators often exhibit rotational symmetry, it is useful to transform Eq. 2.9 to a cylindrical coordinate system (r, φ, z). When the field distribution does not

depend on the angle φ, the wave equation reads

$$\frac{\partial^2 E_0}{\partial r^2} + \frac{1}{r}\frac{\partial E_0}{\partial r} + 2ik\frac{\partial E_0}{\partial z} = 0\,. \tag{2.10}$$

The solutions of this equation are called *modes of propagation* or short *modes* representing transverse waves, i.e. the electric and magnetic field vectors are perpendicular to the direction of propagation, $\boldsymbol{k} \perp \boldsymbol{E} \perp \boldsymbol{H}$, and are consequently called transverse electro-magnetic (TEM) modes. The solution of the lowest order is the TEM_{00}-mode, or Gaussian beam

$$E(r,z) = A(r,z)\, e^{-i(\omega t - \phi_\mathrm{T}(r,z) - \phi_\mathrm{L}(z))} \qquad \text{with} \qquad A(r,z) = E_0 \frac{w_0}{w(z)}\, e^{-\frac{r^2}{w(z)^2}} \tag{2.11}$$

which can be written as the product of an amplitude term $A(r,z)$, which is the radially Gaussian distribution of the electric field and a phase term describing the oscillations of the phase in the direction of propagation similar[1] to plane waves and determines the radius of curvature of the wave fronts. The characteristic parameters of such a beam are

$$w_0 \qquad \text{beam waist at } z = 0 \tag{2.12a}$$

$$z_\mathrm{R} = \frac{\pi w_0^2}{\lambda} \qquad \text{Rayleigh length} \tag{2.12b}$$

$$b = 2z_\mathrm{R} \qquad \text{confocal length or depth of field} \tag{2.12c}$$

$$w(z) = w_0\sqrt{1 + (z/z_\mathrm{R})^2} \qquad \text{beam radius at } z \tag{2.12d}$$

$$R(z) = z\cdot\left(1 + (z_\mathrm{R}/z)^2\right) \qquad \text{curvature of the wave front} \tag{2.12e}$$

$$\phi_\mathrm{T}(r,z) = \frac{kr^2}{2R(z)} \qquad \text{transverse phase term} \tag{2.12f}$$

$$\phi_\mathrm{L}(z) = kz + \zeta(z) \qquad \text{longitudinal phase term} \tag{2.12g}$$

$$\zeta(z) = -\arctan(z/z_\mathrm{R}) \qquad \text{Gouy phase} \tag{2.12h}$$

$$\theta = \lim_{z\to\infty}\frac{w(z)}{z} = \frac{w_0}{z_\mathrm{R}} = \frac{\lambda}{\pi w_0} \qquad \text{far field divergence angle} \tag{2.12i}$$

In terms of these parameters the paraxial approximation means that the beam waist is large compared to the wavelength and that the Rayleigh length of the beam is large compared to the beam waist, which in turn means that the divergence has to be relatively small. As the form of a Gaussian beam is invariant during propagation and it only experiences a spatial broadening, two parameters are sufficient for a complete representation. This can either be the distance from the waste z and the Rayleigh length z_R or the beam radius $w(z)$ and the curvature of the wave fronts $R(z)$. These are

[1] A Gaussian beam acquires a small phase shift compared to a plane wave of the same optical frequency, called the Gouy phase. In the fundamental mode, this is usually negligible, but for higher-order modes, the effect becomes more prominent.

combined in the complex q-parameter

$$q = z + iz_R \qquad \text{or} \qquad \frac{1}{q} = \frac{1}{R(z)} - \frac{i\lambda}{\pi w^2(z)} . \tag{2.13}$$

Using the q-parameter the propagation of a Gaussian beam through an optical system can be described with the $ABCD$-matrices from ray optics [Bé91] according to

$$q' = \frac{A\,q + B}{C\,q + D} . \tag{2.14}$$

This equation is the base for the optimization of the free-space distribution unit as discussed in section 5.5 on pages 108 ff. and the optical cross-correlator of the link stabilization units as discussed in chapter 6 on pages 131 ff. However, real laser beams usually differ from an ideal Gaussian beam. This is quantified with the M^2-factor, which relates the real, for example measured, parameters w_{real} and θ_{real} of the beam to the ideal ones as in Eqs. 2.12d and 2.12i:

$$w_{real} = M \cdot w_0 , \qquad \theta_{real} = M \cdot \theta \qquad \Rightarrow \qquad w_{real} \cdot \theta_{real} = \frac{w_{real}^2}{z_{R,real}} = \frac{\lambda}{\pi} M^2 = \text{const.} \tag{2.15}$$

The M^2-factor is an important quality attribute of a laser beam and should always be considered, for example when implementing a new laser system to an existing setup. Typical values for the laser systems discussed in this thesis and most commercial ones are between $M^2 = 1.1$ and $M^2 = 1.3$.

2.3 Fiber Optics

Optical fiber networks allow for an apparently straightforward and cost-effective way of distributing light over large distances in practically arbitrary environments – in contrast to the free-space beam or pulse propagation described in the section before. The basic physical phenomenon of guiding light in optical fibers is total internal reflection (see e.g. [Hec02]). The most simple optical fiber is the step-index fiber, where a central core with a radius r_{core} and a refractive index n_{core} is surrounded by a cladding with a slightly lower refractive index n_{clad} with a difference of typically 0.005. These types of fibers are characterized by two parameters:

$$\Delta = \frac{n_{core} - n_{clad}}{n_{core}} \qquad \text{and} \qquad V = k r_{core} \sqrt{n_{core}^2 - n_{clad}^2} , \quad k = \frac{2\pi}{\lambda} \tag{2.16}$$

where the V parameter determines the number of modes supported by the fiber. It can be shown [Agr07] that only a single mode is supported for $V < 2.405$ (being the first root of the Bessel function J_0). Such fibers permit of only one possible transverse distribution of the light fields. This type, known as single mode fiber (SMF), is the only type used in the optical synchronization system, but there are various sub-types of SMF such as rare-earth doped gain fibers or dispersion compensating fibers (see also appendix D, pages 239 ff.).

Loss

The transmitted optical power $P(L)$ through a fiber of the length L, which exhibits losses mainly due to infrared absorption (molecular vibrations) and RAYLEIGH scattering, can be expressed by

$$P(L) = P_0 e^{-\alpha L} \qquad \Rightarrow \qquad \alpha_{\mathrm{dB}} = -\frac{10}{L} \log\left(\frac{P(L)}{P_0}\right) = 4.343\alpha \tag{2.17}$$

where α is the attenuation constant. In practice, it is common to express α in units of dB/km as stated above. Modern manufacturing processes allow the attenuation constant to be as low as 0.2 dB/km in the 1560 nm region of interest and thus α is negligible on the length scales in the context of this thesis. However, the fiber links of the European XFEL will have lengths up to 3.5 km and the fiber loss in the optical transmission system can become relevant. Furthermore, the actual losses are larger because of fiber bending and splicing, as well as from using connectors in the transmission lines and must be taken into account in the initial design and layout of optical fiber installations.

2.3.1 Pulse Propagation Equation

The description of the propagation of short and ultrashort laser pulses with durations from few tens of femtoseconds down to ~ 10 fs in optical fibers always must respect dispersive and nonlinear effects, which influence the temporal and spectral properties of the pulses. In order to derive the pulse propagation equation some assumptions and simplifications have to be made, especially regarding the induced polarization $\boldsymbol{P}$ whose actual tensor form can only be calculated from quantum mechanics. Here, however, a scalar approach is made with the optical field assumed to maintain its polarization along the fiber and it is assumed that its magnitude is small enough, such that it can be treated perturbatively. Furthermore, the response of the material to an electric field is assumed to be instantaneous, which is justified by the fact that the time-scale of the electron reconfiguration in the material is in the order of 0.1 fs and much smaller than the optical pulse duration. This allows to expand the polarization in powers of the electric field

$$\boldsymbol{P}(\boldsymbol{r},t) = \underbrace{\varepsilon_0 \chi^{(1)} \boldsymbol{E}(\boldsymbol{r},t)}_{P_{\mathrm{L}}(\boldsymbol{r},t)} + \underbrace{\varepsilon_0 \chi^{(2)} \boldsymbol{E}^2(\boldsymbol{r},t) + \varepsilon_0 \chi^{(3)} \boldsymbol{E}^3(\boldsymbol{r},t) + \ldots}_{P_{\mathrm{NL}}(\boldsymbol{r},t)} \equiv \boldsymbol{P}_{\mathrm{L}}(\boldsymbol{r},t) + \boldsymbol{P}_{\mathrm{NL}}(\boldsymbol{r},t)\,. \tag{2.18}$$

The $\chi^{(2)}$-term is responsible for sum-, difference- and second-harmonic generation and the most important effect for nonlinear optical crystals (see chapter 3 on page 47 ff.), whereas the $\chi^{(3)}$-term causes self- and cross-phase modulation, as well as the KERR effect which are dominant in the case of fiber optics. Similar to the previous section the electric field vector $\boldsymbol{E}(\boldsymbol{r},t)$ is written as a product of a slowly varying pulse envelope $A(z,t)$ and a linear phase term:

$$\boldsymbol{E}(\boldsymbol{r},t) = \frac{1}{2}\,\hat{\boldsymbol{x}}\left(F(x,y)\,A(z,t)\,e^{i\beta_2 z - i\omega t}\right) \tag{2.19}$$

with $\hat{\boldsymbol{x}}$ as a unit vector perpendicular to the direction of propagation. For simplicity, the modal distribution is assumed to be GAUSSian, $F(x,y) = \exp\left\{-(x^2+y^2)/\sigma_w^2\right\}$ with the width σ_w calculated from a fit of the exact BESSEL distribution to a GAUSSian form. The propagation dynamics is then completely determined by the longitudinal pulse envelope function $A(z,t)$ and lengthy algebra finally lead to the pulse propagation equation or generalized nonlinear SCHRÖDINGER equation (NLSE):

$$\frac{\partial A}{\partial z} + \frac{\alpha}{2}A + \frac{i\beta_2}{2}\frac{\partial^2 A}{\partial t'^2} - \frac{\beta_3}{6}\frac{\partial^3}{\partial t'^3} = i\gamma\left(|A|^2 A + \frac{i}{\omega_0}\frac{\partial}{\partial t'}\left(|A|^2 A\right) - T_R A\frac{\partial |A|^2}{\partial t'^2}\right) \tag{2.20}$$

with a moving frame of reference $t' = t - z/v_{gr} = t - \beta_1 z$ traveling with the pulse at the group velocity $v_{gr} = 1/\beta_1$. The quantities β_i are related to dispersive effects, which are, together with the loss of the fiber, described by the left-hand side of the equation and explained in the following section. The right-hand side of the NLSE accounts for the nonlinear effects of self- and cross-phase modulation, as discussed in sections 2.3.6 (page 30 f.) and 2.3.7 (page 32 f.). Additionally, two other effects, which occur for very short and very broadband pulses are taken into account: Self-steepening, described by the term proportional to ω_0^{-1}, causes a reduction of the velocity with which the peak of the pulse travels and by that an increase of the slope of the trailing part of the pulse. The RAMAN-induced frequency shift, accounted for with the term proportional to T_R, leads to a transfer of energy of the shorter wavelength part of the spectrum to the longer wavelength in broadband optical spectra, and can not be neglected for very short pulses with durations $\lesssim 100$ fs.

Solution of the Pulse Propagation Equation

When fiber losses, $\alpha = 0$, as well as the higher-order effects of self-steepening and RAMAN-shift are neglected, the generalized nonlinear SCHRÖDINGER equation reduces to the simple form

$$\frac{\partial A}{\partial z} = i\gamma|A|^2 A - \frac{i\beta_2}{2}\frac{\partial^2 A}{\partial t'^2} \qquad \text{with} \qquad \gamma = \frac{n_2\omega_0}{c_0 S_{eff}}, \tag{2.21}$$

where S_{eff} is the effective core area of the fiber. For negative values of β_2, it has a solution called solitary wave or soliton. In this case, there exists a combination of the pulse duration which is related to the parameter β_2 and the pulse energy which is connected to the parameter γ, where the right-hand side of Eq. 2.21 cancels out, thus leading to $\partial A/\partial z = 0$. Physically, there must be a balance between dispersion and nonlinearity and it is obvious that this balance depends strongly on the type of fiber or a segment of different fibers. When this balance is given, the characteristic pulse shape of an optical soliton is given by a hyperbolic secant

$$|A(t)|^2 = \sqrt{\frac{|\beta_2|}{\gamma\tau_p^2}}\,\operatorname{sech}\left(\frac{t}{\tau_p}\right) = \sqrt{\frac{|\beta_2|}{\gamma\tau_p^2}}\,\frac{1}{\cosh(t/\tau_p)} \tag{2.22}$$

and it can propagate indefinitely without changing its shape.

The complete derivation of Eqs. 2.20 and 2.21 and their solutions, can be found in diverse text-

books, such as [Agro7], with some additional remarks in [Wino8]. In practice, the solution of the pulse propagation equation is retrieved by numerical means, mostly based on the split-step Fourier method, also described in [Agro7].

2.3.2 Chromatic Disperion

As the light is guided in glass the dependence of the material's refractive index $n(\lambda)$ (or $n(\omega)$) on the wavelength (or optical frequency) plays a critical role in the propagation of short pulses, because different spectral components of the pulse travel with different speed given by the group velocity $v_{\mathrm{gr}}(\omega) = c_0/n(\omega)$, which is equivalent to the statement that the different spectral components experience a different phase shift over a length L

$$\phi(\omega) = n(\omega) \cdot k \cdot L = \beta(\omega) \cdot L\,, \qquad \beta(\omega) = n(\omega) \cdot k\,. \tag{2.23}$$

The so-called mode-propagation constant $\beta(\omega)$ can be expanded into a Taylor series

$$\beta(\omega) = n(\omega)\frac{\omega}{c_0} = \beta_0 + \beta_1(\omega - \omega_0) + \frac{1}{2}\beta_2(\omega - \omega_0)^2 + \frac{1}{6}\beta_3(\omega - \omega_0)^3 + \ldots \tag{2.24}$$

with $\beta_j = (\mathrm{d}^j\beta/\mathrm{d}\omega^j)_{\omega=\omega_0}$ and $j = 0, 1, 2, \ldots$. The parameter β_1 describes the movement of the envelope of an optical pulse with the group velocity v_{gr}, whereas the parameter β_2 represents the group velocity dispersion (GVD) and is responsible for pulse broadening. It should be noted that in literature and data sheets often the dispersion parameter D is given which is related to β_2 by

$$D = \frac{\mathrm{d}\beta_1}{\mathrm{d}\lambda} = -\frac{2\pi c}{\lambda^2}\beta_2 \tag{2.25}$$

The third-order dispersion (TOD) term β_3 in Eq. 2.24 should be taken into account for the propagation of optical pulses with durations in the order of 100 fs or less, especially for fibers with lengths $L > 1$ km, for example in case of the European XFEL, for example.

2.3.3 Dispersive Pulse Broadening

For the theoretical treatment and also for practical application, it is useful to introduce two characteristic lengths, namely the dispersion length L_{D} and the nonlinear length L_{NL}, to distinguish between the dispersion dominated pulse evolution in an optical fiber or the second important regime, where the evolution is governed by nonlinear effects. They are defined as

$$L_{\mathrm{D}} = \frac{\tau_p^2}{|\beta_2|} \qquad \text{with the pulse duration } \tau_{\mathrm{p}} \tag{2.26a}$$

$$L_{\mathrm{NL}} = \frac{1}{\gamma P_0} \qquad \text{with the pulse peak power } P_{\mathrm{peak}} \tag{2.26b}$$

and provide length scales where the dispersive or nonlinear effects become important. From the scaling relation N^2_{DNL} the governing effect can be estimated:

$$N^2_{\mathrm{DNL}} \equiv \frac{L_{\mathrm{D}}}{L_{\mathrm{NL}}} = \frac{\gamma P_0 \tau_{\mathrm{p}}^2}{|\beta_2|} \begin{cases} \ll 1 & \text{dispersion dominant regime} \\ \gg 1 & \text{nonlinearity dominant regime.} \end{cases} \tag{2.27}$$

The pulse broadening caused by GVD can most easily be considered as a phase shift applied in the frequency domain using Eqs. 2.23 and 2.24. Using a normalized amplitude U and a time scale T' normalized to the initial pulse duration τ_{p} as per

$$A(z,T') = \sqrt{P_0}\, e^{-\alpha z/2} U(z,T') \qquad \text{and} \qquad T' = \frac{t'}{\tau_{\mathrm{p}}}\,, \tag{2.28}$$

the nonlinear Schrödinger equation 2.20 can be rearranged, called normalized NLSE and satisfied by $U(z,T')$:

$$i\frac{\partial U}{\partial z} = \frac{\mathrm{sgn}(\beta_2)}{2L_{\mathrm{D}}}\frac{\partial^2 U}{\partial T'^2} - \frac{e^{-\alpha z}}{L_{\mathrm{NL}}}|U|^2\, U\,. \tag{2.29}$$

For purely dispersive pulse broadening with $L_{\mathrm{NL}}^{-1} = 0$, this equation can be solved by Fourier transformation of the amplitude $U(z,T')$

$$U(z,T') = \frac{1}{2\pi}\int_{-\infty}^{\infty} \tilde{U}(z,\omega) e^{-i\omega T'}\,\mathrm{d}\omega \tag{2.30}$$

because it fulfills the following ordinary differential equation which is then solved by $\tilde{U}(z,\omega)$:

$$i\frac{\partial \tilde{U}}{\partial z} = -\frac{\beta_2}{2}\omega^2 \tilde{U} \qquad \Rightarrow \qquad \tilde{U}(z,\omega) = \tilde{U}(0,\omega) e^{i\frac{\beta_2}{2}\omega^2 z}\,. \tag{2.31}$$

Thus, each spectral component experiences a phase shift depending on on both its frequency and the distance the pulse propagated in the fiber and the general solution for Eq. 2.29 is given by

$$U(z,T') = \frac{1}{2\pi}\int_{-\infty}^{\infty} \tilde{U}(0,\omega) e^{i\frac{\beta_2}{2}\omega^2 z - i\omega T'}\,\mathrm{d}\omega \quad \text{with} \quad \tilde{U}(0,\omega) = \int_{-\infty}^{\infty} U(0,T') e^{i\omega T}\mathrm{d}T \tag{2.32}$$

which is valid for an arbitrary pulse shape. However, for soliton pulses with their sech^2-shape, these integrals can not be solved analytically. For qualitatively very similar behaving Gaussian pulses $U(0,t) = \exp\left\{-t^2/(2\tau_{\mathrm{p}}^2)\right\}$ the evaluation leads to

$$U(z,t) = \frac{\tau_{\mathrm{p}}}{\sqrt{\tau_{\mathrm{p}}^2 - i\beta_2 z}}\, e^{-\frac{t^2}{2(\tau_{\mathrm{p}}^2 - i\beta_2 z)}} \tag{2.33}$$

After propagation through the fiber the pulse shape is conserved but broadened by a factor depending on the dispersion length L_D:

$$\tau_p(z) = \tau_{p,0}\sqrt{1 + (z/L_D)^2}\,, \tag{2.34}$$

where $\tau_{p,0}$ is the duration of the pulse entering the fiber. This equation can be used, for example, to calculate the pulse durations in the fiber links (see 6.1.2, page 135 f.). A second notable consequence is that the pulse becomes chirped, although the initial pulse had no phase modulation. This is discussed in more detail in [Agro7].

2.3.4 Dispersion Management

As it will be discussed in the later chapters of this thesis, the fiber link end-stations of the optical synchronization systems and the fiber link stabilization scheme itself require short pulse durations closely to the launched reference pulse, making the GVD-induced pulse broadening a serious issue. This can be resolved by the combination of the standard telecommunication fiber and so-called *dispersion-shifted* or dispersion compensating fiber (DCF) in a way that the average GVD is minimized or ideally cancels out completely. The normalized amplitude after the propagation of the pulse through a fiber of length $L_\Sigma = L_1 + L_2$ consisting of two segments with different dispersion properties is according to Eq. 2.32 given by

$$U(L_\Sigma, T') = \frac{1}{2\pi}\int_{-\infty}^{\infty}\tilde{U}(0,\omega)e^{\frac{i}{2}\left(\beta_{2,1}L_1+\beta_{2,2}L_2\right)-i\omega T'}\,\mathrm{d}\omega\,. \tag{2.35}$$

Therefore, the condition for dispersion compensation is, together with Eq. 2.25

$$D_1 \cdot L_1 + D_2 \cdot L_2 = 0 \tag{2.36}$$

which ensures that the pulse duration at the end of the fiber at $z = L_\Sigma$ is the same as the initial one at $z = 0$, while the pulse duration can change dramatically in the intermediate individual segments. In the long fiber links discussed later, Eq. 2.36 is satisfied by compensating the GVD of the standard SMF with relatively short segments of DCF (see appendix D on page 239 ff. for technical details).

2.3.5 Polarization Mode Dispersion

When the polarization of light is additionally considered, a single-mode fiber is not truly single-mode because it supports in reality two modes with orthogonal states of polarization (SOP). These would not couple to each other in an ideal fiber perfect cylindrical symmetry, but in reality this symmetry is broken by small variations of the core shape and concentricity of core and cladding due to the manufacturing process or mechanical stress on the fiber. This results in a modification of the mode propagation constant β along the x and the y directions and defined by the modal birefringence parameter B_m and the beat length L_B on which the two modes mix and exchange their power in a

periodic manner:

$$B_\mathrm{m} = \frac{|\beta_x - \beta_y|}{k_0} = |n_x - n_y| \qquad \Rightarrow \qquad L_\mathrm{B} = \frac{2\pi}{|\beta_x - \beta_y|} = \frac{\lambda}{B_\mathrm{m}} \tag{2.37}$$

where n_x and n_y are the modal refractive indices for the states of polarization. The random changes of the value of B_m in real fibers thus result in a random change of the polarization of the light launched into the fiber. If an input pulse excites both states of polarization, which is usually the case, both components experience different group velocities and the pulse broadens during propagation through the fiber. This effect is called polarization mode dispersion (PMD). Its extent can be estimated from the time delay Δt at the end of a fiber with the length L for the both states and a constant value of B_m

$$\Delta t = \left| \frac{L}{v_{\mathrm{gr},x}} - \frac{L}{v_{\mathrm{gr},y}} \right| = L \cdot |\beta_{1,x} - \beta_{1,y}| \,. \tag{2.38}$$

Due to the statistical nature of the fiber imperfections, however, the effect of PMD is most commonly described by the root-mean-square of Δt, which can be approximated by

$$\sigma_{\Delta t} \approx \Delta\beta_1 \sqrt{2\,L\,l_c} \equiv D_\mathrm{p} \sqrt{L} \qquad \text{with} \qquad \Delta\beta_1 = \frac{\Delta\tau}{L} \tag{2.39}$$

for lengths $L > 100\,\mathrm{m}$ using the differential group delay $\Delta\tau$ and the correlation length l_c on which the polarization states remain correlated. The PMD parameter D_p is typically in the order of $\lesssim 1\,\mathrm{ps}/\sqrt{\mathrm{km}}$ and although in practice thermal and humidity drifts will influence the optical synchronization system more significantly, the effect of PMD-induced group velocity changes and pulse broadening must be kept in mind. In polarization maintaining fibers (PMFs) a large amount of birefringence is intentionally introduced to the fiber, for example by implementing stress-inducing elements into the cladding. By that the cylindrical symmetry is broken intentionally, but the fluctuations of the birefringence parameter are strongly suppressed.

2.3.6 Self-Phase Modulation

The second effect to be considered for the propagation of light through an optical fiber is the phenomenon of self-phase modulation (SPM) which is caused by the intensity dependence of the refractive index $n(\omega, I) = n_0 + n_2 \cdot I$ on the intensity in nonlinear media. It can therefore be seen as temporal analog to the self-focusing for $n_2 > 0$ (see section 2.4.2, page 36). It has in particular to be taken into account when the nonlinear length is smaller than the dispersive length $L_\mathrm{NL} \ll L_\mathrm{D}$, and leads to an intensity dependent phase shift. With the assumptions of a pulse length $\tau_\mathrm{p} \geq 10\,\mathrm{ps}$ and disregarding the GVD effect by setting $\beta_2 = 0$ this phase shift can calculated from Eq. 2.29, which simplifies to

$$\frac{\partial U}{\partial z} = \frac{i e^{-\alpha z}}{L_\mathrm{NL}} |U|^2 \, U \,. \tag{2.40}$$

It can be solved with the ansatz $U = u \cdot e^{i\phi_{\mathrm{NL}}}$ with an amplitude u not changing along the fiber, i.e. $\partial u/\partial z = 0$, as the remaining differential equation for the phase term can be integrated:

$$\frac{\partial \phi_{\mathrm{NL}}}{\partial z} = \frac{e^{-\alpha z}}{L_{\mathrm{NL}}}\, u^2 \qquad \Rightarrow \qquad \phi_{\mathrm{NL}}(L, T') = |U(0, T')|^2\, \frac{L_{\mathrm{eff}}}{L_{\mathrm{NL}}}\,. \tag{2.41}$$

There, $U(0, T')$ is the normalized amplitude of the initial laser pulse at $z = 0$ and L_{eff} the effective length

$$L_{\mathrm{eff}} = \frac{1 - e^{-\alpha L}}{\alpha}\,. \tag{2.42}$$

This quantity accounts for fiber losses, which effectively shorten the fiber length L. The maximum phase shift is given by $\phi_{\mathrm{NL,max}} = L_{\mathrm{eff}}/L_{\mathrm{NL}} = \gamma P_0 L_{\mathrm{eff}}$, which equals to unity just when the pulse propagated the length L_{NL} in the fiber. The time dependence of the nonlinear phase leads to spectral changes because of the different instantaneous frequency across the pulse

$$\delta\omega = -\frac{\partial \phi_{\mathrm{NL}}}{\partial T'} = -\left(\frac{L_{\mathrm{eff}}}{L_{\mathrm{NL}}}\right) \frac{\partial}{\partial T'} |U(0, T')|^2\,. \tag{2.43}$$

As a result, the pulse becomes chirped and the generated frequency components during propagation broaden its spectrum continuously. In case of an unchirped or positively chirped initial pulse, SPM always leads to spectral broadening, whereas on the other hand pulses with a negative initial chirp are spectrally compressed. It must be emphasized that the equations above only hold for comparatively long pulses $\tau_{\mathrm{p}} \geq 10\,\mathrm{ps}$, where the dispersive length L_{D} is much larger than the nonlinear length L_{NL} and also larger than the fiber length L. As the pulses becomes shorter, effects from both the SPM and the GVD have to be considered in combination. This leads to other phenomena, such as the support for optical solitons in the anomalous-dispersion regime or pulse compression in the normal-dispersion regime. In this case, the normalized nonlinear Schrödinger equation must used in the full form

$$i\,\frac{\partial U}{\partial \xi} = \frac{\mathrm{sgn}(\beta_2)}{2}\,\frac{\partial^2 U}{\partial T'^2} - N^2 e^{-\alpha z} |U|^2\, U \tag{2.44}$$

with $\xi = z/L_{\mathrm{D}}$ and $T' = t'/\tau_{\mathrm{p}}$ as normalized distance and normalized time, whereas $\mathrm{sgn}(\beta_2) = \pm 1$ denotes the dispersion regime. Here the scaling relation N^2_{DNL} from Eq. 2.16 is useful, because the the calculated results for a particular value of N hold for different parameter pairs of τ_{p} and P_0, such as $\tau_{\mathrm{p}} = 1\,\mathrm{ps}$ and $P_0 = 1\,\mathrm{W}$, or $\tau_{\mathrm{p}} = 0.1\,\mathrm{ps}$ and $P_0 = 100\,\mathrm{W}$. As the optical synchronization system is based on pulses with durations in the order of 100 fs with peak power ranging up to the kilowatt region, and furthermore the real fiber lengths are in the order of both the dispersive and nonlinear lengths, the optical designs of the individual devices have to be thought out carefully.

2.3.7 Cross-Phase Modulation

If there are two or more pulses propagating in an optical fiber they can interact with each other through the nonlinearity of the medium. Besides BRAGG and BRILLOUIN scattering, harmonic generation and four-wave mixing, the KERR effect couples the light waves through cross-phase modulation (XPM) without any energy transfer between the waves. The physical mechanism is based on the fact that the effective refractive index experienced by one of the pulses does not only depend on the intensity of that particular pulse, but also on the intensity of the other propagating pulse. It is obvious that the light waves have to differ in one of their properties, normally being the wavelength or their state of polarization (see [Agro7, Agro8] and the given references for an extensive review of this topic). In the synchronization system the distribution of the pulse trains is realized with optical fibers in which two soliton pulse trains counter-propagate, such that XPM-induced effects might come into play. However, this has not yet been taken into account for, but as it will bee seen in the following chapters, a comprehensive theoretical treatment of the complete fiber-optic part os the system will be inevitable in the future, especially in the presently on-going planning stage for the synchronization system for the European XFEL.

2.4 Mode-Locking Techniques

Laser pulses with femtosecond duration can only be generated in the stationary regime of the resonator, i.e. the stored energy stays constant on a timely average. This can be achieved by mode-locking which is based on the excitation of a large number of longitudinal resonator modes with a fixed phase relation. The wavelength, wave vector and frequency of the n-th mode is given by the standing-wave condition for a resonator of the length L:

$$n\lambda_n = 2L \qquad \Rightarrow \qquad \omega_n = n \cdot \frac{\pi c_0}{L}\,, \quad k_n = n \cdot \frac{\pi}{L} \tag{2.45}$$

which leads to the mode distance in the frequency domain of

$$\Omega = \omega_{n+1} - \omega_n = \frac{\pi c_0}{L}\,. \tag{2.46}$$

In principle an arbitrary number of modes can coexist in the resonator. The electric field is the superposition of the fields of all the individual modes described by plane waves (Eq. 2.5, p. 22)

$$E(z,t) = \sum_n E_n(z,t) = \sum_n E_{0,n} e^{ik_n z - i\omega_n t} \qquad \text{with} \qquad E_{0,n} = |E_{0,n}| \cdot e^{i\phi_n}\,. \tag{2.47}$$

As the modes build up independently their phases relation is statistically distributed and the summands vanish on average:

$$\sum_{n \neq m} E_m(z,t) E_n^\star(z,t) = 0\,. \tag{2.48}$$

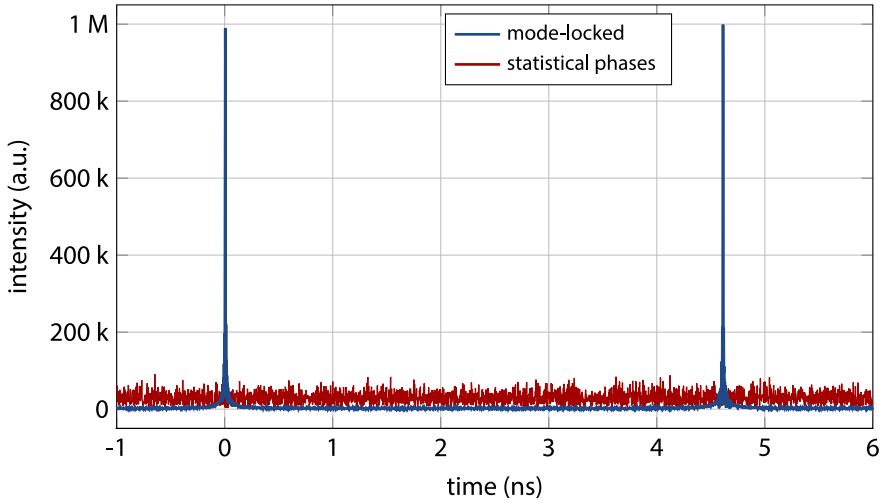

Figure 2.1 | Calculated intensity for the superposition of 1000 resonator modes. The graph shows a comparison between the mode-locked state and the case where random phases are assumed.

In this case the intensity for the number of coexisting modes $N \gg 1$ is given by

$$I(z,t) \propto E(z,t)E^{\star}(z,t) = \sum_{m=1}^{N}\sum_{n=1}^{N} E_m(z,t)E_n^{\star}(z,t)$$
$$= \sum_{m=1}^{N} E_m(z,t)E_m^{\star}(z,t) = \sum_{m=1}^{N} |E_{0,m}|^2 \tag{2.49}$$

which further simplifies with the assumption of equal amplitudes of every mode to

$$I(z,t) = \sum_{m=1}^{N} |E_0|^2 = N|E_0|^2 = N \cdot I_0 \,, \tag{2.50}$$

i.e. the intensity is spatiotemporally constant and the sum of the intensities I_0 of the individual modes. When the phases of all modes, however, is equal and without loss of generality $\phi_n = 0$, the evaluation of Eq. 2.47 yields

$$I(z,t) \propto |E_0|^2 \sum_{m=1}^{N}\sum_{n=1}^{N} e^{i(k_m-k_n)z - i(\omega_m-\omega_n)t} = |E_0|^2 \sum_{m=1}^{N} e^{i(m-n)\frac{\Omega}{c}(z-ct)} \tag{2.51}$$

and is illustrated in Fig. 2.1. If the condition

$$\frac{\Omega}{c}(z-ct) = 2\pi \cdot j \quad \Leftrightarrow \quad z - ct = 2L \cdot j \qquad \text{with } j = 0, 1, 2, 3, \ldots \tag{2.52}$$

is fulfilled, the exponential function in Eq. 2.51 equals unity which leads to a maximum intensity of

$$I_{\max} = N^2|E_0|^2 = N^2 \cdot I_0 \,. \tag{2.53}$$

The spatial and temporal distance of these maxima (the "pulses") can be calculated from Eq. 2.52. At any time there exists one pulse in the resonator and the periodic succession is the resonator's round-trip time T. The inverse of this is called repetition rate of the oscillator:

$$\Delta z = 2L\,, \qquad \Delta t = \frac{2L}{c} \equiv T_{\mathrm{rep}} \qquad \Rightarrow \qquad f_{\mathrm{rep}} = \frac{1}{T_{\mathrm{rep}}}\,. \tag{2.54}$$

To calculate the width of the intensity maxima at a fixed time $t = t_0$ or at a fixed spatial position $z = z_0$ in the resonator, Eq. 2.51 can be considered as interference of N plane waves. Using the textbook equation [YY07, PH98] the intensity is given by (compare interference at a grating with replaced wave vectors by the wave vector difference Δk)

$$I(t) = I_0 \frac{\sin^2\left(\frac{N\Omega}{2}\,t\right)}{\sin^2\left(\frac{\Omega}{2}\,t\right)} \tag{2.55}$$

which leads to the full-width at half-maximum ΔT

$$I(\Delta T) = \frac{I_{\max}}{2} \qquad \Rightarrow \qquad \Delta T = \frac{1}{N}\,\frac{2L}{c} = \frac{1}{N}\,T\,. \tag{2.56}$$

As a result, the pulse shortens with an increasing number of modes. For instance, in a 100 fs (rms) pulse generated by a $f_{\mathrm{rep}} = 200$ MHz laser the number of involved modes is in the order of 2×10^4.

Beside the mandatory broadband gain medium supporting a large number of resonator modes a mechanism to initiate the phase-lock of these modes must be present. The fundamental idea can be understood in the frequency domain, as illustrated in Fig 2.2: The resonator losses (or the gain) has to be modulated with the intermode frequency Ω which leads to the generation of side-bands around the individual modes. These couple to the neighboring modes and force them to oscillate.

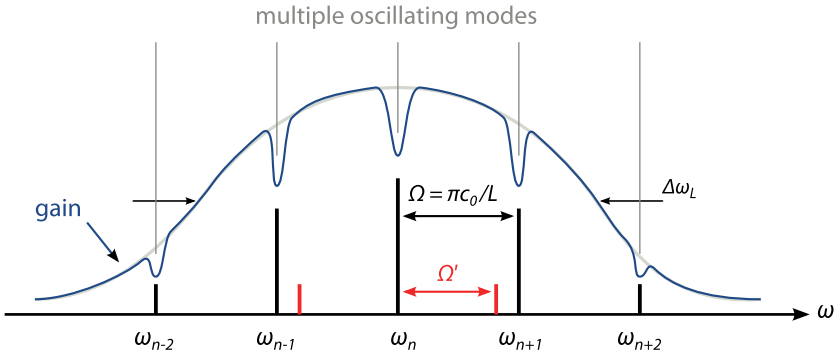

Figure 2.2 | Oscillating modes in a laser resonator with positive net gain. The resonator length is L resulting in a mode spacing of $\Omega = \pi c_0 / L$. Additionally, side-bands at spacings of Ω' are shown which may result e.g. from acousto-optic modulation (see section 2.4.5, p. 39 f.).

As this modulation concerns every mode, all modes supported by the gain medium get a fixed phase relation. By inserting a saturable absorbing medium into the resonator the pulse itself generates

the loss-modulation, because every time the pulse travels through the absorber it becomes saturated and the absorption loss is decreased. As the round-trip time is $T = 2\pi/\Omega$ this modulation occurs periodically in Ω and a single pulse is selected. This technique is called "passive" or "self-induced mode-locking" and starts in most laser systems spontaneously from noise. If not, one intensity maximum to saturate the absorber initially has to be generated by an external disturbance. Technically this is most commonly realized by quickly shaking a mirror of the resonator. Secondly, a laser can be "actively mode-locked" resulting from an external modulation at the frequency Ω either of the resonator losses (by inserting an acousto-optic modulator inside the resonator, for instance) or of the gain of the amplifying medium (for example by pumping it with another mode-locked laser). More details are considered in the following sections, but first the relation between the pulse duration and the spectral bandwidth is briefly to be discussed.

2.4.1 Relation between Pulse Duration and Spectral Bandwidth

The spectral content of a light pulse can be calculated from the Fourier transformation of its time evolution function. In contrast to a plane wave oscillating with the angular frequency ω_0, resulting in the Dirac distribution $\delta(\omega_0)$ in frequency space, the frequency content of a finite pulse with the duration ΔT is larger than this single frequency. Starting with the general Fourier transformations

$$E(t) = \frac{1}{\sqrt{2}} \int_{-\infty}^{\infty} \tilde{E}(\omega) e^{-i\omega t} \mathrm{d}\omega \,, \qquad \tilde{E}(\omega) = \frac{1}{\sqrt{2}} \int_{-\infty}^{\infty} E(t) e^{i\omega t} \mathrm{d}t \tag{2.57}$$

and using the statistical definitions

$$\langle \Delta T^2 \rangle = \frac{\int t^2 |E(t)|^2 \mathrm{d}t}{\int |E(t)|^2 \mathrm{d}t} \,, \qquad \langle \Delta \omega^2 \rangle = \frac{\int \omega^2 |\tilde{E}(\omega)|^2 \mathrm{d}\omega}{\int |\tilde{E}(\omega)|^2 \mathrm{d}\omega} \,, \tag{2.58}$$

it can be shown that these quantities are related by the inequality

$$\Delta T \cdot \Delta \omega \geq \frac{1}{2} \tag{2.59}$$

which is directly related to the quantum mechanical uncertainty principle. This implies that for the production of a light pulse with a particular duration enough spectral bandwidth must be available. A Gaussian pulse, for example, with 1 ps full-width at half-maximum duration has a minimal bandwidth of 441 GHz. The currently routinely achievable pulse durations of Ti:sapphire lasers with a center wavelength at about 800 nm are in the order of 10 fs which require a full-width at half maximum (FWHM) bandwidth exceeding 60 nm, calculated using $|\Delta\lambda/\lambda_0| = \Delta\nu/\nu$. Taking the wings of the distribution into account, the spectra of such short pulses can cover almost the complete the visible spectrum (VIS).

Equality to 1/2 in Eq. 2.59 can only be reached with Gaussian time and spectral envelopes, and if the equality holds, the pulse is said to be "transform-limited" or "Fourier-limited". Since the actual

value of transform limiting factor depends on the actual pulse shape, Eq. 2.59 is usually written as

$$\Delta T \cdot \Delta\omega = 2\pi\, \tau_{\mathrm{FWHM}} \cdot \Delta\nu \geq 2\pi\, c_B \tag{2.60}$$

for practical reasons, where τ_{FWHM} is the full-width at half-maximum pulse duration related to the corresponding physical pulse shape and c_B a constant with a magnitude of 1. The left-hand side of the inequality is called time-bandwidth product (TBP). Table 2.1 gives an overview of the relations for

Table 2.1 | Values of the laser pulse transform-limiting constant. The constant is for practical reasons used in the inequality $\tau_{\mathrm{FWHM}} \cdot \Delta\upsilon \geq c_B$ with τ_{FWHM} and $\Delta\upsilon$ being FWHM quantities.

temporal shape	$E(t) \propto$	τ_{FWHM}	c_B
Gaussian function	$\exp\{-t^2/(2\tau_p^2)\}$	$2.355\ \tau_p$	0.441
hyperbolic secant	$\mathrm{sech}(t/\tau_p)$	$1.763\ \tau_p$	0.315
Lorentz function	$(1 + (t/\tau_p)^2)^{-1}$	$1.287\ \tau_p$	0.142

several pulse profiles. In the laser systems considered within this thesis, Gaussian and sech-pulses are of interest. The basics for the discussed experimental determination of the pulse duration are explained in section 3.5.2 on page 58 f.

2.4.2 Kerr-Lens Mode-Locking

Particularly in titanium-sapphire laser systems the resonator modes can be phase-locked without any external modulation or saturable absorber by a mechanism called "self-locking" of the modes. For such a situation to arise, a highly nonlinear gain medium must induce a transverse narrowing of the pulse at each of its round-trips through the resonator to favor strong intensity maxima at the expense of weak ones, because the strong ones are less subject to resonator losses. This is realized in the Kerr lens mode-locking (KLM) technique where the refractive index of the gain medium depends on the intensity $n = n_0 + n_2 \cdot I$ which is known as Kerr effect. A Gaussian wave therefore experiences an inhomogeneous refractive index while passing the medium. For a positive n_2 the refraction on the axis of the beam is stronger than away from it. By this, the more intense part of the beam is focused stronger as the amplifying medium behaves like a converging lens and a particular single intensity maximum is selected, similar to the passive mode-locking based on a saturable absorbing medium. Additionally, the dependence of the refractive index on the intensity has an important consequence for the time structure of the wave, because the rapid variation of $I(t)$ in time implies a rapid variation of the phase of the pulse. This self-modulation broadens the spectrum of the pulse, i.e. more modes can be supported, and by that the pulse shortens until an equilibrium with the dispersion of the group velocity, which tends to lengthen the pulse, is reached. To minimize the effect from GVD, for example two or four prisms are usually inserted into a titanium-sapphire laser's resonator for dispersion compensation [DR06].

2.4.3 Nonlinear Polarization Evolution

While self- and cross-phase modulation are usually unwanted effects in optical transmission systems they are intentionally exploited in the nonlinear polarization evolution (NPE), or nonlinear polarization rotation (NPR) mode-locking technique [HFH+91]:

Due to the Kerr effect the rotation of the state of polarization of two orthogonally polarized components of a single pulse is intensity dependent and the more-intense peak is rotated further than the wings of the pulse in the fiber. In a ring laser with a short free-space section, as shown in Fig. 2.3, the required elliptical polarization is achieved with a quarter-wave retarder before the light enters the fiber. After the round trip where the pulse experienced the nonlinear polarization rotation two

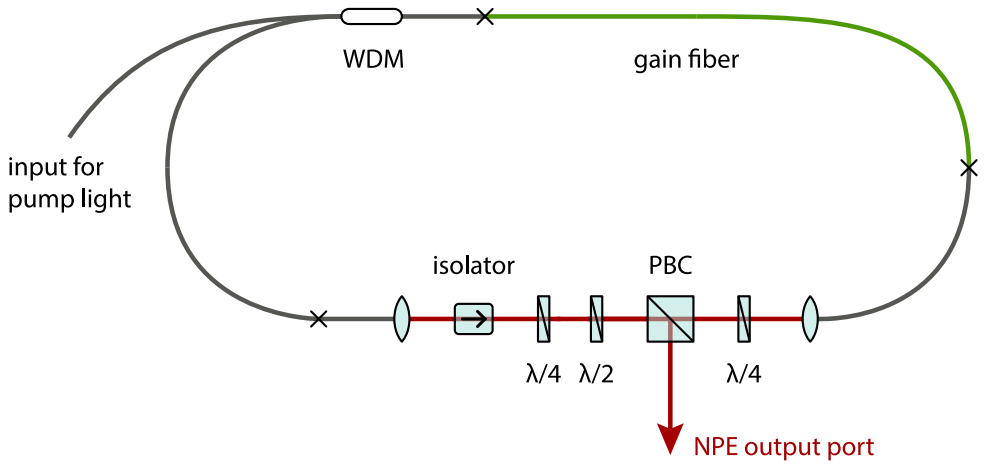

Figure 2.3 | Sketch of a simple fiber ring laser based on nonlinear polarization evolution. The short free-space part of the resonator is used for polarization control and by that establishing the mode-lock state. An optical Faraday isolator ensures unidirectional operation (adapted from [Win08]).

additional retarders are required to rotate the polarization into a state where the center is transmitted through the polarizing beam cube (PBC), thus remaining in the cavity, whereas the wings of the pulse are coupled out. Hence, the combination of the retarders and the polarizing beam splitter effectively act as an artificial saturable absorber. The total phase shift between the two components of the state of polarization with intensities I_x and I_y is the difference of the individual phase shifts caused by SPM and XPM in the fiber of the length L

$$\Delta\phi = \phi_x - \phi_y = L \cdot \left((\beta_x - \beta_y) + \gamma(I_x - I_y) + \frac{2}{3}\gamma(I_x - I_y) \right) . \tag{2.61}$$

If this phase shift and the peak power of the intra-cavity pulse (which is also dependent on the gain of the amplifying fiber and the pump power) are properly balanced, a soliton is supported by the laser as explained in section 2.3.1 (page 25 ff.).

2.4.4 Semiconductor Saturable Absorber Mirrors

The third important mechanism for passive mode-locking is the use of a semiconductor saturable absorber mirror (SESAM), which can be applied to either fiber or bulk lasers and enables femtosecond to nanosecond pulse generation [KWK+93] with a very broad range of possible repetition rates. A SESAM is a mirror structure with an integrated saturable absorber manufactured from semiconductor materials, see Fig. 2.4. Usually, the reflection near the surface of the device is realized with a BRAGG-mirror made from a large-bandgap semiconductor like GaAs or AlAs, such that no absorption can happen in this region. The saturable absorber consists of a periodic structure of semiconductor materials with a direct bandgap slightly lower than the photon energy, like InGaAs with varying indium or arsenide ratios for operation in the $\lambda = 1.55\,\mu m$ region, such that the photons excite electron-hole pairs in the material. As the number of electron-hole pairs which can be created is limited, the absorption saturates. First, the electrons thermalize in the conduction band, occurring on time-scales < 100 fs, and then they recombine with the holes after times in the order of 10 ps to 100 ps and the material can absorb again. These time-scales define the recovery time which is one

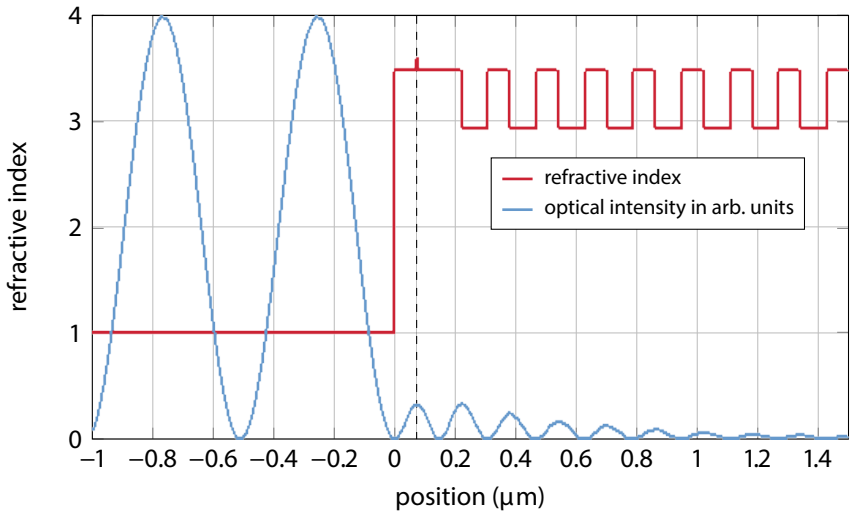

Figure 2.4 | Refractive index and corresponding characteristic optical intensity in a SESAM. The surface of the SESAM is at position 0, while the intensity distribution exhibits a local maximum where the absorber is placed (denoted by the dashed line; illustration adapted from [Pas08a]).

of the important properties in the design of a SESAM. Other critical properties are the modulation depth which defines the maximum nonlinear change of the reflectivity and the the saturation fluence which is the photon fluence of the incident short pulse required for significant saturation of the absorber. Both quantities depend strongly on the employed semiconductor materials and their thickness, as well as the wavelength of the optical field and its penetration into the device. Furthermore, unavoidable non-saturable losses have to be considered which are connected to the damage threshold and the life-time of the SESAM.

Figure 2.5 shows two possible implementations of a SESAM-based laser oscillator. In the fiber

laser, shown on the left, the resonator consists of the gain fiber with a partly reflective end serving as one resonator mirror. The second mirror is the SESAM on which the light is focused (as illustrated) or directly connected to the fiber end. Bulk lasers are build in a classical resonator configuration with

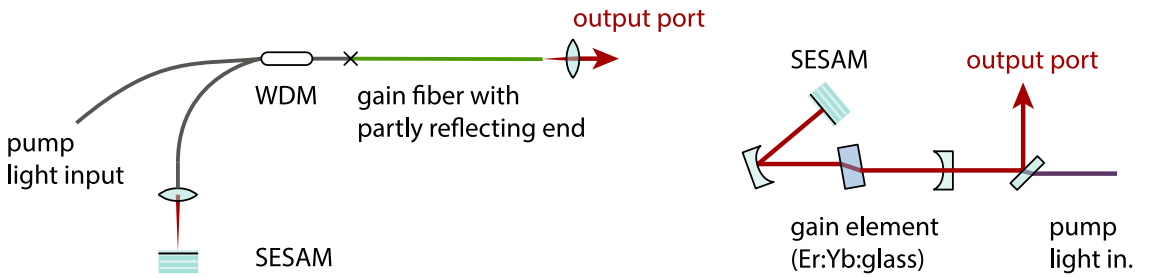

Figure 2.5 | Schematic layout of two different SESAM-based laser oscillators. Left: : Fiber laser with one resonator mirror being the SESAM, while the opposite reflection occurs at the cleave of the gain fiber. **Right:** : Miniature resonator of an Er:Yb:glass bulk laser. These types of lasers can be used in high-speed optical communication systems, with possible repetition rates up to 100 GHz [OSWK08]. Both illustrations are adapted from [Pas08a].

also one mirror being the SESAM and the other one the out-coupling mirror, and at the same time often the pump-light window. In this configuration the resonator can be build extremely small with lengths in the order of 3 mm, thus generating pulse trains with repetition rates exceeding 100 GHz relevant for high-speed telecommunication systems [OSWK08] – and not that much in the context of this thesis.

For femtosecond pulse generation, a GVD-compensating element is additionally required in the resonator. This can be realized, for example, by integrating a Gires-Tournois interferometer (GTI) right into the SESAM structure [KZF+96] for high-repetition rate lasers. The disadvantage of this approach is a relatively small supported spectral bandwidth and thus limiting the achievable pulse duration. Fiber lasers, in contrast, can utilize anomalously dispersive gain fibers eliminating the need for an additional GVD-compensating component in the resonator, thus reducing complexity [BPC+08].

2.4.5 Acousto-Optic Modulation

In contrast to the passive mode-locking techniques described in the previous sections, active mode-locking uses active elements inside the laser resonator to modulates its losses. Considering a sinusoidal modulation with the angular frequency Ω' and a modulation depth α, the time evolution of the electric field of the n-th mode can be written as

$$E_n(t) = E_0 \cos\left(\omega_n t + \phi_n\right) \cdot \left(1 - \alpha \cos(\Omega' t + \phi)\right) . \tag{2.62}$$

Using trigonometric identities Eq. 2.62 can be written as follows, which show that in the frequency domain two side-bands at either side of the mode $E_n(t)$ show up (compare also Fig. 2.2, p. 34):

$$E_n(t) = E_0 \cos(\omega_n t + \phi_n) + E_0 \frac{\alpha}{2} \cos\left((\omega_n - \Omega')t + \phi_n - \phi\right) + E_0 \frac{\alpha}{2} \cos\left((\omega_n + \Omega')t + \phi_n + \phi\right) . \quad (2.63)$$

If the modulation frequency is now close to the inter-mode frequency distance $\Omega'/(2\pi) \simeq \Omega$ of the neighboring modes $n \pm 1$, the side-bands and the longitudinal resonator modes compete inside the amplifying medium for maximum gain. The same holds for external modulation frequencies $m \cdot \Omega'$, with m being an integer, as then the resonator modes $n \pm m$ are coupled to the n-th mode. In this situation, where the modes lock their phases to the sidebands, the amplifying medium is most effectively used and causes a global mode-lock over the whole spectral distribution. This, in turn, is the condition under which the competition of the modes will give to the concentration of all electromagnetic energy of the cavity into a single pulse traveling back and forth inside it.

Usually, the acousto-optic modulator (AOM) is placed directly inside the cavity, see Fig. 2.6. The main elements of an AOM are a transparent medium –normally a crystal or glass– and a piezo-electric transducer, which excites sound waves in the medium and hereby changes of the refractive index. A traversing light beam experiences then Bragg diffraction at this periodic, and traveling, refractive index grating. The scattered beam has a different optical frequency and different direction, which can be controlled by the frequency of the sound wave. If the device is build in a "traveling-

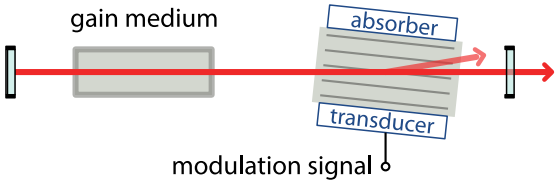

Figure 2.6 | Sketch of a laser resonator with an acousto-optic modulator. The sound wave induced change of the refractive index diffracts part of the laser beam and modulates therefore the resonator losses.

wave geometry", where the sound wave is absorbed on the opposite site of the crystal, bandwidths up to the order of 100 MHz can be achieved. In resonant designs, on the other hand, the bandwidth is reduced, but they allow larger modulation depths, which influence the optical power of the beam.

With a sufficiently high acoustic power up to 95% of the optical power can be diffracted. This allows the use of AOMs not only for resonator loss modulation, but also as pulse pickers to reduce the repetition rate of a pulse train which may be required for subsequent amplification of pulses to high energies.

2.4.6 Electro-Optic Modulation

Electro-optic modulators (EOMs) allow in general for much faster modulation frequencies than AOMs up to several GHz. They are based on the linear electro-optic Pockels effect which describes

the change of the refractive index of certain optical crystals as function of an externally applied electric field E_{ext}. As the index changes are relatively small, these can be approximated by

$$\Delta n = -\frac{n_0^3}{2} r_{\text{eff}} E_{\text{ext}} , \tag{2.64}$$

where n_0 is the unmodified refractive index and r_{eff} describes the electro-optic effect of the given crystal, including its geometry and properties of the light beam to be modulated. The most simple EOM is a phase modulator consisting of one POCKELS cell which changes the phase delay of the laser beam passing through the device depending on the driving voltage. Most commonly these types of EOMs are used together with a periodic, i. e. RF signal to stabilize the resonance frequency of an optical resonator, which may be mode-locked by other means. This is, for example, true for the FLASH photoinjector laser and will be discussed in more detail in chapter 8 on pages 167 ff. It is, however, also possible to use just these electro-optic modulators to initiate the mode-locking of a laser by generating a large number of side-bands in the optical spectrum using a large modulation depth [MBRF96] or creating high repetition rate fiber lasers by harmonic mode-locking [CD96].

Other Applications of Electro-Optic Modulators

In more sophisticated devices with additional optical elements (mainly polarizers, half- and quarter-wave retarders), electro-optic modulators can also be used for polarization modulation, or more importantly amplitude modulation. These are in fact not used in the context of mode-locking, but the key component of the electron BAMs as part of the synchronization system (see section 4.4, p. 67 f. and [Loe09, Boc13]). The modulators can either be built from bulk components or as *photonic integrated circuit* most commonly based on waveguide structures in nonlinear optical crystals, resulting in a very high phase stability. Figure 2.7 shows such a MACH-ZEHNDER-type electro-optic amplitude modulator, where the light wave is split into two arms and depending on the applied RF signal, it experiences a different phase delay. This results in an amplitude modulation when the waves are recombined, because of the constructive and destructive interference depending on the phase relationship between the two arms. In this geometry, high bandwidths exceeding 10-gigahertz region

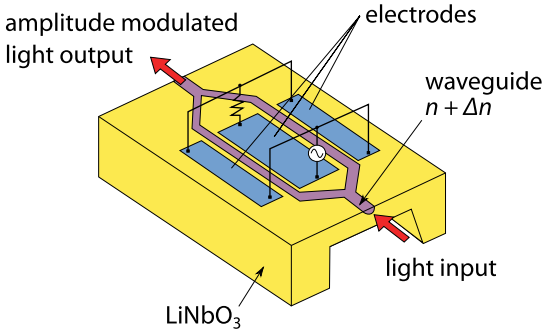

Figure 2.7 | Sketch of a Mach-Zehnder type waveguide electro-optic modulator. The "photonic integrated circuit" is designed as waveguide structure in a lithium niobate crystal (adapted from [BFG+10]).

can be achieved by using a traveling-wave structure, in which the driving RF signal co-propagates in the electrodes along with the optical beam. If the velocities are matched, a highly efficient modulation is possible, even if the wavelength corresponding to the RF frequency is much shorter than the waveguide structure. In any case, the geometry is an important design consideration, because all electro-optic materials are also piezo-electric. Therefore, the electric signal can deform the crystal and influence the refractive index of the material, and RF-induced mechanical vibrations can result in ringing effects. Electro-optic amplitude modulators may also generate phase modulation and vice versa. Furthermore, for the modulation of ultra-short pulses, the KERR effect and chromatic dispersion have to be considered (see section 2.4.2 on page 36 f., section 2.3.2 on page 27 f. and [Paso8b]).

2.5 Noise in Mode-Locked Lasers

In mode-locked lasers noise can occur in many of their characteristic properties such as the pulse duration, optical phase, chirp, pulse energy connected to the average power and phase noise resulting in a timing jitter. The types of noise are more or less coupled to each other and the sources of noise are manifold, from thermal fluctuations and mechanical vibrations, noise of the pump sources –which are usually diode laser modules for the fiber- and SESAM-based lasers relevant in this thesis– or their power supplies to, ultimately, quantum noise. Numerous investigations and analyses have been carried out, see e.g. [HM93] for an analytical model or [Paso4a, Paso4b] for numerical simulations.

In particular the jitter caused by fluctuations of the timing phase of the emitted laser pulse train is of interest, because the repetition rate is the actual timing reference of the optical synchronization system. Therefore, the jitter of the reference would limit the synchronization accuracy of the connected subsystems and the timing stability of the complete system. The second important consideration is the relative intensity noise (RIN), sometimes referred to as amplitude noise, of a laser system. In the context of this thesis, it can affect the performance of optical cross-correlators (see chapter 6, page 131 ff. and chapter 7, page 151 ff.), as well as RF generation from the laser pulse train by means of photodetection, because in the latter process amplitude noise can be converted to phase noise. In the following sections the calculation of the timing jitter and the RIN is briefly summarized, whereas the experimental set-ups for measuring these quantities are explained in more detail in chapter 5 on pages 73 ff. about the characterization of the employed laser systems.

2.5.1 Timing Phase Noise and Timing Jitter

The timing error δt is the temporal deviation of a laser pulse with respect to the position of the pulse in a ideal laser without any noise and is directly related to a phase error, e.g. $\delta\varphi = 2\pi f_{\mathrm{rep}}\,\delta t$ for the fundamental repetition rate. The single side-band phase noise $\ell_\varphi(f_i)$ measured at different offset frequencies $f_i = f_c - f$ with respect to the carrier f_c, is defined as

$$\ell_\varphi(f_i) = \frac{\delta\varphi^2_{\mathrm{rms}}}{\Delta f}\ , \tag{2.65}$$

where $\delta\varphi_{\mathrm{rms}}$ is the rms phase variation of the carrier frequency occurring at the offset frequency f_i while Δf is the measurement bandwidth. The carrier frequency f_c is usually a band-pass filtered harmonic of the laser pulse trains FOURIER comb after photodetection (see section 5.2.5, page 5.2.5 ff.). From the measured single side-band phase noise, the double side-band timing jitter spectral density $S_t(f_i)$ can be calculated by

$$S_t(f_i) = \frac{2}{(2\pi f_c)^2}\,\ell_\varphi(f_i) \tag{2.66}$$

with its integral being the square of the timing jitter δt_{rms} in a particular frequency interval $[f_1, f_2]$:

$$\delta t_{\mathrm{rms}}(f_1, f_2) = \sqrt{\int_{f_1}^{f_2} S_t(f_i)\,\mathrm{d}f_i}\,. \tag{2.67}$$

This quantity is used in the following to compare the different laser systems and to evaluate their timing stability, most often in the offset frequency interval $f_i \in [1\,\mathrm{kHz}, 10\,\mathrm{MHz}]$. Frequency noise below $\lesssim 1\,\mathrm{kHz}$ and the resulting timing jitter of the laser systems can be strongly reduced by phase-locking them to RF oscillators, as those exhibit lower phase noise than laser oscillators in the low frequency region. As it will be seen in section 5.4.3 on pages 101 ff., the cut-off frequency of the phase-locked loop (PLL) plays a significant role for this.

2.5.2 Relative Intensity Noise

The relative intensity noise (RIN) relates the fluctuations of the optical power $\delta P(t)$ to the average power P_{avg} of the laser pulse train. The most obvious way is just to normalize the variation of the optical power, for example measured with a photodetector, to the average power. A resulting number of $\pm 0.5\%$ would then suggest that the optical power stays constant with in a 1% band around the mean. However, as the intensity noise is usually a probability distribution without any sharp "band" character it is more useful to define a rms value of the fluctuations:

$$\delta P_{\mathrm{rms}} = \sqrt{\left\langle P(t) - P_{\mathrm{avg}} \right\rangle}\,. \tag{2.68}$$

Furthermore, the measurement bandwidth must be taken into account, as very fast fluctuations would get averaged out by a slow detector, and the limited measurement time inhibits the detection of drifts which, hence, must be investigated with a very low bandwidth setup (compare section 5.4.4 on pages 105 ff.). To measure the contributions of different noise frequencies the use of a power spectral density $S_{\mathrm{I}}(f)$, similar to the case of phase noise, is most convenient. Conceptually, the detector is subsequently tuned to different offset frequencies and many measurements are taken in a small frequency interval Δf. Within this thesis, a commercial signal source analyzer with a baseband measurement capability is available, enabling exactly this type of measurement. The input signal is the amplified DC component of the voltage V_0 generated by a photo detector. The relative intensity noise δP_{RIN} in a specific frequency interval $[f_1, f_2]$ can then be calculated from the recorded voltage

spectral density $\ell_V(f)$ as per

$$\delta P_{\mathrm{RIN}}(f_1, f_2) = \frac{1}{V_0}\sqrt{\int_{f_1}^{f_2} 10^{\ell_V(f_i)/20}\,\mathrm{d}f_i} \tag{2.69}$$

where the single-sided $\ell_V(f)$ is given in $\mathrm{dBV}/\sqrt{\mathrm{Hz}}$, and this formula is applied in all intensity noise analysis discussed in the following chapters. It is also given in percent, but here the measurement bandwidth and frequency interval is considered.

The power spectral density of a shot-noise or quantum-noise limited laser is given by (see [Paso8a])

$$S_{\mathrm{I,sn}} = \frac{2h\nu}{P_{\mathrm{avg}}} \tag{2.70}$$

where $h\nu = hc_0/\lambda$ is the photon energy. A laser pulse train with an average power of $P_{\mathrm{avg}} = 1\,\mathrm{mW}$ at $\lambda = 1560\,\mathrm{nm}$, for example, exhibits a shot noise limit of $2.55 \times 10^{-16}\,\mathrm{Hz}^{-1}$ which corresponds to $-155.9\,\mathrm{dBc/Hz}$. These values, however, can only be measured when the photodetection process does not limit the noise measurement which is usually the case (see section 5.4.4, p. 105 f. and [Wino8]).

2.6 Erbium-Doped Fiber Amplifiers

Single- and double pass erbium-doped fiber amplifiers (EDFAs) play an important role in the context of the optical synchronization system and are used in several components, as it will become clear in the following chapters. The basic experimental setup of a simple EDFA is depicted in Fig. 2.8. The light enters the amplifying fiber either through a collimator, for example in the free-space distribution unit (see section 5.5, page 108) or fiber-coupled with a connector or simply a splice as in the BAMs (see section 4.4, page 67 and [Boc13]). The gain fiber is pumped with 974 nm or 976 nm

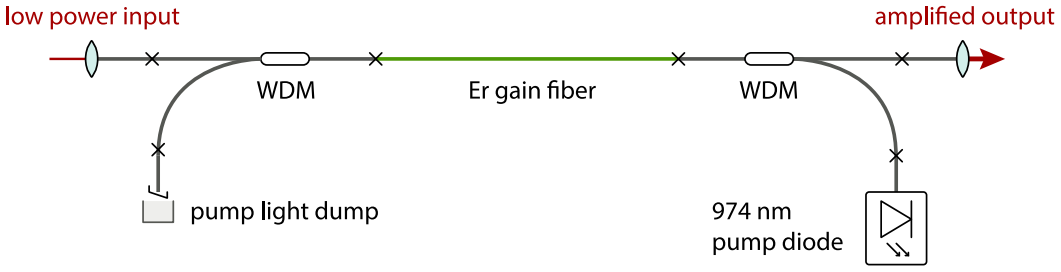

Figure 2.8 | Schematic layout of a simple erbium-doped fiber amplifier. After counter-pumping the gain fiber, the pump light which was not absorbed, is coupled out in this configuration.

light emitted by a pigtailed diode laser and is coupled in utilizing a "980/1550 nm type" wavelength-division multiplexer (WDM) which guides the light wavelength-dependent. It has been shown that counter-pumped EDFAs in the saturation regime exhibit lower timing phase noise [Loeo9, Agro8] because of a lower amplified spontaneous emission (ASE) background. Hence, this configuration

is favored in almost every set-up discussed in this thesis, with an additional WDM to couple out the pump light which might disturb the experiment further downstream of the optical setup chain. The continuous wave (cw) amplification factor is defined as $G = P_{\text{out}}/P_{\text{in}} \equiv P(L)/P(0)$ and can be obtained by solving the equation

$$\frac{\mathrm{d}P}{\mathrm{d}z} = g(\omega)P(z) \qquad \Rightarrow \qquad G(\omega) = \exp\left\{\int_0^L g(\omega)\mathrm{d}z\right\} = \exp\{g(\omega)L\} \tag{2.71}$$

where $g(\omega)$ is the gain coefficient of the amplifying medium and assumed to be constant along the fiber length L, and thus $G(\omega)$ is the amplifier gain spectrum whose bandwidth is always smaller than the gain bandwidth. However, in real optical gain fibers the gain spectrum is considerably modified depending on the composition of the fiber core (see appendix D, in particular Fig. D.3 on page 243). A complete description of optical pulse amplification requires an extensive mathematical framework and is discussed in detail in [Agro8]. Here, only the effect of SPM is briefly mentioned in a simplified picture: As the pulse energy is growing exponentially in case of optical pulses, the effect of SPM becomes stronger, which can be seen when evaluating Eq. 2.44 (page 31) with the loss factor α replaced by $-g(\omega)$. If dispersion effects are neglected, the effective length $L_{\text{eff}} = \left(\exp\{gL\}\right)/g$ (Eq. 2.42, page 31) may become larger than the actual amplifier length L depending on the value of gL, and thus the spectral broadening is dependent on the amplifier gain g.

Additionally, dispersive effects have to be considered. In case of anomalous GVD and for a value of the scaling relation $N^2 = L_{\text{D}}/L_{\text{NL}}$ close to one, the pulse is compressed while being amplified. This is directly related to the soliton nature of the pulse, because to compensate for the increased SPM the pulse duration has to be decreased to maintain the balance between dispersion and nonlinearity, i.e. to keep $N^2 \simeq 1$. This feature of soliton pulse amplification is exploited in the "distribution EDFAs" discussed in section 5.5 on pages 108 below. For the normal dispersion regime it can be shown from the asymptotic solution of the NLSE (see Eq. 2.20, p. 26) that the pulse evolves to a parabolic shape, which is kept although its width and amplitude increase with larger z. This effect is called self-similar pulse evolution. It has, however not been taken into account in theoretical considerations for the laser-optical synchronization system yet. Moreover, effects in EDFAs where pulses are counter-propagating have not been treated theoretically, which turns out to be a severe omission. Such EDFAs are unavoidable in the present fiber link stabilization scheme (compare chapter 6 on pages 131 ff.) and were found to affect its performance significantly….

3 Nonlinear Optics

In this chapter, some basics of nonlinear optics are briefly summarized, as they are essential in laser physics in general and for components of the optical synchronization system like the fiber link stabilization and the Ti:sapphire synchronization in particular. Furthermore, nonlinear optical effects are exploited for picosecond and femtosecond laser pulse diagnostics, which are also discussed. Another example is the optical frequency up-conversion in the photoinjector laser system of FLASH to generate the required photon energy for the emission process in the electron gun.

In the first section of this chapter, calculations are outlined to determine the optimum properties of the nonlinear crystals used in the cross-correlators for Ti:sapphire laser systems and the photo injector laser. In the last section, the concept of correlation functions is introduced, which form the mathematical basics for the detected signals in cross- and autocorrelators based on nonlinear frequency conversion processes of pulsed laser radiation.

3.1 Basics of Frequency Conversion in a Nonlinear Crystal

The frequency conversion of a light wave is possible in nonlinear optical crystals, where the index of refraction n depends on the electric field strength vector $\boldsymbol{E}$ of the light wave:

$$n(\boldsymbol{E}) = n_0 + n_1 \boldsymbol{E} + n_2 \boldsymbol{E}^2 + \dots , \tag{3.1}$$

which can be described by the already introduced dielectric polarization $\boldsymbol{P}(\boldsymbol{E})$, compare Eq. 2.2, page 21, and Eq. 2.18, page 25:

$$\boldsymbol{P}(\boldsymbol{E}) = \varepsilon_0 \chi^{(1)} \boldsymbol{E} + \varepsilon_0 \chi^{(2)} \boldsymbol{E}^2 + \varepsilon_0 \chi^{(3)} \boldsymbol{E}^3 + \dots . \tag{3.2}$$

The square nonlinearity ($\chi^{(2)} \neq 0$) occurs only in crystals without a symmetry center (acentric crystals), whereas in symmetric crystals and in isotropic matter $\chi^{(2)} \equiv 0$. The cubic nonlinearity, however, exists in all crystalline and isotropic materials.

When two light waves with the frequencies ω_1 and ω_2 propagate through an acentric crystals, new frequency components with $\omega_3 = \omega_1 + \omega_2$ or, respectively, $\omega_{3-} = \omega_1 - \omega_2$ can be generated. This three-wave interaction is referred to as sum-frequency generation (SFG) and difference-frequency generation (DFG). In case of equal fundamental frequencies $\omega_1 = \omega_2$, the sum-frequency generation process is called second-harmonic generation (SHG). Successive application of SHG and/or SFG are routinely used to generate ultraviolet (UV) radiation from an infrared (IR) laser, such as the FLASH photo injector laser system with $\omega_4 = 4\omega_1$ (see section 8.1, page 168 f.). To achieve the same ultraviolet

wavelength for a photo injector from a Ti:sapphire laser, a third-harmonic generation (THG) process $\omega_3 = \omega_1 + 2\omega_1$ would have to be deployed.

3.2 Phase-Matching in Uniaxial Crystals

Notable nonlinear effects can only be observed for comparatively high pulse peak power and/or when the light propagates through relatively long crystals and especially the phase-matching condition

$$\boldsymbol{k}_{3,3'} = \boldsymbol{k}_1 \pm \boldsymbol{k}_2 \qquad \text{with} \qquad |\boldsymbol{k}_i| = k_i = \frac{\omega_i\, n(\omega_i)}{c_0} = \frac{2\pi\, n_i}{\lambda_i} \tag{3.3}$$

is fulfilled, where the relative orientation of the wave vectors $\boldsymbol{k}_i$ can be either collinear ("scalar phase-matching") or noncollinear ("vector phase-matching"). The former one is used in all optical cross-correlators described in this thesis, whereas the latter one is realized in the autocorrelators for pulse duration measurements.

The index of refraction $n(\omega)$ or $n(\lambda)$ as a function of the light frequency or wavelength is described by the Sellmeier equation, which reads in its most general form

$$n^2(\lambda) = 1 + \sum_j \frac{B_j \lambda^2}{\lambda^2 - C_j}, \tag{3.4}$$

with the Sellmeier coefficients B_j and C_j. In most cases a reduced form with the additional coefficients A and D

$$n^2(\lambda) = A + \frac{B}{\lambda^2 - C} - D\lambda^2 \tag{3.5}$$

is sufficient and was considered in the calculations for the used crystals[1] . When in an uniaxial crystal the index of refraction n_o of the ordinary[2] beam is larger than for the extraordinary beam, $n_o > n_e$, the crystal is said to be negative; otherwise it is called positive, and the difference $\Delta n = n_e - n_o$ is called birefringence. Furthermore, the refractive index of the extraordinary beam is a function of the angle Θ between the Z axis and the wave vector $\boldsymbol{k}$

$$n^{\mathrm{e}}(\Theta) = \left(\frac{1 + \tan^2\Theta}{1 + (n_o/n_e)^2 \tan^2\Theta} \right)^{1/2} . \tag{3.6}$$

Hence, an extraordinary beam acquires a walk-off and is displaced by an amount δL at the crystal output surface (see Fig. 3.1):

$$\rho(\Theta) = \pm \arctan\!\left((n_o/n_e)^2 \tan^2\Theta \right) \mp \Theta \qquad \Rightarrow \qquad \delta L = L \tan\rho(\Theta) . \tag{3.7}$$

[1] Note that the Sellmeier coefficients in literature for Eq. 3.5 are usually provided for wavelengths given in micrometer.

[2] The light beam, whose polarization is normal to the crystals principle plane is the ordinary beam, whereas the beam polarized in the principle plane is the extraordinary beam. The principle plane is defined by the wave vector $\boldsymbol{k}$ and the Z axis of the crystal.

This walk-off can be useful in the actual implementation of an optical cross-correlator based on sum-frequency generation, for instance of the reference and a Ti:sapphire laser, as the also generated second-harmonic component could be blocked by means of an iris diaphragm.

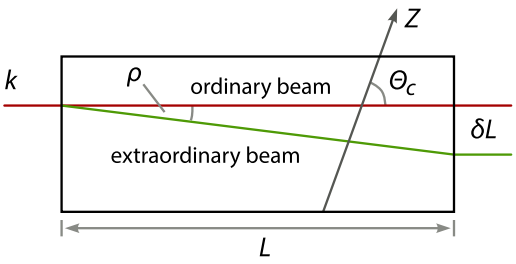

Figure 3.1 | Illustration of the walk-off in a nonlinear optical crystal. The illustration shows the walk-off δL of the extraordinary beam in a nonlinear, negative optical crystal with the length L and the determination of the crystal cut-angle Θ_c.

The phase-matching condition can be fulfilled by several combinations of differently polarized light. If the fundamental waves have the same polarization, the resulting sum-frequency component will be polarized perpendicularly:

- for negative crystals: ordinary-ordinary-extraordinary (ooe), referred to as type-$I^{(-)}$ phase-matching:
  $\Rightarrow \quad \boldsymbol{k}_{o,1} + \boldsymbol{k}_{o,2} = \boldsymbol{k}_3^{\mathrm{e}}(\Theta)$

- for positive crystals: extraordinary-extraordinary-ordinary (eeo) or type-$I^{(+)}$ phase-matching:
  $\Rightarrow \quad \boldsymbol{k}_1^{\mathrm{e}}(\Theta) + \boldsymbol{k}_2^{\mathrm{e}}(\Theta) = \boldsymbol{k}_{o,3}$

If the fundamental light waves are orthogonally polarized, the generated sum-frequency is an extraordinary wave in negative crystals

- ordinary-extraordinary-extraordinary (oee) or type-$II^{(-)}$ phase-matching:
  $\Rightarrow \quad \boldsymbol{k}_{o,1} + \boldsymbol{k}_2^{\mathrm{e}}(\Theta) = \boldsymbol{k}_3^{\mathrm{e}}(\Theta)$

- extraordinary-ordinary-extraordinary (eoe), also known as type-$II^{(-)}$ phase-matching:
  $\Rightarrow \quad \boldsymbol{k}_1^{\mathrm{e}}(\Theta) + \boldsymbol{k}_{o,2} = \boldsymbol{k}_3^{\mathrm{e}}(\Theta)$

and an ordinary wave in positive crystals

- ordinary-extraordinary-ordinary (oeo) or type-$II^{(+)}$ phase-matching:
  $\Rightarrow \quad \boldsymbol{k}_{o,1} + \boldsymbol{k}_2^{\mathrm{e}}(\Theta) = \boldsymbol{k}_{o,3}$

- extraordinary-ordinary-ordinary (eoo), also known as type-$II^{(+)}$ phase-matching:
  $\Rightarrow \quad \boldsymbol{k}_1^{\mathrm{e}}(\Theta) + \boldsymbol{k}_{o,2} = \boldsymbol{k}_{o,3}$.

Table 3.1 | Equations for calculating the phase-matching angle in uniaxial crystals. The formulas, take from [DGN99] allow for the calculation of the phase-matching angle for the most simple case: collinear interaction in uniaxial crystals.

negative uniaxial crystals	positive uniaxial crystals
$\tan^2\Theta_{\mathrm{pm}}^{(\mathrm{ooe})} = (1-U)/(W-1)$	$\tan^2\Theta_{\mathrm{pm}}^{(\mathrm{eeo})} \simeq (1-U)/(U-S)$
$\tan^2\Theta_{\mathrm{pm}}^{(\mathrm{eoe})} \simeq (1-U)/(W-R)$	$\tan^2\Theta_{\mathrm{pm}}^{(\mathrm{oeo})} = (1-V)/(V-Y)$
$\tan^2\Theta_{\mathrm{pm}}^{(\mathrm{oee})} \simeq (1-U)/(W-Q)$	$\tan^2\Theta_{\mathrm{pm}}^{(\mathrm{eoo})} = (1-T)/(T-Z)$

notation:

$U = (A+B)^2/C^2$; $W = (A+B)^2/F^2$; $R = (A+B)^2/(D+B)^2$

$Q = (A+B)^2/(A+E)^2$; $S = (A+B)^2/(D+E)^2$; $V = B^2/(C-A)^2$

$Y = B^2/E^2$; $T = A^2/(C-B)^2$; $Z = A^2/D^2$

$A = n_{o,1}/\lambda_1$; $B = n_{o,2}/\lambda_2$; $C = n_{o,3}/\lambda_3$

$D = n_{e,1}/\lambda_1$; $E = n_{e,2}/\lambda_2$; $F = n_{e,3}/\lambda_3$

Since the dispersion properties of an uniaxial crystal are only functions of the polar angle Θ, the corresponding phase-matching angle Θ_{pm} for a certain scalar three-wave interaction can be calculated from the equations given in table 3.1. These equations can also be generalized to the case of vector phase-matching with the introduction of an angle γ_{vec} between the wave vectors $\boldsymbol{k}_1$ and $\boldsymbol{k}_2$. For an ooe interaction, the abbreviations U and W have then to be replaced by

$$U_{\mathrm{vec}} = (A^2 + B^2 + 2AB\cos\gamma_{\mathrm{vec}})/C^2 \qquad \text{and} \qquad W_{\mathrm{vec}} = (A^2 + B^2 + 2AB\cos\gamma_{\mathrm{vec}})/F^2\,.$$

Although the phase-matching is realized independently of the azimuthal angle φ, the conversion efficiency of the nonlinear process is determined by both φ and Θ_{pm}. Hence, it is crucial to determine the required phase-matching angle for the given parameters of an optical setup.

Since in the optical cross-correlators for Ti:sapphire oscillator (chapter 7, pages 151 ff.) and the photo injector laser synchronization (chapter 8, pages 167 ff.) the negative uniaxial crystal beta barium borate (BBO) is utilized with collinear phase-matching, all following considerations are narrowed to this special case. A fundamental wavelength $\lambda_1 = 1.56\,\mu\mathrm{m}$ of the optical reference and $\lambda_2 = 0.8\,\mu\mathrm{m}$ of a Ti:sapphire oscillator leads to $\Theta_{\mathrm{pm}} = 22.2\,\mathrm{deg}$ for efficient frequency up-conversion to $\lambda_3 = 0.529\,\mu\mathrm{m}$. More information and properties of BBO are summarized in appendix C.1, page 229.

3.3 Frequency Conversion Efficiency

An important figure of merit for the design of the optical cross-correlators within this thesis is the nonlinear frequency conversion efficiency, as it plays a crucial role in the selection of the crystal and in particular the photodetectors for the generated sum- or difference frequency signals. The calculation

of the conversion efficiency is based on the wave equation 2.4, page 22, with a nonlinear term for the dielectric polarization $\boldsymbol{P}_{\mathrm{NL}}$:

$$\nabla^2 \boldsymbol{E}(\boldsymbol{x},t) - \frac{1}{c^2}\frac{\partial^2 \boldsymbol{E}(\boldsymbol{x},t)}{\partial t^2} = \mu_0 \frac{\partial \boldsymbol{P}_{\mathrm{NL}}(\boldsymbol{x},t)}{\partial t^2} \qquad \text{with} \qquad \boldsymbol{P}_{\mathrm{NL}}(\boldsymbol{x},t) = \chi^{(2)} \boldsymbol{E}^2(\boldsymbol{x},t) \tag{3.8}$$

This can be evaluated in the slowly varying envelope approximation (SVEA) when the electric field is considered as superposition of the three interacting waves

$$\boldsymbol{E}(\boldsymbol{x},t) = \frac{1}{2}\sum_{j=1}^{3}\left(\boldsymbol{p}_j A_j(\boldsymbol{x},t)\, \exp\{i\omega_j t - i\boldsymbol{k}_j \boldsymbol{x}\} + \text{c.c.}\right) \tag{3.9}$$

with unit vectors $\boldsymbol{p}_j$ describing the polarization state of the wave. This leads to the coupled, truncated equations (see [DGN99]):

$$\widehat{M}_1 A_1 = i\sigma_1 A_3(\boldsymbol{x},t)\, A_2^\star(\boldsymbol{x},t)\, \exp\{i\Delta k z\} \tag{3.10a}$$
$$\widehat{M}_2 A_2 = i\sigma_2 A_3(\boldsymbol{x},t)\, A_1^\star(\boldsymbol{x},t)\, \exp\{i\Delta k z\} \tag{3.10b}$$
$$\widehat{M}_2 A_3 = i\sigma_3 A_1(\boldsymbol{x},t)\, A_2^\star(\boldsymbol{x},t)\, \exp\{i\Delta k z\} \tag{3.10c}$$

where $A_j(\boldsymbol{x},t)$ are the complex field amplitudes, σ_j the nonlinear coupling coefficients and Δk the total wave mismatch. The operator $\widehat{M}$ is of the form

$$\widehat{M}_j = \frac{\partial}{\partial z} + \rho_j \frac{\partial}{\partial x} + \frac{i}{2k_j}\left(\frac{\partial^2}{\partial x^2} + \frac{\partial^2}{\partial y^2}\right) + v_{\mathrm{gr},j}^{-1}\frac{\partial}{\partial t} + i g_j \frac{\partial^2}{\partial t^2} + \delta_j + Q_j(A_j)\,. \tag{3.11}$$

The parameters ρ_j are the walk-off angles, $v_{\mathrm{gr},j}$ the group velocities, g_j the dispersive spreading coefficients, δ_j the linear absorption coefficients, and Q_j takes the nonlinear (usually two-photon) absorption into account. An exact solution of Eqs. 3.10a to 3.10c is in general not possible and requires numerical methods; only for some special cases analytical solutions exist and the conversion efficiency can be calculated. Whether an effect must be included in the calculation can be decided from the comparison of the length L of the given crystal and several effective length scales:

- aperture length $L_{\mathrm{a}} = d_0/\rho$, where d_0 is the beam diameter
- quasi-static interaction length $L_{\mathrm{qs}} = \tau_{\mathrm{p}}/v_\Delta$, where $v_\Delta = v_{\mathrm{gr},1}^{-1} - v_{\mathrm{gr},2}^{-1}$ is the inverse group velocity mismatch
- diffraction length $L_{\mathrm{dif}} = k d_0^2$
- dispersive spreading length $L_{\mathrm{ds}} = \tau_{\mathrm{p}}^2/g$, which has a similar meaning to the dispersion length in an optical fiber (see section 2.3.3, page 27) with g the *dispersive spreading coefficient*
- nonlinear length $L_{\mathrm{nl}} = 1/(\sigma a_0)$, where $a_0 = \left(a_1^2(0) + a_2^2(0) + a_3^2(0)\right)^{1/2}$ and $a_j = |A_j|$ the field amplitude at the input surface of the crystal at $z = 0$ and σ the *nonlinear coupling coefficient*

When the crystal length is smaller than the effective length, the corresponding effect can be neglected. For example, if $L < L_a$, the anisotropy effect can be ignored by setting the second term in the operator $\widehat{M}$ to zero. This is true for the BBO crystal in the Ti:sapphire's cross-correlator, as there $L_a \approx 1$ mm for a beam diameter of 100 µm and a chosen crystal length of 0.5 µm. The nonlinear length is of special relevance. When $L < L_{nl}$ is fulfilled, a so-called fixed-field approximation (FFA) can be applied. For the sum-frequency generation, this means $a_3(z) \ll a_{1,2}(0)$ and the truncated Eqs. 3.10a to 3.10c transform into linear ones, with

$$\widehat{M}_3^{(FFA)} = -i\,\sigma_3\,a_1(0)\,a_2(0)\,\exp\{i(-\Delta k - \phi_1 - \phi_2)\} \tag{3.12}$$

where the ϕ_j are the phases of the fundamental waves. In this particular case, together with the assumption of negligible diffraction, dispersive spreading, heat effects and absorption, the conversion efficiency for sum-frequency generation $\eta_+ = P_3/\sqrt{P_1 P_2}$ and for difference-frequency generation $\eta_- = P_1/\sqrt{P_2 P_3}$ can be calculated from the ratios

$$\frac{P_3}{P_1} = \frac{8\pi\, d_{\text{eff}}^2 L^2\, P_2}{\varepsilon_0\, c_0\, n_1\, n_2\, n_3\, \lambda_3^2\, w_0^2}\ \text{sinc}^2\left(\frac{|\Delta k|\, L}{2}\right) \qquad \text{for SFG with } \Delta k = k_1 + k_2 - k_3 \tag{3.13a}$$

$$\frac{P_2}{P_1} = \frac{2\pi\, d_{\text{eff}}^2 L^2\, P_1}{\varepsilon_0\, c_0\, n_1^2\, n_2\, \lambda_2^2\, w_0^2}\ \text{sinc}^2\left(\frac{|\Delta k|\, L}{2}\right) \qquad \text{for SHG with } \Delta k = 2k_1 - k_2 \tag{3.13b}$$

$$\frac{P_1}{P_3} = \frac{8\pi\, d_{\text{eff}}^2 L^2\, P_2}{\varepsilon_0\, c_0\, n_1\, n_2\, n_3\, \lambda_1^2\, w_0^2}\ \text{sinc}^2\left(\frac{|\Delta k|\, L}{2}\right) \qquad \text{for DFG with } \Delta k = k_1 + k_2 - k_3\,. \tag{3.13c}$$

The parameter d_{eff} is the effective nonlinearity of the crystal in phase-matching direction and is related to the crystal symmetry, as discussed comprehensively in [DGN99]. It should be noted that the relevant numbers, for instance d_{31} and d_{22} for BBO with $d_{\text{eff}} = d_{31}\sin\Theta - d_{22}\cos\Theta\,\sin\varphi$ are usually provided by the manufacturer of the crystal (see also appendix C.1, p. 229). The focused beam radius is w_0, from Eq. 2.12a on page 23, and is simplistic assumed to be equal for all three waves. For the interaction of pulsed lasers, the optical peak power P_{peak} of the corresponding beam has to substituted for the P_j. Therefore, the conversion efficiency is proportional to the pump power density, to the square of the crystal length, to the square of the effective nonlinearity and the cardinal sine term, which accounts for the wave mismatch – probably due to an imperfect alignment of a collinear cross-correlator setup. Figure 3.2 shows the conversion efficiency of BBO as function of the crystal L for an ooe interaction, which has been found to be favorable over the other possible phase-matching conditions in a negative crystal. Based on the fundamental wavelengths of $\lambda_1 = 1.56$ µm of the reference pulse train and $\lambda_2 = 0.8$ µm of the Ti:sapphire oscillator, the conversion efficiency η_+ has been calculated for different beam waists in the crystal (35 µm and 70 µm) and for different pulse durations of the reference pulse train. The full-width at half-maximum pulse duration of 100 fs is realized when the erbium-doped fiber master laser oscillator (EDFL) is used with a perfectly dispersion compensated fiber link, whereas 200 fs pulses are provided by the SESAM-based master laser oscillator

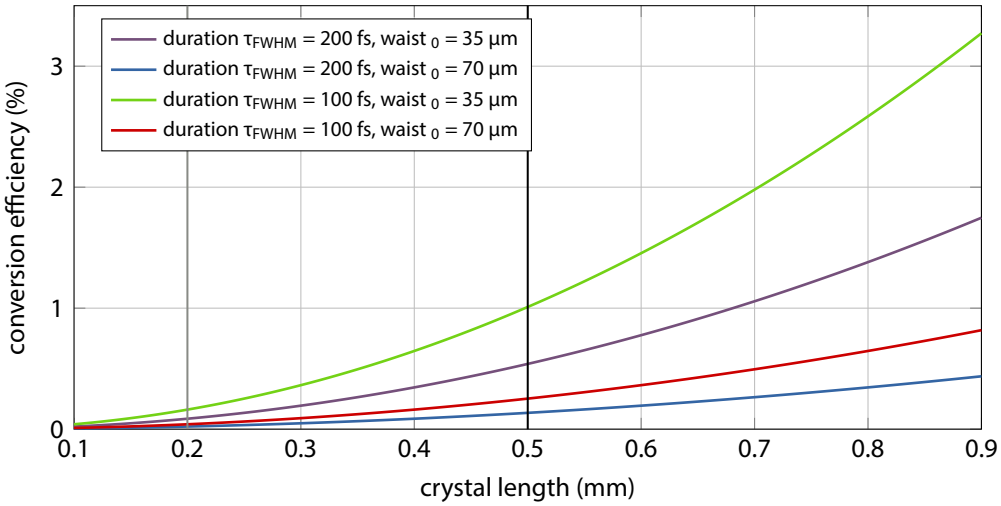

Figure 3.2 | Conversion efficiency of a BBO crystal for Ti:sapphire synchronization. Different reference pulse durations τ_{FWHM} and different beam waists w_0 are evaluated.

(MLO, see chapters 5 and 6 on pages 71 and 131, respectively). The crystal length of the actual device has been chosen to be $L = 0.5\,\mathrm{mm}$ to minimize effects from diffraction, anisotropy and dispersive effects. Since the other parameters are fixed, a strong focussing is desirable to achieve conversion efficiencies to up to 1%. Even then, the average power of the generated sum-frequency component is rather low in the implementation discussed in chapter 7, pages 151 ff. and due to the fact, that it is generated at a repetition rate of 27 MHz, the average power of the SFG is well below 1 µW, requiring sensitive detectors (see section 7.1.1, page 155 f.).

3.4 Wave-Mismatch and Phase-Matching Bandwidth

In practice, the laser radiation can not be described with plane waves, as its beams are divergent, non-monochromatic and often –as in the synchronization system– pulsed. Furthermore, the temperature of the crystal is only stable within certain margins. Therefore, the angular, spectral and temperature bandwidths have to be considered, which allow for an estimation of the maximum permissive divergence, spectral width and temperature instability. This can be expressed using the wave mismatch $\Delta k(T, \nu, \delta\Theta)$ as a function of the temperature T, frequencies of the interacting waves $\nu = \omega/(2\pi)$ and deviation $\delta\Theta = \Theta - \Theta_{\mathrm{pm}}$ from the phase-matching angle:

$$\Delta k(T, \nu, \delta\Theta) \simeq \Delta k(0) + \frac{\partial(\Delta k)}{\partial T}\,\Delta T + \frac{\partial(\Delta k)}{\partial \nu}\,\Delta\nu + \frac{\partial(\Delta k)}{\partial(\delta\Theta)}\,\Delta\Theta\,, \tag{3.14}$$

where $\Delta k(0)$ is the wave mismatch for exact phase-matching. In the fixed-field approximation (FFA), it is possible to derive equations for these three characteristic bandwidths for the phase-matching

acceptance of angular deviation

$$\Delta\Theta = 1.772\,\frac{\pi}{L}\left(\frac{\partial(\Delta k)}{\partial(\delta\Theta)}\right)^{-1}_{\Theta=\Theta_{\mathrm{pm}}}, \tag{3.15}$$

for the phase-mathcing acceptance for temperature changes

$$\Delta T = 1.772\,\frac{\pi}{L}\left(\frac{\partial(\Delta k)}{\partial T}\right)^{-1}_{T=T_{\mathrm{pm}}} \tag{3.16}$$

and the phase-matching acceptance for the different wavelengths involved in the frequency conversion process

$$\Delta\nu = 1.772\,\frac{\pi}{L}\left(\frac{\partial(\Delta k)}{\partial \nu}\right)^{-1}_{\nu=\nu_{\mathrm{pm}}}. \tag{3.17}$$

They depend on the dispersion of the index of refraction and the type of phase-matching. In the following, two example expressions are given for ooe interactions. The first is the spectral bandwidth (also known as "mix-acceptance bandwidth") for SFG, when the interacting wave with the higher frequency has a wide spectrum, such as a Ti:sapphire oscillator:

$$\Delta\nu_2 = \frac{0.886}{L}\left|n_{o,2} - n_3^{\mathrm{e}}(\Theta) - \lambda_2\,\frac{\partial n_{o,2}}{\partial\lambda_2} + \lambda_3\,\frac{\partial n_3^{\mathrm{e}}}{\partial\lambda_3}\right|^{-1}. \tag{3.18}$$

For the parameters of the actual laser oscillator considered in the calculation, the chosen interaction and crystal length, a bandwidth of ~ 65 nm has been determined. Hence, this is a relaxed parameter, as the laser has a spectral width of $\Delta\lambda = 50$ nm (see Fig. 7.1, page 152). By replacing all indices '2' with '1' in Eq. 3.18, the allowed bandwidth for the reference pulse train can be calculated an results in ~ 140 nm, which is even more uncritical. The second example is the internal angular bandwidth of second-harmonic generation (SHG) in an ooe interaction

$$\Delta\Theta = \frac{0.886\,\lambda_3}{L\,\tan\Theta}\,\frac{1 + (n_{o,2}/n_{e,2})^2\tan^2\Theta}{|1 - (n_{o,2}/n_{e,2})^2|\;n_2^{\mathrm{e}}(\Theta)}, \tag{3.19}$$

which has been found to be critical for the UV conversion process in the photoinjector laser system (see section 8.5, page 197). In summary, there are numerous parameters and approximations to consider for the selection of an appropriate nonlinear optical crystal for the development, for instance, of an optical cross-correlator for timing measurement or synchronization, and especially for ultrashort laser pulses. The last sections gave a rough idea of the required calculations, whereas for a broad review the reader is again referred to [DGN99].

3.5 Correlation Functions

The starting point for the following description is the first-order intensity cross-correlation $X_c(\tau)$ which is defined as the convolution[3]

$$X_c(\tau) = \int_{-\infty}^{\infty} I_s(t)\, I_r(t-\tau)\, \mathrm{d}t \tag{3.20}$$

where $I_s(t)$ and $I_r(t)$ are the intensities of a "signal" and a "reference" pulse (see also [DR06]). For two Gaussian pulses with a mutual delay of $\Delta t = t_r - t_s$, different field amplitudes A_i and different pulse durations τ_i given by

$$I_r(t) = A_r^2\, e^{-(t-t_r)^2/\tau_r^2} \qquad \text{and} \qquad I_s(t) = A_s^2\, e^{-(t-t_s)^2/\tau_s^2}\,, \tag{3.21}$$

the evaluation of the integral in Eq. 3.20 yields

$$X_c(\tau) = \frac{A_r^2\, A_s^2\, \sqrt{\pi}}{\sqrt{1/\tau_r^2 + 1/\tau_s^2}}\, \exp\left\{-\frac{-(\tau-\Delta t)^2}{\tau_r^2+\tau_s^2}\right\}. \tag{3.22}$$

It should be noted that the reference laser pulse train of the synchronization system generated by the master laser oscillator (MLO) consists of soliton pulses which have spectral and temporal profiles described by a hyperbolic secant (see section 2.3.1, page 25 f.). However, several equations used in this chapter can not be solved analytically for $I_i(t) = A_i^2\ \mathrm{sech}(t/\tau_i)^2$. Hence, Gaussian temporal shapes are also assumed for the reference and signal pulses as they provide a relatively good approximation for the real pulse shape.

The cross-correlation intensity can be used for a timing measurement, for instance between two lasers, as it is sensitive to the relative time delay Δt of the fundamental pulses. When one of the laser pulses is temporally shifted such that t_i changes, a detector measuring at a fixed $\tau \equiv \tau_0$ will measure another intensity $X_c(\tau_0)$ than in the not-shifted case. When this signal is applied to a phase-locked loop (PLL), this timing change can be compensated by acting on one laser. However, it is obvious, that the cross-correlation intensity also depends on the amplitudes of the correlated pulses. Hence, an amplitude variation would be detected as timing change and misleadingly corrected by the PLL.

3.5.1 Delay/Subtraction Cross-Correlation

In the optical cross-correlators used for relative timing measurement and stabilization of the fundamental pulses, the concept for the phase-locked loop is extended by means of a "delay/subtraction" detection scheme. Therein, the fundamental pulse trains are correlated twice, which is realized by sum-frequency generation in a single nonlinear optical crystal[4]. The balanced optical cross-

[3] Note that pulse durations are always denoted as tau with an index, whereas a simple τ is used as time argument in the correlation functions.

[4] The actual implementation and setup of such cross-correlators is explained in the corresponding section 6.1 on pages 132 ff. for the fiberlink stabilization scheme, section 7.1 on pages 153 ff. for the Ti:sapphire synchronization and section 8.2

correlation function $S_{xc}(\tau, T)$ is then given by

$$S_{xc}(\tau, T) = X_c(\tau) - X_c(\tau + T) \tag{3.23}$$

where T is a time delay the fundamental pulses have to experience before the sum-frequency generation process takes place the second time. This delay can be achieved in different ways:

- Using a dispersive material, such as quartz, leads to different group velocities at different wavelengths because of the dispersion $n(\lambda)$. This is exploited in the "two-color cross-correlator" for the Ti:sapphire laser synchronization (see chapter 7, pages 151 ff.).

- A material with different dispersion for different polarization states can be used when the fundamental pulses have the same wavelength, such as in the fiber link stabilization units (see section 6 on pages 131 ff. and appendix C.3, page 231).

- The fundamental pulses can be separated and recombined with a polarizing beam splitter (when they have a different polarization state) or a dichroic mirror (in a two-color device). In between, the delay is applied by different optical path lengths for the pulses. The latter approach is realized in the cross-correlator for the photoinjector laser system because of its relatively long pulse duration (see section 8.2 on pages 169 ff.).

In order to determine the slope gradient of the delay/subtraction cross-correlation signal and the optimum delay T_{opt}, the derivative

$$\frac{\mathrm{d}S_{xc}(\tau, T)}{\mathrm{d}\tau} = \frac{2}{\left(\tau_r^2 + \tau_s^2\right)} \frac{A_r^2 A_s^2 \sqrt{\pi}}{\sqrt{1/\tau_r^2 + 1/\tau_s^2}} \left((T + \tau) \cdot \exp\left\{ -\frac{(T + \tau)^2}{\tau_r^2 + \tau_s^2} \right\} - \tau \cdot \exp\left\{ -\frac{\tau^2}{\tau_r^2 + \tau_s^2} \right\} \right) \tag{3.24}$$

of Eq. 3.23 has to be evaluated at $\tau = -T/2$. Then, the roots of the derivative of Eq. 3.24 with respect to T yield to the required delay T_{opt} of the pulses such that the slope gradient at the zero-crossing is maximum:

$$\frac{\mathrm{d}}{\mathrm{d}T} \left(\left. \frac{\mathrm{d}S_{xc}(\tau, T)}{\mathrm{d}\tau} \right|_{\tau = -T/2} \right) = 0 \qquad \Rightarrow \qquad T_{opt} = \pm \sqrt{2\left(\tau_r^2 + \tau_s^2\right)} \,. \tag{3.25}$$

Thus, the pulse duration has to be known when designing the optical setup of the cross-correlator, or a possibility to change the delay element afterward has to be provided for cases when, for instance, the reference laser pulse duration changes. This issue is discussed in the chapters about the master laser characterization (sections 5.2.3 and 5.4.2, pages 77 ff. and 97 ff., respectively) and the long-distance timing distribution (section 6.1.3, pages 137 ff.).

on pages 169 ff. for the injector laser stabilization.

Influence of Amplitude and Pulse Duration Fluctuations

The delay/subtraction cross-correlation is, like the single one, also sensitive to amplitude changes of the fundamental pulses. The distinction is, however, that a PLL which operates at the zero-crossing[5] τ_0 of the difference signal, is in a first order approximation not influenced by the amplitude change, as the moment τ_0, which is kept fixed, in fact does not change. This can be seen in Fig. 3.3 as black and red lines, where for the latter trace the amplitude of the pulses was set to be 10% less than nominal. The shown signals have been calculated with a $\tau_r = 150$ fs long reference and a $\tau_s = 200$ fs signal

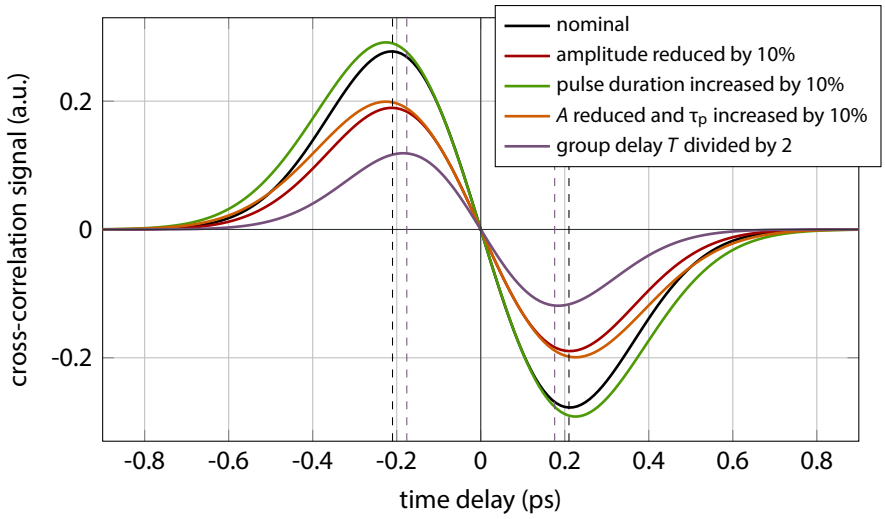

Figure 3.3 | Calculated balanced cross-correlation signal. For comparison of the slope steepness, different amplitudes and durations of the fundamental pulses, as well as for a non-optimal group delay, are considered.

pulse with equal initial amplitudes $A_r = A_s = 1$. Similarly, the influence of a 10% pulse duration increase is also shown in the figure, both for the nominal fundamental pulses and the ones with a reduced amplitude. Here, the slope is hardly changed in a large region around the zero-crossing. Furthermore, the considered magnitude of the changes is rather academic, as in practice amplitude fluctuations are much smaller. Because of this, these two effects are neglected in the implementation of the synchronization schemes within this thesis. An exception is the case, when the balanced optical cross-correlation technique is used for an independent, out-of-loop high-precision timing measurement, for example of two all-optically locked laser oscillators (compare section 7.2 on pages 161 ff.) or an out-of-loop investigation of the fiber link performance. In this case, the difference signal must me normalized to the sum of the individual single cross-correlation intensities

$$B_{xc}(\tau, T) = \frac{X_c(\tau) - X_c(\tau + T)}{X_c(\tau) + X_c(\tau + T)} \tag{3.26}$$

[5] Here, the term "zero-crossing" means the moment, where the balanced cross-correlation signal changes its sign.

which is really independent of amplitude changes and can be referred to as "balanced" detection. Finally, the influence of the group delay T is shown in the figure where it has been halved from the optimum value, Eq. 3.25. The slope around the zero-crossing is significantly less steep for the same fundamental pulses, showing that a careful initial design of an actual device is required, as its performance will degrade with a poorly chosen delay element.

3.5.2 Autocorrelation

In femtosecond pulse diagnostics, a reference pulse much shorter than the pulse to be measured is typically not available. Thus, the limit of Eq. 3.20 with $I_s(t) = I_r(t) \equiv I(t)$ is considered, leading to the first-order autocorrelation

$$A_c^{\text{int}}(\tau) = \int_{-\infty}^{\infty} I(t)\, I(t-\tau)\, \mathrm{d}t \tag{3.27}$$

which is of particular interest for the standard diagnostic methods and characterization of the master laser oscillator, as discussed in chapter 5 (pages 71 ff.). An intensity autocorrelation, as illustrated in Fig. 3.4 (left), is always a symmetric function, which can be understood from the comparison of the overlap integral for positive and negative arguments. This fact results in an important limitation, in the sense that no information on the phase of the pulse being analyzed is provided. There are, however, more sophisticated diagnostic techniques like spectral phase interferometry for direct electric field reconstruction (SPIDER) [IW98] or frequency-resolved optical gating (FROG) [Tre02], but these are not described here, because they are not applied in the context of the synchronization system – yet. The temporal duration of a pulse, as an important figure of merit not only for the laser system itself, but also for the dispersion compensation in the fiber link stabilization units, is usually derived from its autocorrelation. Thereby, a pulse shape is assumed and the duration is determined

Table 3.2 | Typical pulse shapes, spectra, intensity and interferometric autocorrelations. Detailed calculations can be found in [DFMS85]. The FWHM of the intensity autocorrelation function A_c is τ_{ac}.

$E(t')$	$\lvert\tilde{E}(\Omega)\rvert^2$	$\tau_{\text{fwhm}} \cdot \Delta\nu$	$A_c(\tau')$	$\tau_{ac}/\tau_{\text{fwhm}}$	$G_2(\tau') - (1 + 3A_c(\tau'))$
$e^{-t'^2}$	$e^{-\Omega^2}$	0.441	$e^{-\tau'^2/2}$	$\sqrt{2}$	$\pm e^{-(3/8)\tau'^2}$
$\operatorname{sech}(t')$	$\operatorname{sech}\left(\frac{\pi\Omega}{2}\right)$	0.315	$\frac{4(\tau'\cosh\tau' - \sinh\tau')}{\sinh^3\tau'}$	1.543	$\pm\frac{4(\sinh(2\tau') - 2\tau')}{\sinh^3\tau'}$

from known ratios of the FWHM autocorrelation τ_{ac} and that of the pulse. Table 3.2 shows analytical expressions for the pulse spectrum, the intensity autocorrelation and the envelope of the interferometric autocorrelation for Gaussian and sech^2-shaped pulses. The unit t' in the pulse's electric field is chosen such that the function takes its simplest form, and its inverse is used as unit frequency Ω. The FWHM pulse duration τ_{FWHM} can then be calculated from the FWHM τ_{ac} of the autocorrelation function A_c using the shape dependent ratio given in the fifth column. The implementation of

autocorrelators and their use in the synchronization system is discussed in section 5.2.3 (pages 77 f.) on the characterization of the master laser system.

The interferometric autocorrelation, illustrated in Fig. 3.4 (right), can be derived from the field correlation of a MICHAELSON interferometer. It can be shown that the second-order correlation function is given by

$$G_2(\tau) = \int_{-\infty}^{\infty} \left\langle \left| \left(E_1(t-\tau) + E_2(t) \right)^2 \right|^2 \right\rangle \mathrm{d}t \tag{3.28a}$$

$$= A_0(\tau) + \mathrm{Re}\left\{ A_1(\tau) e^{-i\omega_1 \tau} \right\} + \mathrm{Re}\left\{ A_2(\tau) e^{-2i\omega_1 \tau} \right\} . \tag{3.28b}$$

An interferometric autocorrelation signal has three frequency components[6] centered at zero frequency, around ω_1 and $2\omega_1$, respectively. When a low-pass filter is applied to the signal, the correlation reduces to $A_0(\tau)$, which is the sum of a background term and the (background-free) intensity autocorrelation (Eq. 3.27). As any autocorrelation, G_2 is a symmetric function, but it contains the phase information and allows to determine a linear chirp of the measured pulse – in contrast to the intensity autocorrelation. However, this has not been exploited in this thesis, where only intensity autocorrelations were recorded. A very comprehensive review of pulse reconstruction is given for instance in [DR06].

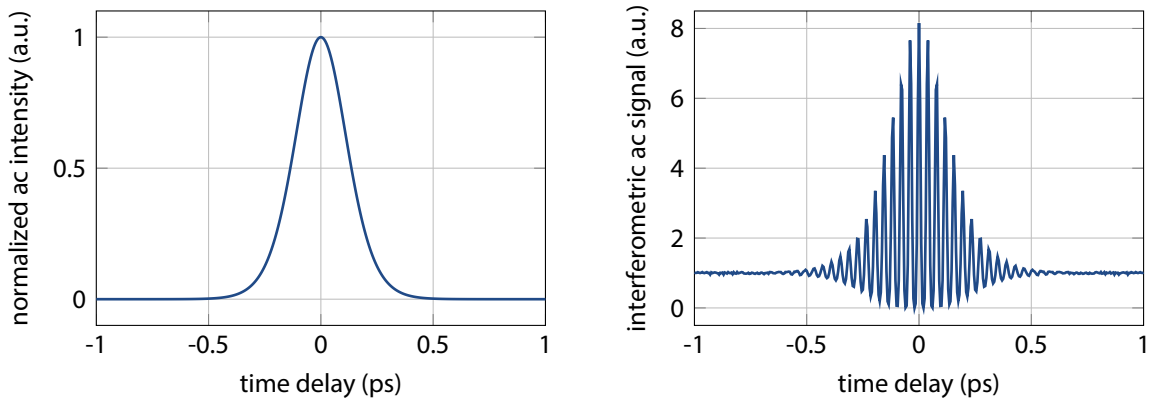

Figure 3.4 | Calculated signals for intensity and interferometric autocorrelation. Intensity (**left**) and interferometric autocorrelation (**right**) of a 100 fs sech^2 pulse. Note that the ratio of the baseline and the signal is always 1:8 for interferometric autocorrelation measurements based on sum-frequency generation.

[6] Here, the term "frequency" refers to the variation of the function $G_2(\tau)$ as function of τ, which is the delay parameter and continuously tuned in the correlation measurement.

4 Pulsed Laser-Based Synchronization System

In this chapter, the implementation of the pulsed laser-based, optical synchronization system at FLASH, its present stage of expansion and the relevant components for this thesis are explained in more detail. It has been substantially upgraded from the principle explained in [KIK+04, KCCK08] mainly with the addition of fiber links to new bunch arrival time monitors [BAF+09, Boc13] and two optical cross-correlators for the integration of external lasers to the system. To ensure reliability of the system, the redundant operation of two master laser oscillators (MLOs) is foreseen. Due to this

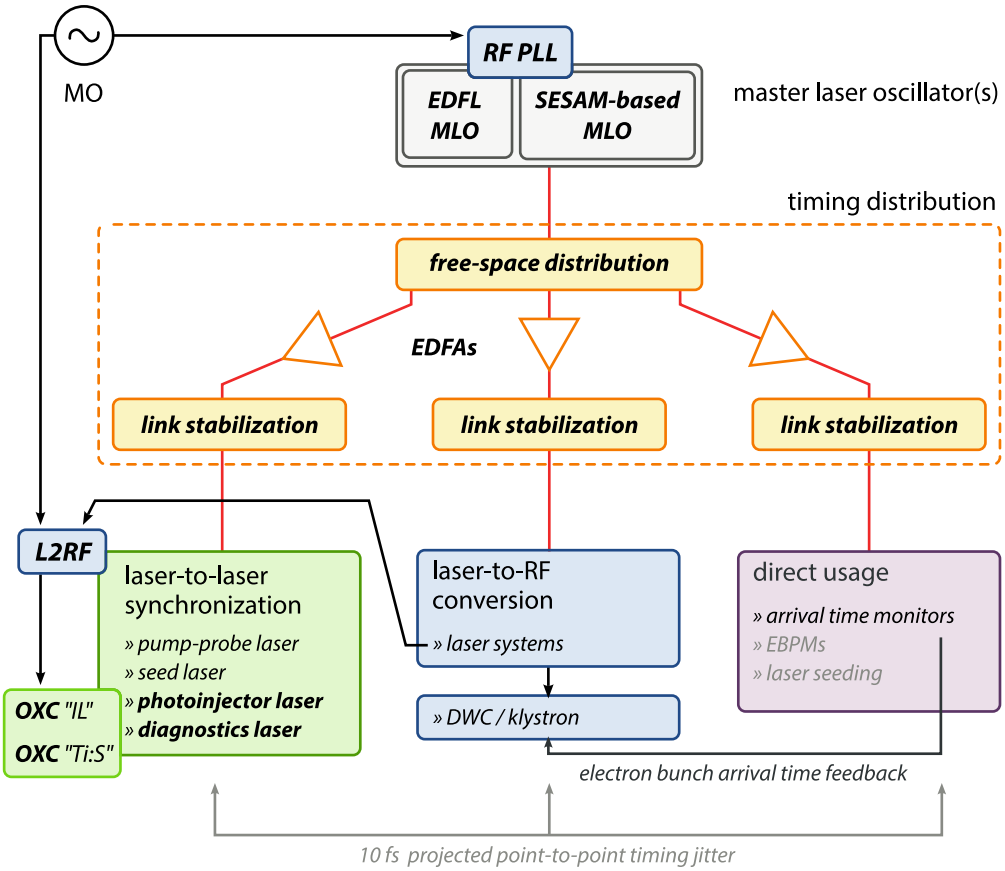

Figure 4.1 | Sketch of the building blocks of the pulsed laser-based synchronization at FLASH. The layout is based on the original ideas (compare Fig. i.2, page 3) but provides more detail on the actual implementation. The topics related to this thesis are printed in a bold typeface.

and the large number of fiber links and possible other consumers of the pulse train emitted by the MLO, a change from the original design had to be made. The so-called free-space distribution unit

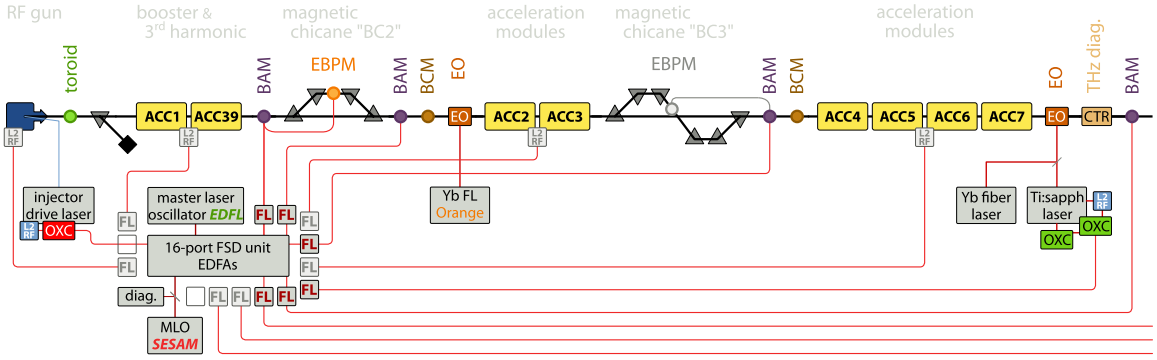

Figure 4.2 | Schematic layout of the FLASH optical synchronization system in the linac section. The system consists of two master laser oscillators, the local distribution unit, six units for fiber link stabilization, three optical cross-correlators and four bunch arrival time monitors.

FSD is an optical setup for splitting the light of both MLOs and providing it to 16 ports. Since every port can only be provided with a comparatively low optical power level, dispersion-compensated erbium-doped fiber amplifiers (EDFAs) are used to connect the fiber link stabilization units to the FSD. Figure 4.1 resembles the schematic principle shown in the introduction (Fig. i.2, page 3), but with more detail on the master laser oscillator, the distribution of the timing information and the synchronization of external laser systems. The connection of the laser-to-laser ("L2L") branch to the laser-to-RF ("L2RF") indicates that for an all-optical synchronization of an external laser an RF-based phase-locked loop (PLL) is a prerequisite as explained later in section 7.1.2 on pages 157 ff.

4.1 RF Synchronization Infrastructure

Presently, the timing and synchronization of the accelerator is derived from a central master RF oscillator (MO). It is operated at the accelerating frequency of $f_{\mathrm{RF}} = 1.3\,\mathrm{GHz}$ and distributed via coaxial cables along the accelerator. To further improve the long-term stability, it is phase-locked to a temperature-stabilized quartz oscillator with a frequency of $f_{\mathrm{RF}}/144 = 9.027777\,\mathrm{MHz}$ [Loro6]. As explained before, a phase stability of 0.005 deg corresponds to 10 fs at the acceleration frequency. In addition to the demanding transport of such a phase-stable signal with a coaxial distribution system, the time drifts in long cables caused by thermal expansion and contraction can be some picosecond per degree temperature change – even for cables with very low temperature coefficients. Since most of the timing-critical devices are located at the beginning of the accelerator, such as the injector and the MO, and at or near the end, such as the pump-probe and seed lasers, the drift in the several hundred meter long cables is a strong limitation.

Nevertheless, all the lasers at the facility –including the master laser oscillator– have to be synchronized to this reference with an RF-synchronization scheme. Since the distributed frequencies include also other sub-harmonics of the accelerating frequency, such as 81.25 MHz, extended phase detection circuits can be built, which are described in the corresponding section 5.3 (page 87 ff.), section 7.1.2 (page 157 ff.) and section 8.1 (page 168 ff.) below. It should be noted that the used mixers,

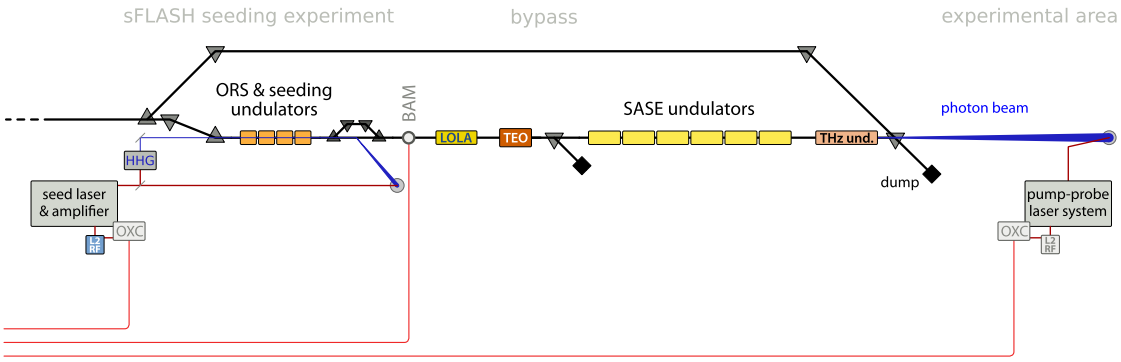

Figure 4.3 | Schematic layout of the FLASH optical synchronization system in the undulator section. In this section, most of the future upgrades will take place, as the seed- and the pump-probe laser oscillators will be locked to the synchronization system, and additional bunch arrival time monitors will be installed.

filters and phase detectors are also temperature sensitive devices, and by this form a second limitation of the RF-based synchronization infrastructure.

4.2 Layout of the Optical Synchronization System at FLASH

First experiments regarding the optical synchronization system were carried out in 2004. Since then, significant developments were made [WLL+06], with a remarkable result of the measurement of 8.4 fs uncorrelated jitter between two electron bunch arrival time monitors (BAMs), which were separated by 60 m and each provided with its own stabilized fiber link from a self-built erbium-doped fiber laser (EDFL). Hence, the resolution of each BAM was ~ 6 fs [LAF+10]. The update of this proof-of-principle experiments began in summer 2009 with steady progress, and in the synchronization hutch located adjacent to the hutches hosting the injector laser and the master RF oscillator in the main accelerator hall components and devices were installed and commissioned. Figures 4.2 and 4.3 schematically show the present stage of expansion of the system. The main existing and commissioned subsystems are

- **two master laser oscillators** of a different type, with the first one being a self-built EDFL based on NPR mode-locking. In the latest step of the expansion (see also remarks below) a commercial SESAM-based laser system, called Origami, has been commissioned. It promises lower timing jitter and maintenance-free operation. A comparison of the two lasers and measurements utilizing the Origami as MLO are discussed in section 5.4 (pages 92 ff.),

- the **free-space distribution unit**, which was commissioned together with the EDFL, after an improvement of the telescope required for imaging the output collimator to the EDFA ones. When the Origami laser had been installed and commissioned, the FSD was again modified and redesigned mirror mounts helped improving the mechanical stability. The FSD is discussed in section 5.5 (pages 108 ff.),

- **six length-stabilized optical fiber links** to the remote locations. They connect four BAMs and the laboratories where the seed and a diagnostic Ti:sapphire oscillators are situated. Due to the individual time of commissioning, the availability of a new dispersion compensating fiber and the in-house-built optical delay lines, as well as several investigations conducted with the link to the EO laboratory, the fiber links are presently different in some regards. They are discussed chapter 6 (pages 131 ff.),

- the first **optical cross-correlator for the synchronization of external Ti:sapphire lasers**, developed in the laboratory of the electro-optic experiment. It uses a similar delay/subtraction (bipolar) detection scheme as the fiber links. In addition, an RF signal can be generated in the laser laboratory from the reference pulse train, such that the laser oscillator can also be phase-locked to this signal – replacing the old RF synchronization setup. The schemes and first results are explained in chapter 7 (pages 151 ff.),

- a similar **optical cross-correlator for the photo injector laser system** as second novel component of the synchronization system. It allows for the measurement of the arrival time of the pulses emitted by the so-called pulse train oscillator (PTO) and in combination with a BAM upstream of the first magnetic chicane the investigation of electron bunch timing jitter in the injector and booster (see chapter 8, p. 167 ff.). It will enable an active stabilization of the laser pulse arrival time and is, furthermore, prepared for the synchronization of the PTO to the reference laser pulse train,

- two already existing and **two additional bunch arrival time monitors**. They had been installed in front (upstream) of the magnetic chicane and behind (downstream) as part of [Boc13]. Since the BAM upstream of the chicane was used for measurements in this thesis, its principle of operation is briefly described in section 4.4 of this chapter,

- a **large horizontal aperture beam position monitor** ("EBPM" in the figure), allowing for the measurement of the electron beam position inside the first magnetic chicane at high resolution with two distinct detection principles – see [Hac10].

Synchronization Laboratory

The synchronization laboratory, which was planned and constructed in [Win08], contains, amongst others, four electronic racks. One of the most important chassis is the RF phase detector for the synchronization of the MLOs. It is temperature stabilized and features two identical RF circuits (see section 5.3, pages 87 ff. and [Hac10]). The racks also hold the electronics for digitizing, regulation and accelerator control system interfaces. Furthermore, the motor- and piezo drivers are realized as rack chassis.

All optical components of the synchronization system are installed on a covered optical table. It accommodates, as sketched in Fig. 4.4, the free-space distribution unit in the center, surrounded by the master laser oscillators, and separate metal boxes, where the erbium-doped fiber amplifiers are

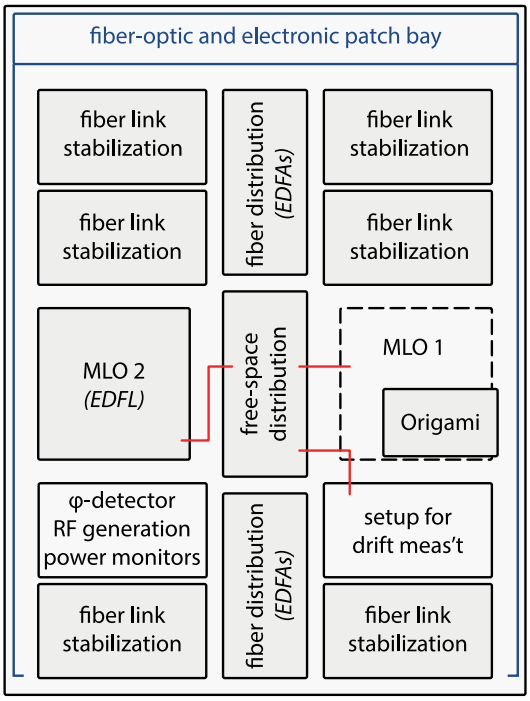

Figure 4.4 | Schematic layout of the optical table in the synchronization laboratory. Around the central free-space- and fiber distribution units, the master laser oscillators and the fiber link stabilizers are grouped.

laid out. On each side of the FSD, four positions for fiber link units are foreseen, and six of those in total eight positions are occupied by the installed links. In one of the remaining spaces, optical power monitor circuits and a setup for the generation of a 2.6 GHz RF signal (see next section) from light at one port in the FSD is installed. The RF signal is used for additional RF phase detectors in the fiber link stabilization units (see section 6.2, p. 140 f.). In the last available space, a drift measurement setup for the evaluation of the distribution EDFAs has been installed (see section 5.6, p. 120 f.). A more detailed description of the synchronization hutch and the reassembly of the interior during the accelerator shutdown is given in appendix B on pages 223 ff.

Historical Remarks on the Master Laser Oscillators

In the beginning of the development of pulsed optical synchronzation systems, the fiber laser systems were chosen to be operating at a repetition rate of 40.625 MHz and later 54.167 MHz [Wino8]. They were built as "stretched pulse" lasers with a ring geometry, because of their proven long-term stability, high pulse energy and peak power. The disadvantage of these relatively low repetition rates is the temporal distance of two subsequent pulses, which are 24.6 ns and 18.5 ns, and making optical delay lines impractically long. Furthermore, the fiber of these laser oscillators are about 4 m and because they are prone to environmental changes like temperature, air flow and humidity, a careful mechanical design with maximum isolation from these changes would have been required to ensure

best possible timing phase noise performance.

To circumvent long optical delays, soliton fiber lasers with repetition rates around 200 MHz in a "sigma configuration" were developed, reducing the distance of two pulses to the order of 1 m in fiber or 4.62 ns, which is especially advantageous for optical cross-correlators, where temporal delay cannot be introduced by adding more fiber (see chapters 7 and 8, pages 151 and 167, respectively). These lasers have a smaller pulse energy at the same average power, which is a disadvantage for some applications like frequency-doubling, thus requiring higher amplification. However, it has been shown that soliton lasers can deliver half of the pulse energy at four times the repetion rate in comparison to stretched pulse lasers.

Ultimately, it was agreed to employ a master laser oscillator at a repetition rate of $f_{\mathrm{MLO}} = f_{\mathrm{RF}}/6 = 216.667\,\mathrm{MHz}$ for maximum compatibility with the existing RF infrastructure at FLASH, as well as electronics and other laser systems. The first laser system was built from off-the-shelf optical and mechanical components as a breadboard setup with no automation, and it was used for many accelerator based measurements along with the prototype bunch arrival time monitors [Loe09, LAF+10]. A second version of this type of laser was constructed with a CNC-milled aluminum main frame, incorporating motorized wave plates, the RF phase detector and a four-port distribution scheme. Because of strategic decisions regarding the redundancy of two laser systems and the number of end-stations of the complete system, this laser could not be used as MLO, but serves now well as experimental laser for various other developments. The third iteration constructed for the comprehensive upgrade of the synchronization system, with cost-effectiveness in mind, turned out to be not deployable because of major mechanical design flaws. During the commissioning of the original laser as a fall-back solution, it was discovered in this thesis that additional diagnostic methods have to be applied to ensure a stable, single-pulse operation (see section 5.2.1, p. 73 f.). This was not achievable with the required average optical power for all components. Therefore, a replica of this breadboard laser system was assembled and commissioned. Albeit being also not fully automated, it is easier to maintain, delivers the required average power and performs better than the prototype. This new laser served as the MLO until the transition to the SESAM-based Origami laser was made.

4.3 Laser-to-RF Conversion

The generation of RF signals from the optical reference pulse train is not only required for controlling the cavity fields in a more advanced status of the synchronization system, but essential for the RF-based phase-locked loops, for instance to synchronize other lasers.

The most simple way, named "direct conversion", to extract an RF signal from the optical pulse train is to detect it with a large bandwidth photodetector. The detector's output is then an electrical pulse train with frequency components at every harmonic of the fundamental repetition rate, up to the cut-off frequency –which can be as high as ~ 100 GHz– of the detector. A suitable harmonic can be band-pass filtered and has usually to be amplified. This enables, for instance, a phase detection of the optical pulse train and a reference, or the RF-based phase detection between two optical pulse trains (L2L synchronization). Since the sensitivity of the phase detector K_ϕ depends on the steep-

ness of the slope at the zero-crossing of the RF signal, the timing resolution is increased at higher harmonics. The major drawbacks of this scheme are drift with temperature and relative humidity changes, the conversion of intensity noise to phase noise[1] in the order of 1 ps/mW to 15 ps/mW, and the limitation of the noise floor by shot noise [Loro8]. Especially the latter is critical in phase noise measurements of mode-locked lasers, which are discussed in the following chapters.

A more elaborate scheme is based on a SAGNAC loop interferometer, for instance to directly lock a local oscillator to the optical pulse train. However, this method is relatively complicated and was found to work only for frequencies higher than a couple of gigahertz. In practice, the direct conversion method turned out to be sufficient at f_{RF} = 1.3 GHz required in the context of this thesis. Further information on the SAGNAC loop technique is provided in [KKL06, KKP04, FAB+09].

4.4 Electron Bunch Arrival Time Monitor

The electron bunch arrival time monitors utilize the optical pulse train, provided by a fiber link, directly, thus circumventing additional sources of jitter from other lasers and PLLs in comparison to, for instance, the electro-optic methods described in section 1.8.1, pages 16 f. Their principle of operation is depicted in Fig. 4.5. The laser pulse train enters a MACH-ZEHNDER type electro-optic amplitude modulator (see section 2.4.6, pages 40 f.) with a bandwidth in the order of 10 GHz. Its input is the signal of a button-type pickup, whose the zero-crossing is a measure for the arrival time of the electron bunch centroid. Due to the large bandwidth of the signal and to avoid drift, the BAM front-end, i.e. the actual device, has to be placed in the tunnel close to the pick-up. When the timing

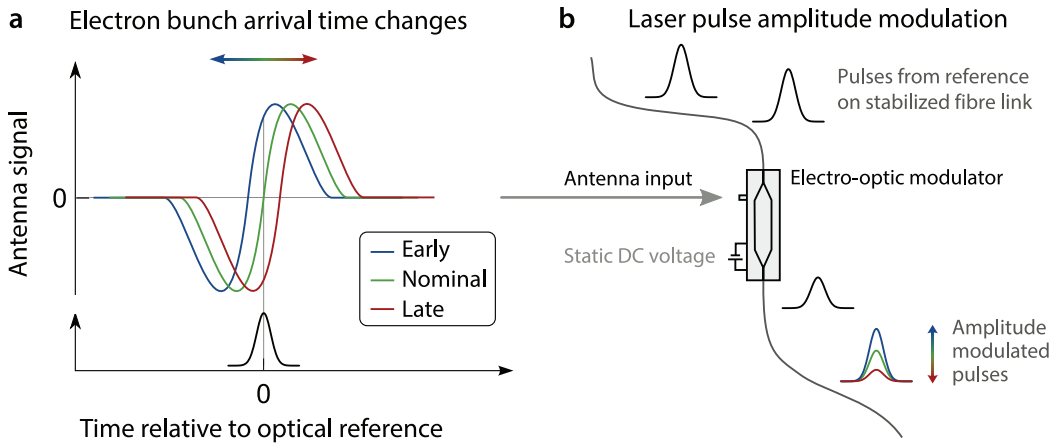

Figure 4.5 | Principle of the electron bunch arrival time measurement. It is based on electro-optic amplitude modulation of one reference laser pulse in the train depending on the transient field of the electron bunch. The illustration is based on sketches by M. K. Bock.

of the laser pulse train is adjusted such that it coincides with that zero-crossing, the subsequent laser pulses will be modulated differently, when an electron bunch with a different arrival time passes the

[1] The conversion depends on the type of the diode, the bias voltage and the optical power level.

pick-up [Loe09]. The baseline and the intensity of the modulated laser pulses is measured with a photodetector and digitized with fast ADCs based on an in-house developed so-called advanced carrier board (ACB). Together with a normalization to a previous laser pulse and the baseline, the influence of most noise sources can be reduced. A more detailed description of the data acquisition is given in [GBF+10b], whereas in [BAF+09, BFG+10] the design and performance of the two new BAMs around the first magnetic chicane are discussed. A more general evaluation and comprehensive studies on the bunch arrival time and its measurement can be found in [Boc13].

Phase Relation of the Synchronization System

Figure 4.6 shows the measured pickup signals as function of the relative timing of the laser pulse and the electron bunch, where the timing of the laser had been scanned with a programmable phase shifter in the synchronization circuit (see section 5.3, page 87 f.). The curves with steeper slopes are

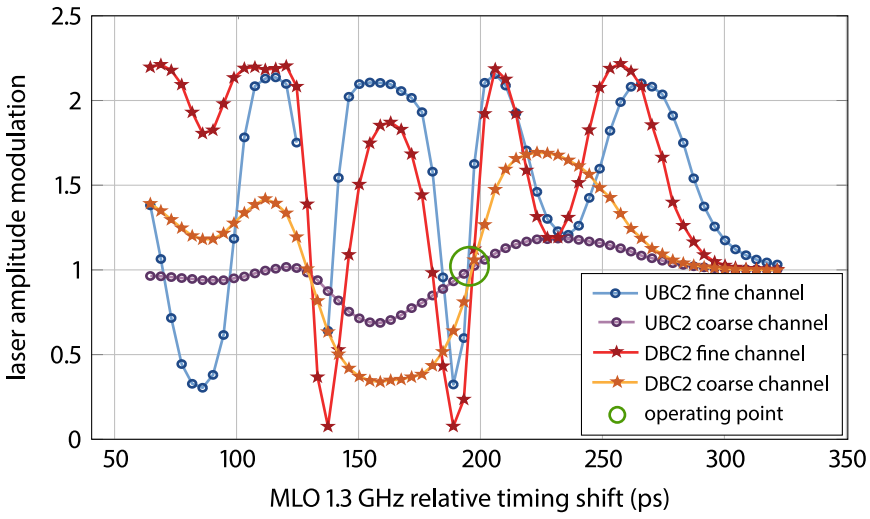

Figure 4.6 | BAM signals from a scan of the relative timing of the MLO and the electron bunch. The graph shows both the fine (steep slope at the operating point) and the coarse (shallow slope at the operating point) signals from two BAMs (adapted from [BFG+10]).

from the "fine" and the other from a "coarse" channel each BAM is equipped with. Naturally, the fine channels have a larger sensitivity at the cost of dynamic range and vice versa.

It can be seen that all four curves cross nearly in one point at a relative time around 200 ps. This is the result from a manual adjustment of the time delay of one of the BAMs: only for the first BAM commissioned, the temporal overlap of the laser pulse and the electron bunch can be set with the phase shifter. Then its phase setting is fixed, and by that the phase setting of all other fiber links. For the next BAM commissioned, this timing has to be set during its commissioning by adjusting the cable length between the pick-up and the EOM, every time requiring a time-consuming access to the accelerator tunnel.

This also affected the optical cross-correlators at the link ends, whose developments began before

the upgrade of the synchronization hutch, which necessitated a new phase setpoint of the master laser oscillator. Usually, the phase of the Ti:sapphire laser is also fixed with respect to the electron bunch for temporal overlap in the diagnostic or user experiment. Hence, the pulse train provided by the fiber link has to be delayed to keep the temporal overlap in the cross-correlator. By this, the focusing is changed and affects the conversion efficiency in a negative way, requiring usually an adaption of the optics.

Typically, this happens only once, but nevertheless, this is a minor weak point of the present implementation. Hence, the phase of the master laser oscillator must be defined as early as possible, and additional optical delay lines can be introduced between the FSD and the link stabilization unit. This moves complexity out of the accelerator tunnel or other end stations and adds it in a better accessible laboratory.

4.5 Longitudinal Accelerator Feedback Overview

As already mentioned, there are several sources of instability in the accelerator, which lead to fluctuations in the arrival time of the electron bunches and therefore the FEL pulses, as well as in the SASE process in general. In particular the arrival time of the electron bunches in the acceleration modules is critical, as it influences total energy, energy spread and compression of the bunches. The main sources of this jitter are the generation of the bunch itself in the photoinjector, as explained in section 1.6.2 on pages 14, where the photoinjector laser and the electron gun have different contributions. Additionally, the amplitude stability of the acceleration fields in the superconducting modules is a critical parameter for the electron bunch arrival time, because energy fluctuations are transformed into arrival time fluctuations in the bunch compressor. The compression itself is mainly influenced by the phase stability of the preceding acceleration fields. Therefore, several feedback loops had been

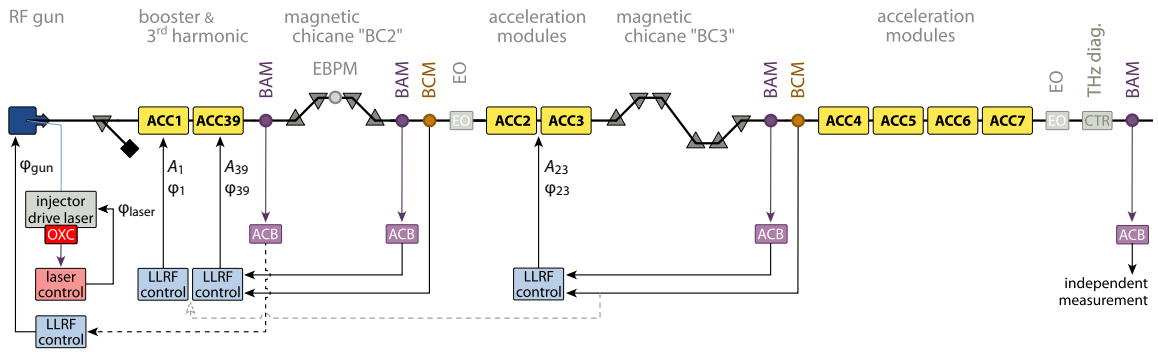

Figure 4.7 | Sketch of the planned FLASH longitudinal accelerator feedback topology. It is envisioned to implement a multiple step feedback topology in which each source of jitter is regulated based on measurement directly succeeding it.

implemented at FLASH. With respect to the optical synchronization infrastructure, two main feedback systems are presently under development, as illustrated in Fig. 4.7:

- Stabilization of the photoinjector laser pulse arrival time on the photocathode, based on the optical cross-correlator (OXC) discussed in chapter 8, pages 167 ff. Presently, this is restricted to only a slow feedback, and a not-learning feed forward as will be explained below.
- Additional correction of the accelerating fields through the low-level RF controller (LLRF) based on arrival time and compression measurements downstream of the acceleration module groups ACC1 & ACC39 and ACC23 with dedicated BAMs (see previous section) and BCMs (see section 1.8.2, page 18). This allows for a fast intra-bunch train feedback to minimize arrival time jitter across the macro-pulse, after a short adaption time.

Later, a slow feedback on the phase of the electron gun is planned, also based on the bunch arrival time monitor upstream of the first magnetic chicane. A more detailed description of the beam-based feedback (BBF), comprehensive studies on the influence of different accelerator parameters and promising results are discussed, for example, in [Loe09, LAF+10, GBF+10a, KBB+10, Boc13].

5 Timing Reference

The timing information for all components of the optical synchronization system and in the future the complete accelerator is the repetition rate of the master laser oscillator. Therefore, it is crucial to understand the behavior of the laser system and to characterize it in various aspects to ensure a reliable short- and long-term operation. In this chapter, the installation and commissioning of a self-built erbium-doped fiber laser (EDFL) as master oscillator, as well as the numerous short-pulse diagnostic methods are described and explained. These methods are afterward applied for the characterization of a commercial SESAM-based laser system which is also installed as an alternative to the EDFL. In order to operate the synchronization system with currently six end-stations and a number of monitor ports, the laser pulse trains of the MLOs must be splitted and distributed to the fiber link stabilization units. This is realized in free-space optics and also discussed in this chapter. Furthermore the synchronization of the lasers to the accelerator's RF oscillator is described, and the long-term stability of the timing reference, consisting of the RF-synchronized lasers and the local distribution to the fiber links, is evaluated.

5.1 Setup and Implementation of an Erbium-Doped Fiber Laser

As mentioned earlier (section 4.2, p. 63 f.), the erbium-doped fiber laser serving as master laser oscillator is a replica of a previously tested system [Loe09], because the original system could not be operated in the desired way. This new laser is built as a laboratory/breadboard setup with off-the-shelf opto-mechanical components which were carefully selected to ensure high mechanical stability. Furthermore, attention was paid during assembly of the laser to ensure easy maintenance and to provide easy access to all components of the system. The laser resonator itself is laid out in a σ-configuration formed by the input- and output collimators and a mirror mounted on a piezo-electric transducer which in turn is mounted on a motorized delay stage, enabling a fine and a coarse repetition rate stabilization (see section 5.3, p. 87). The erbium-doped gain fiber is pumped by two 580 mW PMF-pigtailed 974 nm diode lasers[1], each are combined using a polarization dependent pump combiner. Using a free-space Faraday isolator, the direction of pulse propagation in the laser is chosen to be counter-propagating to the pump light, which was found to be the favorable configuration for low-timing jitter operation. To achieve NPE mode-locking as described in section 2.4.3, page 37 f., a polarizing beam cube (PBC) is used as output coupler in-between the collimators and the mirror. The output beam of the laser passes another Faraday isolator to avoid disturbances in the cavity by back-reflected light. Additional diagnostics ports are directly integrated into the

[1] Bookham/Oclaro LC96UAA74 with a maximum output power of 580 mW when pumped with $I_{\text{pump}} = 1$ A.

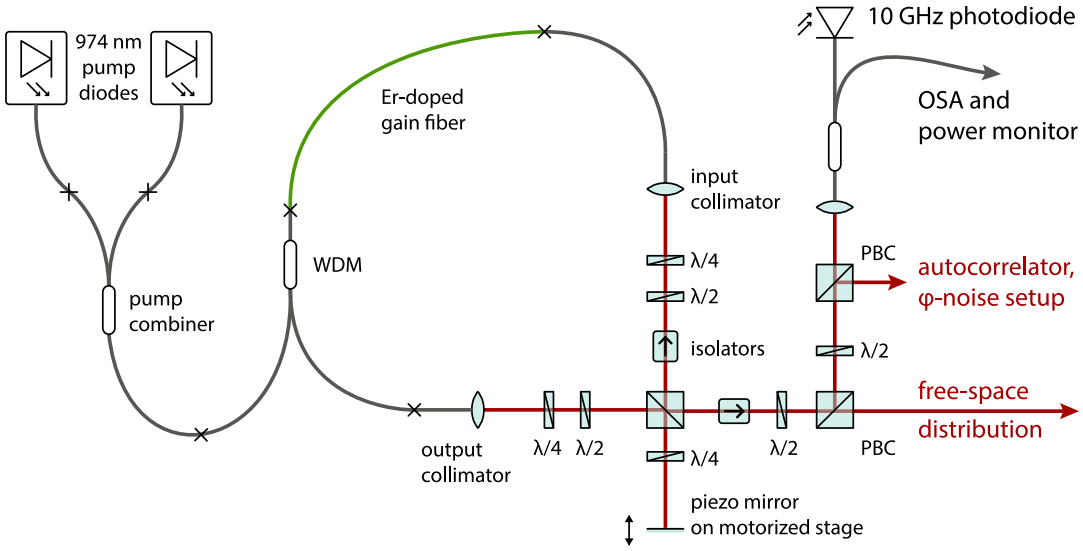

Figure 5.1 | Schematic optical setup of the EDFL master laser oscillator. The resonator is laid out in a σ-configuration confined by the two collimators and the movable mirror. A polarizing beam cube (PBC) serves as NPE output coupler and saturable absorber. The diagnostic components, such as photodiode (upper right) as part of the RF synchronization circuit (see section 5.3, p. 87), are integrated into the housing of the actual implementation.

setup – one in free-space and one fiber-coupled. The collimator is spliced to a 70:30-coupler with the 70% transmission directly spliced to a high-bandwidth InGaAs photodiode[2] providing the electronic Fourier comb of the pulse train required for the synchronization scheme, whereas the 30% tap of the coupler is again split and used for further diagnostics (see section 5.2, p. 73 ff.). In Fig. 5.1 the optical setup is shown schematically, and in table 5.1 the relevant lengths and properties of the resonator's components are summarized. In contrast to previous installations of these type of lasers, the free-space section has been reduced to a minimum possible length for a breadboard setup to enable a longer gain fiber length. The total fiber length is 818.2 mm which results, together with the free-space section of 183.1 mm, in a resonator round-trip time of 4.615 ns and hence a repetition rate of f_{MLO} = 216.667 MHz. The laser emits 215 mW average optical power in cw operation when pumped with a power of ~ 1 W. Mode-locking starts when the quarter-wave retarder in front of the output collimator is rotated slightly, and the average power drops to ~ 130 mW. However, it was discovered that the laser is then operating in a multiple-pulse regime which is very challenging to detect (see below). In order to achieve a stable single-pulse operation, the pump power has to be reduced significantly to about 270 mW where the laser changes its regime to a single pulse mode instantaneously. Then the pump power can be increased iteratively with slight rotation of the quarter-wave retarder to 550 mW where the laser emits approximately 80 mW average optical power. This corresponds to a pulse energy of E_{pulse} = 365 pJ, which is, for the given repetition rate and cavity net dispersion, in very good agreement with the results reported in [TNHI94]. Increasing the pump power beyond

[2] EOTech ET3500F with a 3-dB bandwidth of 10 GHz

Table 5.1 | Lengths and fiber parameters utilized in the master EDFL. In contrast to previous versions of this laser type the length of the free-space section has been reduced to enlarge the gain fiber length. More properties of the optical fibers can be found in appendix D (page 239 ff.).

segment	**type**	**length** mm	β_2(1560 nm) fs^2/mm	**net** β_2 fs^2	γ 1/(W m)
input collimator	SMF-28e	60	-23.16	-1389.6	0.0011
gain fiber	Liekki Er80-8/125	542.7	-20	-10854	0.0013
WDM	ClearLite 980-16	155.5	4.5	699.75	0.0021
output collimator	SMF-28e	60	-23.16	-1389.6	0.0011
free-space		183.1	0	0	0
sum		183.1 + 818.2		-12933.45	

that point breaks the soliton and the laser goes back to cw operation, but once mode-locked in this way, the laser can operate stable on a timescale of months, even with minor disturbances, such as vibrations or slight shocks when working on the optical table. Here the self-aligning mechanism of the soliton with respect to nonlinearity, dispersion and power is advantageous. On the other hand, the rather complex procedure to establish the stable mode-locking regime makes it quite difficult to automate this process, pinpointing one disadvantage of these types of lasers. To further minimize environmental disturbances to the laser, and in particular to prevent the fibers being exposed to air flow, it has been housed completely (see Photo G.1 on page 253). The housing is mounted on the optical table directly and not to the breadboard assembly, further reducing mechanical influences.

5.2 MLO Diagnostics and Characterization

In this section, the applied diagnostic instruments and methods are described and the results obtained from the characterization of the EDFL are discussed. The pulse duration is measured with the commercial SHG-based autocorrelator "APE PulseCheck". Two commercial optical spectrum analyzers are available, both of which allowing for measurements in the wavelength or directly in the optical frequency domain. Furthermore, a 1 GHz and an 8 GHz oscilloscope, as well as 7 GHz and 26 GHz RF spectrum analyzers are available to investigate the output from photodiodes in the frequency domain. The timing phase noise and intensity noise measurements are carried out using an Agilent E5052B signal-source analyzer. Long-term measurements are enabled by distinct optoelectronic monitoring setups connected to ADCs and their DOOCS- and MatLab-based readout.

5.2.1 Detection of Double-Pulse Operation

When the first machined fiber link stabilization unit, described in the following chapter, was commissioned with the original breadboard laser, the scan of the optical delay line revealed two addi-

tional prominent S-shaped signals in a distance of ±34 ps to the expected cross-correlator signal. The only explanation for this is a smaller satellite pulse traveling along with the main pulse in the laser pulse train. Whether the pulse is temporally located 34 ps before or behind the main pulse cannot be distinguished because of the symmetry of the optical cross-correlator setup. Because of the limited bandwidth of the oscilloscope of 8 GHz and the bandwidth of the used photodiode of 10 GHz, corresponding to a signal rise-time of 35 ps, the satellite pulse can not directly be measured in the time-domain with the available equipment. However, with the consulting of the 26 GHz RF

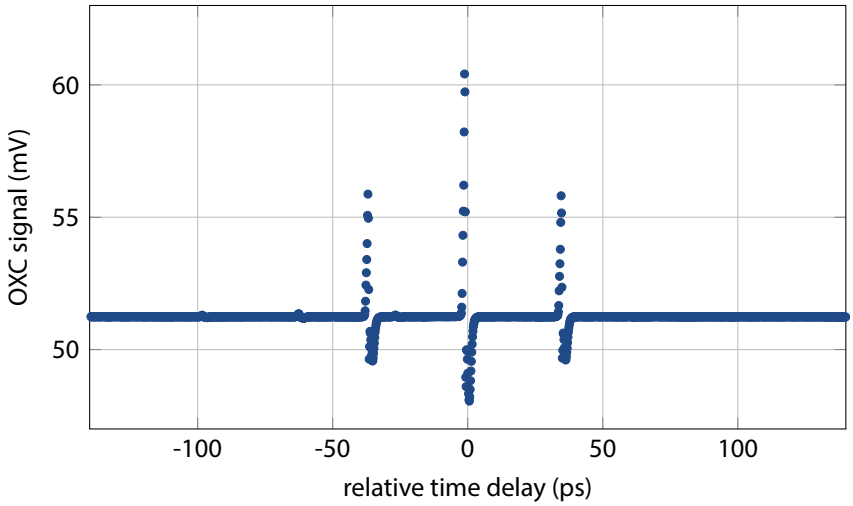

Figure 5.2 | Full range scan of the optical delay line in a fiber link unit. It reveals a satellite pulse in the laser's pulse train with a distance of 34 ps to the main pulse.

spectrum analyzer in addition to the 7 GHz version, which was available in the former theses, this double-pulse regime of the laser can be detected in the frequency domain because of the modulation of the Fourier comb lines.

In Fig. 5.3 the calculated envelopes of the frequency spectra in a double-pulse regime is shown for different intensity ratios of the main pulse and the satellite and for different temporal distances Δt_{dp}. For this calculation, Gaussian pulses with a duration of $\tau_{\mathrm{p}} = 100$ fs are assumed. The satellite pulse has the lower intensity $I_2 < I_1$ and follows the main pulse in a distance of $\Delta t_{\mathrm{dp}} \ll T_{\mathrm{rep}}$. The 3-dB bandwidth of the used photodiode of 10 GHz and a measurement noise floor of −60 dB has been taken into account in the calculation. The upper plot shows the results for the case $I_2 = 0.5 \cdot I_1$. The modulation of the frequency spectrum is very pronounced, even in the lower frequency region and for small temporal distances of < 50 ps. In the lower plot, however, where the calculation is shown for $I_2 = 0.1 \cdot I_1$ being more likely in reality, the modulation for short distances $\delta t < 50$ ps and frequencies below 7 GHz is hardly visible and can be easily overseen or confused with the attenuation of the photodiode in a measurement. In this case, additionally an autocorrelation measurement with large scan range has to be considered. The employed autocorrelator, for instance, has a maximum scan range of 50 ps, thus able to reveal a second pulse with $\Delta t_{\mathrm{dp}} < 25$ ps. For pulse separations of well above 50 ps the modulation is again relatively strong, but that case could also be detected using

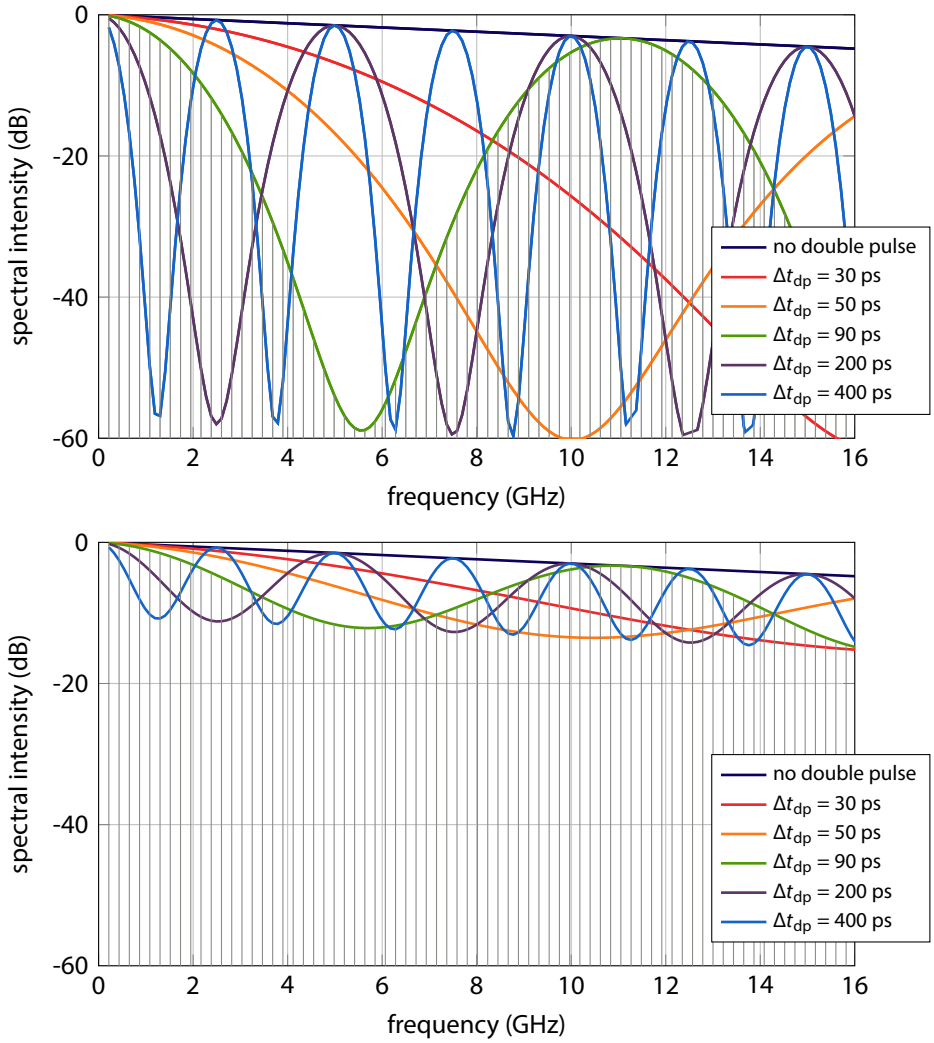

Figure 5.3 | Calculated envelopes of the Fourier comb for laser double pulse operation. The calculation of the envelopes of the Fourier based on a 216 MHz laser with 100-fs-long Gaussian double pulses. The intensity ratios of $I_1/I_2 = 2$ (**top**) and $I_1/I_2 = 10$ (**bottom**) for different temporal pulse spacings are shown. For $\Delta t_{dp} = 90$ ps the individual comb lines are also depicted.

a fast oscilloscope with bandwidth larger than ~ 10 GHz and photodiodes with accordingly high bandwidths.

Figure 5.4 shows the measured frequency spectra taken with the 7 GHz RF spectrum analyzer during the re-commissioning of the prototype MLO in the synchronization hutch. Two different regimes can be distinguished. The dark-colored trace shows a status, where a satellite pulse is traveling temporally relatively close with the main pulse. Around 3 GHz a weak and at the 5 GHz frequency line a stronger modulation is visible. The trace shown in red represents a regime where the EDFL emits a pulse train at twice its nominal repetition rate, consisting of two pulse trains, which are shifted by $\Delta t_{dp} = T_{rep}/2$, but with equal pulse energies in each train. Thus, the signature in the RF spectrum

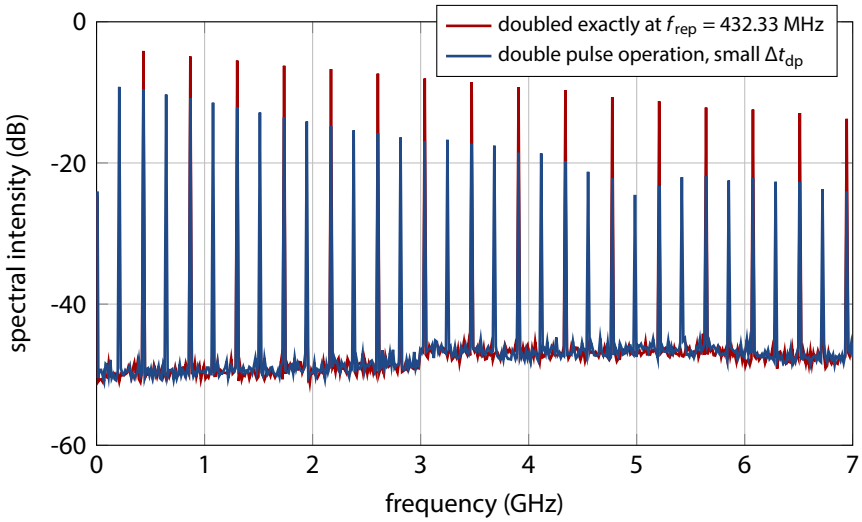

Figure 5.4 | Radio frequency spectra of a prototype MLO operating in double pulse regimes. By adjusting the pump power, two different double pulse regimes are established. The data was taken with a 7 GHz RF spectrum analyzer.

suggests a single-pulse operation at first sight, because then no modulation is visible as it has its local maximum exactly at twice the nominal repetition rate.

Ensuring the single pulse operation of a laser, and in particular the master laser oscillator, is crucial for the optical synchronization system, as there is no or only a very weak coupling of the both pulses in the double pulse regime [Digo1], resulting in a timing jitter of the two individual pulse trains with respect to each other. It is then imaginable that one fiber link, for instance, locks on one pulse train, and another automation routine locks on the other leading to a practically uncorrelated point-to-point synchronization of the fiber link end-stations. After discovering these multiple-pulse regimes in the original MLO quite some effort had been made to operate it in a stable single-pulse regime, but that was not possible and finally led to the decision to built a new master laser oscillator as explained above.

5.2.2 Two-Photon-Absorption

In an insulator or semiconductor two photons can be absorbed if the photon energy is at least half of the band gap energy $2E_{\mathrm{phot}} \geq E_{\mathrm{gap}}$. This process is nonlinear and therefore occurs significantly only at high optical intensities I, because the absorption coefficient depends on the optical intensity $\alpha_{\mathrm{abs}} = \beta_{\mathrm{tpa}} I$, where β_{tpa} is the two-photon absorption (TPA) cross-section. In case of the laser radiation in the 1560 nm region, corresponding to a photon energy of 0.79 eV, adequate semiconductor materials for two-photon absorption are GaAs with a band gap of 1.42 eV [SWVS85] or silicon with a band gap of 1.11 eV at room temperature. The phenomenon can be exploited to detect if a laser is mode-locked, because the optical intensity or peak power increases dramatically in case of the pulsed operation in contrast to the cw optical power. A measurement with light from the aux-

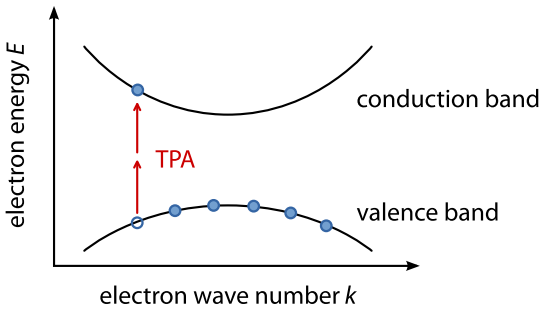

Figure 5.5 | Schematic band model for the two-photon absorption process. With a certain probability, two photons with an energy smaller than the band gap can be absorbed via a virtual intermediate energy level in this oversimplified picture.

iliary diagnostics port of the EDFL focused onto an unbiased silicon photo diode lead to a voltage difference in the order of 10 mV for cw- and mode-locked operation, when the photo current is converted to a voltage with a 50 Ω resistor. Since the peak power depends on the pulse duration, $P_{\text{peak}} = 0.88\, E_{\text{pulse}}/\tau_{\text{p}}$, a permanent measurement with a two-photon absorbing photodiode is highly desirable for MLO diagnostics, because then changes of the pulse duration can be detected when the output voltage is correlated to an independent optical power monitor (see section 5.2.4, pages 80 ff.). Furthermore, two-photon absorption can be exploited to build compact autocorrelators for pulse duration measurements as, for instance, a silicon photo diode can replace the SHG crystal and filter (see section 3.5.2, page 58 f.), because there a signal is only generated when the pulses from both arms overlap temporally as explained in the next section.

5.2.3 Autocorrelation Measurements

One of the important properties of the master laser oscillator is the pulse duration, especially for the dispersion compensation in the fiber links. As discussed in section 3.5.2 (page 58 f.), there are two different autocorrelations to retrieve the pulse duration from, and the commercial autocorrelator used here can be aligned to either measure an intensity or an interferometric (or field-) autocorrelation. The principle of operation for both arrangements is shown in Fig. 5.6. To measure the intensity autocorrelation in a geometry shown in the left panel of the figure, the input beam is split into two arms, each of which usually reflecting the pulse train with a retroreflector (sometimes called "corner cube"). The now displaced beams are focused by a single lens into a crystal with a $\chi^{(2)}$ nonlinearity. The length difference of the arms is realized with an optical delay stage, or simply a loudspeaker, as for femtosecond pulse measurements only displacements in the order of a few hundreds of micrometers are required. When the pulses overlap temporally in the crystal, the sum-frequency is generated and appropriately detected. The optical setup for an interferometric autocorrelator is shown in the right panel of the figure and it resembles a Michaelson interferometer. Both copies of the input pulses travel collinear with the same polarization into the sum-frequency generating crystal, also

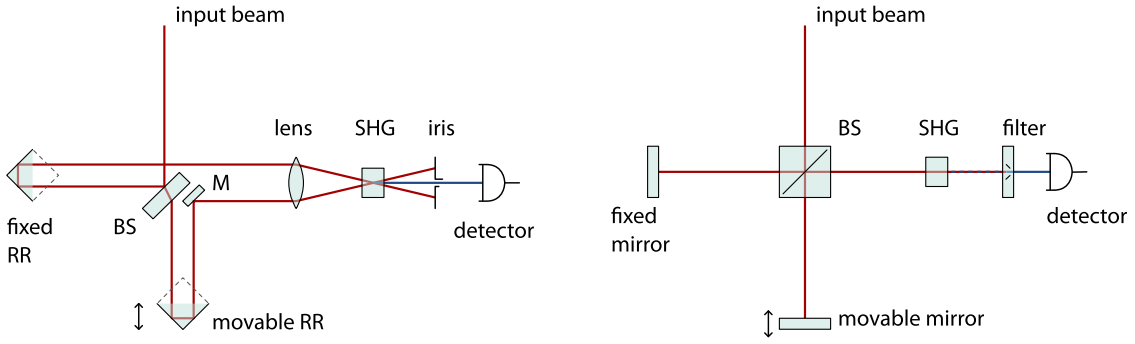

Figure 5.6 | Schematic optical setups of different types of autocorrelators. Left: Intensity autocorrelator. **Right:** Interferometric autocorrelator. Here, optical losses occurs due to the second pass respectively reflexion in the beam cube (BC).

focused by a lens. In both devices, the pulse duration can be retrieved from the recorded from the SFG-signal (see table 3.2, p. 58). An intensity autocorrelator has been setup within this thesis and used for pulse duration measurements in the laser development laboratory. The results discussed in this chapter, however, were measured with the aforementioned commercial device because of its compact size and the limited space available on the optical table. Figure 5.7 shows the autocor-

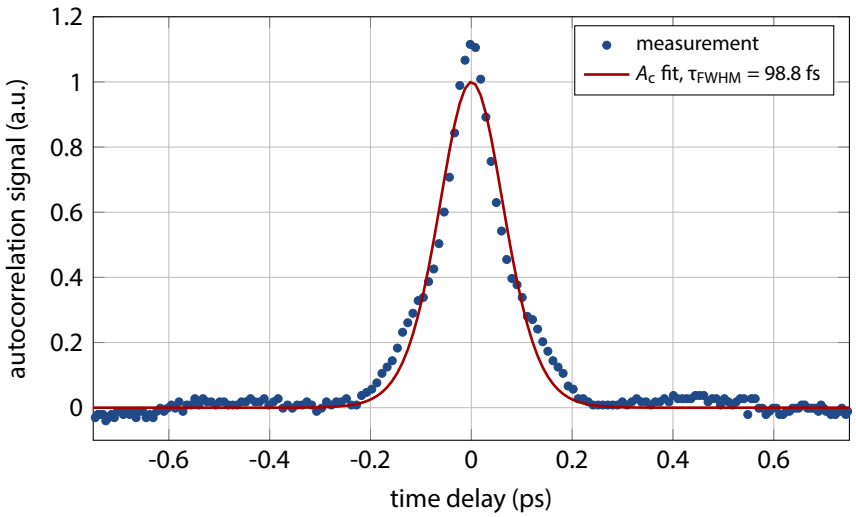

Figure 5.7 | Autocorrelation measurement of the EDFL oscillator. The pulse shape differs from the perfect soliton shape by means of small shoulders in this laser's standard operation regime.

relation function in its nominal operation regime, measured at the additional monitor port in the oscillator setup (compare Fig. 5.1, p. 72). The fit of the function A_c, assuming sech^2-shaped pulses, results in a FWHM pulse duration of τ_{FWHM} = 98.8 fs exactly matching the initial specifications of the laser system. The temporal shape, however, deviates slightly from the expected soliton, especially at the wings of the curve. The reason for this is the existence of the side-bands in the optical

spectrum, shown in Fig. 5.8 which was measured at the same time. These series of side-bands is a well known feature in the spectrum of erbium-doped fiber lasers [Kel92] and are caused by the periodic amplification and loss of the soliton within the resonator round-trip time. Their strong pro-

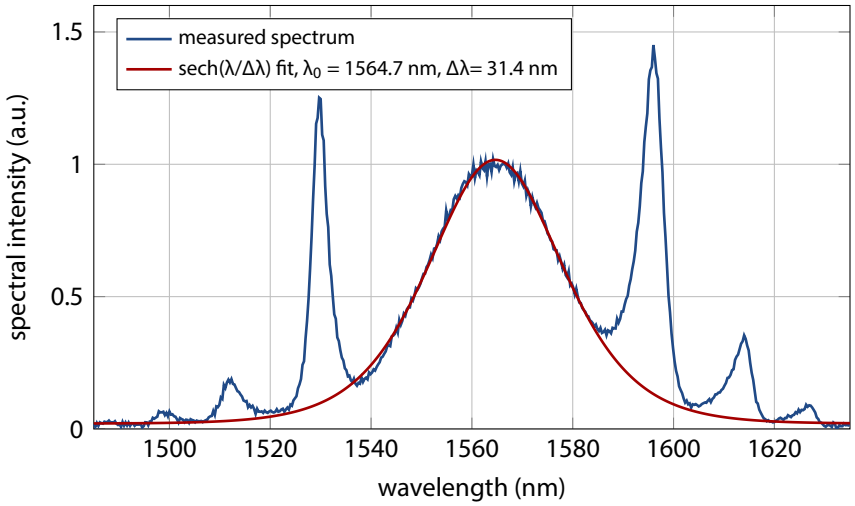

Figure 5.8 | Optical spectrum of the EDFL in its nominal operation regime. The soliton fit neglects the side-bands and yields a center wavelength of $\lambda_0 = 1564.7$ nm and a spectral bandwidth of $\Delta\lambda = 31.4$ nm.

nunciation suggests that the EDFL is operating close to the limit where the soliton breaks and the laser falls back to the cw regime, as described in section 5.1 (page 71 ff.). Referring to section 5.2.1 on pages 73 ff., also in the optical spectrum a modulation caused by double pulses is visible, where the depth and frequency depends on the distance Δt_{dp} of the satellite pulse to the main one. Hence, autocorrelation and optical spectrum measurements are highly desirable as permanent laser diagnostics in the synchronization system. It is planned to implement a very compact autocorrelator directly into the EDFL housing, where the SFG-crystal and the filter are replaced by a two-photon

NOTE ON THE METHOD OF INSTRUMENTATION: ALTHOUGH THE CONTROL UNIT OF THE APE PULSECHECK IS EQUIPPED WITH A DISPLAY SHOWING A NUMBER AND PRETENDING THIS BEING THE PULSE DURATION, ITS CALCULATION SEEMS RATHER ODD: THE MAXIMUM VALUE OF THE AUTOCORRELATION SIGNAL IS DETERMINED FROM THE MAXIMUM PIXEL NUMBER TO THE LOWEST PIXEL ROW OF THE DISPLAY WHEN THE BASELINE IS NOT VISIBLE. BY VARYING THE OFFSET, WHICH IS A FUNCTION PROVIDED BY THE DEVICE, IN PRINCIPLE AN ARBITRARY VALUE FOR THE PULSE DURATION CAN BE SET BY THE EXPERIMENTER. EVEN WHEN THE BASELINE IS VISIBLE, THE DEVICE SEEMS NOT EVERY TIME TO CORRECT THE HALF-MAXIMUM HEIGHT WITH THIS OFFSET. FURTHERMORE, THE CALCULATION IS LIMITED BY THE HORIZONTAL PIXEL COUNT OF 256, RESULTING IN A BAD TEMPORAL RESOLUTION. HOWEVER, THE CONTROL UNIT FEATURES ANALOG OUTPUTS OF THE POSITION ENCODER OF THE TIME DELAY STAGE AND THE AUTOCORRELATION SIGNAL ITSELF. OBSERVING AND MEASURING THESE VOLTAGES WITH AN OSCILLOSCOPE CAN LEAD TO A MUCH MORE PRECISE ANALYSIS OF THE PULSE DURATION.

absorbing photodiode as described in the previous section, simplifying the optical setup and the alignment, as well as increasing robustness.

5.2.4 Relative Intensity Noise and Amplitude Stability

The relative intensity noise (RIN) of the erbium-doped fiber laser has been measured with the setup depicted in Fig. 5.9. The laser pulse train impinges on a biased, 50 Ω-terminated photodiode[3]. Care has to be taken that the photodetector is operated in the linear regime, which is guaranteed by an appropriate attenuation of the average optical power to $P_{\text{avg}} < 1\,\text{mW}$. The electrical output of the detector is then low-pass filtered ($f_{\text{cut}} = 1.9\,\text{MHz}$) and, after amplification with a DC low-noise amplifier (LNA)[4], connected to the baseband input of the signal source analyzer. From the measured

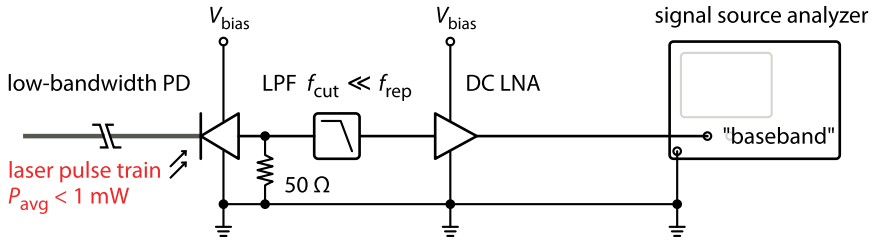

Figure 5.9 | Schematics for laser RIN measurements with a commercial signal source analyzer. It must be ensured that all devices are connected to a common ground to suppress the influence from possible ground loops.

voltage spectral density $\ell_{\text{V}}(f_i)$ the RIN can be calculated using Eq. 2.69, page 44. Figure 5.10 shows the recorded data (dark blue curve) of the free-running EDFL in the frequency range $[10\,\text{Hz}, 20\,\text{MHz}]$ and the integrals evaluated from 10 Hz to three different end frequencies. In this measurement, the described optical monitoring circuit is integrated to the rack chassis which also contains the RF synchronization circuit (see section 5.3, pages 87 ff.). The largest contribution to the calculated RIN are the noise components for frequencies below 1 kHz, resulting in an almost the same total RIN of 0.2551% for the three integrated curves. Remarkable are the frequency lines at 12.5 Hz, which is used in the AC of another particle accelerator on the DESY campus, and the 50 Hz line with its harmonics coming from the mains, as they result in quite large steps in the RIN. It should be noted, however, that the electric circuit is connected to a power-supply with battery-backup and filtering capacitors, and without this the frequency lines from the power grid have been observed to be more than 10 dB higher. The oscillatory structure of the recorded data in $[1\,\text{kHz}, 10\,\text{kHz}]$ is also conspicuous, and the reason for that is not understood, but the laser oscillator can be excluded, as this feature is also visible in the noise floor[5] of the setup shown as the dark line in the figure. In general, the noise floor

[3] EOTech ET3010 with a 3-dB bandwidth of 1.5 GHz, supply voltage $V_{\text{bias}} = 6\,\text{V}$

[4] Here, the term "DC" refers to a frequency range from DC up to a few megahertz, depending on the programmable gain of the amplifier.

[5] The term "noise floor" here means the baseband noise of the complete circuit, measured with a disconnected optical input at the photodiode.

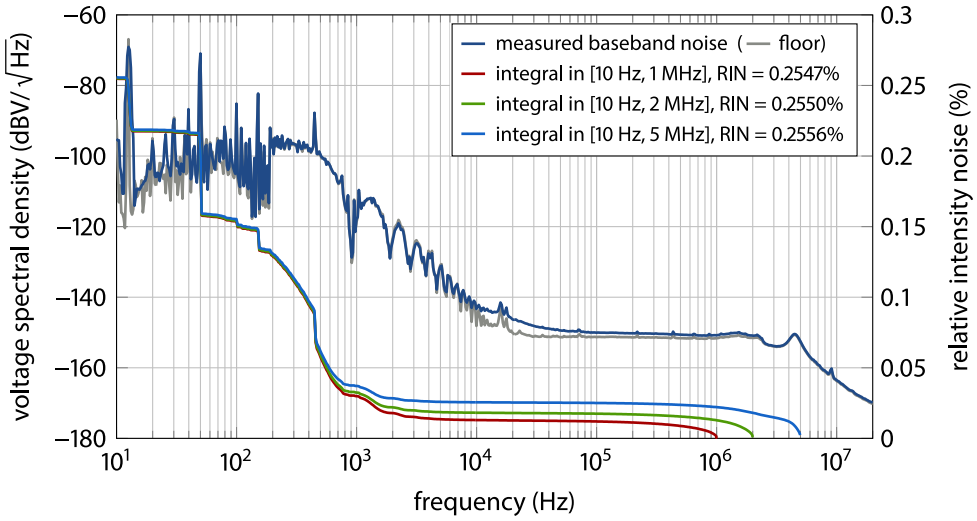

Figure 5.10 | Relative intensity noise of the EDFL measured in the synchronization hutch. The relative intensity noise is evaluated in different frequency intervals. The measurement is strongly limited by the measurement setup noise floor (gray curve in the background).

seems to limit this measurement, and it can be assumed that the laser performs much better, particularly in comparison to similar laser systems investigated in [Loeo9, CSIKo7]. Consequently, the measurements have been repeated with an independent setup. It was neither connected to the opti-

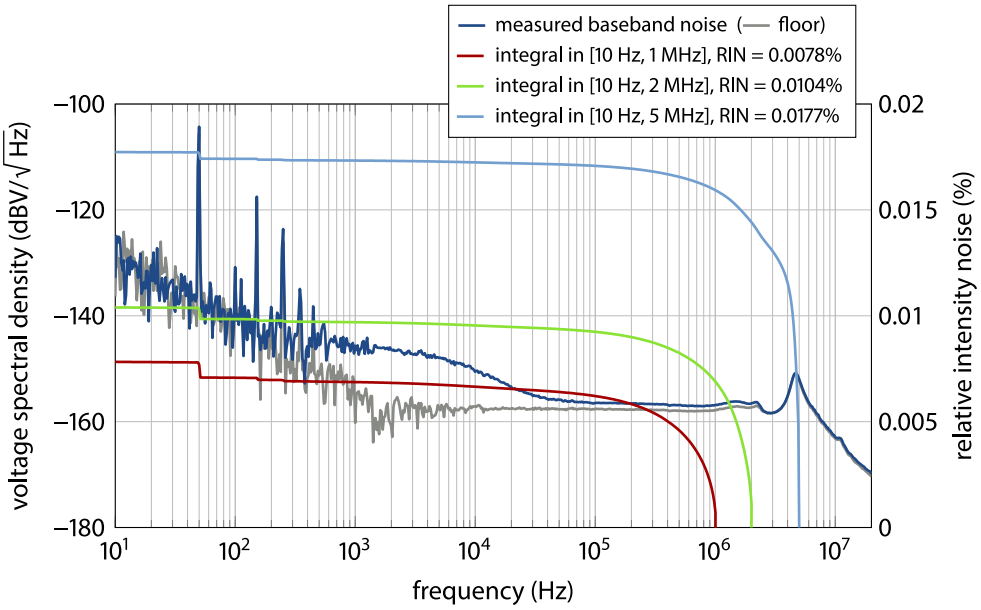

Figure 5.11 | Relative intensity noise of the EDFL measured with a ground-decoupled setup. The noise floor and low-frequency noise is significantly reduced in comparison to Fig. 5.10. Notice the different y-axis scale for the intensity noise.

cal table nor the electronics racks, and a commercial laboratory power supply[6] has been used. Care has been taken to connect all components to a common ground using also the ground connectors provided at the power supply and the SSA. The results are shown in Fig. 5.11 with the same analysis as before. The noise floor could be reduced in the higher frequency region by more than 15 dB and the frequency lines at 50 Hz and its harmonics are suppressed by more than 30 dB due to the excellent performance of the power supply [Huno9] and the grounding. The integral values now differ from each other, because the low-frequency noise does not effect the RIN such as strong as in the measurement discussed before. For the frequency interval from 10 Hz up to 1 MHz the total RIN amounts to an unprecedented value of only 0.0078%. Even if the integral is taken to up to 5 MHz the value is comparable to other laser systems in [10 Hz, 1 MHz]. However, in this case, the filter and amplifier bandwidth of 1.9 MHz and $\lesssim$ 5 MHz influence the voltage spectral density. Furthermore, the measurement is already limited by the photo-detection process from around 30 . . . 40 kHz onwards. To achieve higher limit frequencies the photodiode could be cooled to reduce the thermal noise floor in the detection process. On the other hand, these measurements show already a very good performance, when it is operated with commercial laser diode drivers, though (see next section). Investigations on the long-term stability, i.e. very low frequency noise, are discussed in the last section 5.6 of this chapter (pages 120 ff.).

5.2.5 Timing Phase Noise Measurements

The short-term or high-frequency timing stability of all laser systems discussed here is calculated from the single-sideband timing phase noise $\ell_\varphi(f_i)$ as described in section 2.5.1 on page 42 f. It is measured with the commercial Agilent E5052B signal source analyzer (SSA) using a setup depicted in Fig. 5.12. The laser pulse train impinges a high-bandwidth photodiode reversely biased with a

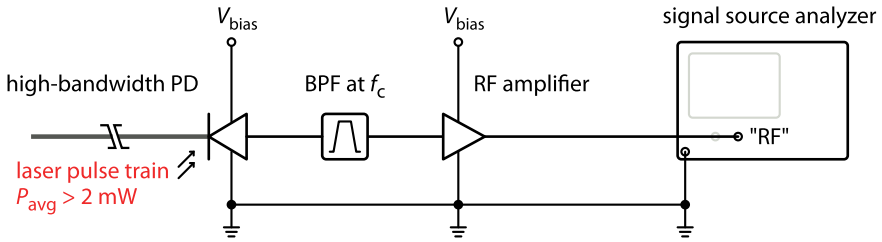

Figure 5.12 | Schematics for timing phase noise measurements with a signal source analyzer. It should be ensured that all devices are connected to a common ground to suppress the influence from possible ground loops.

voltage typically in the order of $V_{bias} = 18$ V. The average power of the pulse train has to be high enough to saturate the photo-detector which happens for the used photodiodes for $P_{avg} > 2$ mW. This is required to minimize the influence of the conversion of amplitude noise to phase noise. From the FOURIER comb the desired harmonic of the laser's repetition rate is filtered with a band-pass as carrier frequency f_c and amplified with a low-noise amplifier. The SSA is capable of measuring the

[6] Toellner TOE 8842-32

phase noise at offset frequencies from 1 Hz up to 100 MHz from this carrier frequency. It is based on a low-bandwidth phase-lock of the device under test (DUT) and a local reference oscillator, which is automatically tuned to f_c. Both RF signals are applied to a microwave mixer with a phase difference of $\pi/2$ resulting in a vanishing output. The residual fluctuations are sampled with an ADC using a high dynamic range. Furthermore, the SSA is equipped with an internal correlation technique which minimizes the influence of the internal oscillator's phase noise and reduces the measurement noise floor by up to 20 dB. The intrinsic uncorrelated phase noise of the LO is suppressed by $\sqrt{N}$ with N the number of correlations. A more detailed discussion about phase noise measurement techniques and its limits using photodiodes can be found in [KCCK07, Wino8], while in, for instance, [Pas10] simulations on timing jitter of fiber lasers are discussed.

Timing Phase Noise of the EDFL with Different Pump Current Drivers

The current of up to 1 A for the pump laser diode modules are provided either by commercial[7] laser diode drivers (LDDs) or driver modules on a VME basis. The development of those modules as 4-channel diode drivers accompanied by matching temperature controllers has been started in the context of a previous thesis in order to have a tight integration into the control system and in order to save cost. The pump laser diode modules on the optical table are connected to the drivers with approximately 10 m long cables. Figure 5.13 shows the single-sideband phase noise (darker colored

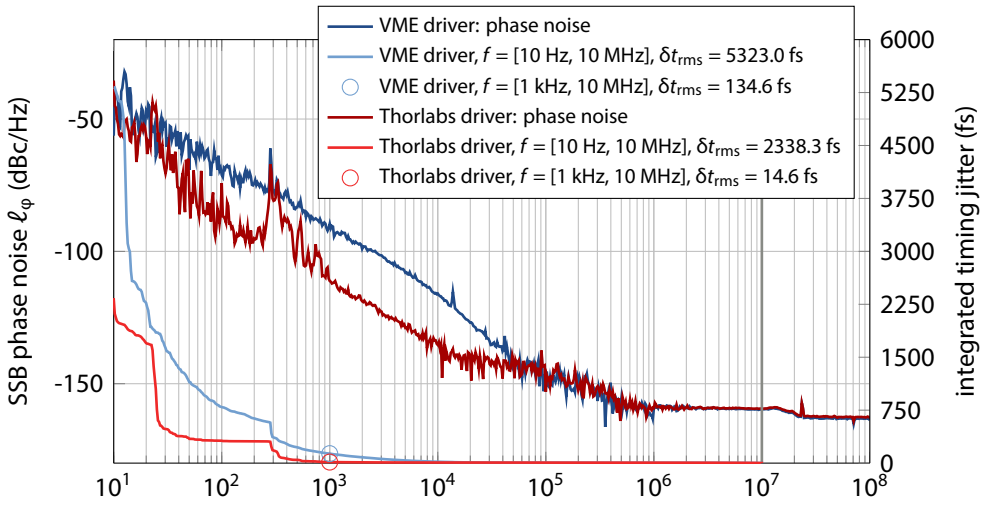

Figure 5.13 | Phase noise of the free-running EDFL compared for Thorlabs and VME pump drivers. The laser is free-running in both measurements.

curves) and the calculated timing jitter (lighter colored curves) of the free-running EDFL for both the commercial and the VME-based driver in the frequency range [10 Hz, 10 MHz] from the carrier frequency of $f_c = 6 \cdot f_{\mathrm{MLO}} = 1.3\,\mathrm{GHz}$. In case of the VME drivers, the integrated jitter amounts to 5.3 ps with the most significant contributions in the lower frequency range. When the laser is

[7] Thorlabs ITC510

operated in the same status with the commercial drivers, the integrated timing jitter reduces to 2.3 ps.

In order to reduce the low-frequency jitter and drift with respect to the accelerator's RF oscillator, the master laser oscillator is synchronized to the MO, with the actual circuit being discussed in section 5.3 (pages 87 ff.). By this, only the laser's noise with frequencies above the cut-off frequency $f_{\mathrm{cut}} \approx 1\,\mathrm{kHz}$ of the corresponding PLL will we present in the optical synchronization system. An evaluation of the integrated jitter from 1 kHz to 10 MHz for both cases leads to $\Delta t_{\mathrm{rms}} = 134.0\,\mathrm{fs}$ for the VME-based and 14.6 fs for the Thorlabs drivers, meaning also the phase noise of the laser up to 1 MHz is significantly higher with the VME-based drivers. From ~ 1 MHz onwards the measurement is limited by the photodetection process thermal noise floor, being in the order of −160 dBc in a 1 Hz bandwidth. In Figure 5.14 the measured phase noise is shown for the phase-locked laser,

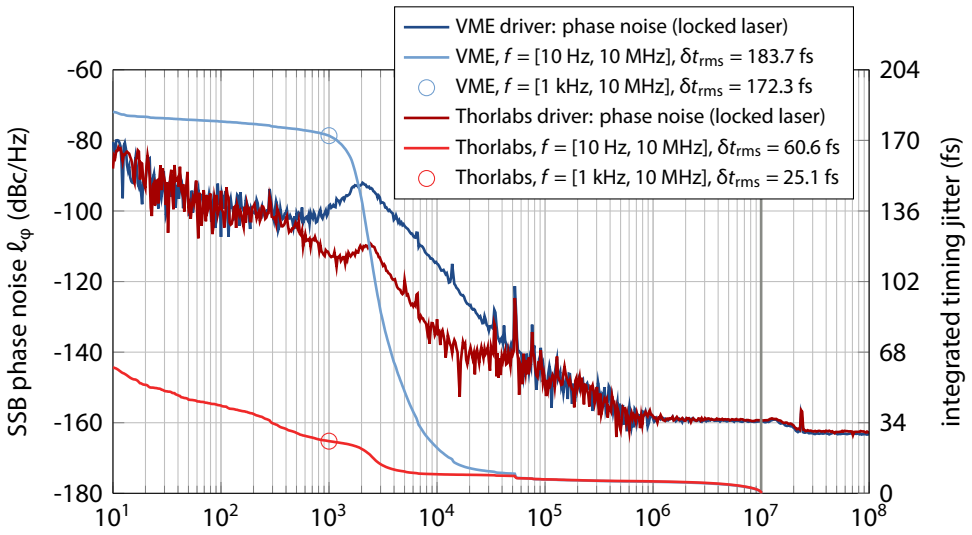

Figure 5.14 | Phase noise of the phase-locked EDFL compared for Thorlabs and VME pump drivers. The laser is phase-locked to the master RF oscillator as in normal operation.

again for both the VME-based and Thorlabs pump laser diode driver. It clearly can be seen that this synchronization reduces the low-frequency jitter significantly, as the integral jitter reduces to $\delta t_{\mathrm{rms}}^{\mathrm{VME}} = 183.7\,\mathrm{fs}$ and $\delta t_{\mathrm{rms}}^{\mathrm{Thorlabs}} = 60.6\,\mathrm{fs}$ in the frequency interval $[10\,\mathrm{Hz}, 10\,\mathrm{MHz}]$. The main contribution in both cases comes from the phase noise measured in the frequency region from 1 kHz to 50 kHz, although for the Thorlabs drivers the noise with frequencies $f_i < 1\,\mathrm{kHz}$ contributes more. The integral jitter in the frequency interval used for most comparisons, $[1\,\mathrm{kHz}, 10\,\mathrm{MHz}]$ amounts to $\delta t_{\mathrm{rms}}^{\mathrm{VME}} = 172.3\,\mathrm{fs}$ and $\delta t_{\mathrm{rms}}^{\mathrm{Thorlabs}} = 25.1\,\mathrm{fs}$, respectively. From the latter value, the jitter of the free-running oscillator and the characteristic of the trace it can be concluded that the cut-off frequency of the PLL is between 1 kHz and 3 kHz. The aforementioned limitation of the photodetection process is better visible in this figure. The step at around 15 MHz results from the limited bandwidth of the used 1.3GHz filter, which is a custom designed 12th order filter made by IMCSD.

Because of the better performance of the laser system when using the Thorlabs drivers, these have been chosen for the standard operation of the laser system, although they have the drawback

not being integrated into the control system. On the other hand, if the laser is set up into a stable regime, there is only limited need to actually control the pump diodes, and the monitoring signals as discussed in this section provide already a lot of information on the laser. Nevertheless, it is crucial to improve the performance of the VME-based laser diode drivers, because they are not only used for the MLO, but also for the erbium-doped fiber amplifiers in the complete synchronization system. Hence, their noise can influence the system's performance in a negative manner. First investigations and measurements at a dedicated setup (see appendix A.4 on pages 210 ff.) has been started, eventually leading to a performance of the VME- or another type of self-developed laser diode driver comparable to the commercial ones.

Influence of the Housing and the Carrier Frequency

The phase noise and timing jitter has furthermore been investigated at different carrier frequencies, as well as the influence of a housing of the laser. The measurements have been carried out during the assembly of the laser in the development laboratory. In figures 5.15 and 5.16 the results are shown. The first figure shows the phase noise for the carriers $f_c = 1.3\,\mathrm{GHz}$ as in the measurements above

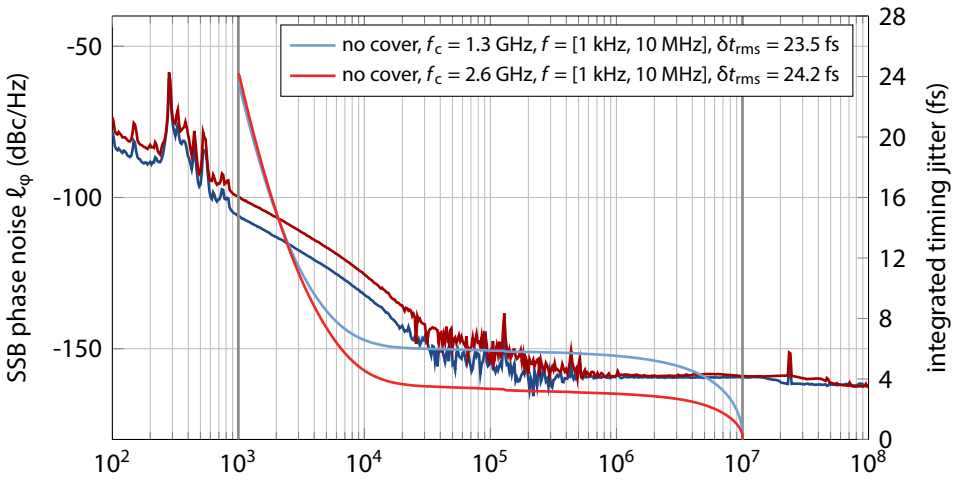

Figure 5.15 | Comparison of phase noise at 1.3 GHz and 2.6 GHz with open laser housing. The laser is free-running in both measurements at different carrier frequencies.

and $f_c = 12 \cdot f_{rep} = 2.6\,\mathrm{GHz}$, as well as the corresponding integrated timing jitter in the interval $[1\,\mathrm{kHz}, 10\,\mathrm{MHz}]$. In this first series of measurements, the data was recorded while the free-running laser oscillator was operated with an open housing and thus exposed to a slight airflow due to the ait conditioning system of the laboratory. The expected (see Eq. 2.66, p. 43) much lower integral amount for the higher carrier frequency is clearly visible from offsets above ~ 5 kHz. Below this, the curves approximate each other resulting in nearly the same total jitter of ~ 24 fs in the evaluated interval, although at a lower timing jitter is expected for higher carrier frequencies. After closing the laser housing and the cover of the optical table, these measurements have been repeated with a couple of minutes wait to allow for a temperature stabilization. As it can be seen in figure 5.16,

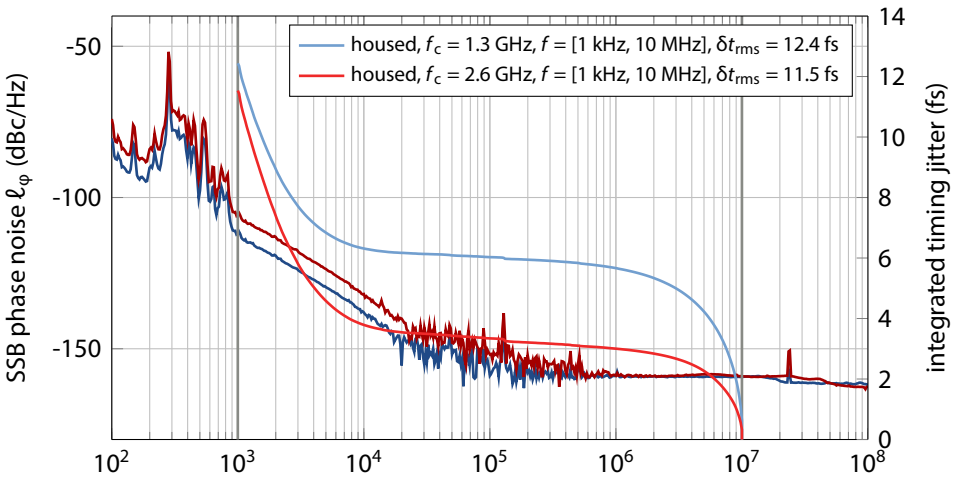

Figure 5.16 | Comparison of phase noise at 1.3 GHz and 2.6 GHz with closed laser housing. The laser is free-running in both measurements at different carrier frequencies. Note the different right-hand y-axis scaling compared to Fig. 5.15.

the effect of approximation of the integral curves shifts slightly to lower frequency offsets, but the difference between the both carrier frequencies is similar for $f_i > 10\,\text{kHz}$ and again limited by the photo detection process. When the integral is evaluated only in the higher frequency interval from 10 kHz to 10 MHz], the total jitter amounts to 6.31 fs for $f_c = 1.3\,\text{GHz}$, which compares very well with the result from the laser built in [Loeo9], and 3.79 fs for $f_c = 2.6\,\text{GHz}$.

Since the integrated timing jitter is an important figure of merit for the performance of the laser operated in different regimes and at different carrier frequencies in the phase noise measurement, the calculated values are summarized in table 5.2. The number which has to be considered for the implementation of the laser and its phase-locked loop (PLL) is written in a bold typeface. This kind of table is used throughout this thesis for timing jitter measurements, and as an easy reference, a complete table is shown in appendix A.8 on page 221. The phase-locked loop for the synchronization to an RF oscillator should be set up at a very high harmonic of the laser's repetition rate, and thus the highest available frequency from the MO of 1.3 GHz has been chosen and is explained in the following section. The investigations at a carrier frequency of 2.6 GHz are of interest, because the fiber link stabilization units discussed in chapter 6 (pages 131 ff.) feature an RF phase detector at that frequency. In the future, even higher carrier frequencies, such as the 9.1 GHz harmonic, will become relevant for extended Ti:sapphire synchronization schemes (see chapter 7 on pages 151 ff.). However, phase noise and timing jitter investigations at this frequency could not be carried out as the available signal source analyzer SSA is limited to 7 GHz. For this, the measurement equipment could be upgraded with another down-mixing module [Agio8].

Table 5.2 | Overview of the integrated timing jitter of the erbium-doped fiber laser. The table also summarizes the integrated timing jitter calculated from phase noise measurements of the EDFL. The last column of the table references to the figure where the corresponding graph is shown.

description	f_c	integrated timing jitter in frequency interval				fig.
	GHz	[10, 10 M]	[100, 10 M]	[1 k, 10 M]	10 k, 10 M]	
erbium-doped fiber master laser oscillator						
free-run., VME LDD, EOT	1.3	5323.0 fs	793.4 fs	**134.6 fs**	19.3 fs	5.13
free-run., Thorlabs LDD, EOT	1.3	2338.3 fs	316.9 fs	**14.6 fs**	7.8 fs	5.13
φ-locked, VME LDD, EOT	1.3	183.7 fs	179.1 fs	**172.2 fs**	21.9 fs	5.14
φ-locked, Thorlabs LDD, EOT	1.3	60.6 fs	42.3 fs	**25.1 fs**	9.2 fs	5.14
free-run., Thorlabs, open hs., u^2t	1.3			**23.5 fs**	6.6 fs	5.15
free-run., Thorlabs, closed hs., u^2t	1.3			**12.4 fs**	6.3 fs	5.16
free-run., Thorlabs, open hs.,u^2t	2.6			**24.2 fs**	4.6 fs	5.15
free-run., Thorlabs, closed hs., u^2t	2.6			**11.5 fs**	3.8 fs	5.16

5.3 Synchronization to the Accelerator's RF Oscillator

In order to reduce the low-frequency jitter of the master laser system and to avoid a long-term drift with respect to the accelerator it has to be synchronized to the master RF oscillator (MO). The synchronization scheme is based on a traditional RF down-mixing circuit as described e.g. in [Win08, Loe09]. However, several extensions have been made and the system evolved to a reliable and robust component of the synchronization system. Obviously, the improvements were mainly made to improve the drift stability of the locking scheme itself, because it can be assumed that then the long-term phase stability of the laser system is ensured by the long-term stability of the RF reference. Details on the implementation can be found in [HAB+09, Hac10], as well as an extensive characterization of the device. Here, the principle of operation, practical aspects and the most important results are discussed.

5.3.1 Phase Detection Scheme

In contrast to the circuits implemented in former thesis, an extended scheme which is based on two rather than only one phase comparisons of the laser and the RF oscillator is utilized. The main phase-locked loop operates at $f_c = f_{RF} = 1.3\,\text{GHz}$, whereas another phase detector at $f_{MLO} = 216\,\text{MHz}$ is used to keep the fast loop in the correct bucket to ultimately ensure consistent overlap with the accelerated electron bunch.

The schematics of the complete RF circuit, which is designed for the synchronization of two different laser systems, are depicted in Fig. 5.17. All components are mounted in a 3U 19-inch rack chassis, with all connectors on the front panel and patched to the according signals from the optical table and the VME-crates containing the digital controllers (see also appendix B, pages 223 ff.). Beginning with

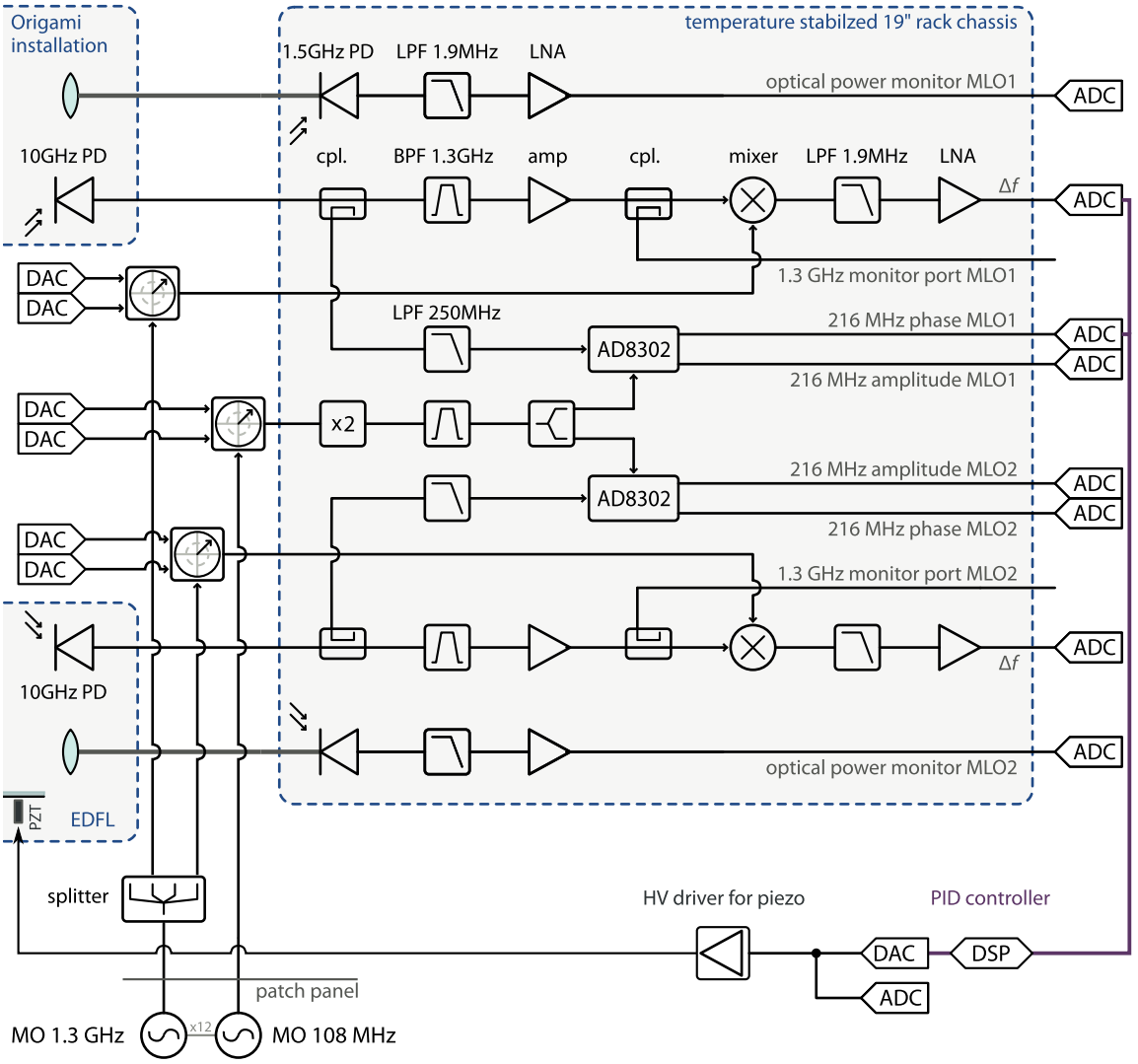

Figure 5.17 | Phase detector RF circuit for synchroniztaion of the two master laser systems. Each laser can be locked to the 1.3 GHz reference signal while another phase detector operating at the fundamental repetition rate f_{MLO} is used to detect the correct bucket of the fast phase-locked loop. The actual controller is only shown for the EDFL.

the high-bandwidth photodiode in the laser system's housing, the highest harmonic corresponding to an RF frequency provided by the master RF oscillator, is filtered from the Fourier comb of the laser pulse train using the same type of filter as described in the phase noise measurement setup. The resulting RF signal $u_{\mathrm{laser}}(t)$ is amplified with a low-noise amplifier and mixed with the RF reference signal $u_{\mathrm{MO}}(t)$ which, in turn, has passed an electronically programmable phase shifter. When the two signals exhibit a relative phase difference of $\pi/2$, the mixer output signal is a superposition of sine

terms containing the difference and the sum of the individual phase jitter terms $\Delta\varphi_{\mathrm{MO}}$ and $\Delta\varphi_{\mathrm{laser}}$:

$$u_{\mathrm{MO}}(t) = u_{0,\mathrm{MO}}\,\sin(\omega_c t + \Delta\varphi_{\mathrm{MO}}) \qquad \text{and} \qquad u_{\mathrm{laser}}(t) = u_{0,\mathrm{laser}}\,\cos(\omega_c t + \Delta\varphi_{\mathrm{laser}}) \tag{5.1}$$

$$\begin{aligned} u_{\mathrm{mix}}(t) &= u_{\mathrm{MO}}(t)\cdot u_{\mathrm{laser}}(t) \\ &= \frac{1}{2}\,u_{0,\mathrm{MO}}\,u_{0,\mathrm{laser}}\left(\sin(2\omega_c t + \Delta\varphi_{\mathrm{MO}} + \Delta\varphi_{\mathrm{laser}}) + \sin(\Delta\varphi_{\mathrm{MO}} - \Delta\varphi_{\mathrm{laser}})\right) \end{aligned} \tag{5.2}$$

To measure the phase difference only, the mixer output is low-pass filtered with a cut-off of 1.9 MHz and amplified with a DC low-noise amplifier (LNA). It is sampled at a rate of $f_{\mathrm{s}}^{\mathrm{ADC}} = 125\,\mathrm{kHz}$ with a VME-based ADC, and the digitized information is transferred via a GigaLink connection to a digital signal processor (DSP), where the digital control loop is implemented on. The calculated correction signal is sent to a DAC again via GigaLink to avoid the latency which would be caused by the VME bus. A fast piezo driver amplifies its input of ±6 V delivered by the DAC, to the required voltage of 0 – 100 V for the piezo actuator inside the laser system.

Because this phase-locked loop (PLL) is operating at 1.3 GHz, which is the sixth harmonic of the laser's repetition rate, there are six zero-crossings on which the PLL can catch. Thus, it can not be guaranteed that the phase between the MO and the laser is the same when the lock has to be re-established in case of a failure. This situation is highly undesirable, as the complete synchronization system relies on a fixed phase relation of the two oscillators, and by that of MLO and the electron beam, as discussed in section 4 on page 68. Therefore, a second PLL operating at the frequency f_{MLO} makes the lock phase of the faster PLL unique. Its RF circuit is similar to the fast PLL: From the photodiode signal, a fraction is tapped off using a directional coupler. After low-pass filtering, the fundamental of the laser is connected to a phase-detector based on the AD8302 chip. The 216 MHz RF reference, however, has to be generated from the 108 MHz signal of the MO, because a 216 MHz signal is not provided. This leads again to an ambiguity of two possible zero-crossings in the fast PLL.

In order to avoid this, the 108 MHz RF reference also has a electronically programmable phase shifter installed, and with the appropriate signals from another pair of DACs, a small phase step is applied to the RF reference signal. That results in an output of the phase detector as shown in Fig. 5.18 for the lock in the correct bucket, measured at the same ADC as the mixer output of the fast PLL. If the fast loop would have caught at the wrong zero-crossing, this phase detector signal would be measured as a step around a different mean output voltage. As a result, the sign of the step and the mean phase detector output can be used to uniquely identify the correct zero-crossing of the fast PLL. If now the phase-lock is first established using the "slow" phase detector, and then switching the input for the PLL over to the output of the 1.3 GHz signal it is guaranteed that the timing of the master laser with respect to the RF reference is as before the loop had been opened. The accuracy of this re-establishment was later found to be less than 100 fs, as discussed in chapter 7 on pages 7 ff.

It has been found that particularly RF filters are highly sensitive to temperature variations and can cause several hundreds of femtoseconds of drift. To minimize this effect, all RF components are mounted on an aluminum plate whose temperature is actively stabilized using Peltier elements and ensures typically a peak-to-peak temperature stability of $\Delta T_{\mathrm{pp}} < 0.03\,^{\circ}\mathrm{C}$ over 12 h, when nobody

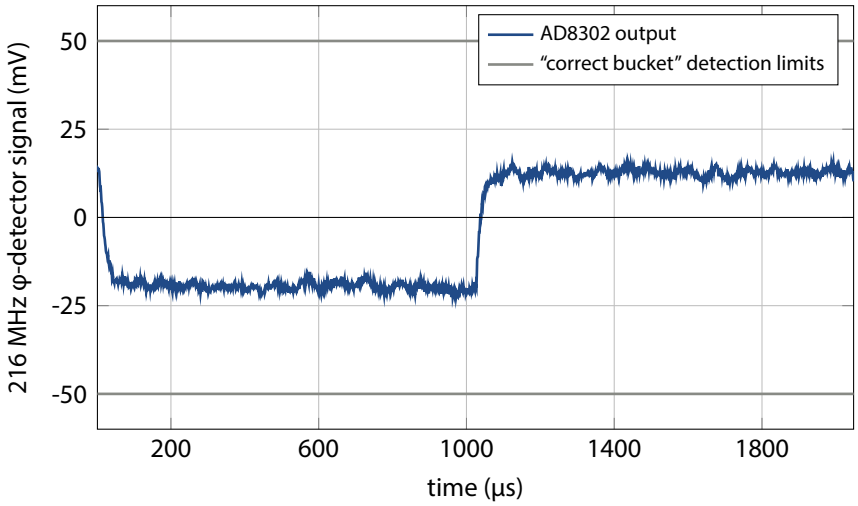

Figure 5.18 | Output of the AD8302 phase detector operated at 216 MHz. The characteristic is observed when the MLO is locked in the correct bucket. This information is used for example in the DOOCS server for the BAM data processing/ The limits are set to allow for an unavoidable slight drift of the detector.

is working in the laboratory. The best result was a peak to peak stability of $< 0.01°C$, limited by the resolution of the PLC used for data recordings. With the temperature stabilization active, the drifts of the RF circuit itself are typically reduced to < 30 fs and to < 7 fs (peak-to-peak) in the best case. These measurements were carried out using the split output of a low-noise 1.3 GHz dielectric resonator oscillator (DRO) as input for the LO and the RF ports, thus canceling out any other noise sources. Based on measurements described also in [Hac10], it was found that a temperature change of $0.1°C$ causes a drift of ~ 10 fs, but as a better temperature stability is guaranteed, those drifts of the RF lock circuit will practically not influence the long-term performance of the optical synchronization system [Hac10]. First investigations on the drift of the synchronized EDFL oscillator led to 77 fs peak-to-peak drift over 24 h, where about 60 fs could be attributed to amplitude changes of the laser. The stability and drift on longer time-scales are discussed in section 5.6 on page 120 below.

In addition to the RF phase detection circuitry, the rack chassis contains optical power monitor circuits for both laser systems to minimize drifts of the photodiode signal from temperature changes, which is especially critical when these signals are used in amplitude stabilization loops. These monitor signals have also been used for the relative intensity noise (RIN) measurements discussed in section 5.2.4 (page 80 ff.) and section 5.4.4 (page 105 ff.).

5.3.2 Controls

The phase-locked loop is running, as already mentioned, a DSP and is implemented as conventional proportional-integral-derivative (PID) controller. Access to the parameters of this system is tightly integrated into the accelerator's control system (DOOCS). With the advent of the compact RF circuit during the commissioning and upgrade of the synchronization system, the DOOCS server had to be adapted accordingly [Ges10], as the robust operation requires fast and correct re-establishment of

the RF lock in case of a failure. The server now supports the two inputs for the PLL and a transition

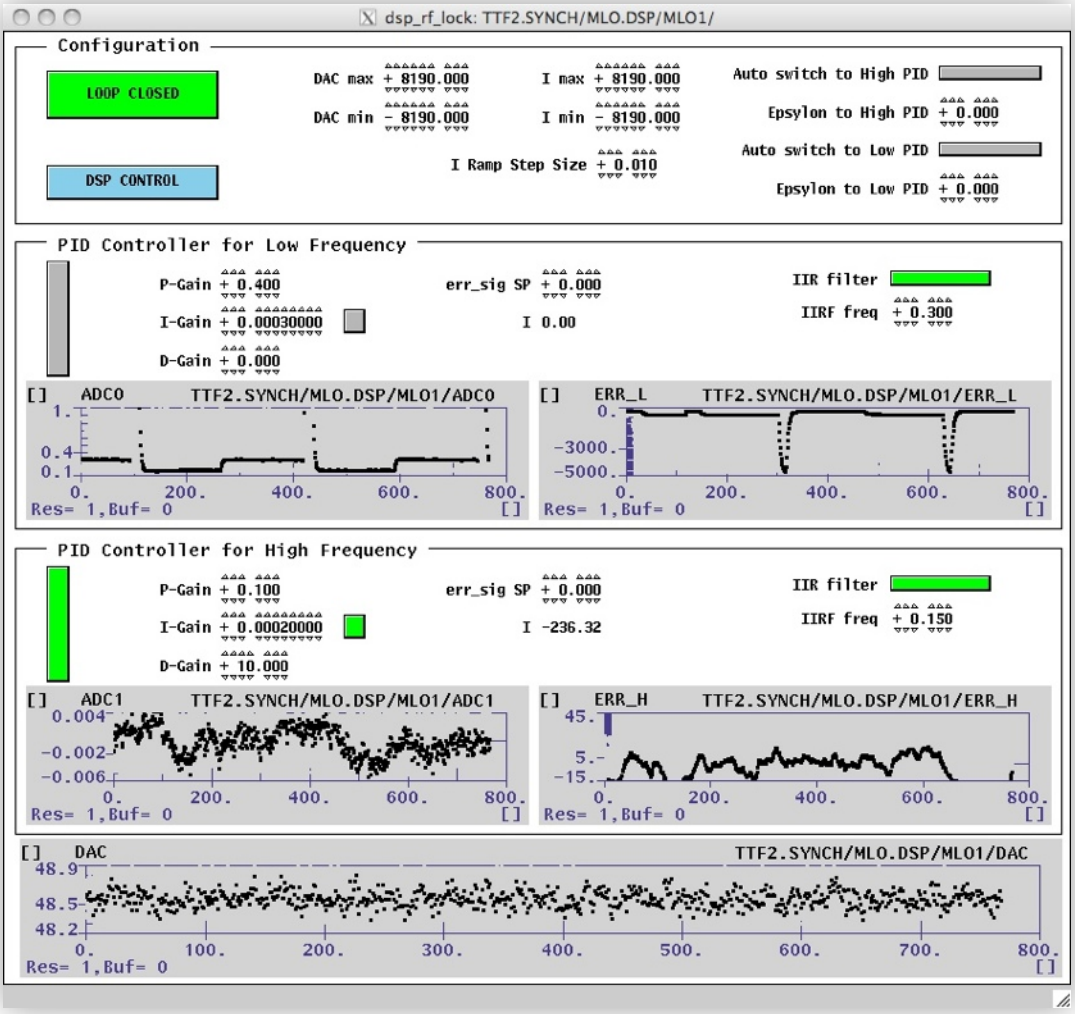

Figure 5.19 | Screenshot of the DOOCS panel for controlling of the DSP-based PLL. The PID controller for the phase-lock is implemented on a VME-based DSP and parameters can be digitally controlled. It is used to synchronize different types of laser oscillators in the optical synchronization system.

between both, such that the 216 MHz PLL catches first in the correct bucket as explained above, and then the PLL at 1.3 GHz takes over to increase the performance of the loop in terms of a much lower jitter. The in-loop timing jitter of the PLL can be calculated from the measured ADC signal, if $K_\varphi = \partial V/\partial\varphi$, which translates voltage changes into time changes, is known. The magnitude of this calibration constant can to some extent set by the last amplifier after the mixer, but above a certain gain, it was found that there is no improvement in the signal-to-noise ratio (SNR). Figure 5.19 shows a screenshot of the DOOCS data display (DDD) panel, which is divided mainly in three parts: In the upper part, the loop lock state can be toggled and the parameters for the transition between the two

loops are defined. The lower two parts represent the two PLLs, which can be individually controlled in terms of *P*-, *I*- and *D*- gain, as well as the error set point and an infinite impulse response filter (IIRF). At the bottom of the panel, the computed output of the DAC is displayed. In the ADC trace of the low-frequency PLL and the calculated error signal the steps applied to the RF reference are also visible.

5.3.3 Actuators

The piezo stack [NEC06] used in the EDFL for the fast repetition rate tuning has a maximum displacement of $\Delta s_{\max} = 6.1\,\mu\text{m}$ at the recommended drive voltage of 100 V resulting in a maximum repetition rate stabilization interval of $\Delta f_{\max} = f_{\text{rep}} \pm \left(f_{\text{rep}}^{-1} - \Delta s_{\max}/c_0\right)^{-1} = \pm 955.2\,\text{Hz}$. For safety reasons, the limits of the voltage V_{piezo} applied to the piezo element are set to 15 V and 85 V, which reduces the repetition rate tuning range to about ±700 Hz. When one of the limits is reached, the coarse repetition rate tuning has to take effect. For this, the piezo-mirror is additionally mounted on a motorized translation stage, which is controlled with another DOOCS server polling the piezo voltage of the DSP loop. The gains and step sizes of the loop are set to exactly move the translation stage to the position where $V_{\text{piezo}} \approx 50\,\text{V}$ to ensure again a maximum dynamic range for the fast feedback. By this, the motor movement is reduced to the minimum, because every move of the translation stage causes a very fast change in the optical output power of the laser, as the mirror vibrates, the efficiency of the coupling to the fiber collimator changes and so the soliton has to align itself to the new configuration. However, these are only little, but observable effects (see section 5.6, pages 120 ff.).

The Origami laser system, in anticipation of the next section, is also equipped with a similar piezo element to be compatible with the existing driver. The tuning range for V_{piezo} from 1 V to 94 V has been measured do be ±808.3 Hz with a slope of (19.5 ± 2.8) Hz/V (see Fig. A.2 in the appendix on page 208). The coarse repetition rate tuning of the laser is realized with a change of the laser cavity temperature. This is a natural choice for the manufacturer, as the laser anyhow has an internal temperature stabilization. Experience shows, that the repetition rate of the laser is extremely stable on the long-run. Furthermore, turning out to be an advantage of this approach, that there are no sudden changes in the optical power, and the slow drift can be compensated with a feedback, as described in section 5.4.4 on pages 105 ff.

It should be noted, that also the EDFL-type lasers could in principle [Wis10] have been equipped with a coarse repetition rate tuning based on temperature changes, but no deeper investigations have been done so far on this topic, as the SESAM-based laser outperforms the EDFL as master laser oscillator in the present status.

5.4 Comparison to SESAM-Based Laser Systems

In this section, the experiences from the commissioning of the Origami laser system and its performance characterization is discussed. The oscillator is based on the passive mode-locking with a

semiconductor saturable absorber mirror (SESAM) as explained in section 2.4.4 on page 38 ff. Since the laser is a commercial one with the resonator enclosed in a compact-sized, sealed housing, neither the exact setup of the resonator is known, nor even the type of the laser. From the small size of the laser head, it could be concluded that a fiber is wound on a temperature stabilized base, which is supported by the fact that a fiber-coupled pump diode is used.[8] On the other hand, from the expertise of the company and the publications on SESAM lasers and their theory, the system may also be an Er:Yb bulk/glass laser, which would require a "several"-times folded cavity, as the resonator length for $f_{\mathrm{MLO}} = 216\,\mathrm{MHz}$ is $c_0/(2 \cdot f_{\mathrm{MLO}}) = 0.694\,\mathrm{m}$ – while the footprint of the housing roughly equals to the size of a sheet DIN A4 paper. In any case, the laser when it was specified had to meet certain requirements for the planned expansion of the optical synchronization system and its robust operation:

- maintenance-free operation
- center wavelength $\lambda_0 = 1560\,\mathrm{nm}$, matching the EDFL
- average optical power $P_{\mathrm{avg}} \geq 120\,\mathrm{mW}$
- pulse duration $\tau_{\mathrm{FWHM}} < 150\,\mathrm{fs}$, ideally transform-limited
- repetition rate $f_{\mathrm{MLO}} = 1.3\,\mathrm{GHz}/6 = 216.666667\,\mathrm{MHz}$
- coarse repetition rate tuning range of at least $\pm 3\,\mathrm{kHz}$
- fine repetition rate using a piezo with a bandwidth $\gg 10\,\mathrm{kHz}$
- integrated timing jitter $\delta t_{\mathrm{rms}} < 5\,\mathrm{fs}$ in $[1\,\mathrm{kHz}, 10\,\mathrm{MHz}]$ at $f_{\mathrm{c}} = 1.3\,\mathrm{GHz}$
- relative intensity noise <0.01% in $[10\,\mathrm{Hz}, 10\,\mathrm{MHz}]$
- input for an external modulation of the pump diode current with a bandwidth of $\geq 500\,\mathrm{Hz}$
- remote control and easy integration into the control system by documentation of digital and/or analog in- and outputs
- to the greatest possible extent insensitive to vibrations and shocks

These custom specification for their laser "Origami-15" were defined in direct cooperation with the company[9] of the laser systems [KSF+09] and it turned out that they are partly at the limit of what is technically possible, especially the pulse duration. When the laser was delivered after 4 months of manufacturing, it has been installed on the optical table in the synchronization laboratory and

[8] A fact that became disclosed soon after colleagues from PSI did their first investigations on this type of laser system. Later, it also was (probably by accident) disclosed that the "coarse tuning", as explained in the previous section, is realized by controlling the temperature of a piece of fiber inside the resonator – instead of the complete resonator itself. About the resonator construction it seems to be known that it is another separate compartment inside the housing. However, there is still no certainty of the type of gain medium...

[9] OneFive GmbH, In Böden 139, CH-8046 Zurich, Switzerland, http://www.onefive.com

characterized in accordance to the list above. A possible issue of the SESAM-based lasers is their limited lifetime. The manufacturer states it to be in the order of 10000 hours or 416 days, which implies a replacement of the laser nearly every year, making the need for the redundant operation of two laser systems even stronger. By this, a significant annual cost factor arises.[10]

Figure 5.20 shows the optical setup for the Origami laser system in the FLASH synchronization laboratory (compare also Fig. 4.4 on page 65 for the general optical table layout). It has been installed

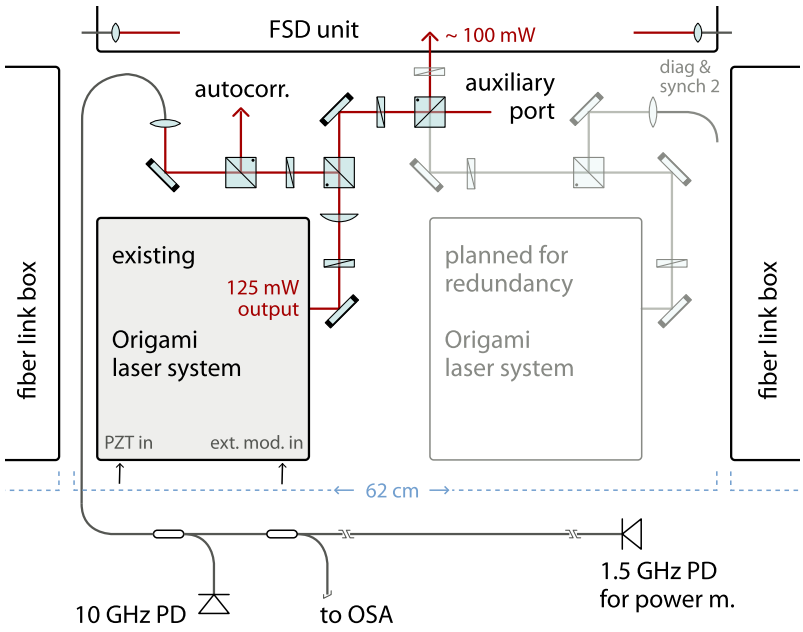

Figure 5.20 | Sketch of the integration of the Origami laser into the exiting system. The optical setup on the table includes a number of diagnostic ports, and only then the light is coupled into the free-space distribution unit (FSD) with its Invar baseplate. Due to the small footprint of the laser system, a second one can be placed next to it for redundancy.

in the space for MLO1, where an area of $620 \times 600\,\mathrm{mm}^2$ is available. Since the laser head has only a footprint of $260 \times 210\,\mathrm{mm}^2$, it is possible to install the second system for redundancy directly next to it, saving the space on the opposite side of the free-space distribution unit currently hosting the EDFL for additional setups and/or diagnostics. It is even imaginable to install a second level of optical components above the Origami installation, because the setup is practically maintenance-free once aligned, and the height of the laser is only 60 mm. From the 125 mW average output power of the laser, 12.5 mW are split off using a combination of a half-wave retarder and a polarizing beam-cube (PBC). After passing another combination of half-wave retarder and PBC, where 5 mW are tapped off for autocorrelation or other diagnostics measurements, this fraction of the laser pulse train is coupled to a short fiber section. Therein, a coupler provides 80% of the light to a fiber connector, where 4.6 mW have been measured. Like in the EDFL setup, this connects to a 10-GHz-bandwidth photodiode used for synchronization, as described in the previous sections. The remaining fraction

[10] The price of a custom-specified Origami-15 laser system is around 38,000 euros (as of 2010).

of the light in the fiber passes a 70%/30% coupler, with the larger amount of optical power (0.8 mW) are transported via a fiber optical patch cord to the amplitude monitor circuit installed in the RF lock chassis. The 30% (0.35 mW) port can be used for determination of the spectral properties using an optical spectrum analyzer (OSA). The main part of the emitted pulses also passes another half-wave retarder and a PBC, which is used to reflect the pulse train into the free-space distribution unit (see section 5.5, pages 108 ff.). The retarder is set to transmit ~ 10 mW of the light through the beam cube to enable further diagnostic measurements, such as an out-of-loop phase detector (see section 5.6, pages 5.6 ff.). Finally, for the free-space distribution and by that the devices of the synchronization system ~ 100 mW are available for distribution to the 16 planned devices. The second laser will be integrated similarly into the optical setup with the same type of synchronization and monitoring fiber installation. Behind the last beam cube, however, another half-wave retarder has then to be introduced in order to rotate the 90 deg rotated state of polarization (SOP), when the second laser is operated. In the future, this will be automated, and the diagnostics will detect if one laser fails and switch to the other in that case.

The Origami laser system is equipped with a control unit housed in a 3U 19-inch rack-mountable chassis with an integrated low-noise laser diode driver. It features a digital input/output (I/O) interface, which is connected to the established Beckhoff-based digital I/O PLC available in the control system. It allows for the control of the coarse repetition rate, toggling the laser emission and readback of several status bits, such as an error or whether the internal temperature stabilization is operating normally. The experience shows, that this interface should be extended. For instance, the laser controller does not report how many steps of the coarse repetition rate have been made, but these are limited by the manufacturer to ±25 (corresponding to $f_{\mathrm{MLO}} \pm 3.1\,\mathrm{kHz}$ at the fundamental) and it could happen, that this maximum number is reached when the environmentally conditions change. In this context, it should also be noted, that the original repetition rate of the pulse train was found to be 2 kHz below the specified value, hence already 16 steps were required to synchronize the laser to the master RF oscillator, leaving only 9 steps in this direction of safe tuning range. The second laser system ordered will be characterized in close cooperation with the manufacturer and colleagues from PSI during the production process to consolidate the expertise and the measurement equipment. Furthermore, the manufacturer offered to extend the digital interface with the required parameters. It will be then also possible, to upgrade the existing controller with the new firmware.

5.4.1 Beam Profile

When the Origami laser system has been commissioned on the optical table in the synchronization hutch, it was discovered that the intensity profile is not round on an infrared (IR) alignment card,[11] as obviously expected for a Gaussian beam. Therefore, the profile was measured using a Spiricon PyroCam III in a distance of 1063 mm from the output window of the laser system. However, the optical components for the coupling into the free-space distribution unit, as described above, were already installed and therefore the light was used from the last beam cube (see Fig. 5.20, p. 94). The

[11] Thorlabs VRC4

average power impinging the array of pyroelectric detectors in the camera was 3 mW. The obtained

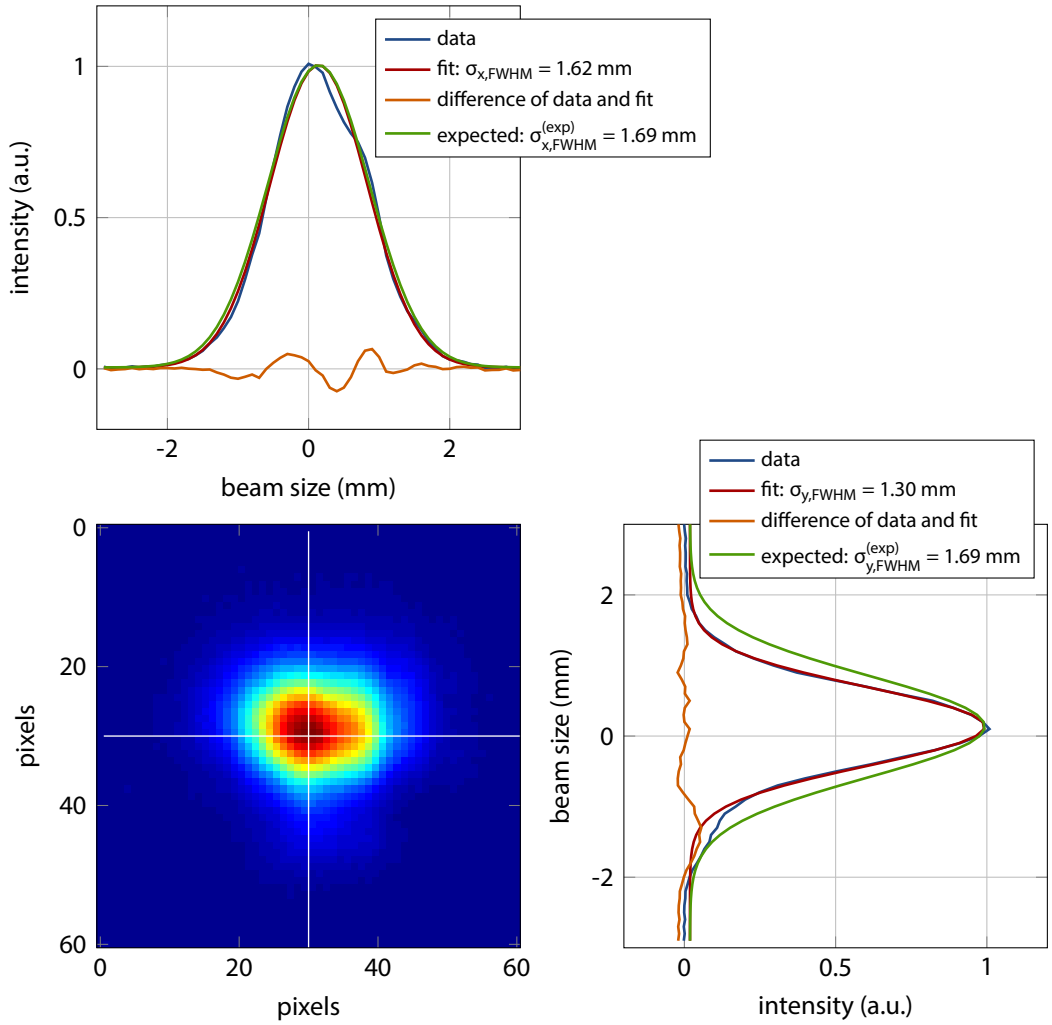

Figure 5.21 | Beam profile of the Origami laser system. The measurement was carried out using a Spiricon PyroCam III placed approximately 1 meter after the laser exit aperture. The theoretical curves take all already installed optical components into account.

profile is shown in Fig. 5.21, where a background image taken before had been subtracted. Two features are prominent: The beam has an elliptical intensity profile, and is significantly smaller in the y-direction. It has a FWHM width of 1.30 mm, obtained from the fit. The expected value of 1.69 mm is calculated by Gaussian beam propagation from the output of the laser up to the detector surface with respect to the installed optical components (see also section 5.5 on pages 108 ff. below). In the x-direction, the measured FWHM beam size of 1.60 mm matches the expected one better, but here, the intensity shows an asymmetric shape which is not covered by the fit. This deviation can clearly be seen in the difference of the data and the fit shown as the orange colored curve in the figure. In order to inspect a possible damage of the output window of the laser system it has been unmounted from the housing. However, the window is intact and the asymmetric pulse shape is also visible

without the window installed. This means that the output coupler, which is located 75 mm behind the window, of the laser resonator itself is damaged, and this can only be fixed by the manufacturer if this should be necessary. Since the coupling into fiber collimators is a critical issue in the free-space distribution unit, the investigations on the intensity distribution and the possible influence on focusing are inevitable in the characterization and the commissioning process of a new laser system. Should the laser output beam profile be determined by emission from a bulk gain material, as e.g. in Ti:sapphire lasers, there are three possibilities to clean the beam profile in terms of astigmatism: first, a combination of cylindrical lenses can be installed to correct for the different beam sizes in the two transverse directions, or secondly, the light can be coupled into a fiber immediately after the laser's output port and coupled out using a collimator with defined and desired parameters for the remaining part of the free-space distribution. Third, the future installments of the laser can be ordered with a fiber output directly from the manufacturer. However, in the latter two approaches problems may arise from high optical intensities in the fibers, causing nonlinear effects affecting other pulse properties (see section 2.3, page 24 ff.).

5.4.2 Pulse Duration and Optical Spectrum

In order to confirm the data sheet [One10] provided by the manufacturer also the pulse duration has been measured with the same commercial autocorrelator setup used for the characterization of the self-built fiber laser (EDFL, section 5.2.3, page 77 f.). The result is shown in Fig. 5.22, together with the EDFL data in the background for comparison. The corresponding fit for soliton pulses

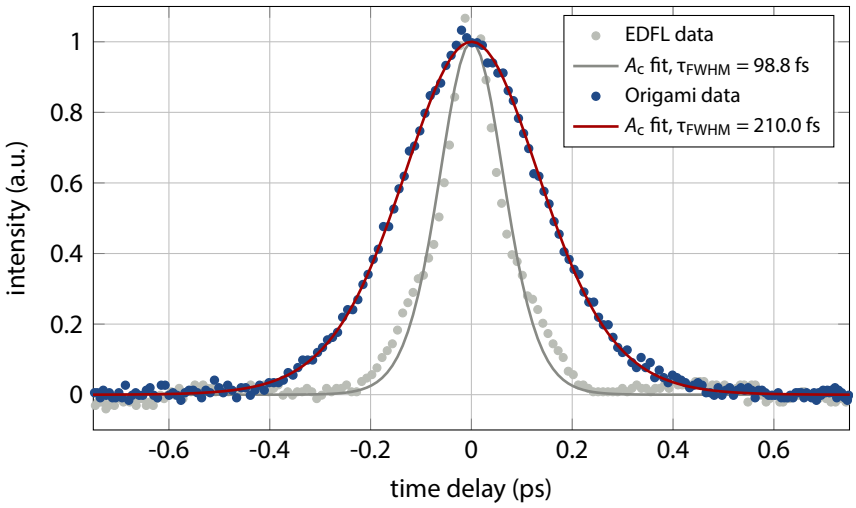

Figure 5.22 | Autocorrelation of the Origami laser oscillator. The pulse duration reconstruction yields 210 fs FWHM which is twice the duration of the EDFL pulse (shown in gray in the background for comparison, see Fig. 5.7, p. 78).

(see table 3.2, page 58) yields a full-width at half-maximum value of τ_{ac} = 324 fs, and hence a pulse duration of τ_{FWHM} = 210 fs, which is about 10% larger than stated in the data sheet (188 fs). It could be argued, that the laser does not meet the specification of a pulse duration less than 150 fs, but is had

not been defined whether the full-width at half-maximum value or the $\tau_p = \tau_{FWHM}/1.76 = 119.3\,fs$ is applicable. On the other hand, shorter pulses are hardly achievable with the employed SESAM technology, as discussed in section 2.4.4 on page 38 f.

The optical spectra of the Origami laser system and the EDFL measured with a calibrated[12] optical spectrum analyzer (OSA) are shown in Fig. 5.23. On the abscissa the wavelength is rep-

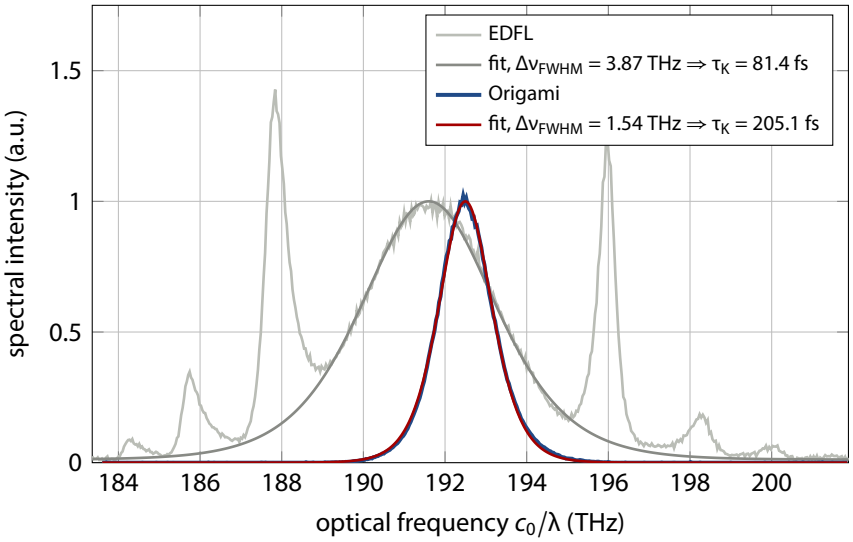

Figure 5.23 | Optical spectrum of the Origami laser oscillator. The spectral bandwidth of the Origami laser ($\Delta\nu \rightarrow \Delta\lambda_{Origami} = 12.42$ nm) is significantly smaller compared to the EDFL ($\Delta\nu \rightarrow \Delta\lambda_{EDFL} = 31.37$ nm) which results in a larger theoretical pulse duration τ_K at the Fourier limit.

resented by the corresponding optical frequency $\nu = c_0/\lambda$. The center of $\nu_0 = 192.56\,THz$ corresponds to $\lambda_0 = 1557.9\,nm$, close to the specified value of 1560 nm, whereas the spectral bandwidth of $\Delta\nu = 1.54\,THz$ leads to $\Delta\lambda = 12.42\,nm$ being 2 nm less than measured by the manufacturer. Using relation 2.60, the the transform-limited pulse duration of the Origami laser is $\tau_K = 205.1\,fs$, or respectively the time-bandwidth product is $\Delta\nu \cdot \tau_{FWHM} = 0.323$. This means that the Origami laser is indeed practically transform-limited as specified and claimed by the manufacturer. In comparison, the EDFL's transform-limited pulse duration, determined from the fit neglecting the sidebands, is $\tau_K = 81.4\,fs$ and by that about 20% less than measured. The time-bandwidth product from the measured quantities is $\Delta\nu \cdot \tau_{FWHM} = 0.382$. When an FFT algorithm is applied to the measured optical spectra, the temporal shape of the pulse can be reconstructed, as shown in Fig. 5.24. For the Origami laser, this temporal profile is in very good agreement with the autocorrelation measurement. In case of the EDFL, however, the pulse duration from this calculation is smaller, because the real pulse is not transform-limited. The oscillatory structure at the wings of the pulse results from the sidebands in the optical spectrum and are the reason for the shoulders observed in the autocorrelation traces.

The impact of the longer pulse duration of the Origami laser, compared to the one of the EDFL,

[12] The used optical spectrum analyzer Yokogawa AQ6370B features optical self-alignment and self-calibration routines to a built-in 1550 nm LED. This procedure is always performed after a transportation of the device or longer stand-by times.

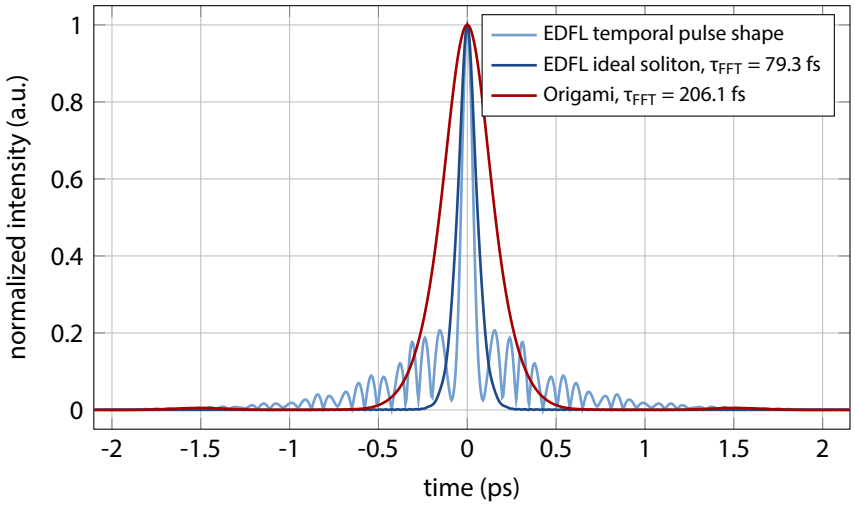

Figure 5.24 | Pulse duration calculation based on optical spectra. The temporal shapes were calculated by Fourier transformation of the optical spectra.

will be always be addressed in the following sections and chapters, because it is particularly important for the optical cross-correlations used in the fiber links (chapter 6, pages 131 ff.), as well as the Ti:sapphire (chapter 7, pages 151 ff.) and photoinjector laser synchronization schemes (chapter 8, pages 167 ff.).

Influence of the Voltage Applied to the Piezo Actuator

The spectral properties and the pulse duration have been investigated as a function of the voltage V_{piezo} applied to the piezo element used for the repetition rate stabilization. This is an important measure, because the piezo changes the length of the cavity and by this the internal dynamics of the laser. In the first measurement, the driver of the piezo was connected to a low-noise laboratory power supply (PS), whose voltage is varied from −5.5 V to 5.5 V. After the driver, this corresponds to $V_{\text{piezo}} = [1.5\,\text{V}, 94\,\text{V}]$. As the laser is equipped with an external modulation input for the current of the pump laser diode, a feedback loop based on the optical power monitor inside the RF lock chassis (to avoid pointing stability issues, see section 5.6, pages 120 ff.) and a DSP-based control loop can be established. In a second series of measurements again the optical spectra and the pulse duration are recorded. The active feedback stabilizes the output power while the voltage of the piezo is changed as in the first series of measurements. Figure 5.25 shows the dependence of the center wavelength and the spectral width without (red trace) and without (green trace) the amplitude feedback engaged. In the latter case, the spectral bandwidth changes by 1.31 nm (peak-to-peak) or 10.83%, while the center wavelength changes by 2.38 nm or 0.15%. Although the active amplitude feedback also affects the internal dynamics of the laser, these effects in the spectral properties are suppressed approximately by a factor of 20. The spectral width now only changes by 0.06 nm (0.52%) and the center wavelength by 0.16 nm (0.01%).

In Fig. 5.26 the results of the autocorrelation measurements is shown. Without a feedback on

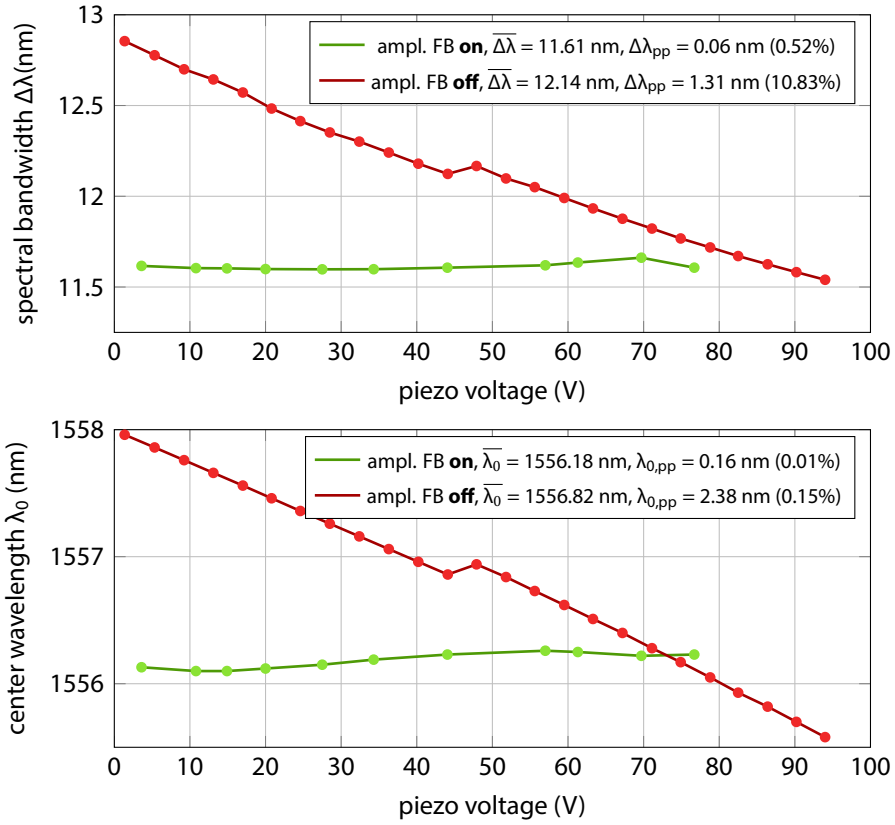

Figure 5.25 | Spectral bandwidth and center wavelength as function of the piezo voltage. The piezo voltage is applied with a DC power supply as input for the driver. In the two measurement series, the amplitude feedback was set to on and off.

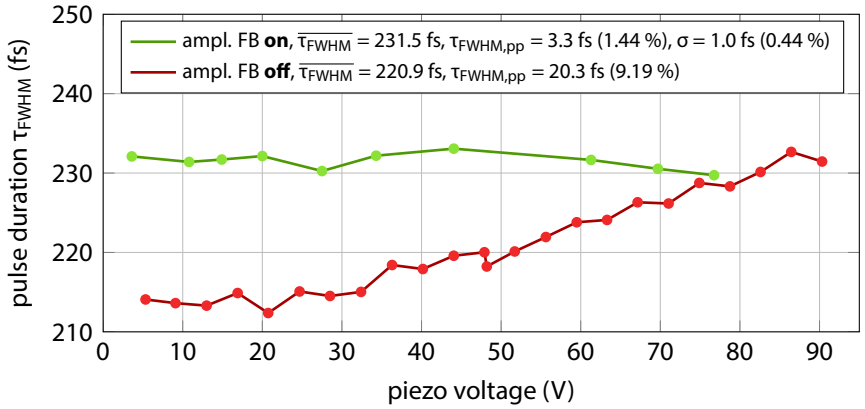

Figure 5.26 | Pulse duration as function of the piezo voltage. In the two measurement series, the amplitude feedback was set to on and off.

the laser amplitude the pulse duration changes by 20.3 fs (peak-to-peak) or 9.19% over the range of the piezo, while this change is suppressed by to 3.3 fs or 1.44% in case of an active feedback. With a

standard deviation of 1 fs, it can be assumed that here the resolution of the autocorrelation analysis is reached.

These investigations strongly suggest that a stabilization of the optical power of the Origami laser is required for the operation as master laser oscillator, because amplitude changes and also a change of the pulse duration would be detected as a timing change in the optical cross-correlators (see section 3.5.1, pages 55 f.) used in the system. During the series of measurements another issue became apparent, as the dynamic range of the external modulation input of the laser is not large enough to cover the induced changes by the piezo element. This can be seen in the graphs as the corresponding data could only be taken up to $V_{\text{piezo}} \simeq 77\,\text{V}$ before the integrator of the loop reached its limit. Hence, either the limit of the piezo-based repetition rate stabilization could be reduced, with the disadvantage that the coarse feedback has to catch more often, or an enlargement of the dynamic range for amplitude stabilization. The latter has been specified for a second laser system, which was ordered for additional research and development with this new type of laser system. At the same time, discussions with the manufacturer took place to strongly reduce the influence of the piezo on the spectral and temporal pulse properties.[13]

5.4.3 Timing Phase Noise Measurements and Synchronization

One of the most important properties of the Origami-15 laser system is its advertised low timing phase noise. An total integrated timing jitter of 3.34 fs in $[1\,\text{kHz}, 10\,\text{MHz}]$ at a carrier frequency of $f_c = 2.998\,\text{GHz}$ had been demonstrated before [Oneo9]. This is the result of a cooperation of PSI

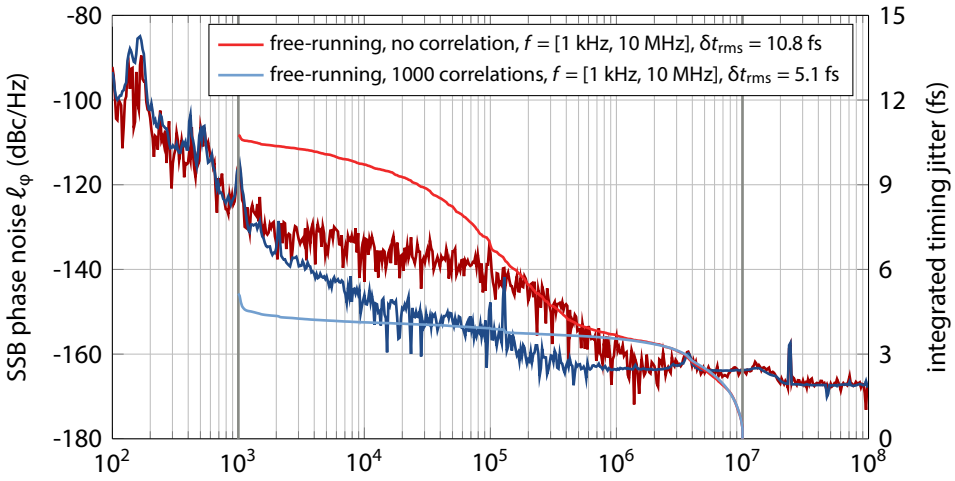

Figure 5.27 | Single-sideband phase noise of the Origami laser oscillator. In the measurement, the resulting integrated timing jitter with and without the SSA's internal correlation capability is compared.

and the manufacturer in order to improve the noise behavior of the laser diode driver and a careful selection of the used components, in particular the photodetector.

[13] Later, it was disclosed that the manufacturer even had to slightly re-design the complete resonator design in order to meet the more stringent specifications.

To evaluate the actual performance of the laser oscillator when integrated into the optical synchronization system, diverse phase noise measurements have been carried out. In the measurement shown in Fig. 5.27 the actual photodetector, which is later integrated into the synchronization circuit, was used. Because of this, also the carrier frequency has been chosen as f_c = 1.3 GHz and the oscillator was free running. When the internal correlation function of the SSA, which suppresses the phase noise of the local oscillator in the device (see section 5.2.5, pages 82 f.), is not used, the integrated timing jitter amounts to 10.8 fs in [1 kHz, 10 MHz]. This value is lower than the determined 12.4 fs for the EDFL in the same frequency range, especially as there were 1000 correlations performed. Employing this capability of the SSA in the phase noise measurements with the Origami, the total jitter reduces to 5.1 fs, practically meeting the specifications. It should be noted that the result in the reference cited above was obtained at almost three times the carrier frequency and with 10000 correlations, which naturally reduces the value of the integrated timing jitter. Comparing the phase noise data taken with 1000 correlations of the EDFL and the Origami, it can be seen that the traces show larger fluctuations from ~ 1 kHz to ~ 12 kHz in the latter case, suggesting a worse performance. This is, however, not the case, as for the EDFL the value of $\ell_\varphi(f_i)$ is measured about 10 dB larger in this region, thus contributing more to the integral. The reason for this might be the intensity noise level of the according laser diode driver, as discussed in section 5.2.5 (pages 82 ff.) and with additional details in appendix A.4 (pages 210 ff.).

This effect is clearly visible in the next series of measurements, which compares the timing jitter of the Origami and the the EDFL at the carrier frequencies of f_c = 1.3 GHz and 2.6 GHz. Furthermore, in these investigations another type of photodiode[14] is used. In both cases, the fiber collimator was installed at the corresponding auxiliary monitor port of the laser setup. At the lower carrier frequency the integrated timing jitter calculated from 1000 correlations amounts to 12.4 fs for the EDFL and to 12.9 fs for the Origami laser. As expected, the total jitter is lower at the higher carrier frequency and amounts to 11.5 fs and 9.4 fs, respectively. Although these numbers are all quite similar, there are significant differences in all four measurements, as it can be seen in Fig. 5.28. For the EDFL the main contribution to the timing jitter is in the frequency interval of [1 kHz, 10 kHz], and while the integrated timing jitter is much lower at larger offset frequencies at the higher carrier, here the curves approximate each other. The Origami's phase noise, on the other hand, suffers from a higher noise floor at high offset frequencies, resulting in the main contribution to the timing jitter in this region, especially in the last evaluated decade. Since the both investigations on the EDFL and the Origami have done with some time in between, not enough attention had been paid to ensure equal optical power levels, such that the photodiode was provided with 5 mW from the Origami, but 11 mW from the EDFL. It is expected to achieve the same noise floor level when these are matched, because the rest of the setup such as used amplifiers and bias voltages were the same in both cases. It is very likely, that these u^{2}t-made photodiode shows a similar or even better performance in further investigations as the normally used ones made by EOTech, but presumably at the cost of higher required optical power levels.

[14] XPDV2120R made by u^{2}t Photonics with an integrated load resistor. The same type without the resistor, but connected through an external bias-tee, had been used in [One09].

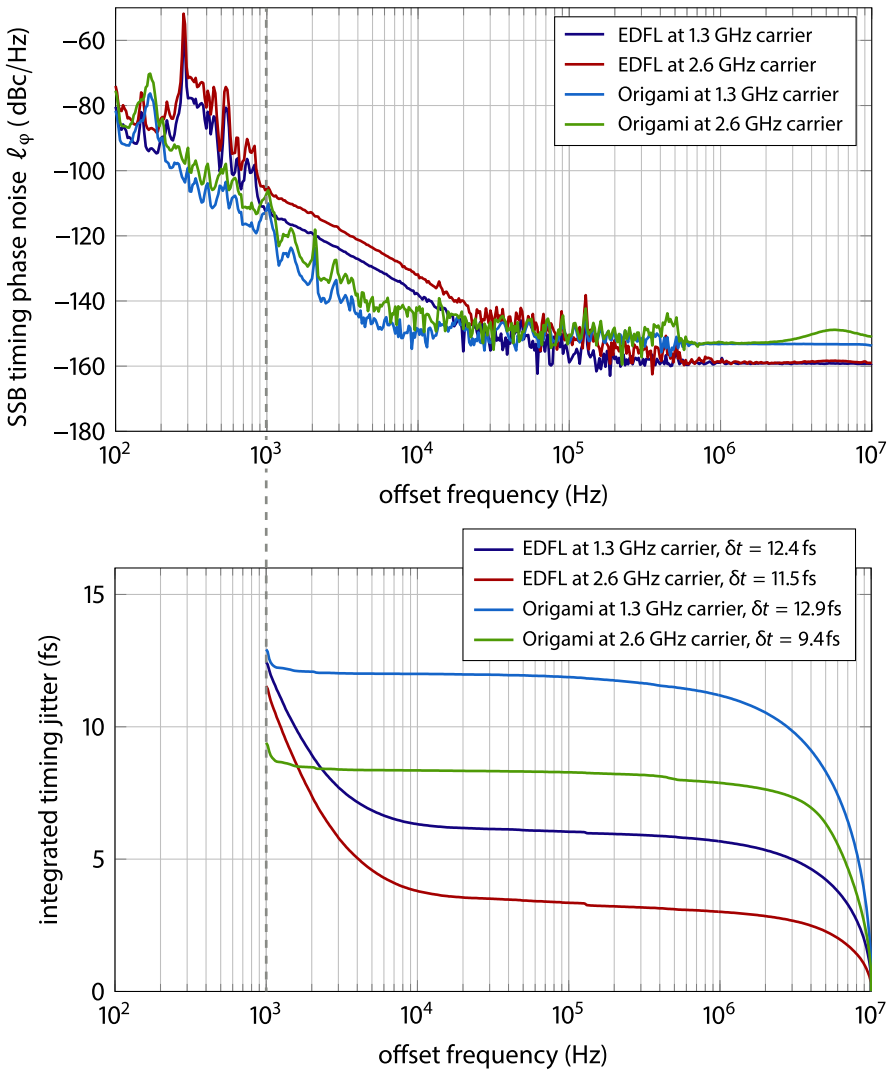

Figure 5.28 | u²t photodiode-based phase noise measurement of both MLOs. In this measurement, a photodiode made by the Berlin-based company u²t was used in contrast to the usual ones made by Michigan-based company EOTech.

For the synchronization of the Origami to the master RF oscillator (MO) the established type of photodiode is used. Figure 5.29 shows a comparison of the laser and the RF reference signal measured with 1000 correlations at a monitor port of the vector modulator. In contrast to the reference signal directly measured at the patch panel with the cables coming from the MO, the vector modulator induces a relatively high noise floor for offset frequencies above 100 kHz. All laser phase noise measurements were carried out truly out-of-loop with an additional EOTech photodiode installed on the optical table and supplied with 4.5 mW optical power at the auxiliary monitor port. From the comparison of the phase noise of this reference signal and the free-running oscillator, it can be concluded, that the laser is performing better in terms of timing jitter than the RF oscillator after the vector modulator vector modulator (VM) down to offset frequencies of 200 Hz. Consequently,

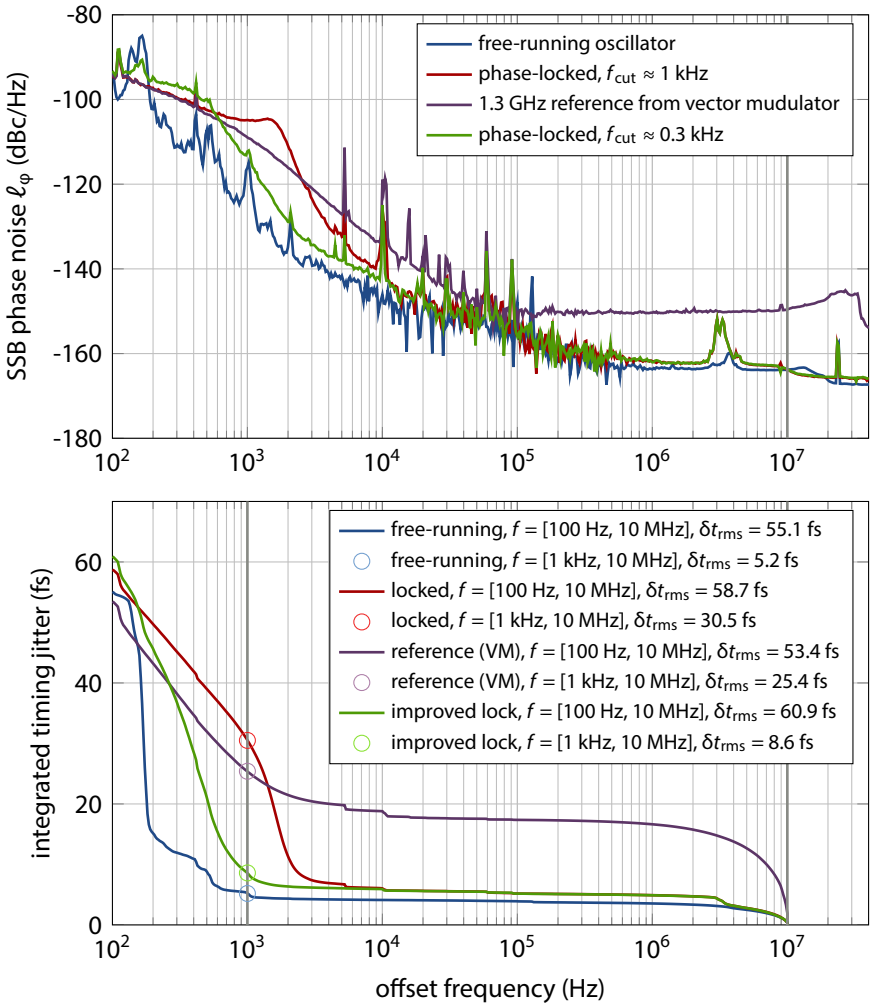

Figure 5.29 | Phase noise and timing jitter of the free-running and phase-locked laser oscillator. The phase noise and timing jitter of the laser is compared the phase noise of the RF reference signal after the vector modulator. With improved loop gains the timing jitter could be reduced significantly in the lower frequency region. It amounts to 5.2 fs (free-running), 30.5 fs (initial, only guessed loop settings) and 8.6 fs (optimized loop settings) in the offset frequency interval f = [1 kHz, 10 MHz].

the integrated timing jitter evaluated down to 100 Hz increases when the laser is RF-locked to the reference. Especially, the red curves shows the situation when PID loop gains are the same as for the EDFL, where the PLL cut-off frequency is in the order of $f_{cut} \approx 2$ kHz leading to a larger phase noise of the reference around this frequency. By a systematic change and particularly a reduction of the loop gains, the cut-off frequency was reduced to $f_{cut} \approx 300$ Hz to reduce the low-frequency timing jitter. For this particular setting the timing jitter almost follows the characteristic of the free-running oscillator with its steep slope, but it should be possible to reduce this frequency further. However, if the loop gains are too small, fast or sudden changes in the laser's noise, for example if accidental something is dropped on the optical table during commissioning or a repair of another device, can

then not be caught. But when there is no installation work, the loop parameters should be carefully adjusted and observed on the long-term (see section 5.6, pages 120 ff.). The evaluation of the phase noise of the free-running oscillator at frequencies from 1 kHz down to 100 Hz reveal a dramatic increase of the jitter at 200 Hz, which might be again due to the intensity noise of the pump laser diode and its driver, but investigations on this can only hardly be carried out, because the manufacturer does not disclose the type of the laser diode.

A summary of the calculated values of the integrated timing jitter is given in table 5.3. In conclusion, the Origami laser systems performs very well in terms of timing jitter, better than the EDFL and even the RF oscillator down to offset frequencies of 200 Hz. From the numbers and the figures it can be seen, that the choice of the photodiode is critical. Although the reported 3.3 fs in [One09] were obtained with a photodiode manufactured by u^2t, the proven ones from EOTech lead to better results here. However, further investigations on this topic are ongoing. Moreover, the synchronization to the RF reference should be improved, as its PLL disturbs the amplitude stability of the laser.

Table 5.3 | Overview of the integrated timing jitter measurements at the Origami. The integrated timing jitter calculated from timing phase noise measurements of the Origami laser. The last column of the table references to the figure where the corresponding graph is shown.

description	f_c	integrated timing jitter in frequency interval				fig.
	GHz	[10, 10 M]	[100, 10 M]	[1 k, 10 M]	[10 k, 10 M]	
Origami SESAM-based master laser oscillator						
free-running, no corr., EOTech	1.3		31.5 fs	**10.8 fs**	9.7 fs	5.27
free-running, 1000 corr., EOTech	1.3		55.1 fs	**5.1 fs**	4.1 fs	5.27
free-running, 1000 corr., u^2t	1.3		129.2 fs	**12.9 fs**	12.0 fs	5.28
free-running, 1000 corr., u^2t	2.6		128.6 fs	**9.4 fs**	8.4 fs	5.28
φ-locked, f_{cut} = 1 kHz, EOTech	1.3		58.7 fs	**30.5 fs**	6.0 fs	5.29
φ-locked, f_{cut} = 300 Hz, EOTech	1.3		60.9 fs	**8.6 fs**	5.9 fs	5.29

5.4.4 Amplitude Stability

The relative intensity noise (RIN) of the Origami laser was measured with the same opto-electrical setups as described in the characterization of the EDFL (see Fig.5.9, p. 80). In the first series of measurements, the amplitude monitor installed in the rack chassis of the synchronization circuit had been used and it was found that the measurement is governed mainly by the noise of the detector (see Fig. A.3 in the appendix on page 209). Therefore, an improved setup with commonly grounded photodiode and amplifier and a low-noise laboratory power supply has been used.

The RIN measurement is carried out for the four possible combinations of free-running and RF-locked oscillator with the aforementioned amplitude stabilization feedback engaged and inactive. The red traces in Fig. 5.30 represent the voltage spectral density and its integral value of the synchronized laser with the amplitude feedback active. The total RIN amounts to 0.017%, where the largest

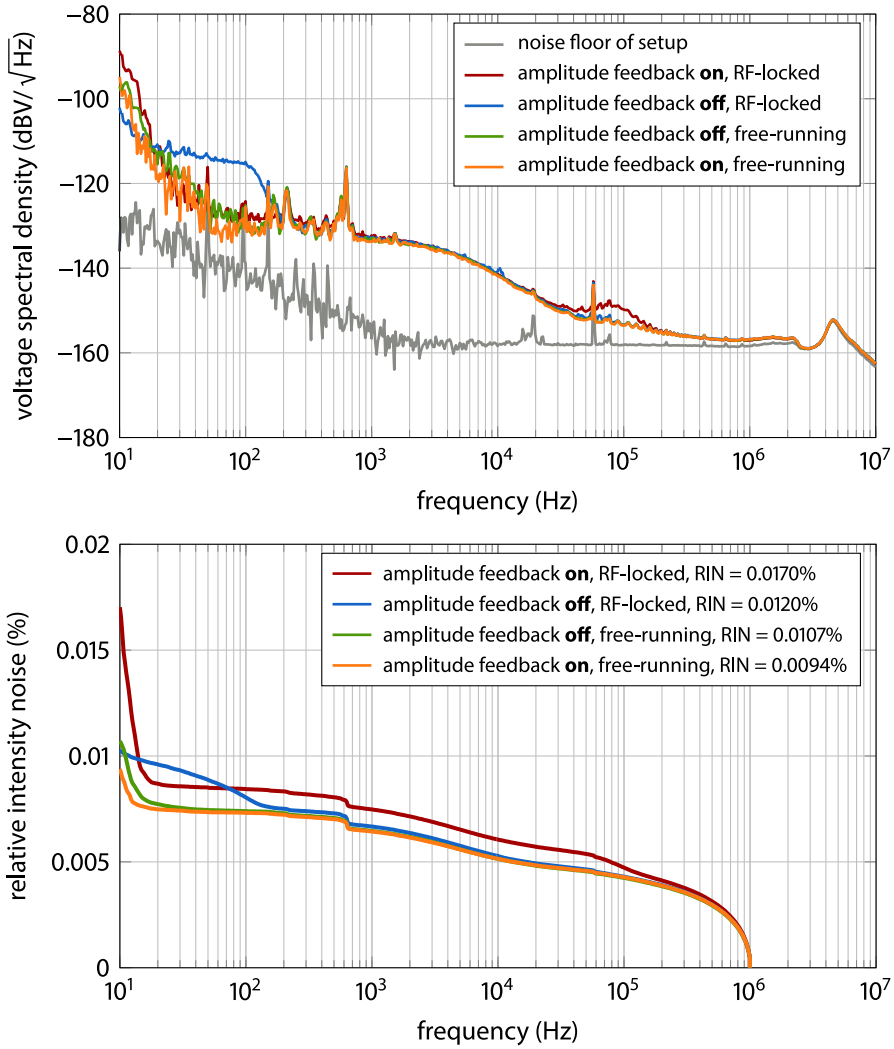

Figure 5.30 | Relative intensity noise of the free-running Origami laser oscillator. The data was recorded with a dedicated measurement setup as described in section 5.2.4 and shown on page 80. It is evaluated in different frequency intervals. The gray curve in the background shows the noise floor of the setup with no optical input.

contribution is the intensity noise at frequencies in the first measured decade [10 Hz, 100 Hz], particularly below 20 Hz. The reason for this is most likely the bandwidth of the amplitude stabilization feedback loop, since it had to be chosen very low, because the external modulation input of the laser does not work with higher modulation frequencies than ~ 50 Hz. This was found experimentally by connecting a function generator to the input, tuning the frequency and amplitude of the generated AC voltage and trying to find a correlation in the monitored optical power. The lowest frequency the used function generator can provide is 50 Hz, but no modulation could be observed in the optical power. With a DC voltage applied, on the other hand, the optical power could be varied in the specified range. Hence, only a very slow amplitude feedback can be established. It should be noted, that

the original specification required this frequency to be 500 Hz, so the manufacturer has to mend on this aspect. When the amplitude stabilization is turned off, but with the RF-lock PLL still active, the data shown in blue is recorded, which features a shoulder at 150 Hz contributing the second-most to the total RIN of 0.0102%. The frequency corresponds approximately to the estimated cut-off frequency of the RF-lock PLL, as discussed in the previous section and is a direct consequence of the known dependency of the piezo movement on the optical power of the laser (see also supplementary Fig. A.2 in the appendix on page 208). When the laser is free-running without the amplitude stabilization, its RIN calculates to 0.0107%, but the largest contribution is again be found in the 15 Hz region. The same holds, when the amplitude stabilization is switched on, without a synchronization to the RF oscillator. The RIN is slightly lower in this case and amounts to 0.0094%. Generally, the relative intensity noise of the Origami laser is a bit larger than that of the EDFL, but still matches the initial specifications. Remarkably at low frequencies, the measured voltage spectral density $\ell_V(f_i)$ closely resembles the noise of the setup (see Fig. 5.11, page 81), whereas the Origami's ℓ_V is about 20 dB higher at some frequencies. It can be assumed already from these measurements that the laser

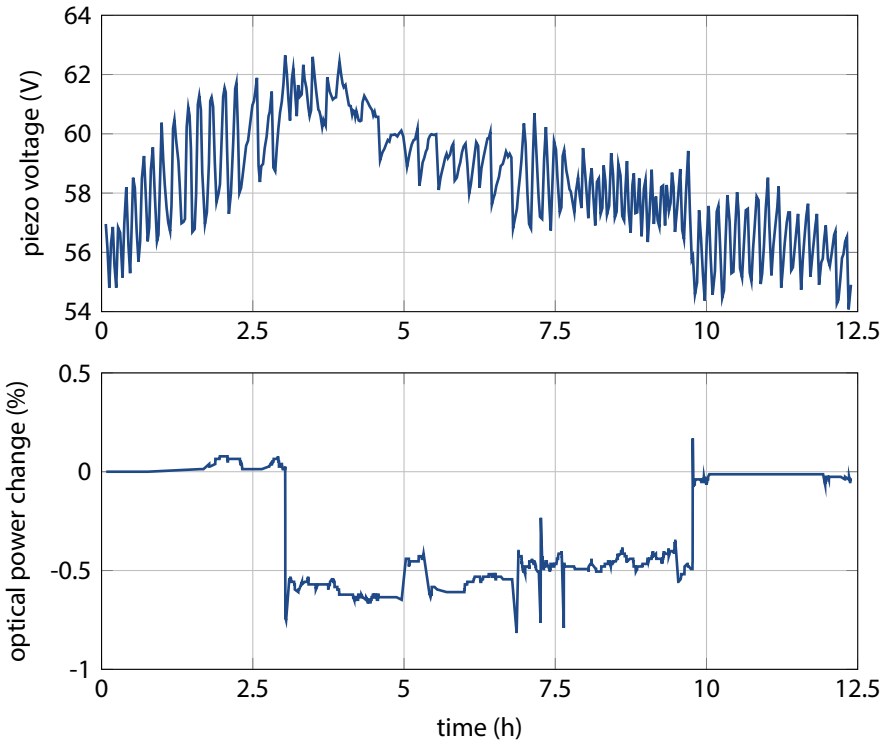

Figure 5.31 | Piezo voltage and optical power of the Origami laser over about 12 hours. At around 12:30 the amplitude feedback went off and was again engaged at 19:00. The data was retrieved from the control system long-term archive.

will drift on the long-run, i. e. at even lower frequencies. The results of the corresponding investigations are presented in section 5.6 on pages 120 ff.

Since the piezo voltage of the synchronization PLL does not only influence the optical power of

the laser, but also the spectral and temporal properties, it is evident to stabilize the laser's optical power with the active feedback for a reliable long-term operation. In section 5.4.2 (page 97 ff.), it has been already mentioned that the range of the external amplitude modulation does not cover the range of the optical power change induced by the piezo voltage. Consequently, it can happen that the integrator of the PLL approaches the limit of the allowed modulation and the feedback loop is not working anymore. In this case, the optical power normally drops, as shown in Fig. 5.31 (lower plot), where data reconstructed from the long-term archive of the accelerator's control system for a course of 12 h. At around 12:30, the amplitude feedback stopped working as the piezo voltage (upper plot) exceeds a certain voltage and the output power of the laser changes by 0.5%. For the following 6.5 h the trend of the piezo voltage is to lower values, and correspondingly, the optical power increases slightly. Furthermore, it shows some some spikes and steps, which may result from external disturbances, for example when an experimenter was working in the room. At 19:00, the amplitude stabilization feedback was engaged again, when the piezo voltage reached an uncritical region. Thus, a reasonable amplitude stabilization loop can only be setup when the external modulation range is large enough to compensate for the complete change induced by the piezo element (see also section A.2 in the appendix on page 208 ff.). It should be noted that the observed fast oscillation in the piezo voltage with a period of approximately 10 min could be traced back to the internal temperature stabilization of the Origami laser resonator.

Although the new SESAM-based laser system has some minor issues, with the amplitude feedback active and with the improved phase-locked loop to the accelerator's MO, it can operate uninterrupted on long time-scales and its pulse train can be distributed to the components of the optical synchronization system as an alternative to the EDFL.

5.5 Local Distribution and Splitting of the Master Laser Pulse Train

The reference laser pulse train of the master laser oscillator must be distributed to the front-ends of the optical synchronization system which are usually connected by an individually length-stabilized fiber link. For this purpose a distribution scheme has been suggested [Wino8] which is installed on the optical table where the master laser oscillators (MLOs) are located. It is based on free-space optics and in particular using half-wave retarders and polarizing beam cubes, allowing for the distribution of two laser pulse trains to up to 16 devices. This approach has a number of advantages compared to completely fiber-based or hybrid distribution schemes which were also under consideration:

- dispersive pulse broadening negligible as only a small number of optical components is used
- no pulse distortion and broadening due to nonlinear effects
- minimized drift caused by airflow, temperature or humidity changes
- allows for setting the optical power for each connected device individually
- allows to split the available optical power to a reduced number of ports

- enables the choice between standard single mode fiber or polarization maintaining fiber on a port by port decision, and even changeable after installation.

The optical setup of this free-space distribution unit (FSD) is depicted in Fig. 5.32. The single pulse train enters the FSD through a telescope and then passes a series of polarizing beam cubes preceded by a half-wave retarder. This allows for precise control of the ratio between transmitted and reflected light finally guided to each port. The redundant operation of two laser systems is achieved by combining their light with a first beam cube (BC1) requiring a perpendicular linear polarization of the beams entering the FSD. However, for one laser system an additional retarder (indicated by the arrow in the illustration) in front of the second beam cube (BC2) has to be introduced to ensure the correct splitting ratio, if it is not set to a ratio of 50%:50%. In case of the fiber link stabilization units, the light is coupled into a dispersion-compensated erbium-doped fiber amplifier (see section 5.5.3 below) and then fed to the optical cross-correlator inside the device and the actual link. Other, presently unused, ports are used for optical power monitoring, the phase detector for coarse timing stabilization of the fiber links and a direct connection to the photoinjector laser.

Mechanically, the compact and space-saving designed unit is based on an *Invar* plate which has a very low thermal expansion coefficient minimizing the influence of temperature changes, and by that timing changes caused by changes in the optical path lengths. The beam cubes and the retarders are both installed within custom-designed mounting blocks made from aluminum. These blocks and the supports of the mirror mounts are screwed to the base with additional dowel pins to ensure a well-defined optical axis through the beam cubes. Since efficient coupling of light into fiber collimators is only possible within tight tolerances, each port features at least one additional kinematic mirror mount to align, along with the kinematic mount of the collimator itself, the transverse position and angle of the beam at the collimating lens. Because of the divergence of laser beams, also approximately equal beam path lengths are required for all ports which was taken into account for during the design process of the unit. It should be noted that the mirror mounts of the original design had to be replaced by mechanically more stable ones as the quality of foreseen mounts [Wino8] did not match the required stability and repeatability. During this reconstruction of the support blocks it has also been discovered that the thickness of the mirrors was not considered initially, and has also been corrected in the second iteration of the unit.

5.5.1 Beam Propagation in the Free-Space Distribution Unit

In order to couple light efficiently from one fiber collimator into a another in a particular distance, an imaging system is required because of the divergence of a laser beam propagating in free-space. Therefore, at the beam entrance of the free-space distribution a Kepler telescope consisting of two converging lenses is foreseen. During the initial commissioning of the FSD on the optical table it was discovered, that the efficiency of coupling light into the collimators could not exceed about 50%. Here, the efficiency is defined as the ratio of the average optical power measured at a connector spliced to the collimator and the optical power measured in front of the collimator, normalized to the transmittance of the connector/fiber/collimator combination, which has to be measured beforehand.

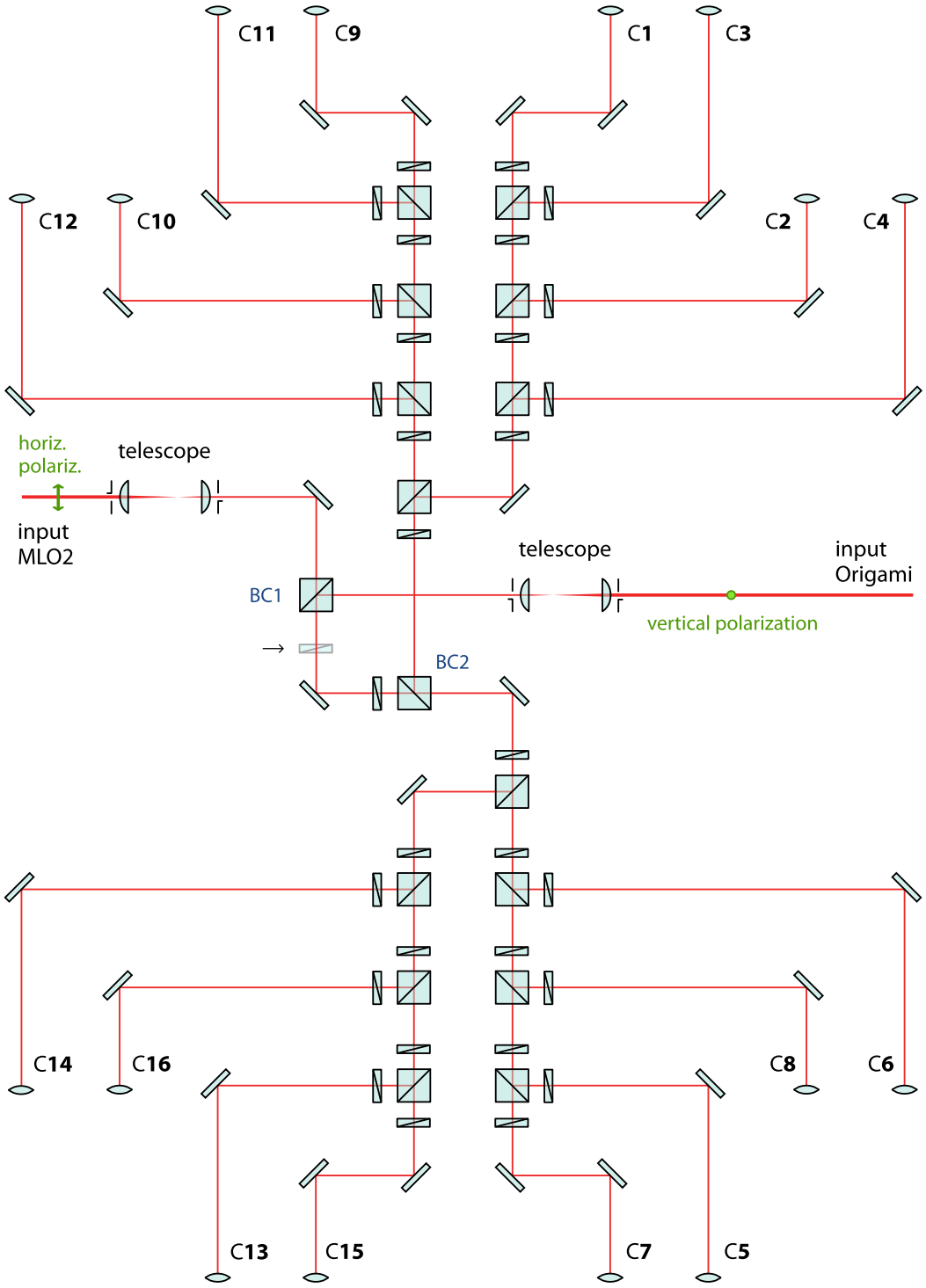

Figure 5.32 | Sketch of the optical setup and geometric beam path of the FSD. It allows for distribution of the laser pulse train of two laser systems to up to 16 devices (see also Fig. 4.4 on page 65) Usually, the light is coupled into a fiber collimator which requires a careful and systematic alignment of the unit.

The reason for these values to be lower than expected were twofold: First, the telescope design was not well thought out in the first place and secondly, the originally planned laser system could not be used, but the prototype laser from [Loe09] – see the historical remarks in section 4.2, pages 63 f. Therefore, the telescope has been optimized by means of the GAUSSian beam propagation from the laser's output collimator to the individual ports of the FSD [Sch09]. The outcome of the simulations required a new mechanical construction of the telescope, in which initially omitted iris diaphragms are integrated for an easier adjustment of the beam path (see also supplementary figures G.3 and G.4 on pages 255 and 256 in the appendix). With this new optical setup, the specified average coupling efficiency of 80% can be achieved, as discussed in the following section.

After the initial alignment of the beam path in the free-space distribution unit with the new telescopes, but before the final splitting of the optical power to the individual ports, the pulse duration of both laser systems has been measured. The beams left the FSD at port 5 (see Fig. 5.32, page 110,

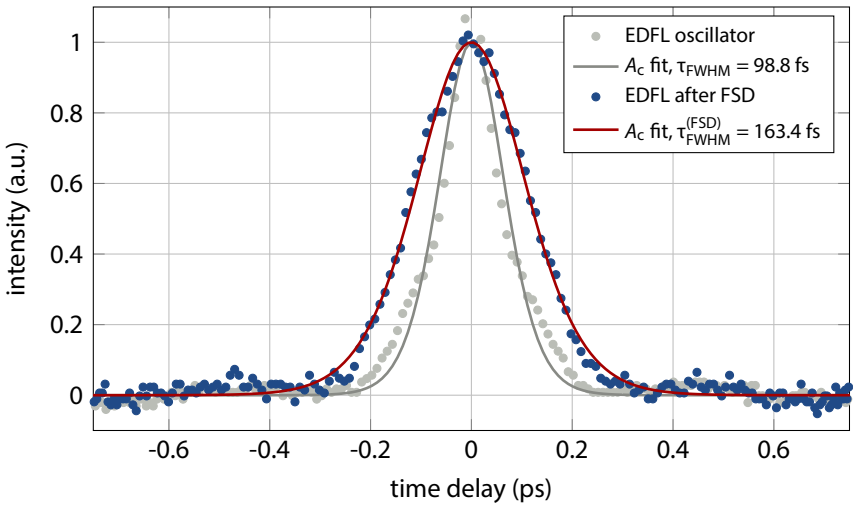

Figure 5.33 | EDFL pulse duration before and after propagating through the FSD. The pulse is broadened caused by chromatic dispersion in the retarders and the polarizing beam cubes.

again) and passed the maximum number of beam cubes and retarders. By that, the worst case of the influence of dispersive effects from the glass material of the optical components has been evaluated. The pulse duration of the EDFL becomes significantly larger, as shown in Fig. 5.33, and was measured to be τ_{FWHM} = 163.4 fs. However, the autocorrelation trace approaches more the one expected shape for the sech^2-shaped pulse, in contrast to the autocorrelation measured at the exit of the oscillator. The temporal pulse shape of the Origami laser, on the other hand, is not influenced by the propagation through the FSD. Its duration measured at the port is τ_{FWHM} = 216.9 fs, as can be seen in Fig. 5.34. The reason for this behavior might be the larger spectral bandwidth of the EDFL, such that wavelength-dependent effects from the coating of the optical components, the retardation of the retarders and the reflectivity of the mirrors come into play. Finally, the knowledge of the pulse duration is furthermore essential for the design of the fiber amplifiers, which connect the corresponding devices to the FSD (see section 5.5.3 below on pages 115 ff.).

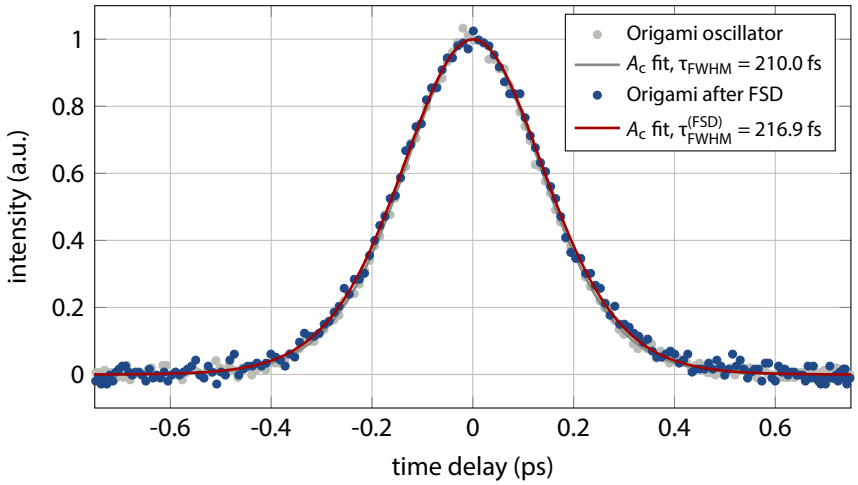

Figure 5.34 | Origami pulse duration before and after propagating through the FSD. The pulse is only slightly broadened caused by chromatic dispersion in the retarders and the polarizing beam cubes compared to the EDFL because of its larger original duration and narrower optical spectrum.

5.5.2 Optical Power Split-Up & Budget

The split-up of the available average optical power delivered by each of the master laser oscillators to the various consumers is an important task during the commissioning of the free-space distribution unit, particularly with regard to power of the EDFL, as it is lower than initially assumed. This leads to the following specification for the splitting of the available power in the current stage of expansion, taken also the loss from all optical components into account:

- 5.5 mW for each of the four installed fiber links to the BAMs
- 6.0 mW for the fiber link to the EO beam diagnostics laboratory, because the distribution EDFA exhibits more loss due to the installed isolator (see chapter 6, pages 131 ff.)
- 5.5 mW for the fiber link to the sFLASH ("HHG") laser laboratory
- 5.5 mW for the direct fiber connection to the injector laser hutch
- 4.0 mW for the LO generation used in the phase detector for the coarse timing stabilization of the fiber links
- 0.5 mW for two optical power monitors, installed at opposite sides of the FSD

Two additional ports of the FSD have 5.5 mW allocated and are foreseen for EDFA drift measurements (see section 5.6.4, page 128 ff.) and further expansion of the synchronization system without the need for an anew change of the retarder settings, as this is a time-consuming task and inevitably would interrupt the operation of the system.

Table 5.4 lists the actually measured optical powers P_{EDFL} and P_{Origami} for both laser systems after the Origami laser has been commissioned as master laser oscillator (MLO), and for both cases the

sum of the measured powers closely matches the power delivered by the laser. The total transmission P_Σ/P_1 of the distribution unit due to the loss of all optical elements also agrees with the expected value of 82.1%. This is calculated from the mean m_{PBC} of the transmission and reflexion coefficients of the used beam cubes (see supplementary measurement shown in Fig. A.1 on page 207) and the transmission coefficient of the retarders ($r_{\mathrm{loss}} < 0.5\%$ loss from reflexion per surface, see [Mea10]) with the beam passing 5.25 beam cubes and retarders on average:

$$P_\Sigma/P_1 = (m_{\mathrm{PBC}})^{5.25} \cdot ((1 - r_{\mathrm{loss}})^2)^{5.25} = 97.3^{5.25} \cdot (0.995)^2)^{5.25} = 0.82.$$

The table also lists the optical power measured at the connector of the patch cord for the four ports of the FSD where presently no EDFA is installed and the achieved coupling efficiency η which also takes the transmission of the used patch cords (between 0.98 and 1) into account. It is about 8% lower for

Table 5.4 | Allocation of the optical power in the free-space distribution unit. The overview includes the currently installed devices. The table is divided according to the upper and lower part of the optical setup (see Fig. 5.32, page 110; IL = injector laser).

C#	device	P_{nominal} mW	P_{EDFL} mW	$P_{\mathrm{conn.}}$ mW	η_{EDFL}	P_{Origami} mW	$P_{\mathrm{conn.}}$ mW	η_{Origami}
1	BAM 4DBC3	5.5	6.10			9.28		
3	BAM 18ACC7	5.5	5.80			9.20		
9	BAM 1UBC2	5.5	5.32			4.50		
11	BAM 3DBC2	5.5	5.51			4.63		
12	monitor	0.5	0.75	0.63	84.0%	0.62	0.44	71.0%
5	open port	5.5	5.24			4.77		
6	sync. IL	5.5	5.42	4.67	86.2%	4.60	3.20	69.6%
7	sync. HHG lab.	5.5	5.80			4.50		
8	monitor	0.5	0.48	0.36	76.5%	0.40	0.30	76.5%
13	φ-detector	4.0	4.11	3.30	81.9%	3.40	2.63	78.9%
15	sync. EO lab.	6.0	6.24			5.11		
		$\Sigma = 49.5$	$\Sigma = 50.77$		$\overline{\eta} = 82.2\%$	$\Sigma = 51.01$		$\overline{\eta} = 74.0\%$
measured power at BC1			64.9		$\pm$ 4.1%	64.8		$\pm$ 4.1%
transmission η_{FSD}			78.2%			78.7%		

the Origami laser systems for two reasons: First, the FSD has been optimized for the EDFL operation, because the Origami laser was not available when the FSD had been commissioned, and secondly the beam profile and propagation issues of the Origami laser (see section 5.4.1, pages 95). From tables 5.4 and 5.5 it can also be seen that the free-space measured optical power for the Origami laser is lower at all ports ($P_{\mathrm{nominal}}/P_{\mathrm{fs}} \Rightarrow \bar{r} = 0.88$) except for C1 and C3, where it is significantly higher. This is most likely just due to an imperfect setting of the retarder in front of BC2, which is supported by the similar standard deviation of the nominal and the measured power in front of the collimators for

both laser systems. It should be possible to achieve a better matching of the power levels at all ports for both lasers by adjusting the polarization with the additional retarder in front of BC2 which was not available for this measurements.

A similar investigation (data not shown) has been done on the ports with EDFAs installed, both with no pump current applied and for a moderate pump current of $I_p = 100\,\mathrm{mA}$. Since the efficiency of the coupling of light into the collimators of the EDFAs cannot be measured directly, the average efficiency $\overline{\eta}$ of the first measurement had been taken into account for the calculation of the transmission coefficients. In the not-pumped case, the average transmission amounted to $(11.0 \pm 1.3)\%$ and for the pumped EDFA $(81.2 \pm 14.7)\%$ with the EDFL as master oscillator in place. This is in relative good agreement with former EDFA investigations, which led to the "100 mA pump current corresponds to ≈ 100% transmission" rule of thumb. For the Origami laser, however, the transmission in

Table 5.5 | Free-space power ratios and in the FSD and coupling efficiency. The data is shown for both laser systems. In the calculation of the mean value in the third column (marked by a star), the first two values were not considered.

			EDFL		Origami	
C#	device	$P_{EDFL}/P_{Origami}$	η_{coll}	$P_{nom.}/P_{meas.}$	η_{coll}	$P_{nom.}/P_{meas.}$
1	BAM 4DBC3	0.65		1.11		1.69
3	BAM 18ACC7	0.63		1.05		1.67
9	BAM 1UBC2	1.19		0.96		0.82
11	BAM 3DBC2	1.19		1.00		0.84
12	monitor	1.21	0.84	1.5	0.71	1.24
5	open port	1.10		0.95		0.87
6	sync. IL	1.18	0.68	0.99	0.70	0.84
7	sync. HHG	1.29		1.05		0.82
8	monitor	1.20	0.76	0.96	0.77	0.80
13	φ-detector	1.21	0.82	1.03	0.79	0.85
15	sync. EO lab.	1.22		1.05		0.85
mean		1.20*	0.82	1.06	0.74	0.88
σ		0.05	0.04	0.15	0.04	0.14

the not-pumped case amounted to $(3.9 \pm 1.6)\%$. The reason is the strong wavelength dependence of the erbium-doped gain fiber used in the EDFA (see supplementary Fig. D.3 on page 243 in appendix D), as the center wavelength of the Origami laser spectrum is closer to the absorption maximum. The relative transmission in the amplifying case is similar to the EDFL with a mean value of 70.7%, but it shows a larger deviation of 23.9%.

In general, the distribution of the laser pulse train in the FSD with reasonable optical power levels for all connected device works well and no additional losses had been observed. The power splitting and the coupling efficiency using the Origami laser, which was installed after the FSD was optimized for the EDFL, can be improved, but is partly caused by the laser itself (see section 5.4.1, pages 95 f.).

5.5.3 Influence of the Distribution EDFA on Spectral and Temporal Properties

The erbium-doped fiber amplifiers, which connect the ports of the free-space distribution unit to the individual devices must be build in a dispersion compensated manner (see section 2.3.4 on page 29 f.), because most of the devices are fiber link stabilization units, which require short pulse durations for their optical cross-correlator. Therefore, a gain fiber with a positive mode propagation constant of $\beta_2 = 12\,\mathrm{fs}^2/\mathrm{mm}$ (see supplementary information in section D.3, pages 243 ff.) has been chosen to compensate the dispersion of the single mode fiber used as collimator pigtails. Based on the measured pulse duration at one port of the FSD, the evolution of the pulse duration in the EDFAs has been calculated for both, but only GVD-induced pulse broadening has been taken into account for. Figure 5.35 shows the result for four of the installed EDFAs for both laser systems. In case of the

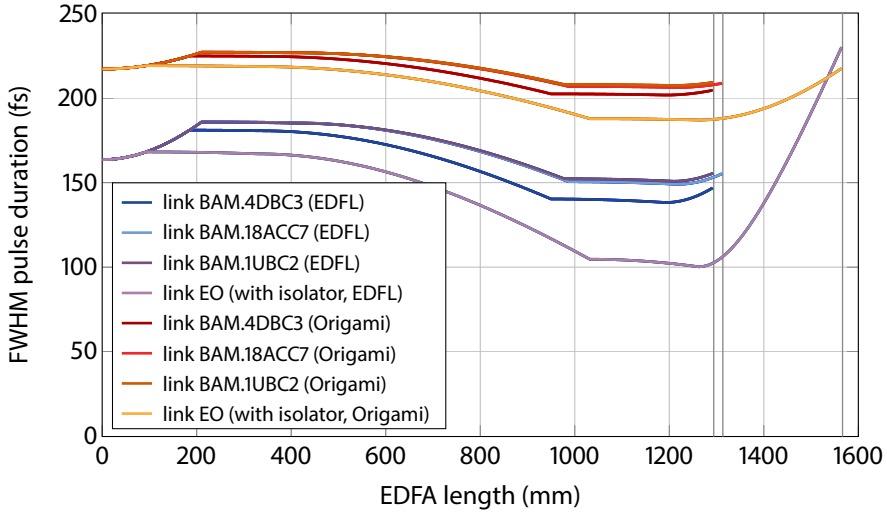

Figure 5.35 | Evolution of pulse duration in the EDFAs connecting the fiber link devices to the FSD. In the calculation, which is based on the originally measured pulse durations, only takes chromatic dispersion into account.

EDFL acting as master laser, the EDFA of link 4DBC3 is overcompensated, such that the initial pulse is shortened by approximately 20 fs, whereas the pulse duration at the end of the EDFAs of links 18ACC7 and 1UBC2 are close to the original one. The EDFA for the link to the EO laboratory has been rebuild and equipped with a Faraday isolator (see section 6.3, pages 144 ff.), when the Origami laser system was already installed and thus the dispersion compensation of the additional SMF used in the isolator has been adapted to the longer initial pulse duration of the Origami laser. In this case, the pulse duration at the end of the amplifier is perfectly matching the duration at the beginning (topmost orange curve in the figure). However, due to the shorter pulse duration of the EDFL, and by that the shorter dispersive length L_D as per Eq. 2.26a (see page 27) in the SMF, the dispersion compensation does not match and the pulse leaves the EDFA significantly longer. In the other amplifiers, the dispersion is compensated relatively good also for the Origami laser, although the EDFAs were designed for the EDFL, and the pulses leave these with a slightly shorter duration than the initial one.

Table 5.6 | Power and dispersive and nonlinear lengths of the distribution EDFAs. The table gives an overview on peak power, dispersive lengths and nonlinear lengths at the entrance of the gain fiber, as well as the FWHM pulse duration τ_{FWHM}^{exit} at the end of the distribution EDFAs.

laser	**EDFL**					**Origami**				
link	P_{peak}	L_{NL}	L_D	N^2	τ_{FWHM}^{exit}	P_{peak}	L_{NL}	L_D	N^2	τ_{FWHM}^{exit}
	W	m	m		fs	W	m	m		fs
4DBC3	198.42	0.87	1.79	0.49	146.5	159.54	1.35	2.23	0.61	204.0
18ACC7	193.31	0.92	1.84	0.50	154.8	158.01	1.38	2.25	0.61	208.1
1UBC2	193.60	0.92	1.83	0.50	155.1	158.10	1.37	2.25	0.61	208.7
EO (28G)	214.62	0.75	1.65	0.45	229.5	163.97	1.28	2.17	0.59	216.9

Due to the small core diameter of the erbium-doped fiber (see appendix D, pages 239 ff., for detailed properties of the used fibers) and the high gain in the order of 10 . . . 20 dB of the amplifier, nonlinear effects could come into play. In table 5.6, the peak power P_{peak} of the pulse at the entrance of the gain fiber, as well as the dispersive length L_D, the nonlinear length L_{NL} from Eq. 2.26b (see page 27) and the corresponding scaling relation $N^2 = L_D/L_{NL}$ (see page 28) are summarized for the four amplifiers. Although the values of N^2 are smaller than one, they are large enough to suggest that also nonlinear effects such as self-phase modulation should be consider in a more comprehensive theoretical treatment.

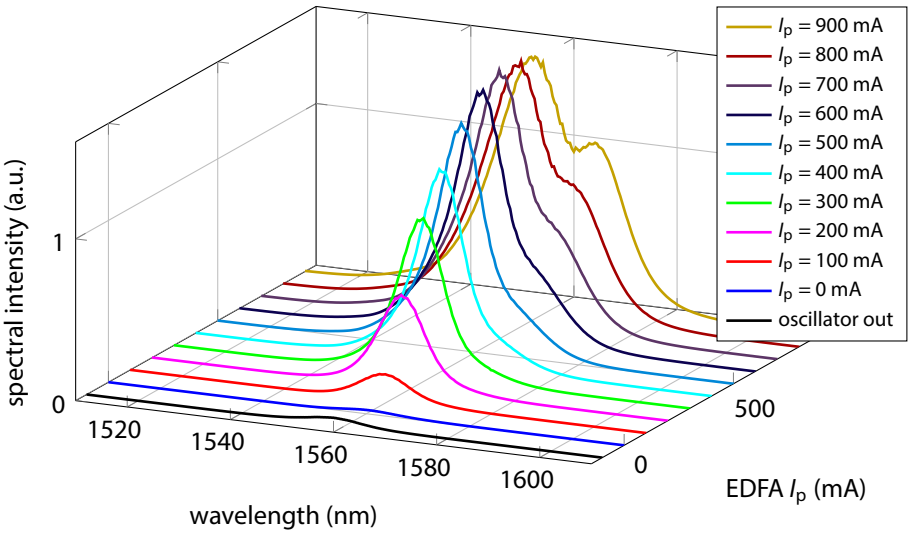

Figure 5.36 | Optical spectra of the Origami laser after amplification. The data is acquired after amplification in an EDFA used in the local distribution and connection of the fiber link stabilizers to the FSD.

Experimentally, this becomes evident, when the optical spectra and the pulse duration are measured after the amplifier at different pump currents, and by that different peak powers inside the gain fiber and the subsequent coupler- and collimator pigtail fibers. In Fig. 5.36, data from link 4DBC3 is

shown and it can be seen that the optical spectrum broadens asymmetrically with increasing pump power and develops a second local maximum at a higher wavelength than the central part, which itself shifts to shorter wavelength. Most likely, the reason for this behavior is self-phase modulation, which causes a generation of new frequency components due to the KERR effect (see section 2.3.6, pages 30 f.). The pulse duration increases significantly already at relatively low pump currents between 100 mA and 200 mA and then stays constant at about 250 fs FWHM. Only in the not-pumped case the pulse duration matches the calculated one. Figure 5.37 gives an overview of the change of the three characteristic properties pulse duration τ_{FWHM}, center wavelength λ_0 and full-width at half-maximum spectral bandwidth $\Delta\lambda$. Most notably, the latter increases by more than 100%. The

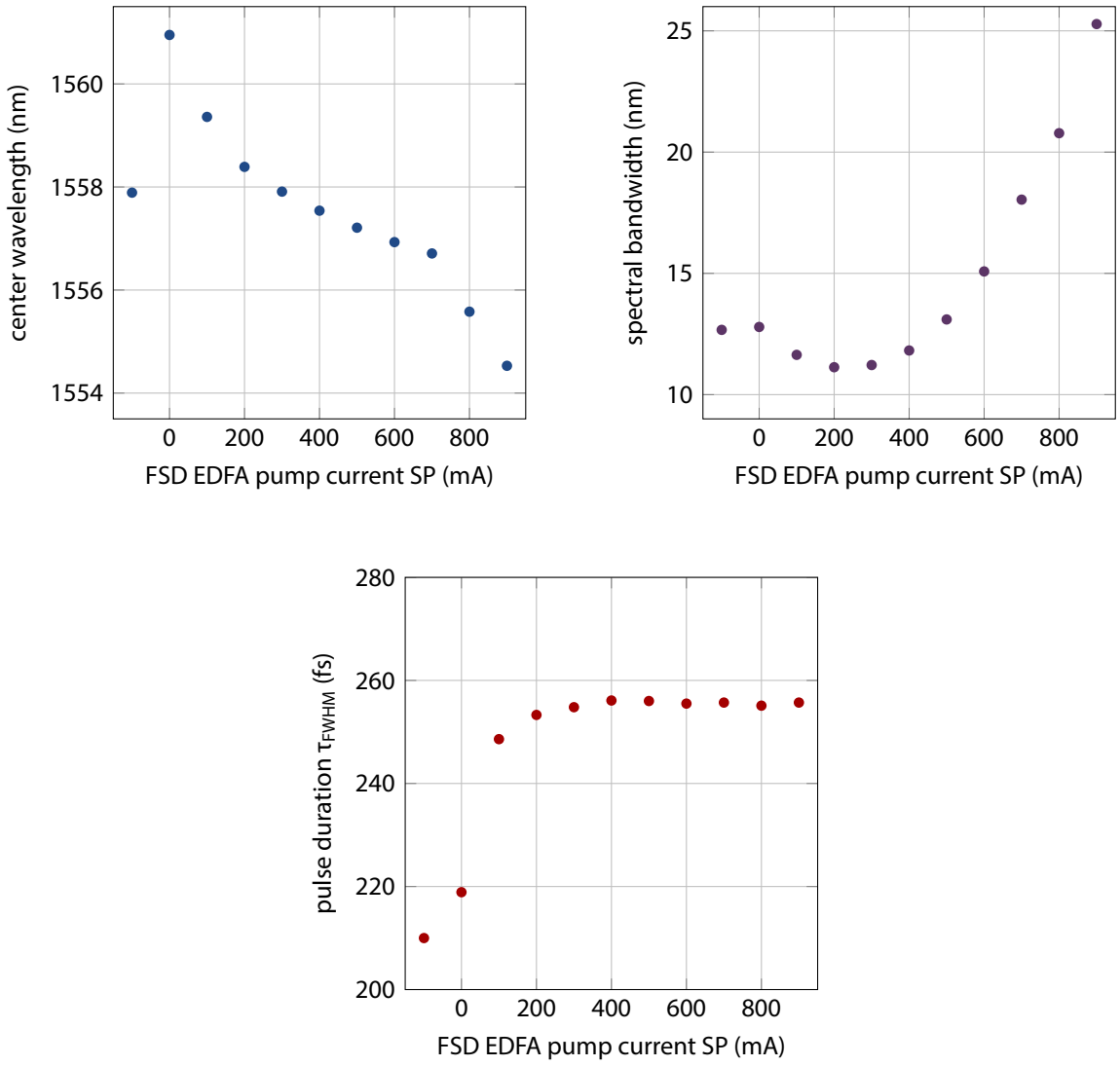

Figure 5.37 | Influence of the EDFA pump current on the optical spectrum and pulse length. Dependence of the center wavelength (**left**), spectral bandwidth (**right**) and pulse duration (**bottom**) on the distribution's EDFA pump current. The measurements were carried out using the Origami laser input pulses.

different temporal and spectral properties for different pump currents of the EDFA can influence the sum-frequency generation in the fiber link stabilization unit, as the conversion process heavily depends on these. Since in the future only Origami laser systems will be deployed as master laser oscillators (MLOs), the design of the fiber amplifiers has to be adapted for this type of laser and they need to be carefully characterized to optimize the performance of the fiber links.

5.5.4 Considerations for a Future Upgrade of the Distribution Scheme

Based on the observations discussed above, and in anticipation of the following section on the long-term reliability and stability of the free-space distribution scheme, it became apparent that the scheme has to be modified and optimized. After brainstorming, a first sketches came up, and in this second iteration of the local distribution of the master laser oscillator pulse train, the idea of staying in free-space is still pursued. Hybrid schemes or pure fiber-based layouts were considered non-optimal because of the short pulse duration and the high optical power with the resulting need for dispersion compensation and the problems with nonlinearities. Although temporal drift from thermal expansion is similar for aluminum and standard fiber with $\sim 50 \ldots 70\,\mathrm{fs/(m \cdot K)}$, fibers are sensitive to changes in the humidity of the surrounding air. This effect is negligible for free-space setup. Therefore, the most important considerations had been:

- single, common baseplate for the laser systems and the actual distribution optics
- use Invar or SuperInvar to minimize influence of thermal expansion

As the Origami laser systems have a small footprint, two of them will be mounted next to each other. The remaining available space on the optical table and the baseplate, respectively, can be utilized optimally keeping the following considerations in mind:

- Stay with 16 ports of cross-correlator based fiber links, and in principle copy the existing distribution setup (compare Fig. 5.32, page 110), but ensure that the geometric path is equal and as short as possible for each port.
- Use custom-engineered optic mounts to make the setup as compact as possible.
- Optimize the imaging system for highest possible efficiency for coupling light into the fiber collimators at the 16 ports. Taking the beam parameters (section 5.4.1, pages 95 f.) of the Origami laser into account, based on ideas in [Boc13], a Galilean beam expander with an additional focusing lens seems to be promising.
- Add one dedicated port for the connection of the photoinjector laser system, and be prepared for the connection of more than one laser (see section 8.2.3, pages 174 ff.).
- For a future upgrade, add two ports for the connection of a "short link" subsystem [Lam11, Zem08]. This will require one "reference" port and one port, where a temporal delay corresponding to one period at 10.4 GHz, or 28.8 mm, can be set.

- Install a four quadrant detector, or a camera, to monitor possible remaining pointing instabilities of the reference laser beam.

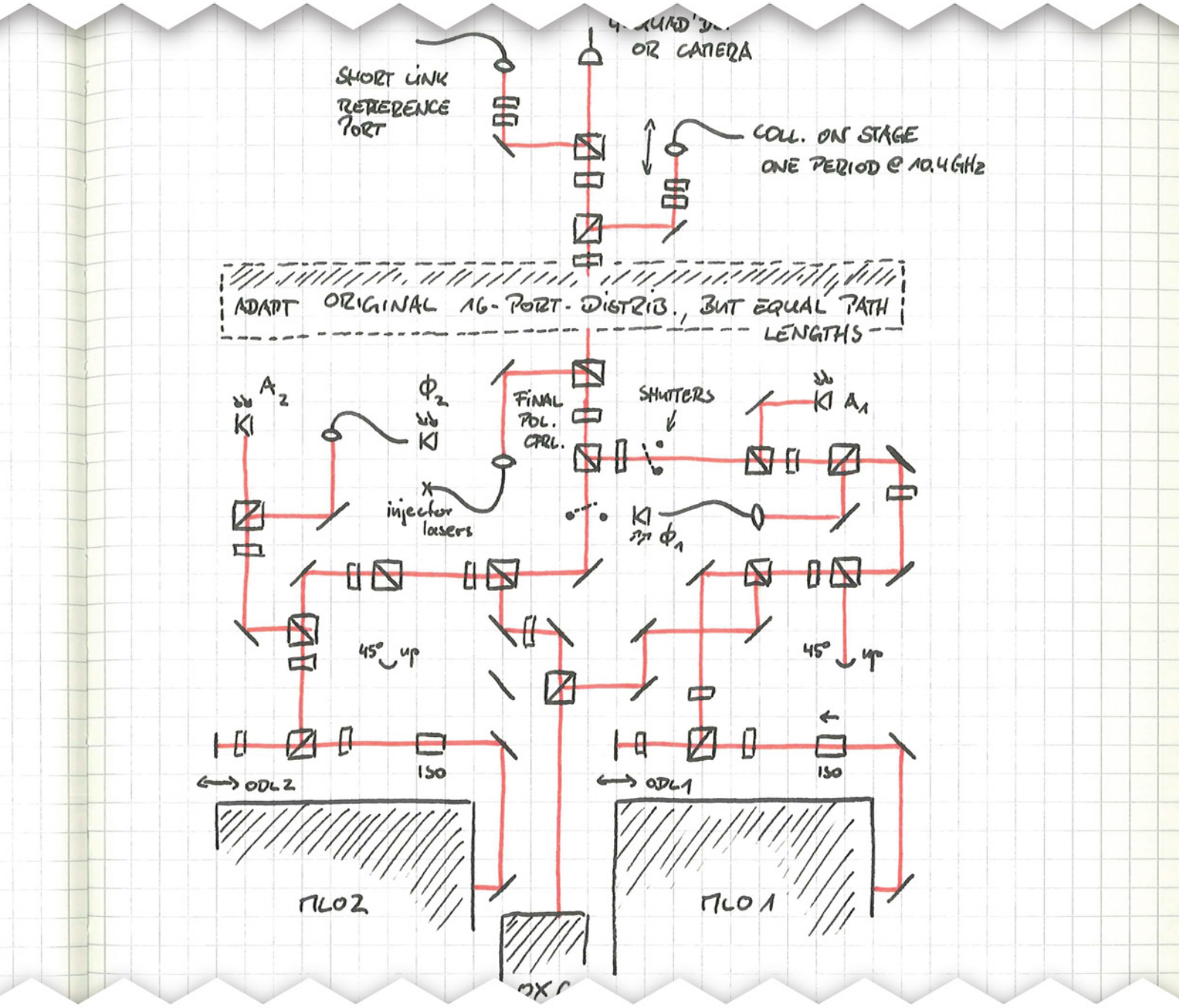

For the redundant operation of the two MLOs, in this design remote-controllable shutters have to be used to block the beam of the laser not serving as real master. Additionally, several ideas,

diagnostic measures and operation-critical aspects have to be taken into account:

- Each laser must be permanently synchronized to the accelerator's master RF oscillator (MO), and therefore individual PLLs are required (see section 5.3.1, pages 87 ff.).
- Install free-space photodiodes for measurement of the optical power independent of the beam pointing for each laser, and prepare for a corresponding feedback.
- Measure the timing between the two laser systems with femtosecond precision with an optical cross-correlator. For this, the pulse trains have to be combined independently of the combination for the main distribution while the path lengths also must be the same, such that temporal overlap in the OXC corresponds to exactly the same timing for the two pulse trains in the main distribution.
- Equip both lasers with a motorized optical delay stage to correct for timing drifts detected with the OXC.
- Detect if the laser is mode-locked at all. This can either be realized by exploiting TPA (see section 5.2.2, page 76) or by measuring the power in one of the FOURIER comb lines, which will require a modification of the phase detector assembly in the rack.
- Install an additional port at each laser for future expansion of the diagnostics, for instance pulse duration or optical spectrum measurements.
- Install a $c_0/(2 \cdot f_{\mathrm{MLO}}) \simeq 700\,\mathrm{mm}$-long optical delay line at each port to cope with all possible temporal overlap requirements at the end-stations.

Finally, the complete distribution scheme and the diagnostics must be integrated into the accelerator's control system. A corresponding DOOCS server must be able to detect the failure based on the many diagnostic measures of one laser and ideally switch over to the other one fully automated. In particular, the timing relation to the accelerator should be kept as close as possible, meaning with sub-picosecond accuracy (see section 4.4 on page 68 f.).

5.6 Long-Term Drift Behavior

In this section, measurements on the long-term stability and drift behavior of the master laser oscillators and the free-space distribution unit (FSD) are discussed. The data of the according monitoring channels (compare also appendix B, pages 223 ff.) is recorded through the accelerator control system (DOOCS) using a MATLAB script with a data acquisition rate of 0.1 Hz for a particular period of time. This has the advantage over the simple DOOCS history feature, that at any time all channels are read out with the same "general event number". In the future, all relevant DOOCS channels used in the optical synchronization system will be integrated into the DAQ system of the accelerator, which will simplify these types of measurements and enable the evaluation of the drift for arbitrary periods.

5.6.1 Amplitude and Timing Stability of the Origami SESAM-Based Laser System

The Origami laser system has been surveyed twice over a period of 160 h, i. e. nearly one week each. The first measurement has been carried out immediately after the laser had been commissioned and characterized. For the second measurement, the amplitude stabilization feedback had been setup and enabled. In both cases, the laser was synchronized to the master RF oscillator. Figure 5.38 shows a comparison of the drift and fluctuation of the optical power. Without the feedback, the optical

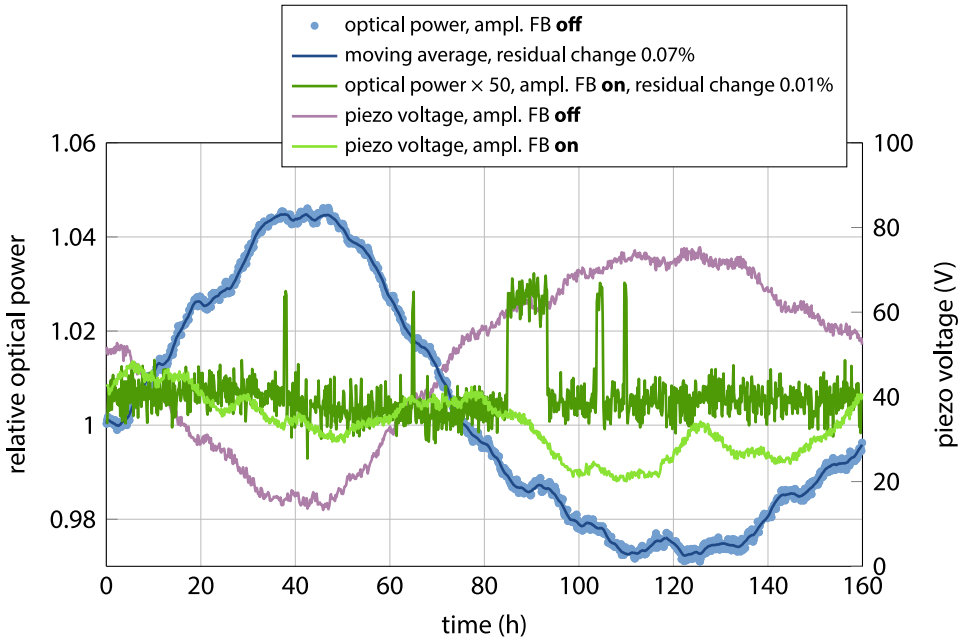

Figure 5.38 | Drift of the optical power of the Origami laser over 160 hours. The graphs show a comparison between the long-term drift behavior when the amplitude feedback is active and when it is not.

power changes by 7.58% (peak-to-peak, light blue trace) and is governed by the variation of the voltage applied to the piezo element (violet curve, see also Fig. A.2 on page 208 in the appendix). The residual fluctuation of the optical power amounts to 0.07% rms, where the residue is defined here as the difference of the measured data and a 1-hour moving average (dark blue curve) subtracted from it. Although the drift has been removed mathematically, these numbers are relatively large compared to the short-term performance described in 5.4.4, pages 105 ff. Since that large changes of the optical power are unacceptable for a permanent operation of the laser in the synchronization system, the measurement has been repeated with the aforementioned amplitude stabilization feedback enabled. The relative optical power for the 160-hour period is shown magnified by a factor of 50 in the figure (dark green trace). In this case, the amplitude changes peak-to-peak by 0.11%. It should be noted that the observed sudden jumps in the data trace are most likely caused by mechanical disturbances on the optical table by an experimenter, for instance when the cover of the table is opened, and not by the laser oscillator. The ratio of the peak-to-peak change with and without amplitude stabilization is almost 70, thus a significant improvement is achieved with the feedback loop. The calculated residual

fluctuations amount to 0.0065% rms. However, there is still a slight drift observed suggesting that the loop gains were not been chosen optimally.

In addition to the optical power, the timing change with respect to the master RF oscillator has been measured in both cases. For this, an out-of-loop phase detector with a second photo diode at the auxiliary port of the optical setup had been installed (see Fig. 5.20, page 94). The RF circuit, consisting of a filter, an amplifier and a mixer, was a replica of the one used in the synchronization chassis. In Fig 5.39 the result for both series of measurements are compared. As expected, the timing drifts significantly, when there is no amplitude stabilization feedback. The change amounts to 5.47 ps peak-to-peak over the 160-hour period, with 50 fs residual timing jitter, when the drift is artificially removed from the data. It is shown magnified by a factor of 10 in the figure (violet). In case of the

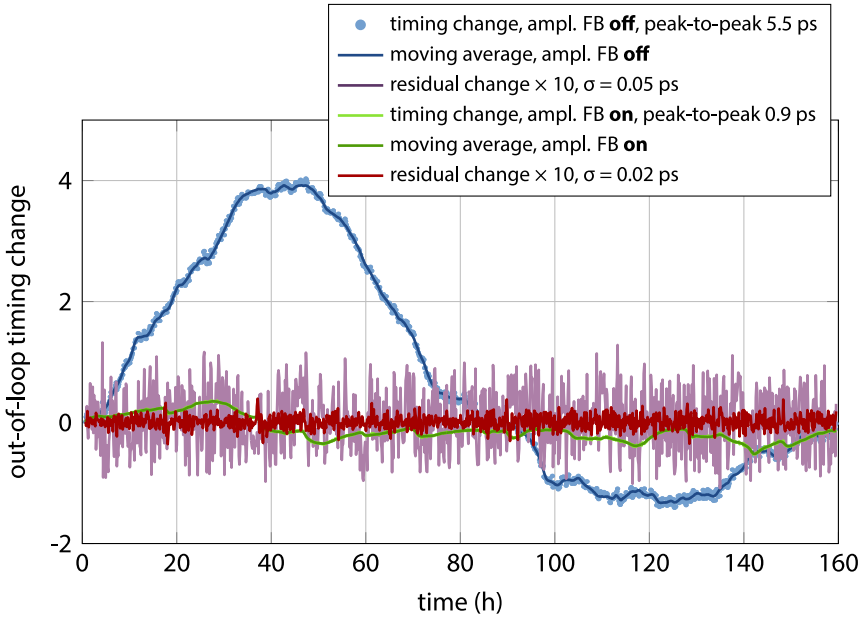

Figure 5.39 | Timing drift measured with an out-of-loop phase detector over 160 hours. The graphs show a comparison between the long-term timing change when the amplitude feedback is active and when it is not.

Origami laser, the active amplitude stabilization feedback is crucial, because then the timing change already reduces to 0.92 ps peak-to-peak, but still a drift is observable. When the drift is removed from the data in this measurement, the residual timing jitter is in the order of 20 fs, showing a very good synchronization of the the laser to the master RF oscillator. However, these drifts are critical not for the current state of the optical synchronization system, because the timing of the accelerator subsystems is not defined by the MLO but only the MO. In the far future, however, the situation could become more critical, because parts of the machine will follow the drifts of the laser, when more and more subsystems requiring optical or derived RF signals are connected to the MLO, as well when external lasers are locked to the optical reference. For an absolute timing stability, drifts of the laser timing has to be reduced to a minimum. Presently, there are several explanations for the observed

residual drift, but none of them could be verified or disproved. The remaining change of the optical power could lead to an AM-to-PM process, there could be a pointing instability or the temperature of the photo detector and the RF cable connecting the phase detector to the MO patch panel changes, all of which being detected as a timing change. The effect of AM-to-PM conversion [CV06, Wino8] is particularly visible in the amplitude-unstabilized case.

Figure 5.40 (left) shows the measured out-of-loop timing change versus the relative optical power with the measurement period encoded in the color of the plot. Despite some minor deviations, with probable reasons as mentioned above, the both quantities are highly correlated. For the utilized pho-

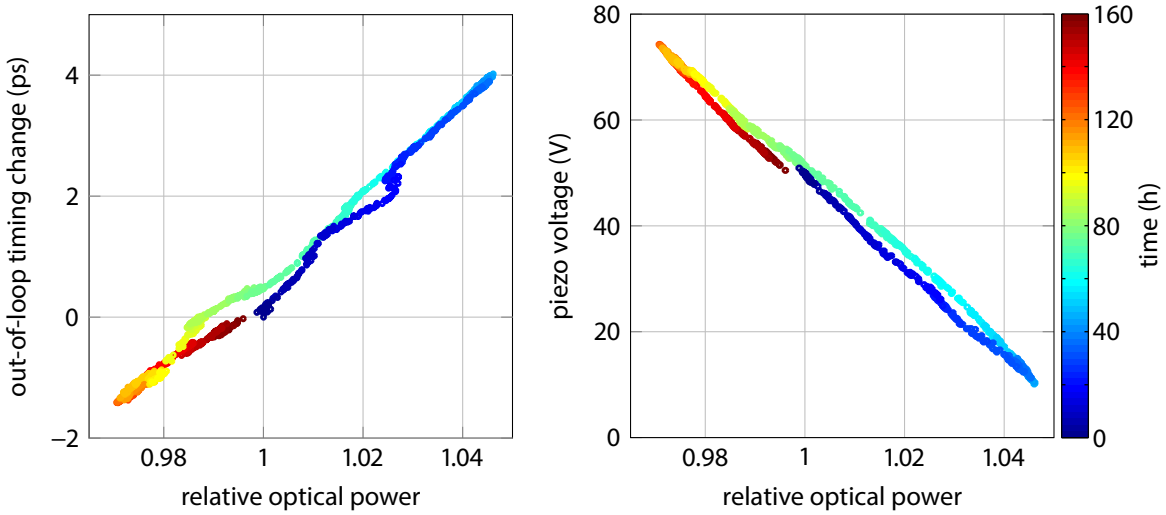

Figure 5.40 | Correlation analysis of the optical power, piezo voltage and timing change. Left: Correlation of the optical power and the out-of-loop timing change. **Right:** correlation of the optical power and the voltage applied to the piezo actuator for synchronization. The colorbar with time information applies to both axes. The underlying time domain data is shown in Figs. 5.39 and 5.38 (pages 122 and 121).

todiode in the out-of-loop phase detector, the AM-to-PM coefficient was found to be 13.42 ps/mW corresponding to 0.45 ps/% for the according optical power level. The main reason for the optical power change is the change of the resonator length by means of the piezo element, as the correlation plot on the right-hand side of the figure confirms.

During the measurement periods, also the temperature of the conditioned air in synchronization hutch and on the optical table have been monitored. Figure 5.41 shows the data from the second survey of six temperature sensors, which are installed inside the EDFA fiber distribution boxes (FDB, see also Fig. 4.4 on page 65) and of one centered above the cover of the optical table in 1 m height (air sensor). Its data show a spike after around 115 h, with a peak-to-peak change of 0.73°C, whereas the rms of the fluctuation amount to 0.04°C. The spike and a smaller change approximately 20 h before are indications of environmental changes in the laboratory, as they lead to significant subsequent changes of the FDB temperatures. For the first box, a peak-to-peak change of 0.44°C and an rms value of 0.11°C have been determined, for the second one 0.70°C and 0.09°C, respectively. A careful investigation reveals additionally a connection to the optical power changes shown in Fig. 5.38. When

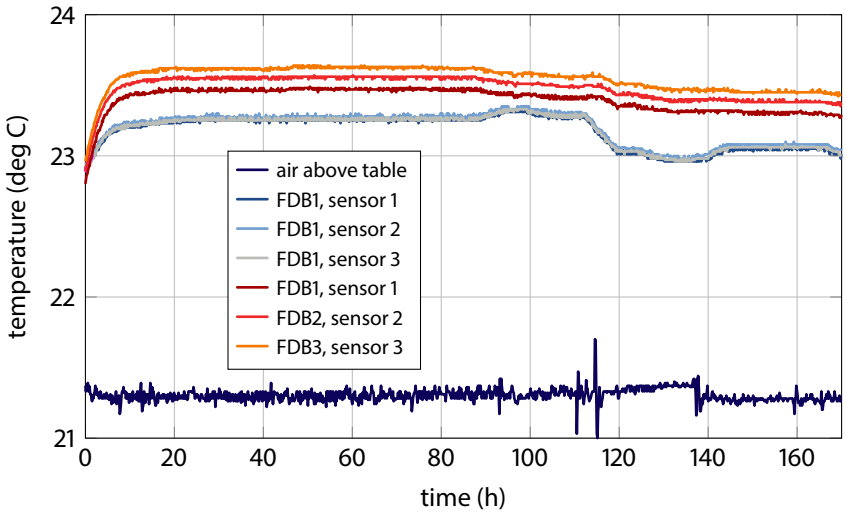

Figure 5.41 | Temperature stability of the optical table over 160 hours. The temperature sensors were placed in the covered compartments where the fiber amplifiers are installed, as well as just below the overall cover of the optical table.

only the quiet period from 20 h to 80 h is analyzed, the peak-to-peak change of the air temperature is 0.200°C with an rms value of 0.029°C. Within these 60 h, the temperature fluctuations of the first FDB are 0.008°C rms with a drift of 0.040°C, when all three sensors are averaged. From the data of the second box, values of 0.009°C rms and 0.037°C are found.

Consequently, during the routine operation of the synchronization system, care has to be taken not to change the temperature and air flow conditions in the laboratory, as a change of 0.7°C inside the FDB would result in a timing change by ~ 35 fs of the unstabilized fiber section of the corresponding devices.

5.6.2 Amplitude and Timing Stability of the Erbium-Doped Fiber Laser

The measurement period for the EDFL stability investigation was 240 h, i. e. 10 days. The laser was also synchronized to RF oscillator and had an out-of-loop phase detector installed, with the photodiode provided with 5 mW average power from the monitor port in the laser housing (see Fig. 5.1, page 72). The optical power has been measured by means of the amplitude monitor inside the RF lock chassis, and is shown in Fig. 5.42 (upper plot). Being not actively stabilized, it changes by 1.81% peak-to-peak with residual fluctuations of 0.02%, when the slow drift is removed from the data. However, there are several steep changes visible. These are caused by the move of the motorized delay stage, when the voltage applied to the piezo stack reached on of its limits (Fig. 5.42, lower plot). This coarse repetition rate tuning was required only 15 times during the measurement period of 240 h. Hence, the repetition rate of the laser stayed within ±700 Hz over a period of 16 hours on average (see section 5.3.3, page 92 ff.). The motor did not always move such, that the piezo voltage stalled around 50 V. These over- and undershoots suggest that the gain settings of the coarse PLL, step size and

piezo voltage limits can be improved to minimize the movement of the translation stage, which naturally also exhibits only a limited repeatability. The dip in the optical power after 90 h was caused by a sudden temperature change (see supplementary Fig. B.2 on page 225 in the appendix).

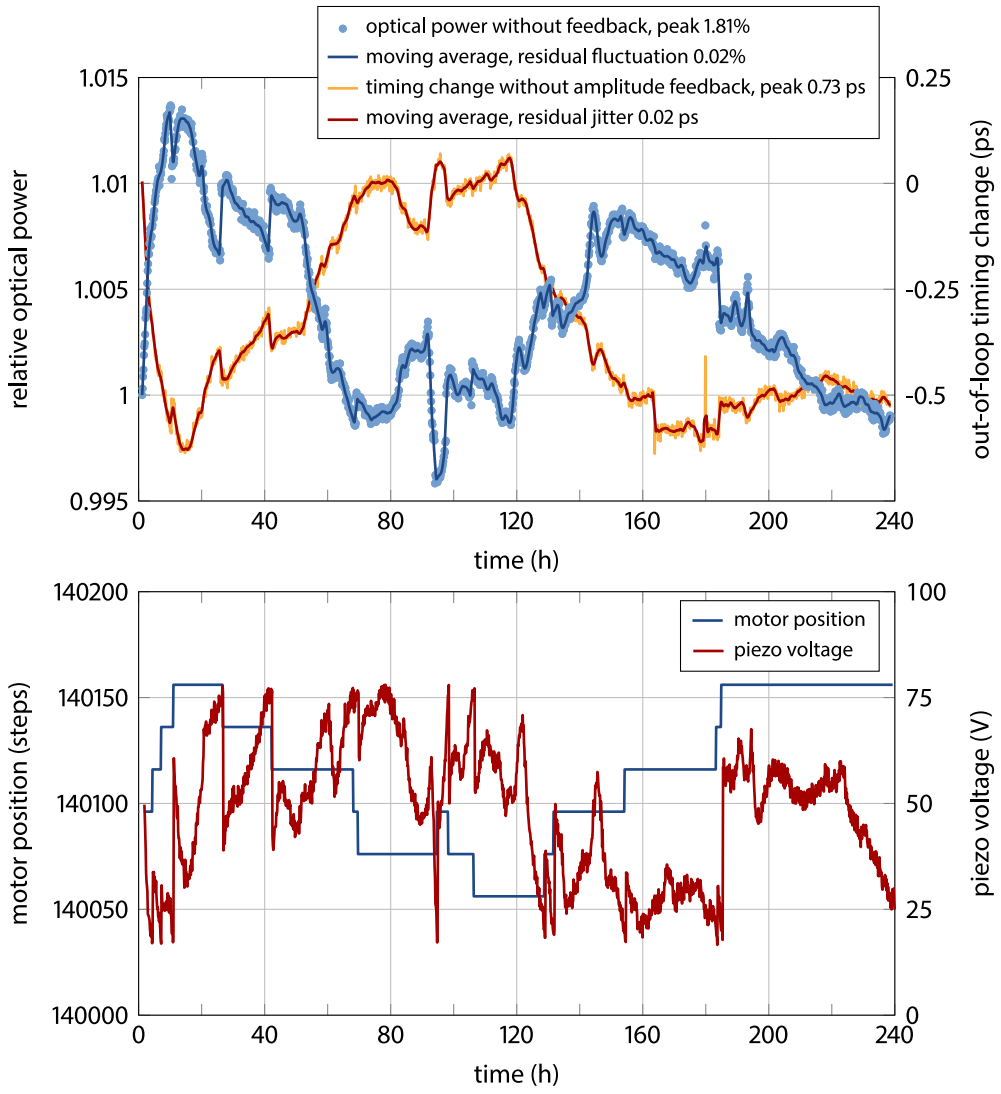

Figure 5.42 | Optical power drift and out-of-loop timing change over a period of 240 hours. Compared to the Origami laser system (shown in shown in Figs. 5.39 and 5.38 on pages 122 and 121), the EDFL exhibits a more stable behavior. The laser was phase-locked to the master RF oscillator which caused the the piezo actuator and the motorized stage to act (**bottom**).

In the figure, the measured out-of-loop timing change with a peak-to-peak change of 0.73 ps is also shown. The according residual jitter amounts to 18 fs rms. In contrast to the Origami laser, however, the correlation between the optical power change and the timing change is less pronounced, as can be seen in Fig. 5.43. The plot, which in principle represents the AM-to-PM coefficient, if this is the only effect, shows two distinct regions for the first ≈ 160 h and the remaining time with a

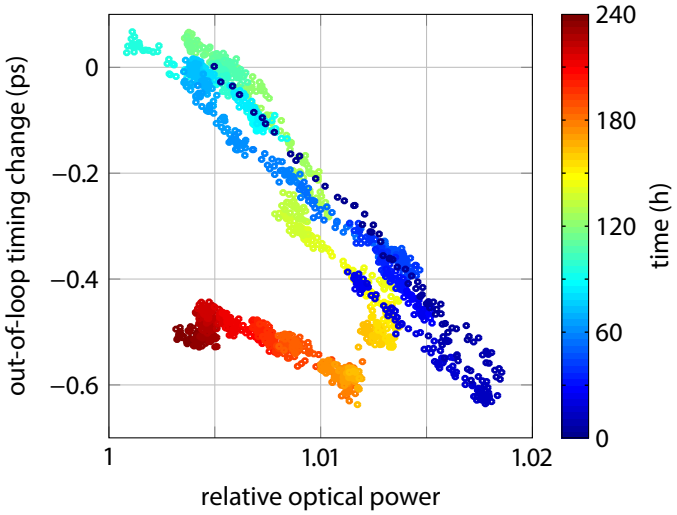

Figure 5.43 | Correlation analysis of the EDFL optical power and timing change. The plot is based on the measurements shown in Fig. 5.42 on page 125.

significantly different relation between the two measurements. This behavior can already be guessed from Fig. 5.42, where the timing change and the optical power change with different signs, but in the last 40 h, the timing changes to more negative values as does the optical power. The reason for this is not understood, and requires further investigation in a repetition of the measurement. Furthermore, it is necessary to commission an amplitude stabilization for this laser, which was not available at that time, and to evaluate the performance of the stabilized EDFL in comparison to the Origami laser. Moreover, the coarse repetition rate tuning based on the translation stage, which causes severe optical power changes when moving, could be replaced by a temperature controlled compartment, in which the fiber part of the laser resonator is installed.

In conclusion, the self-built EDFL performs almost four times better in terms of amplitude stability compared to the Origami laser, when the latter is not actively stabilized with feedback. The timing change, measured for both lasers with the same out-of-loop phase detector, shows a similar and low timing jitter for both lasers. The long-term drift of the EDFL is slightly lower than that of the Origami laser, even when it is actively stabilized. An optimization of the loop gain and the missing investigations with an amplitude-stabilized EDFL can lead to an even more reduced drift with respect to the accelerator.

5.6.3 Drifts in the Free-Space Distribution Unit

Two ports on the opposite sides (C04 and C13) of the free-space distribution (FSD, compare Fig. 5.32 on page 110) unit are equipped with fiber collimators connected to amplitude monitoring photodiodes and provided with 0.5 mW average optical power (see also table 5.4, page 113). The relative change of the optical power is shown in the left plot of Fig. 5.44, which was recorded during the EDFL measurement. At port C04, a significant peak-to-peak change of 3.56% is measured (light blue

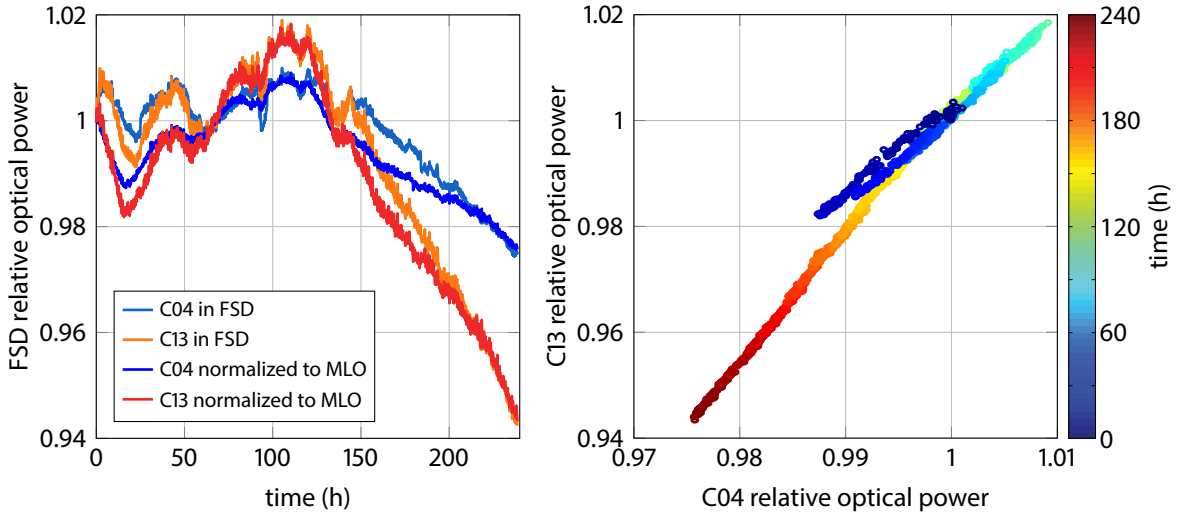

Figure 5.44 | Drift of the optical power in the free-space distribution unit. Left: The data was recorded at two monitoring ports and is shown both as is and corrected for the MLO power drift. **Right:** correlation of the two corrected monitoring ports.

trace), at port C13 7.67%, which is even more than twice as large. In order to remove the effect of the MLO's power variation, each data point has been normalized to the according one of the EDFL – which is, although being recorded with different ADCs, justified, because the data is taken with the same general event number of the FLASH timing system. However, these curves show a similar peak-to-peak change, and only slightly lower residual fluctuations of 0.17% from 0.22% for C04 and 0.28% from 0.31% for C13. Since the optical power changes at the both ports are highly correlated (see right-hand plot of Fig. 5.44) with a width of 1.03% and only minor changes of their relation within the first 100 h, it can be concluded, that there must be a pointing instability between the EDFL and the free-space distribution unit on a slow time-scale. This might be possible, as the FSD is not completely fixed on the optical table, but rather clamped by means of eight strong springs at the four sides of the device. The reason for this construction is the different thermal expansion coefficient of steel, which the surface of the optical table is made of, and the much lower one of Invar, which the base plate of the FSD is made of.

Two conclusions can be drawn now: First, as the correlation between the opposite-sided ports is very high, the decision to use Invar as the base plate for the FSD to minimize thermal effects, is correct. Secondly, the pointing stability of the beam entering the FSD must be improved. Considering the beam path of the first MLO into the FSD, it will be possible to transmit a small fraction of the optical power straight through the first beam cube (PBC) and measure the beam position with two high resolution quadrant detectors. Using this signal, a feedback loop could be established with two piezo-controlled kinematic mirror mounts. This would also work around the situation if the laser oscillators themselves show pointing instabilities, but this has to be investigated before starting such a project, which will require a complete re-assembly of the opto-mechanical setup of the MLOs (see further considerations in section 5.5.4 on pages 118 ff. before). A more simple solution to minimize

drifts caused by mechanical changes between the laser and the FSD is to design a common Invar base plate for the optical components distributing the laser pulse trains to the required number of output ports, as well as the lasers themselves. However, this approach is still prone to pointing instabilities of the laser (see section 5.5.4 above, page 118).

5.6.4 Timing Stability of the Fiber Amplifier in the Distribution Scheme

The introduction of erbium-doped fiber amplifiers to connect the fiber link stabilization units to the free-space distribution unit is a major conceptual change in comparison to the former proof-of-principle experiments. In [Loe09], phase noise measurements had shown that they less than 1 fs timing jitter to the pulse train on short time scales. However, for the routine operation of the synchronization system it is important to know if there is any timing drift and if the low timing jitter behavior is kept on longer time scales. To investigate this, first experiments have been carried out using a setup depicted in Fig. 5.45 which is based on an optical cross-correlator. The reference pulse train is taken

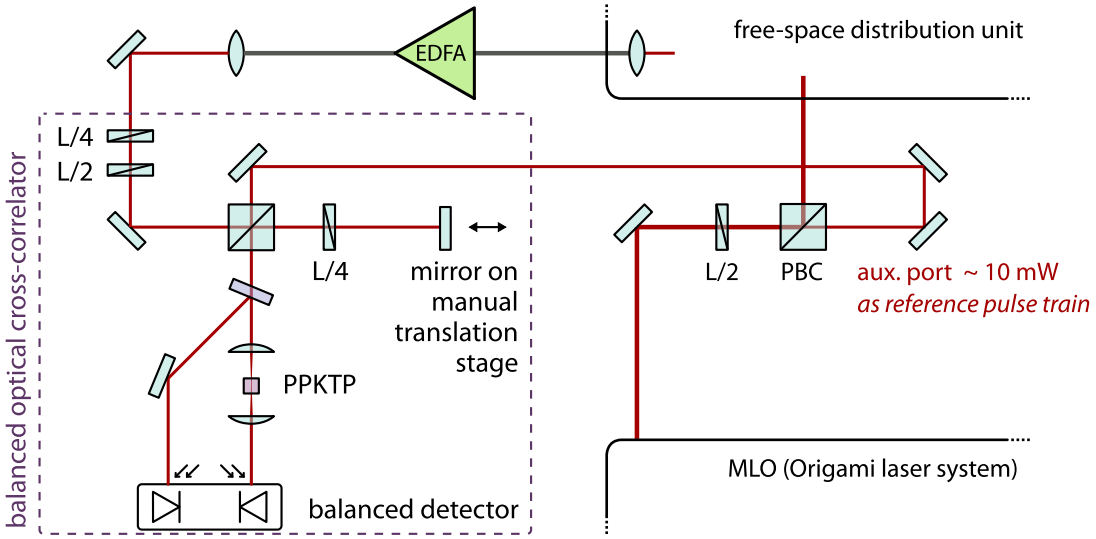

Figure 5.45 | Optical setup for drift measurement of a distribution EDFA. The timing drift of the EDFA is evaluated against reference pulses emitted by the Origami master laser oscillator. The optical cross-correlator for the timing measurement is built equally to the ones in the fiber link stabilization units (see chapter 6, p. 131).

from the auxiliary port of the Origami optical setup (see also Fig. 5.20, page 94), whereas the pulse train to be measured passes the free-space distribution unit and the EDFA to replicate the situation as for the fiber links. The balanced cross-correlation scheme for the timing measurement is adapted from the fiber link stabilization units and explained in more detail in section 6.1 on pages 132. At this point it is sufficient to know that the zero-crossing of the difference signal of two sum-frequency components generated in a PPKTP crystal is highly sensitive to timing changes of the two fundamental pulse trains as shown in Fig. 5.46. To calibrate the optical cross-correlator by means of that signal, the mutual delay of the fundamental pulse trains can be changed by moving a mirror mounted on

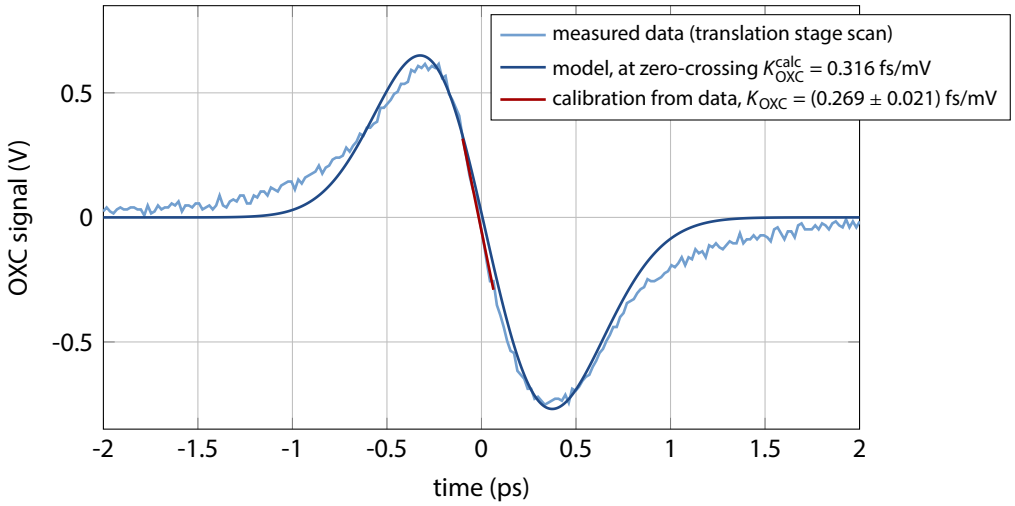

Figure 5.46 | Measured and calculated calibration curves of the OXC for EDFA drift measurement. The data is recorded by scanning the optical delay line for the reference pulse train. The model is based on Gaussian pulses as explained in section 3.5 (page 55 ff.).

manual translation stage, while at the same time sampling the cross-correlator photodetector output with an oscilloscope. The time scale of the oscilloscope can then be translated into the relative time delay of the pulses by adjusting the measured data such, that the trace fits the theoretical curve (see section 3.5.1, page 55 f.; shown in dark blue in the figure). This is justified because the calculated curve, is based on the measured durations of the reference and the amplified pulse. These amount to $\tau_{\mathrm{MLO}} = 210.0\,\mathrm{fs}$ (FWHM, see Fig. 5.22, page 97) and $\tau_{\mathrm{EDFA}} = 266.7\,\mathrm{fs}$ FWHM, respectively. Most notably, however, are the tails of the measured cross-correlator signal wider than in the calculation. This is caused by a slightly distorted pulse shape of the amplified pulse as discussed in section 5.5.3 (pages 115), although the EDFA is only pumped with a current of $I_{\mathrm{p}} = 220\,\mathrm{mA}$ to minimize those distortions. Furthermore, the measured data is steeper around the zero-crossing, which is expressed by the slope fit of $K_{\mathrm{OXC}} = (0.269 \pm 0.021)\,\mathrm{fs/mV}$ in contrast to the slope of the calculation at $t = 0$ of $K_{\mathrm{OXC}}^{\mathrm{calc}} = (\partial V/\partial t)^{-1}|_{t=0} = 0.316\,\mathrm{fs/mV}$. This is caused by the temporal shift of the maximum by 80 fs, which in turn is caused by a discrepancy of the calculated and the observed group velocity dispersion in the nonlinear crystal (see chapter 3, pages 47 ff. and section 6.1, pages 132 ff.).

After the optical cross-correlator, which has a dynamic range of ±100 fs in this configuration, had been set to the zero-crossing, the cover of the optical table (see appendix B, pages 223 ff.) has been closed and a first drift measurement over a period of 16 h was started. In Fig. 5.47 it can be seen that the timing changes by about 30 fs within the first 2 h and continues to drift in a slower fashion. At the end of the measurement period, the timing has changed by 52.3 fs (peak-to-peak). The reason for this behavior is the temperature change on the optical table when the cover is closed. When the slow drift, calculated as 10-minute moving average, is removed from the data the residual jitter amounts to 0.605 fs, which means that the EDFA does not contribute significantly to the fast timing jitter of the pulse train. A second drift measurement over a period of 66 h has been started subsequently to

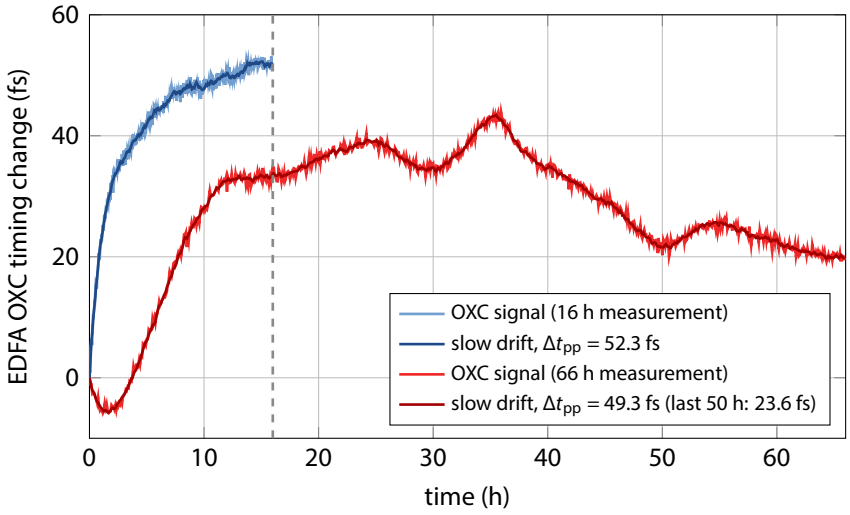

Figure 5.47 | Timing drift of a distribution EDFA. Two measurements were carried out, one for 16 hours and one for 66 hours, each with a sample rate of 0.1 Hz. When the slow drift (moving average) is subtracted from the data, the residual timing fluctuation amounts to 0.61 fs and 0.56 fs, respectively.

investigate if there is any drift on even longer time scales than in the first measurement and if the system stabilizes after roughly 16 hours as suggested by the first measurement. In contrast to that the timing drifted by 10 fs in the negative direction for 1.5 h before the characteristic of the curve resembles that of the first measurement. The timing stabilized after approximately 13 h. In the last 50 h period of the measurement, a drift with a peak-to-peak change of 23.6 fs and a residual jitter of 0.564 fs is observed. When the first 16 h are taken into account, the peak-to-peak change amounts to 46.2 fs with a residual jitter of 0.562 fs, which is very similar to the first measurement.

In conclusion, the distribution EDFAs are not critical components of the timing reference in terms of fast jitter, but their contribution to the drift can not be neglected in the point-to-point timing stability between two devices of the system, as discussed in chapter 4 on pages 61 ff. In a first approach, all EDFAs should be assembled and set up using exactly the same fiber lengths, which ensures a common mode drift for all connected devices. Furthermore, an investigation of the drift behavior at higher pump diode currents, as set for the fiber link units, have to be carried out, and also the drift and timing jitter of two distribution EDFAs against each other should be determined.

6 Long-Distance Stable Timing Distribution – Optical Fiber Links

The timing information provided by the pulse train of the master laser oscillator (MLO) must be distributed to the various remote devices at the accelerator, such as bunch arrival time monitors and external laser laboratories, without deteriorating its accuracy. For this, a scheme based on actively length-stabilized optical fibers had been developed [KIK+04, KCZ+07].

Its principle of operation is depicted in Fig. 6.1. The laser pulses emitted by the MLO enter the optical setup of the stabilization unit only after passing an erbium-doped fiber amplifier (EDFA, see section 5.5, page 108 ff.). In the fiber link stabilization unit, the pulses are split into a reference entering an optical cross-correlator direcly and a fraction send to the fiber link. At its end station, the pulses

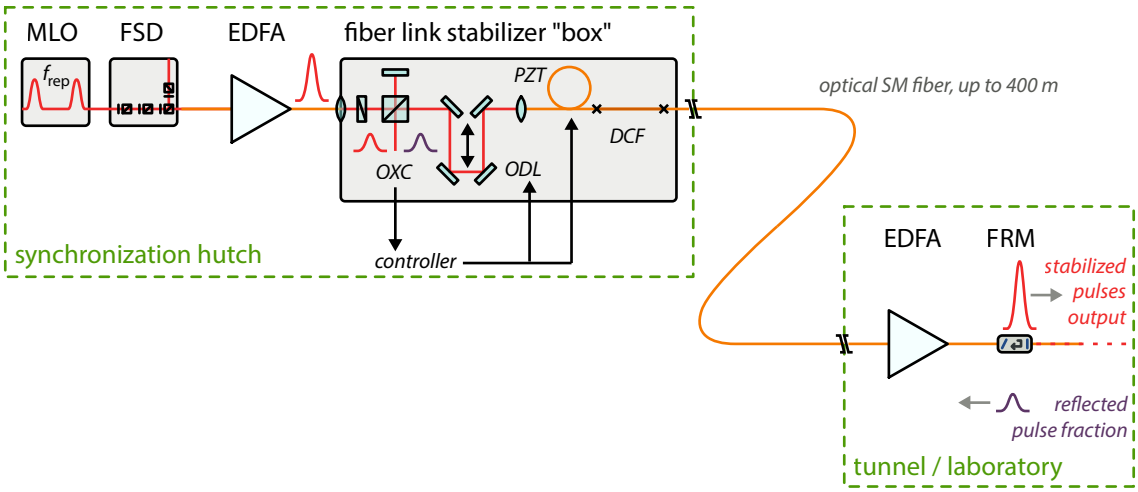

Figure 6.1 | Sketch of the fiber link stabilization and distribution scheme. The pulses from the MLO and the FSD are amplified (EDFA) and then split in the link box to enter an optical cross-correlator (OXC) or to travel down the link. At the link end, a fraction of the pulse energy is reflected in an Faraday rotating mirror (FRM) with its state of polarization rotated, travels back and also enters the cross-correlator. Based on the temporal relation of two pulses in the OXC, the length of the link fiber is adjusted with a piezo-based fiber stretcher (PZT) and an optical delay line (ODL). To compensate for pulse broadening, a special dispersion compensating fiber (DCF) is incorporated into the link.

are amplified with another EDFA and can be used for the synchroniztion of the corresponding device, but a fraction of the optical power is reflected back by a Faraday rotating mirror (FRM), which at

the same time rotates the pulses' state of polarization by 90 deg. The length-stabilization of the fiber link is based on an optical cross-correlation of the reference and the reflected pulse trains. Since the output of the optical cross-correlator (OXC) is highly sensitive to timing changes of the correlated pulse trains (see section 3.5.1, pages 55 ff.), this signal is used for acting on the link length, and by that on the transit time of the pulses, with two actuators: A piezoelectric fiber-stretcher and motorized optical delay line (ODL). These can compensate for fast and small timing changes, and for slow and large ones, respectively. A similar scheme is applied in the synchronization of mode-locked lasers to adjust the resonator length (see 5.3.3, pages 92 f.).

At FLASH, successful experiments with prototype setups with link lengths of up to 400 m have been carried out in [Loe09]. In measurements with a second, out-of-loop optical cross-correlator beside the one used for the stabilization of the link a residual timing jitter of 4.4 fs had been demonstrated. Based on those results, an engineered opto-mechanical design was proposed.

In this chapter, the most important results and experiences from the commissioning of these new, integrated link stabilization units are discussed. The comprehensive characterization, detailed investigations on the performance of the fiber link distribution scheme and required re-designs can be found in another PhD thesis [Boc13].

6.1 Fiber Link Stabilization Scheme

The free-space optical setup of the stabilization unit to measure the relative timing of returning pulses from the link end and the reference pulses is shown schematically in Fig. 6.2. The latter enter the device as amplified pulses from a port of the free-space distribution unit (FSD). A telescope is required for an efficient coupling of light from the input fiber collimator (denoted by C.IN in the figure) into to the link fiber collimator (C.OUT). Using a polarizing beam cube (PBC), the pulses are split into two arms, where one fraction is directly send to the actual cross-correlator. The ratio of the splitting can be set with a combination of a quarter- and a half-wave retarder in front of the PBC. The transmitted fraction to be send to the link end[1] is reflected by a mirror, which is mounted on a motorized delay stage for the coarse compensation of timing changes. The introduction of a quarter-wave retarder between the PBC and the mirror ensures a rotation of the linear state of polarization (SOP) by 90 deg, such that this pulse train is reflected inside the PBC when it impinges it the second time. This pulse train is coupled into the fiber components of the link, composed of the piezoelectric fiber stretcher, a dispersion compensating fiber (see section 6.1.2 on pages 135 f. below) and the actual link fiber laid out in the accelerator tunnel to the corresponding end stations (see table B.1, page 223). Since the Faraday rotating mirror at the link end not only reflects a fraction of the light, but also rotates its polarization state by 90 deg, the returning pulse train is transmitted through the PBC and now enter also the cross-correlator arm.

The actual cross-correlation of the two pulse trains is realized in a periodically poled potassium titanyl phosphate (PPKTP) crystal with a poling period of 46.2 µm and being phase-matched for collinear type-II$^{(+)}$ interaction (see section 3.2, pages 48 ff. and appendix C.3, page 231 f.). This

[1] The pulse train traveling from the PBC to the link end is also referred to as "forward" pulse.

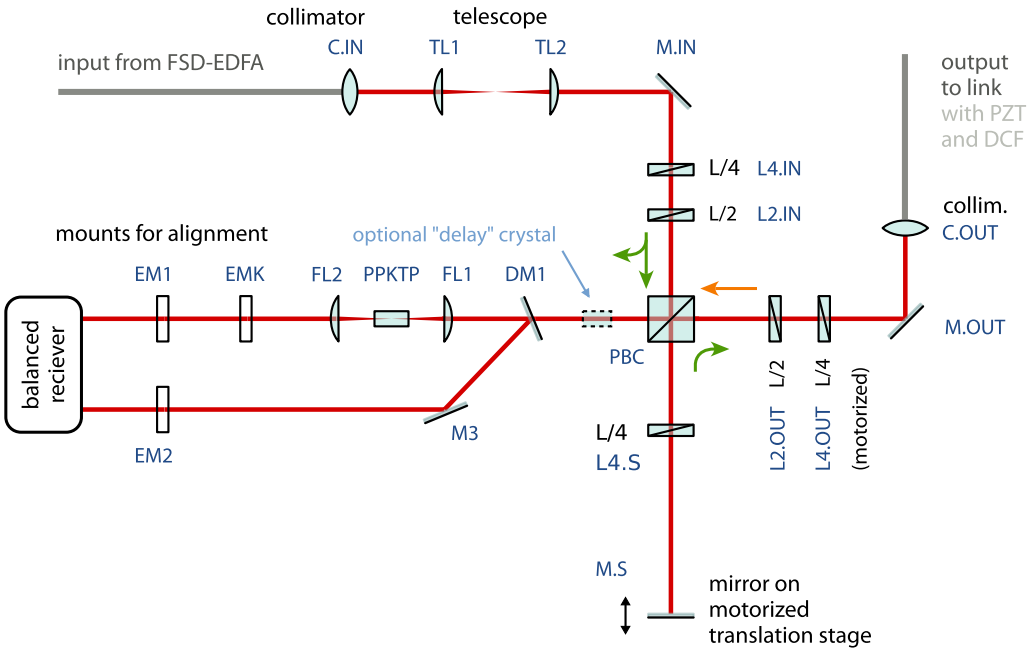

Figure 6.2 | Free-space optical setup in the fiber link stabilization scheme. The green arrows indicate the propagation of the reference pulses, the orange ones that of the returning pulses from the fiber link end.

type of interaction is background-free, as both perpendicular polarization states are required for the second-harmonic generation (SHG) process, in contrast to type-I phase-matching. The fundamental laser radiation is focused into the crystal using a lens (FL1) with a short focal length. The generated second-harmonic component, when the pulses overlap temporally, impinges one detector of a so-called balanced receiver[2]. The required delay T_{opt} (Eq. 3.25, page 56), before the SHG process takes place the second time for the delay/subtraction detection scheme, is created by the nonlinear crystal itself, since KTP exhibits a large birefringence. Furthermore, the backside of the crystal is coated high-reflective (HR) for the fundamental wavelength, making another dichroic mirror unnecessary. The SHG component generated by the back-reflected pulse inside the crystal is guided with a dichroic mirror (DM, installed between the PBC and the focusing lens FL1), and another mirror onto the second detector of the balanced receiver. Its output is then the bipolar signal, whose region around the zero-crossing is highly sensitive to timing changes of the fundamental pulse trains.

This method allows for the detection of timing changes happening on a slower time scale than the round trip time of the pulses in the fiber link, which amounts to ~ 3.8 µs for a 400 m long link. Since the main sources for timing changes in the link result from thermal expansion/contraction of the fiber, temperature or humidity induced changes of its refractive index or mechanical stress by vibrations, are comparatively slow, those can be compensated with a stabilization loop based on the cross-correlator signal.

[2]New Focus, Model 2307, also integrated into the opto-mechanical design.

The integration of the major parts of the link stabilization scheme into a relatively compact enclosure turned out to be very practicable. It allows for the assembly and initial optical alignment of the device in another laboratory. In the synchronization laboratory, the unit can be placed at its final position on the optical table (see Fig. 4.4, page 65) and the link fiber can be connected to the corresponding receptacle on the patch bay. After mounting the input collimator in the FSD and coupling light into the EDFA, in principle only one, but the most critical fiber splice for the optimum dispersion compensation and finding the temporal overlap has to be made, as is discussed in the following two sections.

An illustration of the mechanical setup and the commissioning is shown in the appendix (Fig. G.6, page 257, Photo G.7, page 258 and Photo G.8, page 259).

6.1.1 Packaging of Optics and Electronics

In addition to the free-space optic part of the cross-correlator, the fiber link units were designed to hold the required fiber components consisting of the dispersion compensating fiber, the piezoelectric stretcher and the major parts of the EDFA. Furthermore, the unit includes optical power monitors for both the reference pulse train send to the link and the returning pulse train, as well as an RF-based phase detector.

The optical power monitors, in analogy to the ones used for the monitoring of the MLOs, consist of a photodiode, a low-pass filter and a low-noise amplifier. Their optical input signals are provided by the taps of a fiber coupler, which follows the collimator of the link fiber (see Fig. 6.3). The photodiode signal of the returning pulse train is splitted for the optical power monitor and the RF phase detector. In the latter, the harmonic at 2.6 GHz is filtered from the FOURIER comb and compared with a corresponding reference signal, which is generated from a photodiode directly connected to the free-space distribution unit. By this, the output signal of the phase detector is also sensitive to timing changes of the returning pulse train and is monitored in the present status. The output of the balanced receiver is digitized with an ADC and fed to a digital PID controller implemented on a DSP which is of the same type as used for the MLOs (see section 5.3.2, pages 90 ff.). The commercial fiber stretcher[3] consists of a hollow cylinder made from lead zirconia titanate (PZT), on which 40 m optical fiber are wound. The controller acts on the fiber stretcher via a low-noise amplifier, which provides the desired voltage of ±200 V for the linear reaction range of the piezoelectric material. With an optical path change of about 20 fs/V, this fast actuator can compensate approximately 8 ps timing change in the link. When this limit is reached, the controller moves the optical delay line to adjust the piezo voltage again around zero for a maximum dynamic range, until the delay stage has to be moved another time.

The fiber link stabilization units and their operation is completely integrated into the accelerator's control system. The corresponding DOOCS server allows, for instance, to automatically search for the signal by scanning the motor and close the regulation loop in case of a failure. It has been extended from the original implementation in [Loe09] with several exception handlers, such as a

[3] OptiPhase PZ2, with two layers of standard single-mode fiber.

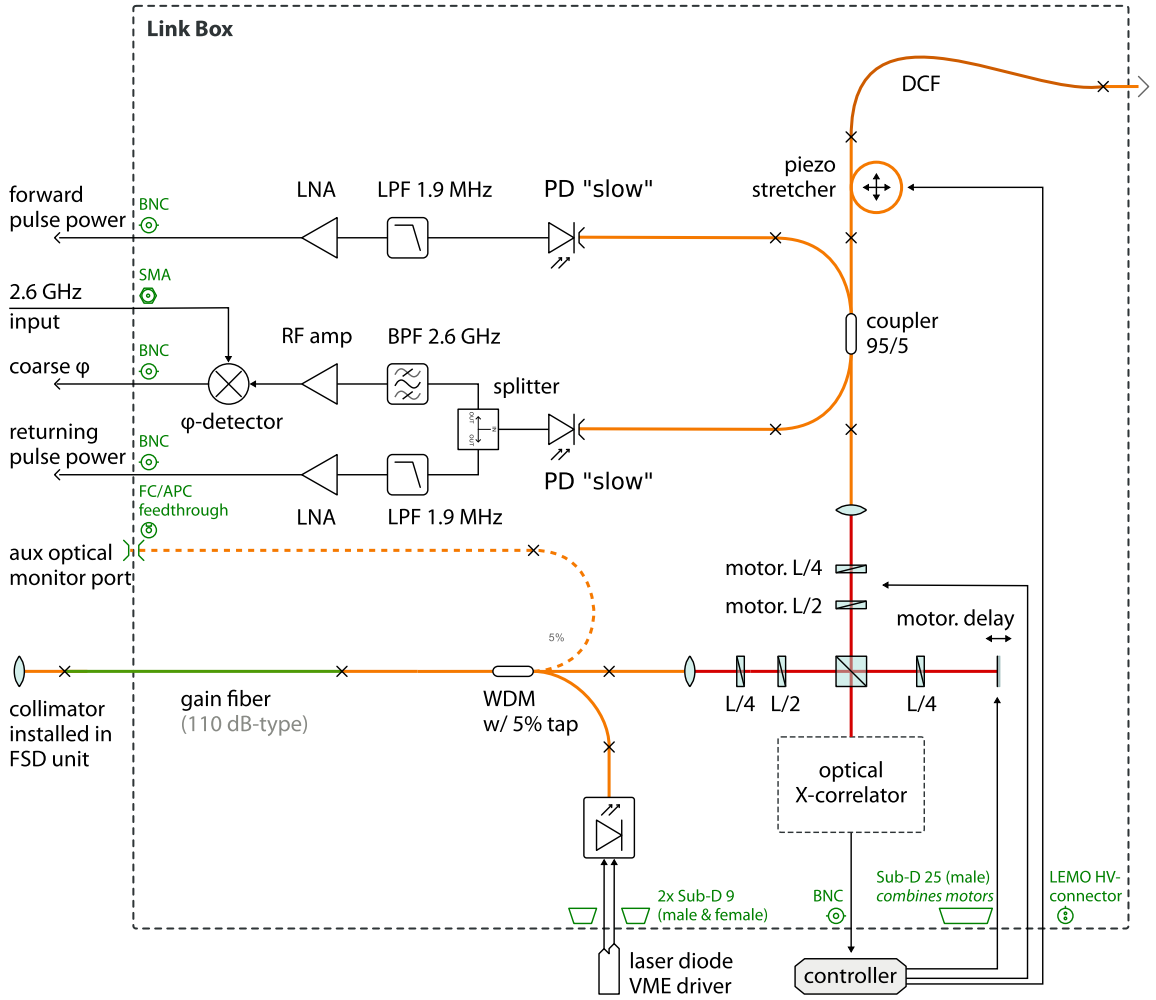

Figure 6.3 | Schematic layout of the fiber link stabilization enclosure. The fiber link stabilization unit includes the fiber amplifier to connect to the FSD, the free-space optical cross-correlator and optical delay line, the fiber stretcher and the dispersion compensating fiber, as well as monitoring electronics.

check whether the master laser oscillator is synchronized to the accelerator. This information can, in turn, be used by the DOOCS servers of the bunch arrival time monitors (BAM), for example to notify a machine operator, that the BAM data is invalid as long as the regulation loop of the link is not closed.

6.1.2 Dispersion Compensation

The optical cross-correlators in the fiber link stabilization scheme and the devices at the remote locations provided with the timing information require short pulse durations comparable to the one generated in the MLO. This is particularly important for the synchronization of external lasers by another optical cross-correlator.

Therefore, a dispersion compensating fiber (DCF) is incorporated to the link to counteract the dis-

persive pulse broadening (see section 2.3.3, pages 27 f.) the pulses experience while traveling through the standard single-mode fiber to the remote location. The required length can be calculated from Eq. 2.36 (page 29) and has to be considered for each fiber link individually, because their total fiber lengths are different. In particular the lengths of the fibers installed along the accelerator tunnel to the various end stations are not equal (see table B.1 on page 223 in the appendix), but also the used patch cords and the pigtails of the fiber components vary from link to link. In contrast to the prototype fiber links, a new type of DCF was used (see appendix D.2, page 242 f.), which has a larger (negative) dispersion parameter of $D \approx -170\,\mathrm{ps}/(\mathrm{nm}\cdot\mathrm{km})$ in comparison to $D^{(\mathrm{old})} \approx -120\,\mathrm{ps}/(\mathrm{nm}\cdot\mathrm{km})$ of the original one. This results in a ratio of $L_{\mathrm{SMF}}/L_{\mathrm{DCF}} = D_{\mathrm{DCF}}/D_{\mathrm{SMF}} \approx 9.5$ for the required fiber lengths. DCF typically has a very small core diameter, resulting in larger undesirable nonlinearities. Hence, the use of the new type of fiber is beneficial in the fiber links, which are operated at relatively high optical power, because the length of the DCF can be kept shorter.

For the commissioning of a fiber link in the synchronization laboratory, the required DCF length is cut with some safety margin and spliced into the fiber installation. The pulse duration of the returning pulses from the link has to be measured, which can be accomplished by removing the balanced receiver and guiding the light, which now exits the optical setup of the link, to an autocorrelator. If the pulse duration is too large, the DCF has to be cut back, each time by breaking and remaking one splice. Figure 6.4 shows the autocorrelation of the reference pulses (blue trace) and the returning ones

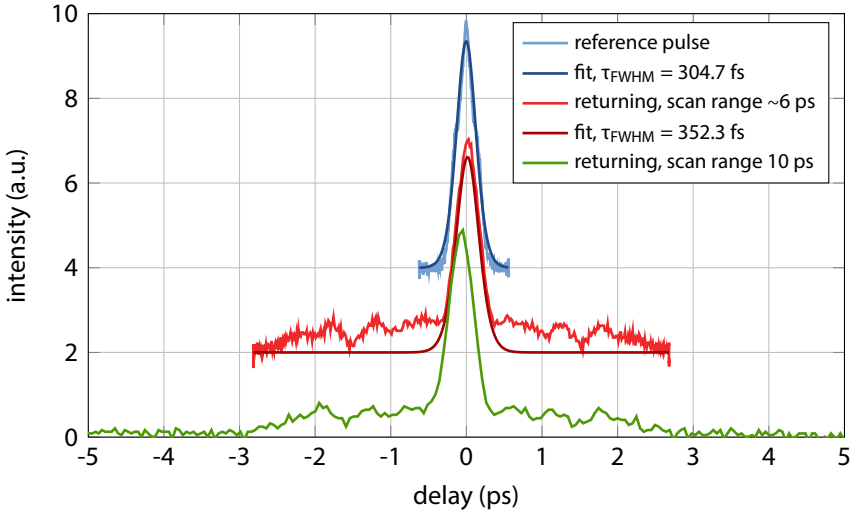

Figure 6.4 | Comparison of the duration of a reference and a returning pulse from the link. The data was recorded after the DCF had been cut optimally for the shortest possible duration of the returning pulse. The EDFA at the fiber link end is pumped with 1.3 W. The offset in the data had been added mathematically for better visualization.

(red trace), where the returning pulse is sufficiently short with 352 fs FWHM, compared to 305 fs of the reference. In the pulse shape, the observed shoulders are caused by nonlinear effects and/or dispersion of higher order. The effect of these distortions on the cross-correlator performance have not been studied until now, as it is difficult to reproduce the distortions observed in the synchronization

laboratory in another laser laboratory, because of the (present) uniqueness of each link.

To achieve a temporal overlap of the pulses in the PPKTP crystal, the fibers have to be cut again. The autocorrelator is replaced by a fiber collimator and the signal of a high-bandwidth photodiode is sampled with a fast oscilloscope. When both pulse trains are coupled into the fiber, the oscilloscope can be used to determine their temporal offset. When then both the SMF link fiber and the DCF are cut in the ratio $D_{\mathrm{DCF}}/D_{\mathrm{SMF}}$, the temporal spacing will change while the pulse duration of the returning pulse will remain short. Using this technique, the overlap can be found within 50 ps to 100 ps limited by the resolution of the oscilloscope and the bandwidth of the photodiode. This is within the range of the optical delay line, which then has to be moved to ultimately find temporal overlap and by this the cross-correlator signal.

It should be noted that the DCF does not compensate the third-order dispersion β_3, which is supposed to have a magnitude of approximately 10% of the second order dispersion. An additional compensation for this remaining dispersion can in particular become important for the fiber links installed at the European XFEL, as their lengths will range up to 3.5 km.

6.1.3 Commissioning Experiences

During the continuous extension and improvement of the synchronization system, six engineered fiber link units have been commissioned up to now. Each time, another link was required, the experiences from its predecessors were considered during the assembly and commissioning. Prominent problems identified with the new opto-mechanics of the fiber links and their solutions are briefly discussed in the following.

Optical Delay Line

The motorized translation stage for the coarse timing compensation was also custom-designed[4] along with the complete integrated design of the fiber link stabilization unit. This was caused by the fact, that commercial translation stages did not offer the desired travel range, or had too large dimensions to fit into the mechanical design. However, the some of the manufacturing tolerances were not specified tight enough initially. This led to a degradation of the coupling efficiency into the fiber collimator of the link due to the pitch and yaw of the mirror mounted on the stage. A measurement of the optical power at the forward monitor port at the link end (for the exact location of the port see the setup in Fig. 6.11 below on page 145) over a range of ±11 ps with respect to the position of the stage, where the cross-correlator signal is observed, is shown in Fig. 6.5. The relative optical power is governed by a strong oscillation with a peak-to-peak variation of approximately 67%. Its period corresponds to a full rotation of the spindle in the stage. The errorbars in the plot represent the standard deviation of 10 measurements at each scan step. When this is averaged over the scan range, an optical power fluctuation of 3.8% is determined. The main contributions to this number are the much larger errors at the local minima of the oscillation. However, this measurement represents

[4] …but not by the author of this thesis, but rather by Bernd Beyer under scientific advice first from Florian Löhl and then from Marie Kristin Bock who also investigated the performance of the stage [Boc13]

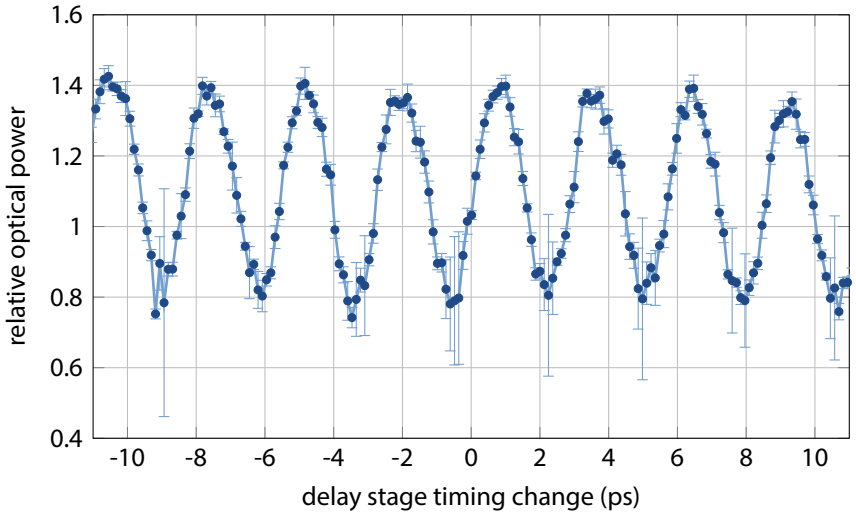

Figure 6.5 | Relative optical power at link end as function of delay stage position. The data was recorded at a monitor port in the forward direction. The translation stage used was the first version of the engineered design.

the worst case ever observed when the fiber links were commissioned. The mechanical design of the translation stage meanwhile underwent several iteration, which resulted in a strong suppression of the oscillations in first tests.

Time Delay Offset at the Link End

A much more critical problem with the delay line and the overall optical design of the fiber link stabilization was discovered during electron bunch arrival time studies [Sch10a], as the absolute arrival time t_{end} of the laser pulses at the link end is influenced by the delay the stage has to move to compensate for a coarse timing change. An illustration of this is shown in Fig. 6.6. In a fiber link with a certain total length L, the transit time of the pulses in forward direction and of the returning ones is given by

$$t_{\mathrm{fw}} = t_{\mathrm{s}} + t_{\mathrm{p}} + t_L \equiv t_{\mathrm{end}} \quad \text{(forward)} \qquad \text{and} \qquad t_{\mathrm{ret}} = t_{\mathrm{p}} + t_L \quad \text{(returning)} \tag{6.1}$$

where t_{S}, t_{P} and t_L are the times the pulses travel in the delay stage, the fiber-stretcher and the actual link, respectively. In this case, the optical cross-correlator will detect a relative time delay τ_{OXC} (situation 'a' in the figure). Consider now a length change of the link by Δl (single-pass), resulting in a timing change of Δt (single-pass). The optical cross-correlator then detects a total timing change of $\tau'_{\mathrm{OXC}} - \tau_{\mathrm{OXC}} = 2\Delta t$ (situation 'b' in the figure). When this timing change is corrected with the piezo-based fiber stretcher (PZT) by application of a correction $t_{\mathrm{P}} \rightarrow t_{\mathrm{P}} + \delta t_{\mathrm{P}}$, the arrival time of the pulses of the link end is again t_{end}, as the required correction $\delta t_{\mathrm{P}} = -\Delta t$ is applied to both the forward traveling pulses and the returning (situation 'c' in the figure). The situation is different, when the correction $t_{\mathrm{S}} \rightarrow t_{\mathrm{S}} + \delta t_{\mathrm{S}}$ must be applied with the optical delay stage, when the fiber-stretcher reaches

one of its limits for the correction. Since again a total correction of $2\Delta t$ is required, the transit time through the stage must be reduced by $\delta t_S = -2\Delta t$, because the pulses pass the delay stage only in forward direction. This results in a change of the absolute arrival time at the link end

$$t'_{\text{end}} = t_S + \Delta t + t_P + t_L \neq t_{\text{end}} \,. \tag{6.2}$$

Hence, the pulse arrival time at the link end changes absolutely by Δt. As a result, in the bunch arrival time monitors (BAMs), for instance, a change of the electron bunch arrival time is detected. This wrong arrival time determination is in particular critical, if the BAM is part of an arrival time

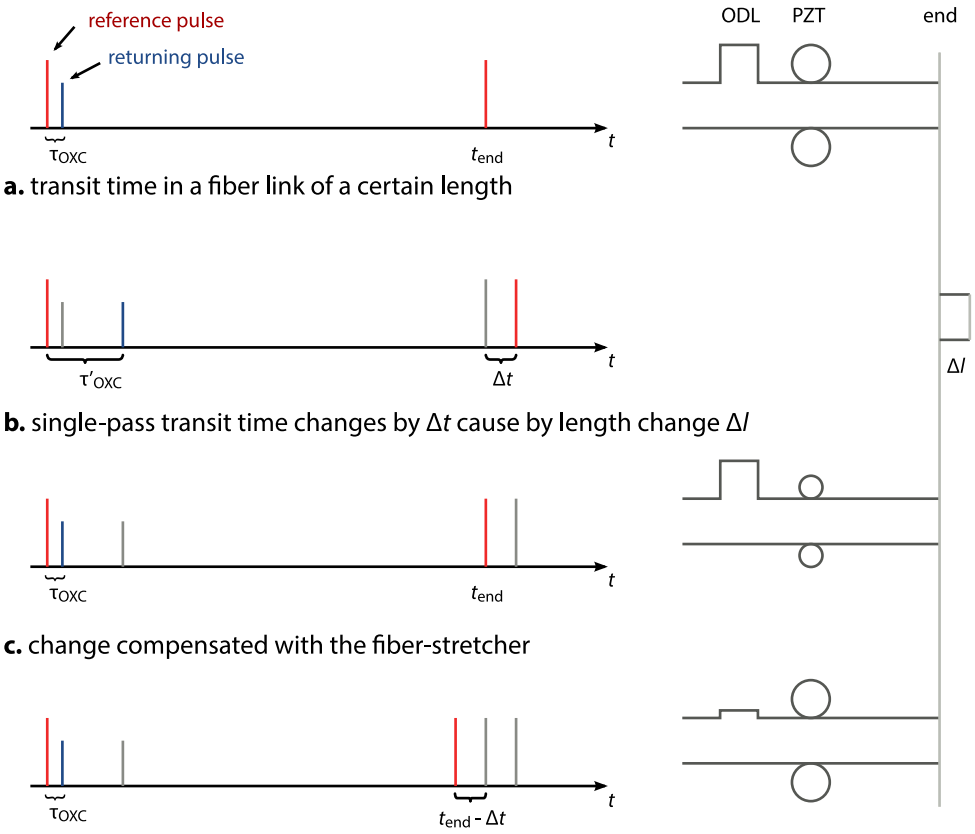

Figure 6.6 | Sketch of transit-time stabilization in the fiber link. When a length change of the fiber link is compensated with the fiber stretcher (PZT), the arrival time at the fiber link end station remains stable, as supposed. If the optical delay stage (ODL, denoted MS in Fig. 6.2 on page 133) in the mistakenly designed devices is used, the arrival time changes.

feedback (see section 4.5, page 69) because then the falsely corrected fiber link time will we applied to the electron beam.

All devices connected to the fiber links are equipped with motorized optical delay lines. These are presently used to compensate for this laser pulse arrival time change induced by the fiber link

by moving in the opposite direction. Although this is a major design flaw of the fiber links, the workaround ensures a reliable operation of the corresponding end stations.

In a presently ongoing major re-design of the fiber link stabilization units, the delay stage is correctly positioned within the optical beam path for the forward and the returning pulse trains. Both problems with the optical delay line are addressed and are discussed in detail in [Boc13].

Impacts of the Fiber Link on the Distribution EDFA

The fiber link stabilization scheme depends on the state of polarization of the light. The laser pulse train in forward direction has a certain linear polarization, which is rotated by 90 deg by the Faraday rotating mirror (FRM) at the link end and allows for the splitting and combing the pulse trains with a polarizing beam cube (PBC). Due to the finite extinction ratios of the FRM and the PBC and the effect of polarization mode dispersion (PMD, see section 2.3.5, page 29) in the fiber, it is possible that a fraction of the returning pulse train is not transmitted through the PBC into the cross-correlator, but propagates back into the EDFA, which connects the link unit to the FSD.

It has been observed that this influences the gain of the erbium-doped fiber in the the amplifier, because it experiences now co- and counter-propagating pulse. However, it is not possible to measure the optical power of the fraction with the "wrong" polarization directly, and the effects of two counter-propagating pulse trains in the EDFA, for example by cross-phase modulation (XPM), have not been studied yet. However, the planning of an experimental setup for further investigations and a theoretical treatment has started recently. In the actual fiber link setup, the effect of the counter-propagating pulses can strongly be suppressed by the introduction of a fiber-coupled Faraday isolator between the gain fiber and the output collimator of the EDFA. On the other hand, this enlarges undesirably the length of the uncompensated fiber section. Consequently, in the next iteration of the fiber link design, a free-space Faraday isolator is foreseen.

6.2 Performance

The most important figure of merit for the performance of the fiber link stabilization unit is the timing jitter of the transmitted pulse train on short and long timescales. While the investigations on the short-term jitter is discussed in the next section, Fig. 6.7 shows a comparison of the measured rms timing jitter for two fiber links over a period of 240 h. The data recorded with a rate of 0.1 Hz using control system-integrated ADCs,[5] after a calibration of the cross-correlator had been performed. The fiber links in question are the presently longest link with a total length of 340 m (single-pass) to the EO laboratory, where the development setup for the synchronization of a Ti:sapphire lasers by means of an optical cross-correlator is located, and the shortest link with a length of 98 m to the bunch arrival time monitor upstream of the first magnetic chicane in the accelerator tunnel. In case of the shorter link (blue curve), the average timing jitter amounts to 0.9 fs with no significant changes over

[5] Every 10 seconds, a trace of 2048 data points is recorded, where the sample points repeat with 1 MHz. The mean of these data points is plotted as one data point in the figure.

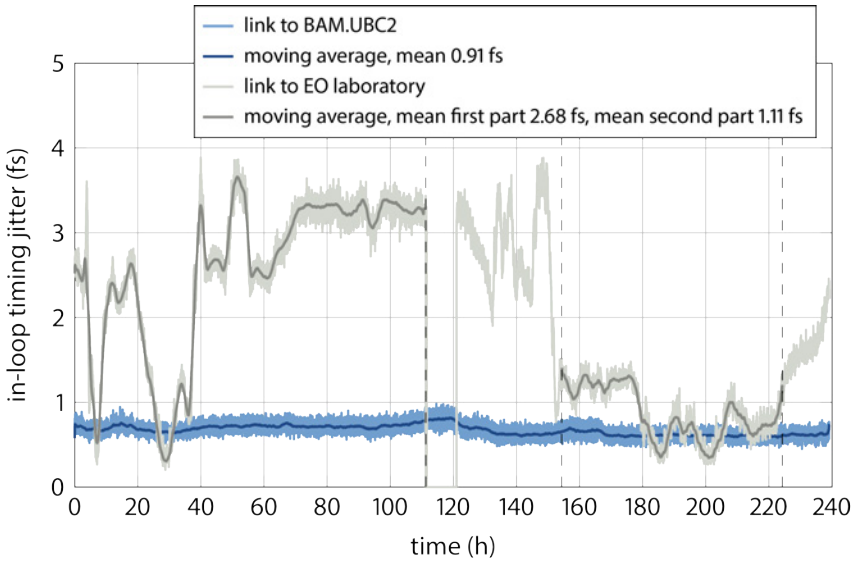

Figure 6.7 | Long-term timing jitter and drift measurement on two fiber links. In the measurement, the to-date longest, over 300-meter-long, fiber link and the shortest one with about 100 m length have been investigated.

the measurement period. The longest link exhibits variations in the timing jitter of 3.5 fs, and the happened more often in the first 50 h of the measurement. The average timing jitter in the first 115 h amounts to 2.7 fs. Over a period of 65 h, when only little fluctuations were observed, the timing jitter is reduced to 1.1 fs on average. The reason for the larger fluctuations are most likely caused by its more than three times larger length, and by the fact that this link is subject to additional environmental influences, because the fiber the accelerator tunnel at the location of the EO experiment and ends in an external laboratory.

It must be emphasized that the timing jitter shown in the figure was measured in-loop as the fluctuations of the error signal of the controller, hence the numbers must be taken with a grain of salt. A more relevant number would be the timing change and the residual jitter measured out-of-loop. In such a measurement the timing between the pulse train at the end of a fiber link and a pulse train directly emitted by the MLO is determined with another optical cross-correlator. This is presently not possible due to these restrictions:

- Naturally, the end of the fiber links are located at remote locations and the light can not be transported back to the synchronization laboratory.

- Although a link, where a fiber laid out in the accelerator tunnel, but has an end in the synchronization laboratory could in principle be build, a complete engineered fiber link unit is required. However, currently all existing units are commissioned for their designated links.

It is, obviously, planned to investigate the performance of the links with a dedicated out-of-loop setup, when the manufacturing of new link mechanics is completed.

RF-Based Phase Detector

As another aspect of the term "performance" also the robustness and reliability of a component of the synchronization system can be considered. With the RF-based phase detector and the optical cross-correlator in the the fiber link stabilization unit, there are two detectors for timing changes of the reference and the returning pulse train. They have, obviously, a significantly different sensitivity for the detection of timing changes, but at the same time a significantly different dynamic range. Figure 6.8 shows the output signals of both detectors recorded for a relative time delay of 25 ps of the pulse trains, which was applied using the optical delay line in the fiber link optical setup. Obviously,

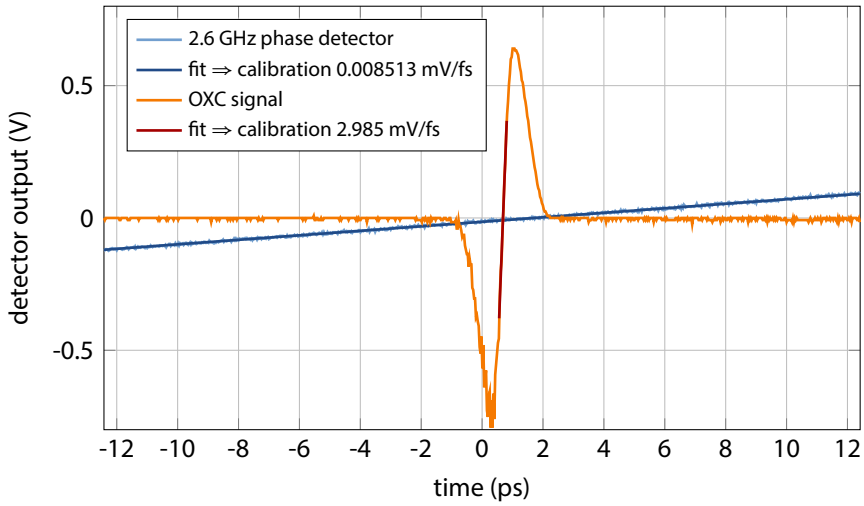

Figure 6.8 | Comparison of the OXC and the RF phase detector sensitivity. The optical method is almost a factor of 350 more sensitive, but at the cost of the dynamic range.

the optical cross-correlator is more sensitive around its zero-crossing with a calibration constant, which is the slope in that region, of $K_{\mathrm{OXC}} = 2.985\,\mathrm{mV/fs}$, which is a factor of 350 better than the sensitivity of the phase detector with $K_{\phi} = 0.009\,\mathrm{mV/fs}$. High sensitivity is always at the cost of dynamic range. Due to this, the cross-correlator signal has to be found reproducibly, when the loop had to be closed again, for instance after a failure. For this, the RF phase detector can be used. As the period of a 2.6 GHz RF signal is 384.6 ps and the delay stage can change the relative timing of the pulses by 313 ps, the position of the stage for temporal overlap in the cross-correlator can always be found by measuring the output of the phase detector. In a planned extension of the DOOCS server for the fiber link stabilization unit, this will be included and automated.

The RF phase detector and the optical cross-correlator have been used to measure the timing drift of a fiber link when it is not actively stabilized, shown in Fig. 6.9 for a period of 5 min. The RF phase detector signal (light gray) exhibits much more noise than the cross-correlator (light red). From a moving average (dark gray), a peak-to-peak change of 501 fs has been determined. At the same time, the optical cross-correlator signal detected a timing change of 388 fs, which is 77% of the value from the phase detector. Although there is an influence of imperfect calibrations, the phase detector sig-

nal suffers from a slow oscillation superimposed on the signal. For comparison, the detector signals

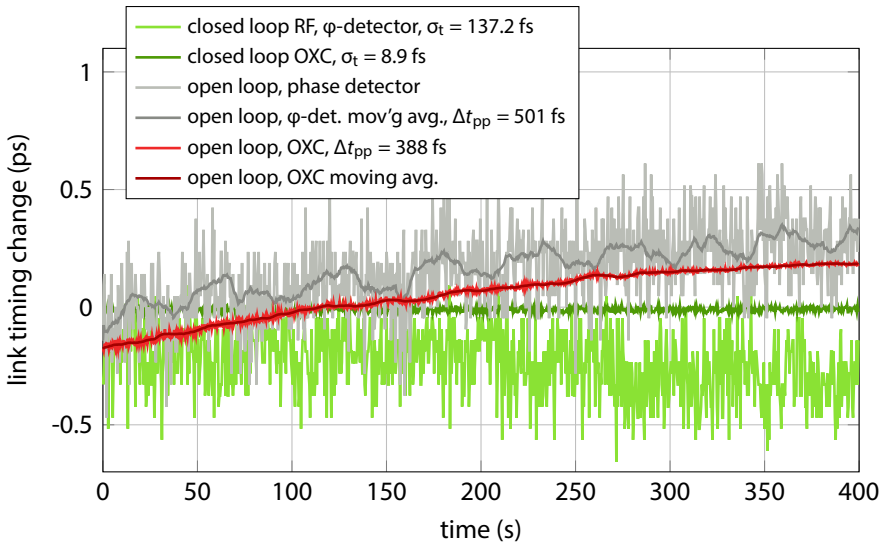

Figure 6.9 | Mid-term timing drift of a 300-meter-long fiber link. In the investigation two measurements were performed: First, data was acquired in normal, closed loop operation; secondly, the active stabilization was disabled and data was recorded for the same period of time. In both measurements, the RF-based phase detector and the optical cross-correlator signal is evaluated.

are shown for the closed loop operation of the link, recorded prior to the drift measurement. From the optical cross-correlator signal (dark green), a timing jitter of 8.9 fs (rms) had been determined, which was relatively bad due to ongoing other work in the laboratory. Nevertheless, the timing jitter calculated from the RF phase detector signal (light green) amounts to 137.2 fs at the same time. Furthermore, the oscillation is also visible here.

These measurements clearly show the advantages of the laser-based timing detection schemes, but it must be noted that the electronic phase detector is not optimized for high precision measurements in this case.

Spectral Distortion at the Link End

At the link end, the consumers usually require high optical power levels, for instance for efficient sum-frequency generation in cross-correlators for external lasers or to compensate for the PMF-splice loss and the insertion loss of the EOM in the bunch arrival time monitor (BAM). The installation of another fiber amplifier behind the FRM is highly undesirable, as its fibers are then not actively stabilized and prone to drifts, in particular in setups without active temperature stabilization, such as the cross-correlators for laser synchronization being in the development phase. Furthermore, it has been discovered that those EDFAs can severely affect the performance of the fiber link stabilization. Therefore, the EDFA in front of the FRM, as part of the link, is operated with a comparatively high pump current, occasionally boosting the pulse energy to more than 300 pJ. At the same time, the pulse duration at the link end is short, resulting in a high peak power. This leads to temporal and

spectral pulse distortions (the latter are shown in Fig. 6.10) caused by self-phase modulation (SPM) and cross-phase modulation (XPM) due to nonlinear effects. In the figure, it can be seen that pulse

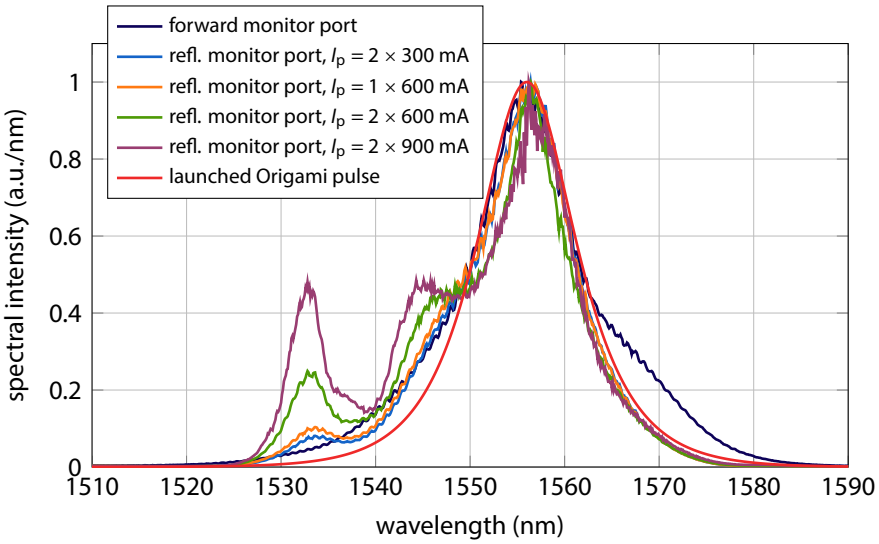

Figure 6.10 | Optical spectra of the Origami laser pulse at the link end. The spectrum is measured at a monitor port after passing the EDFA at the link end and after reflection by the FRM. The EDFA was pumped with different currents.

arriving at the link end (dark violet curve, measured at the forward monitor port), is spectrally broadened compared to the launched pulse (red), when the distribution EDFA, which connects the link unit to the FSD is operated with high pump currents. In the other measurements, its pump current had been slightly reduced and kept constant, while the amplification of the EDFA at the link end was varied. While the center wavelength stays practically constant for different pump currents, new spectral components arise when the EDFA is ramped up. The effect becomes very prominent for large pump currents – in this case $I_p = 2 \cdot 900\,\mathrm{mA}$ in a double-pumped configuration, corresponding to a pump power in the EDFA of more than 1 W.

As a result, both EDFAs required in the present scheme for the fiber link stabilization should be kept at the minimum power levels the connected device can accept to avoid a degradation of their performance from pulse distortions. In future developments, this has to be considered for the end stations. Furthermore, a change of the stabilization scheme might be possible, or a reduction of nonlinear effects by installation of the EDFA at another position in the fiber link.

6.3 Amplitude Stability and Timing Phase Noise

For the development of the optical cross-correlator for the Ti:sapphire laser (see chapter 7 , pages 151 ff.), an RF signal generated from the optical pulse train is required. It was discovered that this signal exhibits a substantially larger integrated timing jitter calculated from phase noise measurements, than is expected. In theory, the signal must be comparable to the one of the initial pulse train generated

by the master laser oscillator. The cause for the significant distortion could be identified as intensity noise of the transmitted pulse train.

For a systematic study, a setup as depicted in Fig. 6.11 was used. The forward monitor port of the

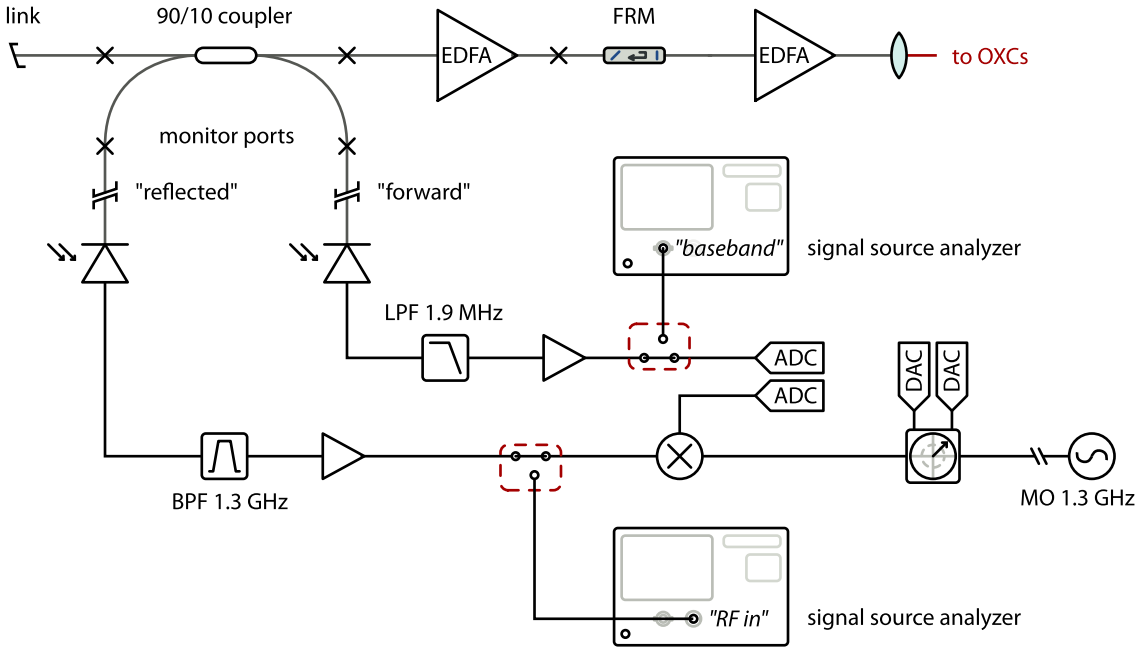

Figure 6.11 | Optical and electrical setup for noise investigations at the link end. The optical power of the arriving pulse train is monitored by means of a low-pass filtered and amplified signal of a low-bandwidth photodiode. The tapped-off light of the FRM-reflected pulse train is used for LO generation and this signal is down-mixed with the RF reference signal. The intensity- and timing phase noise is measured with the SSA.

fiber link is connected to an already described optical power monitor. Its signal can either be digitized with an ADC (as in the measurement shown in Fig. 6.5, page 138) or measured with the signal source analyzer (SSA) to determine the relative intensity noise (RIN) on fast time scales. From the coupler port of the reflected light, a 1.3 GHz RF signal is generated as it provides a higher optical power level after the amplification compared to the forward monitor. The phase noise of the signal can be measured with the corresponding operation modus of the SSA. Alternatively, the generated signal can be down-mixed with the RF signal provided by the master RF oscillator (MO). This enables a measurement of the arrival time of the laser pulse train with respect to the MO.

Before the amplitude- and phase noise investigations were conducted, the phase comparison setup had been used to investigate the influence of the optical power variation induced by the movement of the delay stage, as discussed in section 6.1.3, pages 137 ff. Figure 6.12 shows the output of the phase detector for a scan range of ±11 ps. In the measured timing change, the same oscillation is visible as in the optical power (see again Fig. 6.5, page 138), which had been recorded at the same time. This is caused by the AM-to-PM conversion process, i.e. amplitude noise of the optical signal is translated into a phase fluctuation of the generated RF signal. A linear fit to the data reveals a slope

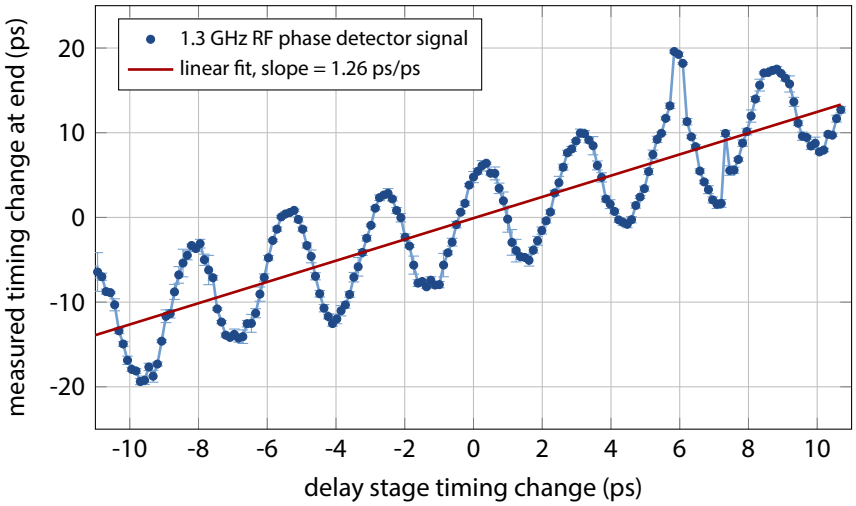

Figure 6.12 | RF-based detection of timing changes at the link end in a delay stage scan. Timing changes occur at the fiber link end when the delay stage in the stabilization unit is moved, as measured with an RF-based phase detector in the EO laboratory.

of 1.26, hence 26% larger than expected, which can be contributed to calibration errors and the drift of the fiber link during the measurement period. Due to constraints in the accelerator control system, the communication with the motor controller results in a duration of this scan of 20 min, in which the link is estimated to drift by ~ 1 ps. A measurement of the link drift was not possible, since the RF phase detector was not available at that time.

In analogy to the investigations on the optical power, the errorbars represent the standard deviation of 10 measurements and their average amounts to 330 fs over the measurement range of 22 ps, also caused by the rather large optical power fluctuations discussed above. The fiber link under investigation here was not equipped with the newest version of the delay stage yet, because the presently four available ones were installed in the fiber links for the BAMs, since they are more critical for the electron beam diagnostics. After its upgrade these measurements will be repeated.

For the measurement of the intensity noise (RIN) at the forward monitor port and its impact on the phase noise on fast time scales, the signal source analyzer had been used. The upper plot of Fig. 6.13 shows the relative intensity noise calculated from the voltage spectral density of the amplified photodiode signal, Eq. 2.69, page 44, for three different cases.

- **closed loop**, as normal operation mode of the link: the PLL of the fiber link stabilization is closed and keeps the optical cross-correlator signal at the zero-crossing. In the frequency range of $[1\,\mathrm{kHz}, 10\,\mathrm{MHz}]$, the RIN amounts to 1.00%. Contributions to this integral come from frequencies up to 500 kHz, with a prominent plateau in its characteristic.

- **open loop**: The data had been taken directly after opening the regulation loop. By this, the timing of the pulse trains did not change significantly from the closed loop operation. However, the characteristic of the curve changed and the main contribution comes from frequencies up

~ 60 kHz. In this case, the total RIN for the measurement range amounts to 1.55%.

- When the **delay is stage moved** several millimeters, and by this the pulses do not overlap temporally in the cross-correlator, the characteristic is changed again, and only frequencies up to 2 kHz contribute significantly to the integral. That amounts to 0.74% in the complete range.

In the last case, the total RIN is still rather large, compared to the laser systems providing the pulse train (see section 5.4.4, pages 105 ff.). The measured phase noise, shown as blue trace in the lower plot

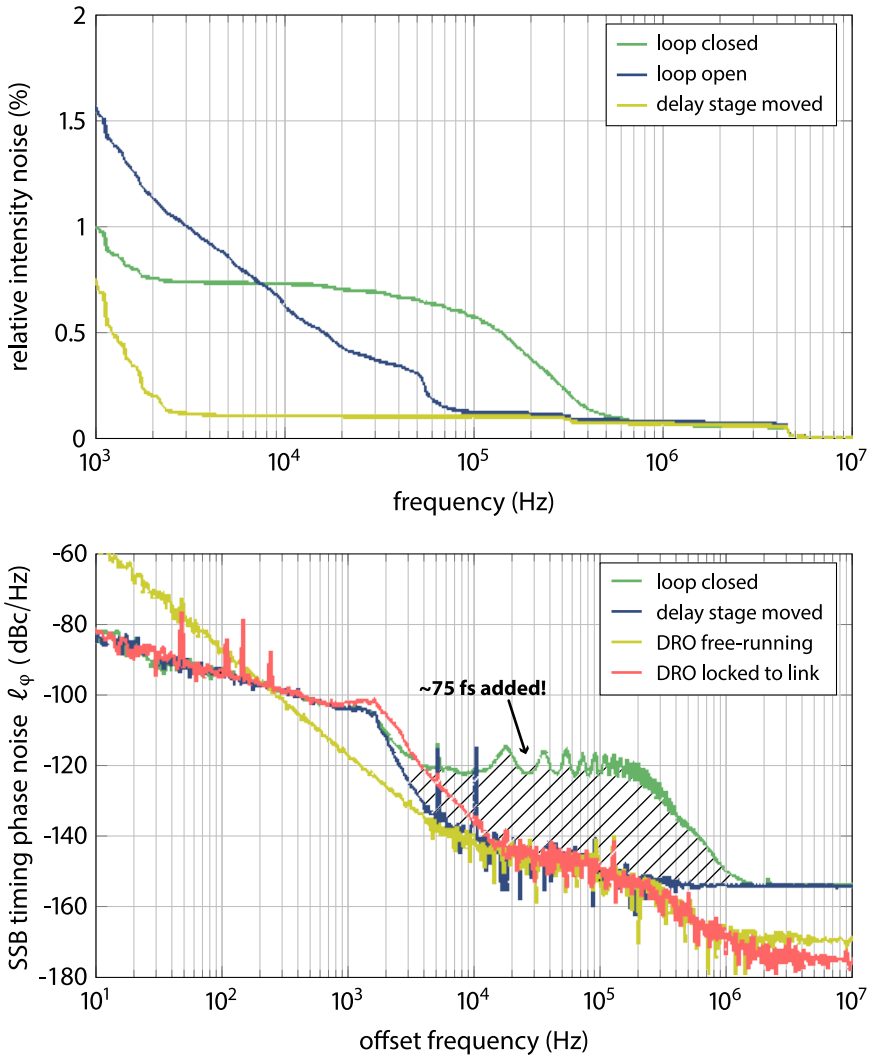

Figure 6.13 | Relative intensity noise and timing phase noise at the fiber link end. The relative intensity noise is calculated from the optical power monitor baseband spectrum, while the timing phase noise is measured using the photodiode normally used for synchronization. For low-noise RF extraction at a fiber link end, it is required to phase-lock another RF oscillator with low bandwidth.

in the figure, has an expected characteristic (compare to Fig. 5.27, page 101) in this case. However, when the pulses are overlapped in the cross-correlator and the loop is closed, the phase noise (green

trace) is substantially increased for frequencies of 3 kHz to 1 MHz. Moreover, its characteristic is very similar to the intensity noise in this frequency region, superimposed by a strong oscillation. The shaded area in the figure depicts that this increase of phase noise adds 75 fs timing jitter to the integral. Thus, the generated RF signal is, for instance, not suited for the synchronization of external laser systems.

To overcome this without changing the fiber link, a dielectric resonator oscillator (DRO) can first be locked to the RF generated from the optical pulse train. Here, the PLL cut-off frequency has to be lower than ~ 1 kHz, where the phase noise is not yet influenced by the large intensity noise of the fiber link in its locked case. Then, the external laser can then be locked to the DRO. Details on this approach can be found in [FBB+10].

The influence of the relative temporal position of the reference and the returning pulse train can also be observed in the cross-correlator which is actually used for the fiber link stabilization. Figure 6.14 shows such cross-correlator signals, which were recorded during the commissioning of one fiber link stabilization unit. The data (shown as dots; solid lines are fits) exhibits larger fluctuations

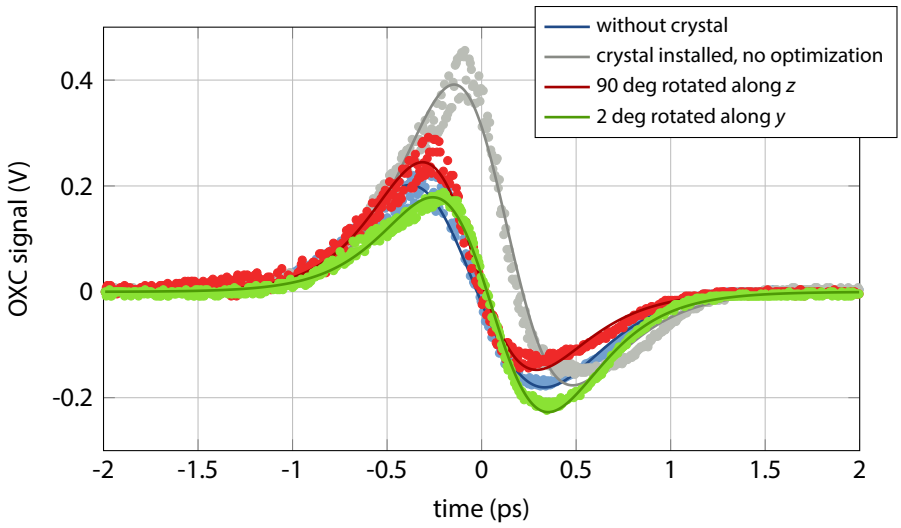

Figure 6.14 | Optical cross-correlator signal for different geometric YVO crystal orientations. After the YVO_4 crystal had been introduced to the optical cross-correlator setup, calibration curves were recorded for different orientations of the crystal.

for more negative time delays. When the pulses of both pulse trains temporally overlap in the PPKTP crystal, they also coincide in the polarizing beam cube. It had been suspected, that the glue and/or the coating between the prisms the PBC is constructed of, is affected by the high power in the pulses, which amounts in sum to ~ 5 kW.

Therefore, an yttrium orthovanadate (yttrium orthovanadate (YVO), see appendix C.7, page 237) crystal had been introduced between the splitting/combining beam cube and the actual nonlinear crystal for a series of experiments. Due to the large birefringence of the crystal of $\Delta n \approx 0.2$, the pulse trains, which are orthogonally polarized, are temporally shifted with respect to each other. By this, they do not overlap in the beam cube when they do in the PPKTP crystal. The corresponding cross-

correlator signals are shown in the figure for three different geometric orientations of the crystal. It can be seen, that the fluctuations of the data points can be reduced for a particular orientation of the crystal (red), but it should also be noted, that these tests were made with in existing fiber link where space for additional components is limited. Further investigations with the new link design, in which the installation of such a crystal is possible, will show, to which level the noise can be mitigated or completely eliminated.

Another source of noise was identified as cross-talk from other fiber links connected to the free-space distribution unit (FSD), as the amplified spontaneous emission (ASE) from an EDFA propagates in both directions of the gain fiber and consequently also into the FSD. There it can couple into other fiber collimators, for example installed at the opposite side of a two-PBC combination (compare for example C3 and C11 in Fig. 5.32, page 110). In order to reduce the influence of ASE, which is unpolarized, the pump currents of the EDFAs must be kept low, as Faraday isolators can not be used in this case. Furthermore, there are fractions of the returning pulse trains counter-propagating through the EDFA into the FSD. Under the assumption that the EDFA does not change the polarization state, such a pulse train is perpendicularly polarized to the original one and can couple into another EDFA (e.g. from C7 into C15). This is possible, since the mechanics is manufactured with

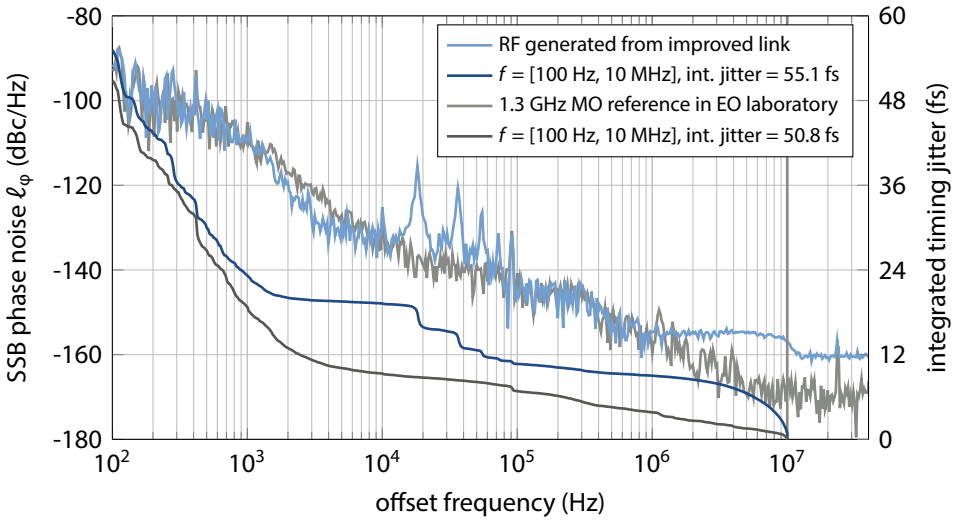

Figure 6.15 | Phase noise and timing jitter of RF generated from improved link. The measurement was carried out after the YVO_4 crystal was introduced in the fiber link stabilization unit. For comparison, the corresponding reference signal from the MO is also shown.

very tight tolerances and the optical alignment can be done very precisely. Initially, there were no beam blocks foreseen between such beam cube combination, but were be installed afterwards.

With the beam blocks installed in the free-space distribution unit, a Faraday isolator in the EDFA and with comparatively low pump currents of both EDFAs of the fiber link, the phase noise at the end of the fiber link to the EO laboratory could be reduced, as shown in Fig. 6.15 (blue curves). Although there are still peaks visible in the decade from 10 kHz to 100 kHz, the integrated timing jitter up to 10 MHz amounts to 55.1 fs, and in $[1\,\text{kHz}, 10\,\text{MHz}]$ to 23.2 fs. While this is still larger

than the timing jitter of the master laser oscillator in the same frequency interval (10.8 fs rms, see also table A.1, page 221), it is comparable to the 1.3 GHz reference signal in the laboratory provided by the master RF oscillator.

Hence, this optical reference pulse train can be used for the synchronization of a Ti:sapphire laser oscillator, as described in the next chapter. It should be noted, that the BAMs are much less sensitive to this amplitude noise than the optical cross-correlators for external lasers, as their digitizing principle by sampling the baseline and the peak (see section 4.4, page 67 f., and in particular [GBF+10b, Boc13]) acts as high-pass filter at not less than 1 MHz. Until the source of the amplitude noise has been identified and analyzed completely, furthermore the DRO-based method can be deployed to generate low-phase noise RF signals from the optical pulse train. This adds, however, more complexity and is rather expensive. Ultimately, the fiber link optical setup must be modified to avoid these sources of jitter, which probably requires a significant change in the stabilization principle.

7 Synchronization of Independent Laser Oscillators

One of the unique features of pulsed optical synchronization systems is the possibility to directly lock other laser oscillators to the distributed reference pulse trains by means of optical cross-correlation, promising femtosecond jitter and drift-free synchronization. In principle, the optical cross-correlator is, like in the fiber link stabilization units, based on sum-frequency generation and delay/subtraction detection. There is, however, one important difference: here, two individual oscillators are involved, which can be separated by several hundred meters or even kilometres. Consequently, these two oscillators have to be pre-synchronized by an RF-based phase-locked loop before the temporal overlap in the nonlinear optical crystal can be adjusted. Once a signal is detected, the regulation loop can switch over to this error signal.

In this chapter, the experimental setup and results of the first optical cross-correlator for a commercial Ti:sapphire laser oscillator are discussed. The scheme is, however, not limited to Ti:sapphire lasers but can easily adapted to other wavelengths, repetition rates and/or pulse durations, as it will be explained in the following sections. Furthermore, the difficulties and problems encountered during the development of the device are addressed.

Ti:sapphire Oscillator used for the Development

The titanium-sapphire laser system to be optically synchronized is a commercial Micra-5 made by Coherent [Coh07]. It is based on an X-folded cavity with two-prism GVD compensation (see section 2.4.2, page 36). The emitted pulse train has a repetition rate of $f_{\mathrm{TiS}} = f_{\mathrm{RF}}/16 = 81.25\,\mathrm{MHz}$ with an average power of 500 mW, resulting in more than 6 nJ pulse energy. The optical setup in the laboratory allows to use the major fraction of the available optical power for seeding a Ti:sapphire amplifier system or, normally, for electro-optic bunch diagnostics at the accelerator (see section 1.8.1, pages 16 ff.). Approximately 15%, however, are tapped off for the optical cross-correlator, the RF synchronization scheme and pulse diagnostics. The left plot of Fig. 7.1 shows the measured autocorrelation of the emitted laser pulses. The pulse duration amounts to $\tau_{\mathrm{TiS}} = 167.5\,\mathrm{fs}$, which is relatively long compared to the capability ($\ll 50\,\mathrm{fs}$ according to the manufacturer) of the laser. However, the laser beam propagates through a two-lens telescope installed 400 mm after the output window to optimize the transport of the laser into the accelerator tunnel. Because the fraction of light for the optical cross-correlator is tapped off after the telescope, this is the pulse duration to consider, for instance in the calculations of the nonlinear processes in the BBO crystal (see chaper 3, pages 47 ff. and appendix C.1, page 229). The photodiode used for the RF synchronization is fiber coupled and

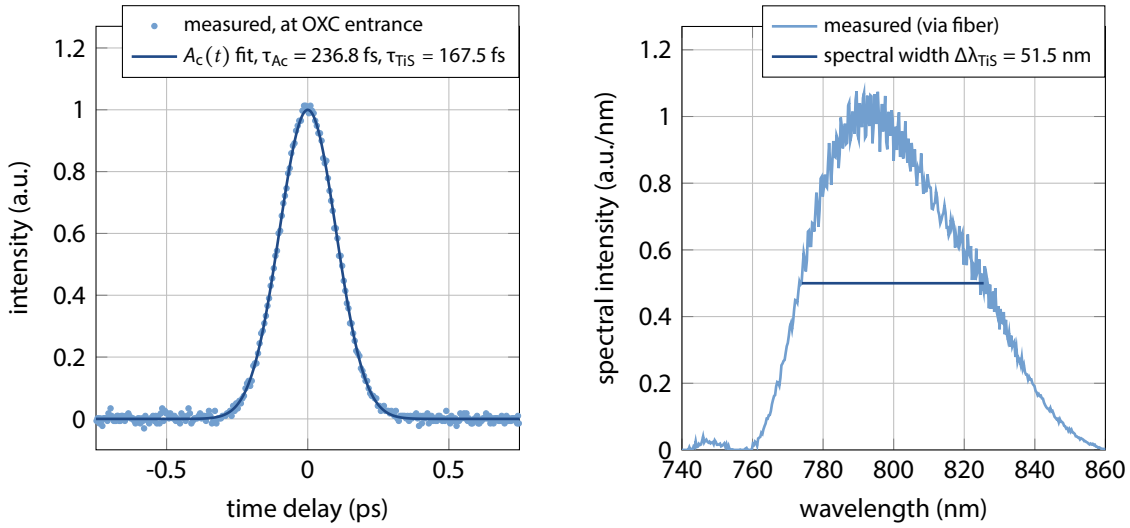

Figure 7.1 | Autocorrelation and optical spectrum of the Micra Ti:sapphire oscillator. The commercial laser system is normally used in the electro-optic beam diagnostic experiment. In the laser diagnostics section, the pulses entered the autocorrelator after passing a telescope and several mirrors, whereas the optical spectrum has been measured at a fiber collimator which is used for the synchronization photodiode.

the corresponding fiber collimator is impinged by light which is tapped off by Fresnel reflection from the beam using a 1 mm thin quartz window. This fiber was also used to measure the optical spectrum of the laser shown in the right plot of Fig. 7.1. It is centered at λ_{TiS} = 795 nm and has a full-width at half-maximum of $\Delta\lambda_{TiS}$ = 51.5 nm determined directly from the data. It should be noted that the prisms in the laser cavity can be used to tune the spectral width in the range from 30 nm to 120 nm by the insertion or removal of glass, but it has found that the laser operates most stable with a ~ 50 nm wide spectrum. By this, the mix-acceptance bandwidth of the BBO crystal, as discussed in section 3.4 (pages 53 ff.), is slightly under-utilized for the sum-frequency generation process.

Phase Noise and Timing Jitter

As explained in section 5.2.5, pages 82 ff., the integrated timing jitter δt_{rms} calculated from the recorded phase noise at certain carrier frequencies f_c is an important figure of merit of the short-term timing stability of the laser and an estimation for the expected synchronization accuracy. Figure 7.2 shows phase noise measurements at f_c = 1.3 GHz and f_c = 2.6 GHz measured using the photodiode[1] normally used in the synchronization circuit. From the integrals, it can be seen that the timing jitter significantly increases at 1 kHz, hence the PLL for synchronization to a reference signal should have a corner frequency larger than this (see also Fig. 6.15, page 149). At higher frequencies, i. e. in the interval [1 kHz, 10 MHz], the laser shows a good performance with δt_{rms} = 17.9 fs at 1.3 GHz and δt_{rms} = 11.3 fs at 2.6 GHz. The measurement is again limited by the photodetection process, as the noise floor at very high offset frequencies contributes most to the integrals. The timing jitter for

[1] EOTech ET4000F, bias voltage V_{bias} = 15 V, optical power ~ 1.3 mW

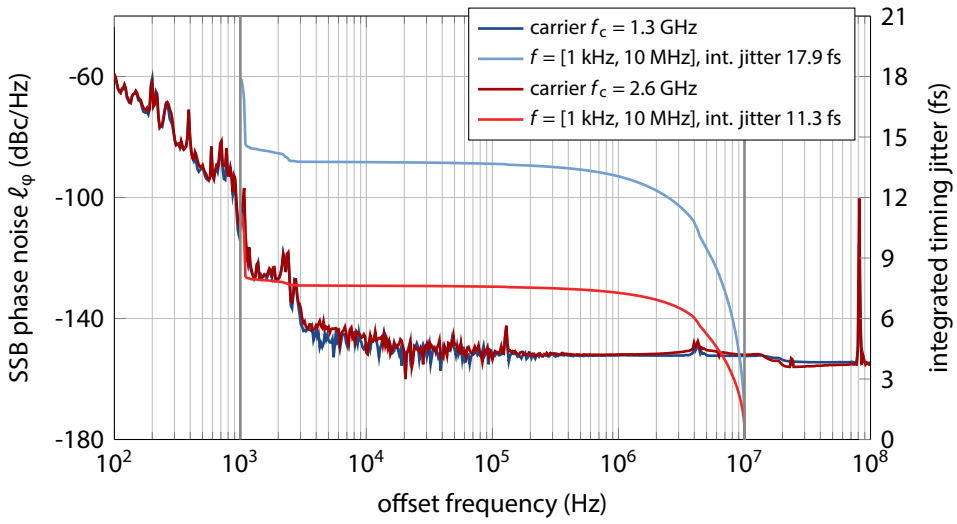

Figure 7.2 | Timing phase noise and integrated jitter of the Micra Ti:sapphire oscillator. The measurement was carried out at 1.3 GHz and 2.6 GHz carrier frequencies. The laser was free-running and the SSA-internal correlation tool was used.

other frequency intervals calculated from this measurement is given in table A.1 on page 221 in the appendix.

7.1 Implementation and Development Setup

The implementation of the complete setup for the all-optical synchronization is shown in Fig. 7.3. Beside the Ti:sapphire oscillator, it consists of five major parts: the optical reference to lock on, the cross-correlator generating the error signal, the digital regulation loop, an extended RF phase detector and a second optical cross-correlator for out-of-loop timing measurement. The setup furthermore allows to switch between two different optical references during the development, being

- a stretched-pulse erbium-doped fiber laser (EDFL, built in [Wino8]) with a repetition rate of 40.625 MHz and an average output power of 20 mW and hence a pulse energy of E_p = 0.49 nJ. Its pulse duration is in the order of τ_{FWHM} = 250 fs after five meters of fiber. It was used as reference mainly before the fiber link was completed and for measurements when the amplitude noise of the link (see section 6.3, pages 144 ff.) hindered the development of the optical cross-correlator.

- the pulse train of the master laser oscillator (MLO), distributed via a stabilized fiber link to the laboratory, with the repetition rate f_{MLO} = 216.667 MHz. After the Faraday rotating mirror (FRM) at the link end, up to 35 mW average optical power are available.

The advantage of the locally installed EDFL is its repetition rate of $f_{TiS}/2$ = 40.625 MHz, because the laser pulses will temporally overlap in the cross-correlator this frequency, leading to a higher average

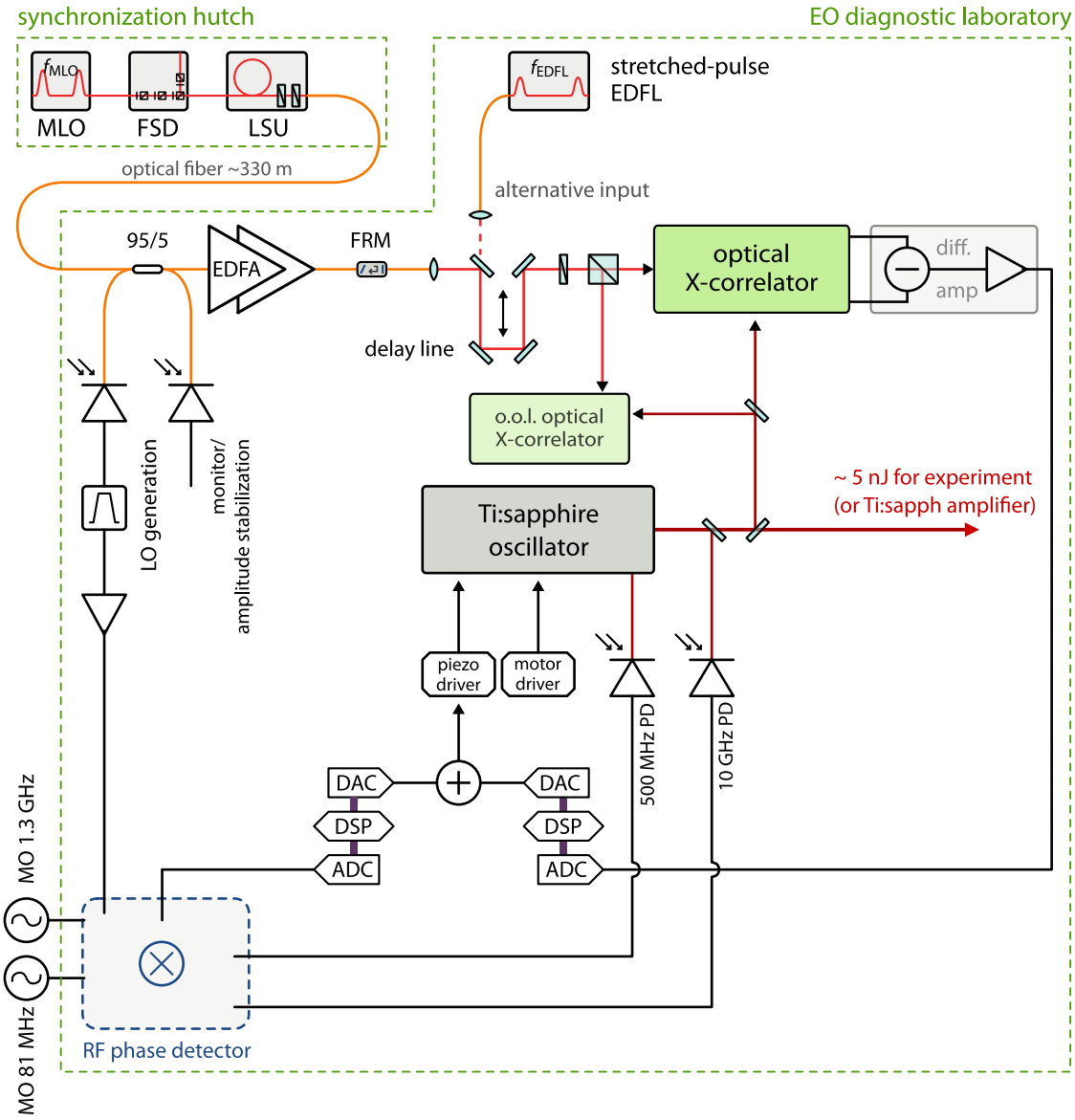

Figure 7.3 | Overview of RF- and all-optical synchronization for the Ti:S oscillator. The laser oscillator can be phase-locked to the optical reference by means of an RF phase detector and an optical cross-correlator. Another, independent cross-correlator is used to measure the timing stability.

power of the generated sum-frequency signal. In case of the optical reference pulse train of the MLO, the repetition rate f_{SFG} of the sum-frequency pulse train is (compare appendix F, pages 251 f.)

$$T_{SFG} = 3 \cdot (f_{TiS})^{-1} = 8 \cdot (f_{MLO})^{-1} = 36.923\,\text{ns} \quad \Rightarrow \quad f_{SFG} = T_{SFG}^{-1} = 27.083\,\text{MHz}\,. \tag{7.1}$$

Therefore, only every third reference pulse and every eighth pulse from the Ti:sapphire oscillator will temporally overlap. The lower average power of the generated sum-frequency signals can be,

however, compensated for with the used photodetectors to some extent, as will be explained below.

The reference pulse train passes an optical delay line (ODL) before entering both cross-correlators. This allows for a calibration of those and for changing the relative timing of the oscillator with respect to the reference pulse train in a range of ±450 ps. The pulse train of the oscillator entering the cross-correlator is a tapped-off fraction of its beam, as explained above. The average power available in each of the cross-correlators is about 15 mW.

The phase-locked loop based on the optical cross-correlator can only catch, when the error signal is generated in a way such that the relative time delay of the pulse trains can be adjusted to sample the signal around the zero-crossing. This requires a tight synchronization of the oscillator and the reference by means of an RF-based scheme, explained in section 7.1.2 on pages 157 below. Therefore, the end of the fiber link is equipped with a 95/5-coupler with one port connected to a standard circuit for direct conversion, consisting of a large-bandwidth photodiode, a bandpass-filter at 1.3 GHz and an amplifier. The second tap is used for monitoring the optical power of the link. The output of the phase detector is sent to a digital PID controller based on the same hardware (ADC → DSP → DAC) and software as for the synchronization of the MLO (see section 5.3, pages 87 ff.). A second, identical controller is fed with the output signal of the cross-correlator as error signal. The output signals of the two regulations are connected to a variable combiner, which allows weighting its inputs for the switch between the two PLLs. The combined signal is amplified with a low-noise high-voltage driver and acts on a piezo actuator in the resonator of the Ti:sapphire oscillator by moving a mirror and thus adjusting the resonator length.

7.1.1 Two-Color Optical Cross-Correlator

The optical cross-correlator is based on the twice the detection of the sum-frequency (SFG) component generated by the fundamental light waves. The used beta barium borate (BBO) crystal is phase-matched for a collinear ooe interaction (see section 3.2, pages 48 ff.) and has a length of 0.5 mm (see sections 3.3, pages 50 ff. and appendix C.1, page 229). The optical setup of the development setup is shown schematically in Fig. 7.4. The pulse trains of the optical reference (λ_1 = 1560 nm) and the Ti:sapphire oscillator (λ_2 = 800 nm) enter the device through a first dichroic mirror. They are reflected at a second dichroic mirror, which is high-reflective (HR) for both wavelengths, and are focused into the BBO crystal using a lens with a focal length of f = 40 mm. The fundamentals are, together with the generated sum-frequency component at $\lambda_3 = (\lambda_1^{-1} + \lambda_2^{-1})^{-1}$ = 528.8 nm, collimated with a second lens of the same type and impinge the third dichroic mirror, which is high-transmissive (HT) for λ_3. After spatial and spectral filtering to minimize the effect from the alongside generated second-harmonics[2] of both fundamentals, the first SFG intensity is measured with a photomultiplier tube (PMT). The fundamentals are reflected at the third dichroic mirror, pass a 3 mm thin quartz slab, get reflected and pass the silica slab again. By this, their relative temporal position is exchanged for the second process of sum-frequency generation, as the now backwards traveling pulses are again focused into the BBO crystal. This SFG signal passes the first dichroic mirror the pulses were reflected

[2] Due to the relatively broad spectra of the fundamentals and the high power of the fundamental waves, the second-harmonic generation (SHG), albeit with a very low conversion efficiency, can not be suppressed

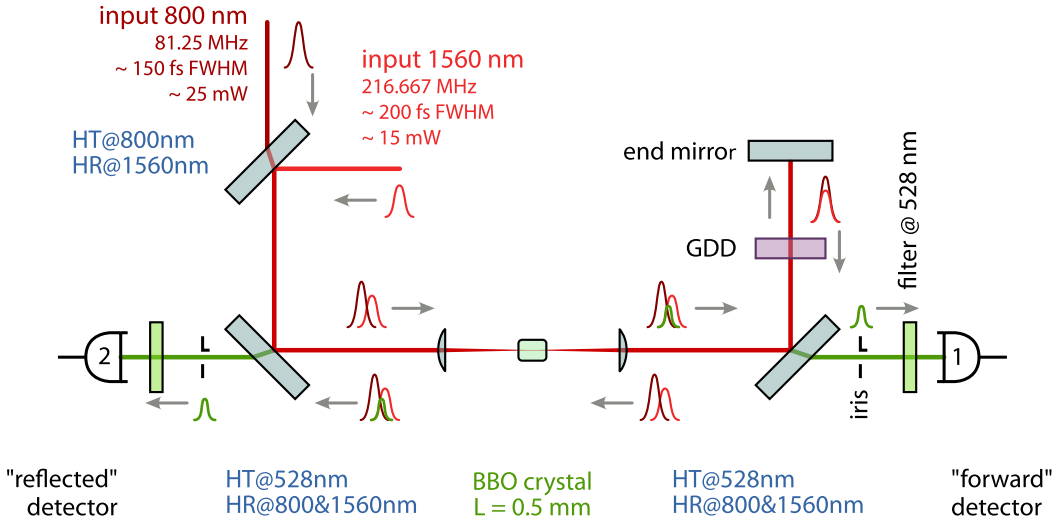

Figure 7.4 | Schematic setup of the two-color single crystal optical cross-correlator. The pulse propagation is indicated by the gray arrows, while it is also stated at which wavelengths the dichroic mirrors are highly reflective (HR) and highly transmissive (HT).

before, and is detected with the second PMT. Due to the pulse swap with the quartz slab (GDD in the figure), the difference of the SFG intensities is a bipolar signal with a certain slope around its zero-crossing. When the thickness of the quartz slab is chosen according to the pulse duration to induce an optimum delay T_{opt} (see Eq. 3.25, page 56), this slope is maximum resulting in maximum sensitivity to timing changes of the fundamental pulse trains. In order to adapt to other pulse durations, the delay element can be exchanged. This turned out to be necessary, when the master laser oscillator was changed from the EDFL-MLO to the SESAM-based laser with a longer pulse duration.

The PMTs[3] used for the detection of the sum-frequency signals have their peak sensitivity close to the wavelength corresponding to the SFG light and feature a programmable gain from 100 to 10^6, which had been useful during the original commissioning of the device. The output signals of the PMTs are subtracted in a transimpedance amplifier (TIA) with differential inputs[4].

Mechanically, the prototype setup is build from typical off-the-shelf components on a double layer breadboard, where the lower layer contains the fiber installation of the link end (see photographs G.9 and G.10 on pages 259 and 260 in the appendix). The second cross-correlator, used for out-of-loop timing measurements, is built almost equally, only without the fiber layer and with an additional optical delay line in the beam path of the Ti:sapphire pulse train to enable an independent calibration. In principle, the latter device can be used for another Ti:sapphire laser system in a later stage of the expansion of the synchronization system, given that out-of-loop studies are not required any more.

[3] Hamamatsu H6780-20, see data sheet [Ham07]
[4] Femto DLPVA-100-B-D, see data sheet [Fem06].

NOTE ON THE ALIGNMENT OF THE OXC: THE INITIALLY REQUIRED PHASE RELATION OR "TEMPORAL OVERLAP" OF THE REFERENCE AND THE TI:S PULSES CAN BE FOUND WITH THE HELP OF A FIBER COLLIMATOR INSTALLED INSTEAD OF THE END MIRROR OF THE CORRELATOR SETUP. THEN THE PULSE TRAIN CAN BE OBSERVED WITH A HIGH-BANDWIDTH PHOTODIODE AND A "FAST" OSCILLOSCOPE: WITH A SCAN OF THE RELATIVE TIMING OF THE PULSE TRAINS, THE DELAY CAN BE ADJUSTED WITH AN ACCURACY OF ABOUT 20 PICOSECONDS. NOW THE OPTICAL DELAY LINE CAN BE ADJUSTED TO FIND THE TEMPORAL OVERLAP IN THE CRYSTAL BY OBSERVING THE FORWARD SFG INTENSITY. THIS BECOMES MORE COMPLICATED WHEN THE PHASE RELATION OF THE TI:S OSCILLATOR IS ALREADY FIXED WITH RESPECT TO THE ACCELERATOR, E.G. KNOWN FROM A FORMER EXPERIMENT (SUCH AS THE ELECTRO-OPTIC DIAGNOSTICS; OR THE SEED LASER AND THE ELECTRON BUNCH). FURTHERMORE, THE PHASE RELATION OF THE MLO PULSES WITH RESPECT TO THE ACCELERATOR IS ALSO FIXED BY THE BUNCH ARRIVAL TIME MONITORS. CONSEQUENTLY, AN ADDITIONAL FIXED DELAY BY ADDING GEOMETRIC BEAM PATH HAS TO BE INTRODUCED. THIS, IN TURN, MAY AFFECT THE BEAM PROPAGATION IN THE DEVICE, BY MEANS OF DIVERGENCE AND BEAM SIZE, AND HAS TO BE TAKEN INTO ACCOUNT IN EFFICIENCY CALCULATIONS FOR EXAMPLE. HERE, A DEGRADATION BY A FACTOR OF TWO WAS OBSEREVD.

7.1.2 Extended RF Phase Detector

The RF phase detection principle for the synchronization of the Ti:sapphire oscillator, based on down-mixing harmonics of the laser's repetition rate, is very similar to the one utilized for phase-lock of the MLOs, which is discussed in detail in section 5.3.1, page 87 f. The major differences, explained in the following, are the PLL at the fundamental repetition rate f_{TiS} of the laser oscillator, and the addition of a loop at a very high harmonic of $112 \cdot f_{\mathrm{TiS}} = 42 \cdot f_{\mathrm{MLO}} = 9.1\,\mathrm{GHz}$. The successive lock to the optical pulse train at first the fundamental (to find the correct phase relation as explained in the chapter on the master laser synchronization), then at the intermediate frequency of 1.3 GHz and finally at 9.1 GHz promises an even tighter RF-based synchronization of the laser [FBB+10]. However, the PLL at the highest harmonic was not yet available in the investigations described in the next sections, and a characterization in terms of phase noise and the performance of the corresponding components was only partly possible, as the required measurement equipment is not completely available yet. The 9.1 GHz-branch is shown in a lighter color in the block diagram of the synchronization circuit in Fig. 7.5. The 1.3 GHz phase-locked loop can be used for either locking the laser to the optical reference pulse train or the signal of the master RF oscillator (MO). Presently, the switch between this possibilities has to be done manually, but in the future it will be useful to employ an automatic switch over to the RF reference, for example in case of a malfunction of the fiber link. Furthermore, a programmable phase shifter is installed in this branch to adjust the phase relation of the oscillator and the reference, as explained earlier. The reference signal for the coarse lock at the fundamental repetition rate $f_{\mathrm{TiS}} = 81.250\,\mathrm{MHz}$ of the laser is always provided by the master RF oscillator, as it can not be directly extracted from the optical pulse train as $f_{\mathrm{TiS}} < f_{\mathrm{MLO}} = 216.667\,\mathrm{MHz}$. The corresponding sig-

nal of the laser oscillator is extracted from a built-in photodiode. That makes this lowest-frequency

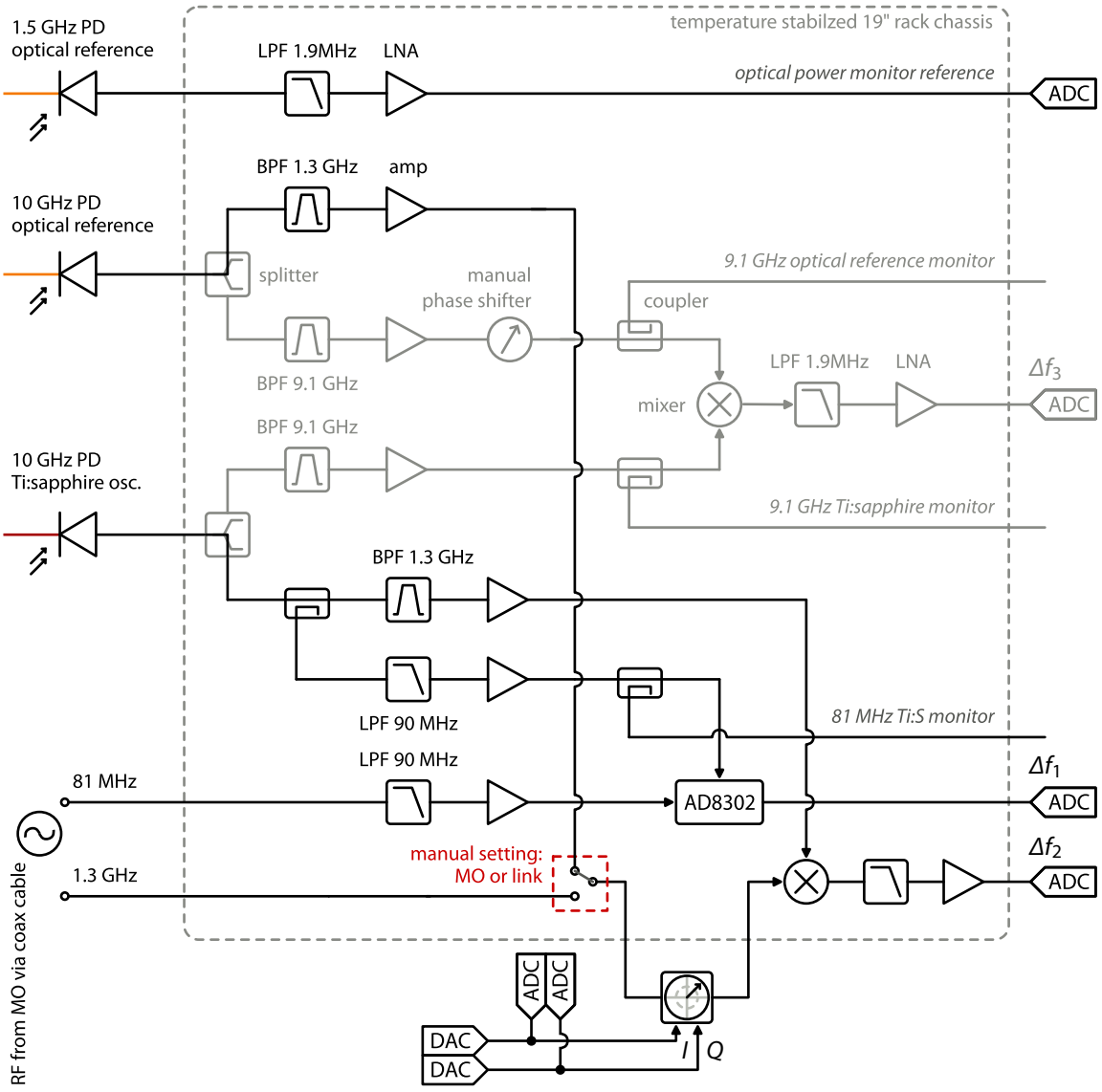

Figure 7.5 | Extended RF phase detection scheme for laser-to-laser synchronization. The scheme is based on a phase detector operating at the fundamental repetition rate of the laser and a phase detector at a carrier frequency of 1.3 GHz. The input of this PLL can either be extracted from the optical reference or the one from the master RF oscillator (MO). It is foreseen to extend the scheme to a third phase detector operating at 9.1 GHz.

branch subject to drifts compared to the higher frequency PLLs. However, since a phase detection circuit based on an AD8302 chip with an output voltage of ±900 mV is used, the corresponding output of the 16 possible zero-crossings of the 1.3 GHz RF signal can easily be distinguished. By that, the correct bucket can be found reproducibly in case the loop has to be reestablished, even when the input of the 1.3 GHz PLL is switched from the RF reference distribution to the RF signal generated

from the optical reference pulse train. Based on the good experiences with the temperature stabilization of the RF-lock rack chassis for the MLO, it is planned to assemble a similar rack chassis for this RF-circuit as well.

7.1.3 Calibration

When the temporal overlap of Ti:sapphire pulses and the reference pulse train in the crystal has been found, the optical cross-correlator can be calibrated. In any case, an RF-based synchronization is essential to keep the laser pulse trains appropriately phase-locked. Otherwise, the independent drift and fast timing jitter of the separated, individual laser oscillators prohibits a detection of the SFG signals. This is a harsh contrast to the cross-correlators in the fiber link stabilization units, where the reference pulses and the reflected ones originate from the same pulse train, such that their timing jitter and drift experienced in the transit through the link is negligible in the corresponding calibration (see section 6.1, pages 132 ff.). In the following discussion, this fact should be kept in mind.

The actual calibration, i.e. recording the cross-correlator output signal while varying the relative timing Δt of the pulse trains, can be realized in several ways:

- The motorized optical delay stage can be moved, which allows for extremely small time steps in the scan. Due to the slow communication of the accelerator's control system and the motor driver, this method can take up to 15 min for a 4 ps. During that time, the lasers can drift with respect to each other, which would distort the measurement.
- The programmable phase shifter (vector modulator) in the 1.3 GHz PLL can be scanned. The minimum time step in this method is in the order of 30 fs limited by the electronic circuit. This method takes about 2 min for a scan of 4 ps.
- The vector modulator can be used to apply a phase slope to the reference signal, resulting in the required time delay Δt. This method is practically equivalent to the detection of the SHG signal in autocorrelators (see section 5.2.3, pages 77 f.) and explained below. Since the DAC controlling the vector modulator and the ADC sampling the cross-correlator output signal are triggered by the machine timing system, this method takes in theory only 0.1 s, but in practice ~ 1 s including the communication through the control system.

Consider the Ti:sapphire oscillator phase-locked with at certain phase setpoint φ_0 of the vector modulator. Then, the delay function $\varphi_{\mathrm{cal}}(t)$ with a linear slope α can be applied by

$$\varphi(t) = \varphi_0 + \varphi_{\mathrm{cal}}(t) \qquad \text{with} \qquad \varphi_{\mathrm{cal}}(t) = 2\pi \cdot f_{\mathrm{lock}} \cdot (t_0 + \alpha\, t) \quad \text{and} \quad \alpha = \frac{\Delta f}{f_{\mathrm{lock}}}\,, \tag{7.2}$$

where $f_{\mathrm{lock}} = 1.3\,\mathrm{GHz}$ the frequency of the PLL. The frequency shift Δf, which defines the time delay of the fundamental pulses, is typically in the order of 1.5 Hz. The voltages V_I and V_Q, which have to be set in the vector modulator, are given by

$$z(t) = V_{\mathrm{nom}} \cdot e^{i\varphi(t)} \qquad \Rightarrow \qquad V_I(t) = \mathrm{Re}\{z(t)\} \quad \text{and} \quad V_Q(t) = \mathrm{Im}\{z(t)\}\,. \tag{7.3}$$

The knowledge of the applied slope α allows the ADC sampling points to be converted to the relative timing of the lasers with $\Delta t = \alpha \, \Delta t_{\mathrm{ADC}}$, where t_{ADC} is the temporal distance of the ADC sampling points of usually 1 µs. An example implementation of this calibration method as a MatLab script can be found in appendix E, pages 247 ff. In Fig. 7.6, a comparison of the calibration curve recorded

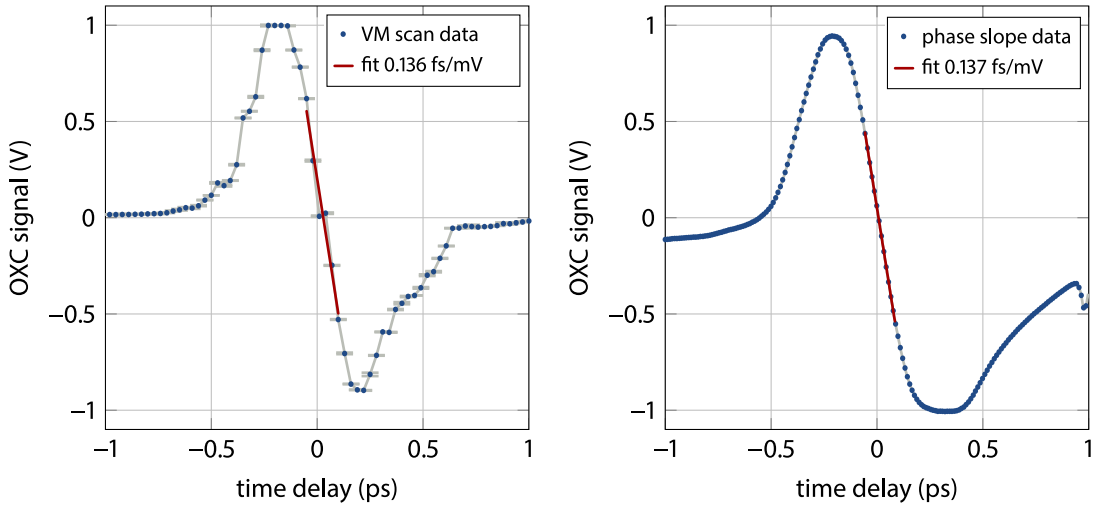

Figure 7.6 | Comparison of different methods for calibration of the optical cross-correlator. Left: The motor in the optical delay line is scanned. **Right:** A phase slope is applied in the PLL using the vector modulator. In both measurements, the laser is synchronized to the optical reference by means of the RF phase detector.

during a scan of the vector modulator (left plot) and with the phase slope method (right plot). The measurements were recorded consecutively and result in nearly the same calibration constant of $K_{\mathrm{OXC}}^{(\mathrm{scan})} = 7.353\,\mathrm{mV/fs}$ and $K_{\mathrm{OXC}}^{(\mathrm{slope})} = 7.299\,\mathrm{mV/fs}$, respectively. However, in the first method, the discrete scanning steps are clearly visible, and since the slope is relatively steep, only ten data points can be taken between the maximum and the minimum of the balanced signal. Moreover, the curve is less smooth due to the aforementioned jitter of the of the lasers, although every data point represents the mean of five measurements. The phase slope technique, on the other hand, shows a broader signal in the negative voltage range, albeit the positive characteristic in the two measurements is highly comparable. This issue requires further investigations, but in principle, this method seems to be ready for the implementation in the planned control system server for the optical cross-correlators.

Influence of the Optical Power

The calibration has been performed for different optical power levels of the reference pulse train, as it had been found that the EDFA at the link end should only be pumped moderately (see section 6.3, pages 144 ff.), resulting in lower power levels than initially assumed in the original design of the cross-correlator. The left plot in Fig. 7.7 shows the value of the calibration constant K_{OXC}, which is given in units of millivolt per femtosecond, hence larger values are better. The error bars represent the uncertainty of the linear fit around the zero-crossing. The right plot in the figure shows the

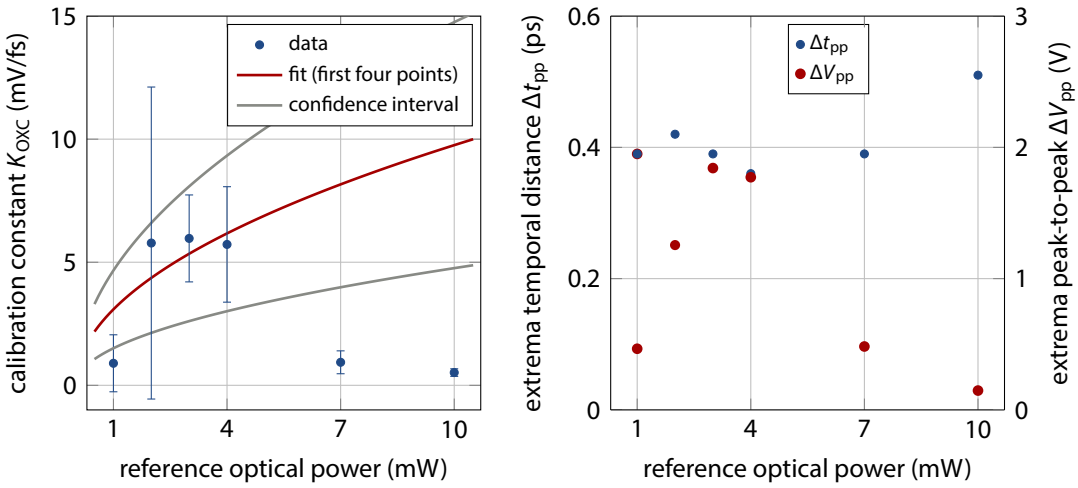

Figure 7.7 | Calibration constant of the OXC as function of the reference optical power. Left: Calculated calibration constant K_{OXC} from the balanced signal; **Right:** temporal distance Δt_{pp} of the both extrema and their peak-to-peak signal ΔV_{pp}.

measured temporal distance Δt_{pp} of the extrema of the balanced signal, as well as its peak-to-peak voltage ΔV_{pp}. From the data, it can be concluded, that optical power levels in the order of 3 mW to 4 mW already lead to an optimum performance, at least for the device under test. Although it differs from the expected behavior, this is an important result, as the fiber link stabilization units providing the optical reference pulse train, have a better performance at low optical power levels. However, the required power levels of both the reference pulse train and the Ti:sapphire laser for the maximum conversion efficiency of the SFG process should be investigated individually for each cross-correlator being built in the future, as it depends on other factors, such as the pulse duration and the focusing into the crystal (see section 3.3, pages 50 ff.).

7.2 Timing Jitter Analysis

The optical cross-correlators can be used for out-of-loop timing jitter and drift measurements. In the following two section, this is discussed for the three possibilities for the phase-lock of the Ti:sapphire oscillator to the accelerator, being the

- RF-based synchronization to the master RF oscillator, where the reference signal is provided by the coaxial RF distribution system,
- RF-based synchronization to a signal generated from the optical reference pulse train, distributed to the laboratory via an actively stabilized fiber link,

and most importantly

- synchronization to an optical reference pulse with a PLL fed with the output signal of one optical cross-correlator.

For the last possibility, commonly referred to as "all-optical" or simply "optical" synchronization, a second cross-correlator is required for the out-of-loop measurement. In all measurements, the timing change is measured with respect to the optical reference pulse train.

7.2.1 RF-Based Synchronization

In a first series of measurements, shown as gray trace in Fig. 7.8, the timing drift has been measured over one hour, when the laser oscillator was synchronized to the master RF oscillator (MO) using the 1.3 GHz PLL described above.

After the calibration, the phase of the laser was set to measure the fluctuations of the cross-correlator signal around the zero-crossing, and data was taken with a rate of 0.1 Hz, with the result shown in Fig. 7.8. Similar to the other drift measurements, at every measurement step 2048 points

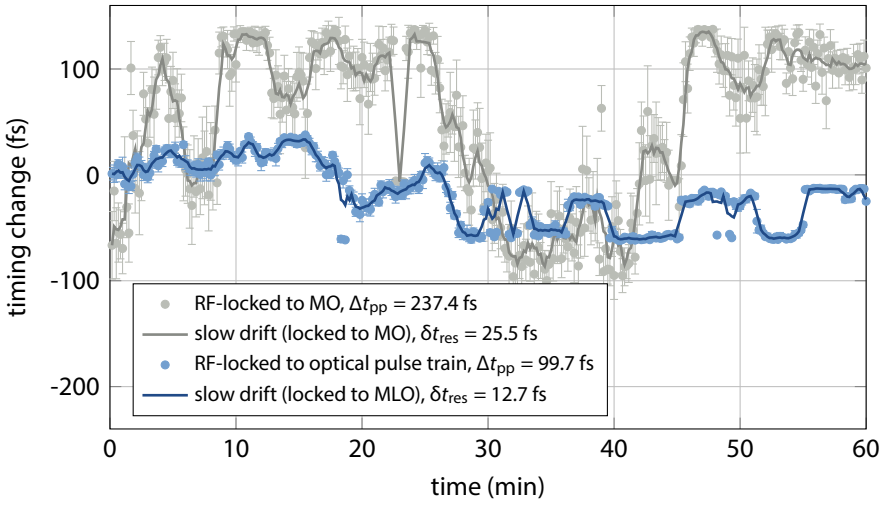

Figure 7.8 | Timing drift of the Ti:sapphire laser locked to the RF reference. Comparison of the timing drift over 1 hour of the RF-locked Ti:sapphire oscillator to the RF reference and to an RF signal generated from the optical pulse train, measured with an independent optical cross-correlator.

are sampled with an ADC integrated to the control system at a rate of 1 MHz. The errorbars in the figure represent the standard deviation of these digitized bursts. The slow drift, calculated from a 1-minute moving averaging, amounts to 237 fs peak-to-peak. By subtracting the slow drift from the data, a residual jitter of 25.5 fs rms has been determined. The jitter and in particular the observed drift seems to be mainly caused by the drift of the coaxial reference signal distribution and the phase distortions, for instance induced by electromagnetic interference. This can be seen from a consecutive measurement, where the reference signal is generated from the optical pulse train with a direct conversion circuit. The slow drift is reduced by almost a factor of 2.5 over the 1-hour measurement and amounts to 100 fs (peak-to-peak, shown in dark blue in the plot). Moreover, the residual jitter is also reduced by approximately a factor of 2 to 12.7 fs rms. Since the Ti:sapphire laser is in this case locked and measured against the same optical pulse train, this jitter is only made up from the jitter of the RF generation process, the PLL, the laser oscillator and the optical cross-correlator itself,

in which the latter can be neglected [DS10]. Hence, the RF-based synchronization scheme shows a sufficient performance on long timescales.

To evaluate the performance on short timescales, or high frequencies, the voltage spectral density of the cross-correlator signal at the zero-crossing has been measured with the signal source analyzer (SSA). Using the calibration constant, the timing jitter spectral density can be calculated and integrated in certain frequency intervals, as shown in Fig. 7.9. In the whole measurement range of

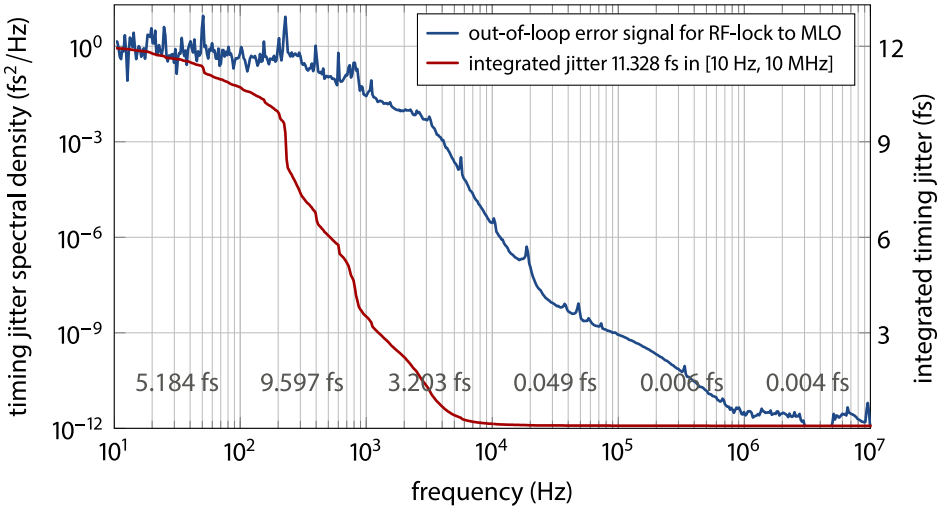

Figure 7.9 | Residual timing jitter of the RF-based synchronization circuit. The signal is obtained from the baseband spectrum of the optical cross-correlator output, and by this being an independent, out-of-loop measurement.

[10 Hz, 10 MHz], the integrated timing jitter of the complete synchronization scheme amounts to 11.3 fs rms, which is only slightly less than determined from the drift measurement. Therefore, it can be assumed that there are no significant contributions to the timing jitter for frequencies below 1 Hz. Rather, the main contribution to the integral is approximately the offset frequency range from 50 Hz to 4 kHz, as also the numbers in the individual decades suggest. Using this measurement method, the loop gains of the 1.3 GHz PLL could be improved, but a comparison with the best demonstrated timing jitter performance of this type of RF synchronization circuit of ~ 7 fs rms [Hac10] shows that this lower limit is also being approached here.

For completeness it should be mentioned that during the first measurement, the therein contributing timing jitter of the fiber link was on average 1.1 fs rms while the MLO was synchronized to the master RF oscillator with an average jitter of 28.3 fs (rms, data not shown, but comparable to Fig. 5.39 and Fig. 6.7 on pages 122 and 141, respectively).

7.2.2 All-Optical Synchronization

It is possible to lock the Ti:sapphire laser onto the zero-crossing of the cross-correlator signal. For this, the signal is fed into a second digital controller and using the variable combiner for the outputs of the regulations (see section 7.1, pages 153 ff.), their weighting is slowly moved from the RF-based PLL

to the cross-correlator loop. This is not automated up to now, as the reaction of the laser oscillator strongly depends on the error signal delivered by the cross-correlator, which in turn depends, for instance, on the phase- and amplitude noise of the reference pulse train (see section 6.3, pages 144 ff.). Rather, the lock can presently only be established for a couple of minutes. During those times, no systematic study and improvement of the loop gains had been possible[5]. However, it is possible to calibrate the second, out-of-loop cross-correlator and to measure the drift for the time the laser oscillator remains optically synchronized. In Fig. 7.10, the out-of-loop signal over a period of 12 min

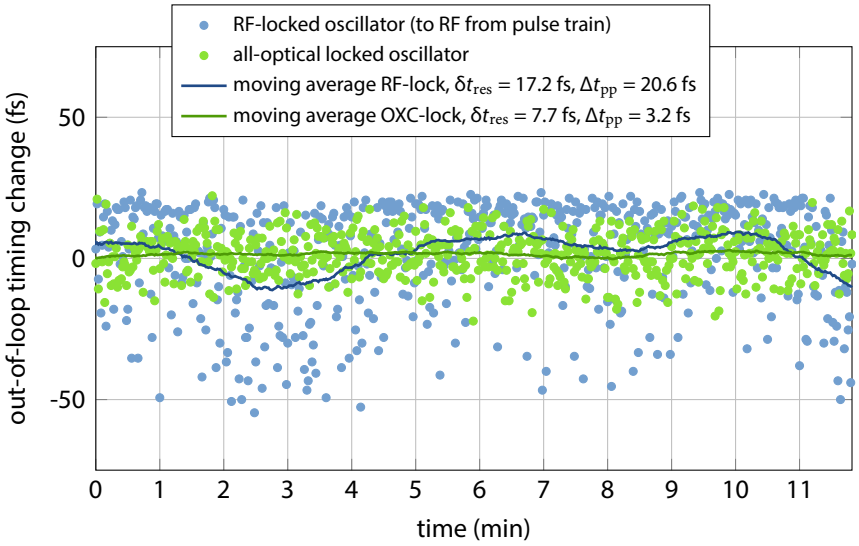

Figure 7.10 | Out-of-loop timing drift of an all-optically locked Ti:sapphire oscillator. Comparison of the Ti:sapphire laser locked to the reference pulse train by means of an RF-based PLL and an optical cross-correlator. The measurement is conducted with a second, out-of-loop cross-correlator. In the RF-based PLL, the reference signal is generated from the optical reference pulse train.

is shown (green dots[6]), together with the performance of the prior measured performance of the RF synchronization for comparison. The slow timing change, which amounts to $\Delta t_{pp} = 3.2$ fs peak-to-peak over the measured period, it can be seen, that the regulation loop based on the optical cross-correlator leads practically to a drift-free synchronization of the Ti:sapphire oscillator. In the same period, the RF-based phase-lock loop, which was measured before, exhibits a peak-to-peak timing change of 21 fs. The residual timing jitter for the optical synchronization is 7.7 fs rms, which is larger than expected, but nevertheless below the initially targeted 10 fs.

In analogy to the RF-based synchronization measurements, the voltage spectral density of the out-of-loop cross-correlator has been measured when the laser oscillator was locked with the first cross-correlator. The corresponding timing jitter spectral density and the integral in the offset frequency interval of $[10\,\text{Hz}, 10\,\text{MHz}]$ is shown in Fig. 7.11. The evaluation of the integral yields a residual timing jitter of the optical synchronization of 3.5 fs at the measured high frequencies. Most notable, the largest contribution to the integral is the broad peak around 9 kHz, which is caused by imperfect loop

[5] This issue is discussed in section 7.3 below.
[6] The data had been recorded with an oscilloscope in this measurement.

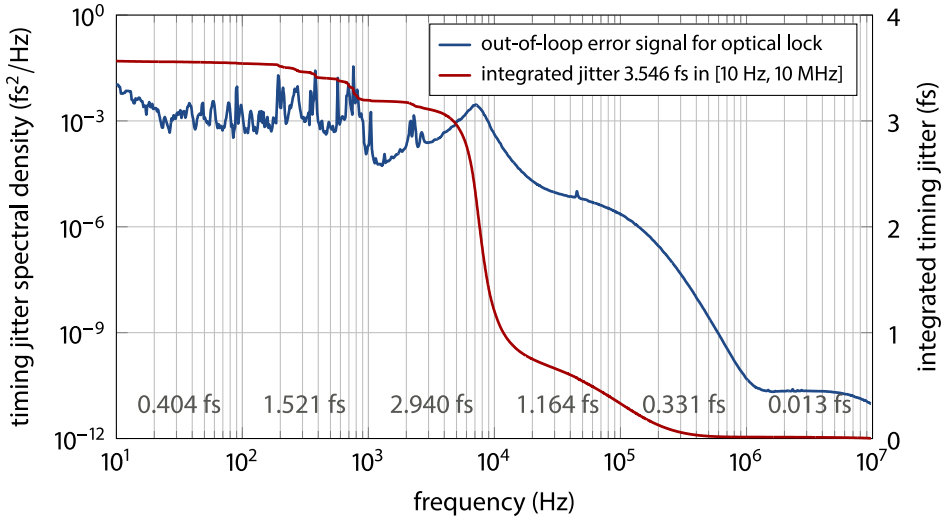

Figure 7.11 | High-frequency timing jitter of the PLL based on the optical cross-correlator. The signal is obtained from the independent, out-of-loop optical cross-correlation signal of the second device.

gains and most likely, the *P*-part of the PID-controller was set too high. With a careful optimization of the loop gains in further studies, together with the fact that the jitter spectral density at low frequencies is less in comparison to the RF-based PLL, a synchronization of the Ti:sapphire oscillator to the femtosecond level seems to be within reach.

7.3 Further Considerations

Until the optical lock can be established routinely, several further investigations are required. Some of them are discussed in this section.

It was found that the switch from the RF-based PLL to the optical error signal depends critically on the *P*, *I* and *D* gain parameters of the regulation loop. Initially, these parameters for the optical cross-correlator loop were chosen similar to those of the optical cross-correlators in the fiber link stabilization loops. However, they differ significantly in magnitude from the optimum values of the RF-based PLL for the given Ti:sapphire laser oscillator. Those were found experimentally to ensure the synchronization with the lowest possible timing jitter, as explained above. Hence, the cross-correlator loop gains have to be optimized in a trial-and-error process. Based on the settings of the fiber link gain values, they have to be adapted to the reaction of the Ti:sapphire laser. Once the phase-lock is established, a systematic improvement is difficult before the oscillator looses the lock, for example if for some reason its drift is too large compared to the relatively small dynamic range of the cross-correlator signal.

At this point, the fundamental difference of the cross-correlation scheme in the fiber link stabilization units and the synchronization of an individual Ti:sapphire laser should be emphasized. In the former case, the correlated pulses originate from the same pulse train, travel forth and back in

the fiber to the end station, and are correlated with fresh pulses of the same train. The timing drift and jitter they experience through their transit comparatively low (see Fig. 6.9, page 143). Due to this, the relative timing of the pulses traveled through the link and the reference pulses is stable and a cross-correlator signal can be detected for a couple of minutes after the loop has been opened before they drift out of the dynamic range. This makes it easy for the PLL to catch onto this signal and the fiber link stabilization scheme very robust.

In case of the individual oscillator, the timing of its pulse train with respect to the phase reference varies by a larger amount with a much larger jitter, resulting in a minuscule sum-frequency signal. Hence, a prior RF-based synchronization is required, with the difficulty to switch from one lock to another.

In this context, the actual implementation suffers from the amplitude noise observed in the fiber links, whose cause has not ultimately been found and extinguished up to now. Due to the AM-to-PM conversion in the photodiode, the induced phase noise in the RF signal generated from the reference pulse train negatively influences the performance of RF-based PLL and by this the initiation of the optical lock.

Although a successful synchronization of a Ti:sapphire laser to an optical reference has been reported in literature, see for instance [SKK+03, MSK+01], in many experimental setups used in the publications the laser systems were of similar type and located in the same laboratory with corresponding environmental stabilization. This results in similar conditions for the two laser systems as in the fiber link stabilization scheme. In case of the optical synchronization system, the laser oscillators to be locked and the optical reference are separated by several hundreds of meters and as a result, they experience different distortions, such as temperature or microphonics, leading to individual changes of their dynamics.

Moreover, several minor, but in principle uncritical problems and difficulties have been identified in the discussed experimental setup, such as electromagnetic interference (EMI) in the laboratory affecting the performance of the driver for the piezo element or trouble with the digital hardware. Additionally, other types of crystals and photodetectors must be investigated in terms of conversion efficiency and noise, as for instance a much larger SFG signal will allow for the use of photodiodes instead of the photo multiplier tubes, which in turn promises a better signal-to-noise ratio.

Nevertheless, the presented results suggest a successful integration of Ti:sapphire lasers into the optical synchronization system soon. It is also interesting to note that similar optical cross-correlators can be used to measure and probably stabilize the timing of a Ti:sapphire amplifier and its seed laser oscillator. More interestingly, this type of cross-correlator can be used for an important key experiment to determine the performance of the synchronization system, as it enables to measure the timing jitter of the pulse trains emitted by two individual Ti:sapphire oscillators, each optically locked to different fiber links. Finally, when the Ti:sapphire oscillator of the pump-probe laser system is synchronized to the optical reference, and together with the BAM-based arrival time feedback, the timing jitter between the X-ray pulse generated in the FEL and an optical laser pulse will be evaluated in a suitable pump-probe experiment.

This will be the figure-of-merit for future user experiments at FLASH.

8 Connection of the Photoinjector Laser

Stable X-ray pulse timing with low jitter of the electron bunches begins with the electron source of the accelerator, because changes in the longitudinal properties of the bunches in the beginning of the acceleration process affect the compression and finally the lasing performance of the FEL, and is especially critical in the case of linear compression when the third-harmonic cavity, ACC39, is used. The FLASH photoinjector, consisting of the laser system driving the photoemission process from the photocathode and the electron gun itself, has to be stabilized in a twofold way: first, the laser pulse arrival time on the photocathode and secondly, the RF phase of the gun's acceleration cavity. In the present planning of the arrival time feedback topology, it is destined to stabilize the latter using information from the bunch arrival time monitor upstream of the first magnetic chicane. The laser system will be synchronized to the master laser oscillator (MLO) by means of an optical cross-correlator, similar to the scheme described in the previous chapter for the Ti:sapphire lasers.

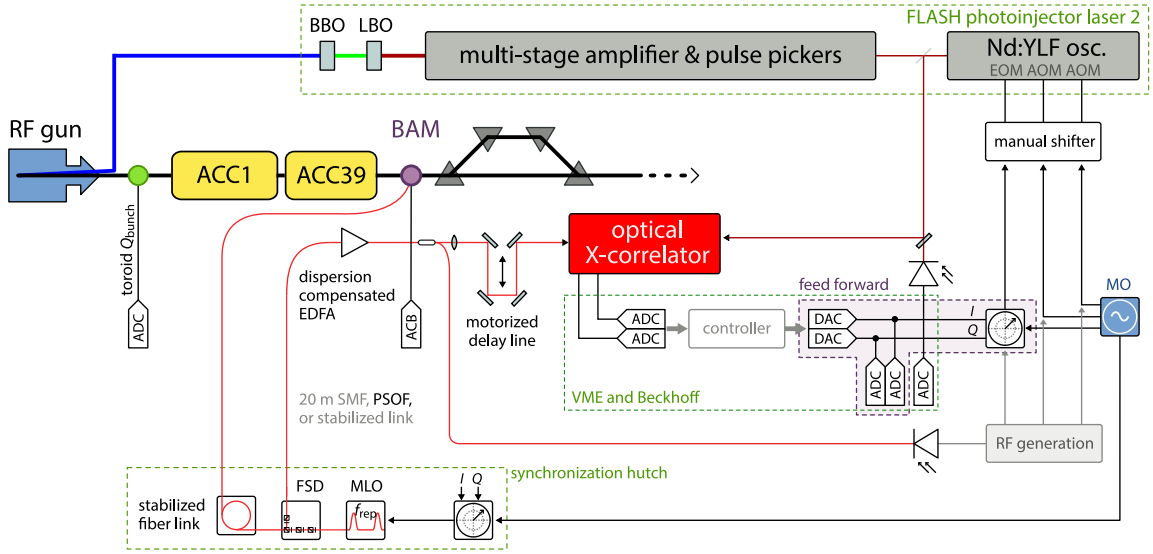

Figure 8.1 | Context for the optical cross-correlator for injector laser synchronization. The control signal is generated from the PTO and the MLO pulse trains and can be fed back to the phase of the RF driving the EOM inside the PTO's cavity. The electron bunch arrival time monitor upstream of the first magnetic chicane provides an independent measurement. The highlighted components –DACs, ADCs and the vector modulator– were installed first and allowed for a feed forward correction before the cross-correlator was available.

This chapter is devoted to the implementation and the characterization of such an optical cross-correlator, the investigation on the photoinjector laser performance and the influence of the electron

on the electron bunch arrival time. Figure 8.1 shows the connection of the optical cross-correlator (OXC) to the photoinjector laser system, the booster section of the accelerator up to the first magnetic chicane (compare Fig. 1.1, page 6) and the optical synchronization infrastructure. A small fraction of the oscillator's pulse train is tapped off, before the main fraction enters the amplifier chain with pulse pickers, the wavelength conversion stage and finally being send to the photocathode. The tapped part is guided to the OXC setup by means of free-space optics with a fixed delay line. The optical reference pulse train is delivered to the device via an optical fiber directly from the free-space distribution unit (FSD) in the synchronization hutch. The sum-frequency signals of the optical cross-correlator are sampled with standard ADCs installed in a VME crate. This crate will also run the feedback controller and thus has a DAC built in, which delivers the *I* and *Q* signals for the vector modulator, which in turn is used as phase and amplitude modulator for the RF signal driving an EOM inside the laser oscillator resonator. In order to investigate the relation between the laser pulse and the electron bunch arrival time, the BAM upstream of the first magnetic chicane has to be used, because at this point, the arrival time jitter is not influenced by the bunch compression process yet (see section 1.4, page 10 f.).

8.1 Photoinjector Laser System

The time structure (compare section 1.7, page 15) of the accelerator requires a special design of the laser system, which then defines the initial properties of the electron bunch such as its charge and pulse duration. In order to meet the specifications, the injector laser system is laid out in a master oscillator power amplifier (MOPA) configuration made of the following main building blocks:

- a diode-pumped, actively mode-locked laser, referred to as pulse train oscillator (PTO)
- an amplification stage with multiple fiber-coupled single- and double-pass amplifiers
- a wavelength conversion stage which converts the infrared radiation to the required ultraviolet region by two-tier second-harmonic generation (SHG) in LBO and BBO crystals.
- a beamline with corresponding imaging optics to the RF gun in the tunnel, featuring also a variable attenuator for the adjustment of the bunch charge and a spatial filtering of the intensity profile.

This allows for the generation of macro-pulses with the required 800 µs duration at 10 Hz bursts and up to ≈ 50 µJ energy of the ultraviolet pulse at a wavelength of 262 nm and a repetition rate of 1 MHz. The overall optical setup is depicted in Fig. 8.2. Since the pulse train oscillator is going to be stabilized to the optical reference, a basic description of only this part of the system is given here. More details on the complete laser can be found in [WKT05, SGK+06].

The PTO is a 10 Hz burst-mode oscillator with neodymium-doped yttrium lithium fluoride (YLF) as laser material, which allows for high single pulse energy in the order of 280 nJ. The repetition rate of the pulse train in each burst is 27.083 MHz, being the 48th sub-harmonic of the 1.3 GHz RF signal that drives the acceleration modules. Mode-locking is achieved actively with the use of two acousto-optic modulators (AOMs, see section 2.4.5 on pages 39 f.) and an electro-optic phase modulator

(EOM, see section 2.4.6 on pages 40 f.). The low-frequency AOM is driven at 13.542 MHz providing a gating of the pulses at the repetition rate of the oscillator of 27.083 MHz. The EOM is operated at 1.3 GHz and defines the synchronization to the accelerator's master RF oscillator (MO) and more importantly the arrival time of the laser pulses on the photocathode via its phase. This oscillator con-

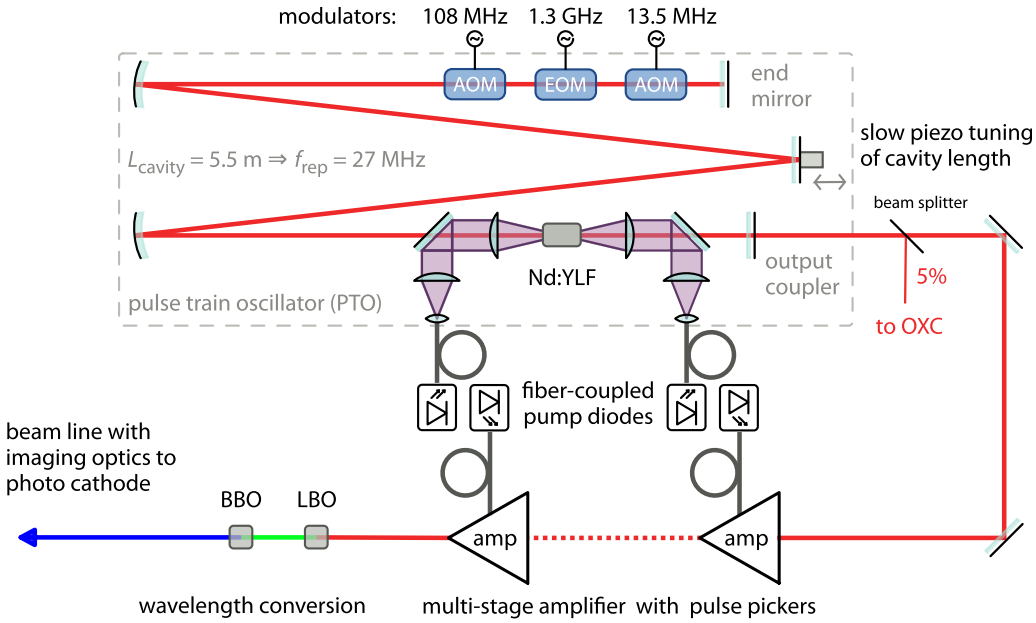

Figure 8.2 | Schematic layout of the optical setup of the photo injector laser system. It consists of the actively mode-locked pulse train oscillator with a slow piezo-based stabilization of the cavity length, the amplifier chain, the wavelength conversion stage and the beam line to the photo cathode in the electron gun.

figuration, however, is sensitive to alignment changes which can lead to the generation of unwanted pre- and post-pulses. To suppress this effect, the second AOM is driven at an intermediate frequency of 108.33 MHz also provided by the MO. The pulse duration of the individual Gauss ian-shaped pulses is in the order of τ_p = 6.5 ps rms or τ_{PTO} = 15 ps FWHM. Before this pulse train enters the amplification stage, approximately 5%, corresponding to $E_{PTO} \sim 14$ nJ is tapped of using a pellicle beamsplitter[1] and sent to the optical cross-correlator.

8.2 Two-Color, Picosecond-Pulse Optical Cross-Correlator

With the optical cross-correlator, the arrival time of the laser pulse train emitted by the PTO can be measured with respect to the optical reference – the master laser oscillator (MLO). The scheme and optical setup is also based on two-branch sum-frequency generation (SFG) in a single BBO crystal and very similar to the one used for the synchronization of Ti:sapphire laser systems described in

[1] Thorlabs BP108. Over time, it seems that the tension of the polymer foil degrades and therefore the beam splitter has to be replaced with a more robust one. At the time of the original installation, however, the then-introduced beam offset was not acceptable.

chapter 7 (pages 151 ff.). The main difference is the much longer pulse duration of approximately 15 ps generated by the PTO in contrast to the reference pulse, which is in the order of 300 fs, and its eight times lower repetition rate – only produced in bursts. This has considerable effects on the design of the device and the efficiency of the nonlinear process. Furthermore, it is assumed, that the amplification and wavelength conversion processes does not add jitter to the pulse arrival time, and this fact is important to remember when speaking of the laser pulse arrival time on the photocathode, because there might be unknown sources of jitter. To overcome this limitation, it should be possible to build an optical cross-correlator (probably based on difference-frequency generation, DFG), which can measure the timing of the ultraviolet pulse train even in a single-shot manner, but this is a future project not covered here. The implementation of the actual device is comparatively compact, given that a fiber amplifier for the reference pulse train and some electronic and RF circuits are additionally integrated. It is housed against stray light and installed next to the PTO on the optical table in the temperature stabilized laser hutch.

8.2.1 Principle of Operation

In Fig. 8.3 the optical setup and the beam propagation for the delay/subtraction detection with only one crystal is shown. The reference laser pulse train, with an average optical power of $P_{\mathrm{ref}} = 50\,\mathrm{mW}$, passes the first dichroic mirror, which reflects the PTO pulse train. Then the collinear beams pass a second dichroic mirror and are focused into the 5-mm-long type-$I^{(-)}$ phase-matched BBO crystal (see section 3.2, pages 48 ff.), where a sum-frequency component with a wavelength of $\lambda_{\mathrm{SFG}} = 626.5\,\mathrm{nm}$ and the lower repetition rate of $f_{\mathrm{SFG}} = f_{\mathrm{MLO}}/8 = 27.083\,\mathrm{MHz}$ is generated. All three pulse trains are collimated by a second lens and experience another dichroic mirror, which reflects the sum-frequency beam to the first detector. The fundamental pulses are separated by a fourth dichroic mirror. The optical path to the end mirrors for both pulses is set differently, such that the reflected

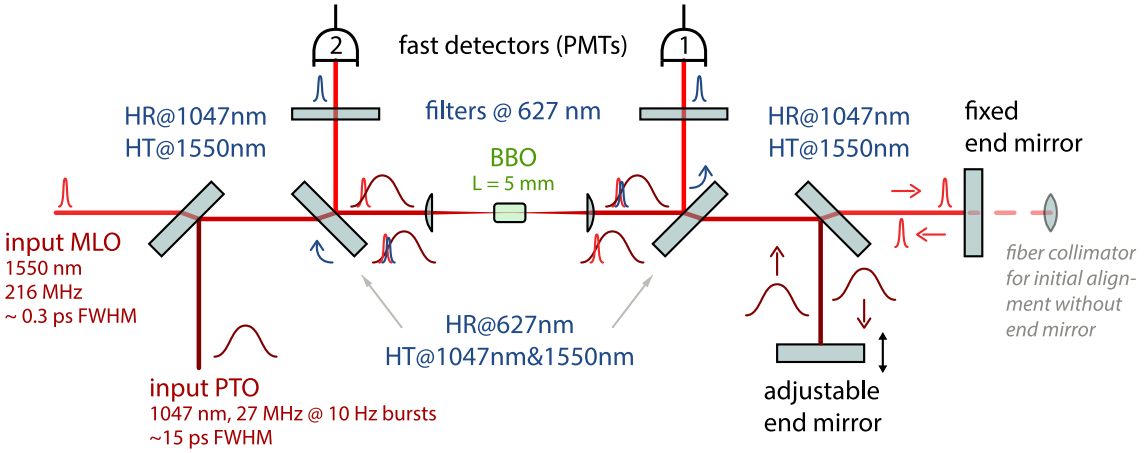

Figure 8.3 | Sketch of the beam path in the optical cross-correlator. The device is laid out for collinear interaction in a single crystal for forward and reflected pulses. The required group delay is applied by separation and recombination of the fundamental pulses and a different optical path length.

and recombined pulse trains ideally have the mutual delay of $\Delta t_{\mathrm{swap}} \equiv T_{\mathrm{opt}} = \sqrt{2 \cdot (\tau_{\mathrm{ref}}^2 + \tau_{\mathrm{PTO}}^2)}$, see Eq. 3.25 on page 56. When these pulses are again focused into the nonlinear crystal, the sum-frequency is generated on the opposite edge of the PTO pulses compared to the the first one and hence the maximum intensity is measured with a temporal shift of T_{opt}. This is done with the second detector after separating the sum-frequency light from the fundamentals with the second dichroic mirror the fundamental beams passed initially. As the intensity of the SFG signals is very weak, photomultiplier tube modules[2] (PMT) with integrated electronics and adjustable sensitivity are used for detection. In front of each detector an optical band-pass filter, based on interference, is placed. These types of filters have a typical transmission of 70% to 80%, thus lowering the weak SFG intensity further. The filters are however crucial, because in the BBO crystal, also the second-harmonic components at wavelength of 523.5 nm and 780 nm of both fundamental pulses are generated and would be detected by the sensitive PMTs. As the filters and the dichroic mirrors are not perfect, the detection of that light cannot be suppressed completely, which results in slightly different offset voltages of the SFG signals' baselines. This can be seen in Fig. 8.4, where a typical calibration curve is shown. The relative time delay of the fundamental pulses is varied by moving a motorized

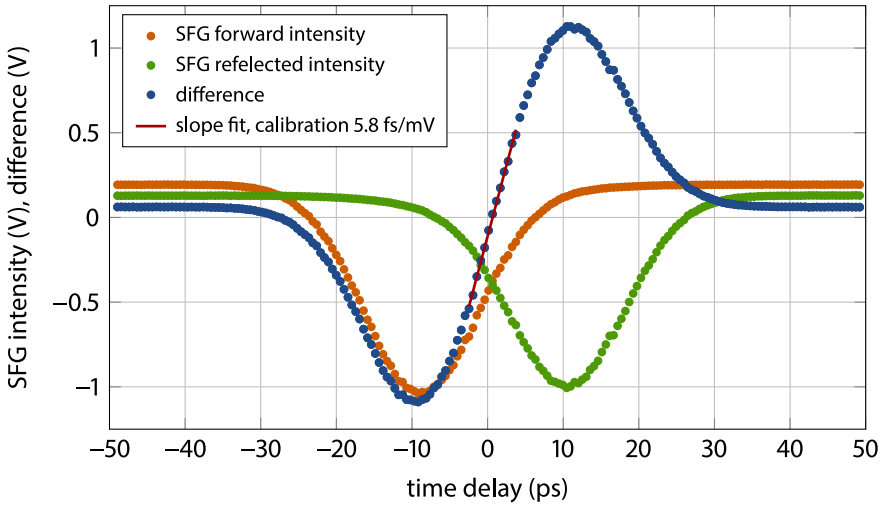

Figure 8.4 | Typical cross-correlator signals and calibration characteristics. The curves are obtained by scanning the motorized delay stage. The region around the zero-crossing of the difference signal gives approximately the dynamic range of the device.

delay stage and the SFG signals (green and orange in the plot) are recorded at the same time. When the pulse swap delay Δt_{swap} before the second sum-frequency generation is set correctly, the region of the difference $V_{\mathrm{OXC}} = V_{\mathrm{SFG},1} - V_{\mathrm{SFG},2}$ around the zero-crossing has a maximum slope $\partial V_{\mathrm{diff}}/\partial t$. In the figure, this is not exactly the case as the crossing of both SFG signals occurs at a voltage of −0.4 V, whereas the optimum would be −0.55 V. Thus, a slightly better resolution, expressed with a larger value of the calibration constant $K_{\mathrm{OXC}} = (\partial V_{\mathrm{diff}}/\partial t)|_{t=0}$, is possible. For an exact adjustment of Δt_{swap} and to compensate, for instance, changes by temperature drift or pulse duration change

[2] Hamamatsu H6780-20, see data sheet [Hamo7], similar to the ones used in the Ti:sapphire optical cross-correlator

of the PTO, it is foreseen to motorize the movable end mirror of the optical cross-correlator setup.

FROM THE EXPERIMENTER'S POINT OF VIEW THE INITIAL ALIGNMENT OF THE DEVICE IS NOT A TRIVIAL TASK, BECAUSE THE PTO PULSE TRAIN FLICKERS WITH IT'S 10 HZ BURSTS ON THE IR ALIGNMENT DISC, AND IT IS STRONGLY OUTSHINED BY THE CONTINUOUS REFERENCE PULSES, EVEN WHEN SET TO VERY LOW POWER AS THE USED CARDS ARE OPTIMIZED FOR THE OPTICAL C-BAND, I.E. THE 1550 NM SPECTRAL REGION. TO ESTABLISH TEMPORAL OVERLAP OF THE PULSES IN THE BBO XTAL, THE LAST DICHROIC MIRROR AND THE STRAIGHT END MIRROR HAVE TO BE REMOVED. THEN, THE COLLINEAR BEAMS CAN BOTH BE COUPLED INTO A FIBER WITH A COLLIMATOR. WHEN USING AN APPROPRIATE PHOTODIODE --HERE, AN INGAAS PHOTODIODE WITH A BANDWIDTH OF ~10 GHZ WAS USED. HOWEVER, THE SENSITIVITY OF INGAAS AT 1047 NANOMETER IS ABOUT A FACTOR OF FIVE LESS THAN AT 1560 NM. THIS IS LUCKILY COMPENSATED PARTLY BY THE HIGH PULSE ENERGY IN THE PTO TRAIN-- CONNECTED TO A FAST OSCILLOSCOPE THE RELATIVE DELAY OF THE PULSES CAN BE DETERMINED AND THEN ADJUSTED. IT SHOULD BE NOTED THAT A TRIGGER FROM THE MACHINE SHOULD BE USED, AS TRIGGERING TO ONE OF THE PULSE TRAINS CAN OBFUSCATE THE RELATIVE DELAY MEASUREMENT.

FURTHERMORE, A FIBER COLLIMATOR AT THIS LOCATION IS ALSO USEFUL FOR THE INITIAL GEOMETRIC ALIGNMENT OF THE COLLINEAR PROPAGATION: WHEN THE BEAM COMBINING DICHOIC MIRROR (OR ANOTHER MIRROR WHICH IS ALREADY REFLECTING BOTH BEAMS) IS SLIGHTLY MANIPULATED, THE EFFICIENCY OF THE COUPLING INTO THE FIBER MUST WORSEN OR IMPROVE FOR BOTH BEAMS AT THE SAME TIME. IF IT IS OBSERVED THAT THE INTENSITY OF ONE OF THE PULSES ON THE OSCILLOSCOPE INCREASES WHILE THE OTHER ONE DECREASES, THE BEAMS HAVE A MUTUAL ANGLE AND DO NOT TRAVEL COLLINEAR ON THE OPTIC AXIS OF THE CROSS-CORRELATOR. ADDITIONALLY IT SHOULD BE NOTED THAT THE RELATIVE TIMING CAN ONLY BE DET WHEN THE REFERENCE PHASE FOR THE MLO WITH RESPECT TO THE RF OSCILLATOR ("THE MACHINE") HAD ALREADY BEEN SET WITH ONE BAM, AS EXPLAINED BEFORE. THEN, A FIXED DELAY MUST ONLY BE INSTALLED ONCE, AND A SHORT ODL IS SUFFICIENT FOR CALIBRATION AND COMPENSATION OF POSSIBLE DRIFTS OF THE PHOTOINJECTOR LASER

8.2.2 Electronics Integration

The implementation of the device does not only consist of the optical cross-correlator optics, but also several opto-electronic and electronic components, which are connected digitizing hardware, as schematically shown in Fig. 8.5. The PTO pulses pass a combination of a half-wave retarder and a polarizing beam cube (PBC) before they enter the cross-correlator. A tapped-off fraction of the light is coupled into a fiber collimator, which is connected to a standard amplitude monitoring circuit, as already used in previously described setups.

Similarly, the reference laser pulse train from the fiber collimator of the link is also splitted by a retarder/polarizing beam cube combination. For this, the elliptically polarized light coming from the collimator has to be linearly polarized, which is realized with a quarter- and a consecutive half-wave retarder, both of which are motorized and adjustable through the control system. Approximately 10 mW of the average optical power is transmitted through the beam cube, coupled back into a fiber and split in the ratio of 80/20. The lower power fraction of 1.2 mW is used for optical power detection.

The efficiency of the fiber coupling is only about 60%, because no imaging optics is used. Together

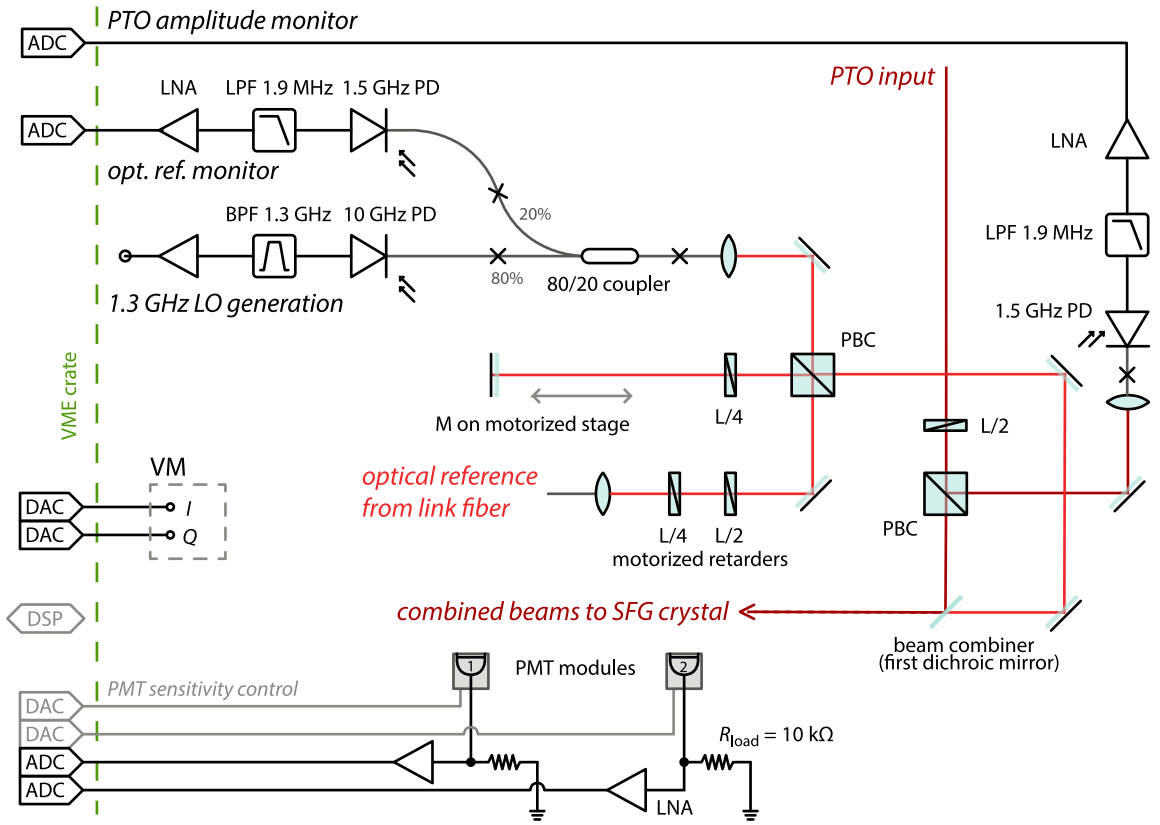

Figure 8.5 | Optical and electrical components of the OXC setup. In addition to the photomultiplier tubes (shown in the principle of operation, Fig. 8.3, page 170), their amplifiers, the optical power monitors and the 1.3 GHz RF generation are all integrated into the housing of the device.

with the motorized retarders, this allows for the setup of a simple 2-point control loop for optical power stabilization (see section A.5 on page 212 f. in the appendix). The remaining optical power of ~ 4.8 mW at the fiber coupler is guided to a photodiode with a bandwidth of 10 GHz to generate an 1.3 GHz local oscillator (LO) signal. When the LO signal would be used to drive the EOM inside the PTO, the arrival time of its laser pulse train is defined by the master laser oscillator and not by the master RF oscillator, which is an option for future operation. The main fraction of the reference pulse train is reflected by the first PBC passes a quarter-wave retarder. After reflection from a mirror mounted on a remote-controllable motorized delay stage, the beam passes the quarter-retarder again. For the correct setting of the retarder, the linear polarization state of the light is rotated by $\pi/2$ and thus it is transmitted through the beam cube and is combined with the PTO pulse train by the first dichroic mirror as described above. From the originally measured 80 mW of optical power around 50 mW are available in front of the BBO crystal due to the amplitude monitor, the LO generation, and losses from the various optical components.

The photomultiplier tubes (PMTs) for the detection of the sum-frequency signals have the high-

voltage (HV) generation integrated. The gain is adjustable from ~ 10^2 to ~ 10^5 by means of an externally applied control voltage V_c from 0.2 V to 0.9 V. At present, this voltage can varied with a potentiometer in a simple analog circuit. It is set to ≃ 0.25 V such that the SFG intensities do not saturate the ADCs after amplification with a low-noise DC LNA while using the complete (negative) range from 0 V to −1.1 V. It would be possible to directly provide the control voltage by two DAC channels, which would then enable the remote control of the sensitivity of the PMTs, for example to increase the slope of the difference signal at its zero-crossing. On the other hand, the resolution of the cross-correlator is defined by the SNR, and it was found that this worsens for large gain settings of the PMTs. Another relevant parameter limiting the resolution is the optical power of the reference laser pulse train. Up to now, the laser diode driver of the required EDFA can not be remotely controlled, as the transport of the DC current from the VME-based driver to the pump laser diode requires a cable length of 20 m, because the VME crate is installed in the laboratory in the next room. After solving this with a closely installed laser diode driver, the integration to the control system would enable further studies on the optical power dependence of the cross-correlation signal.

8.2.3 Optical Link to the Master Laser Oscillator

In the present state, depicted in Fig. 8.6, the reference laser pulse train from the master laser oscillator is transported to the injector laser hutch through a 20 m long special single-mode phase-stable optical fiber (PSOF), which exhibits a very low phase drift with temperature and humidity changes. It is connected to a fiber collimator inside the free-space distribution unit (FSD). The average optical power at the patch cord's end is 4.5 mW. In order to achieve a higher pulse energy for the SFG process, an erbium-doped fiber amplifier (EDFA) has also been integrated into the housing of the cross-correlator. With the use of 68 cm Er110/4-125 gain fiber (see section D.3, page 243 ff. in the

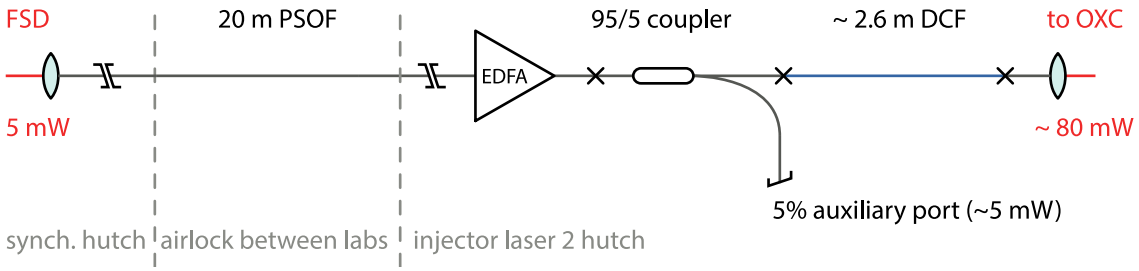

Figure 8.6 | Schematics of the fiber link from the FSD to the injector laser optical cross-correlator. It consistss of 20 m special phase-stable optical fiber (PSOF), dispersion compensating fiber (DCF), and fiber amplifier (EDFA) to provide an average optical power of approximately 80 mW for the amplitude monitor, LO generation and the optical cross-correlator.

appendix) the average power is boosted to 100 mW when the pump laser diode is operated at 0.8 A, which corresponds to 415 mW pump power. A fiber coupler with the splitting ratio 95%/5% provides a 5 mW auxiliary port for monitoring purposes or further developments or additional diagnostics. The high-power port of the coupler is spliced to the SMF pigtail of a dispersion-compensating fiber (DCF) module (see appendix D.2, page 242). The required length of the DCF has been determined

experimentally using the EDFL master laser oscillator: As the pulse duration of $\tau_{\mathrm{EDFL}} = 163.4\,\mathrm{fs}$ at the port of the FSD is known (see section 5.5.1, pages 109 ff.), the DCF could be cut away in small pieces at the end of the link while at the same time observing the pulse duration with an autocorrelator until the minimum pulse duration is reached. In case of the EDFL, this is $\tau_{\mathrm{EDFL}\rightarrow\mathrm{OXC}} = 220.1\,\mathrm{fs}$, whereas the initially longer pulses from the Origami laser are measured to have a duration of $\tau_{\mathrm{ref}} \equiv \tau_{\mathrm{Origami}\rightarrow\mathrm{OXC}} = 284.9\,\mathrm{fs}$ (see Fig. 8.7, left plot). The figure shows in the right plot the optical spectrum

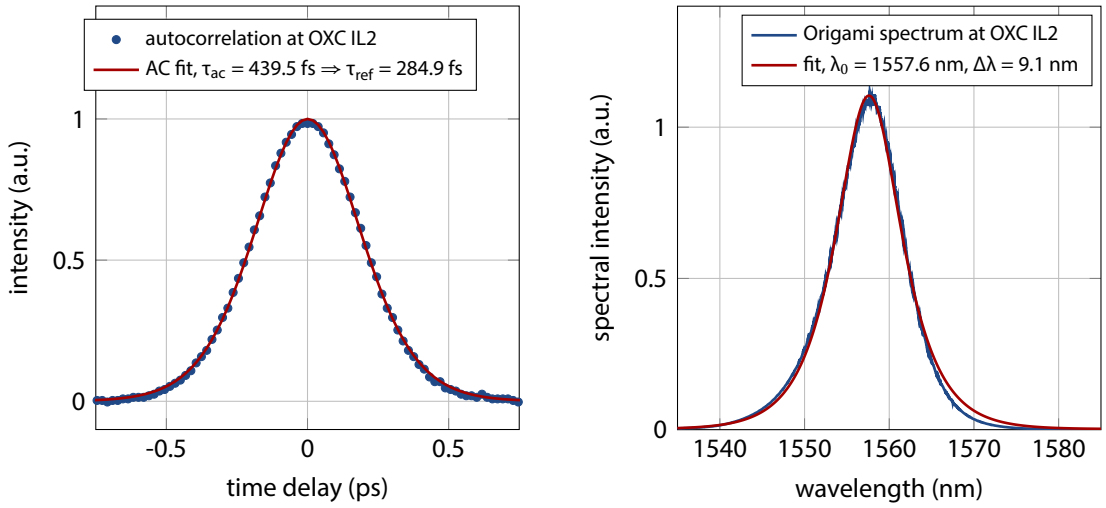

Figure 8.7 | Intensity autocorrelation and optical spectrum of the reference pulses at the OXC. The autocorrelation trace (**left**) and optical spectrum (**right**) of the reference laser pulses measured after amplification and dispersion compensation.

measured at the auxiliary port of the coupler, hence after strong amplification in a gain fiber with a small core diameter. The spectrum has narrowed to $\Delta\lambda = 9.1\,\mathrm{nm}$ (FWHM) from the 12.4 nm (compare Fig. 5.23, page 98) of the launched Origami pulse. Furthermore, a slight asymmetry of the spectral wings can be observed, which might result from nonlinear effects like self-phase modulation (SPM) in the gain fiber. Nevertheless, the time-bandwidth product (TBP) of $\Delta\nu \cdot \tau_{\mathrm{Origami}\rightarrow\mathrm{OXC}} = 0.32$, where $\Delta\nu = \Delta\lambda \cdot c_0/\lambda^2$, agrees surprisingly good with the one determined directly from the Origami oscillator pulse.

Obviously, the used simple fiber connection to the MLO is prone to drifts, mainly caused by temperature and humidity changes. However, the fiber cable is installed in a tube, which runs from the optical table in the synchronization hutch through the laser safety airlock and the hutch of the old injector laser to the optical cross-correlator. By that, it is supposed that the fiber is not exposed to large temperature changes, because all laboratories are air-conditioned. In a future upgrade, the patch cord will be replaced by an actively length-stabilized link. Because of the short length, an RF-based phase detection scheme can be applied in this link, which has proven to achieve accuracies well below 5 fs (see [ZAB+09, Lam11]), while being significantly cheaper than the cross-correlator based fiber link units.

8.3 Control System Integration

Nearly all read-back values provided by the optical cross-correlator and its controls are accessible through the accelerator's control system (DOOCS). Since the device is still an experiment under construction, rather than a standard diagnostics tool, only an "expert panel" for the graphical user interface DOOCS data display (DDD) is provided at the moment and a screenshot is shown in Fig. 8.8. It displays the raw sum-frequency detector signals over 2048 µs, beginning 700 µs before the laser

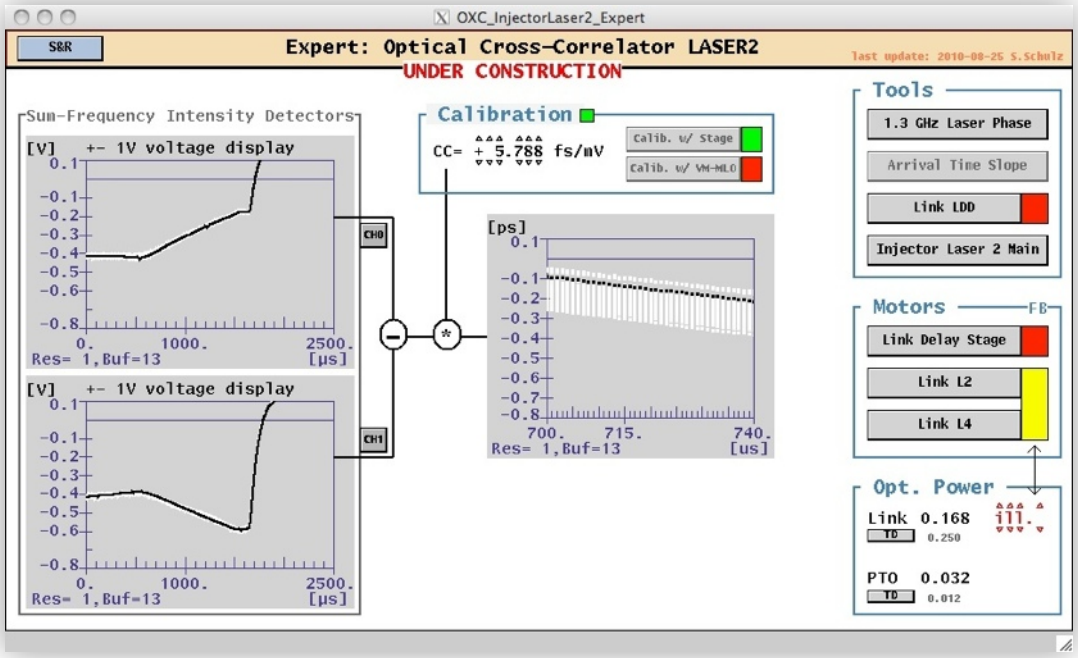

Figure 8.8 | Screenshot of the DOOCS expert panel for the cross-correlator. The panel, which is presently under development, provides an overview of the most important data and the access to various tools and other related panels.

pulse, which will actually generate the first electron bunch. By this, almost the complete burst of the PTO pulse train is covered, and the time before the generation of the first electron bunch can be used for adaptive feed forward or feedback purposes. The graph in the center of the panel shows the laser pulse arrival time with respect to the optical reference as the difference of the SFG intensities multiplied with the calibration constant, i. e. $t_{\mathrm{PTO}}^{(\mathrm{arr})} = V_{\mathrm{OXC}} \cdot (K_{\mathrm{OXC}})^{-1}$. In order to provide this information, currently a DOOCS server software of a BPM is used, because there is no dedicated server for optical cross-correlators available yet. Hence, the device is controlled additionally by a number of MatLab scripts, which, for instance, determine the calibration constant either by moving the motorized delay stage (see Fig. 8.4) or by scanning the phase of the master laser oscillator RF lock (see section 5.3, pages 87 ff.). The latter one, although being much faster, is usually not possible, because it would shift the timing of the complete optical synchronization system and, for example, the BAMs

can not measure the electron bunch arrival time during the calibration of this OXC. Furthermore, the panel allows the access to the motors, and more importantly establishing motor feedback loops to keep the optical cross-correlator within its dynamic range by moving the translation stage accordingly, and to stabilize the optical power of the reference laser pulse train (see appendix A.5, page 212). The planned DOOCS server will combine all this functionality, in addition to a regular calibration and the aforementioned adaptive feed forward and/or feedback loop. It will first run on a DSP in the same VME crate, similar to the control loop used for the RF lock of the master laser oscillators, and eventually on a MTCA.4 crate[3] with advanced hardware allowing for single-shot signal processing.

For feed forward correction of the amplitude and the phase of the RF signal, which drives the EOM inside the laser resonator via the vector modulator, a DOOCS server has already been implemented. This allows in particular for the application of a phase slope $\partial\varphi_{\mathrm{EOM}}/\partial t$ across the laser macro-pulse, which translates into an arrival time change of the pulses on the photocathode. The server does a linear interpolation between six sample points $\big(t_i, (A_i, \varphi_i)\big)$ and calculates the corresponding DAC output voltages $V_I(t_i) = A_i \cos\varphi_i$ and $V_Q(t_i) = A_i \sin\varphi_i$ of the I and Q channels for the vector modulator. The output voltage of the DAC, which is actually applied only when the corresponding button is pressed on the expert panel, is monitored using two channels of an ADC to cross-check the correct write of the calculated table to the DAC's memory. The timing of the DAC and ADC is shown schematically in Fig. 8.9, with a positive slope across the macro-pulse as an example. A screenshot of the actual expert panel is depicted in Fig. 8.10 where the graphs show the DAC

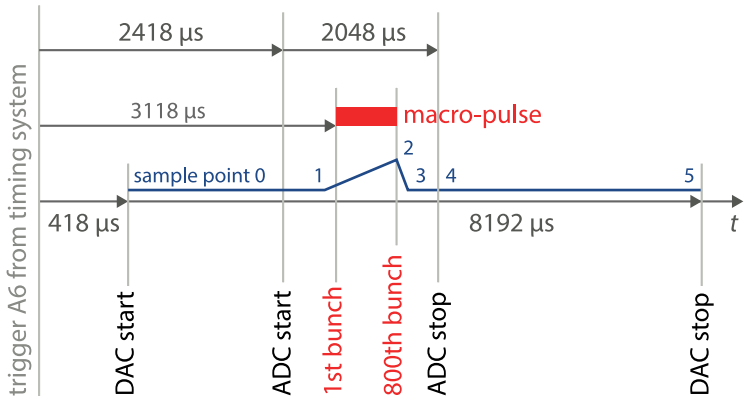

Figure 8.9 | Timing of the vector modulator phase and amplitude control. The DAC starts triggered 2000 µs before the readback ADC with its lower number of sample points. For the shown example, only five sample points are required to generate the slope. A step would, for instance, require all six available points (compare Figure 8.10).

setpoint (SP) and the ADC read back value (RBV) tables for the both channels. Below the graphs, the six amplitude and phase sample points can be configured. Here, a negative slope is applied to the phase, beginning with node 1 at a sample point 200 µs before the first electron-generating laser pulse at $t_2 = 2700$ µs. The slope ends at $t_3 = 3500$ µs and is ramped down to the original value within

[3] http://mtca.desy.de

another 900 µs. With this timing configuration, the phase slope across the macro-pulse can conveniently be stated in units of deg/ms. For this, also a MATLAB-based graphical user interface (GUI) is available for machine operators, which calculates and sets the correct sample points and values for an arbitrary slope. More complicated patterns and particularly a step (within 1 µs) are possible for

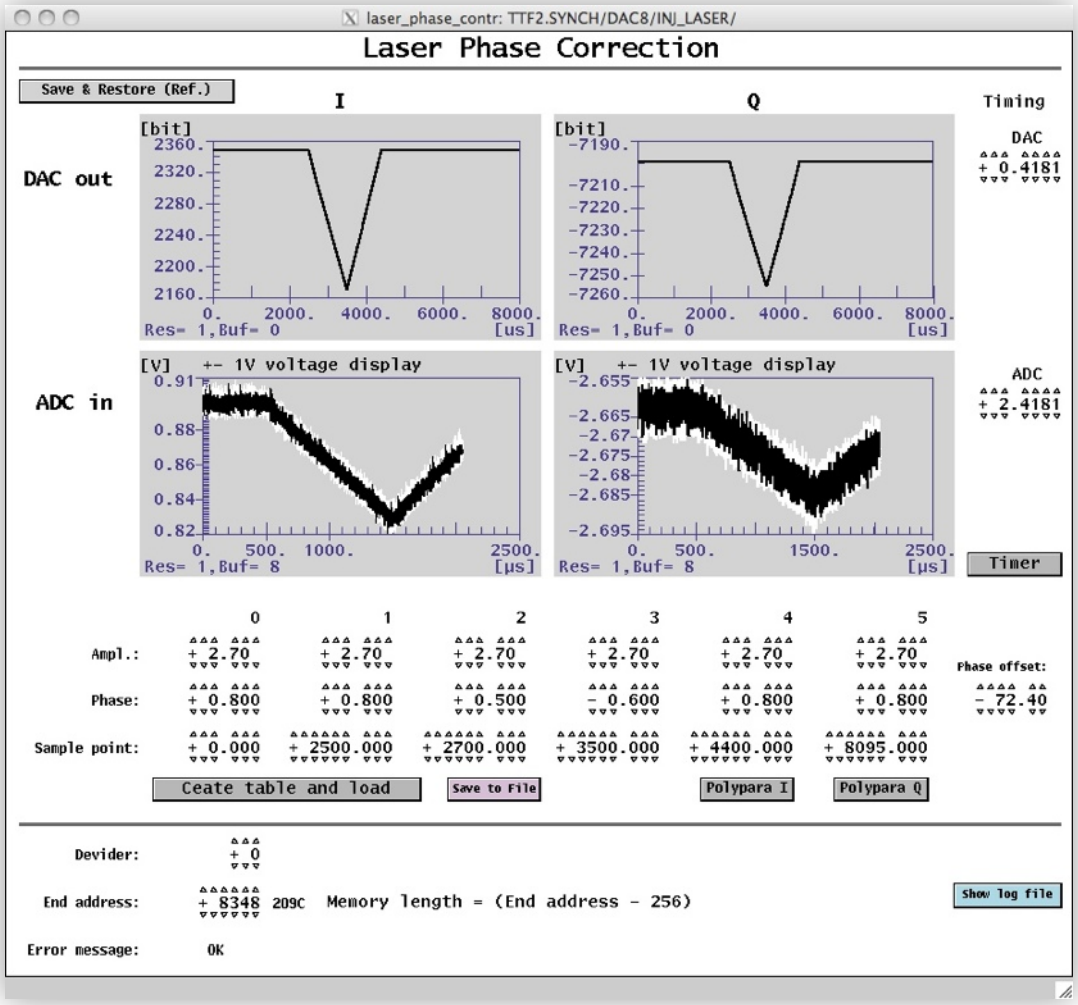

Figure 8.10 | Screenshot of the DOOCS expert panel for the photoinjector laser phase setting. Beside a single-valued phase setpoint, the server allows for setting arbitrary phase and amplitude values at arbitrary sample points. This can be used to create a phase slope, as shown, which translates into an arrival time change of the laser pulses.

systematic studies and system identification. Furthermore, the server allows for the setting of a total phase offset φ_{laser}, which is not only required for the commissioning the vector modulator in order to set the correct phase for the EOM as before, but also as a parameter for specific measurements. It should be noted that same type of server is used to generate the phase step of the 108 MHz signal for the synchronization of the master laser oscillators.

8.4 Laser Pulse Duration Measurements

The optical cross-correlator is a natural choice for the determination of the PTO's pulse duration, as a much shorter reference pulse to sample it is available (see section 3.5, pages 55 ff.). From the calibration routine, which scans the relative time delay of both pulses while recording the SFG signals, the pulse duration can directly be retrieved. The left panel of Fig. 8.11 shows the data from the calibra-

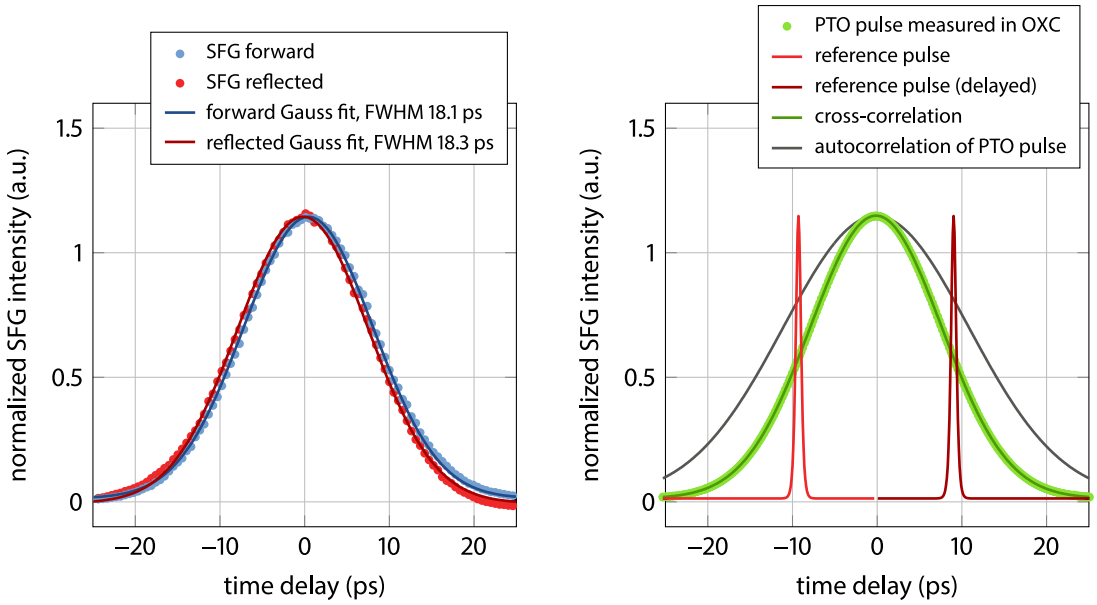

Figure 8.11 | Pulse duration of the photoinjector laser oscillator. The pulse duration is determined from the cross-correlation with the reference pulse in both arms of the device (**left**). A deconvolution is not applied as the reference pulse is much shorter as can be seen from the calculated shapes (**right**).

tion timing scan (Fig. 8.4, p. 171) scaled and centered. From Gaussian fits a FWHM pulse duration of $\tau_{\mathrm{PTO}} = (18.2 \pm 0.1)\,\mathrm{ps}$ is determined, corresponding to $\tau_{\mathrm{p}} = 7.7\,\mathrm{ps}$ rms. A deconvolution of the PTO pulse and the reference pulse is not required, as the comparison of a calculated Gaussian pulse (with $\tau_{\mathrm{PTO}} = 18.2\,\mathrm{ps}$, green dots in the right panel of the figure) and the intensity cross-correlation of this pulse and a reference pulse with $\tau_{\mathrm{ref}} = 284\,\mathrm{fs}$ FWHM shows. To illustrate the ratio the pulse durations, the reference pulse is shown twice with a temporal shift of $\pm\,\tau_{\mathrm{XC}}/2$. These are the actual temporal positions where the sum-frequency is generated for the forward traveling and the reflected pulses during the normal operation of the optical cross-correlator. The result for the PTO pulse duration is comparable to measurements using a streak camera [KT10] which reported 22.6 ps FWHM. However, it must be noted that in those measurements the ultraviolet, i.e. frequency up-converted pulse had been investigated. A direct comparison is only possible, when a cross-correlation of the UV- and the reference laser pulse train is available. This would then also allow for investigations on the influence of the amplification and wavelength conversion process not only on the pulse duration, but even more importantly on the timing drift and jitter of the pulse train guided to the photocathode as it will be discussed in section 8.5.3, pages 186 ff. below.

8.5 Arrival Time Measurements

Before the optical cross-correlator will be used to actively stabilize the photoinjector laser pulse arrival time, several pre-studies had been carried out. In addition, the influence of the laser on the electron bunch arrival time can be investigated using the bunch arrival time monitor (BAM "1UBC2", see also Fig. 4.2, page 62) upstream of the first magnetic chicane. The influence of the electron gun can be investigated using specific emission phase settings, as discussed in section 1.6.2 on page 14.

8.5.1 Pulse Train Oscillator

To determine the stability of the pulse train oscillator, the arrival time from the cross-correlator has

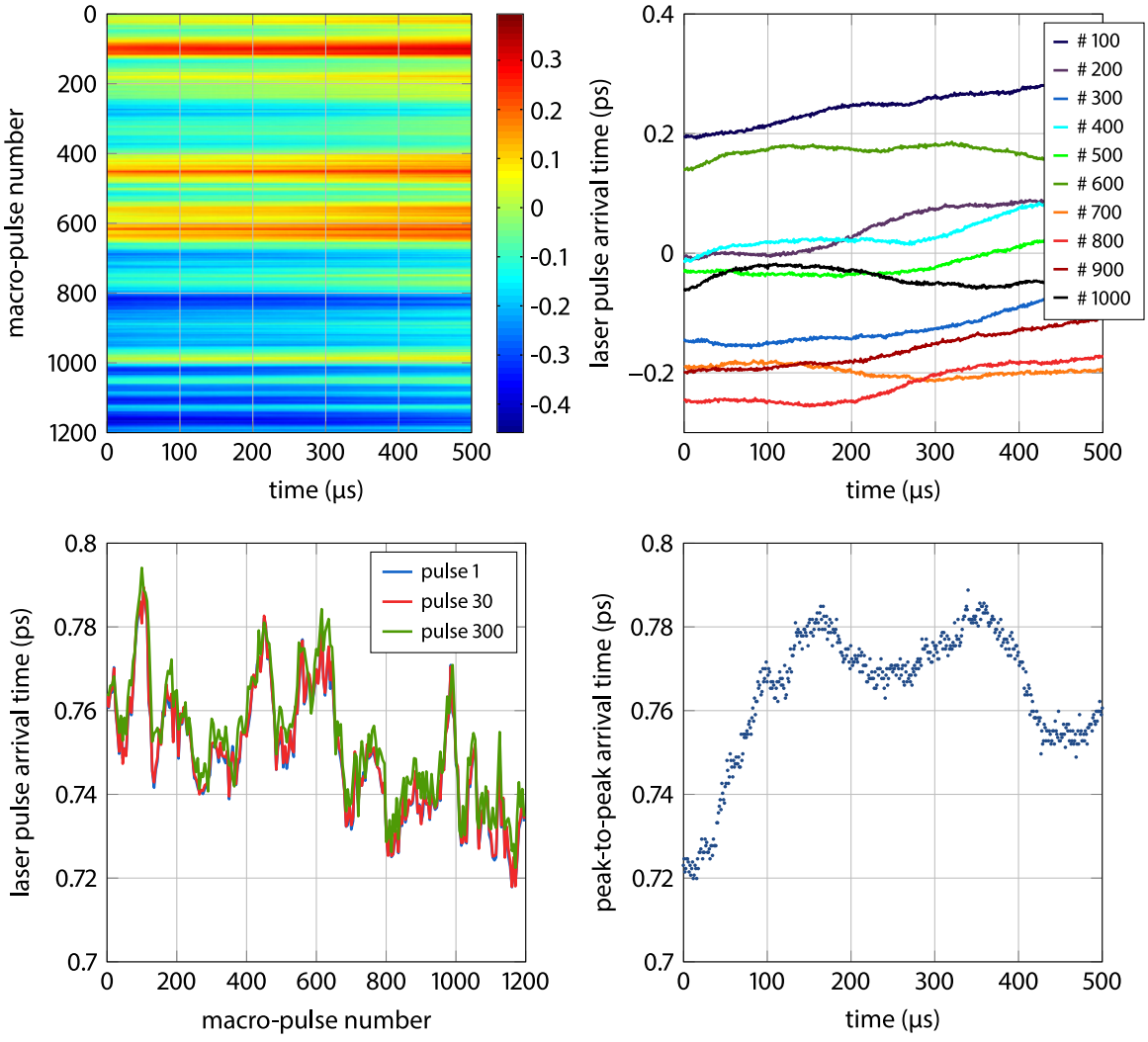

Figure 8.12 | Laser pulse arrival time of 1200 consecutive bursts. From the two-dimensional (**top left**) data the arrival time of every 100th burst (**top right**), the variation of particular pulses (**bottom left**) and the maximum change across the burst (**bottom right**) is extracted.

been recorded for 1200 subsequent bursts ("macro-pulses") with a rate of 10 Hz. The upper left plot of Fig. 8.12 is a two-dimensional representation of the arrival times shown by different colors. The trigger was set such that the laser pulse with the index 0 is actually the first one generating an electron bunch after amplification and wavelength conversion. From the regular line structure of the picture, it can be concluded that the laser pulse arrival time is relatively constant across one individual pulse train, which can also be seen in the upper right plot of the figure where the arrival time of every 100th train is shown. However, the absolute arrival time of the complete train changes within a range of (750 ± 30) fs, which can be seen in the lower part of the figure. The left plot shows the arrival time variation of the first pulse, the 30th and the 300th. These are the timings of the first electron bunch, the 30th electron bunch at 1 MHz operation and the 30th electron bunch at 100 kHz operation – which are often used at FLASH. There is hardly a difference observable between the traces, but the peak-to-peak variation is relatively large with very fasts variations in the order of 400 fs, for example around the shot number 100, 700 and 1000. The peak-to-peak variation of the arrival time within the 1200 trains of all 500 pulses is shown in the lower right plot. The first pulses changes less, but only by approximately 40 fs or ~ 5%.

This leads to the conclusion, that only the intra-train stability of the oscillator is very good and this is confirmed, when the repetitive error from all 1200 macropulses is calculated by subtracting the mean arrival time offset of each train.

The blue dots shown in Fig. 8.13 represent the arrival time of all measured macropulses normalized to the average arrival time, which enables the calculation of a mean arrival time of every single pulse. The rms variation of the repetitive error amounts to 3.5 fs across the 500 µs long observed

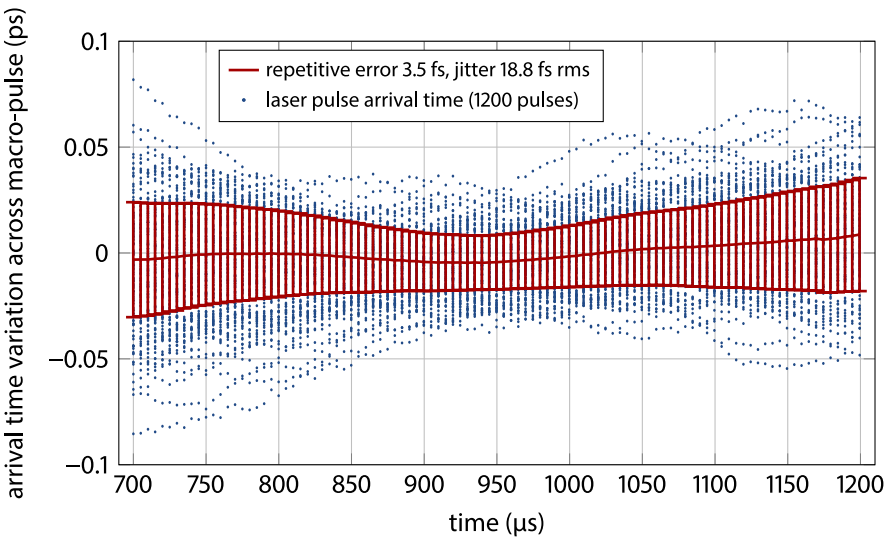

Figure 8.13 | Repetitive error and jitter of the PTO burst arrival time over a period of 2 minutes. Data was acquired at a rate of 10 Hz, i.e. 1200 macro-pulses and is shown after removal of the mean offset variation. The plot shows a 500-µs-long cut-out of the burst, starting with the one which actually generates an alectron bunch.

pulse train. The jitter of the individual pulses, shown as error bars, is larger at the beginning and the end of the pulse train. Until now, the cause of this "bow tie"-like pattern has not been found. How-

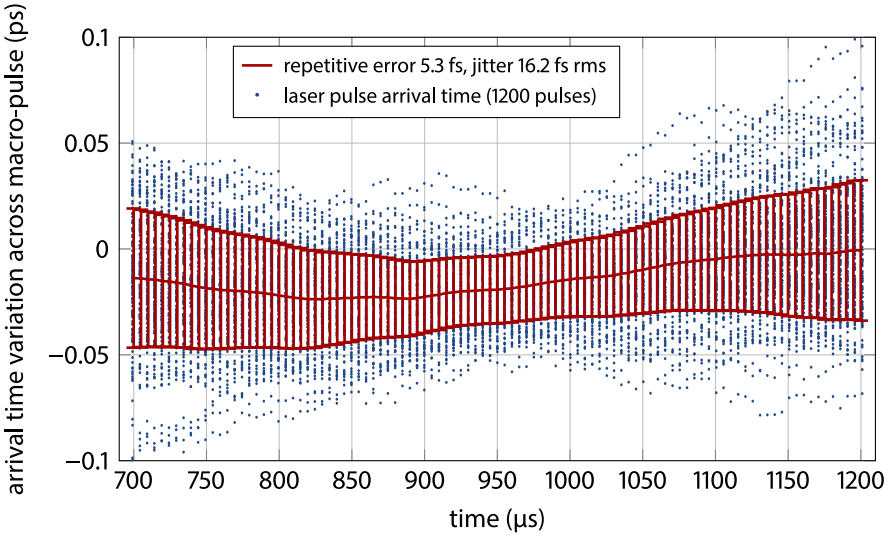

Figure 8.14 | Repetitive error and jitter of the PTO burst arrival time over a period of 3.3 hours. Data was acquired at a rate of 0.1 Hz, while processing and analysis is analog to the data shown in Figure 8.13.

ever, the mean of the jitter value amounts only to 18.7 fs, and shows the tight synchronization of the PTO to the accelerator's RF oscillator on the measured 2-minute time scale. When the measurement is repeated with 1200 macropulses and a data recording rate of 1 Hz, corresponding to 20 min, a repetitive error of 11.1 fs and a pulse-to-pulse jitter of 16.6 fs rms have been found (plot not shown), with a similar pattern of the arrival time distribution. Almost the same value for the jitter, 16.2 fs rms, has been determined from a measurement over a period of 3.3 h, which has been carried out again with 1200 macropulse, but with a data recording rate of 0.1 Hz (Fig. 8.14). The offset-removed repetitive error was found to be 5.3 fs and by that not significantly larger than the 100 times shorter period shown before. From the more than twice as large repetitive error in the 20 min measurement the conclusion might be drawn, that there are fluctuations on the second time-scale, which are not seen in the longest measurement due to the much slower sampling rate. Nevertheless, the timing drift and jitter of the PTO, in particular with respect to the optical reference, is very low and hence will hardly influence the correlation measurements using the optical cross-correlator and the first bunch arrival time monitor.

8.5.2 Gun-Based Arrival Time Measurements

Before the optical cross-correlator and the electron bunch arrival time monitor upstream of the first chicane were operational, the relative timing of the photo injector laser pulses and the RF gun phase, an indirect technique has been used. It is based on the dependence of the emitted electron bunch charge on the operation phase of the accelerating RF fed into the gun, which is shown in Fig. 8.15.

When the electrical field gradient at the photocathode is decelerating ($\varphi_{\text{gun}} > 0\,\text{deg}$) at the time the

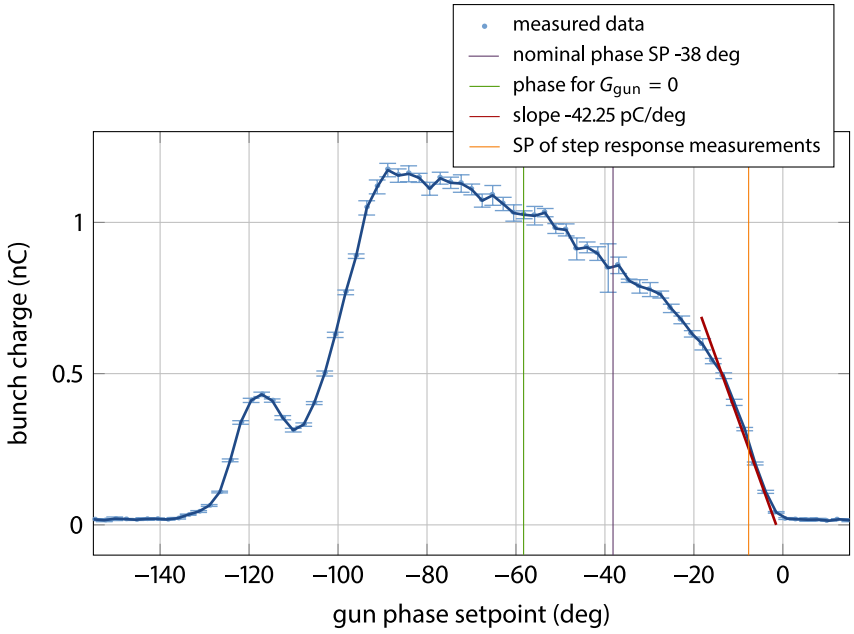

Figure 8.15 | Scan of the electron gun RF phase. The charge is measured with a monitor directly downstream of the gun. The vertical lines indicate designated phase setpoints used for nominal operation and special measurements.

laser pulse impinges, no electrons can exit the gun and the toroid monitor (see section 1.6, pages 12 ff.) delivers no signal. Once charge is detected by the toroid, the zero-emission phase is defined. For small negative emission phases,[4] roughly half of the electrons exit the cavity and can be detected. The steepness of the slope depends for low charges primarily on the duration of the PTO laser pulse. At an emission phase of around −30 deg all electrons leave the gun. The most effective and thus usually set operation emission phase is $\varphi_{\text{gun}} \equiv \varphi_{\text{nom}} = -38\,\text{deg}$. Although a flat top in the scan is expected, when the the emission phase exceeds the laser pulse duration, the charge increases further due to collective effects and the lowering of the working function of the CsTe photocathode due to the Schottky effect for increasing electrical fields. For a phase setpoint beyond ~ 90 deg, the RF field decelerates the electron beam in the full-cell and it gets lost. Details of the emission process can be found e.g. in [HBG+05, HKF05] and the references cited therein.

The steep slope between the zero-crossing and the nominal phase setpoint can be used to determine the relative timing of the photo injector laser and the gun, as a monitored charge variation can be translated into a timing variation [SHK+06]. In the presented measurement, an absolute value of the slope of 42.3 pC/deg has been determined, corresponding to 19.7 pC/ps at the 1.3 GHz accelerating frequency. As the charge can be read out on a single shot basis, i.e. with 1 MHz, the timing variation of every electron bunch in long macropulses can be measured. However, the toroid has a resolution of about 4 pC, which results in a lower limit for the observable timing change of $\sigma_Q = 202$ fs

[4] The sign is convention at FLASH.

for single shots. Furthermore, the generated charge depends on the amplitude of the individual laser pulses, which is typically only stable within 2% (rms). At $\varphi_{\text{gun}} \equiv \varphi_{\text{slope}} = -8$ deg, a charge of 270 pC is measured. Hence, a 2% variation limits the sensitivity to $\sigma_A = 265$ fs. Together, this limits the single shot timing resolution to $\sigma_{\text{res}} = (\sigma_Q^2 + \sigma_A^2)^{1/2} = 333$ fs. For long bunch trains the toroid limit can be neglected. Although the toroid readout can be improved and the amplitude of the laser measured or even stabilized, the resolution of the BAM and the optical cross-correlator based on optical measurement can never be reached.

Laser and Electron Bunch Response to a Phase Step

The planned stabilization of the photo injector laser is based on the pulse arrival time measurement using the optical cross-correlator. An adaptive feed forward or feedback algorithm will already act on the laser pulse train before the actual pulses are picked out to generate the electron bunches. By this, the arrival time can be stabilized from the first bunch on. However, the response time of the photo injector laser must be known, as it could limit the performance of the stabilization algorithm. In order to investigate the laser response time, only the vector modulator for the 1.3 GHz signal of the EOM with its control DAC and the monitoring ADC has been installed in a first experiment (marked by the box labelled "feed forward" in Fig. 8.1 on page 167). Using the new DOOCS server for the DAC (see section 8.3, page 176 ff.), phase steps have been applied after 3 µs of a 60 µs long electron macro-pulse. The influence on the timing of the macro-pulse has been measured with the method described above, where at a gun emission phase of $\varphi_{\text{gun}} = -8$ deg a change of the charge can be translated in a timing change. The left plot of Fig. 8.16 shows the result for the four different phase steps ±1 deg, ±2 deg and the nominal operation. Most notably, the laser requires around 7 µs to react on the phase step. Secondly, the step is not transferred one-to-one by the laser, but rather only in the order of 60% to 70%. On the other hand, the macropulse had a duration of only 60 µs, and it has been found out that the set phase step value is reached to up to 90%, when the step is applied to the laser 45 µs before the first electron bunch.

It should be noted, that the measurement method can not distinguish between timing and amplitude changes of the laser. Therefore, the cause of an oscillation with a frequency of around 70 kHz in the gun response, for example reported in [Loe09], was not clear. Later measurements showed, that indeed the amplitude of the laser pulse train is modulated by the applied phase step, as shown in the right plot of Fig. 8.16. The measured response of the electron gun in the left plot of the figure had to be corrected with the observed amplitude modulation.

Although the modulation seems rather large, it must be considered that the applied phase steps of ±1 deg are quite academic. A correction of the arrival time of, for instance, 100 fs requires a phase change of 0.05 deg. Taking the good timing stability of the laser, as discussed in the previous section, into account, the feed forward or feedback will have to apply even lower phase corrections across the macropulse – making the amplitude modulation negligible in the first investigations.

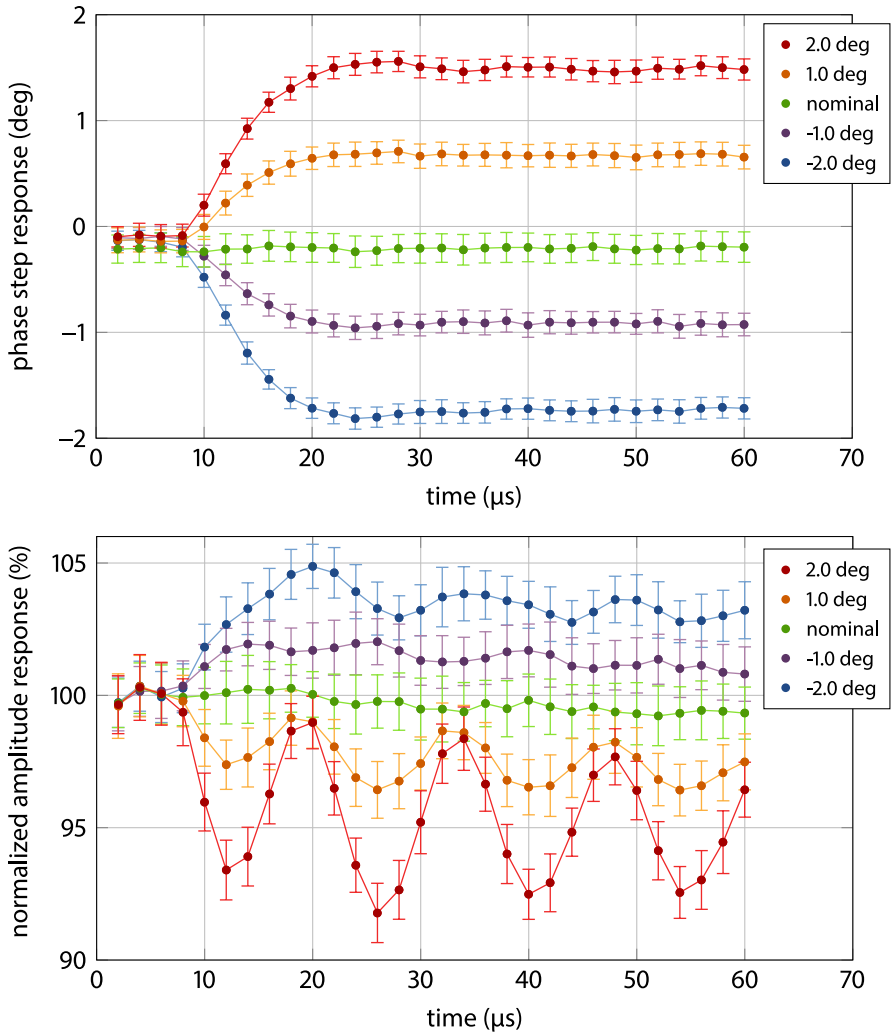

Figure 8.16 | Response of the laser and the electron gun to a phase step. The phase step is applied to the electro-optic modulator inside the photoinjector laser resonator via the vector modulator while the response was measured using the toroid-based technique.

Feed Forward Timing Correction

For a long time, and particularly before the upgrade of FLASH, where the gun had been replaced and the new photo injector laser was commissioned, a slope in the arrival time, measured again with the charge-based technique, had been observed. An example is shown as the red trace in Fig. 8.17, where the arrival time of a 725 µs long macropulse of 30 bunches with 25 µs spacing changes by 6.3 ps. At that time, the RF controller of the electron gun could be excluded as cause for the change, and as a consequence, the arrival time of the laser pulse train was manipulated by a feed forward correction. With a slope of $\partial\varphi_{\text{laser}}/\partial t = 3.75\,\text{deg/ms}$ applied, the timing change could be reduced by a factor of 10 to 0.6 ps. This was only possible with the upgraded DOOCS server for the phase shifter (vector modulator), as explained in section 8.3 on pages 176 before. The remaining variations

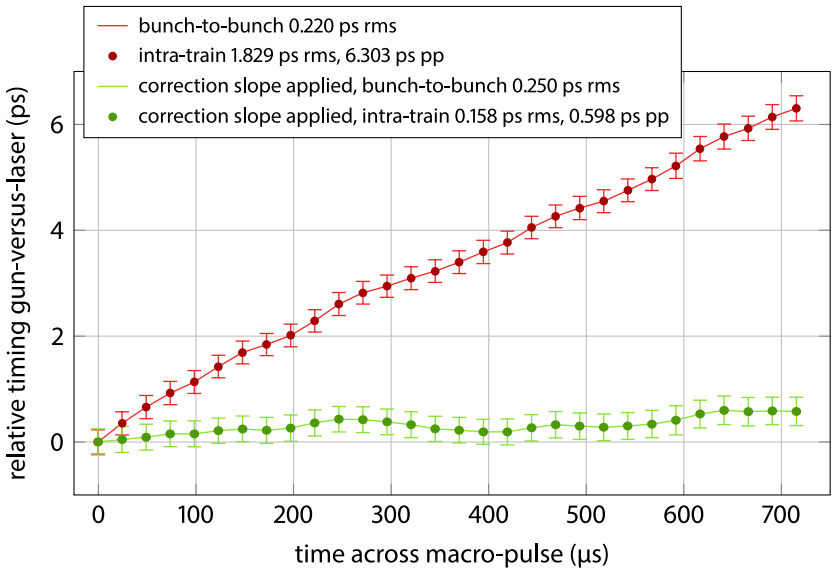

Figure 8.17 | Feed-forward timing correction of the photoinjector laser pulse arrival time. The timing correction with respect to the electron gun was applied as phase slope on the electro-optic modulator inside the photoinjector laser resonator.

might be corrected with a more complicated feed forward pattern, but an adaptive feed forward of a closed loop based on the optical cross-correlator, or a corresponding feedback algorithm will offer more flexibility, especially for intra-bunch train timing manipulation and stabilization.

8.5.3 BAM-Based Arrival Time Measurements

Beam-based measurements using the optical cross-correlator (OXC) for the photoinjector laser and the bunch arrival time monitor (BAM "1UBC2") for the electron beam offer a significantly better resolution than the gun-charge method. They allow for distinguishing the effects caused by the laser and those of the electron gun accelerating fields. Systematic studies have been carried out with varying parameters such as the laser phase, the gun phase and the gun amplitude in small ranges around their nominal setpoints to study their influence on the arrival time. In addition, slopes in phase or amplitude were applied to the RF driving the EOM to evaluation system reaction, which provides important information for the planned arrival time feedback loops.

Nominal Gun Emission Phase

In a first measurement, the offset phase φ_{laser} of the RF driving the EOM has been varied within a range of ±0.5 deg using the digital control of the vector modulator. This has to result in an arrival time change of the PTO laser pulse train with the theoretical dependence $a_0 = 2.137$ ps/deg for the frequency of 1.3 GHz of accelerating structures.

As can be seen in the upper plot of Fig. 8.18 (green markers), a linear fit to the laser pulse arrival

time leads to a slope of $|a_{\mathrm{O}}^{\mathrm{laser}}| = 2.269\,\mathrm{ps/deg}$ which agrees relatively well with the expected value. The slope of the arrival time (blue markers in the figure) of the electron bunches upstream of the magnetic chicane caused by the laser phase change is $|a_{\mathrm{U}}^{\mathrm{laser}}| = 1.318\,\mathrm{ps/deg}$, which corresponds to 61.7% of a_0. Since the emission phase of the gun is set to its nominal value $\varphi_{\mathrm{gun}} = \varphi_{\mathrm{nom}}$ in this measurement,

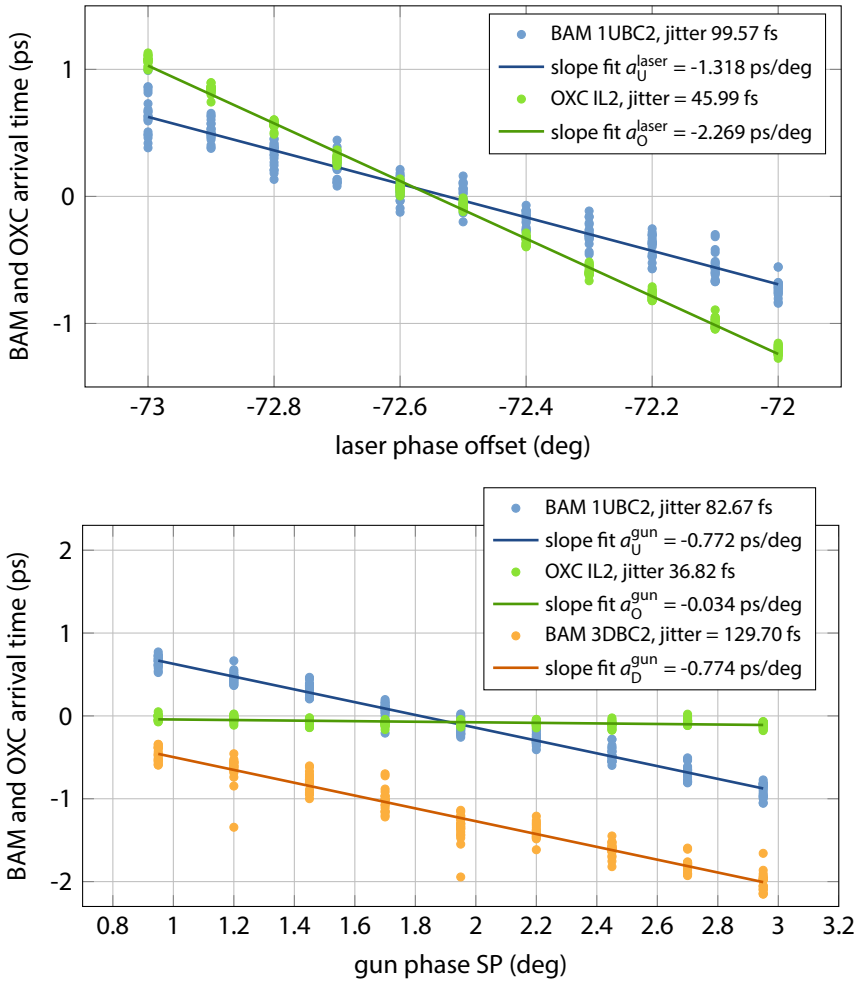

Figure 8.18 | Electron bunch and laser pulse arrival time versus nominal gun and laser phase. The data was recorded as a function of the laser phase (**top**) and the gun phase (**bottom**) around their nominal values.

the result is in extremely good agreement with the simulations discussed in section 1.6.2, pages 14 f., where ~ 60% arrival time change must be caused by the laser and hence ~ 40% by the gun, when the influence of the acceleration modules is neglected. In order to cross-check this, the gun phase has been varied by $\varphi_{\mathrm{gun}} = \varphi_{\mathrm{nom}} \pm 1\,\mathrm{deg}$. The slope of the electron bunch arrival time amounts to $|a_{\mathrm{U}}^{\mathrm{gun}}| = 0.772\,\mathrm{ps/deg}$ and thus 36.1% of a_0, whereas the laser pulse arrival time is obviously not influenced and stays constant within $\lesssim 40\,\mathrm{fs}$. Adding both electron arrival time slopes yields $|a_{\mathrm{U}}^{\mathrm{laser}} + a_{\mathrm{U}}^{\mathrm{gun}}| = 2.09\,\mathrm{ps/deg}$, which agrees again very well with the expected value. The missing 2% are contributed to unavoidable but small calibration errors and measurement inaccuracy. During the measurements,

the machine was quite stable, as the electron bunch arrival time jitter amounts to 100 fs in the first and to 83 fs in the second measurement. In the plot of the gun phase scan, additionally the arrival time data of the BAM downstream of the magnetic chicane is shown. Here, an arrival time jitter of 130 fs is calculated, caused by an imperfect setup of the accelerating RF in the booster module. The arrival time slope, on the other hand, amounts to $|a_{\mathrm{D}}^{\mathrm{gun}}| = 0.774\,\mathrm{ps/deg}$ and is nearly equal to the one of the upstream BAM. This is also expected because the acceleration modules ACC1 and ACC39 have been set to their on-crest phases.

As the typical duration of these parameter scans is in the order of ten minutes, the drift of the arrival time has been investigated on this time scale and is shown in Fig. 8.19. The electron bunch

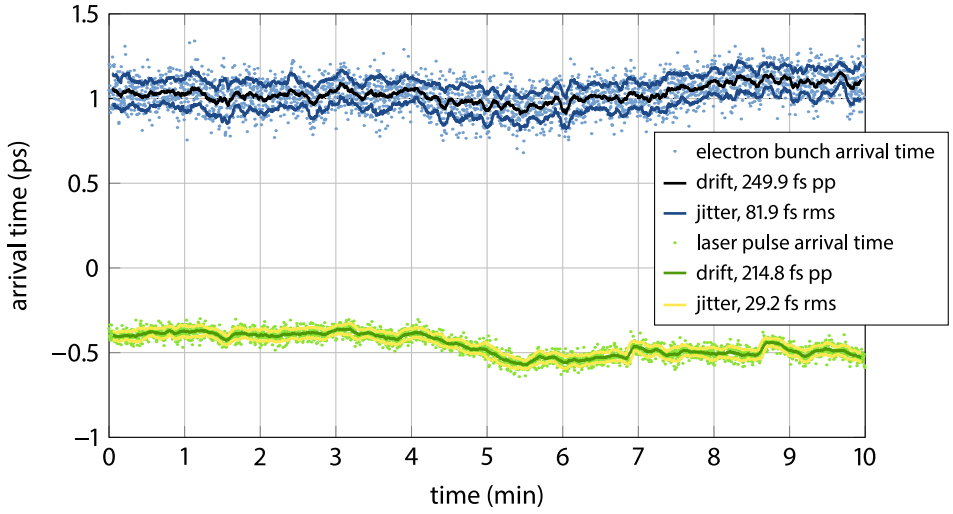

Figure 8.19 | Arrival time drift over a period of 10 minutes. The electron bunch arrival time is recorded with the BAM upstream of the first bunch compressor and the laser pulses are detectd with the optical cross-correlator. The gun is operated at it nominal emission phase $\varphi_{\mathrm{gun}} = \varphi_{\mathrm{nom}}$

arrival time changes by 250 fs peak-to-peak, determined from the smoothed trace shown in black. The previously measured timing jitter in the order of ~ 80 fs is reproducible. It is calculated as rms fluctuation after the slow drift had been subtracted from the data. The laser pulse train drifts by 215 fs with a residual jitter of 29.4 fs, which is even better than in the scans. A common drift tendency is visible for the two traces, but a correlation could not be analyzed, due to problems with the "general event number" of the control system in the data recording program (see [Boc13]).

From the data, also the repetitive errors across the electron bunch macro-pulse and the laser pulse train, as shown in Fig. 8.20, can be calculated. The laser (bottom plot in the figure) shows an good performance for the used 120 µs long macro-pulse with a repetitive error of 3.5 fs over the measurement period. Interestingly, the same "bow tie"-like pattern as for the more than four times longer pulse train discussed in section 8.5.1 is observed. The cause for this has yet to be found out. The absolute electron bunch arrival time, with a repetitive jitter of 51 fs and shown in the top plot of the figure, changes by 1.56 ps across the macro-pulse duration. This is caused by a slope of the RF gun phase, as shown in the middle plot of the figure by the readback values

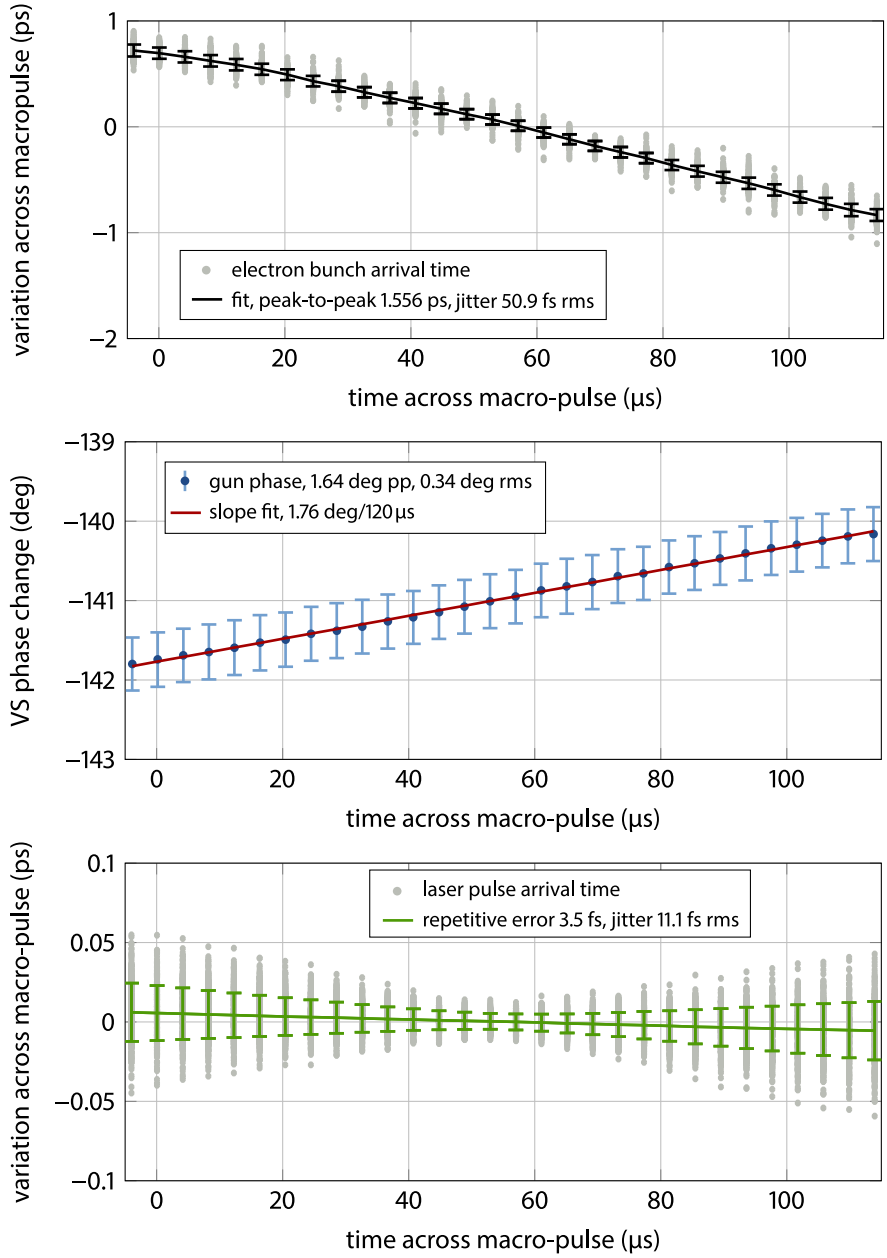

Figure 8.20 | Repetitive error of the electron bunch and laser pulse trains. The intra-train arrival times of the electron bunches (**top**) and the laser pulses (**bottom**) are taken from the drift measurement in Fig. 8.19. The gun emission phase, retrieved from the vector sum (VS) of the LLRF controller, changes considerably by 1.64 deg across the macro-pulse duration.

(RBV) of the low-level radio frequency (LLRF) controller vector sum (VS) phase. A phase slope of $\partial\varphi_{\mathrm{gun}}/\partial t_{\mathrm{mp}} = 1.76\,\mathrm{deg}/120\,\mu\mathrm{s} \Rightarrow 3.76\,\mathrm{ps}/120\,\mu\mathrm{s}$ was retrieved. However, from the gun phase scan it is known that the timing change of the gun contributes by 36.1% to the electron bunch arrival time and hence the slope results in 1.35 ps timing change across the macro-pulse from the RF phase. Since

the controller features a slope compensation, these kinds of measurements, showing that the laser pulse arrival time is constant, can be used to set such a slope up in order to flatten the electron bunch arrival time for the normal operation of the machine.

Offset Gun Emission Phase

As discussed in section 1.6.2 on pages 14 f., it should be possible to set the gun emission phase to a value $\varphi_{\text{gun}} = \varphi_0 = \varphi_{\text{nom}} - 20\,\text{deg}$, such that the electron bunch arrival time is not influenced by variations of it. At this phase (marked with a green vertical line in Fig. 8.15, page 183), it is assumed that $G_{\text{gun}} \simeq 0$ in Eq. 1.5, page 14. As a result, the arrival time is only influenced by the laser as per $\delta t_{\text{bunch}} = G_{\text{laser}}\,\delta t_{\text{laser}}$ with $G_{\text{laser}} \simeq 1$. Using the optical cross-correlator and the BAM "1UBC2" upstream of the chicane a measurement of this relation and several other studies at this emission phase were enabled for the first time: The upper plot of Fig. 8.21 shows the arrival time change during

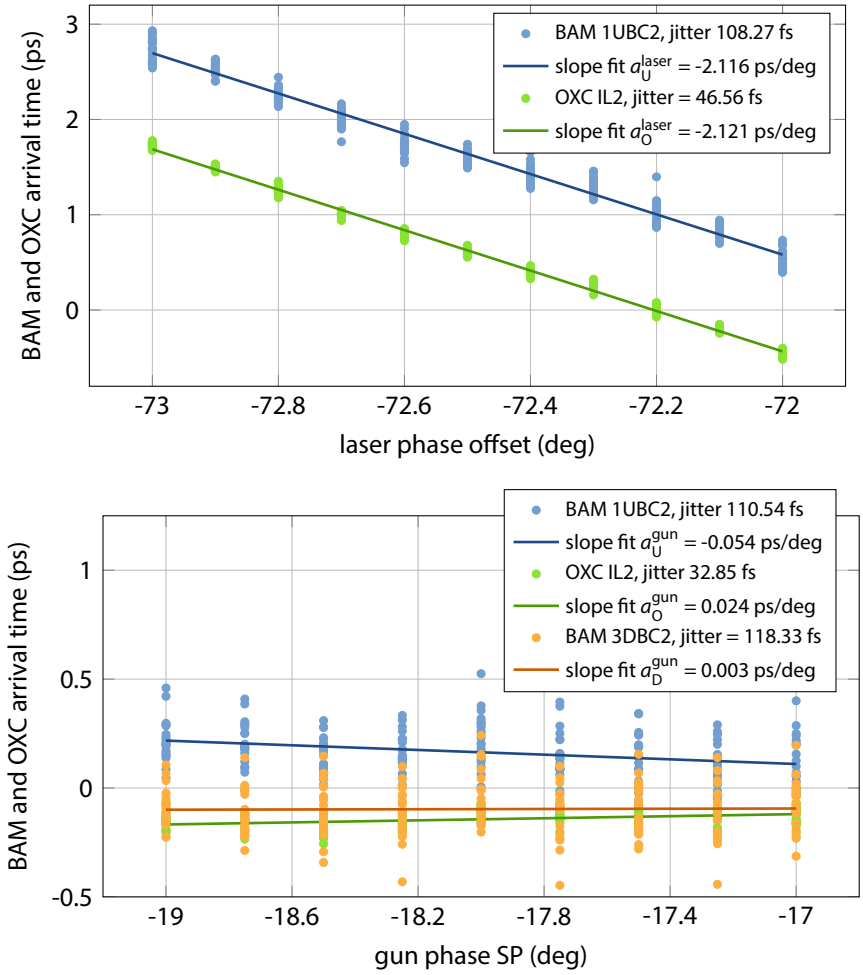

Figure 8.21 | Electron bunch and laser pulse arrival time versus offset gun and laser phase. The data was recorded as a function of the nominal laser phase (**top**), while the gun phase (**bottom**) was offset by -20 deg from its nominal value.

a scan of the phase $\varphi_{\text{laser}} \pm 0.5$ deg of the RF signal driving the EOM in the PTO resonator. The linear slope fits for both the laser pulse and the electron bunch arrival time result in similar values $|a_{\text{U}}^{\text{laser}}| = 2.116\,\text{ps/deg} \simeq |a_{\text{O}}^{\text{laser}}| = 2.121\,\text{ps/deg}$ which are, moreover, in excellent agreement with the expected slope of $a_0 = 2.137\,\text{ps/deg}$. In order to cross-check that the gun phase does not play a role at this emission phase, it was varied by ±1 deg around its setpoint[5] in a second measurement. It was found, as shown in the lower plot of the figure, that the arrival time slopes amount to 54 fs/deg for the electron bunch and 24 fs/deg for the laser pulse train – being practically zero. For the BAM downstream of the magnetic chicane an even lower slope value has been calculated. The first acceleration module and the third-harmonic cavity have been operated on-crest to minimize their influence and to allow for the comparison of the both BAMs around the magnetic chicane. The electron bunch arrival time jitter is in the order of 100 fs in all measurements, which is slightly worse than in the measurements at the nominal gun emission phase, but still very reasonable.

The influence of the laser pulse arrival time change on the electron bunch through the first acceleration and the third-harmonic modules is shown in Fig. 8.22 for the laser phase scan. In the correlation plot, the slope of 0.98 indicates the nearly one-to-one transport of the arrival time changes, whereas the correlation width of 98 fs is mainly governed by the electron bunch arrival time jitter.

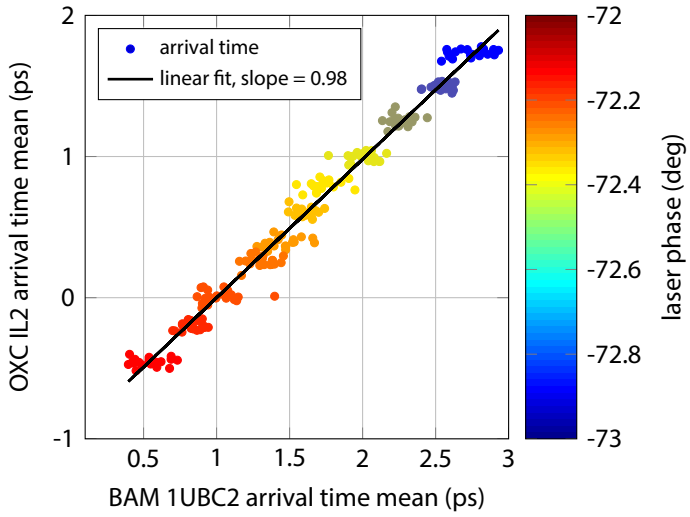

Figure 8.22 | Correlation of the electron bunch and the laser pulse arrival time. The arrival times of the electron bunch train and the photoinjector laser pulse pulse burst are shown as function of the laser phase φ_{laser} (encoded in color) at the gun emission phase $\varphi_{\text{gun}} = \varphi_{\text{nom}}$ - 20 deg.

In analogy to the investigations at the nominal emission phase, also at the emission phase discussed here, a drift measurement over a period of 10 min has been carried out, whose result is shown in Fig. 8.23. In comparison to the drift measurement at the nominal gun emission phase, the electron bunch arrival shows a larger drift of 398 fs peak-to-peak and the 20% increased jitter of 100 fs. At the

[5] The abscissa of the plot actually shows the setpoint from the control system. The nominal phase DOOCS setpoint was +1.95 deg in these measurements, as also shown in Fig. 8.15, page 183), and hence the zero-crossing, which has been determined before the investigations, at $\varphi_0^{\text{SP}} = +40$ deg.

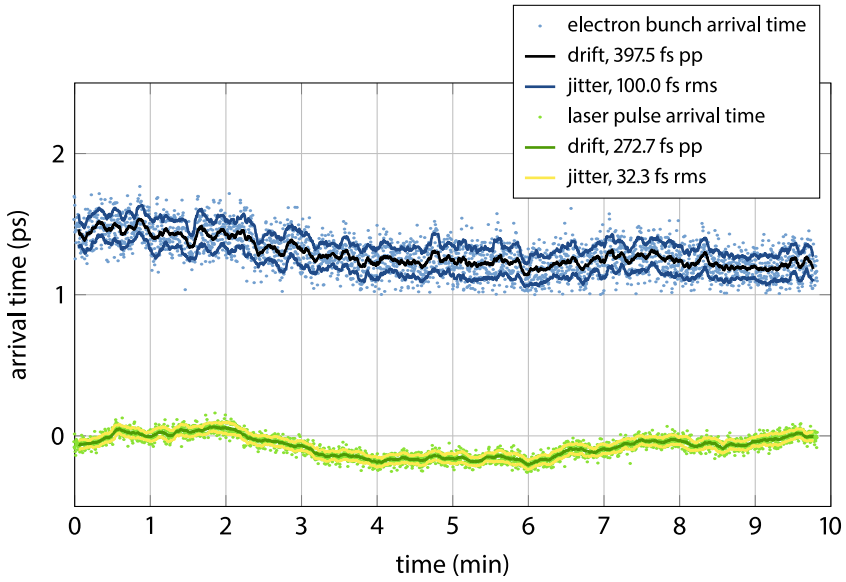

Figure 8.23 | Arrival time drift over a period of 10 minutes at offset gun phase. The drift measurement from Fig. 8.19 is repeated with the offset gun phase of $\varphi_{gun} = \varphi_{nom}$ - 20 deg.

same time, the laser pulse arrival time also drifted more and amounts to 273 fs. The arrival time jitter of the laser pulses, on the other hand, is only 9% larger in this measurement in comparison to the operation at the nominal gun emission phase. As the influence of gun emission phase changes in this case is practically zero, the considerably larger timing jitter of the electron bunches and the fact, that a common drift tendency is not visible over the complete measurement period results from changes of the gun acceleration gradient.

Furthermore, the repetitive errors have also be determined from this measurement and are shown in Fig. 8.24. The laser pulse train has a repetitive error of 1.2 fs and thus electron bunch arrival time jitter does not depend on the laser. Again, the "bow tie" pattern is observed, where the first and the last pulses have a larger timing jitter than the ones in the center of the pulse train. It should be noted, however, that the accelerator could only be operated with a bunch repetition rate of f_{bunch} = 1 MHz in this measurement, and hence the investigated macro-pulse is just 30 µs long. This explains the significantly lower repetitive error of the laser in comparison to Fig. 8.14. The electron bunch arrival time differs from this, as it shows a saturation curve like pattern in the first 5 µs of the macro-pulse followed by a slight decrease of the arrival time by ≈ 50 fs beginning 13 µs after the first bunch. Particularly the first effect results in the relatively large values for the repetitive error of 37 fs and rms arrival time jitter of 65 fs as they are calculated from the complete bunch train. Since the influence of the gun emission phase is practically suppressed, the reason for the much larger electron arrival time jitter are most likely changes in the gun gradient.

The overall pattern of the arrival time can be caused by transient effects in the wavelength conversion to the UV with the LBO and BBO crystals, or the amplification stage of the photoinjector laser, or a combination of those effects. However, these can not be observed by the actual optical

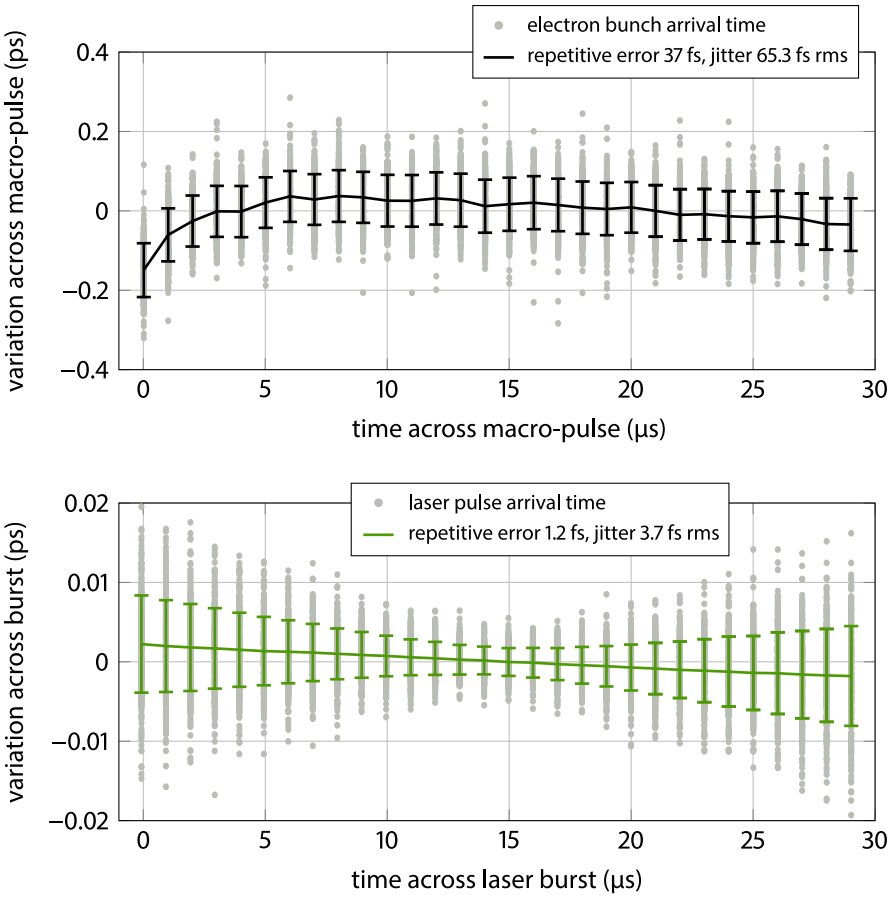

Figure 8.24 | Repetitive error of the electron bunch and laser pulse trains for offset gun phase. The data of the drift measurement in Fig. 8.23 is analyzed. The gun emission phase is $\varphi_{gun} = \varphi_{nom}$ - 20 deg.

cross-correlator in the near infrared (NIR) region, because its input pulse train is tapped off immediately after the oscillator of the injector laser system. Therefore, it is highly desirable, to design and implement an optical cross-correlator for the UV pulse train actually send to the photocathode. Until then, only indirect measurements using the NIR cross-correlator, the BAM and the gun set to the offset emission phase can be used for arrival time studies in the injector and booster, as presented in the following sections.

Response to a Laser Pulse Arrival Time Slope

In section 8.5.1 it has been explained that a slope in the arrival time of the electron bunch had been observed using the toroid-based technique of the gun. These measurements have been repeated, where the optical cross-correlator provides additionally the direct measurement of the laser pulse arrival time. Furthermore, it is an advantage to be able to set the gun emission phase to the offset phase at $\varphi_{gun} = \varphi_0 = \varphi_{nom} - 20$ deg to strongly suppress its influence. Using the digital control of the vector modulator (see section 8.3, pages 176 ff.), different slopes $\partial\varphi_{laser}/\partial t$ ranging from −7 deg/ms

to 0 deg/ms have been applied to the phase of the RF signal which drives the EOM in the PTO's resonator. For this measurement, the bunch repetition rate was set to 100 kHz with $N_{\mathrm{bunch}} = 30$ in order to be able to study the slope influence for a 300 µs long pulse train. The left plot of Fig. 8.25

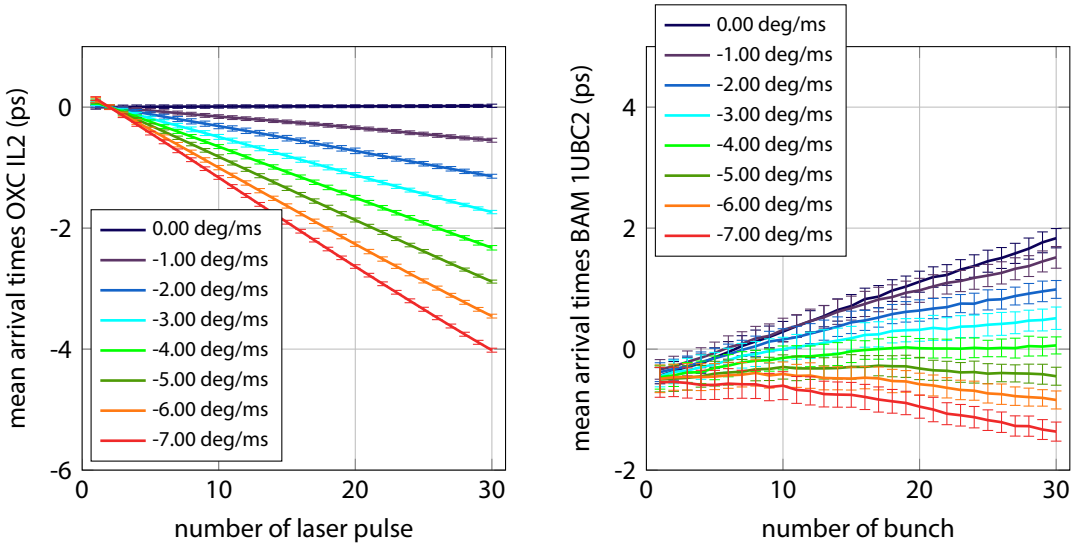

Figure 8.25 | Scan of a phase slope applied to the RF driving the EOM. The influence on the electron bunch train arrival time across the macropulse (**right**) of a phase slope applied to the RF driving the EOM (**left**) of the laser oscillator is investigated at a gun phase of $\varphi_{\mathrm{gun}} = \varphi_{\mathrm{nom}}$ - 20 deg with a bunch repetition rate of $f_{\mathrm{bunch}} = 100$ kHz.

shows the laser pulse train arrival time slopes for the different phase slopes, which react within 10% accuracy as expected. For example, for $\partial\varphi_{\mathrm{laser}}/\partial t = -5$ deg/ms a timing change of 3.02 ps is expected over the pulse duration, and from the data 3.21 ps are determined. The right plot of the figure shows the influenced arrival time of the electron bunches. When no phase slope of the laser is applied, a positive slope with a peak-to-peak change of 2.38 ps is observed. For larger negative phase slopes applied to the laser, the electron bunch arrival time becomes more flat and shows only a slight curved characteristic for $\partial\varphi_{\mathrm{laser}}/\partial t = -5$ deg/ms. The fact that a correction by the laser pulse train of 3.02 ps is required to compensate for 2.38 ps electron bunch arrival time suggests a connection to another parameter, which is also influenced by the laser phase, because at the set offset gun emission phase, timing changes from the laser are transported one-to-one to the BAM upstream of the chicane (see Fig. 8.22, page 191). Nevertheless, this feed forward method can be used to roughly flatten the arrival time of the bunch train before it is compressed, until the investigation of all other parameters is completed and understood, as well as addressed correspondingly.

Influence of a Change in the Amplitude of the EOM-Driving RF

The amplitude of the RF signal, which drives the EOM, and by this the phase modulation depth can be also be varied by the output voltage $V_{\mathrm{VM}} = (V_I^2 + V_Q^2)^{1/2}$ controlling the vector modulator. Akin to the phase slope, also an amplitude slope $\partial V_{\mathrm{VM}}/\partial t$ can be applied. In Fig. 8.26 the influence of

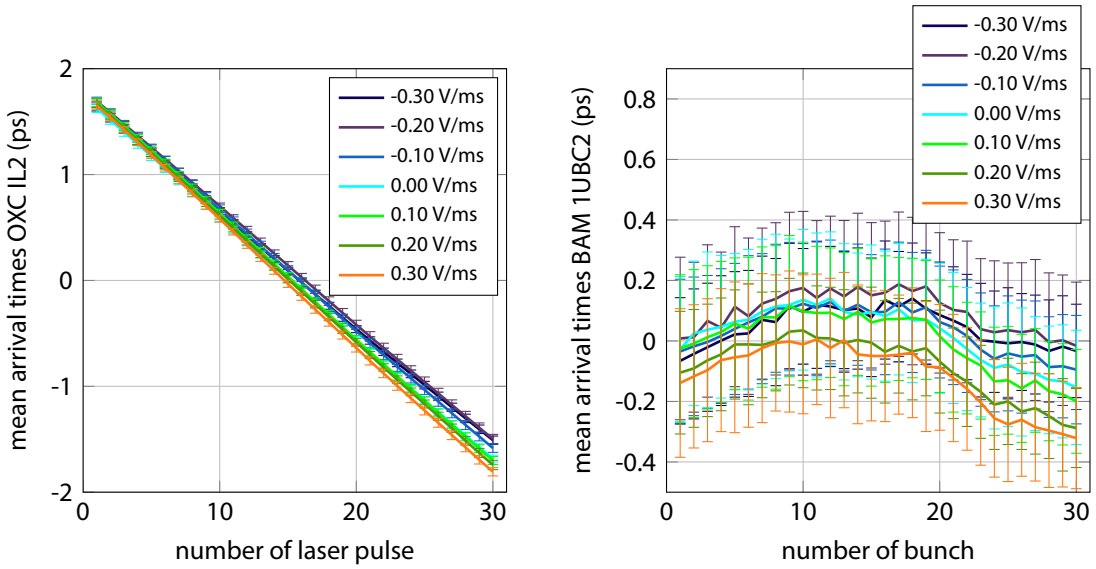

Figure 8.26 | Scan of the RF amplitude slope applied to the EOM in the PTO. The influence on the electron bunch train arrival time across the macropulse (**right**) of an RF amplitude slope applied to the EOM (**left**), realized with corresponding DAC voltages for the I and Q inputs of the vector modulator is investigated at the offset gun phase.

different slopes in the range of ±0.30 V/ms on the arrival times is shown. Across the macro-pulse duration, this corresponds to a maximum change by 3.4%, as the nominal voltage is $V_{\mathrm{VM}} = 2.70\,\mathrm{V}$, which was found before to result in the lowest phase noise at the RF output of the vector modulator (see Fig. A.12 on page 218 in the appendix). The slope of the laser pulse train arrival time results from the phase slope discussed in the previous section, which is applied at the same time to have a more or less constant arrival time at the BAM across the electron macro-pulse, as shown in the right plot of the figure. Therein, two effects are visible: first, the offset arrival time changes for the different RF amplitude slopes in the order of 200 fs. Although for every slope setpoint 20 bunch trains have been averaged, the induced timing changes are within the measurement error. For example, the mean arrival time with the largest slope is actually lower then the one of the setpoint before. The second visible feature is a slight divergence of the curves, i.e. there is a larger difference in the arrival time of the 30th bunch than the one of the first bunch. This can also be seen in the arrival time of the laser pulse train. Both effects are expected to be more prominent when the measurement is repeated with either a longer macro-pulse or larger amplitude slopes. However, the overall curved characteristic seems not to be influenced by the laser amplitude or a slope thereof.

Influence of the Electron Gun RF Amplitude

As already mentioned, the accelerating gradient of the electron gun also influences the electron bunch arrival time, and consequently, it has also been investigated at the flat top emission phase $\varphi_{\mathrm{gun}} = \varphi_0 = \varphi_{\mathrm{nom}} - 20\,\mathrm{deg}$. For this, the forward power setpoint (SP) of the RF fed to the gun has been varied

within a range of ~ ±1% around its nominal value of 3.25 (in arbitrary units), while the arrival time has been measured analog to the investigations discussed above. The top left plot of Fig. 8.28 shows the arrival time across the laser pulse train. In this measurement, the macro-pulse consisted again of

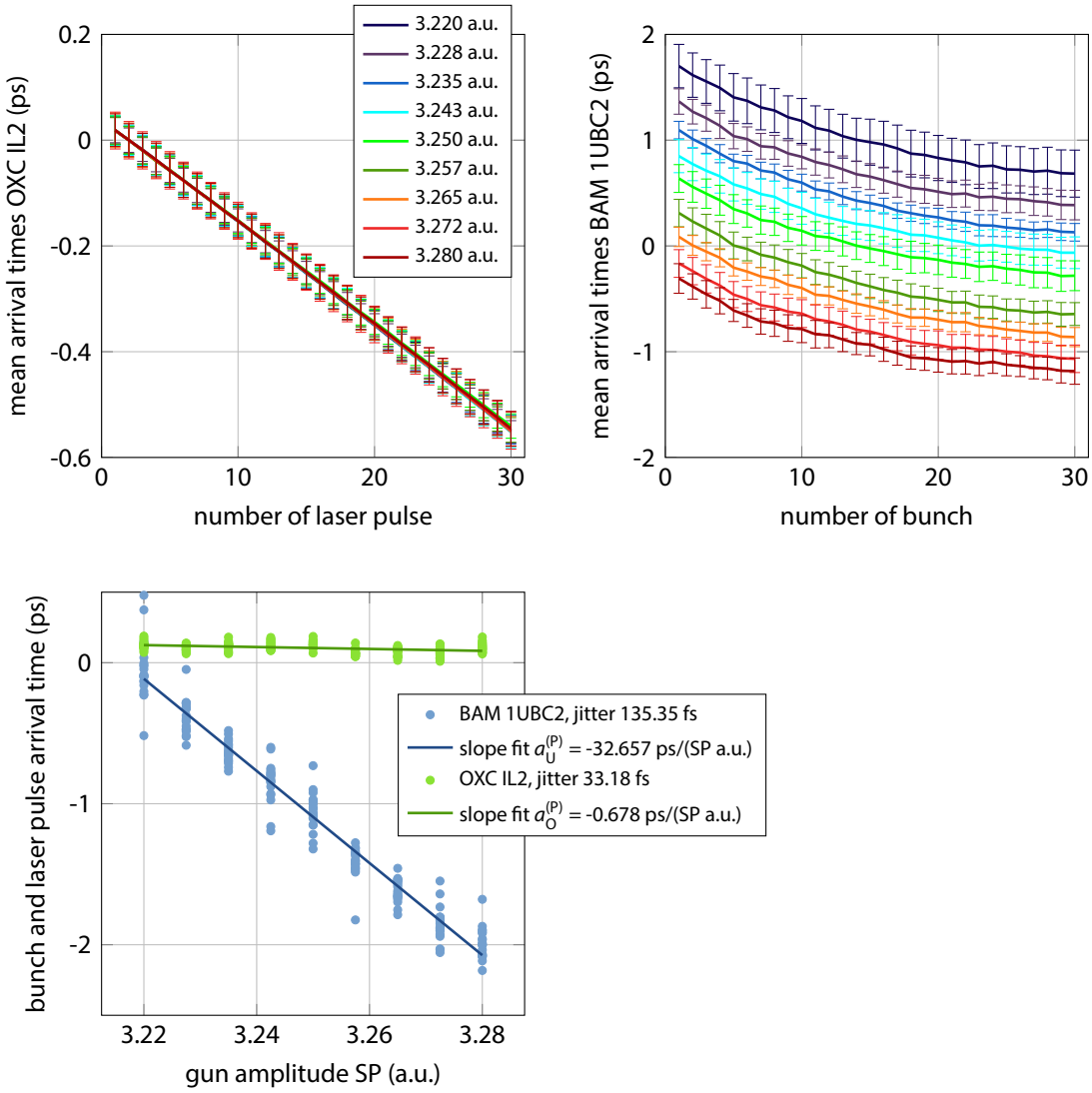

Figure 8.27 | Influence of the gun RF amplitude on the arrival time at offset gun phase. The mean arrival times of the laser with a phase slope applied and the electron bunch across the macropulse (**top**, the legend holds for both plots) and the first pulse and bunch (**bottom left**) is investigated at the offset emission phase $\varphi_{gun} = \varphi_{nom}$ - 20 deg.

N_{bunch} = 30 electron bunches at a repetition rate of f_{bunch} = 500 kHz.[6] The slope is artificially applied via the phase control of the EOM, as discussed above. The electron bunch arrival time, shown in the top right plot in the figure, reveals a curvature in these measurement and does not flatten until the 30th

[6] The resulting duration of the macro-pulse of 60 µs was the maximum allowed by the accelerator's machine protection system (MPS) in the dedicated measurement shift.

bunch, which a longer macro-pulse would have shown presumably. A maximum change of 2.38 ps from the first to the last bunch in the train has been determined. The influence of the gun gradient, however, precipitates in a change of the arrival time of the whole macro-pulse without altering the characteristic of the curves. The lower left plot of the figure shows the arrival time data versus the amplitude setpoint, from which the mean arrival times across the macro-pulse have been calculated. The laser pulse arrival time changed by 678 fs during the measurement, due to the fact that after setting another gun power value, a waiting period of about 60 s is required to let the gun temperature regulation stabilize the cavity (see section 1.6.1, pages 13 f.). During this time, the photoinjector laser can drift (see section 8.5.1, pages 180 ff.). The timing jitter of the laser is at 33 fs as low as in the former investigations, whereas the electron bunch arrival time jitter again is significantly larger and amounts to 135 fs. The slope with an absolute value of $|a_{\mathrm{U}}^{(P)}| = 32.657\,\mathrm{ps/(SP\ a.u.)}$ or correspondingly $\sim 1.061\,\mathrm{ps/(\%\ SP\ change)}$ is calculated from all 20 shots, which were recorded at every setpoint. Although the dependency on the gun amplitude is rather large, it has to be taken into account that the contribution from the gun to the arrival time is reduced at the nominal emission phase (see above). Nevertheless, it seems desirable to establish a better stability of the gun amplitude than the formerly measured 0.2% residual rms, as this already corresponds to 200 fs timing change.

Arrival Time Dependency on the Bunch Repetition Rate

It has been observed that the FEL pulse energy reduces significantly for specific machine settings when the number of electron bunches is increased or decreased, without touching any other knobs except the number of laser pulses on the photocathode. Therefore, initial investigations have been carried out to evaluate the electron beam arrival time change in dependency on the number N_{bunch} in the macro-pulse and the bunch repetition rate f_{bunch}. For this, the arrival time of two bunches and 20 consecutive macro-pulses has been recorded before the number of bunches is increased by two. After a 30-second-long pause, again the arrival time of 20 macro-pulses is measured. This procedure is repeated up to $N_{\mathrm{bunch}} = 24$. In the topmost plot of Fig. 8.28, these data points are shown for different repetition rates and hence different lengths of the macro-pulse. The peak-to-peak change of the arrival times varies from 0.24 ps to 0.65 ps, whereas the largest change is only visible for the longest macro-pulse with a duration of 240 µs. These variations, however, could also be caused by a drift within the 12 minutes the measurement takes, for example of the gun amplitude, because there is no regular pattern observable. It should be noted, that the emission phase was set to the offset phase and using the phase slope of the EOM, the arrival time has been flattened before the measurement.

A different picture is drawn when the BBO crystal, which is the second frequency up-converter after the amplification and pulse picking of the injector laser pulse train (see section 8.1, pages 168 f.), is slightly tilted and the measurement repeated. The peak-to-peak arrival time change increases to the range from 1.13 ps to 1.55 ps, as shown in the middle plot of the figure versus the macro-pulse duration. Interestingly, the characteristic curvature of the averaged arrival times is more or less independent on the macro-pulse duration, but on the number of electron bunches within the train, as shown in the lower plot of the figure, where all arrival times show a minimum between six and ten bunches. This leads to several speculations: In addition to the modified phase-matching in the

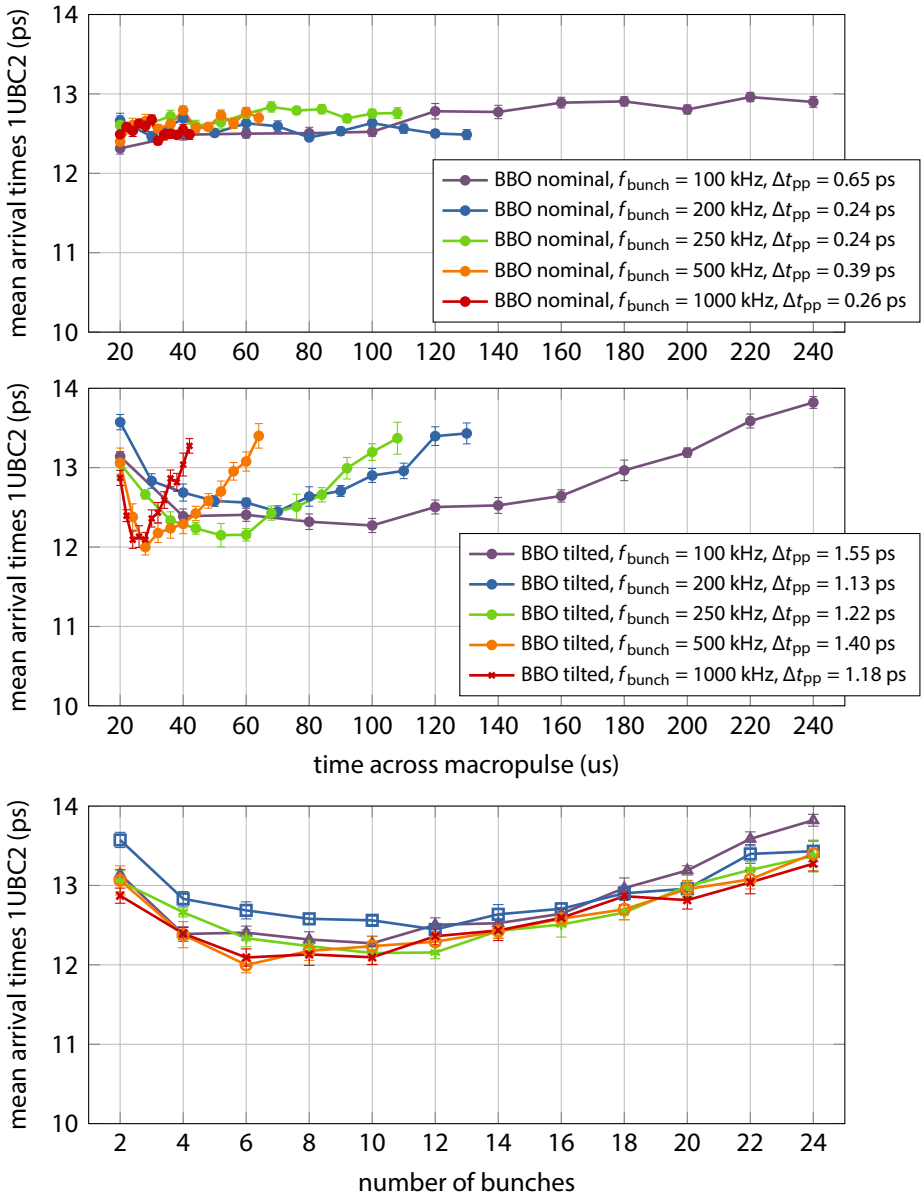

Figure 8.28 | Electron bunch arrival time for different repetition rates and bunch numbers. Change of the electron bunch arrival time when changing the number of bunches N_{bunch} at different repetition rates f_{bunch}. The measurements were done at the nominal BBO crystal position (**top**) and for the crystal tilted (**middle**, **bottom**). Note that the lower plots show the same data, but over time and over the number of bunches.

BBO crystal caused by its tilt, a temperature change and by this also a change of the phase matching might be induced with an increasing number of laser pulses, as these are picked before the wavelength conversion stage (see chapter 3, pages 47 ff.). The significance of this effect should be addressed in calculations, which take the exact geometry and crystal properties into account. Furthermore, there might be a pointing instability of the laser and/or the amplifier, because during standard operation of

the accelerator, an arrival time change of up to 5 ps has been observed when changing the number of bunches from 1 to 30. On the other hand, the laser beam is spatially filtered before impinging the first conversion crystal [Sch10c], which can suppress those pointing instabilities. Finally, yet unlikely, this might be related to the observed "bow-tie" pattern across the macro-pulse measured with the optical cross-correlator, which has also be found to be independent on the pulse duration. In fact, the pulse train oscillator should not be influenced by the wavelength conversion process happening later in the system, but is has been observed that the optical power monitor of the PTO inside the cross-correlator setup (see Fig. 8.5, page 173) shows a slightly different characteristic for different operating states of the pump diodes of the amplification stage, which could be caused by electrical cross-talk in the laboratory. In conclusion, a number of investigations have yet to be carried out in order to find the optimum operating conditions for the photoinjector laser to produce the lowest timing jitter electron bunches.

Summary and Outlook

Optical synchronization systems, based on the timing-stable distribution of a laser pulse train emitted by a master laser oscillator, are key for taking full advantage of the ultra-short extreme ultraviolet and X-ray pulses generated by a free-electron laser – being it based on the SASE process or seeded by an external laser. They enable improved internal operation of the accelerator and therefore a more stable FEL pulse generation, when feedbacks are applied based on the intrinsically more accurate laser-based diagnostics. In particular, however, they allow for the synchronization of external laser systems directly to the reference pulse train. Those include the photoinjector drive laser, and the typically Ti:sapphire-based seed- and pump-probe laser oscillators.

In this thesis, an optical cross-correlation scheme has been developed and used to demonstrate the practically drift-free synchronization of a Ti:sapphire laser oscillator to a reference laser pulse train with sub-10 fs timing jitter. This cross-correlation scheme has been adapted to the pulse parameters of the FLASH photoinjector laser, which enables the measurement of the laser pulse arrival time with respect to the optical reference with a resolution of better than 10 fs – for picosecond-long pulses. Furthermore, many critical components of the laser-based synchronization system at FLASH underwent a comprehensive survey during a significant extension of the system, based on proof-of-principle experiments in former theses.

The centerpiece of the optical synchronization system is a passively mode-locked laser, whose repetition rate serves as timing reference. Caused by the unsatisfactory outcome of investigations on former prototypes, a new nonlinear polarization rotation mode-locked erbium-doped fiber laser has been built. It emits a train of 100 fs pulses with an average output power of more than 70 mW – the minimum required by the extended synchronization system. The timing phase noise was found to be very low in offset frequencies beyond the locking bandwidth of the PLL used to synchronize the laser to the accelerator. Its integrated timing jitter from 1 kHz to 10 MHz is 12 fs rms at a 1.3 GHz carrier frequency. The relative intensity noise was in the order of 10^{-5} for frequencies in $[10\,\mathrm{Hz}, 10\,\mathrm{MHz}]$, while a long-term stability of 1.8% over a period of 10 days without any feedback could be observed. During that time, a slow timing drift of about half a picosecond was observed, but the measurement was limited by unavoidable AM-to-PM conversion in the used photodiode, such that the laser is assumed to drift much less. The measurements show that the oscillator is amongst the best erbium-doped fiber lasers presently available, and suitable as master laser oscillator for the synchronization system.

This self-built laser, however, had to compete with a commercial SESAM-based laser system becoming available only during the course of this thesis and was therefore compared in every aspect. Its timing jitter was found to be 5 fs with a relative intensity noise also of 10^{-5} in the same offset frequency intervals. Caused by a relatively strong dependence of the optical power on the actuator of the synchronization PLL, an amplitude feedback was commissioned, reducing the long-term drift to 0.11% over the period of one week. Due to the superior performance of the laser in terms of timing jitter and a more reliable "push button" operation, the optical synchronization system was transitioned to this master laser oscillator. However, care was taken to be able to operate alternatively with the erbium-doped fiber laser. Minor problems of the laser system which were identified during the commissioning were solved in cooperation with the manufacturer and will be considered in future systems, in particular with respect to the reliability needs of the upcoming European XFEL.

The extension of the synchronization system to more than two end-stations and the desired redundant operation of two master laser oscillators required a major conceptual change for distributing the light of the lasers to the fiber link stabilization units – in comparison to the proof-of-principle experiments in former theses. An optical setup had been suggested and was designed before in there, where the light is split up to 16 ports. The individual link units are then connected via an erbium-doped fiber amplifier to achieve high optical power levels for the link stabilization. The engineered opto-mechanical setup, called free-space distribution unit, was installed and commissioned within this thesis. Several minor issues were discovered and resolved, for instance the imaging system from the output of the laser to the fiber collimators of the amplifiers, or the mechanical stability of the mirror mounts. However, the optical power loss due to unwanted reflection and finite extinction ratio of the optical components were apparently originally not considered at all. Notably, that was another reason for the assembly of the new master laser system with higher optical output power. Furthermore, in the optimized setup a very careful optical alignment increased the coupling efficiency into the fiber collimators from originally ~ 50% to more than 80%, which approaches the calculated limit. The overall mechanical stability benefits from a redesign of the mirror-mounts. Long-term measurements revealed that additional, significant changes are required for performance and reliability reasons, as there are strong influences caused by pointing and temperature changes.

Due to the larger number of end stations, erbium-doped fiber amplifiers had to be introduced between the free-space distribution and the fiber link stabilization units. These fibers are not actively stabilized and therefore prone to drifts. It was found that the peak timing drift of such an amplifier is 24 fs with a residual rms timing jitter of 0.6 fs over a period of 50 hours under normal operating conditions. Although the additional fast timing jitter contributes to the overall jitter from the reference to an end station, it is below its projected maximum tolerable jitter of 1 fs and will not limit the performance of any end station. The drift can be attributed to the temperature and relative humidity on the covered optical table. Although in a quiet period, a peak-to-peak temperature change of only 0.04°C and fluctuations of 0.008°C rms have been measured over a period of 60 hours inside the box, where the fiber amplifiers are laid out, situation is usually worse by a factor of five to ten, which explains the drift found above.

The reference laser pulse train is distributed to the remote locations at the accelerator via actively length-stabilized fiber links, which were developed in a former thesis. Therein, also an engineered mechanical design had been suggested. Within this thesis, several units have been successfully commissioned to connect more end-stations, such as additional bunch arrival time monitors, to the master laser oscillator. Each installation benefited from the experience of its predecessors, since more and more teething troubles could be addressed. Particular attention was paid to the fiber link connection to the optical cross-correlator for the Ti:sapphire laser, since the transmitted pulse train exhibited a large intensity noise at the link end. It was found to be directly related to the relative timing of the reference pulse train and the reflected one in the link. Numerous experiments were conducted without a final, conclusive result. However, the problem can be worked around and mitigated by operating the fiber link at low optical power levels and ensuring minimum cross-talk from other fiber links. This measures allowed to reduce the amplitude and phase noise of an extracted RF signal to a level where the synchronization of a Ti:sapphire laser is possible with 12 fs rms timing jitter. The amplitude noise is also present in the other fiber links, but the electron bunch arrival time monitors seem to be only negligible affected by this, since their measurement technique acts like a filter. An ultimate solution for the noise problem, however, is yet to be found.

The Ti:sapphire oscillator of the electro-optic bunch diagnostic setup can not only be locked with an RF phase detector to the reference laser pulse train, but also with an all-optical scheme based on optical cross-correlation. The lock was stable over a couple of minutes, and over these periods, a timing jitter in the order of 8 fs with practically no drift was determined from a true out-of-loop measurement using a second, identical optical cross-correlator. An analysis of fast fluctuations in [10 Hz, 10 MHz] led to the conclusion that a timing jitter of 3 fs or below is feasible.

A novel component of the laser-base synchronization system, and of particular importance for the operation of the accelerator, is the optical cross-correlator which was installed at the photoinjector laser. Presently, it allows for the measurement of the arrival time of the pulses emitted by the injector laser oscillator with respect to the optical reference with a timing resolution of better than 10 fs, limited by the photodetection process. It allows to study the timing stability of the oscillator, but especially in combination with the bunch arrival time monitor upstream of the first magnetic chicane, the influence of the injector laser and the electron gun on the bunch arrival time can be investigated for the first time. Additionally, simulations from former thesis on the arrival time in the injector could be confirmed experimentally.

Future Tasks and Challenges

The survey of the individual subsystems and the experiences during their commissioning and upgrades revealed a number issues and possible room for improvements:

The erbium-doped fiber master laser oscillator has a shorter pulse duration than the SESAM-based laser. Thus, the optical cross-correlators in the fiber link stabilization units and at the end

stations can benefit from a better sensitivity. Further research on the output power, reliability, stability and automation could eventually make EDFLs again an alternative to the commercial, SESAM-based system. But since reliability and robustness, in combination with an ultra-low timing jitter are essential for the operation of the synchronization system, a second SESAM-based laser will be installed for redundancy. In the ideal case, the switch between the lasers has to happen automatically, when one laser fails, which is especially important for the reliability of the upcoming European XFEL.

In a redesign of the free-space distribution unit, a maximum suppression of cross-talk between the connected devices must be guaranteed. Furthermore, compact master laser oscillators, such as the commercial ones, should be directly integrated into the optical setup to minimize mechanical drifts. Envisioned future versions of the BAMs may require optical delay lines between the distribution and the fiber link units, enforcing a redesign of the distribution setup. Also, a hybrid free-space/fiber-based distribution scheme is imaginable, but presently not favorable. To address the issue with the individual erbium-doped fiber amplifier to the different fiber links, a high-power amplifier could be developed. This would allow to provide the fiber links with sufficient optical power in free-space, thus eliminating additional drift from the existing amplifiers. Then, to avoid drift of the high-power amplifier, the required light for the photodiode of the synchronization phase-locked loop would be tapped at the output of the amplifier. The chirped-pulse amplification approach seems promising for such a development to reduce nonlinear pulse distortion.

The fiber link stabilization units have been redesigned recently and are presently manufactured. Major changes have been made to the delay line and the free-space optical setup, allowing for the compensation of a much larger timing change of the fiber and an improved coupling efficiency into the fiber collimator nearly over the complete travel range. For the fiber links at the European XFEL with lengths of up to 3.5 km, the compensation of the third-order dispersion may be required. The new fiber link design is prepared for an update with a corresponding optical setup.

The all-optical synchronization scheme for the Ti:sapphire lasers requires a careful system identification by means of control theory, which will allow for an optimization of the regulation loop. For this, apparently the regulation speed of the digital PLL must be increased, which also may require a new driver for the piezo actuator with a larger bandwidth. It is furthermore envisioned to implement an algorithm to lock the laser first with an RF-based scheme to find the correct phase with respect to the accelerator, and then to switch over to the cross-correlator error signal.

Since electron bunch arrival time jitter in the injector critically influences the timing jitter of the FEL pulse, an active stabilization of the photoinjector laser oscillator, based on the optical cross-correlator, is foreseen. Then, a feedback for the phase of the RF gun phase can be realized based on the bunch arrival time upstream of the magnetic chicane. Furthermore, it is planned to setup another cross-correlator for the arrival-time measurement of the ultraviolet pulses of the injector laser, since the amplification and conversion of the infrared radiation of the oscillator can be another source

for timing jitter and drift. Another cross-correlator will be used for the new injector laser for future low-charge operation, which requires a modified design due to the different pulse properties.

In addition to a continued improvement, more general future goals of the synchronization system include the measurement of the point-to-point jitter based on two optically locked Ti:sapphire oscillators, out-of-loop measurements of the fiber link timing stability and ultimately the measurement of the timing jitter between an external laser and the FEL pulse in a pump-probe approach.

Conclusion

The optical synchronization infrastructure at FLASH is a highly complex system with many components and subsystems, which have to be understood in great detail. This ranges from optical fiber interconnections over the internal dynamics of a mode-locked femtosecond laser up to the electron bunch arrival time measurement and stabilization in the accelerator. At the same time, the system is very versatile and due to its modular design, it enables the integration of new developments or, for instance, the move to a different type of master laser oscillator without significant impact on its overall performance, but increasing its robustness.

The substantial progress discussed in this thesis towards a reliable optical synchronization infrastructure will makes pump-probe experiments with an external laser and the FEL pulses with a timing resolution in the order of 10 fs feasible in the near future.

A Additional Measurements and Supplementary Information

This appendix is a compilation of several supplementary measurements and additional information which can alleviate the understanding of the main results discussed in this thesis.

A.1 Transmission and Reflection of Polarizing Beam Cubes

In order to ensure minimum optical losses in the free-space distribution unit the delivered batch of broadband coated PBCs were characterized with respect to transmission and reflection coefficients. In the first measurement the beam cube is exposed to linearly polarized light and using a half-wave

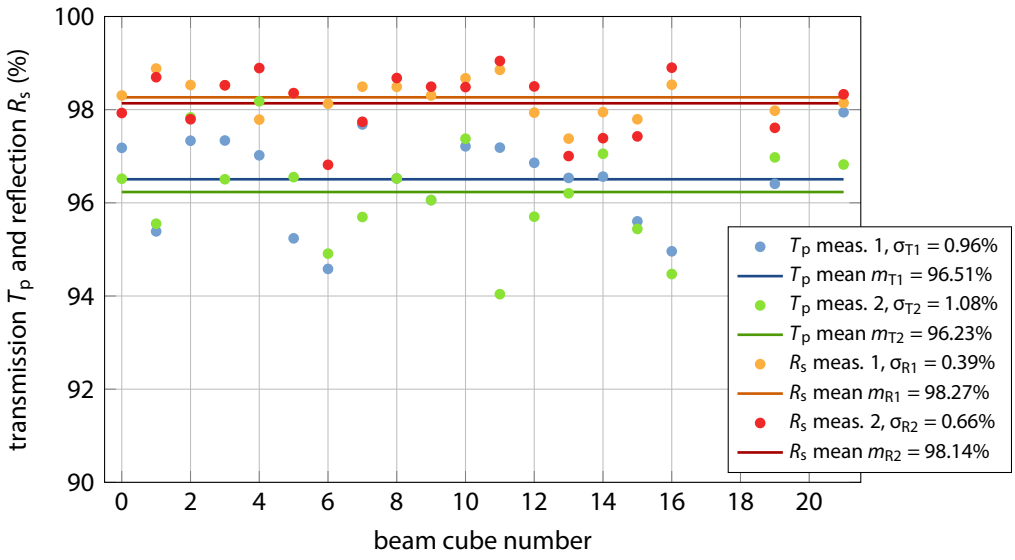

Figure A.1 | Transmission and reflection of a batch of polarizing beam cubes. The beam cubes, made by Newport as *05FC16BC.9*, are investigated at a wavelength of 1560 nm. The specification of the manufacturer [New10] states a typical transmission of $T_p > 90\%$ and a reflexion of $R_s > 99.5\%$, which could not be confirmed.

retarder in front of the beam cube the maximum transmission T_p is determined. Then the PBC is rotated by 90 degree and the measurement is repeated. By this, both sides of the dielectric coating of the cube are evaluated. Now the detector is rotated by 90 degree and the half-wave retarder is adjusted to determine the maximum reflection coefficient R_s. By another 90 degree rotation of the

PBC the other dielectric coating in the cube is lit and the reflection coefficient is determined for this side as well, but requires the detector to be mounted on the opposite side of the cube as before. This quality assurance allowed for the selection of the 16 cubes based on Fig. A.1 with the smallest optical losses for mounting in the free-space distribution unit, as only minimum loss can be tolerated there.

A.2 Dependency of the Repetition Rate and the Optical Power on the Piezo Voltage in the Origami Laser System

Figure A.2 shows (on the left-hand ordinate, × markers) the fundamental repetition rate change Δf_{rep} as a function of the voltage V_{piezo} applied to the piezo element, measured using a photodetector and an RF spectrum analyzer. It is possible to tune the fundamental repetition rate f_{MLO} within the range of ±860 Hz with piezo voltages in the range from 0 V to 100 V. Larger drifts must be compensated by the coarse repetition rate, which is controlled digitally and acts on the temperature of the optical cavity of the laser. It has been observed that the oscillator's repetition rate stays within the range covered by the piezo over a period in the order of a week. Thus, a coarse repetition rate tuning, which can cover a range of $\Delta f_{\mathrm{coarse}} = \pm 3.1$ kHz, is only rarely required. However, the optical power (shown

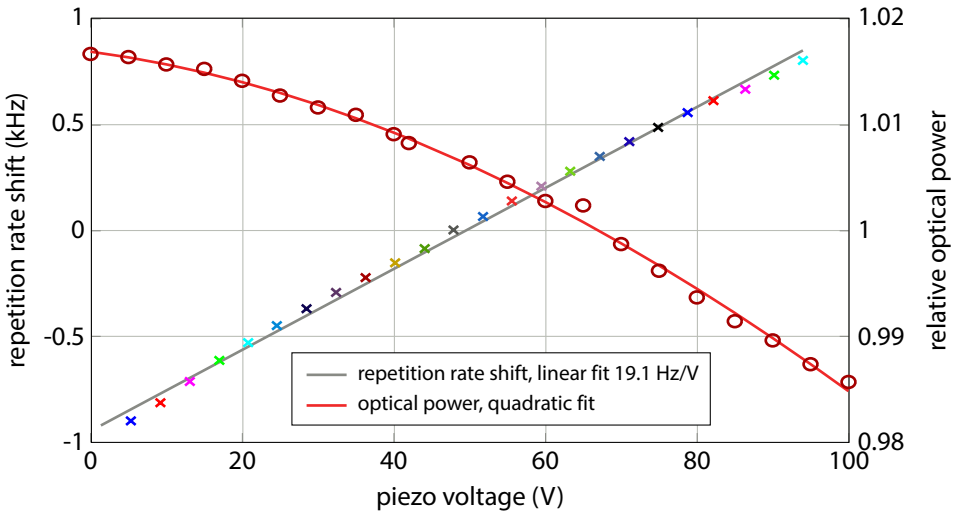

Figure A.2 | Repetion rate and optical power change versus applied piezo voltage. Intended change of repetition rate and and unwanted variation of the optical power of the Origami laser as function of the voltage V_{piezo} applied to the piezo actuator.

on the right-hand ordinate in the figure) depends on the voltage applied to the piezo element, because the internal laser dynamics change when the piezo element changes the length of the resonator. For the complete range, a peak-to-peak variation of more than 3% has been measured. The dependency is not linear and is showing a stronger influence at higher voltages. From this characteristic of the curve it can be concluded, that the manufacturer optimized the laser without a voltage applied to the piezo element. It has been agreed with the company, however, that future laser systems must have the

best performance with $V_{\text{piezo}} = 50\,\text{V}$, as the PLL for the synchronization to the MO keeps the piezo around this voltage. More importantly, the laser is already equipped with an external optical power modulation input which enables the operation of a feedback acting on the optical power independent on the repetition rate feedback.

A.3 Relative Intensity Noise of the Origami Laser System Measured at the RF-Lock Chassis

In section 5.4.4 (pages 105 f.) the amplitude stability and relative intensity noise (RIN) of the Origami laser is discussed. The measurements were carried out using a low-noise laboratory power supply for powering the required amplifier and biasing the photodiode, while for normal operation an amplitude stabilization feedback with a detection circuit integrated into the rack chassis of the RF synchronization PLL is used. The intensity noise calculated from the baseband noise of this particular

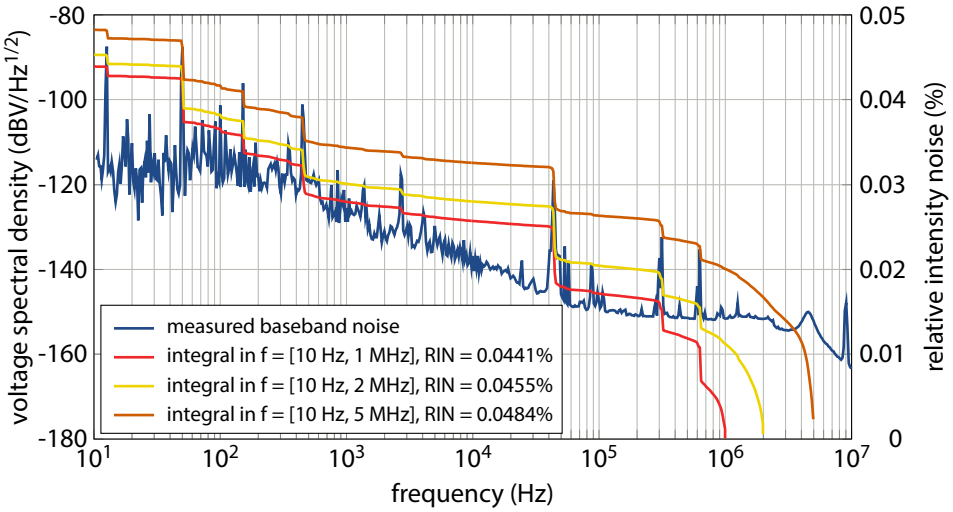

Figure A.3 | Relative intensity noise of the free-running Origami oscillator. The relative intensity noise does not change significantly for different integration intervals. The measurement was carried out with the output of the monitor port of the RF lock chassis in the synchronization laboratory and is spoiled by electronic noise and possible electromagnetic interference.

monitor is shown in Fig. A.3. The total RIN in each of the three frequency intervals amounts to about 0.04%. Especially the low frequency region contributes to these values with the 50 Hz line and its harmonics from the mains power grid. Other remarkable contribution come from frequency lines at 42 kHz, ~ 300 kHz and ~ 600 kHz. Due to the very low bandwidth of ~ 20 Hz of the optical power feedback, this purely electrical noise is not applied to the laser by the loop (see 5.30, p. 106).

The larger integrated intensity noise for both the erbium-laser (see section 5.2.4, pages 80 ff.) and the Origami laser system when measured at the rack chassis in comparison to a dedicated RIN measurement setup is caused by the electronics in the racks. Although the rack chassis is connected to

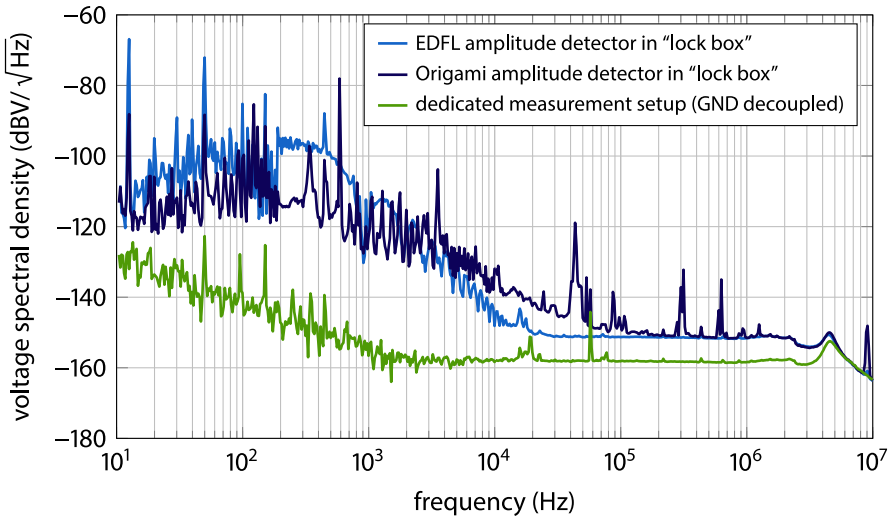

Figure A.4 | Noise floor comparison of different amplitude detection circuits. The noise floor of different amplitude detection circuits in the synchronization hutch measured after disconnecting the optical input. In the rack ("lock box") electromagnetic interference deteriorates the measurement significantly.

a power supply with battery backup and filters for the line power noise, there is significant noise observable in the floor of both amplitude detection circuits in the chassis, shown in Fig. A.4. The data has been recorded with the optical input disconnected. In case of a dedicated setup, where the photodiode, the DC-LNA, their power supplies and the signal source analyzer (SSA) are properly grounded and in particular decoupled from the ground of the optical table and the racks, a 10 dB lower noise floor is achieved (green trace in the figure). Such a setup allows for a more precise determination of the RIN of a laser system, but for optimization of the amplitude feedback, the characteristic from the rack chassis has to be considered.

A.4 Laser Diode Driver Test Setup

In section 5.2.5 it is discussed that the erbium-doped fiber master laser oscillator shows a large inte-

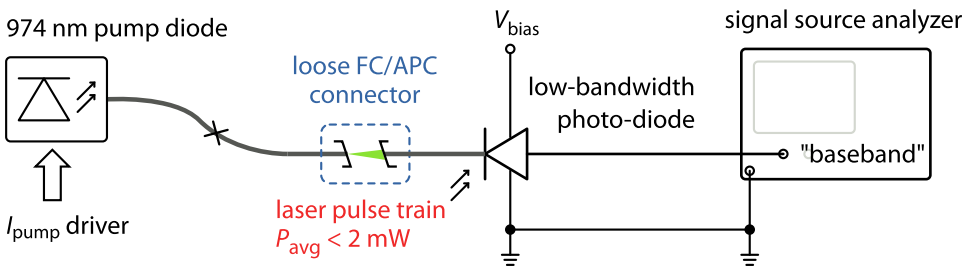

Figure A.5 | Setup for intensity noise measurements of laser diode drivers. A photodiode is used to measure the relative intensity noise directly, where attenuation is provided by a loose connector.

grated timing jitter when operated with the VME-based laser diode drivers, apparently because of their intensity noise in the according frequency region. To investigate this, an experiment as sketched in Fig. A.5 had been set up. The current for the laser diode is either provided by a Thorlabs or the VME laser diode driver (LDD). Its fiber is spliced to a connector which is loosely coupled to another fiber connected to the photodiode to reduce the optical power impinging the photodiode to $P < 2\,\mathrm{mW}$. The biased photodiode is directly connected to the baseband input of the signal source analyzer to prevent the noise of the amplifier obfuscate the noise of the driver. At pump currents of 0.5 A the laser diode emits 260 mW optical power which is reduced by a factor of 200 to 1.3 mW after the loose FC/APC connection. This leads to a voltage of 250 mV converted from the photo current into a 50 Ω resistor. Figure A.6 shows the results for the Thorlabs driver (red curve) and two channels

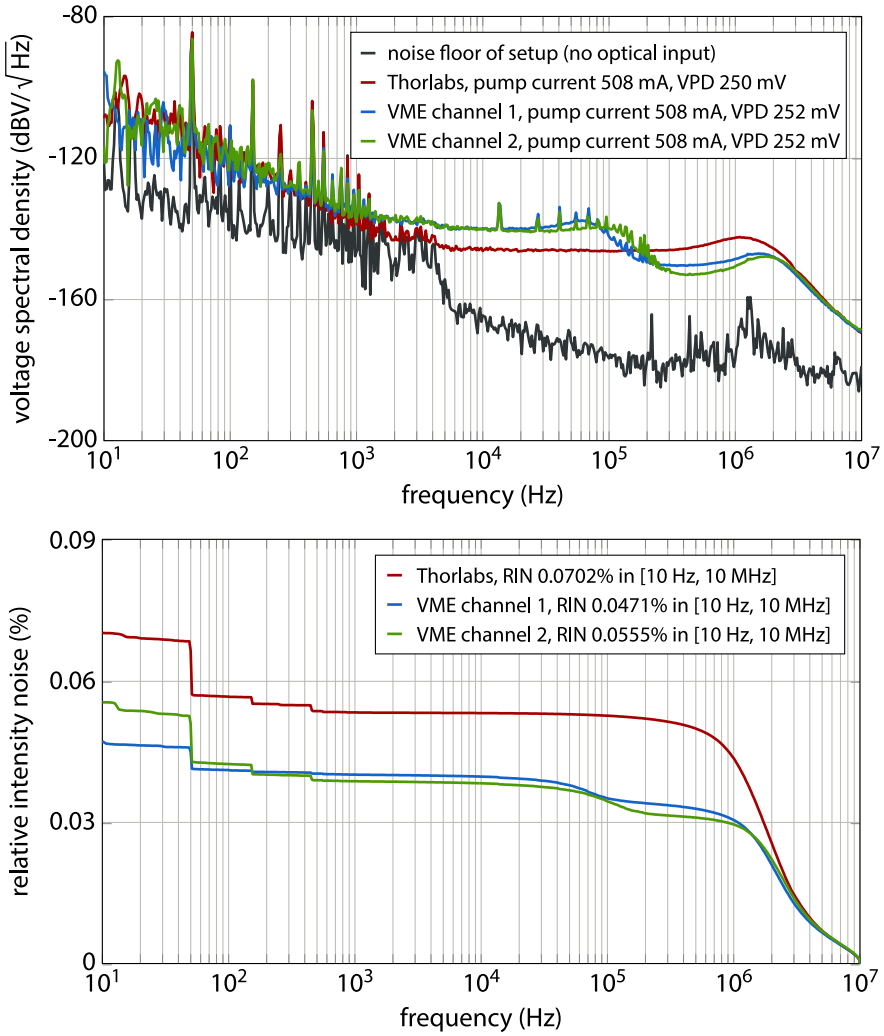

Figure A.6 | Intensity noise of a pump laser diode module. The relative intensity noise is measured using different drivers. In this test measurement under laboratory conditions, the noise of the VME-based drivers is lower, resulting from smaller high-frequency contributions.

of the VME LDD driver. Although the total RIN of the Thorlabs driver with 0.07% is higher than the ~ 0.05% for the VME driver, it can be seen that in the latter case the noise in the frequency region from 1 kHz to 100 kHz contributes more to the RIN. Exactly in these two decades the EDFL shows a large phase noise, resulting in a large timing jitter (see Fig. 5.13, page 83 and Fig. 5.14, page 84). The larger noise of the Thorlabs driver at low frequencies is not too critical, as the laser is synchronized to the master RF oscillator (MO) with a bandwidth of around 1 kHz, thus the phase noise below this frequency will be strongly suppressed. As the time of this writing, further investigations on the noise of the VME modules are ongoing to improve and beat the commercial ones, because not only the integration to the control system is preferable, but also the cost is much less for the VME drivers per channel (~ 300 euros) in contrast to the Thorlabs drivers (~ 2500 euros).

A.5 Additional Measurements on the Photoinjector Laser System

Polarization Controller of the Fiber Connection to the MLO

In section 8.2.3, the optical connection of the optical cross-correlator for the photoinjector laser system to the master laser oscillator with a not actively stabilized PSOF patch cord before the dispersion-compensated EDFA is described. In addition to the also with this type of fiber unavoidable, yet small, transit time drifts, also the state of polarization of the transmitted light is changing with temperature and humidity fluctuation. This results in a change of the splitting ratio in the polarizing beam cube

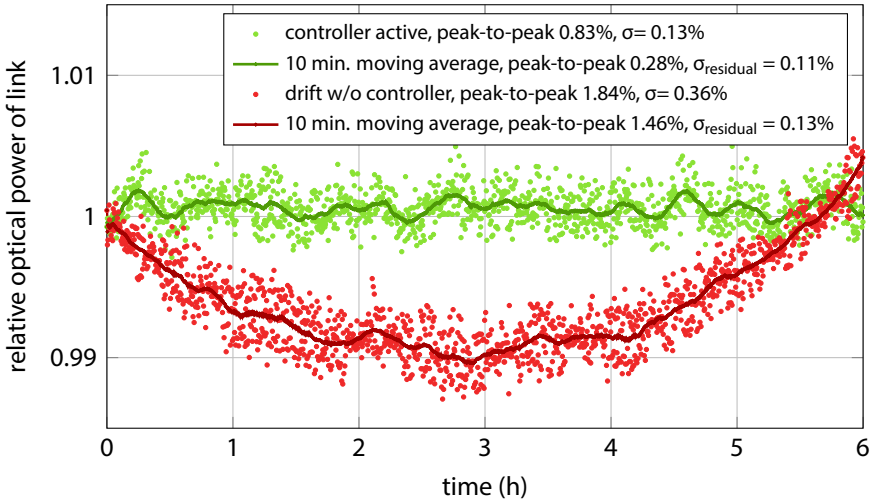

Figure A.7 | Optical power drift compensation of the reference signal in the cross-correlator. The dark blue curve shows the drift over a course of 6 hours. The light blue curve shows the optical power with an active stabilization loop based on a PBC and a motorized half-wave plate.

after the generation of linear polarized light with the quarter- and half-wave retarders (see Fig. 8.5, p. 173). Therefore, a simple two-point controller has been implemented as a MATLAB script, which rotates in the present state the motorized half-wave retarder based on the measurement of the fiber-coupled optical power monitor after the light has passed the beam cube. Figure A.7 shows a compar-

ison of the optical power level over a period of six hours with an active (green) and an inactive loop (red). When the optical power is not stabilized, the peak-to-peak drift amounts to Δ_{pp} = 1.84% for all data points or $\Delta_{pp,avg}$ = 1.46% for a 10-minute averaging window. In case of the active feedback, the peak-to-peak change is reduced to Δ_{pp} = 0.83% and an average of $\Delta_{pp,avg}$ = 0.28 %. The residual optical power fluctuations after subtracting the slow drift amount to $\sigma_{residual}$ = 0.11% (stabilized case) and $\sigma_{residual}$ = 0.13% (unstabilized case). The value for the stabilized case is nearly equal to the one of the unstabilized link, because the bandwidth of the feedback loop is only 0.3 Hz due to the motor movement. A significant improvement to suppress the higher frequency fluctuations can be made when the drive current of the EDFA's pump laser diode would be used as feedback actuator, but for the present setup that was not possible (see section 8.2.3, page 174). The amplitude stability would become particularly relevant in experiments where the 1.3 GHz LO signal is generated from the optical pulse train to suppress a timing drift due to AM-to-PM conversion in the photodiode.

Pulse Pattern of the Photoinjector Laser System

The PTO emits bursts at a rate of 10 Hz with approximately 3 ms duration and a intra-burst repetition rate of 27.083 MHz. This pulse train, indicated in yellow in Fig. A.8, starts with relaxation oscillations which are typical for pulsed lasers. These oscillations settle within 700 µs. A first Pockels cell cuts out an approximately 1.3 ms long train from the stable region with a repetition rate of either 1 MHz for normal operation of FLASH or 3 MHz for the high-current mode (see section 1.7, page 15). This train is sent to the multi-stage amplifier, and shown in magenta in the screenshot. The amplitude flatness of this shorter burst can be controlled by the trigger delay of the amplifier's pulsed pump diodes. A second Pockels cell is used to generate the pulse pattern for the bunch pattern of the accelerator. This is accomplished by feeding the appropriate number of trigger pulses at the desired repetition rate into the driver of this second cell. Finally, this train is guided to the wavelength conversion stage. After the LBO crystal, i.e. the first second-harmonic generation process, leakage light is detected by a photodiode and shown as the green trace in the figure[1]. Note that the pulse pickers are not shown explicitly in the schematics in Fig. 8.2. More detail on the complete injector laser system, although the slightly different one used before the 2009/2010 FLASH upgrade, can be found in [WKT05].

Response of the Pulse Train Oscillator to a Phase Step

In section 8.5.2 (page 182 ff.), the response of the photoinjector laser to a phase steps has been investigated using the gun emission phase method. These measurements were carried out before the upgrade of FLASH in 2009/2010, and hence the older injector laser system as described in [WKT05] was used. The optical cross-correlator installed at the new photoinjector laser enables a direct and more precise measurement of the PTO's response to phase steps without the detour via the electron gun and the toroid charge monitor. Figure A.9 shows the response of the PTO to phase steps of ±1 deg and ±2 deg applied to the EOM in comparison to the unmodified phase. The arrival time is shown for a macropulse duration of 501 µs. The curves differ significantly to the ones shown in

[1] Note the coincidence of the detected light with a wavelength of 523.5 nm and the the color of the oscilloscope trace…

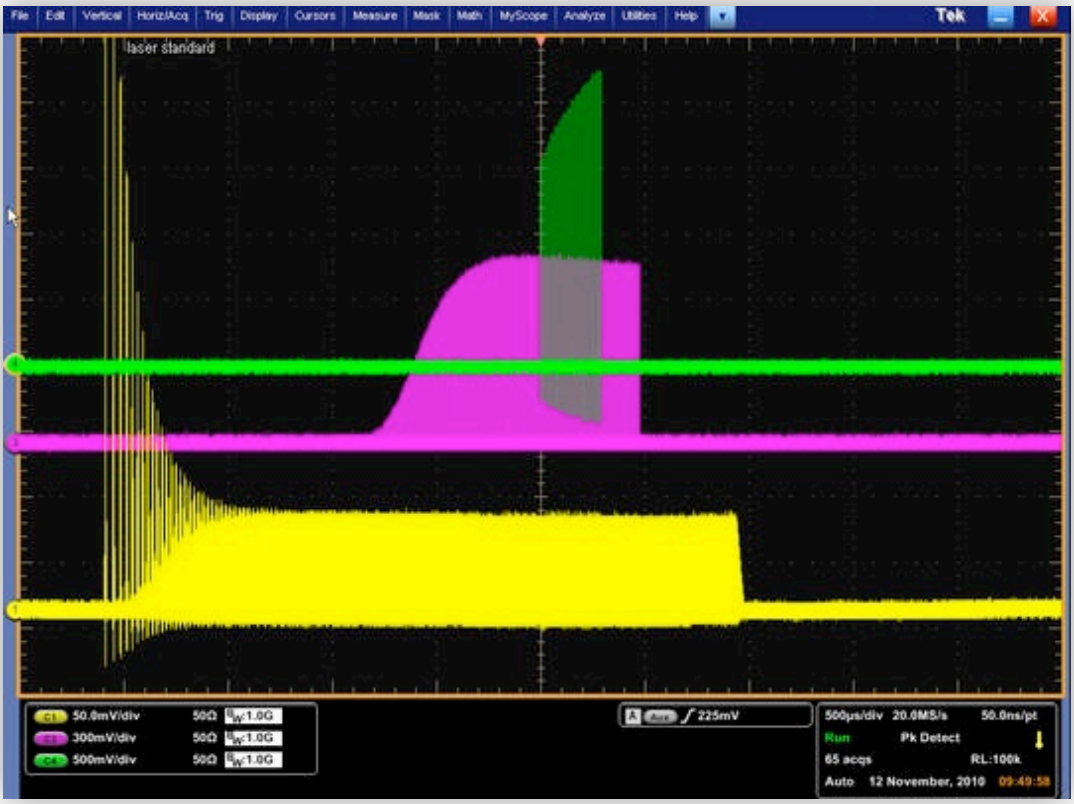

Figure A.8 | Screenshot of the oscilloscope used for permanent monitoring the injector laser. The individual traces show photodiode signals of the oscillator (yellow), the amplified pulses (magenta) and the ones actually sent to the photocathode (green). The time scale on the abscissa is 500 µs/div, while the traces are intentionally shifted vertically for increased readability.

Fig. 8.16, where the laser reacted in less than 10 µs, but there the set phase was only reached within 60% to 70%. Here, the expected timing change of ±2.137 ps for the ±1 deg steps and ±4.274 ps for the ±2 deg steps are reached. However, fits of the function $T_{\mathrm{EOM}} = T_{\mathrm{max}} \left(1 - e^{t/t_{\mathrm{r}}}\right)$ lead to rising times in the order of $t_{\mathrm{r}} = 90$ µs. Thus, there must be a limiting component in the chain. The vector modulator input channels for I and Q are low-pass filtered, as described above, but with a bandwidth in the order of 100 kHz and this can not explain the slow response. The photomultiplier tubes, which are used to detect the generated sum-frequency as basis for the arrival time calculation are also bandwidth-limited by the use of a load resistor of 10 kΩ to improve the signal-to-noise ratio, but their bandwidth remains in the order of hundreds of kilohertz. In the present state with the feed forward correction, the slow response is not that critical, as a phase slope, for instance, applied to the EOM can begin several hundreds of microseconds before the first pulse is picked for the electron bunch generation. For a future adaptive feed forward or feedback loop, the response time of the PTO becomes more important. In order to cross-check and improve the situation, a number of further investigations has to be carried out, but naturally this requires dedicated studies shifts at the accelerator, as experi-

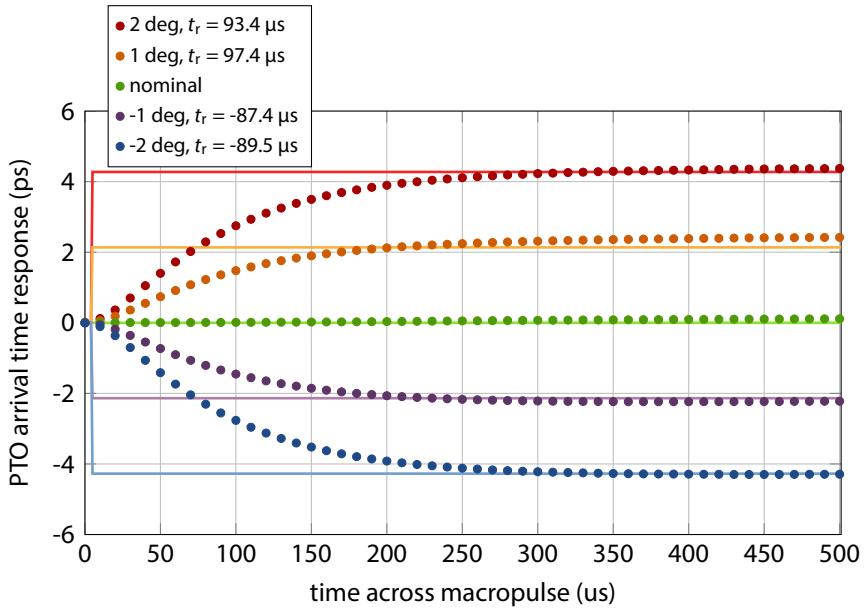

Figure A.9 | Step response of the PTO measured with the optical cross-correlator. Response of the pulse train oscillator (dots) to different phase steps applied to the EOM inside the laser resonator (solid lines).

ments with the injector laser system can not be carried out during normal operation of the machine. Ultimately, an arrival time correlation measurement with the first BAM must be carried out, similar to the ones described in section 8.5.3, in particular at the special gun offset phase where phase fluctuations are strongly suppressed (see pages 190 ff.). This will allow for a cross-check of the determined step response of the laser oscillator.

A.6 Fast Calibration of an Optical Cross-Correlator

In section 7.1.3 (page 159 ff.), a method for the fast calibration of an optical cross-correlator using a vector modulator in the reference signal of the 1.3 GHz-PLL has been explained. Figure A.10 shows the ADC signals digitized with corresponding ADCs. The upper plot shows the output of the differential amplifier used to subtract the detected SFG intensities with analog electronics. The lower plot shows the setpoints of the *Q*- and *I*-channels written to the DAC driving the vectormodulator and the corresponding readback values of monitoring ADCs. For better visualization, constant values have been added to the data, which has been recorded using the MatLab script explained in appendix E, page 247 ff. The phase shift applied to the Ti:sapphire by the slope in the *Q*- and *I*- channels corresponds to −1 ps to 1 ps around the original value, allowing for the translation of the ADC sampling points to time. By this, the method is similar to autocorrelation measurements, where a time delay is continuously sweeped. Due to the burst mode operation of the accelerator, the data can be recorded within one bunch trigger cycle. In the future, it is planned to integrate this calibration functionality into the DOOCS server controlling the DAC hardware, similar as explained in section 8.3

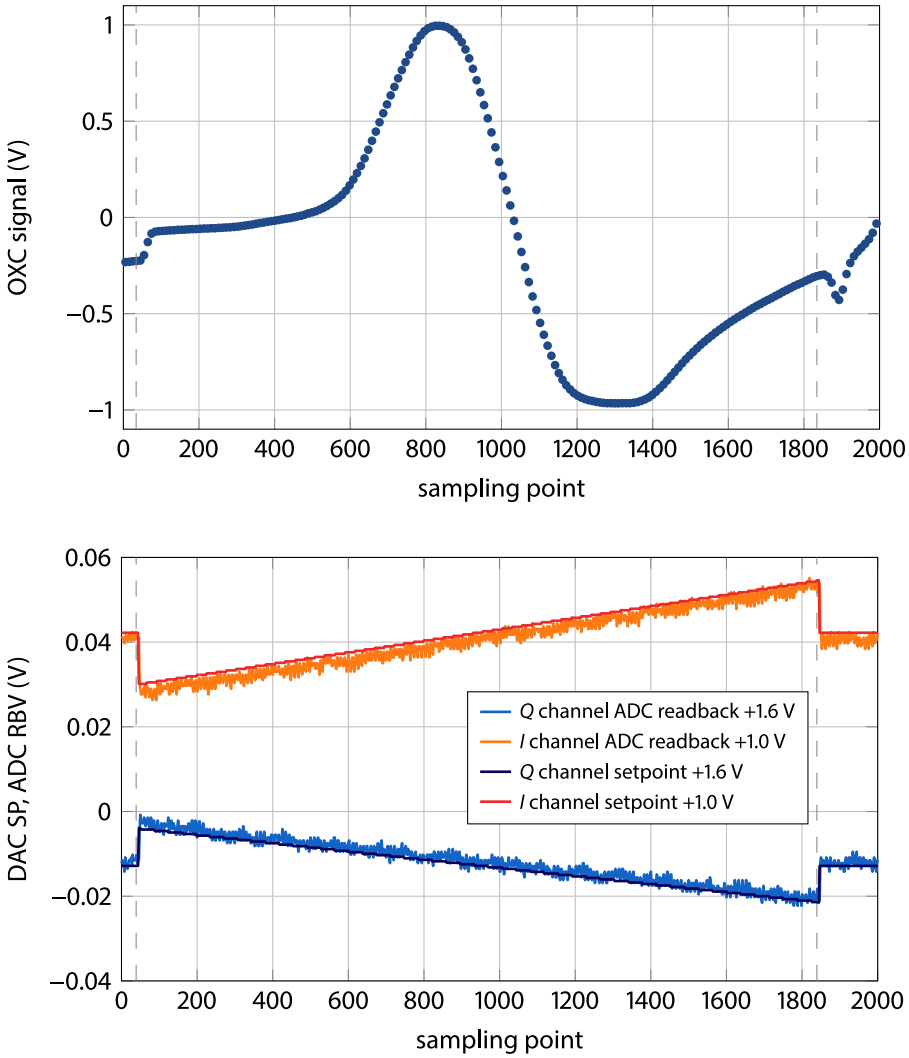

Figure A.10 | Raw data of the phase slope OXC calibration method. Top: Sampled output signal of the cross-correlator; **Bottom:** Calculated DAC setpoint (SP) values for the *I* and *Q* channel written to the DAC and signal of the monitoring ADCs (RBV).

(page 176 ff). Moreover, a similar fast calibration technique is planned for the automated calibration of fiber link stabilization units.

A.7 Phase Noise of the RF Reference in the Synchronization Laboratory and the Injector Laser Container

To estimate the added timing jitter performance of locking the master laser oscillator to the master RF oscillator (MO), its phase noise has been measured at the patch panel in the synchronization hutch, and after the vector modulator (VM, compare Fig. 5.17, page 88). The reference shows an

excellent performance, even at high offset frequencies resulting in an integrated timing jitter of 33.3 fs in [100 Hz, 10 MHz] as shown in Fig. A.11. After the vector modulator, however, the noise increases

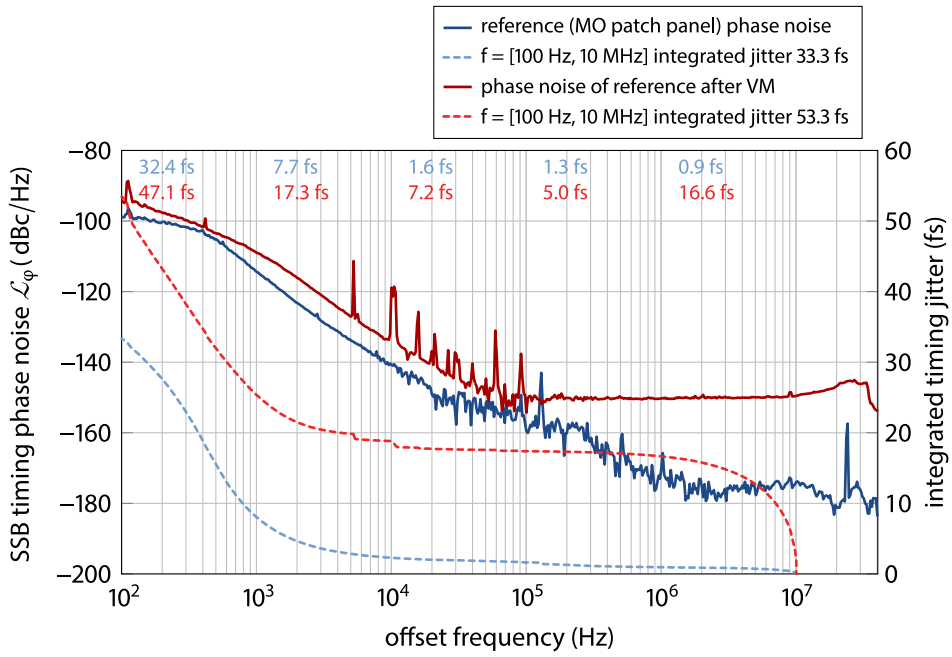

Figure A.11 | Phase noise and integrated timing jitter of the 1.3 GHz reference. Comparison of phase noise and integrated timing jitter of the 1.3 GHz reference measured before (blue traces) and after (red traces) the vector modulator. Both measurements were recorded with the SSA-internal correlation function ($N = 1000$, see section 5.2.5, p. 82).

significantly resulting in a total jitter of 53.4 fs in the same frequency interval. The main contribution is the much higher noise floor from 100 kHz onwards. The lines visible in the two decades before are caused by the DC voltage driving the I- and Q-channels of the vector modulator, but they do contribute only by approximately 1 fs to the integral. More critical is the much larger contribution in the frequency interval [1 kHz, 100 kHz], where the timing jitter amounts to 18.7 fs with the vector modulator in comparison to the 7.9 fs timing jitter of the reference. On the other hand, in case of the master laser oscillator (MLO) synchronization, the PLL is operated with a low cut-off frequency in the order of 1 kHz or even less to reduce the laser's noise below this frequency and avoid drifts with respect to the accelerator. Hence, the high-frequency noise will not effect the performance of this loop. But still, these measurements show that not only the lasers themselves, but also the reference must be investigated carefully, because for instance Ti:sapphire oscillators, will be synchronized with very high locking bandwidths in the order of 100 kHz in the future. From the data sheet the used vector modulator chip[2] should have a noise floor of −159 dBc, but due to the electronic input circuit, practically only a noise floor of the measured −150 dBc can be achieved. Ideally, for applications with high locking bandwidths passive waveguide-based phase shifters should be used.

[2] Hittite HMC497LP SiGe Wideband Direct Modulator RFIC, 100 . . . 4000 MHz

Vector Modulator Noise in the Injector Laser Laboratory

The photoinjector laser stabilization, as discussed in chapter 8 on pages 167 ff., also requires a vector modulator to be introduced to the RF signal driving the EOM inside the laser resonator. During the commissioning of the optical cross-correlator, the influence of the vector modulator on the phase noise and timing jitter has been investigated using the setup shown in Fig. A.12. The dark blue

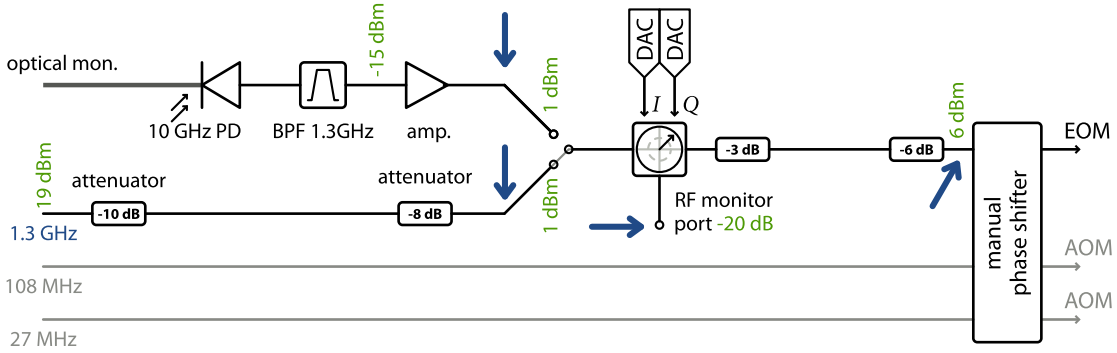

Figure A.12 | Schematics of the RF components used at the PTO including LO generation. In the present state, the RF signals with frequencies of 27 MHz, 108 MHz and 1.3 GHz are provided directly by the master RF oscillator (MO) via a patch panel in the laboratory. The 1.3 GHz branch incorporates a DOOCS-controllable phase shifter for arrival time manipulation of the emitted laser pulse train. The voltage generated by the DACs driving the vector modulator is set to $V_{VM} = (V_I^2 + V_Q^2)^{1/2} = 2.70$ V, resulting in the lowest integrated timing jitter at the input of the manual phase shifter. The phase noise has been investigated at the positions marked with a blue arrow. After this optimization, the power levels were set using appropriate attenuators to restore the original situation, which did not feature the vector modulator. As an alternative to the MO, an 1.3 GHz RF signal generated from the reference laser pulse can be used. In this case, the arrival time is defined by the MLO rather than the MO. In a future upgrade, it is planned to generate the lower frequencies of the AOMs also from this pulse train in order to minimize the effects from drifts. This also requires the installation of a stabilized fiber link from the MLO to the injector laser (see section 8.2.3, p. 174 f.).

traces in Fig. A.13 show the reference signal delivered by the MO. As expected, it shows a very good performance due to the short cable length to the MO itself. The integrated timing jitter amounts to 80.4 fs in the frequency range of [10 Hz, 10 MHz]. However, when the vector modulator was installed (compare Fig. A.12) with appropriate adaption of the power levels, the phase noise performance is degraded significantly by the high frequency noise (red trace in Fig. A.13). Not only the high noise floor, but particularly the frequency line at 308 kHz leads to an integrated jitter of 135.3 fs in the same frequency range as before. Since such a degradation is unacceptable for the operation of the accelerator's photoinjector laser, in numerous investigations it was found that the DAC and the monitoring ADC in combination with the long, but unavoidable, cable length are the reason for this due to electromagnetic interference (EMI). With a modification of the I and Q input stages of the vector modulator by means of a 100-kHz low-pass filter, the noise could strongly be suppressed, shown as light blue curves in the figure. The prominent line at 308 kHz, for instance, is reduced by ~ 25 dB and the integrated timing jitter amounts to 75.8 fs. Larger contributions in the higher frequency range

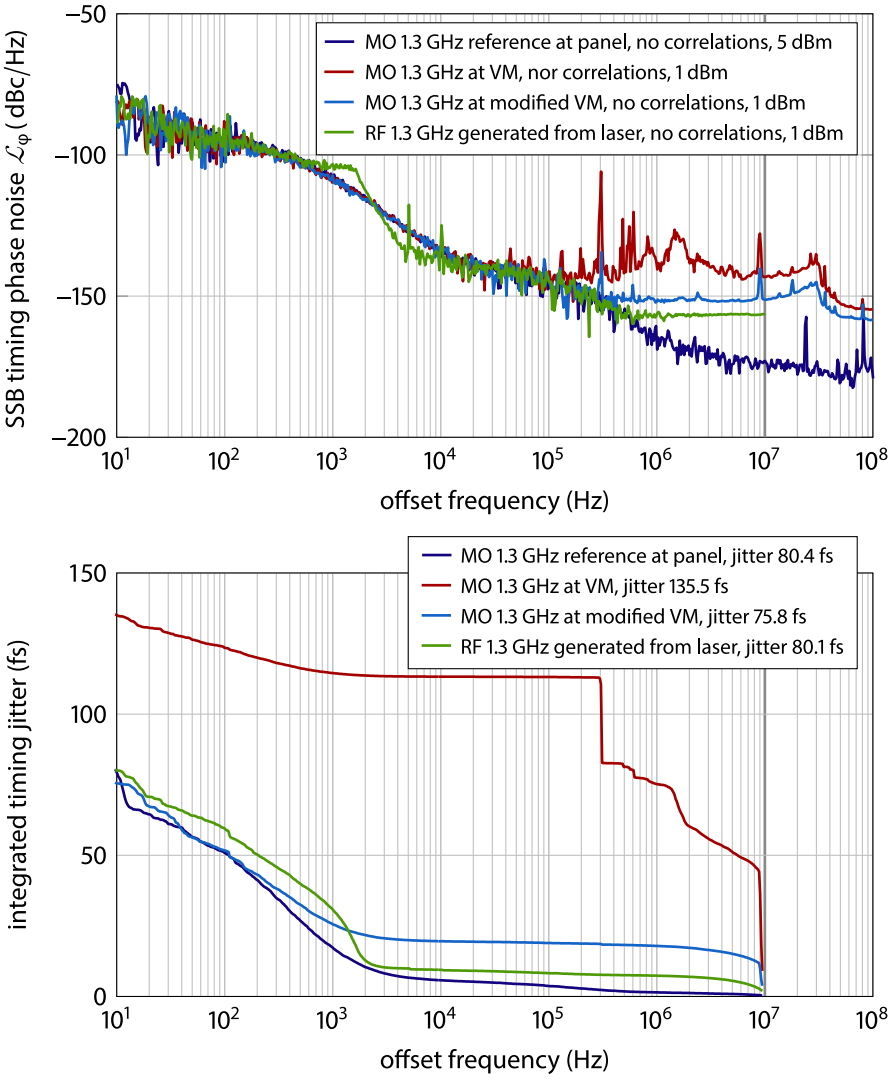

Figure A.13 | Phase noise and integrated timing jitter of the EOM-driving RF for the PTO. The phase noise (**top**) of the RF signals was measured at the points indicated in Fig. A.12. One of these signals is used drive the EOM inside the PTO laser cavity, where a change of the signal requires hardware re-cabling.

are due to the higher noise floor in comparison to the RF reference without the VM. The drawback of the low-pass filter, however, is the limitation of the achievable bandwidth of the planned phase stabilization feedback for the laser. On the other hand, as discussed in section 8.2, pages 169 ff., the photodetection in the optical cross-correlator (OXC) is also bandwidth limited in the same order of magnitude in the present implementation. The figure furthermore shows the phase noise of the 1.3 GHz LO signal generated from the reference laser pulse train of the Origami laser by the standard scheme by means of a photodiode, a band-pass filter (BPF) and an amplifier. This signal can be used to drive the EOM in dedicated laser pulse and electron bunch arrival time studies (see section 8.5, pages 180 ff.). Most notable, the phase noise curve (green) shows a kink at around 2 kHz, which leads

to a significant contribution to the integrated timing jitter. At the time of the measurement, the loop gains of the Origami laser were not yet optimized, thus the phase noise in the frequency region of 200 Hz to 2 kHz is higher than it could be (see section 5.4.3, pages 101 ff.). Nonetheless, the total jitter in the complete evaluated frequency interval amounts to 80 fs, which is comparable to the MO-RF signals and at least no degradation of the PTO performance is expected, when using the 1.3 GHz signal for synchronization to the MLO.

A.8 Summary of Timing Jitter Based on Phase Noise Measurements

The integrated timing jitter of numerous devices, such as the master laser oscillators in different operating regimes, has been calculated from many phase noise measurements. Moreover, the integration has been carried out in different frequency intervals to investigate different effects. Table A.1 on the next page provides an overview and includes references to the corresponding figure in this thesis, where the results are discussed. Note that the data given for the "noisy link", marked with a star (*), is taken from one exemplary measurements. Under particular circumstances, values ranging from ~ 200 fs up to 4 ps have been observed in the frequency range [1 kHz, 10 MHz] (see section 6.3, pages 144 ff.).

Table A.1 | Overview of the integrated timing jitter calculated from phase noise. The basis for the evaluation are the numerous subsystems of the synchronization infrastructure.

description	f_c	integrated timing jitter in frequency interval				Fig.
	GHz	[10, 10M]	[100, 10M]	[1k, 10M]	[10k, 10M]	
master RF oscillator (distributed to laboratories)						
patch panel in synch lab., 1000 corr.	1.3		33.3 fs	8.0 fs	2.2 fs	A.11
after splitting and VM, 1000 corr.	1.3		53.3 fs	25.4 fs	18.8 fs	A.11
patch panel in inj. laser hutch	1.3	80.4 fs	51.4 fs	17.6 fs	5.7 fs	A.13
after original VM (no filter)	1.3	135.3 fs	123.9 fs	114.6 fs	113.2 fs	A.13
after improved VM (IQ filter)	1.3	75.8 fs	52.0 fs	25.8 fs	19.5 fs	A.13
after splitting in EO laboratory	1.3		50.8 fs	18.8 fs	9.3 fs	6.15
HHG laboratory (see [FBB+10])	1.3			45.1 fs	41.8 fs	
older erbium-doped fiber laser with 40 MHz repetition rate						
free-running, 1000 corr.	1.3		290.5 fs	17.0 fs	15.2 fs	(7.3)
erbium-doped fiber master laser oscillator						
free running, VME LDD, EOT	1.3	5323.0 fs	793.4 fs	134.6 fs	19.3 fs	5.13
free running, Thorlabs LDD, EOT	1.3	2338.3 fs	316.9 fs	14.6 fs	7.8 fs	5.13
φ-locked, VME LDD, EOT	1.3	183.7 fs	179.1 fs	172.2 fs	21.9 fs	5.14
φ-locked, Thorlabs LDD, EOT	1.3	60.6 fs	42.3 fs	25.1 fs	9.2 fs	5.14
free running, Thorl., open housing, u^2t	1.3			23.5 fs	6.6 fs	5.15
free running, Thorl., closed housing, u^2t	1.3			12.4 fs	6.3 fs	5.16
free running, Thorl., open housing, u^2t	2.6			24.2 fs	4.6 fs	5.15
free running, Thorl., closed housing, u^2t	2.6			11.5 fs	3.8 fs	5.16
RF generated from optical pulse train (for laser synchronization)						
inj. laser, with VM (IQ filter)	1.3	80.1 fs	59.7 fs	30.9 fs	9.4 fs	A.13
EO lab., noisy * link, no VM	1.3		83.9 fs	75.2 fs	72.9 fs	
EO lab., impr. link, no VM	1.3		55.1 fs	23.2 fs	19.3 fs	6.15
Origami SESAM-based master laser oscillator						
free running, no corr., EOT	1.3		31.5 fs	10.8 fs	9.7 fs	5.27
free running, 1000 corr., EOT	1.3		55.1,fs	5.1 fs	4.1 fs	5.27
free running, 1000 corr., u^2t	1.3		129.2 fs	12.9 fs	12.0 fs	5.28
free running, 1000 corr., u^2t	2.6		128.6 fs	9.4 fs	8.4 fs	5.28
φ-locked, f_{cut} = 1 kHz, EOT	1.3		58.7 fs	30.5 fs	6.0 fs	5.29
φ-locked, f_{cut} = 300 Hz, EOT	1.3		60.9 fs	8.6 fs	5.9 fs	5.29
Micra Ti:sapphire oscillator used for EO bunch diagnostics						
free-running, no corr.	1.3		793.0 fs	22.5 fs	17.7 fs	
free-running, 1000 corr.	1.3		1063.8 fs	18.0 fs	13.8 fs	7.2
free-running, no corr.	2.6		664.8 fs	9.9 fs	8.7 fs	
free-running, 1000 corr.	2.6		541.4 fs	11.4 fs	7.6 fs	7.2

B Reassembly and Upgrade of the Synchronization Laboratory Infrastructure

The master laser oscillator (MLO) and the fiber link stabilization units (LSUs) as the central components of the optical syncronization system are installed in a laboratory in direct vicinity to the photoinjector laser hutch. The planing and installation of the so-called "synchronization hutch" inside the main accelerator hall was part of a former thesis [Wino8]. Back then, the optical setups consisted two laser systems in development –one erbium-doped fiber laser (EDFL) and one ytterbium-doped fiber laser (YDFL)– and the two fiber link stabilization prototypes, which were used for the proof-of-principle experiments being topic of [Loeo9]. Within that thesis, the optical fibers[1] to the various

Table B.1 | Overview of the optical fibers installed at the accelerator facility. The table is divided into the currently used (upper part) and the future optical links.

location/use	identifier	tunnel, z	laboratory	length
BAMs 1UBC2 & 3DBC2	BC2 (P2)	21 m	–	53.8 (+8) m ("U")
			–	53.8 (+15) m ("D")
BAM 4DBC3	BC3 (P4)	76 m	–	97 (+12) m
BAM 18ACC7	ACC7 (P6)	142.5 m	–	180 (+2) m
synch's EO & HHG Ti:S	ORS (P8)	–	28G/007	230 (+20) m
LLRF ACC1	ACC1 (P1)	12 m	–	
LLRF ACC23	ACC23 (P3)	45.5 m	–	
LLRF ACC4567	ACC456 (P5)	113 m	–	
HHG tunnel, BAM 1SFELC	OCAS (P7)	192 m	–	229 m
synch. pump-probe Ti:S	PP (P10)	–	28C/laser	361.4 m
special diagnostics	EXP (P9)	–	28C/expt.	

end-stations at the facility had been planned and commissioned. An overview of the locations and lengths[2] from the rack next to the hutch, where they accumulate in so-called splice cassettes, is given

[1] Exactly speaking, to each location a fiber bundle consisting of 24 individual SMF-28e fibers embedded in a single, gel-filled cable were installed. These bundles end in break-out boxes, where they are patched to a panel with FC/APC receptacles. At the BAM end-stations the fibers do not only provide the optical fiber link, but 4 other fibers are used to transport the modulated pulse train back to the synchronization hutch.

[2] It should be noted that the fiber length was measured by the installation company during the assembly with a telecom-grade OTDR. This technique is designed for very long-haul fiber networks in the kilometer range and hence a limited

in table B.1. From the patch panels inside this rack, the optical fiber link units are connected to the fiber link stabilization units via another patch panel and an individual fiber patch cord of the appropriate length. The reassembly of the optical table was one of the major changes in the infrastructure of the synchronization hutch and required a careful planning. It is laid out to host 16 fiber link stabilization boxes, two master laser oscillators, the distribution unit and ensures a stable installation of the EDFA fibers connecting the links to the FSD. Furthermore, space for the electrical connections cannot be neglected, as well as for the autocorrelator required for the commissioning of the fiber links. As the dimensions of the optical table are $2.0 \times 1.4\,\mathrm{m}^2$ the links have to be installed in two levels. Initially (i.e. from [Wino8]), it was planned to place all devices on a aluminum plates which in turn are bedded onto a 5 cm thick sheet of lead foam in order to reduce the influence of mechanical vibrations. However, during the commissioning of the MLO and the first two fiber link units it became obvious that this approach is not optimal, as the plates deform when loaded with a new device, such as a link box, which weighs in at around 20 kg. It was found to be especially critical that the aluminum consisted of 3 separated plates screwed to each other. The effect has been inves-

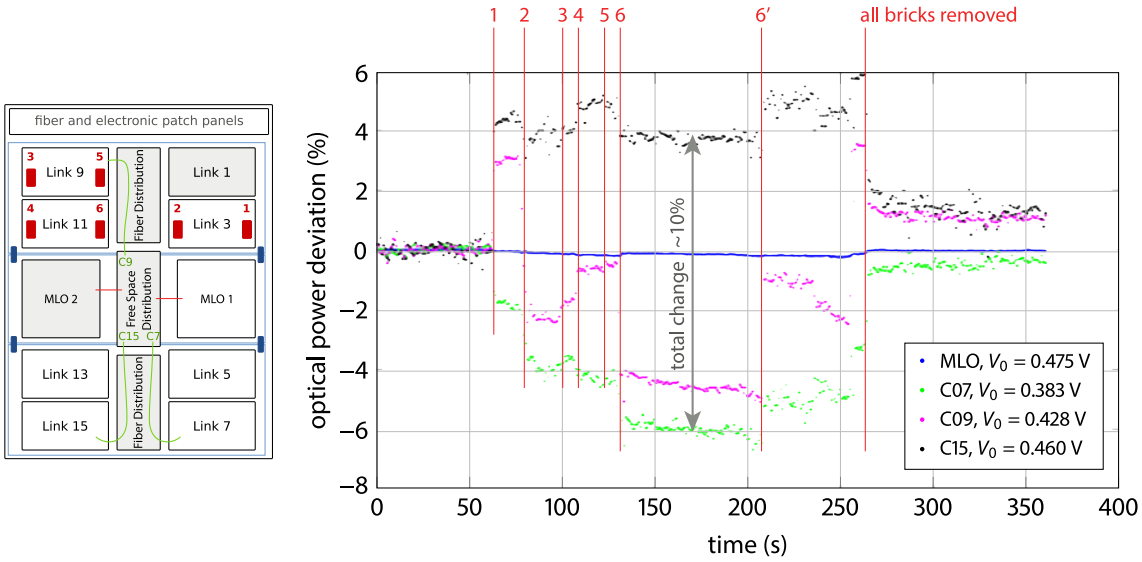

Figure B.1 | Influence of the mounting of new devices on the optical power. The test was performed with the originally planned optical table with three separated aluminum sheet on lead foam. The installation of new devices was simulated by putting weights at the corresponding positions while monitoring the change of the optical power measured at three collimator ports of the FSD.

tigated by a measurement of the optical power change in the free-space distribution unit at three collimator ports (FSD, see also Fig. 5.32, page 110) while putting lead blocks onto the table with a weight nearly equal to that of the link boxes. In Fig. B.1 the output of the optical power monitors

accuracy in the order of ±2 m. This complicates the commissioning of the fiber links, because the DCF can then only be cut with uncertainty of ±0.2 m.

is shown for the subsequent addition of more weight to the aluminum plate (depicted by the blue outlines in the schematic drawing). After the 6th lead block a peak-to-peak change of $\Delta P_{\mathrm{pp}} \approx 10\%$ between the ports C07 and C15 was observed, although these ports are directly next to each other in the FSD. At the time denoted by 6' an additional force has been applied locally, which leads also to a significant change. This is an important result, because of the compactness of the complete assembly and the limited space, it is unavoidable for an experimenter to support himself on the table when, for instance, aligning the FSD. Moreover, and very critical, the applied forces changed the optical alignment irreversibly as after removing the lead blocks from the table, the optical power monitors did not show their original values. From these measurements, it was decided to remove the lead foam an the aluminum plates and to install all components directly onto the optical table – which naturally caused some delay in the commissioning process of the complete system. However, after the removal and the re-installation of the devices, the measurement was repeated and the maximum change of the optical power was measured to be well below 1%. To investigate the influence of vibrations, the optical table was exposed to different acoustical frequencies with different amplitudes using a loudspeaker. At the same time the optical power change (see section 5.2.4, page 80 f.) and the baseband spectrum of highly sensitive seismographic acceleration sensors for the three room axes placed on the optical table have been measured. It was found that the excitation frequencies are visible in all spectra, but the contribution to the RIN was in either case negligible in contrast to the 50 Hz line and its harmonics from the electrical mains. Here it paid out, that the optical table was installed decoupled from the concrete base of the accelerator hall.

Another important change in contrast to the prototype system is the installation of a cover of the optical table to prevent the components exposed to an air-flow and to further minimize the influence of temperature changes. In a long-term drift measurement (see section 5.6, pages 120 ff.) also the

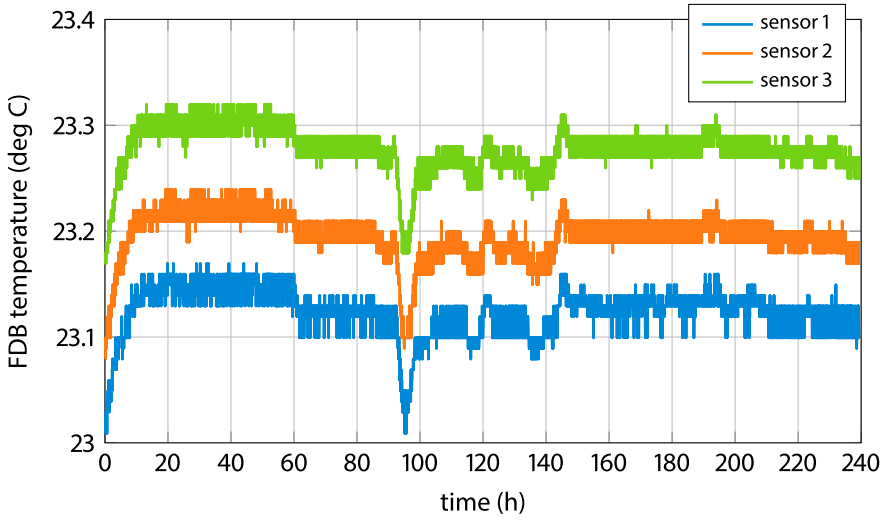

Figure B.2 | Temperature stability over 240 hours inside the cover of the optical table. The temperature sensors were installed at the positions where the temperature-sensitive EDFAs are laid out.

temperatures on the optical table and the room has been recorded. Figure B.2 shows the data of three

sensors which are installed next to the EDFA fibers, as they are most sensitive of temperature changes, because they belong to the distribution and are not actively stabilized. The peak-to-peak temperature change amounts to less than 0.16°C and a root-mean-square of 0.02°C, which is more or less limited by the measurement resolution, except in the beginning of the measurement and the relatively large change after 95 hours. Neglecting these, the rms value is $\Delta T_{\mathrm{rms}} \ll 0.01°\mathrm{C}$, thus practically the drift of the fibers has no influence.

The second major concern during the massive upgrade and expansion of the synchronization system are electronic controls, as well as readback and monitoring. In the prototype system, the laser, the links and each BAM with its digital front-end advanced carrier board (ACB) had its own VME crate. In the upgraded version, however, two crates are forseen for eight link stabilization loops each, together with the monitoring channels and laser diode drivers. Furthermore, it was planned to install the ACB of at least on BAM also in these crates. Another crate is used for the digital PLL of the and the amplitude feedback loop of the two master laser oscillators. A fourth VME crate should

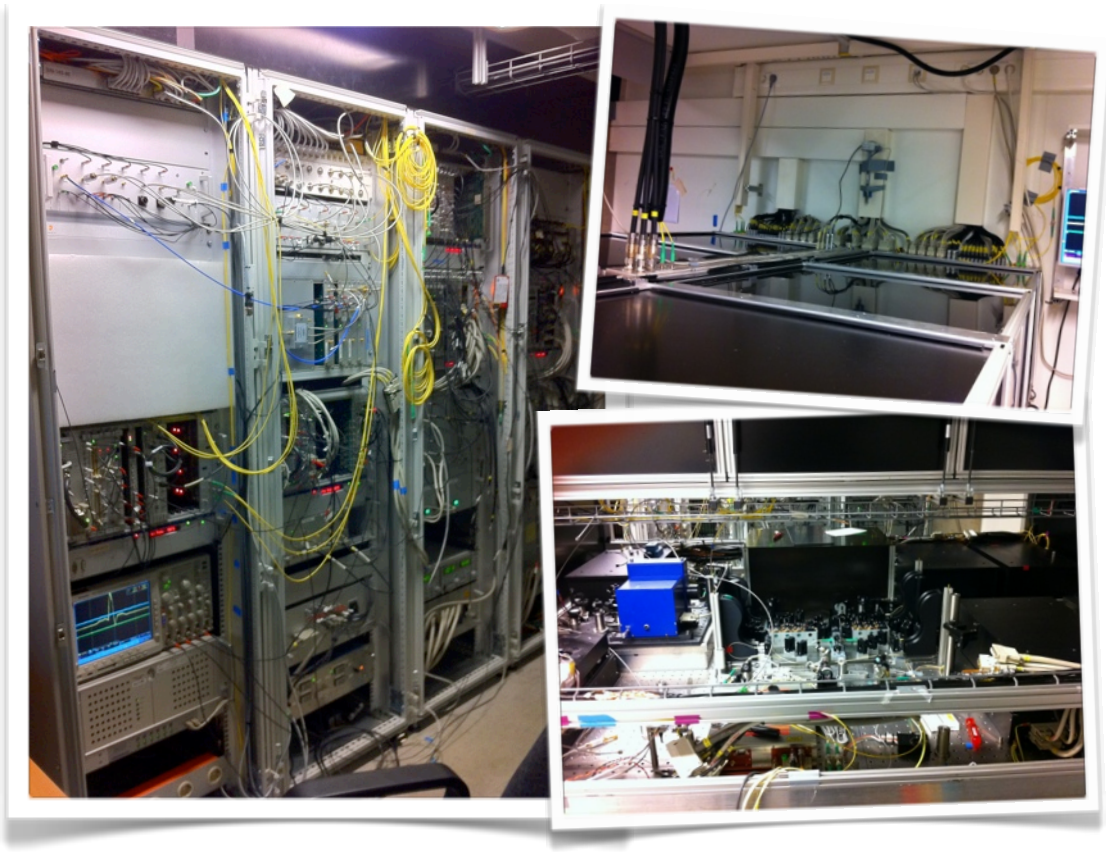

Figure B.3 | Photograph of the interior of the synchronization hutch, late 2010. Left: : Electronic racks containing the controls and monitoring electronics for the synchronization system inside the laster laboratory. The cabling required careful planning of the installations of the VME crates, the PLC units and patch panel locations, as there were more than 500 cables to install. **Right:** : Views of the optical table with closed cover (**top**), where more than 300 cables at the patch bay can be seen, and opened (**bottom**) showing the Origami laser system, the free-space distribution unit and the fiber link stabilization units.

have the remaining ACBs for the BAMs and the large horizontal aperture beam position monitor (EBPM). These crates are installed in four standard, full-height 19-inch racks, together with the RF lock chassis, RF- and optical EBPM chassis [Hac10], motor control PLC[3] chassis, the temperature monitoring PLC and power supplies with a battery backup for the critical components (see Fig. B.3). After the complete installation, two major issues arose: Firstly, various software bugs prevented the concurrent operation of the DSP-based control loops, the ACBs and a couple of ADCs in the same VME crate. The solution to this was to install a fifth crate containing only the monitoring ADC channels, and, obviously, a debugging of the ACB/BAM server including its firmware. Secondly, the racks became warm with temperatures more than 12°C above the room temperature. As they are not closed with doors, this led to an undesirable temperature gradient in the laboratory. Only an extensive –and expensive– upgrade of the air conditioning system, including an active exhaustion of the warm air from the racks improved the situation.

The planning of the required cabling and rack layout was also a complicated and time consuming task, as, for instance, each link requires three motor drivers, three monitoring ADC channels, one laser diode driver, a current source and a two-channel DSP-based regulation loop, which, in turn, requires a high-voltage (HV) driver for the piezo stretcher[4]. Together with the laser control and monitoring signals the number of cables from the optical table to the side of the laboratory where the four racks are located sum up to approximately 300. These cables were mostly individually assembled in-house, such that they fit from the patch panel of optical table to their corresponding device in the rack, like the motor controller PLC. The analog channels, like power monitors or the cross-correlator signal are patched through a panel in each rack, allowing for more transparency and flexibility in the connections, which was particularly useful when the fifth VME crate had to be installed.
Since the installation, setup and commissioning of the optical synchronization system is intentionally not planned to be fixed once and for all –there are many problems to solve, partly major changes and new developments– it turned out to be useful to have a number of spare channels in the control and readback electronics. That allowed for the installation of additional monitoring channels, for example of the FSD. On the optical table, the space of link 13 (see Fig. B.1) is, contrary to the planning, occupied by three optical power monitoring setups and the laser-to-RF conversion setup, whose signal is used in the 2.6 GHz phase detector of the fiber link units. Due to the small footprint of the Origami laser system, the second one for redundancy can be installed on the same side of the FSD as the first one. The nascent space on the optical table currently being occupied by the breadboard EDFL can be used for further diagnostics like permanent measurement of the pulse duration and the optical spectrum, as discussed in section 5.2 (page 73 ff.). In the next iteration, the fiber link stabilization units are supposed to operate maintenance free. Therefore, in the second level of the table, an optical fiber link stabilization unit known as "short link" based an RF-based phase detection scheme, but nonetheless providing femtosecond accuracy [Zem08, Lam11], is envisioned to be installed to connect the injector laser system to the master laser oscillator. It is also imaginable, that a Sagnac loop interferometer

[3] In German, the abbreviation SPS is commonly used.
[4] In this context, it should be emphasized that special cables and connectors had to be introduced to comply with the the according VDE regulations for safety…

[KKL06] will be installed as phase detector for the synchronization of the MLO to the RF oscillator.

Control System Integration

As a rough estimate the optical synchronization system has more than 1000 digital and analog output and input channels permanently available in the accelerator's control system. In the labs where components are developed and manufactured additionally around 300 channels are used temporarily. As the control system is very versatile it is a tremendous task to set up all channel parameters initially and especially to monitor all signals. Therefore, an overview panel, shown in Fig. B.4, in the graphical user interface DOOCS data display (DDD) was created to summarize the status of the most important components. The panel reflects the actual topology of the system based on the redundant

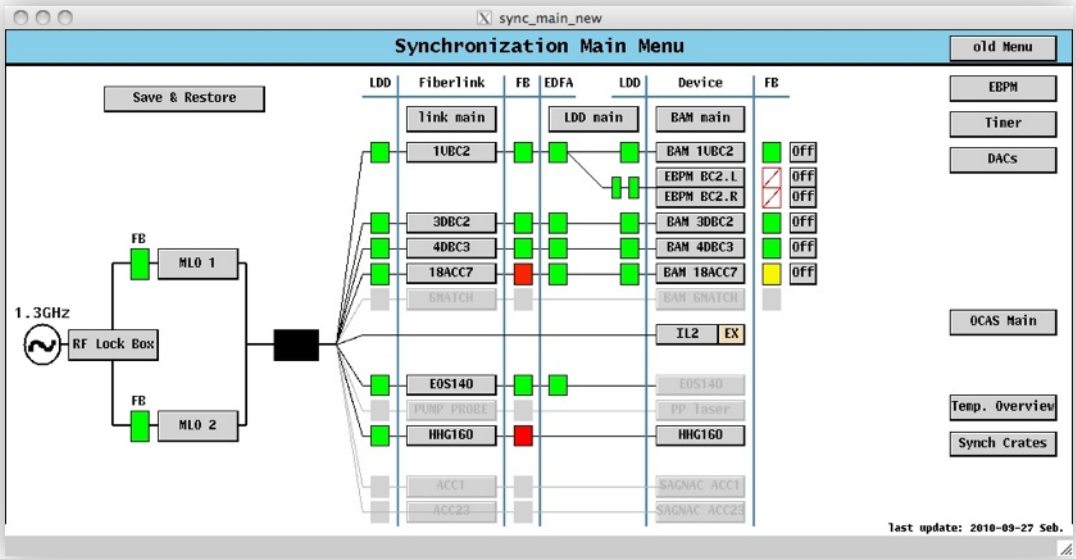

Figure B.4 | Screenshot of the main synchronization system DOOCS panel. The panel layout resembles the actual topology of the system and provides an overview of the system's health with different types of indicators. Furthermore, it enables access to all individual components via deeper-level panels and tools (compare e.g. section 8.3, p. 176 ff.)

operation of two MLOs, the splitting and the distribution to the devices across the accelerator facility. The fiber links, for instance, have indicators for the operation of the FSD-EDFA laser diode driver, the driver for the EDFA at the link end and an indicator if their FB loop is engaged. For the BAMs also the status of the laser diode driver and in particular the state of the DOOCS server delivering the arrival time data is indicated. In the figure it can be seen that the BAM.18ACC7, for example, showing a yellow indicator is in principle operational but currently stopped providing arrival time data, as its exception handler detected that the according fiber link is not locked to the laser, in turn indicated by the red box next to the fiber link's button. Those buttons open expert interfaces with additional information, monitoring, tools, controls etc.

C Properties of Selected (Nonlinear) Optical Crystals

In many laser systems and numerous optical setups nonlinear optical processes in crystals are exploited, as explained in chapter 3, pages 47 ff. This appendix summarizes selected properties of the most commonly used crystals and their application in setups at FLASH and within the optical synchroniztaion system. Most of the data is taken from [DGN99] and the publications cited therein.

C.1 Beta Barium Borate (BBO)

Beta barium borate, which is also known as β-barium borate, β-BaB_2O_4 or short BBO, is a negative ($n_o > n_e$) uniaxial crystal with a trigonal crystal system. It belongs to the crystallographic point group $3m$ and its nonlinear optical coefficients are

$$d_{22} = \pm 2.3 \times 10^{-12}\,\mathrm{m/V} \quad \text{and} \quad d_{31} = \mp 0.16 \times 10^{-12}\,\mathrm{m/V} \quad \text{at } \lambda = 1.0642\,\mu\mathrm{m} \tag{C.1}$$

BBO has a large birefringence (approximately six times larger than KDP, for instance) and a wide transmission range from the deep ultraviolet (UV, 0.189 µm) to the infrared (IR, 3.5 µm). Furthermore, it has a large damage threshold (~ 10 GW/cm^2 for 100 ps pulse duration at 1064 nm) and a low temperature-dependence of the refractive indices. In the wavelength range from 0.4 µm to 1.0 µm, the temperature derivatives of the refractive indices are

$$\frac{\mathrm{d}n_o}{\mathrm{d}T} = -16.6 \times 10^{-6}\,\mathrm{K}^{-1} \qquad \text{and} \qquad \frac{\mathrm{d}n_e}{\mathrm{d}T} = -9.3 \times 10^{-6}\,\mathrm{K}^{-1}\,. \tag{C.2}$$

This leads to a large usable temperature phase-matching bandwidth from Eq. 3.16, page 54, of ΔT = 55 K. However, BBO crystals are slightly hygroscopic.

The dispersion relations described by the Sellmeier equations 3.5, page 48 matching the experimental data best [Kat86] read at a temperature of 20°C

$$n_o^2 = 2.7359 + \frac{0.01878}{\lambda^2 - 0.01822} - 0.01354\lambda^2 \tag{C.3a}$$

$$n_e^2 = 2.3753 + \frac{0.01224}{\lambda^2 - 0.01667} - 0.01516\lambda^2\,, \tag{C.3b}$$

where the wavelength λ is given in µm. The calculations for the optical cross-correlators discussed in chapter 3 are based on these equations. Table C.1 summarizes the refractive indices at the rele-

vant wavelength in this thesis. Because of its well-known and extensively studied properties, BBO is commonly used for frequency mixing in all possible phase-matching configurations (see section 3.2, pages 48 ff.), especially auto- and cross-correlators for short laser pulses and THz radiation, for optical parametric oscillation (OPO), as well as material for fast Pockels cells.

Table C.1 | Refractive indices of BBO at selected wavelengths. In the table, the indices of the ordinary and extraordinary beams in a BBO crystal at the relevant wavelength for this thesis is shown.

λ (µm)	0.2618	0.4000	0.5235	0.5288	0.6265	0.8000	1.5600
n_o	1.7631	1.6930	1.6750	1.6745	1.6676	1.6606	1.6464
n_e	1.6157	1.5679	1.5552	1.5549	1.5498	1.5444	1.5308
$n^e(\Theta_{pm})$	1.6750	1.6606		1.6559	1.6515		

At FLASH, different BBO crystals are used in the optical cross-correlators for the synchronization of Ti:sapphire oscillators and the photoinjector laser system, in electro-optic electron bunch diagnostic experiments (EOTD, compare section 1.8.1, pages 16 ff.), as well as the second frequency-doubler in the conversion stage of the photoinjector laser itself. There, it converts the LBO-generated 532 nm radiation to the UV, which then impinges the photocathode of the electron gun.

Furthermore, BBO is suited for the construction of an optical cross-correlator for those UV pulses with the optical reference pulses in the IR. The phase-matching condition is fulfilled for both sum-frequency (SFG) and difference-frequency generation (DFG).

C.2 Bismuth Triborate (BiBO)

Bismuth triborate, BiB_3O_6, BiBO,[1] is a comparatively new developed nonlinear optical crystal. It is now typically used for frequency doubling (SHG) of ~ 950 nm radiation for the generation of blue laser light. In general, BiBO crystals exhibit a 3.5 . . . 4 times larger conversion efficiency than LBO, and a 1.5 . . . 2 times larger conversion efficiency than BBO, and it can be phase-matched for many different applications, hence the suitability for the optical cross-correlators should be evaluated carefully. Its usable wavelength range, however prohibits the application at the photoinjector laser for measurements in the ultraviolet, as it only starts from 0.286 µm, but ranges up to 2.5 µm which is again comparable to BBO.

BiBO crystals have a monoclinic structure and belong to the point group 2 with the lattice parameters $a = 7.116$ Å, $b = 4.993$ Å, $c = 6.508$ Å and $Z = 105.62°$ and the thermal expansion coefficients $\alpha_a = 4.8 \times 10^{-5}/\mathrm{K}$, $\alpha_b = 4.4 \times 10^{-6}/\mathrm{K}$ and $\alpha_c = -2.69 \times 10^{-5}/\mathrm{K}$.

[1] Not to be confused with a particular yellow bird starring in the Sesame Street.

The simplified Sellmeier equations (Eq. 3.5, page 48) for the three crystal axes read [BDE+09]:

$$n_X^2 = 3.07403 + \frac{0.03231}{\lambda^2 - 0.03163} - 0.013376\,\lambda^2 \tag{C.4a}$$

$$n_Y^2 = 3.16940 + \frac{0.03717}{\lambda^2 - 0.03483} - 0.01827\,\lambda^2 \tag{C.4b}$$

$$n_Z^2 = 3.6545 + \frac{0.05112}{\lambda^2 - 0.03713} - 0.02261\,\lambda^2\,. \tag{C.4c}$$

with the wavelength λ, as usual, given in micrometers. The nonlinear coefficients of BiBO are

$$\begin{aligned} &d_{11} = 2.53\,\mathrm{pm/V} \quad d_{12} = 2.3\,\mathrm{pm/V} \quad d_{13} = -1.3\,\mathrm{pm/V} \quad d_{14} = 2.3\,\mathrm{pm/V} \\ &d_{25} = 2.4\,\mathrm{pm/V} \quad d_{26} = 2.8\,\mathrm{pm/V} \\ &d_{35} = -0.9\,\mathrm{pm/V} \quad d_{36} = 2.4\,\mathrm{pm/V} \end{aligned} \tag{C.5}$$

which, depending on the interaction type allow for a larger effective nonlinear coefficient d_{eff} compared to BBO or LBO, for instance (see section 3.2, pages 48 ff.).

Furthermore, BiBO is not hygroscopic, and there is no degradation of conversion efficiency over time under the influence of radioactive radiation [CRT+11]. This has to be considered, when an optical cross-correlator would be installed in the accelerator tunnel, as it is imaginable for the sFLASH experiment with an 800 nm pilot beam, or any other experiment where the timing between an external laser pulse near or in the beam vacuum pipe needs to be known with femtosecond precision.

C.3 Potassium Titanyl Phosphate (KTP)

Potassium titanyl phosphate (KTP) is a positive biaxial crystal and can be manufactured with the hydrothermal-grow or flux-grow methods. It is by far most common used for second-harmonic generation (SHG) of infrared laser radiation to the visible spectral range, for instance in green laser pointers, but it can also be used for optical parametric oscillation (OPO), in electro-optic modulators (EOMs) or as material for optical waveguides. It is, however, restricted to low and medium power densities, in contrast to LBO (see section C.4, page 232 f. below) for instance.

KTP belongs to the crystallographic point group $mm2$ with the assignment $(X, Y, Z) \rightarrow (a, b, c)$ of the dielectric and the crystallographic axes (see Fig. C.1).

Periodically poled potassium titanyl phosphate (PPKTP) consists of regularly spaced ferroelectric domains with alternating orientations within the crystal. It can be wavelength-tailored for sum-, difference- and second harmonic generation with high conversion efficiencies – with an enhancement of up to a factor 20 compared to a bulk crystal. For this, the structure must achieve quasi phase-matching (QPM). In the optical cross-correlators for the link stabilization unit, the poling period is $46.2\,\mu\mathrm{m} \approx 60 \cdot \lambda_{\mathrm{SHG}}$ in a crystal of 4 mm length. For optimum focusing, the maximum

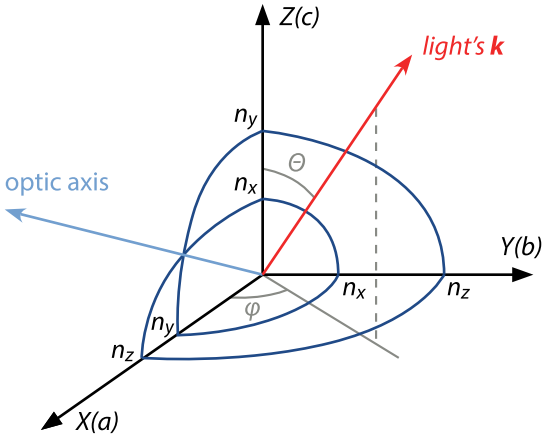

Figure C.1 | Dependence of the refractive index in KTP on light propagation direction. The refractive index in the biaxial crystal KTP on depends on light propagation direction and polarization, shown for the first octant of the dielectric reference frame. Notation: Θ is the polar angle, φ the azimuthal angle, V_z is the angle between one of the optical axes and the Z axis.

conversion efficiency

$$\eta_+ = \frac{8\pi^2 Z_0}{\lambda^3} \cdot \frac{{d_{\text{eff}}}^2}{n^3} \cdot 5.68 \cdot l_w \cdot \frac{P_{\text{peak}}}{\sqrt{2}} \tag{C.6}$$

has been reported [KCZ+07] for the used type-*II* phase-matched SHG, where Z_0 is the characteristic impedance of vacuum, λ the wavelength of the input and l_w the walk-off length. Experimentally, a conversion efficiency of $\eta_{\text{SHG}} = 4 \times 10^{-4}$ was found in the same reference. It can be assumed that in the fiber link stabilization units (see section 6.1, pages 132 ff.) a similar value is achieved, as the laser pulse parameters are comparable.

C.4 Lithium Triborate (LBO)

Lithium triborate, LiB_3O_5, LBO, is a negative biaxial crystal of the point group $mm2$ with the assignment $(X, Y, Z) \rightarrow (a, c, b)$ of the dielectric and the crystallographic axes in an orthorhombic structure. Its lattice parameters are $a = 8.4473$ Å, $b = 7.3788$ Å and $c = 5.1395$ Å.

The dispersion relation for the three crystal axes are at $T = 20°\text{C}$ with $[\lambda] = \mu\text{m}$ given by

$$n_X^2 = 2.4542 + \frac{0.01125}{\lambda^2 - 0.01135} - 0.01388\,\lambda^2 \tag{C.7a}$$

$$n_Y^2 = 2.5390 + \frac{0.01270}{\lambda^2 - 0.01189} - 0.01848\,\lambda^2 \tag{C.7b}$$

$$n_Z^2 = 2.5865 + \frac{0.01277}{\lambda^2 - 0.01223} - 0.01861\,\lambda^2\,. \tag{C.7c}$$

with a temperature dependence as per

$$\frac{\mathrm{d}n_X}{\mathrm{d}T} = -1.8 \times 10^6\,\mathrm{K}^{-1} \tag{C.8a}$$

$$\frac{\mathrm{d}n_Y}{\mathrm{d}T} = -13.6 \times 10^6\,\mathrm{K}^{-1} \tag{C.8b}$$

$$\frac{\mathrm{d}n_Z}{\mathrm{d}T} = (-6.3 - 2.1\,\lambda) \times 10^6\,\mathrm{K}^{-1} \tag{C.8c}$$

for a temperature range of 20°C to 65°C and a wavelength range of 0.4 µm to 1.0 µm, with a dependence on the wavelength in Z direction. The effective nonlinear coefficients depends on the phase-matching direction and is given three-wave interaction in the principle planes as [DN93]

- XY plane: $d_{\mathrm{ooe}} = d_{32}\,\cos\varphi$
- YZ plane: $d_{\mathrm{oeo}} = d_{\mathrm{eoo}} = d_{31}\,\cos\Theta$
- XZ plane with $\Theta < V_Z$: $d_{\mathrm{eoe}} = d_{\mathrm{oee}} = d_{32}\,\sin^2\Theta + d_{31}\,\cos^2\Theta$
- XZ plane with $\Theta > V_Z$: $d_{\mathrm{eeo}} = d_{32}\,\sin^2\Theta + d_{31}\,\cos^2\Theta$

where V_Z is the angle between the optical axis and the Z axis. In an arbitrary direction, the nonlinear coefficients are reported to be at $\lambda = 1.064$ µm in the same reference

$$d_{31} = \mp 0.67\,\mathrm{pm/V} \tag{C.9a}$$

$$d_{32} = \pm 0.85\,\mathrm{pm/V} \tag{C.9b}$$

$$d_{33} = \pm 0.04\,\mathrm{pm/V}\,. \tag{C.9c}$$

In literature, LBO has been used for many different applications in the wavelengths range from 0.35 µm to ~ 1.2 µm. However, it's by far most prominent (and commercial) use is intra-cavity second-harmonic generation (SHG) of 1.064 µm radiation in Nd:YAG diode-pump solid state lasers (DPSSLs) for pumping Ti:sapphire laser oscillators and amplifiers.

At FLASH, an LBO crystal is also used in the photoinjector laser system for conversion the amplified infrared pulse train to green, which is then converted to ultraviolet and send to the photocathode (see section 8.1, pages 168 f.).

C.5 Lithium Iodate (LiIO)

Lithium iodate, $LiIO_3$, LiIO, is just like BiBO a relatively new developed negative uniaxial crystal for nonlinear optical applications. The crystals are grown from an aqueous solution, which results in absence of inclusions or absorption bands over the wide transparency range of 0.28 µm to 4 µm. It is, however, highly hygroscopic and has to be carefully protected from moisture.

The advantage of this type of crystal, whose structure exhibits hexagonal symmetry with lattice constants of $a = 5.4815\,\text{Å}$ and $c = 5.1709\,\text{Å}$, are the relatively high nonlinear coefficients of

$$d_{15} = 2.2\,\text{pm/V} \quad \text{and} \quad d_{31} = -7.1\,\text{pm/V} \quad \text{and} \quad d_{32} = -7.0\,\text{pm/V}\,. \tag{C.10}$$

The form of the dispersion relations for lithium iodate is different from the crystals discussed above and for the ordinary and the extraordinary beam they are given by [BDE+09]

$$n_o^2 = 2.03132 + \frac{1.37623\,\lambda^2}{\lambda^2 - 0.0350823} + \frac{1.06745\,\lambda^2}{\lambda^2 - 169.0} \tag{C.11a}$$

$$n_e^2 = 1.83086 + \frac{1.08807\,\lambda^2}{\lambda^2 - 0.0313810} + \frac{0.0554582\,\lambda^2}{\lambda^2 - 158.76} \tag{C.11b}$$

and show that the crystal is highly birefringent. An initial, brief evaluation leads to the conclusion that this type of crystal could be useful for optical cross-correlation of single-color laser pulses, for example between a Ti:sapphire laser oscillator and the correspondingly seeded amplifier. The required pulse exchange (see Eq. 3.25, page 56) for the delay/subtraction method can happen inside the crystal, similar to the PPKTP crystal in the fiber link stabilization unit (see section 6.1, pages 132 ff.). Therefore, an additional splitting of the fundamental pulses would not be needed in this type of cross-correlator.

C.6 Lithium Niobate (LN)

Lithium niobate, $LiNbO_3$ or short LN, is a popular and well-known crystal for nonlinear optical applications. It is also a commonly used material for optical waveguides and modulators (see e. g. section 2.4.6, pages 40 f.), and can also be used as piezoelectric sensor.

The crystal has a negative uniaxial birefringence, a trigonal crystal system with the lattice constants $a = 5.148\,\text{Å}$ and $c = 13.863\,\text{Å}$, thermal expansion coefficients $\alpha_a = 15 \times 10^{-6}/\text{K}$ and $\alpha_c = 5 \times 10^{-6}/\text{K}$ and belongs to the point group $3m$. It is transparent for wavelengths from 0.4 µm to ~ 5.5 µm, which makes it perfect for applications in the near infrared (NIR).

Depending on the manufacturing process, three types of crystal composition have to be distinguished, as there is

- lithium-rich lithium niobate
- lithium niobate grown from stoichiometric melt (mole ratio Li/Nb = 1)
- lithium niobate grown from congruent melt (mole ratio Li/Nb = 0.946)

which results in slightly different (nonlinear) optical properties. For lithium-rich lithium niobate, the temperature dependent Sellmeier equations are given by ([DGN99], with λ in µm and temperature

T in K):

$$n_o^2 = 4.913 + 1.6 \times 10^{-8} \times (T^2 - 88506.25) + \frac{0.1163 + 0.94 \times 10^{-8} \times (T^2 - 88506.25)}{\lambda^2 - (0.2201 + 3.98 \times 10^{-8} \times (T^2 - 88506.25))} - 0.0273\,\lambda^2 \tag{C.12a}$$

$$n_e^2 = 4.546 + 2.72 \times 10^{-7} \times (T^2 - 88506.25) + \frac{0.0917 + 1.93 \times 10^{-8} \times (T^2 - 88506.25)}{\lambda^2 - (0.2148 + 5.3 \times 10^{-8} \times (T^2 - 88506.25))} - 0.0303\,\lambda^2 \tag{C.12b}$$

while they read as follows for lithium niobate from stoichiometric melt

$$n_o^2 = 4.913 + \frac{0.01173 + 1.65 \times 10^{-8} \times T^2}{\lambda^2 - (0.212 + 2.7 \times 10^{-8} \times T^2)} - 0.0278\,\lambda^2 \tag{C.13a}$$

$$n_e^2 = 4.5567 + 2.605 \times 10^{-7} \times T^2 + \frac{0.097 + 2.7 \times 10^{-8} \times T^2}{\lambda^2 - (0.201 + 5.4 \times 10^{-8} \times T^2)} - 0.0224\,\lambda^2 \tag{C.13b}$$

and for lithium niobate from congruent melt

$$n_o^2 = 4.9048 + 2.1429 \times 10^{-8} \times (T^2 - 88506.25) + \frac{0.11775 + 2.2314 \times 10^{-8} \times (T^2 - 88506.25)}{\lambda^2 - (0.21802 + 2.9671 \times 10^{-8} \times (T^2 - 88506.25))} - 0.027153\,\lambda^2 \tag{C.14a}$$

$$n_e^2 = 4.582 + 2.2971 \times 10^{-7} \times (T^2 - 88506.25) + \frac{0.09921 + 5.2716 \times 10^{-8} \times (T^2 - 88506.25)}{\lambda^2 - (0.2109 + 4.9143 \times 10^{-8} \times (T^2 - 88506.25))} - 0.02194\,\lambda^2\,. \tag{C.14b}$$

In phase-matching direction, the effective nonlinear expressions are given by

$$d_{\mathrm{ooe}} = d_{31}\ \sin\Theta - d_{22}\ \cos\Theta\ \sin 3\varphi \tag{C.15a}$$

$$d_{\mathrm{eoe}} = d_{\mathrm{oee}} = d_{22}\ \cos^2\Theta\ \cos 3\varphi \tag{C.15b}$$

with the following nonlinear coefficients for the stoichiometric melt

$$d_{22}(1.058\,\mu\mathrm{m}) = (2.46 \pm 0.23)\,\mathrm{pm/V} \tag{C.16a}$$

$$d_{31}(1.058\,\mu\mathrm{m}) = -(4.64 \pm 0.66)\,\mathrm{pm/V} \tag{C.16b}$$

$$d_{33}(1.058\,\mu\mathrm{m}) = -(41.7 \pm 7.8)\,\mathrm{pm/V} \tag{C.16c}$$

and these for material from the congruent melt

$$d_{22}(1.06\,\mu\text{m}) = (2.10 \pm 0.21)\,\text{pm/V} \tag{C.17a}$$

$$d_{31}(1.06\,\mu\text{m}) = -(4.35 \pm 0.44)\,\text{pm/V} \tag{C.17b}$$

$$d_{33}(1.06\,\mu\text{m}) = -(27.2 \pm 2.7)\,\text{pm/V}\,. \tag{C.17c}$$

Lithium niobate can also be doped with magnesium oxide (MgO), which reduces the photorefractive damage – that is increasing the damage threshold for medium-power applications, where undoped material can not be used.

Periodically-Poled Lithium Niobate

Furthermore, lithium niobate can be periodically poled, where the ferroelectric domains point alternatively to the $+c$ and the $-c$ direction. These types of crystal, made for quasi phase-matching (QPM) can exploit the largest value of the nonlinear tensor, d_{33}, and results in $2/\pi$ of the maximum value, which is approximately 17 pm/V. For finding the poling period and the optimum phase-matching temperature in [Jun97] another Sellmeier equations is given for the extra-ordinary beam in periodically poled lithium niobate (PPLN)

$$n_e^2 = 5.35583 + 4.629 \times 10^{-7} f + \frac{0.100473 + 3.862 \times 10^{-8} f}{\lambda^2 - (0.20692 - 0.89 \times 10^{-8} f)^2} + \frac{100 + 2.657 \times 10^{-5} f}{\lambda^2 - (11.34927)^2} - 1.5334 \times 10^{-2} \lambda^2 \tag{C.18a}$$

which is valid for temperatures from 20°C to 250°C, wavelengths from 0.4 µm to 5 µm and where $f = (T - 24.5)(T + 570.82)$. Typically, the poling period ranges from 5 µm to 35 µm, where the shorter ones are required for second-harmonic (SHG) and sum-frequency generation (SFG) while for optical parametric oscillation (OPO) longer poling periods are favorable.

In particular, a crystal poled for SFG of 1.55 µm and the wavelength region around 0.8 µm became available commercially recently [Cov13a]. Since the conversion efficiency has a quadratic dependence on the nonlinear coefficient (see Eqs. 3.13a–3.13c, page 52) and the coefficient is approximately eight times larger compared to BBO, PPLN is the most promising candidate for future iterations of the optical cross-correlators for the synchronization of Ti:sapphire laser oscillators to the optical reference pulse train (see chapter 7, pages 151 ff.). The expected significantly larger sum-frequency signal will most likely allow for the use of photodiodes instead of the presently employed photomultiplier tubes (PMTs), thus providing a better signal-to-noise ratio (SNR). With a custom-manufactured PPLN crystal, also the infrared cross-correlator for the photoinjector laser (see chapter 8, pages 167 ff.) may be improved. A drawback is the fact that optimum phase-matching is achieved for temperatures way above room temperature, as shown in Fig. C.2 which requires a crystal mount equipped with an oven and a controller.

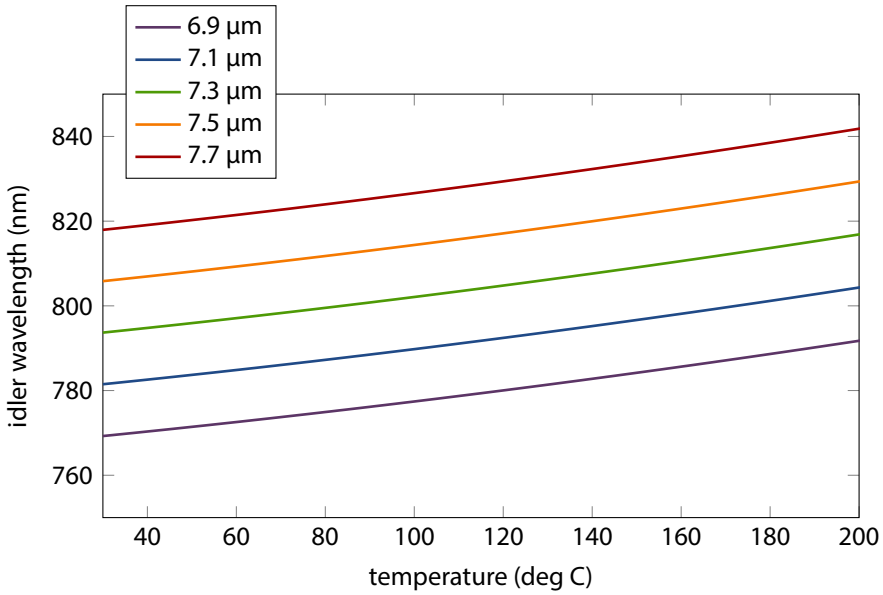

Figure C.2 | Phase-matching of MgO-doped periodically poled lithium niobate. The graph shows the sum-frequency tuning curve as function of the temperature for different idler wavelengths and poling periods for a fixed pump wavelength of 1550 nm (data source [Cov13b]).

C.7 Yttrium Orthovanadate (YVO)

Although yttrium orthovanadate (YVO) is not a nonlinear optical crystal, some of its properties are also compiled here, because such a crystal was used in the fiber link stabilization units. Most commonly, yttrium orthovanadate is used in polarization optics including fiber optic isolators and circulators because of its its large birefringence of $\Delta n \gtrsim 0.2$ and its wide transparency range (0.4 µm – 2.2 µm), and it is used as synthetic substitute for calcite ($CaCO_3$) and rutile (TiO_2). It can also be used as host material in diode-pump solid state lasers (DPSSLs) instead of YLF, for instance.

YVO_4 is a positive uniaxial crystal with a tetragonal crystal structure and belongs to the point group $4/mmm$. The refractive indices are related to the crystal cell by $n_o = n_a = n_b$ and $n_e = n_c$. Their dispersion relation is given by the Sellmeier equations

$$n_o^2 = 3.77834 + \frac{0.06973}{\lambda^2 - 0.04724} - 0.0108133\,\lambda^2 \tag{C.19a}$$

$$n_e^2 = 4.59905 + \frac{0.110534}{\lambda^2 - 0.04813} - 0.0122676\,\lambda^2\,, \tag{C.19b}$$

resulting in refractive indices of $n_o(1.56\,\mu m) = 1.94454$ and $n_e(1.56\,\mu m) = 2.14838$ and therefore a birefringence of $\Delta n = 0.20384$ at the wavelength the synchronization system is based on. This birefringence had been used to generate a mutual delay of the reference pulse train and the returning pulse train in the fiber link stabilization units (see section 6.3, pages 144 ff.). The thermal optical coefficients are given by $dn_o/dT = 8.5 \times 10^{-6}\,K^{-1}$ and $dn_e/dT = 3.0 \times 10^{-6}\,K^{-1}$, whereas the thermal

expansion coefficients are $\alpha_a = 4.43 \times 10^{-6}\,\mathrm{K}^{-1}$ and $\alpha_c = 11.37 \times 10^{-6}\,\mathrm{K}^{-1}$.

The advantages of YVO_4 in comparison to calcite, albeit that having a slightly larger birefringence, are its lower temperature dependence and the better mechanical properties. Furthermore, yttrium orthovanadate can be produced in better optical qualitys and it is non-hygroscopic.

D Properties of Selected Optical Fibers

The optical synchronization system was chosen to operate at the telecommunication wavelength around 1550 nm (so-called C-band), because, among other reasons, there are many different fiber-optic components readily available at low cost, which should allow for straightforward implementation of optical setups and experiments. Furthermore, the existence of dispersion compensating fiber (DCF) in this wavelength region actually facilitates the current design of the synchronization system and in particular the stabilized fiber links. As there are also numerous types of fibers available on the market, the properties of the most important ones for the system are compiled in the following sections for reference.

From the experimenter's respectively implementor's point of view also the different connector types have to be considered, especially as they are partly not compatible with each other. Although there exist many other types, the relevant connectors for single-mode fibers used in the context of this thesis are the "ferrule connector with physical contact (FC/PC)", "ferrule connector with ultra-high quality polished physical contact (FC/UPC)" and "ferrule connector with angled physical contact (FC/APC)", with the latter one being preferred because of its lowest back-reflection although it exhibits a larger insertion loss. In many applications in the context of the synchronization system back-reflections result in larger difficulties or performance degradation as higher loss in the fiber-optic transmission line. All matings must be done very carefully as the key must be aligned properly

Table D.1 | Properties of different types of optical fiber connectors. The different fiber connectors are mainly classified by their return loss, but they also partly incompatible due to geometric reasons.

connector type	ferrule polish	insertion loss	return loss	mates to		
		(typical)	(typical)	FC/PC	FC/UPC	FC/APC
FC/PC	flat	≤ 0.2 dB	-45 dB	yes	yes	no
FC/UPC	flat	≤ 0.2 dB	-55 dB	yes	yes	no
FC/APC	8°-angled	≤ 0.3 dB	-65 dB	no	no	yes

to the receptacle. Also, the fiber core at the tip of the ferrule is easily scratched and care should be taken not to contaminate the ferrule with dust or other particles, especially in experimental setups in the laboratory as this can significantly increase the insertion loss of the connectors and reduce their 500-matings life-time dramatically. Ideally, the ferrule should be inspected with a dedicated viewer device and cleaned if necessary. To complicate things further, there are two different key widths available on the market for APC connectors and receptacles, differing by just 0.1 mm. Particularly

for polarization maintaining fibers incompatible connectors can degrade the signal transmission as the optical axes of the fibers may become misaligned. This may even lead to intensity noise of the transmitted pulse train if, for example, narrow-key connectors are mated with a wide-key receptacle installed in an environment exhibiting mechanical vibrations – such as vacuum pumps inside the accelerator tunnel.

D.1 Standard Single Mode Fibers

Corning SMF-28e

Corning SMF-28e optical single-mode fiber is the de-facto standard in the telecommunication industry and is therefore produced at a very high quality at low cost. It can be used both in the 1310 nm wavelength region nearly without dispersion and in the 1550 nm wavelength region with relatively low dispersion. The data sheet [Coro2] of the Corning SMF-28e fiber states the dispersion formula with the zero-dispersion wavelength range 1302 nm $< \lambda_D <$ 1312 nm and the zero-dispersion slope $S_D = 0.092\,\mathrm{ps}/(\mathrm{nm}^2\,\mathrm{km})$:

$$D_{\mathrm{SMF28e}}(\lambda) = \frac{S_D}{4}\left(\lambda - \frac{\lambda_D^4}{\lambda^3}\right) \qquad \text{for } 1200\,\mathrm{nm} \le \lambda \le 1600\,\mathrm{nm} \tag{D.1}$$

Using this formula and Eq. 2.25, p. 27, the dispersion parameter D and the group velocity mode propagation constant β_2 are shown in Fig. D.1. In the figure also the center wavelengths of the both master laser oscillators λ_0^{E} and λ_0^{O} are shown as vertical lines, together with their FWHM spectral bandwidth in a lighter color. Within those, the value of β_2 changes already by $-3.3\,\mathrm{ps}^2/\mathrm{km}$ and

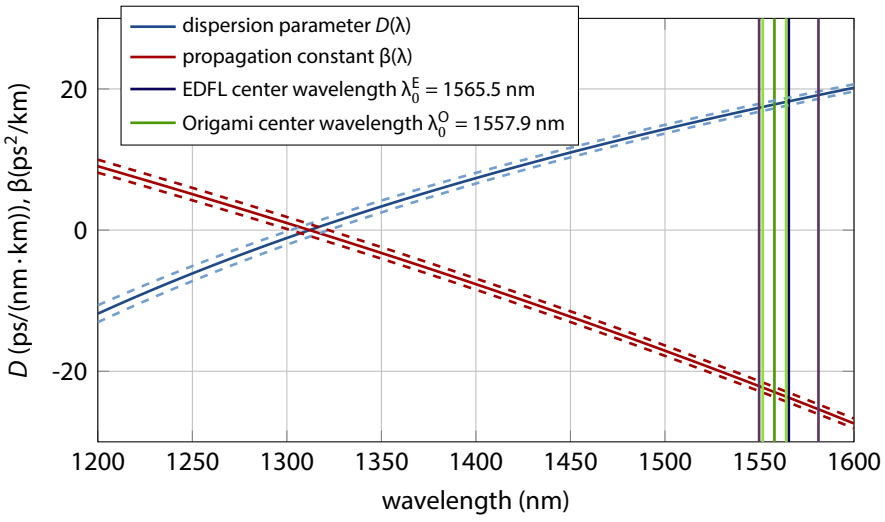

Figure D.1 | Dispersion and mode propagation constant of SMF-28e optical fiber. Characteristic of $D(\lambda)$ and $\beta(\lambda)$ of SMF-28e optical fiber. The operation wavelength ranges of the EDFL and the Origami laser are denoted by the vertical bars. The dashed lines take the uncertainty of the zero-dispersion wavelength into account.

$-1.3\,\mathrm{ps}^2/\mathrm{km}$, respectively. The third-order dispersion constant for this type of fiber is $\beta_3 = 86\,\mathrm{fs}^3/\mathrm{m}$ and the γ-parameter governing the nonlinearity of the fiber is $\gamma = 0.0011\,\mathrm{W}^{-1}\mathrm{m}^{-1}$ [OUI10]. The polarization mode dispersion (PMD) parameter has a low value of $D_\mathrm{p} \leq 0.1\,\mathrm{ps}/\sqrt{\mathrm{km}}$ due to the tight geometric specifications of $2r_\mathrm{core} = 8.2\,\mu\mathrm{m}$ and a core-cladding concentricity of $\leq 0.5\%$, with a cladding diameter of $(125 \pm 0.7)\,\mu\mathrm{m}$. The fiber has a mode field diameter (MFD) of $(10.4 \pm 0.8)\,\mu\mathrm{m}$ at the wavelength 1550 nm and a numerical aperture (NA)[1] of 0.14. The effective group index of refraction is $n_\mathrm{core}(1550\,\mathrm{nm}) = 1.4682$ with an index difference to the cladding of 0.36%. The attenuation of SMF-28e optical fiber is very low with $\alpha_\mathrm{dB} \leq 0.2\,\mathrm{dB/km}$ at 1550 nm.

OFS 980 (Lucent 980)

OFS ClearLite CL980-16, formerly known and commonly referred to as OFS980 or Lucent980 coupler fiber, is a high-NA fiber optimized for EDFA and EDFL pump light coupling, and thus providing single-mode propagation for both 980 nm and 1550 nm light. Only WDMs made with this particular type of fiber are used in the optical synchronization system. For future developments, however, another type named CL980-20 should be used when building EDFAs with the Liekki 110-dB gain fiber, as their mode field diameter and numerical aperture are perfectly matched for efficient coupling of pump light into the gain fiber (see tables D.2 and D.3).

Table D.2 | Optical and geometrical properties of OFS980 pump coupler fiber. The data was taken from [OFS05] with additions from [OUI10]. The values marked with an asterisk (*) are calculated with the assumption of the same glass host material.

	ClearLite CL980-16	**ClearLite CL980-20**	unit
operating wavelength	980 and 1550	980 and 1550	nm
cut-off wavelength λ_cut	≤ 960	≤ 960	nm
MFD at 980 nm	5.0 ± 0.3	4.0 ± 0.3	µm
MFD at 1550 nm	7.5 ± 0.75	6.5 ± 0.3	µm
attenuation α_dB at 980 nm	≤ 3.0	≤ 3.5	dB/km
refractive index difference	0.65	1	%
numerical aperture	0.16	0.20	–
group velocity propagation constant β_2	4.5	(not disclosed)	$\mathrm{fs}^2/\mathrm{mm}$
third-order dispersion constant β_3	109	(not disclosed)	fs^3/m
nonlinear parameter γ at 1550 nm	0.0021	0.002816 (*)	$\mathrm{W}^{-1}\mathrm{m}^{-1}$
core diameter $2\,r_\mathrm{core}$	4.0	3.6	µm
core concentricity error	≤ 0.2	≤ 0.2	µm
cladding diameter	125 ± 2	125 ± 2	µm

[1] The numerical aperture of an optical fiber is defined as $\mathrm{NA} = n_0^{-1} \cdot \sqrt{n_\mathrm{clad}^2 - n_\mathrm{core}^2}$.

D.2 Dispersion Compensating Fibers

The dispersion compensation in the fiber-optic link is, as explained in chapter 6, pages 131 ff., realized with an appropriate segment of DCF (see also section 2.3.4, page 29). In the first proof-of-principle experiments demonstrated in [Loe09], a DCF manufactured by *Avanex* with an average dispersion of $D(1550\,\mathrm{nm}) \approx -124\,\mathrm{ps/(nm\cdot km)}$ was used. This fiber could only be spliced to SMF with an insertion loss of $\sim 1.6\,\mathrm{dB}$ per splice resulting in more than 50% loss of optical power only by this fiber in the link.

In the engineered versions of the fiber link units commissioned within this thesis, the G.652 LLWBDK dispersion compensating modules made by *OFS* are used. They were delivered as SMF-pigtailed modules, where the 70 m long DCF segment is spliced on each side to an intermediate fiber of an unknown type which in turn is spliced to the SMF pigtails. This allowed the manufacturer to reduce the insertion loss for a complete module to an average value of $\overline{\mathrm{IL}}_{70} = (0.75 \pm 0.15)\,\mathrm{dB}$ for ten modules (see Fig. D.2 and [OFS09a]). However, each link requires its individual segment of DCF and thus the modules were cut accordingly, but then the fiber of one module can be used for two links. By an empirical (read trial-and-error) improvement of the splice parameters, the loss

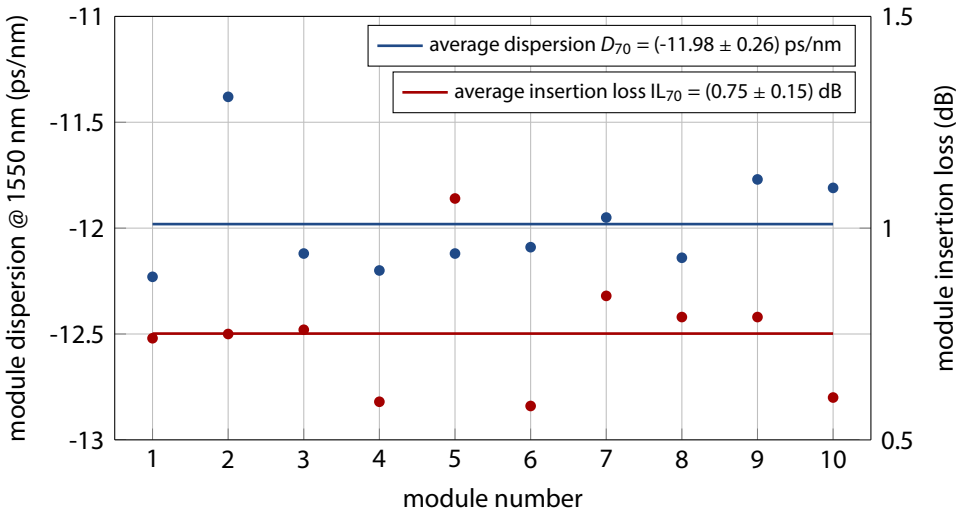

Figure D.2 | Dispersion and insertion loss of the OFS DCF modules. Fluctuation of the dispersion D_{70}(1550 nm) and insertion loss of the delivered 70-m-long OFS DCF modules.

of the second splice of SMF to the DCF could be reduced to a reproducible value of 1.1 dB, resulting in a loss of $\sim 1.5\,\mathrm{dB}$ for a single-pass through the DCF segment in the links. Furthermore, the amount of dispersion compensation of this fiber is larger compared to the old one and amounts to $\overline{D}_{70}(1550\,\mathrm{nm}) = (-11.98 \pm 0.26)\,\mathrm{ps/nm}$ for the modules. This results in $D_{\mathrm{DCF}}(1550\,\mathrm{nm}) = (-171.14 \pm 3.75)\,\mathrm{ps/(nm\cdot km)}$ which gives almost a ratio of ten to the dispersion of SMF. The reduction of the fiber length can help mitigate nonlinear effects which might arise due to its small core diameter. The DCF has a typical intrinsic loss of $\alpha_{\mathrm{dB}} = 0.44\,\mathrm{dB/km}$ and an effective core area of $S_{\mathrm{eff}} = 21.4\,\mu\mathrm{m}$ [OFS09b].

D.3 Erbium-Doped Gain Fibers

The gain spectrum of isolated erbium ions is homogeneous and its gain coefficient can be written as

$$g_{\mathrm{Er}}(\omega) = \frac{g_0}{1 + (\omega - \omega_a)^2\, T_2^2 + P/P_{\mathrm{sat}}} \tag{D.2}$$

where g_0 is the peak gain value, ω the angular frequency and P the power of the signal being amplified and ω_a the atomic transition frequency [Agro7]. The saturation power P_{sat} depends on the fluorescence time and the transition cross-section between the excited and the ground state. The parameter T_2 is the dipole relaxation time and typically in the order of 100 fs, which determines the bandwidth of the amplifier. However, in doped fibers the spectrum is considerably broadened by the silica host and can be, to some extent, tailored by co-doping with other materials such as ytterbium, aluminum or germanium. In this case, the gain spectrum is obtained from

$$g(\omega) = \int_{-\infty}^{\infty} g_{\mathrm{Er}}(\omega) f_a(\omega)\, \mathrm{d}\omega_a \tag{D.3}$$

where $f_a(\omega_a)$ is a distribution function which depends on the glass and the doping composition of the fiber core. Figure D.3 shows the absorption and emission spectra of a commercially available erbium-doped fiber which is used as gain medium in the lasers and amplifiers described in this thesis. The fact that the spectrum is strongly varying over the wavelength region has notable influence on the amplification of short laser pulses which naturally exhibit large spectral bandwidths.

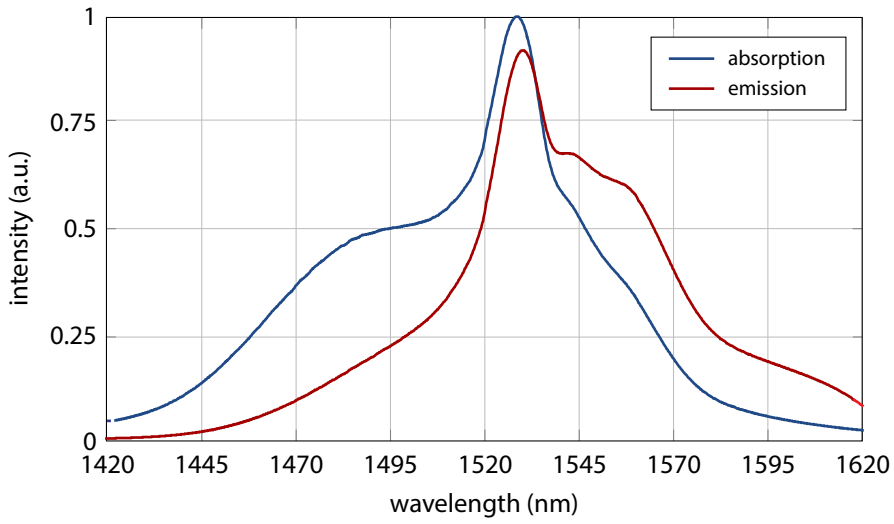

Figure D.3 | Erbium-doped fiber characteristics. Absorption and emission spectra of *Liekki* erbium-doped gain fiber (from [Tho10]).

Liekki Er80-8/125 and Liekki Er110-4/125

The Liekki Er80-8/125 and Liekki Er110-4/125 are highly erbium-doped gain fiber (ErF) designed for medium and high power short pulse EDFAs and EDFLs. The large peak absorption allows for a large gain and at the same time short fiber lengths, thus reducing nonlinear effects. However, the latter are higher in the Er110-4/125 fiber, because of its smaller core and by that mode field diameter. Since the fiber lengths of the EDFAs used and built with the context of this thesis are shorter than ~ 1 m, these effects have, probably unwisely, not been taken into account for at all. As manufacturers of optical

Table D.3 | Optical and geometrical properties of Liekki erbium-doped fibers. Overview of relevant parameters of the gain fibers used in the EDFAs and EDFLs utilized in this thesis. The values marked with an asterisk (*) are calculated.

	Er80-8/125	**Er110-4/125**	unit
MFD at 1550 nm	9.5 ± 0.8	6.5 ± 0.5	µm
peak core absorption at 1530 nm	80 ± 8	110 ± 10	dB/m
nominal core NA	0.13 ± 0.02	0.20 ± 0.02	–
cut-off wavelength λ_{cut}	1100–1400	800–980	nm
group velocity propagation constant β_2	-20	12	fs^2/mm
third-order dispersion constant β_3	(not disclosed)	(not disclosed)	fs^3/m
nonlinear parameter γ	0.001318 (*)	0.002816 (*)	$W^{-1}m^{-1}$
core concentricity error	≤ 0.2	≤ 0.2	µm
cladding diameter	125 ± 2	125 ± 2	µm

fibers sometimes offer sparse information in their data sheets [Lie08, Lie09], or only provide them under a non-disclosure agreement, missing values are gathered additionally from [BSM+10, OWS+11] in table D.3.

Splice Parameters

As some manufactures of optical fibers provide optimized splice parameters for their products these should be obviously considered in experimental setups and implementations. Table D.4 shows exemplary the recommended parameters for the Liekki erbium gain fiber Er110-4/125 obtained from the "Liekki EasySplice" software [Lie07] in comparison to the default program of the available splicers (Fujikura FSM-45PM, firmware version 1.49 and Fujikura FSM-60S, firmware version 1.26). Parameters which differ are highlighted in a bold typeface. Most notable are the significantly different arc duration, arc power and gap settings during the actual splice. However, in the EDFAs discussed in this thesis the gain fiber is normally spliced to OFS980 fiber which differs from SMF-28 (see Fig. 2.8, page 44). Parameters for this particular kind of splice are, however, not available from data sheets or support documentation, but could be determined experimentally. Moreover, there is a notable difference in this most often used splice program between both of the splices manufactured by the

same company, for example for the loss estimation or gap settings. This suggests a careful investigation and optimization of the parameters for splices of these fibers to SMF-28 and OFS980, especially as there is no data available for the also used Er80-8/125 fiber. Moreover, there is a notable difference

Table D.4 | Recommended splice parameters for Liekki Er110-4/125. Manufacturer-recommended parameters for splicing Liekki Er110-4/125 erbium-doped gain fiber to SMF-28 standard single mode fiber with Fujikura splicers, which were available in this thesis.

parameter	Liekki recommended	FSM-45PM default	FSM-60S default
fiber type	special	SM-SM1	SM-SM1
alignment	core	core	core
focus	**auto**	**0.25 (L), 0.25 (R)**	**0.25 (L), 0.25 (R)**
ECF	**0.35**	**0.30**	**0.30**
auto power	on	on	on
cleave limit	**3.0 deg**	**2.0 deg**	**2.0 deg**
loss limit	**0.75 dB**	**0.2 dB**	**0.2 dB**
core angle limit	1.0 deg	1.0 deg	1.0 deg
cleaning arc	150 ms	150 ms	150 ms
gap	15 µm	15 µm	15 µm
gapset position	center	center	center
prefuse power	20 bit	20 bit	standard
prefuse time	180 ms	180 ms	180 ms
overlap	**3 µm**	**15 µm**	**10 µm**
arc 1 power	**17 bit**	**20 bit**	**standard**
arc 1 time	**5000 ms**	**2000 ms**	**2000 ms**
arc 2 power	**17 bit**	**20 bit**	**standard**
arc 2 time	off	off	off
arc 2 on-time	180 ms	180 ms	180 ms
arc 2 off-time	0 ms	off	0 ms
re-arc time	800 ms	800 ms	800 ms
taper splice	off	off	off
taper wait	400 ms	400 ms	400 ms
taper speed	**100 bit**	**100 bit**	**20 bit**
taper time	100 ms	100 ms	N/A
estimation mode	core	core	core fine
MFD left	**2.5 µm**	**9.3 µm**	**9.3 µm**
MFD right	**5.4 µm**	**9.3 µm**	**9.3 µm**
minimum loss	0.00 dB	0.00 dB	off
core step	**100**	**100**	**70**
core curve	**100**	**70**	**150**
MFD mismatch	off	off	off

in this most often used splice program between both of the splices manufactured by the same company, for example for the loss estimation or gap settings. This suggests a careful investigation and optimization of the parameters for splices of these fibers to SMF-28 and OFS980, especially as there is no data available for the also used Er80-8/125 fiber.

E MATLAB Code

In this appendix some useful MatLab routines are listed. The comments, beginning with a % character, explain the code.

Fast Calibration of an Optical Cross-Correlator with a Phase Slope

The following MatLab script was implemented for the calibration of the optical cross-correlator for the Ti:sapphire laser in the EO laboratory. Within one macro-pulse trigger cycle, a phase slope, based on Eqs. 7.2 and 7.3 (see page 159), is applied to the RF reference signal to which the oscillator is locked. This makes the calibration procedure very fast in comparison to scanning the vector modulator or the optical delay stage. In the future, this functionality will be implemented in a corresponding control system (DOOCS) server for the cross-correlator. The code can even be adapted for the calibration of the fiber link optical cross-correlators, as the piezo stretchers (section 6.1, pages 132 ff.) are also driven by the same type of fast DACs.

```
%   initialization, set options etc.
opts.RFfreq   = 1.3e9;  % frequency of the PLL

opts.MaxBits  = 2^14-1; % using a 14-bit DAC
opts.MaxVolt  = 6.33;   % maximum output voltage when MaxBits are applied
opts.NomVolt  = 4.00;   % nominal operating voltage (lowest phase noise in RF)
opts.SlMinMax = 1;      % ps; min./max. of phase slope around current phase
opts.SlDuratn = 1800;   % sample points of the slope
opts.SlStart  = 200;    % sample points before slope starts

%   definition of DOOCS addresses
DAddr.DACBase = 'TTF2.SYNCH/TISA.DAC/EO140.TISA/';
DAddr.DACCh_Q = strcat(DAddr.DACBase, 'DPM1.DATA_1_W');
DAddr.DACCh_I = strcat(DAddr.DACBase, 'DPM2.DATA_1_W');
%
DAddr.ADCBase   = 'TTF2.SYNCH/YDFL.ADC/EO140.YDFL/';
DAddr.ADC_OXC   = strcat(DAddr.ADCBase, 'CH02.VOLTAGE.TD'); % OXC signal
DAddr.ADC_OptP  = strcat(DAddr.ADCBase, 'CH01.VOLTAGE.TD'); % optical power
DAddr.ADC_PhDet = strcat(DAddr.ADCBase, 'CH00.VOLTAGE.TD'); % 81 MHz phase det.
DAddr.ADC_QRBV  = strcat(DAddr.ADCBase, 'CH07.VOLTAGE.TD'); % Q readback value
DAddr.ADC_IRBV  = strcat(DAddr.ADCBase, 'CH06.VOLTAGE.TD'); % I readback value
DAddr.BufferNr  = strcat(DAddr.ADCBase, 'CURRENT');         % current buffer no

```

```
%   number of loops of data acquistion if averaging is desired
opts.Nshots = 10;


%   create file name for saving
fn = ttf_filename(sprintf('Calib_VMPhaseSlope_D%d_M%.1f_S%d.mat', ...
                          opts.SlDuratn, opts.SlMinMax, opts.SlStart));

%%  calculation
s = (1:opts.SlDuratn);
x = opts.SlMinMax*1e-12 * (-1 + 1/(opts.SlDuratn/2)*s);
%   calculate \phi_{cal}(t)
phit = x * 2 * pi * opts.RFfreq;

%   get current I and Q values from DAC (as vector)...
I0 = ttfr(DAddr.DACCh_I);
Q0 = ttfr(DAddr.DACCh_Q);
%   and calculate phase
phi0 = angle(I0 + 1i*Q0);
%   insert slope to phase vector
phi = phi0;
phi(opts.SlStart+1:length(phit)+opts.SlStart) = ...
                        phi0(opts.SlStart+1:length(phit)+opts.SlStart)' + phit;

%   calculate new I and Q values (as bit counts, not as voltage)
Z = opts.NomVolt/opts.MaxVolt * opts.MaxBits/2 * exp(1i * phi);
I = round(real(Z));
Q = round(imag(Z));

%   initialize arrays for data taking
Data.ADC_OXC   = zeros(opts.Nshots, 2048);
Data.ADC_OptP  = zeros(opts.Nshots, 2048);
Data.ADC_PhDet = zeros(opts.Nshots, 2048);
Data.ADC_QRBV  = zeros(opts.Nshots, 2048);
Data.ADC_IRBV  = zeros(opts.Nshots, 2048);

%%  apply I and Q values to DAC
ttfw(Q, DAddr.DACCh_Q);
ttfw(I, DAddr.DACCh_I);
pause(0.01);
ttfw(1, strcat(DAddr.DACBase, 'WRITE_NEW_DATA_IN_MEMORY'));  pause(1);


%%  loop for data taking
%
%   get ADC buffer number
BuffNumNew = ttfr(DAddr.BufferNr);
BuffNumOld = BuffNumNew;
%
```

```
for k = 1:opts.Nshots
    tic
    % wait for new buffer number
    while BuffNumNew == BuffNumOld
        pause(0.01);
        BuffNumNew = ttfr(DAddr.BufferNr);
    end
    % take data
    Data.ADC_OXC(k,:)   = ttfr(DAddr.ADC_OXC);
    Data.ADC_OptP(k,:)  = ttfr(DAddr.ADC_OptP);
    Data.ADC_PhDet(k,:) = ttfr(DAddr.ADC_PhDet);
    Data.ADC_QRBV(k,:)  = ttfr(DAddr.ADC_QRBV);
    Data.ADC_IRBV(k,:)  = ttfr(DAddr.ADC_IRBV);
    %
    pause(0.1-toc);
end


%%  set back original values
ttfw(Q0, DAddr.DACCh_Q);
ttfw(I0, DAddr.DACCh_I);
pause(0.01);
ttfw(1, strcat(DAddr.DACBase, 'WRITE_NEW_DATA_IN_MEMORY'));

%%  determine calibration constant from mean of measured data
Data.OXC_Mean = mean(Data.ADC_OXC(:, ...
                     opts.SlStart+1:opts.SlDuratn+opts.SlStart), 1);
Data.OXC_Std  = std(Data.ADC_OXC(:, ...
                    opts.SlStart+1:opts.SlDuratn+opts.SlStart), 0, 2);
%   with time vector t
t = (-opts.SlMinMax:2/opts.SlDuratn:opts.SlMinMax-2/opts.SlDuratn);
%   using a linear slope around the zero-crossing
Data.Calib = calculateCalibSlope(t, Data.OXC_Mean);

%%  save data to file
save(fn);
```

The variable `Data.Calib.constant` now contains the calibration constant K_{OXC}, i.e. the slope of the bipolar cross-correlation signal around its zero-crossing.

Determination of the Calibration Constant

This function calculates that constant from the input parameters `t`, as the vector containing the time axis, and the balanced cross-correlation signal `y`.

```
function calib = calculateCalibSlope(t, y)
    %   determine extrema
    [y_max, y_maxind] = max(y);
    [y_min, y_minind] = min(y);
```

```
    %   ensure monotonic increasing indices in region-of-interest
    if y_maxind > y_minind
        roiidx = (y_minind:y_maxind)';
    else
        roiidx = (y_maxind:y_minind)';
    end
    %   cut region-of-interest from time vector and signal
    troi = t(roiidx);
    yroi = y(roiidx);
    %   determine peak-to-peak signal
    y_pp = y_max - y_min;
    %   assume linear region around +- 1/4 around zero (bipolar signal!)
    linidx = find( (yroi > -y_pp/4) & (yroi < y_pp/4) );
    %   further confine time and signal to linear region
    calib.tlin = troi(linidx);
    ylin = yroi(linidx);
    %   fit linear slope
    plin = polyfit(calib.tlin, ylin, 1);
    calib.flin = polyval(plin, calib.tlin);
    %   return calibration constant; plin(1) is in units of [signal]/[time]
    calib.constant = abs(plin(1));
return
```

F Frequency and Timescales

FLASH, as free-electron laser generating X-ray wavelength pulses with durations of a few tens of femtoseconds has been in operation for years now, and presumably will be for the next two decades. In experiments, data acquisition times can be hours, but are typically on the minute and second timescale, or are even single-shot. During an experiment, for instance employing an optical pump and X-ray probe, the synchronization between the two independent sources should be ideally below the individual pulse durations. This inevitably requires an infrastructure even more accurate.

As a result, the timescales which have to be considered in the implementation of the laser-based optical synchronization system cover more than twenty orders of magnitude. Figure F.1 gives an overview of these time-, frequency- and the corresponding length-scales.

In practice, the actual subsystems of the synchronization infrastructure incorporate a variety of components operating at different radio frequencies – a prime example being the RF phase detector circuits of the MLO and titanium-sapphire (Ti:S) laser oscillators (see section 5.3.1, pages 87 ff. and section 7.1.2, page 157 ff., respectively) – which are summarized in table F.1 together with their ratios.

Table F.1 | Frequency conversion factors. Overview of conversion factors for the radio frequencies utilized in subsystems of the laser-based optical synchronization infrastructure at FLASH. The most common ones in this thesis are printed in bold.

f (MHz)	**1.003**	**9.028**	13.542	**27.083**	**40.625**	54.167	**81.250**	108.333	**216.667**	**1300**	**2600**	9100
1.003		9	13	27	40	54	81	108	216	1296	2592	9072
9.028	1/9		3/2	3	9/2	6	9	12	24	144	288	1008
13.542	1/13	2/3		2	3	4	6	8	16	96	192	672
27.083	1/27	1/3	1/2		3/2	2	**3**	4	**8**	48	96	336
40.625	1/40	2/9	1/3	2/3		4/3	**2**	8/3	16/3	32	64	224
54.167	1/54	1/6	1/4	1/2	3/4		3/2	2	4	24	48	168
81.250	1/81	1/9	1/6	**1/3**	**1/2**	2/3		4/3	**8/3**	16	32	112
108.333	1/108	1/12	1/8	1/4	3/8	1/2	3/4		2	**12**	24	84
216.667	1/216	1/24	1/16	**1/8**	3/16	1/4	**3/8**	1/2		**6**	12	42
1300.	1/1296	1/144	1/96	1/48	1/32	1/24	**1/16**	1/12	**1/6**		**2**	7
2600.	1/2592	1/288	1/192	1/96	1/64	1/48	1/32	1/24	**1/12**	**1/2**		7/2
9100.	1/9072	1/1008	1/672	1/336	1/224	1/168	1/112	1/84	1/42	1/7	2/7	

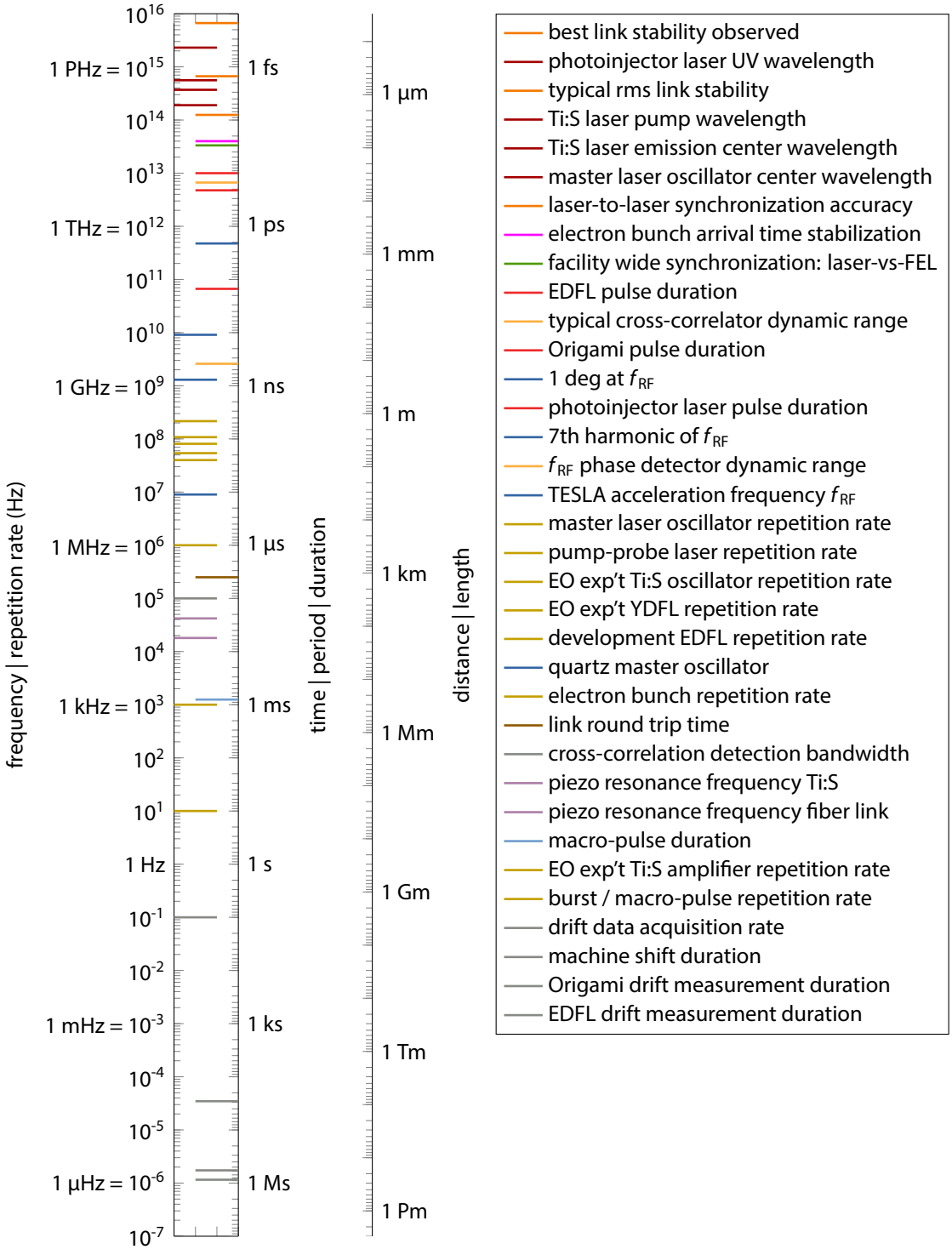

Figure F.1 | Frequency-, time- and length scales relevant for optical synchronization at FLASH. On the left, the figure provides an overview on the time- and frequency scales relevant in this thesis while on the right the corresponding length scales are illustrated.

G Photographs and Drawings of Selected Experiments and Setups

This chapter comprises a collection of photographs and technical drawings of selected setups and experiments described in the main text. Most building blocks of the synchronization system are a combination of mechanical, optical, fiber-optic and electronic parts, and the time required to plan, assemble, commission and characterize those subsystems should not be underestimated.

Master Laser Oscillators

Figure G.1 shows the self-built erbium-doped master laser oscillator (EDFL/MLO) during its commissioning in the synchronization hutch without its cover. The "plus"-shaped section in the center of

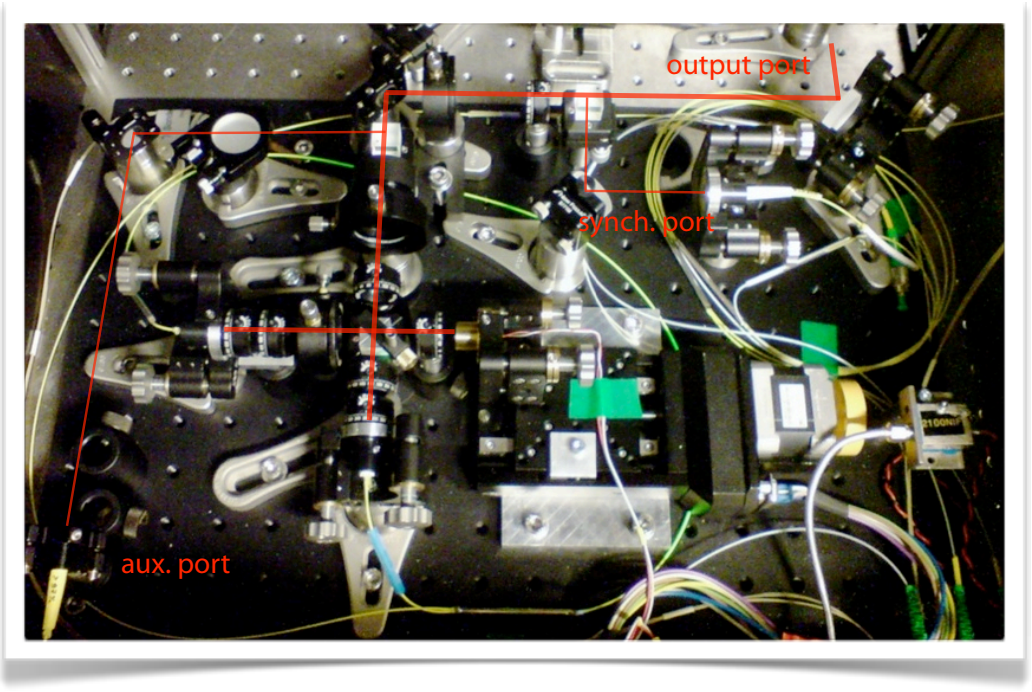

Figure G.1 | Photograph of the EDFL installed in the synchronization hutch. The self-built laser system is shown with open housing during commissioning in the synchronization hutch. The two fiber-coupled pump laser diodes are mounted at the right wall of the housing and are not shown in the image. The red lines sketch the beam propagation inside the device.

the image, formed by the wave plates, the piezo-mounted mirror and the output polarizer of the laser resonator, defines the σ-configuration with the NPE output port. The optical delay stage for coarse repetition rate tuning takes most of the space. The mirror and the fiber collimator next to it are part of the synchronization circuit (see Fig. 5.1, page 72). The mirror in the upper right corner is the final exit mirror, whereas the fiber collimator in the lower left provides an additional monitor port, for instance for out-of-loop drift- or phase noise measurements. The commercial Origami SESAM-based master laser oscillator is located on the opposite site of the free-space distribution unit (FSD, see also Fig. 4.4 on page 65). The optical setup for coupling the beam into the FSD and into the fiber collimator of the photodiode used for synchronization is shown in Fig. G.2. Due to the small footprint of the laser system, it is possible to install a second Origami laser for redundancy right next to it. In this case, the beam path of the laser systems are combined using the polarizing beam cube (PBC) where the light of the auxiliary port is tapped off. For the operation of the second laser, another half-wave

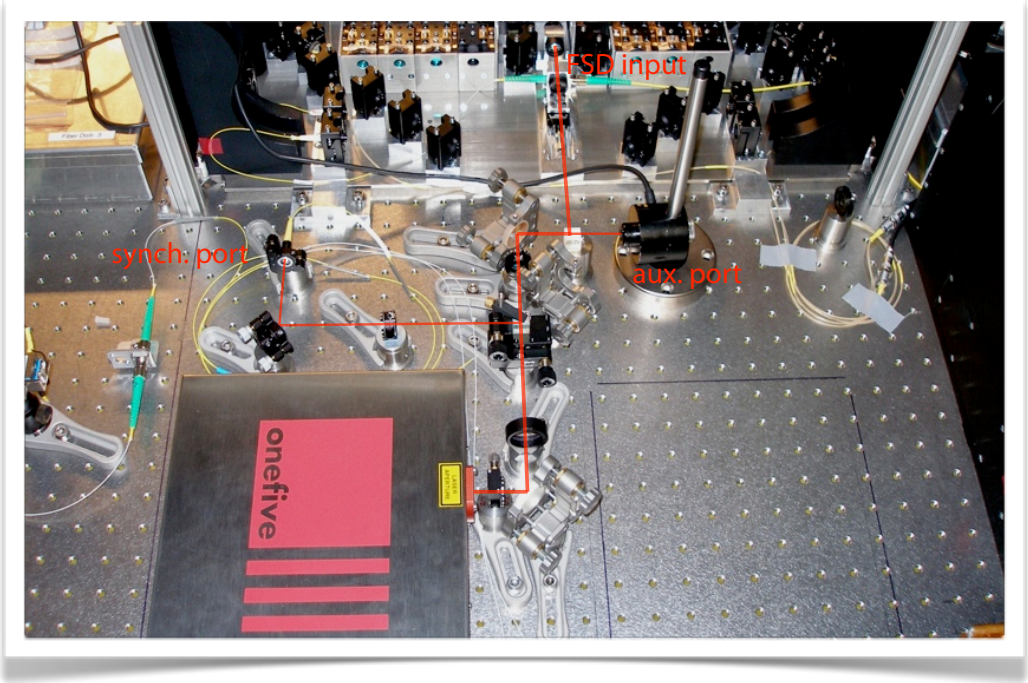

Figure G.2 | Integration of the Origami into the setup of the optical table. It is placed where the installation of the second EDFL had been foreseen. In the background of the picture, the free-space distribution unit can be seen.

retarder has to be introduced between this beam cube and the FSD input to rotate the transmitted horizontal polarization to the vertical plane required by the first PBC in the FSD. It is planned to automate the switching of the two laser systems in case of a failure of one. Furthermore, the auxiliary port will be used with both laser systems for additional online diagnostics, such as a two-photon absorption (TPA, see section 5.2.2 on page 76 f.) photodiode, an autocorrelator (see section 5.2.3 on page 77 f.) and a spectrometer in the future.

Free-Space Distribution Unit

The compact optical setup of the free-space distribution unit (FSD) is based on custom-designed beam cube mounts and allows the distribution of the pulse trains of two laser systems to up 16 devices by means of fiber collimators. For an optimal coupling efficiency, two adjustable mounts are required – one mirror and the fiber collimator mount itself. Figure G.3 shows a 3D model of the

Figure G.3 | 3D CAD model of the free-space distribution unit. The device is shown in its slightly upgraded version "1.1" with more stable mirror mounts compared to the original design.

FSD from the CAD software. The blocks with the turquoise-colored pads are the custom-designed mounts for the PBC and half-wave retarder combination (see also Fig. 5.32 on page 110). The telescopes of the both input ports are shown on the dark blue and pink bases, and they are equipped with iris diaphragms for easier alignment. The leftmost and rightmost kinematic mounts (shown in white) hold the fiber collimators of the corresponding ports. The complete optical setup is built on an Invar baseplate, which has a very low thermal expansion coefficient to minimize the influence of temperature-induced changes of the beam path length. The curved structures in the upper left and upper right corners of the unit are used to hold the optical fibers of the second link unit layer in place. These are left out in the lower left and lower right corner in the illustration. The required mechanical and optical components for the assembly are 41 kinematic mounts, 16 polarizing beam cubes, 25 mirrors, four lenses and 20 half-wave retarders. When polarization-maintaining fiber (PMF) would be used at a port, an additional half-wave retarder is required and can be mounted in the PBC assembly. The CAD program is also used to determine the geometric beam path length from the telescopes to the individual fiber collimators, as discussed in section 5.5 (page 108 ff.). Figure G.4 shows a di-

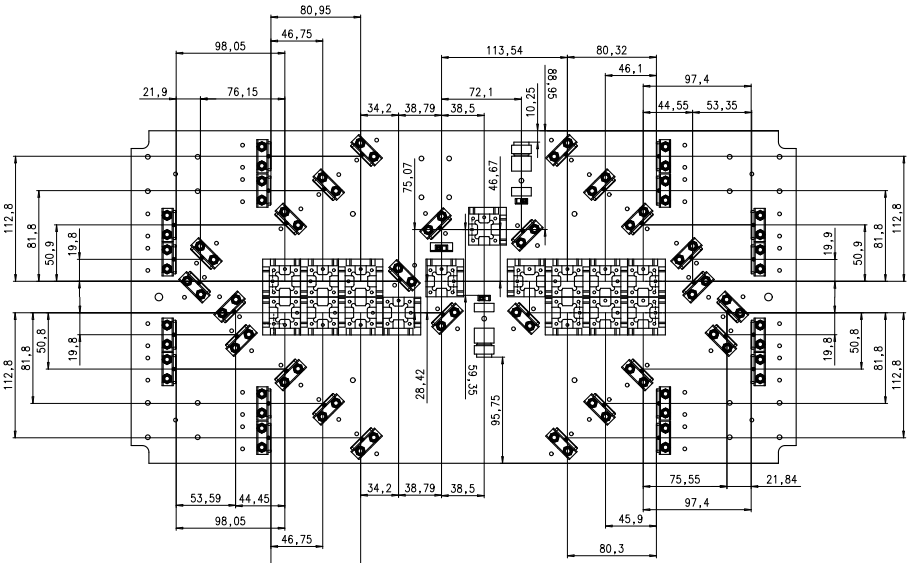

Figure G.4 | Construction drawing and geometric path lengths in the FSD. The figure shows an excerpt from the original construction drawings of the FSD to determine the geometric beam path lengths from the telescope to the 16 ports of the device.

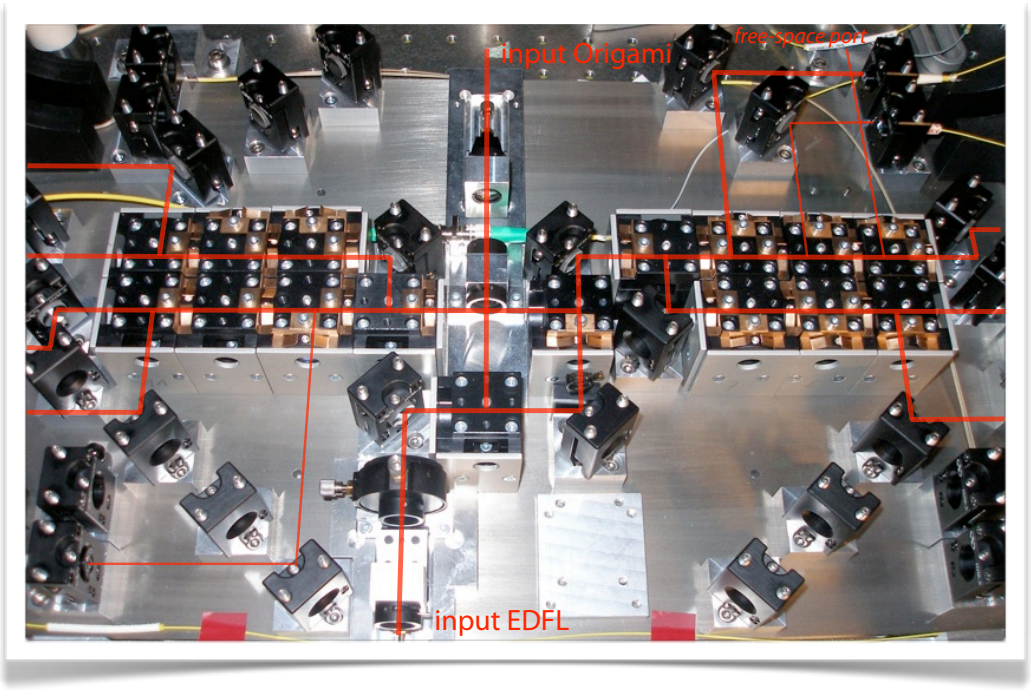

Figure G.5 | Photograph of the free-space distribution unit. The beam propagation for the installed devices through the setup is overlaid.

mensioned construction drawing of the unit. In the status shown in Fig. G.5 the FSD is set up to distribute light to six fiber link stabilization units, two monitor ports, the fiber to the optical cross-

correlator of the photo injector laser, the 2.6 GHz phase detector and one free-space port, for instance for autocorrelation measurements (see section 5.5.2, page 112 ff.). Five additional ports are available.

Fiber Link Stabilization Unit

The fiber link stabilization units had been designed as compact boxes [Loeo9]. They contain electronics for phase detection and optical power monitoring, the fiber installation with piezo stretcher, dispersion-compensating fiber (DCF) and pump laser diode of the distribution EDFA, as well as the free-space optical cross-correlator. These different installations are organized in three layers, as shown in Fig. G.6. In the photograph (Fig. G.7, left), which shows the assembly of a fiber link box, the

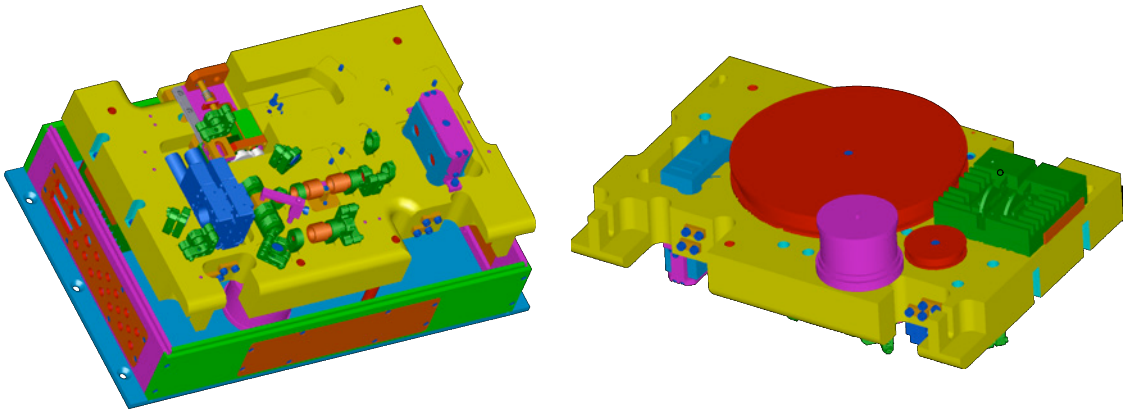

Figure G.6 | 3D CAD views of the machined fiber link stabilization unit. Left: Free-space optics consisting of the EDFA collimator, the telescope, the optical cross-correlator with balanced detector, the delay stage and the link fiber collimator. **Right:** Fiber layer occupied by a large spool on which the DCF is wound, the mount for the pump laser diode of the EDFA and the piezo stretcher.

electronics and the fiber installation can be seen. On the opposite side of the thick aluminum base plate, the components of the optical cross-correlator are mounted. The plate is attached to the box with hinges to allow access to the fibers and the electronics in an easy way. The optical and electrical connections to the device are realized through a panel at one side of the unit. It provides connections for the current and temperature controller of the EDFA pump laser diode, the three motors, two temperature sensors, current supply for the photodetectors, the output signals of the balanced detector, the optical power monitors and the 2.6 GHz phase detector, the RF input for it, the high-voltage (HV) connector of the piezo stretcher, as well as the fiber connector for the actual link. An exception is the optical fiber of the distribution EDFA, which leads outwards from the opposite site of the box due to the arrangement of the devices on the optical table. It should be noted, that the complete assembly and optical alignment of the fiber link unit can be done outside the synchronization hutch. There, only the final splice of the piezo stretcher to the DCF has to be made after the correct lengths for short returning pulses from the link and temporal overlap in the PPKTP crystal have been determined experimentally (see also section 6.1.2, page 135 ff.). For this, a robust optical setup with

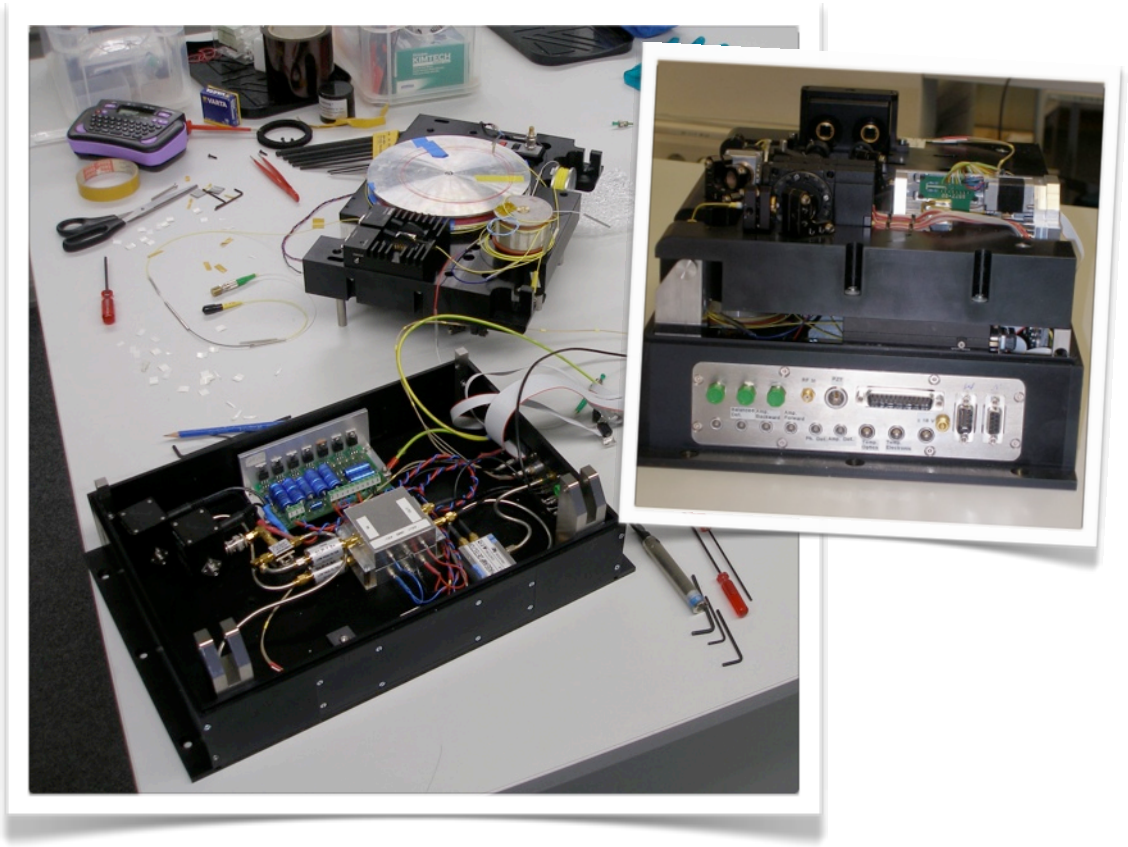

Figure G.7 | Assembly of a fiber link stabilization unit. Assembled box (**left**) and a view of the connector panel and parts of the optical cross-correlator (**right**).

an autocorrelator and a high-bandwidth photodiode has been assembled, which universally can be used for the commissioning of all link units. Furthermore, the footprint of the link boxes and the fiber splicer are similar, such that its placement on the optical table during the commissioning of a link does not interfere with the other, already installed devices. The photograph (Fig. G.8) shows the installation process of a fiber link stabilization unit. Next to the link box the fiber splicer is located. The blue box in the upper left part is the commercial autocorrelator used for the determination of the pulse duration for the dispersion compensation. The Origami laser system, which also can be seen in the picture, provides the timing reference for the other, operational fiber links through the free-space distribution unit. The fiber link end, at which the pulse train is reflected partly, can be designed in different ways, as explained in section 6.3 (page 144 ff.). Figure G.9 shows a photograph of the fiber installation of a double-pumped EDFA with precedent monitor ports. Together with the pump laser diodes, the link end consists of approximately 8 m fiber, which has to be installed inside the device using the particular stabilized pulse train. In the depicted case, this is the optical cross-correlator for the synchronization of the Ti:sapphire laser of the EOSD experiment (see section 1.8.1, page 16 ff.). The light from the monitor ports (connectors at upper left in the picture) are used for LO generation and RIN measurements, see section 6.3 on pages 144 ff.

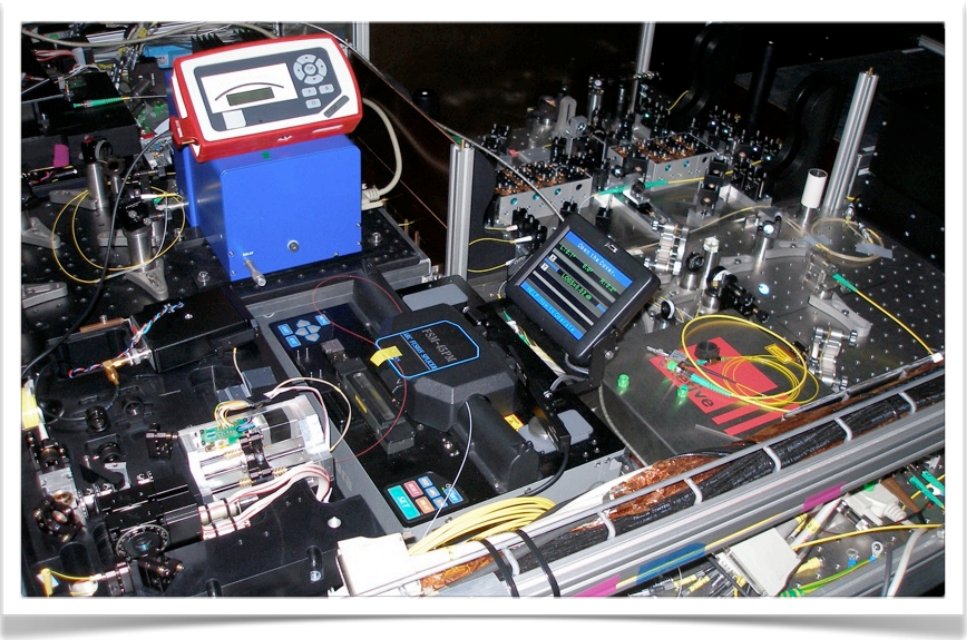

Figure G.8 | Photograph taken during the commissioning of a fiber link stabilization unit. The box, shown in the lower left part of the photo will be the connection to the HHG laboratory.

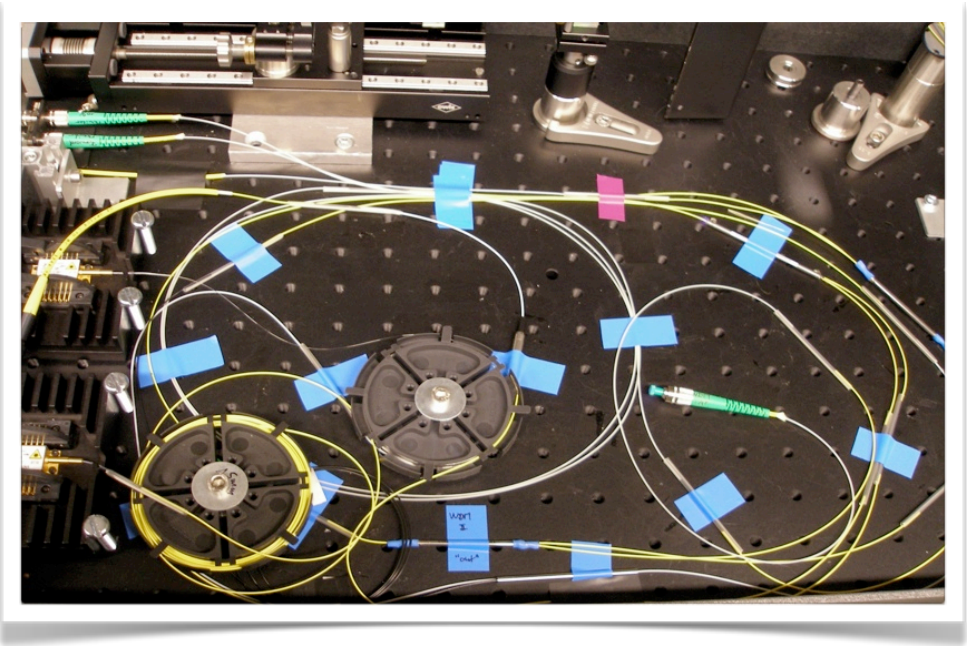

Figure G.9 | Fiber installation of the end of the link to the EO laboratory. The fiber link end consists of a double-pumped EDFA and features several monitor ports for diagnostics of the transmitted reference pulse train.

Optical Cross-Correlators

The optical cross-correlator (OXC) for the Ti:sapphire synchronization is described in chapter 7 (pages 151 ff.). For development, a breadboard setup with two layers had been chosen. The lower one contains the fiber link end installation shown in G.9 with its two required pump laser diodes. The upper layer contains the free-space optic part of the actual cross-correlator. For easier alignment of the collinear propagation of the two laser beams and for enhanced mechanical stability, a construction known as "cage system" manufactured by Thorlabs is used. The timing of the optically locked

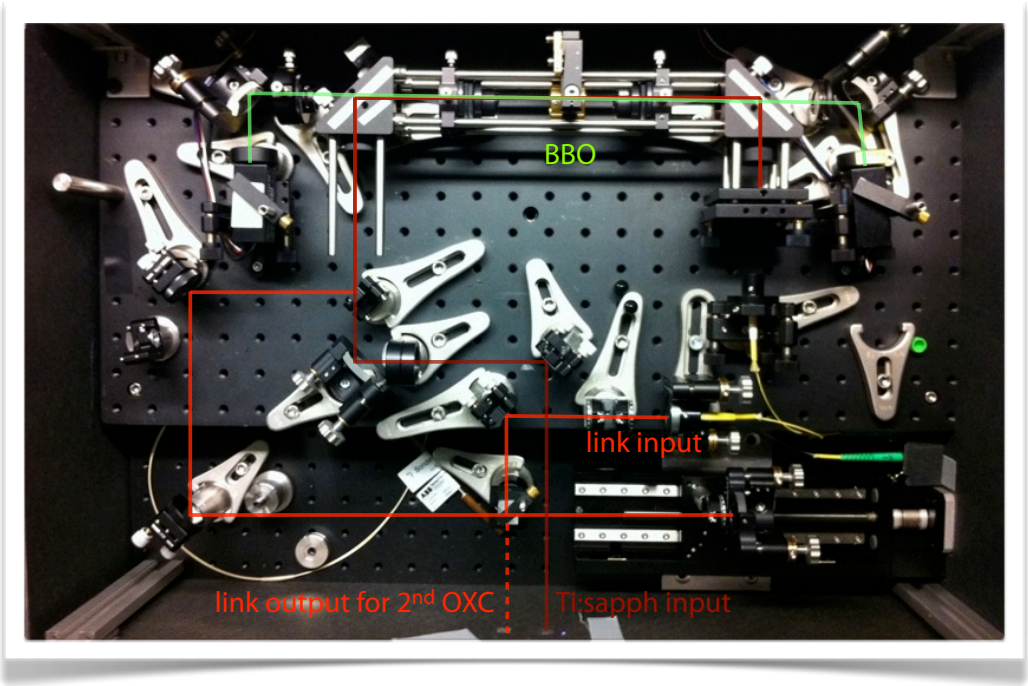

Figure G.10 | Photograph of the optics of the Ti:sapphire optical cross-correlator. The optical cross-correlator is used for Ti:sapphire laser synchronization in the special diagnostics laboratory at FLASH.

Ti:sapphire laser system can be shifted by ±450 ps with respect to the reference pulse train provided by the fiber link with an optical delay line (shown in the lower right in the figure). Furthermore, a fraction of the reference pulse train is tapped off and can be used for out-of-loop timing measurements with a second cross-correlator (see section 7.2, page 161 ff.). The generated sum-frequency signals are detected with compact photomultiplier tube (PMT) modules with controllable sensitivity. The electronic part of the setup are not integrated to the device in this proof-of-principle setup.

The optical cross-correlator setup, as shown in Fig. G.11, for the photoinjector laser pulse arrival time measurements and, in the future, for stabilization or synchronization is built on a breadboard of the the size 600 × 450 mm^2 and located in direct vicinity to the PTO on the optical table. In contrast to the OXC described above, it contains not only the free-space optical part of the correlator with its delay line (also ±450 ps range), but also the opto-electronics for monitoring the optical powers and generation of an 1.3 GHz LO signal, as well as the fiber optics with an EDFA and dispersion compen-

sation (see section 8.2, page 169 ff.). Furthermore, the required quarter- and half-wave retarders of the fiber link end are motorized and used as actuators of an optical power stabilization loop. Similar to the fiber link units, all electrical and optical connections are made through a patch panel.

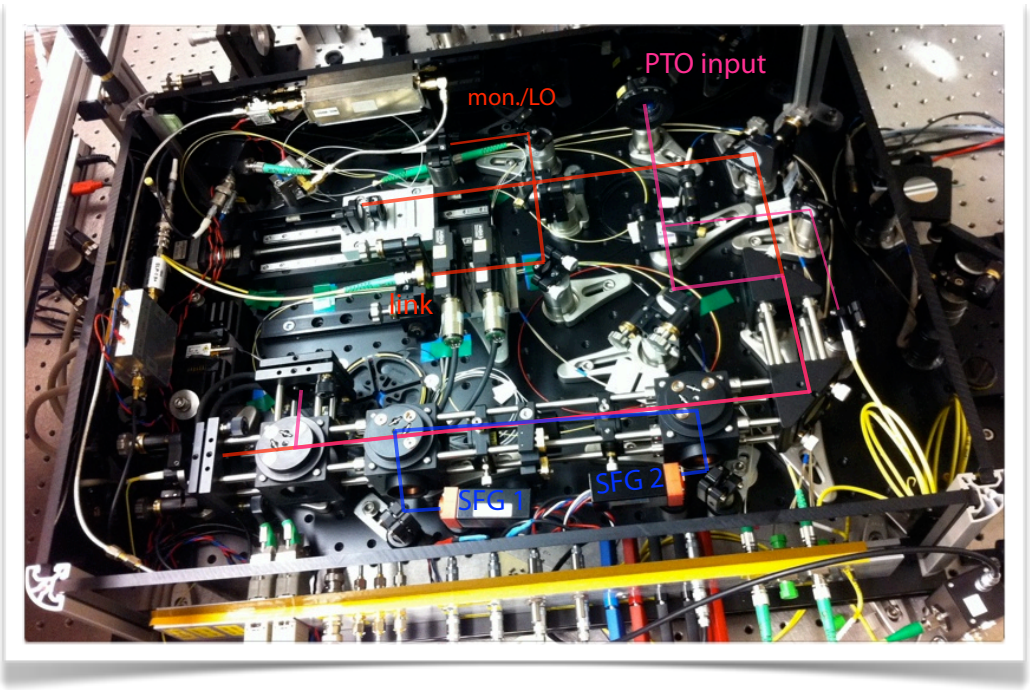

Figure G.11 | Photograph of the optical cross-correlator at the photo injector laser. The optical cross-correlator presently used for the photoinjector laser pulse arrival time measurements and, in the future, stabilization/synchronization.

Bibliography

[AAA+07] W. Ackermann, et al., *Operation of a free-electron laser from the extreme ultraviolet to the water window*, Nature Photonics 1 (2007), no. 6, 336–342.

[ABC+07] M. Altarelli, et al., *The European X-Ray Free-Electron Laser - Technical Design Report*, DESY XFEL Project Group and Project Team, http://xfel.eu, 2007.

[AFK+08] V. R. Arsov, et al., *Electro-optic Bunch Arrival Time Measurement at FLASH*, Proceedings of EPAC 2008, Genoa, Italy, 2008, 3348–3350.

[Agi08] *Fast, Easy and Accurate Phase Noise Measurements using the Agilent E5052B SSA with the E5053*, Application Note, Agilent Technologies, http://cp.literature.agilent.com/litweb/pdf/5989-8373EN.pdf, May 2008.

[Agr07] G. P. Agrawal, *Nonlinear Fiber Optics*, fourth ed., Academic Press, 30 Corporate Drive, Suite 400, Burlington, MA 01803, USA, 2007.

[Agr08] ———, *Applications of Nonlinear Fiber Optics*, second ed., Academic Press, 30 Corporate Drive, Suite 400, Burlington, MA 01803, USA, 2008.

[Azi09] A. Azima, *An Electro-Optical Timing Diagnostic for Pump-Probe Experiments at the Free-Electron Laser in Hamburg FLASH*, Ph.D. thesis, University of Hamburg, June 2009, DESY-THESIS-2009-027.

[BAC+10] J. Boedewadt, et al., *sFLASH - First Results of Direct Seeding at FLASH*, Proceedings of FEL 2010, Malmö, Sweden, 2010, 330–335.

[BAF+09] M. K. Bock, et al., *New Beam Arrival Time Monitor Used in a Time-of-Flight Injector Measurement*, Proceedings of FEL 2009, Liverpool, UK, 2009, 659–662.

[BDE+09] M. Bass, C. DeCusatis, J. Enoch, V. Lakshminarayanan, G. Li, C. MacDonald, V. Mahajan, and E. van Stryland, *Handbook of Optics*, McGraw Hill Professional, October 2009.

[Beh10] C. Behrens, *Detection and Spectral Measurements of Coherent Synchrotron Radiation at FLASH*, Diploma thesis, University of Hamburg, 2010, DESY-THESIS-2010-002.

[BFG+10] M. K. Bock, et al., *Recent Developments of the Bunch Arrival Time Monitor with Femtosecond Resolution at FLASH*, Proceedings of IPAC'10, Kyōto, Japan, 2010, 2405–2407.

[BGZ09] C. Behrens, C. Gerth, and I. Zagorodnov, *Numerical Performance Studies on the new Sliced-Beam-Parameter Measurement Setup for FLASH*, Proceedings of FEL 2009, Liverpool, UK, 2009, 599–602.

[BNSW10] C. Behrens, D. Nicoletti, B. Schmidt, and S. Wesch, *Upgrade and Evaluation of the Bunch Compression Monitor at the Free-Electron Laser in Hamburg (FLASH)*, Proceedings of IPAC'10, Kyōto, Japan, 2010, 912–914.

[Boc13] M. K. Bock, *Measuring the Electron Bunch Timing with Femtosecond Resolution at FLASH*, Ph.D. thesis, University of Hamburg, March 2013, DESY-THESIS-2013-008.

[BPC+08] H. Byun, D. Pudo, J. Chen, E. P. Ippen, and F. X. Kärtner, *High-repetition-rate, 491 MHz, femtosecond fiber laser with low timing jitter*, Optics Letters **33** (2008), no. 19, 2221–2223.

[Bre11] J. Breunlin, *Commissioning of an Electro-Optic Electron Bunch Length Monitor at FLASH*, Diploma thesis, University of Hamburg, 2011, DESY-THESIS-2011-017.

[BSM+10] H. Byun, M. Y. Sander, A. Motamedi, H. Shen, G. S. Petrich, L. A. Kolodziejski, E. P. Ippen, and F. X. Kärtner, *Compact, stable 1 GHz femtosecond Er-doped fiber lasers*, Applied Optics **49** (2010), no. 29, 5577–5582.

[BSSW10] J. Breunlin, B. Schmidt, B. Steffen, and L.-G. Wissmann, *Commissioning of an Electro-Optic Electron Bunch Length Monitor at FLASH*, Proceedings of FEL 2010, Malmö, Sweden, 2010, 139–142.

[Bé91] P. A. Bélanger, *Beam propagation and the ABCD ray matrices*, Optics Letters **16** (1991), no. 4, 196–198.

[CAB+10] F. Curbis, et al., *Characterization of Seeded FEL Pulses at FLASH: Status, Challenges and Opportunities*, Proceedings of FEL 2010, Malmö, Sweden, 2010, 298–301.

[CD96] T. F. Carruthers, and I. N. Duling, III, *10-GHz, 1.3-ps erbium fiber laser employing soliton pulse shortening*, Optics Letters **21** (1996), no. 23, 1927–1929.

[Coh07] *Micra Broadband Ultrafast Ti:Sapphire Oscillators*, Coherent, Inc., http://coherent.com/Lasers/index.cfm?fuseaction=forms.DownloadsFile&DLID=6199&origin=%27lasers%27&page=1470&ID=1470&loc=834&Named=Micra%20Data%20Sheet, 2007.

[Cor02] *Corning SMF-28 Product Information*, Corning Inc., http://www.photonics.byu.edu/FiberOpticConnectors.parts/images/smf28.pdf, April 2002.

[Cov13a] *Device Specification MSFG1-xx*, Covesion Ltd., http://www.covesion.com/assets/downloads/MSFG1-0.5.pdf, 2013.

[Cov13b] *MSFG1-0.5-xx Phase Matching Data v1.0*, Covesion Ltd., http://www.covesion.com/assets/downloads/data/MSFG1data.csv, 2013.

[CRT+11] A. Ciapponi, W. Riede, G. Tzeremes, H. Schröder, and P. Mahnke, *Non-linear optical frequency conversion crystals for space applications*, Proc. SPIE 7912, Solid State Lasers XX: Technology and Devices, 791205, February 2011.

[CSIK07] J. Chen, J. W. Sickler, E. P. Ippen, and F. X. Kärtner, *High repetition rate, low jitter, low intensity noise, fundamentally mode-locked 167 fs soliton Er-fiber laser*, Optics Letters **32** (2007), no. 11, 1566–1568.

[CV06] M. Currie, and I. Vurgaftman, *Microwave Phase Retardation in Saturated InGaAs Photodetectors*, IEEE Photonics Technology Letters **18** (2006), no. 13, 1433–1435.

[DES10] *FLASH eröffnet den Blick durchs Wasserfenster*, DESY News, September 28, http://www.desy.de/aktuelles/@@news-view?id=101&lang=ger, 2010.

[DFMS85] J.-C. M. Diels, J. J. Fontaine, I. C. McMichael, and F. Simoni, *Control and measurement of ultrashort pulse shapes (in amplitude and phase) with femtosecond accuracy*, Applied Optics **24** (1985), no. 9, 1270–1282.

[DGN99] V. G. Dmitriev, G. G. Gurzadyan, and D. N. Nikogosyan, *Handbook of Nonlinear Optical Crystals*, third revised ed., Springer, Berlin, 1999.

[DHMR+09] H. Delsim-Hashemi, V. Miltchev, J. Rossbach, Y. Holler, A. Schöps, M. Tischer, and I. Vasserman, *Status of the sFLASH Undulator System*, Proceedings of FEL 2009, Liverpool, UK, 2009, 500–502.

[Dig01] M. J. F. Digonnet (ed.), *Rare-Earth-Doped Fiber Lasers and Amplifiers*, second revised and expanded ed., Marcel Dekker, Inc., 270 Madison Avenue, New York, NY 10016, 2001.

[DN93] V. G. Dmitriev, and D. N. Nikogosyan, *Effective nonlinearity coefficients for three-wave interactions in biaxial crystal of mm2 point group symmetry*, Optics Communications **95** (1993), no. 1–3, 173–182.

[DR06] J.-C. Diels, and W. Rudolph, *Ultrashort Laser Pulse Phenomena*, second ed., Academic Press, 30 Corporate Drive, Suite 400, Burlington, MA 01803, USA, 2006.

[DS10] M. Danailov, and P. Sigalotti, *Noise of the balanced cross-correlator in development for Ti:sapphire synchronization*, private communication, April 2010.

[EAA+10] P. Emma, et al., *First lasing and operation of an angstrom-wavelength free-electron laser*, Nature Photonics **4** (2010), no. 9, 641–647.

[EBH10] H. Edwards, C. Behrens, and E. R. Harms, *3.9 GHz Cavity Module for Linear Bunch Compression at FLASH*, Proceedings of LINAC2010, Tsukuba, Japan, 2010, 41–45.

[Emm01] P. Emma, *X-Band RF Harmonic Compensation for Linear Bunch Compression in the LCLS*, Technical Report, SLAC-TN-05-004, November 2001.

[FAB+09] M. Felber, et al., *Long-Term Femtosecond Stable RF Signal Generation from Optical Pulse Trains*, Proceedings of PAC 2009, Vancouver, Canada, 2009, 4165–4168.

[FBB+10] M. Felber, et al., *RF-based Synchronization of the Seed and Pump-Probe Lasers to the Optical Synchronization System at FLASH*, Proceedings of FEL 2010, Malmö, Sweden, 2010, 544–547.

[Fel10] J. Feldhaus, *FLASH - the first soft x-ray free electron laser (FEL) user facility*, Journal of Physics B: Atomic, Molecular and Optical Physics **43** (2010), no. 19, 194002(8).

[Fem06] *Datasheet DLPVA-100-B Series*, FEMTO Messtechnik GmbH, http://www.femto.de/datasheet/DE-DLPVA-100-B_5.pdf, July 2006.

[FWG+09] U. Frühling, et al., *Single-shot terahertz-field-driven X-ray streak camera*, Nature Photonics **3** (2009), 523–528.

[GBF+10a] P. Gessler, M. K. Bock, M. Felber, K. E. Hacker, W. Koprek, F. Ludwig, H. Schlarb, B. Schmidt, and S. Schulz, *Longitudinal Bunch Arrival-Time Feedback at FLASH*, Proceedings of FEL 2010, Malmö, Sweden, 2010, 578–580.

[GBF+10b] P. Gessler, M. K. Bock, M. Felber, K. E. Hacker, F. Ludwig, H. Schlarb, B. Schmidt, S. Schulz, and J. Szewinski, *Real-Time Sampling and Processing Hardware for Bunch Arrival-Time Monitors at FLASH and XFEL*, Proceedings of FEL 2010, Malmö, Sweden, 2010, 585–587.

[Ges10] P. Gessler, *Modifications of the DOOCS laser lock DSP server*, group internal seminar, May 2010.

[GHR+07] O. Grimm, Y. Holler, J. Rossbach, N. Morozov, A. Chesnov, E. Matushevsky, D. Petrov, and E. Syresin, *Magnetic Measurements with the FLASH Infrared Undulator*, TESLA FEL Report 2007-08, December 2007.

[HAB+09] K. E. Hacker, et al., *Design and Drift Performance of the FLASH Master Laser Oscillator RF-Lock*, Proceedings of FEL 2009, Liverpool, UK, 2009, 663–666.

[Hac10] K. E. Hacker, *Measuring the Electron Beam Energy in a Magnetic Bunch Compressor Chicane*, Ph.D. thesis, University of Hamburg, June 2010, DESY-THESIS-2010-037.

[Ham07] *Metal PMT Photosensor Module H6780-20 Data Sheet*, Hamamatsu Corporation, http://sales.hamamatsu.com/assets/pdf/parts_H/H6780-20.pdf, 2007.

[HBG+05] J. H. Han, et al., *Emission Mechanisms in a Photocathode RF Gun*, Proceedings of 2005 Particle Accelerator Conference, Knoxville, USA, 2005, 856–858.

[Hec02] E. Hecht, *Optics*, fourth ed., Addison Wesley, 1301 Sansome St., San Francisco, CA 94111, USA, 2002.

[HFF+10] K. Honkavaara, B. Faatz, J. Feldhaus, S. Schreiber, R. Treusch, and J. Rossbach, *FLASH Upgrade*, Proceedings of IPAC'10, Kyōto, Japan, 2010, 1290–1292.

[HFH+91] M. Hofer, M. E. Fermann, F. Haberl, M. H. Ober, and A. J. Schmidt, *Mode locking with cross-phase and self-phase modulation*, Optics Letters **16** (1991), no. 7, 502–504.

[HKF05] J. H. Han, M. Krasilnikov, and K. Flöttmann, *Secondary electron emission in a photocathode rf gun*, Physical Review Special Topics - Accelerators and Beams **8** (2005), no. 3, 033501–1–033501–9.

[HM93] H. A. Haus, and A. Mecozzi, *Noise of mode-locked lasers*, IEEE Journal of Quantum Electronics **29** (1993), no. 3, 983–996.

[Hun09] S. Hunziker, *Power supply influence on direct conversion*, private communication, November 2009.

[IW98] C. Iaconis, and I. A. Walmsley, *Spectral phase interferometry for direct electric-field reconstruction of ultrashort optical pulses*, Optics Letters **23** (1998), no. 10, 792–794.

[Jun97] D. H. Jundt, *Temperature-dependent Sellmeier equation for the index of refraction, ne, in congruent lithium niobate*, Optics Letters **22** (1997), no. 20, 1553–1555.

[Kat86] K. Kato, *Second-Harmonic Generation to 2048A in Beta-Bariumborat*, IEEE Journal of Quantum Electronics **7** (1986), no. 22, 1013–1014.

[KBB+10] W. Koprek, et al., *Intra-Train Longitudinal Feedback for Beam Stabilization at FLASH*, Proceedings of FEL 2010, Malmö, Sweden, 2010, 537–543.

[KCCK07] J. Kim, J. Chen, J. Cox, and F. X. Kärtner, *Attosecond-resolution timing jitter characterization of free-running mode-locked lasers*, Optics Letters **32** (2007), no. 24, 3519–3521.

[KCCK08] J. Kim, J. A. Cox, J. Chen, and F. X. Kärtner, *Drift-free femtosecond timing synchronization of remote optical and microwave sources*, Nature Photonics **2** (2008), 733–736.

[KCZ+07] J. Kim, J. Chen, Z. Zhang, F. N. C. Wong, F. X. Kärtner, F. Löhl, and H. Schlarb, *Long-term femtosecond timing link stabilization using a single-crystal balanced cross correlator*, Opt. Lett. **32** (2007), no. 9, 1044–1046.

[Kel92] S. M. J. Kelly, *Characteristic sideband instability of periodically amplified average soliton*, Electronics Letters **28** (1992), no. 8, 806–807.

[KIK+04] J. Kim, F. Ö. Ilday, F. X. Kärtner, O. D. Mücke, M. H. Perrott, W. S. Graves, D. E. Moncton, and T. Zwart, *Large-Scale Timing Distribution and RF-Synchronization for FEL Facilities*, Proceedings of FEL 2004, Trieste, Italy, 2004, 339–342.

[KKL06] J. Kim, F. X. Kärtner, and F. Ludwig, *Balanced optical-microwave phase detectors for optoelectronic phase-locked loops*, Optics Letters **31** (2006), no. 24, 3659–3661.

[KKP04] J. Kim, F. X. Kärtner, and M. H. Perrott, *Femtosecond synchronization of radio frequency signals with optical pulse trains*, Optics Letters **29** (2004), no. 17, 2076–2078.

[KSF+09] L. Krainer, G. J. Spühler, M. Felber, H. Schlarb, and S. Schulz, *Specification of the Origami-15 for the optical synchronization syste of FLASH*, private meeting, November 2009.

[KT10] K. Klose, and R. Tarkeshian, *Laser pulse duration measurement with streak camera*, private communication, see also http://ttfinfo.desy.de/TTFelog/show.jsp?dir=/2010/16/20.04_M&pos=2010-04-20T11:50:08, April 2010.

[KWK+93] U. Keller, et al., *Semiconductor Saturable Absorber Mirrors (SESAMs) for Femtosecond and Nanosecond Pulse Generation in Solid-State Lasers*, IEEE Journal of Selected Topics in Quantum Electronics **2** (1993), 435–445.

[KZF+96] D. Kopf, G. Zhang, R. Fluck, M. Moser, and U. Keller, *All-in-one dispersion-compensating saturable absorber mirror for compact femtosecond laser sources*, Optics Letters **21** (1996), no. 7, 486–488.

[LAF+10] F. Löhl, et al., *Electron Bunch Timing with Femtosecond Precision in a Superconducting Free-Electron Laser*, Physical Review Letters **104** (2010), no. 14, 144801(4).

[Lam11] T. Lamb, *Femtosekundengenaue Stabilisierung von optischen Glasfaserstrecken basierend auf HF-Leistungsmessung*, Diploma thesis, University of Magdeburg, January 2011.

[LHG+08] G. Lambert, et al., *Injection of harmonics generated in gas in a free-electron laser providing intense and coherent extreme-ultraviolet light*, Nature Physics **4** (2008), 296–300.

[Lie07] *Liekki EasySplice Software, Version 1.7*, nLIGHT Corporation, http://www.nlight.net/easysplice, August 2007.

[Lie08] *Data Sheet of Er110-4/125 High Power Erbium Fiber*, nLIGHT Corporation, http://www.nlight.net/nlight-files/file/datasheets/Fibers/nLIGHT_LIEKKI-Er110-4-125_080728.pdf, July 2008.

[Lie09] *Data Sheet of Er80-8/125 High Power Erbium Fiber*, nLIGHT Corporation, http://www.nlight.net/nlight-files/file/datasheets/Fibers/nLIGHT_LIEKKI-Er80-x-125_090121.pdf, January 2009.

[Loe09] F. Loehl, *Optical Synchronization of a Free-Electron Laser with Femtosecond Precision*, Ph.D. thesis, University of Hamburg, September 2009, DESY-THESIS-2009-031.

[Lor06] B. Lorbeer, *Performance of the Master Oscillator for FLASH at DESY*, Project Thesis, TESLA-FEL-2006-12, October 2006.

[Lor08] _____, *Laser to RF Conversion Techniques for the Laser Based Synchronization System at FLASH in Comparison*, Master's thesis, Hamburg University of Technology (TUHH), November 2008.

[LS97] R. Lai, and A. J. Sievers, *On using the coherent far IR radiation produced by a charged-pARTICLE bunch to determine its shape: I Analysis*, Nuclear Instruments and Methods in Physics Research Section A **397** (1997), no. 2-3, 221 – 231.

[MAB+09] V. Miltchev, et al., *Technical Design of the XUV Seeding Experiment at FLASH*, Proceedings of FEL 2009, Liverpool, UK, 2009, 503–506.

[MBRF96] G. M. Macfarlane, A. S. Bell, E. Riis, and A. I. Ferguson, *Optical comb generator as an efficient short-pulse source*, Optics Letters **21** (1996), no. 7, 534–536.

[Mea10] *Data Sheet of Meadowlark Precision Polymer Retarders*, Meadowlark Optics, Inc., http://www.meadowlarkoptics.com/products/RetardersPrecisionPolymer.php, August 2010.

[MSK+01] L.-S. Ma, R. K. Shelton, H. C. Kapteyn, M. M. Murnane, and J. Ye, *Sub-10-femtosecond active synchronization of two passively mode-locked Ti:sapphire oscillators*, Physical Review A: Atomic, Molecular, and Optical Physics **64** (2001), no. 2, 021802.

[NEC06] *AE0203D08F Specification Sheet*, Thorlabs, Inc., http://www.thorlabs.de/Thorcat/15600/15640-S01.pdf, July 2006.

[New10] *Data Sheet of Broadband Polarizing Cube Beamsplitter 05FC16PB.9*, Newport Corporation, http://search.newport.com/?q=*&x2=sku&q2=05FC16PB.9, August 2010.

[OFS05] *Specifications of ClearLite 980 Photonic Fibers*, OFS Optics, http://www.specialtyphotonics.com/pdf/products/022_023.pdf, May 2005.

[OFS09a] *OFS LLWBDK DC Modules Test Report*, OFS Optics, internal documentation, May 2009.

[OFS09b] *G.652 Product Comparison*, OFS Optics, available on request, May 2009.

[One09] *Ultra low timing jitter performance & characterization of Origami femtosecond laser series*, OneFive GmbH, http://onefive.com/pdf/20090613_ultra_low_noise_whitepaper.pdf, June 2009.

[One10] *Origami-15 Serial Number 072 Data Sheet*, OneFive GmbH, provided with laser, internal documentation, April 2010.

[OSWK08] A. E. Oehler, T. Südmeyer, K. J. Weingarten, and U. Keller, *100 GHz passively mode-locked Er:Yb:glass laser at 1.5 µm with 1.6-ps pulses*, Optics Express **16** (2008), no. 26, 21930–21935.

[OUI10] B. Oktem, C. Ülgüdür, and F. Ö. Ilday, *Soliton–similariton fibre laser*, Nature Photonics **4** (2010), 307–311.

[OWS+11] C. Ouyang, H. Wang, P. Shum, S. Fu, J. H. Wong, K. Wu, D. R. C. S. Lim, V. K. H. Wong, and K. E. K. Lee, *Properties of a vector soliton laser passively mode-locked by a fiber-based semiconductor saturable absorber operating in transmission*, Optics Communications **284** (2011), no. 2, 619–624.

[Pas04a] R. Paschotta, *Noise of mode-locked lasers (Part I): numerical model*, Applied Physics B **79** (2004), 153–162.

[Pas04b] ———, *Noise of mode-locked lasers (Part II): timing jitter and other fluctuations*, Applied Physics B **79** (2004), 163–173.

[Pas08a] R. Paschotta, *Encyclopedia of Laser Physics and Technology*, first ed., vol. II, Wiley VCH, Berlin, 2008.

[Pas08b] ———, *Encyclopedia of Laser Physics and Technology*, first ed., vol. I, Wiley VCH, Berlin, 2008.

[Pas10] ———, *Timing jitter and phase noise of mode-locked fiber lasers*, Optics Express **18** (2010), no. 5, 5041–5054.

[PH98] R. Poprawe, and G. Herziger, *Lasertechnik I*, Lecture Notes, RWTH Aachen University, September 1998.

[RASA+11] H. Redlin, A. Al-Shemmary, A. Azima, N. Stojanovic, F. Tavella, I. Will, and S. Düsterer, *The FLASH pump–probe laser system: Setup, characterization and optical beamlines*, Nuclear Instruments and Methods in Physics Research Section A: Accelerators, Spectrometers, Detectors and Associated Equipment **635** (2011), no. 1, Supplement, S88–S93.

[Roe08] M. Roehrs, *Investigation of the Phase Space Distribution of Electron Bunches at the FLASH-Linac Using a Transverse Deflecting Structure*, Ph.D. thesis, University of Hamburg, June 2008, DESY-THESIS-2008-012.

[SAB+09] B. Steffen, et al., *Electro-optic time profile monitors for femtosecond electron bunches at the soft x-ray free-electron laser FLASH*, Physical Review Special Topics - Accelerators and Beams **12** (2009), no. 3, 032802.

[SAL+05] H. Schlarb, V. Ayvazyan, F. Ludwig, D. Noelle, B. Schmidt, S. Simrock, A. Winter, and F. X. Kärtner, *Next Generation Synchronization System for the VUV-FEL at DESY*, Proceedings of FEL 2005, Stanford, USA, 2005, 118–121.

[Sch09] H. Schlarb, *Tolerance study on free-space distribution for FLASH*, group internal seminar, February 2009.

[Sch10a] _____, *Ladies and gentlemen, how can this be?*, FLA eLogBook, http://ttfinfo.desy.de/FLAelog/show.jsp?dir=/2010/05&pos=2010-05-18T00:40:05, April 2010.

[Sch10b] J. R. Schneider, *FLASH—from accelerator test facility to the first single-pass soft x-ray free-electron laser*, Journal of Physics B: Atomic, Molecular and Optical Physics **43** (2010), no. 19, 194001(9).

[Sch10c] S. Schreiber, *Details on the wavelength conversion stage of the photo injector laser*, private communication, November 2010.

[SDR08] P. Schmüser, M. Dohlus, and J. Rossbach, *Ultraviolet and Soft X-Ray Free-Electron Lasers*, first ed., Springer, Berlin, 2008.

[SFF+10] S. Schreiber, B. Faatz, J. Feldhaus, K. Honkavaara, R. Treusch, M. Vogt, and J. Rossbach, *FLASH Upgrade and First Results*, Proceedings of FEL 2010, Malmö, Sweden, 2010, 198–201.

[SGK+06] S. Schreiber, M. Görler, K. Klose, M. Staack, L. Fröhlich, I. Will, and I. Templin, *Experience with the Photoinjector Laser at FLASH*, Proceedings of FEL 2006, Berlin, Germany, 2006, 590–593.

[SHK+06] H. Schlarb, N. Heidbrook, H. Kapitza, F. Ludwig, and N. Nagad, *Precision RF Gun Phase Monitor System for FLASH*, Proceedings of EPAC 2006, Edinburgh, UK, 2006, 1052–1054.

[SKK+03] T. R. Schibli, et al., *Attosecond active synchronization of passively mode-locked lasers by balanced cross correlation*, Optics Letters **28** (2003), no. 11, 947–949.

[Ste07] B. Steffen, *Electro-Optic Methods for Longitudinal Bunch Diagnostics at FLASH*, Ph.D. thesis, University of Hamburg, July 2007, DESY-THESIS-2007-020.

[SWVS85] E. W. V. Stryland, M. A. Woodall, H. Vanherzeele, and M. J. Soileau, *Energy band-gap dependence of two-photon absorption*, Optics Letters **10** (1985), no. 10, 490–492.

[TAB+10] R. Tarkeshian, et al., *Femtosecond Temporal Overlap of Injected Electron Beam and EUV Pulse at sFLASH*, Proceedings of IPAC'10, Kyōto, Japan, 2010, 915–917.

[TAvB+09] K. Tiedtke, et al., *The soft x-ray free-electron laser FLASH at DESY: beamlines, diagnostics and end-stations*, New Journal of Physics **11** (2009), no. 2, 023029(16).

[Tho10] *Specifications and Graphs of Liekki Highly Doped Er Fibers*, Thorlabs GmbH, http://www.thorlabs.de/catalogpages/v20/867.pdf, August 2010.

[TNHI94] K. Tamura, L. E. Nelson, H. A. Haus, and E. P. Ippen, *Soliton versus nonsoliton operation of fiber ring lasers*, Applied Physics Letters **64** (1994), no. 2, 149–151.

[Tre02] R. Trebino, *Frequency-Resolved Optical Gating: The Measurement of Ultrashort Laser Pulses*, Springer Science+Business LLC, 2002.

[VAB+10] E. Vogel, et al., *Test and Commissioning of the Third Harmonic RF System for FLASH*, Proceedings of IPAC'10, Kyōto, Japan, 2010, 4281–4283.

[vTM+08] J. van Tilborg, C. Tóth, N. H. Matlis, G. R. Plateau, and W. P. Leemans, *Electro-optic techniques in electron beam diagnostics*, Proceedings of BIW08, Lake Tahoe, USA, 2008, 65–74.

[WAB+09] L.-G. Wissmann, et al., *Electro-Optic Electron Bunch Diagnostic At FLASH Using an Ytterbium Fiber Laser*, Proceedings of FEL 2009, Liverpool, UK, 2009, 627–630.

[Wes08] S. Wesch, *Spektroskopie kohärenter Übergangsstrahlung zur Strukturanalyse von Elektronenpaketen bei FLASH*, Diploma thesis, University of Hamburg, 2008.

[Wes12] _____, *Echtzeitbestimmung longitudinaler Elektronenstrahlparameter mittels absoluter Intensitäts- und Spektralmeßung einzelner kohärenter THz Strahlungspulse*, Ph.D. thesis, University of Hamburg, December 2012, DESY-THESIS-2012-052.

[Wie98a] H. Wiedemann, *Particle Accelerator Physics I*, second ed., vol. I, Springer, Berlin, 1998.

[Wie98b] _____, *Particle Accelerator Physics II*, second ed., vol. II, Springer, Berlin, 1998.

[Win08] A. Winter, *Fiber Laser Master Oscillators for Optical Synchronization Systems*, Ph.D. thesis, University of Hamburg, April 2008, DESY-THESIS-2008-010.

[Wis10] L.-G. Wissmann, *Coarse repetition rate tuning via cavity temperature changes*, private communication, August 2010.

[Wis12] _____, *A Robust Fibre Laser System for Electro-Optic Electron Bunch Profile Measurements at FLASH*, Ph.D. thesis, University of Hamburg, August 2012, DESY-THESIS-2012-023.

[WKT05] I. Will, G. Koss, and I. Templin, *The upgraded photocathode laser of the TESLA Test Facility*, Nuclear Instruments and Methods in Physics Research A **541** (2005), 467–477.

[WLL+06] A. Winter, F. Loehl, F. Ludwig, H. Schlarb, B. Schmidt, and P. Schmüser, *Layout of the Optical Synchronization System for FLASH*, Proceedings of EPAC 2006, Edinburgh, UK, 2006, 1061–1063.

[WRD+05] I. Will, H. Redlin, S. Düsterer, J. Feldhaus, and E. Plönjes, *Optical Laser Synchronized to the DESY VUV-FEL for Two-Color Pump-Probe Experiments*, Proceedings of FEL 2005, Stanford, USA, 2005, 690–693.

[YY07] A. Yariv, and P. Yeh, *Photonics*, sixth ed., Oxford University Press, New York, Oxford, 2007.

[ZAB+09] J. Zemella, et al., *RF-Based Detector for Measuring Fiber Length Changes With Sub-5 Femtosecond Long-Term Stability over 50 h.*, Proceedings of FEL 2009, Liverpool, UK, 2009, 780–783.

[Zem08] J. Zemella, *Driftfreier Detektor zur Messung des Zeitversatzes zweier verschiedener Laserpulszüge*, Diploma thesis, University of Hamburg, 2008.

List of Publications

[1] S. Ackermann, A. Azima, S. Bajt, J. Bödewadt, F. Curbis, H. Dachraoui, H. Delsim-Hashemi, M. Drescher, S. Düsterer, B. Faatz, M. Felber, J. Feldhaus, E. Hass, U. Hipp, K. Honkavaara, R. Ischebeck, S. Khan, T. Laarmann, C. Lechner, Th. Maltezopoulos, V. Miltchev, M. Mittenzwey, M. Rehders, J. Rönsch-Schulenburg, J. Rossbach, H. Schlarb, S. Schreiber, L. Schroedter, M. Schulz, **S. Schulz**, R. Tarkeshian, M. Tischer, V. Wacker, and M. Wieland, *Generation of Coherent 19- and 38-nm Radiation at a Free-Electron Laser Directly Seeded at 38 nm*, Physical Review Letters **111** (2013), 114801.

[2] V. R. Arsov, M. K. Bock, M. Felber, P. Geßler, K. E. Hacker, F. Löhl, F. Ludwig, K.-H. Matthiesen, H. Schlarb, B. Schmidt, **S. Schulz**, A. Winter, L.-G. Wissmann, and J. Zemella, *Temporal Profiles of the Coherent Transition Radiation Measured at FLASH with Electro-Optical Spectral Decoding*, Proceedings of DIPAC09, Basel, Switzerland, 2009, pp. 272–274.

[3] V. R. Arsov, M. Felber, E.-A. Knabbe, F. Löhl, B. Lorbeer, F. Ludwig, K.-H. Matthiesen, H. Schlarb, B. Schmidt, P. Schmüser, **S. Schulz**, B. Steffen, A. Winter, and J. Zemella, *Electro-optic Bunch Arrival Time Measurement at FLASH*, Proceedings of EPAC08, Genoa, Italy, 2008, pp. 3348–3350.

[4] M. K. Bock, V. R. Arsov, M. Felber, P. Gessler, K. E. Hacker, F. Löhl, F. Ludwig, H. Schlarb, B. Schmidt, **S. Schulz**, A. Winter, L.-G. Wissmann, and J. Zemella, *New Beam Arrival Time Monitor Used in a Time-Of-Flight Injector Measurement*, Proceedings of FEL2009, Liverpool, UK, 2009, pp. 659–662.

[5] M. K. Bock, M. Bousonville, M. Felber, P. Gessler, T. Lamb, S. Ruzin, H. Schlarb, B. Schmidt, and **S. Schulz**, *Benchmarking the Performance of the Present Bunch Arrival Time Monitors at FLASH*, Proceedings of DIPAC2011, Hamburg, Germany, 2011, pp. 365–367.

[6] M. K. Bock, M. Felber, P. Gessler, K. E. Hacker, F. Ludwig, H. Schlarb, B. Schmidt, **S. Schulz**, L.-G. Wissmann, and J. Zemella, *Recent Developments of the Bunch Arrival Time Monitor with Femtosecond Resolution at FLASH*, Proceedings of IPAC'10, Kyōto, Japan, 2010, pp. 2405–2407.

[7] M. K. Bock, T. Lamb, M. Bousonville, M. Felber, P. Gessler, H. Schlarb, B. Schmidt, and **S. Schulz**, *Report on the Redesign of the Fibre Link Stabilisation Units at FLASH*, Proceedings of FEL2011, Shanghai, China, 2011, pp. 370–373.

[8] J. Bödewadt, A. Azima, F. Curbis, H. Delsim-Hashemi, M. Drescher, S. Düsterer, J. Feldhaus, R. Ischebeck, S. Khan, T. Laarmann, Th. Maltezopoulos, A. Meseck, V. Miltchev, M. Mittenzwey, J. Rossbach, H. Schlarb, **S. Schulz**, R. Tarkeshian, and M. Wieland, *Status of the XUV Seeding Experiment at FLASH*, Proceedings of PAC09, Vancouver, BC, Canada, 2009, pp. 1251–1253.

[9] M. Felber, V. R. Arsov, M. Bock, P. Gessler, K. Hacker, F. Löhl, F. Ludwig, K.-H. Matthiesen, H. Schlarb, B. Schmidt, **S. Schulz**, A. Winter, L. Wissmann, and J. Zemella, *Long-Term Femtosecond Stable RF Signal Generation from Optical Pulse Trains*, Proceedings of PAC09, Vancouver, BC, Canada, 2009, pp. 4165–4167.

[10] M. Felber, M. K. Bock, M. Bousonville, P. Gessler, T. Lamb, S. Ruzin, H. Schlarb, B. Schmidt, and **S Schulz**, *Upgrade of the Optical Synchronization System for FLASH II*, Proceedings of FEL2011, Shanghai, China, 2011, pp. 496–498.

[11] M. Felber, M. K. Bock, J. Breunlin, P. Gessler, K. E. Hacker, T. Lamb, F. Ludwig, H. Schlarb, B. Schmidt, **S. Schulz**, and L.-G. Wissmann, *RF-based Synchronization of the Seed and Pump-Probe Lasers to the Optical Synchronization System at FLASH*, Proceedings of FEL2010, Malmö, Sweden, 2010, pp. 544–547.

[12] M. Felber, M. Hoffmann, U. Mavric, H. Schlarb, **S. Schulz**, and W. Jalmuzna, *Laser Synchronization at REGAE using Phase Detection at an Intermediate Frequency*, Proceedings of IPAC12, New Orleans, Louisiana, USA, 2012, pp. 2624–2626.

[13] P. Gessler, M. K. Bock, C. Bohm, M. Bousonville, K. Czuba, M. Felber, A. Hidvegi, M. Hoffmann, T. Jezynski, T. Lamb, F. Ludwig, D. R. Makowski, G. Petrosyan, L. M. Petrosyan, K. Rehlich, **S. Schulz**, P. Vetrov, and M. Zimmer, *Next Generation Electronics based on µTCA for Beam-Diagnostics at FLASH and XFEL*, Proceedings of DIPAC2011, Hamburg, Germany, 2011, pp. 294–296.

[14] P. Gessler, M. K. Bock, M. Felber, K. E. Hacker, W. Koprek, F. Ludwig, H. Schlarb, B. Schmidt, and **S. Schulz**, *Longitudinal Bunch Arrival-Time Feedback at FLASH*, Proceedings of FEL2010, Malmö, Sweden, 2010, pp. 578–580.

[15] P. Gessler, M. K. Bock, M. Felber, K. E. Hacker, F. Ludwig, H. Schlarb, B. Schmidt, **S. Schulz**, and J. Szewiński, *Real-Time Sampling and Processing Hardware for Bunch Arrival-Time Monitors at FLASH and XFEL*, Proceedings of FEL2010, Malmö, Sweden, 2010, pp. 585–587.

[16] K. E. Hacker, V. R. Arsov, M. K. Bock, M. Felber, P. Gessler, F. Löhl, F. Ludwig, H. Schlarb, B. Schmidt, **S. Schulz**, A. Winter, L.-G. Wissmann, and J. Zemella, *Demonstration of a BPM with 5 Micron Resolution over a 10 cm Range*, Proceedings of FEL2009, Liverpool, UK, 2009, pp. 667–670.

[17] _____, *Design and Drift Performance of the FLASH Master Laser Oscillator RF-Lock*, Proceedings of FEL2009, Liverpool, UK, 2009, pp. 663–666.

[18] M. C. Hoffmann, A. Cavalleri, B. Schmidt, **S. Schulz**, S. Wesch, and S. Wunderlich, *Coherent Single Cycle Pulses with MV/cm Field Strengths from a Relativistic Transition Radiation Light Source*, Optics Letters **36** (2011), no. 23, 4473–4475.

[19] M. C. Hoffmann, **S. Schulz**, S. Wesch, S. Wunderlich, and B. Schmidt, *MV/cm THz pulses from a coherent transition radiation source*, Infrared, Millimeter and Terahertz Waves (IRMMW-THz), 2011 36th International Conference on, October 2011, pp. 1–2.

[20] W. Koprek, C. Behrens, M. K. Bock, M. Felber, P. Gessler, H. Schlarb, C. Schmidt, **S. Schulz**, B. Steffen, J. Szewiński, and S. Wesch, *Intra-train Longitudinal Feedback for Beam Stabilization at FLASH*, Proceedings of FEL2010, Malmö, Sweden, 2010, pp. 537–543.

[21] M. Kuntzsch, M. K. Bock, M. Bousonville, A. Büchner, M. Felber, M. Gensch, A. Jochmann, T. Kirschke, T. Lamb, U. Lehnert, H. Schlarb, **S. Schulz**, and F. Röser, *Concept of Femtosecond Timing and Synchronization Scheme at ELBE*, Proceedings of IPAC2011, San Sebastián, Spain, 2011, pp. 565–567.

[22] M. Kuntzsch, S. Findeisen, M. Gensch, B. W. Green, J. Hauser, S. Kovalev, U. Lehnert, P. Michel, F. Röser, Ch. Schneider, R. Schurig, A. Al-Shemmary, M. Bousonville, M. K. Czwalinna, T. Golz, H. Schlarb, B. Schmidt, **S. Schulz**, N. Stojanovic, S. Vilcins, and E. Hass, *Electron Bunch Diagnostic at the Upgraded ELBE Accelerator: Status and Challenges*, Proceedings of IBIC 2013, Oxford, UK, 2013, pp. 23–25.

[23] T. Lamb, M. K. Bock, M. Bousonville, M. Felber, P. Gessler, E. Janas, F. Ludwig, S. Ruzin, H. Schlarb, B. Schmidt, and **S. Schulz**, *Femtosecond Stable Laser-to-RF Phase Detection Using Optical Modulators*, Proceedings of FEL2011, Shanghai, China, 2011, pp. 551–554.

[24] T. Lamb, M. K. Bock, M. Bousonville, M. Felber, P. Gessler, F. Ludwig, S. Ruzin, H. Schlarb, B. Schmidt, and **S. Schulz**, *Development of an Alternative, Photodiode-Based, Femtosecond Stable Detection Principle for the Link Stabilization in the Optical Synchronization Systems at FLASH and XFEL*, Proceedings of DIPAC2011, Hamburg, Germany, 2011, pp. 380–382.

[25] T. Lamb, M. K. Bock, M. Felber, S. Jabłoński, F. Ludwig, H. Schlarb, and **S. Schulz**, *Characterization of the Engineered Photodiode-based Fiber Link Stabilization Scheme for Optical Synchronization Systems*, Proceedings of IPAC12, New Orleans, Louisiana, USA, 2012, pp. 2627–2629.

[26] T. Lamb, M. K. Czwalinna, M. Felber, C. Gerth, H. Schlarb, **S. Schulz**, C. Sydlo, M. Titberidze, F. Zummack, E. Janas, and J. Szewiński, *Femtosecond Stable Laser-to-RF Phase Detection for Optical Synchronization Systems*, Proceedings of IBIC 2013, Oxford, UK, 2013, pp. 447–450.

[27] F. Löhl, V. Arsov, M. Felber, K. Hacker, W. Jalmuzna, B. Lorbeer, F. Ludwig, K.-H. Matthiesen, H. Schlarb, B. Schmidt, P. Schmüser, **S. Schulz**, J. Szewiński, A. Winter, and J. Zemella, *Electron Bunch Timing with Femtosecond Precision in a Superconducting Free-Electron Laser*, Physical Review Letters **104** (2010), no. 14, 144801.

[28] F. Löhl, V. R. Arsov, C. Behrens, M. Felber, L. Fröhlich, K. E. Hacker, W. Jalmuzna, B. Lorbeer, F. Ludwig, K.-H. Matthiesen, H. Schlarb, B. Schmidt, **S. Schulz**, J. Szewiński, S. Wesch, A. Winter, and J. Zemella, *Observation of 40 fs Synchronization of Electron Bunches for FELs*, Proceedings of FEL08, Gyeongju, Korea, 2008, pp. 490–493.

[29] F. Löhl, V. R. Arsov, M. Felber, K. E. Hacker, W. Jalmuzna, B. Lorbeer, F. Ludwig, K.-H. Matthiesen, H. Schlarb, B. Schmidt, **S. Schulz**, J. Szewiński, A. Winter, and J. Zemella, *Measurement and Stabilization of the Bunch Arrival Time at FLASH*, Proceedings of EPAC08, Genoa, Italy, 2008, pp. 3360–3362.

[30] F. Löhl, V. R. Arsov, M. Felber, K. E. Hacker, B. Lorbeer, F. Ludwig, K.-H. Matthiesen, H. Schlarb, B. Schmidt, **S. Schulz**, A. Winter, and J. Zemella, *Experimental Determination of the Timing Stability of the Optical Synchronization System at FLASH*, Proceedings of EPAC08, Genoa, Italy, 2008, pp. 1386–1388.

[31] **S. Schulz**, V. Arsov, M. K. Bock, M. Felber, P. Gessler, K. E. Hacker, F. Ludwig, H. Schlarb, B. Schmidt, L.-G. Wissmann, and J. Zemella, *Precision Synchronization of the FLASH Photoinjector Laser*, Proceedings of IPAC'10, Kyōto, Japan, 2010, pp. 2875–2877.

[32] **S. Schulz**, V. R. Arsov, M. K. Bock, M. Felber, P. Gessler, K. E. Hacker, F. Löhl, F. Ludwig, K.-H. Matthiesen, H. Schlarb, B. Schmidt, A. Winter, L.-G. Wissmann, and J. Zemella, *All-Optical Synchronization of Distributed Laser Systems at FLASH*, Proceedings of PAC09, Vancouver, BC, Canada, 2009, pp. 4174–4176.

[33] **S. Schulz**, V. R. Arsov, M. K. Bock, M. Felber, P. Gessler, K. E. Hacker, F. Löhl, F. Ludwig, H. Schlarb, B. Schmidt, A. Winter, L.-G. Wissmann, and J. Zemella, *Progress Towards a Permanent Optical Synchronization Infrastructure at FLASH*, Proceedings of FEL2009, Liverpool, UK, 2009, pp. 671–674.

[34] **S. Schulz**, V. R. Arsov, M. Felber, F. Löhl, B. Lorbeer, F. Ludwig, K.-H. Matthiesen, H. Schlarb, B. Schmidt, P. Schmüser, B. Steffen, A. Winter, and J. Zemella, *An Optical Cross-Correlation Scheme to Synchronize Distributed Laser Systems at FLASH*, Proceedings of EPAC08, Genoa, Italy, 2008, pp. 3366–3368.

[35] **S. Schulz**, M. K. Bock, M. Bousonville, M. Felber, P. Gessler, T. Lamb, F. Ludwig, S. Ruzin, H. Schlarb, and B. Schmidt, *Progress and Status of the Laser-Based Synchronization System at FLASH*, Proceedings of DIPAC2011, Hamburg, Germany, 2011, pp. 383–385.

[36] **S. Schulz**, M. K. Bock, M. Felber, P. Gessler, K. E. Hacker, T. Lamb, F. Ludwig, H. Schlarb, B. Schmidt, and L.-G. Wissmann, *Performance of the FLASH Optical Synchronization System with a Commercial SESAM-Based Erbium Laser*, Proceedings of FEL2010, Malmö, Sweden, 2010, pp. 581–584.

[37] **S. Schulz**, M. Bousonville, M. K. Czwalinna, M. Felber, M. Heuer, T. Lamb, J. Müller, P. Peier, S. Ruzin, H. Schlarb, B. Steffen, C. Sydlo, F. Zummack, T. Kozak, P. Predki, and A. Kuhl, *Past, Present and Future Aspects of Laser-Based Synchronization at FLASH*, Proceedings of IBIC 2013, Oxford, UK, 2013, pp. 753–756.

[38] **S. Schulz**, M. K. Czwalinna, M. Felber, P. Prędki, S. Schefer, H. Schlarb, and U. Wegner, *Femtosecond-precision synchronization of the pump-probe optical laser for user experiments at FLASH*, Proceedings of SPIE 8778, Advances in X-ray Free-Electron Lasers II: Instrumentation, 2013, p. 87780R.

[39] **S. Schulz** and the LBSynch team, *Installation progress of the optical synchronization system at FLASH*, 48th ICFA Advanced Beam Dynamics Workshop on Future Light Sources, Menlo Park, CA, USA, 2010, talk, slides available at https://portal.slac.stanford.edu/sites/ad_public/events/FLS2010/Lists/WorkingGroup6/Public_View.aspx, summary available at http://fla.desy.de/localfsExplorer_read?currentPath=/afs/desy.de/group/fla/www/publications/2010/FLS2010/Summary_FLS2010_SebastianSchulz.pdf.

[40] C. Sydlo, M. K. Czwalinna, M. Felber, C. Gerth, S. Jabłoński, T. Lamb, H. Schlarb, **S. Schulz**, and F. Zummack, *Development Status of Optical Synchronization for the European XFEL*, Proceedings of IBIC 2013, Oxford, UK, 2013, pp. 135–138.

[41] L.-G. Wissmann, V. R. Arsov, M. K. Bock, M. Felber, P. Gessler, K. Hacker, F. Löhl, F. Ludwig, H. Schlarb, B. Schmidt, **S. Schulz**, S. Wesch, A. Winter, and J. Zemella, *Electro-Optic Electron Bunch Diagnostic at FLASH using an Ytterbium Fiber Laser*, Proceedings of FEL2009, Liverpool, UK, 2009, pp. 627–630.

[42] S. Wunderlich, M. C. Hoffmann, S. Schefer, B. Schmidt, **S. Schulz**, and S. Wesch, *Characterization of Single-cycle THz Pulses at the CTR Source at FLASH*, Proceedings of FEL2012, Nara, Japan, 2012, pp. 500–502.

[43] J. Zemella, V. R. Arsov, M. K. Bock, M. Felber, P. Gessler, K. E. Hacker, F. Löhl, F. Ludwig, H. Schlarb, B. Schmidt, **S. Schulz**, A. Winter, and L.-G. Wissmann, *RF-Based Detector for Measuring Fiber Length Changes with Sub-5 Femtosecond Long-Term Stability Over 50h*, Proceedings of FEL2009, Liverpool, UK, 2009, pp. 780–783.

[44] J. Zemella, V. R. Arsov, M. Felber, K. E. Hacker, F. Löhl, B. Lorbeer, F. Ludwig, K.-H. Matthiesen, H. Schlarb, B. Schmidt, **S. Schulz**, and A. Winter, *Drift-Free, Cost-Effective Detection Principle to Measure the Timing Overlap Between Two Optical Pulse Trains*, Proceedings of FEL08, Gyeongju, Korea, 2008, pp. 401–404.

[45] F. Zummack, M. K. Czwalinna, M. Felber, S. Jabłoński, T. Lamb, H. Schlarb, **S. Schulz**, and C. Sydlo, *Status of the Fiber Link Stabilization Units at FLASH*, Proceedings of IBIC 2013, Oxford, UK, 2013, pp. 139–142.

Acknowledgments

This thesis is the result of three and a half year work in the innovative and hard-working FLA group at DESY. It would not have been possible, and especially not in its coverage, without the support of many people to who this page is dedicated to.
First of all, I like to thank PD Dr. Bernhard Schmidt for the kind hosting in his group, providing me with a workspace, several laboratories and equipment, and for acting as referee for this thesis.
I am grateful to Prof. Dr. Markus Drescher and Dr. Jens Osterhoff for acting as second referees for this work and my defense.
For usually challenging questions and serious discussions, many thanks to Prof. Dr. Jörg Roßbach and Prof. Dr. Peter Schmüser.
Without the encouragement of Prof. Dr. Manfred Tonutti, who enabled me to visit DESY several times during my studies in Aachen, I probably would never have had the idea to write my thesis in Hamburg.
Prof. Dr. Shaukat Khan arranged a contract within the a BMBF project, so I'm grateful for the slightly higher earnings and additional travel expenses, which helped me come around in the past three years.
Very special thanks go to my supervisor, mentor and spiritus rector of the synchronization system at FLASH, Dr. Holger Schlarb. I highly appreciate that he taught me uncountable things in uncountable fields of knowledge on uncountable occasions.
I am also grateful to all colleagues who proof-read parts of this thesis, each time making it probably a little better.
Invaluable support came from our technical staff, especially Matthias Hoffmann, Albert Schleiermacher and Bernd Beyer, since they could provide me with every exotic cable or weird connector, and helped with the setup of several experiments.
And many thanks to Ingrid Nikodem, Ursula Djuanda and Iris Kerkhoff not only for helping me through the jungles of bureaucracy and the IT infrastructure.
To the complete FLASH team and controls group many thanks for their support and funny, yet always instructive day and night shifts, especially to Dr. Siegfried Schreiber for endorsing my setup and the measurements at the photoinjector laser.

Likewise many thanks to my numerous present and former colleagues, fellow diploma, master and PhD students at FLA and from many other groups at DESY and the accelerator physics group at the University of Hamburg. Everyone contributed something – being it a tempered debate, a cozy coffee or a breaking idea...

Naturally, I would also like to thank the many friends from Hamburg, Kölle, Berlin, Aachen and all around the world – in particular Larissa, for everything; and my family, especially Papa. ★

Glossary, Acronyms and Symbols

Within the topics covered in this thesis – accelerator physics, laser physics and technology, radio frequency basics and timing- and synchronization systems – a fairly large number of abbreviations evolved and is being routinely used in publications and the daily routine, as well as in the illustrations in this thesis. For reference, therefore, a list of the most common acronyms and symbols is provided.

Glossary

BAM (**bunch arrival time monitor**). Device to measure the arrival time of all electron bunches within a macro-pulse. Based on mixing a radio frequency signal generated in an antenna at the beam pipe when the electron bunches pass by with a laser pulse in an electro-optic amplitude modulator. The arrival time information is encoded in the depth of the modulation and can be retrieved with near real-time sampling schemes. 16, 41, 44, 70, 135, 143, 180, 215

EDFA (**erbium-doped fiber amplifier**). Usually a short piece of erbium-doped gain fiber, with pump light coupled in counter-propagating fashion through wavelength-division multiplexers, to boost the optical power of laser pulses in the fiber link stabilization unit, the free-space distribution unit of the bunch arrival time monitors. 44, 62, 131, 160, 212, 244, 260

EDFL (**erbium-doped fiber laser**). Laser oscillator constructed mainly as fiber-optic device, in particular with erbium-doped fiber as active material. Here passively mode-locked to generate laser pulses with 100 femtosecond duration at tens to hundreds of megahertz repetition rate to serve as master laser oscillator for the optical synchronization system. 4, 52, 63, 124, 153, 175, 223, 244, 253

FSD (**free-space distribution unit**). Optical setup to split the pulse train emitted by the master laser oscillator into 16 or more beams for the connection of the individual fiber link stabilization units. Based on the linear state of polarization, half-wave retarders and polarizing beam splitters. 62, 63, 109, 112, 126, 132, 174, 224, 254

LSU (**fiber link stabilization unit**). Optical setup for the active transit time-stabilization through an optical fiber, typically with the length of several hundreds of meters, based on optical cross-correlation of pulses traveled forth- and back the link and fresh ones. 223

machine Usually the term refers to the accelerator facility as a whole. 5

MLO (**master laser oscillator**). Usually a passively mode-locked laser oscillator emitting pulses with durations in the hundreds of femtoseconds range. The repetition rate, tens or hundreds of megahertz,

constitutes the timing information of the synchronization system. In literature also abbreviated OMO (optical master oscillator) and LMO (laser master oscillator). 2, 4, 53, 55, 61, 66, 108, 119, 131, 153, 167, 217, 220, 223, 251, 253

OXC (**optical cross-correlator**). Hardware implementation of a mathematical convolution, realized here as temporal overlap of ultra-short laser pulses in a nonlinear optical crystal for generation of a sum-frequency signal. 4, 70, 132, 219, 260

PTO (**pulse train oscillator**). Actively mode-locked laser oscillator, producing bursts of high-energy picosecond infrared pulses for subsequent amplification and frequency conversion to the ultraviolet for the photoemission process in the electron gun. 168, 179, 213, 260

Acronyms

c.c. complex conjugate. 51

AC alternating current. 80, 106
ACB advanced carrier board. 68, 226
ADC analog-to-digital converter. 127, 134, 155, 159, 162, 174, 177, 218
AOM acousto-optic modulator. 40, 168
ASE amplified spontaneous emission. 44, 149
ASTRA a space-charge tracking code. 14

BBF beam-based feedback. 70
BBO beta barium borate. 17, 50, 52, 155, 168, 192, 229, 236
BCM bunch compression monitor. 5, 17, 70
BiBO bismuth triborate. 230
BPF band-pass filter. 219
BPM beam position monitor. 15, 176

CAD computer-aided design. 255
CNC computer numerical control. 66
CsTe caesium telluride. 13, 183
CTR coherent transition radiation. 6, 15
cw continuous wave. 45, 72

DAC digital-to-analog converter. 89, 155, 159, 174, 177, 218, 247
DC direct current. 43, 80, 89, 106, 174, 210, 217
DCF dispersion compensating fiber. 29, 135, 174, 224, 239, 242, 257
DDD DOOCS data display. 91, 176, 228
DESY Deutsches Elektronen-Synchrotron. 1

DFG difference-frequency generation. 47, 52, 230
DOOCS distributed object-oriented control system. 90, 120, 134, 176, 247
DPSSL diode-pump solid state laser. 233, 237
DRO dielectric resonator oscillator. 90, 148
DSP digital signal processor. 89, 90, 99, 134, 155, 177
DUT device under test. 83
DWC down-converter. 3

EBPM large horizontal aperture beam position monitor. 227
eeo extraordinary-extraordinary-ordinary. 49, 233
EMI electromagnetic interference. 166, 218
EO electro-optic. 16
eoe extraordinary-ordinary-extraordinary. 49, 233, 235
EOM electro-optic modulator. 40, 143, 169, 218, 231
eoo extraordinary-ordinary-ordinary. 49, 233
EOS electro-optic sampling. 16
EOSD electro-optic spectral decoding. 17, 258
EOTD electro-optic temporal decoding. 17, 230
ErF erbium-doped gain fiber. 244

FB feedback. 228
FC/APC ferrule connector with angled physical contact. 211, 223, 239
FC/PC ferrule connector with physical contact. 239
FC/UPC ferrule connector with ultra-high quality polished physical contact. 239
FDB fiber distribution box. 123
FEL free-electron laser. 1, 5, 13
FFA fixed-field approximation. 52, 53
FFT fast Fourier transformation. 98
FLASH Free-Electron Laser in Hamburg. 1
FRM Faraday rotating mirror. 131, 153
FROG frequency-resolved optical gating. 58
FWHM full-width at half-maximum. 36, 58, 240

GTI Gires-Tournois interferometer. 39
GUI graphical user interface. 178
GVD group velocity dispersion. 27–29, 36, 45, 115, 151

HHG high-harmonic generation. 6, 9, 259
HR high-reflective. 133, 155, 156
HT high-transmittive. 155, 156
HV high-voltage. 173, 257

I/O input/output. 95
IIRF infinite impulse response filter. 92
ILC International Linear Collider. 15
IR infrared. 47, 95, 229

KDP monopotassium phosphate. 229
KLM KERR lens mode-locking. 36
KTP potassium titanyl phosphate. 231

LBO lithium triborate. 168, 192, 213, 231, 232
LCLS Linac Coherent Light Source. 1
LDD laser diode driver. 83, 211
LED light emitting diode. 98
LiIO lithium iodate. 233
linac linear accelerator. 1, 5
LLRF low-level radio frequency. 12, 70, 189
LNA low-noise amplifier. 80, 89, 174, 210
LO local oscillator. 90, 173, 213, 219, 258, 260

MFD mode field diameter. 241, 244
MgO magnesium oxide. 236
MO master RF oscillator. 2, 103, 108, 120, 157, 162, 169, 212, 216, 218
MOPA master oscillator power amplifier. 168
MPS machine protection system. 196
MS Milena S. 139
MTCA Micro Telecommunications Computing Architecture. 177

NA numerical aperture. 241, 244
NC normal-conducting. 13
NIR near infrared. 193, 234
NLSE nonlinear SCHRÖDINGER equation. 22, 26, 28
NPE nonlinear polarization evolution. 37, 254
NPR nonlinear polarization rotation. 37

ODL optical delay line. 132, 155
oee ordinary-extraordinary-extraordinary. 49, 233, 235
oeo ordinary-extraordinary-ordinary. 49, 233
ooe ordinary-ordinary-extraordinary. 49, 52, 54, 155, 233, 235
OPO optical parametric oscillation. 230, 231, 236
ORS optical replica synthesizer. 6
OSA optical spectrum analyzer. 95, 98
OTDR optical time-domain reflectometry. 223

PBC polarizing beam cube. 37, 94, 127, 132, 172, 254
PID proportional-integral-derivative. 90, 104, 134, 155, 165
PLC programmable logic controller. 95
PLL phase-locked loop. 43, 55, 89, 104, 120, 157, 209, 217
PMD polarization mode dispersion. 30, 241
PMF polarization maintaining fiber. 30, 143, 255
PMT photomultiplier tube. 155, 171, 173, 236, 260
PPKTP periodically poled potassium titanyl phosphate. 128, 132, 137, 231, 234, 257
PPLN periodically poled lithium niobate. 236
PS power supply. 99
PSI Paul Scherrer Institut. 95, 101
PSOF phase-stable optical fiber. 174, 212
PZT lead zirconia titanate. 134

QPM quasi phase-matching. 231, 236

RBV read back value. 177
RF radio frequency. 2, 13, 41, 42, 90, 134, 209, 227, 247, 251
RIN relative intensity noise. 42, 43, 80, 90, 105, 209, 212
rms root mean square. 43, 121, 140

SASE self-amplified spontaneous emission. 1, 5, 6, 9, 69
SESAM semiconductor saturable absorber mirror. 4, 38, 52, 63, 93, 254
SFG sum-frequency generation. 47, 52, 54, 155, 230, 236
sFLASH seeded-FLASH project. 9, 231
SHG second-harmonic generation. 47, 52, 54, 73, 133, 155, 168, 230, 231, 233, 236
SLAC Stanford Linear Accelerator Center. 1
SMF single mode fiber. 24, 29, 242
SNR signal-to-noise ratio. 91, 174, 236
SOP state of polarization. 16, 29, 95, 132
SP setpoint. 177, 195
SPIDER spectral phase interferometry for direct electric field reconstruction. 58
SPM self-phase modulation. 30, 37, 45, 144, 175
SSA signal source analyzer. 82, 102, 145, 163, 210
SVEA slowly varying envelope approximation. 22, 51

TBP time-bandwidth product. 36, 175
TDS transverse deflecting structure. 6, 15
TEM transverse electro-magnetic. 12, 23
TESLA teraelectronvolt energy superconducting linear accelerator. 5
THG third-harmonic generation. 48
Ti:S titanium-sapphire. 251

TIA transimpedance amplifier. 156
TOD third-order dispersion. 27
TPA two-photon absorption. 76, 120, 254
TTF TESLA test facility. 5

UV ultraviolet. 13, 47, 54, 179, 192, 229

VIS visible spectrum. 35
VM vector modulator. 103, 216
VME Versa Module Eurocard. 83, 89, 177, 211, 226
VS vector sum. 12, 189
VUV vacuum-ultraviolet. 5

WDM wavelength-division multiplexer. 44, 45, 241

XPM cross-phase modulation. 32, 37, 144
XUV extreme ultraviolet. 9

YDFL ytterbium-doped fiber laser. 17, 223
YLF yttrium lithium fluoride. 168, 237
YVO yttrium orthovanadate. 148, 237

Symbols

$A_{\mathbf{c}}^{\mathbf{int}}(\tau)$ first-order intensity autocorrelation. 58
$\beta(\omega)$ mode-propagation constant. 27
$B_{\mathbf{u}}$ undulator magnetic field. 7
$B_{\mathbf{xc}}(\tau, T)$ balanced cross-correlation. 57
D dispersion parameter. 136
$d_{\mathbf{eff}}$ effective nonlinearity of a crystal. 52, 232
Δn birefringence of a crystal; difference $n_{\mathrm{e}} - n_{\mathrm{o}}$. 48, 237
$\rho(\Theta)$ walk-off angle in a birefringent crystal. 48
$\delta t_{\mathbf{bunch}}$ electron bunch arrival time. 11, 14
η_{+} sum-frequency generation conversion efficiency. 52, 232
η_{-} difference-frequency generation conversion efficiency. 52
f_{39} acceleration frequency of the third-harmonic cavities, $3 \cdot f_{\mathrm{RF}}$. 11
$f_{\mathbf{bunch}}$ electron bunch repetition rate within macro-pulse. 192, 196, 197
f_c carrier frequency. 87, 152
f_{MLO} repetition rate of the optical reference oscillator. 66, 72, 87, 93, 120, 154, 157, 170, 208
$f_{\mathbf{rep}}$ repetition rate, usually pulse repetition rate of a mode-locked laser. 34
f_{RF} acceleration frequency of the superconducting cavities, 1.3 GHz. 11, 12, 14, 62, 66, 87, 151

f_{TiS} repetition rate of the Ti:sapphire oscillator. 151, 154, 157
G_{ACC1} weighting factor of acceleration module contribution to bunch arrival time. 14
G_{gun} weighting factor of electron gun contribution to bunch arrival time. 14
G_j weighting factor of contribution to bunch arrival time, $j \in$ (laser, gun, ACC1). 14
G_{laser} weighting factor of photoinjector laser contribution to bunch arrival time. 14, 190
K_{OXC} calibration constant of an optical cross-correlator. 129, 142, 160, 171, 176, 249
K_ϕ phase dependent calibration constant of a mixer output. 142
K_{u} undulator parameter. 8
L_{a} aperture length in a nonlinear optical crystal. 51
λ_{u} undulator period. 7
L_{D} dispersion length in optical fibers. 27
L_{dif} diffraction length in a nonlinear optical crystal. 51
L_{ds} dispersive spreading length in a nonlinear optical crystal. 51
L_{NL} nonlinear length in an optical fibers. 27
L_{nl} nonlinear length in a nonlinear optical crystal (attention: $L_{\mathrm{nl}} \neq L_{\mathrm{NL}}$). 51
$\ell_\varphi(f_i)$ single side-band phase noise. 42, 82, 102
L_{qs} quasi-static interaction length in a nonlinear optical crystal. 51
L_{u} undulator length. 7
$\ell_{\mathrm{V}}(f_i)$ voltage spectral density. 80, 107
N_{bunch} number of electron bunches in macro-pulse. 194, 196, 197
N^2_{DNL} scaling relation in fiber optics, $N^2_{\mathrm{DNL}} = L_{\mathrm{D}}/L_{\mathrm{NL}}$. 28, 31
n_e refractive index of the extraordinary beam. 48
$n^{\mathrm{e}}(\Theta)$ refractive index of the extraordinary beam as function of polar angle. 48
n_o refractive index of the ordinary beam. 48
φ_{gun} electron gun emission phase. 13, 183, 187, 190, 193, 195
φ_{laser} phase setpoint of EOM in photoinjector laser oscillator. 186, 191, 193
φ_{nom} nominal gun emission phase. 14, 183, 187, 190, 193, 195
φ_0 offset gun emission phase with $G_{\mathrm{gun}} \simeq 0$. 14, 190, 193, 195
P_{peak} optical peak power; for a soliton pulse holds $P_{\mathrm{peak}} = 0.88 \cdot E_{\mathrm{pulse}}/\tau_{\mathrm{p}}$. 27, 52, 77, 116, 232
R_{56} linear dispersion parameter of a magnetic chicane. 11
$R(z)$ curvature of phase fronts of a Gaussian beam. 23
$S_{\mathrm{xc}}(\tau, T)$ delay/subtraction cross-correlation. 56
τ_{ac} FWHM of an intensity- or the envelope of an interferometric autocorrelation. 58
τ_{EDFL} FWHM duration of the erbium-doped fiber master laser oscillator pulses. 175
τ_{FWHM} full-width at half-maximum duration of an optical pulse. 36
τ_{p} physical pulse duration dependent on pulse shape. 27, 29, 51, 179
τ_{PTO} FWHM duration of the photoinjector laser oscillator. 179
τ_{TiS} FWHM pulse duration of a Ti:sapphire laser system. 151
Θ_{pm} phase-matching angle in a nonlinear optical crystal. 50
T_{rep} pulse repetition period. 34

v_{gr} group velocity. 26, 27
w_0 waist of a GAUSSian beam. 23, 52
$w(z)$ radius of a GAUSSian beam. 23
$X_{\mathrm{c}}(\tau)$ first-order intensity cross-correlation. 55
z_{R} RAYLEIGH length. 23

Index